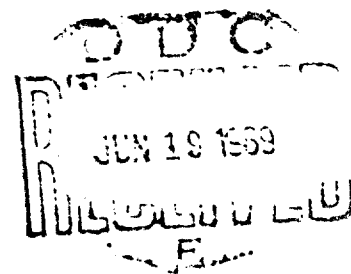Bulletin 39
Part 4
(of 6 Parts)

AD688788

THE
SHOCK AND VIBRATION
BULLETIN

APRIL 1969

A Publication of
THE SHOCK AND VIBRATION
INFORMATION CENTER
Naval Research Laboratory, Washington, D.C.

DDC
JUN 19 1969
E

Office of
The Director of Defense
Research and Engineering
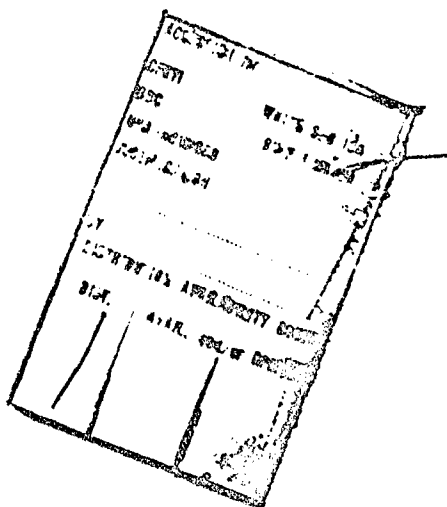
SYMPOSIUM MANAGEMENT

THE SHOCK AND VIBRATION INFORMATION CENTER

William W. Mutch, Director
Henry C. Pusey, Coordinator
Rudolph H. Volin, Coordinator
Katherine G. Jahnel, Administrative Secretary

Bulletin Production

Graphic Arts Branch, Technical Information Division,
Naval Research Laboratory

Bulletin 39
Part 4
(of 6 Parts)

THE
SHOCK AND VIBRATION
BULLETIN

APRIL 1969

A Publication of
THE SHOCK AND VIBRATION
INFORMATION CENTER
Naval Research Laboratory, Washington, D.C.

The 39th Symposium on Shock and Vibration was held in Pacific Grove, California, on 22-24 October 1968. The U.S. Army was host.

Office of
The Director of Defense
Research and Engineering

CONTENTS

PART 4

Damping

*This paper not presented at Symposium.

Isolation

PAPERS APPEARING IN PART 1

Part 1 - Classified
(Unclassified Titles)

---

*This paper not presented at Symposium.

*This paper not presented at Symposium.

v

---

*This paper not presented at Symposium.

---

*This paper not presented at Symposium.

*This paper not presented at Symposium.

*DESIGN AND VIBRATION ANALYSIS OF A NAVAL SHIP PROPULSION SYSTEM WITH A DIGITAL COMPUTER
   Stephen T. W. Liang, Naval Ship Research and Development Center, Washington, D.C.

---

*This paper not presented at Symposium.

DAMPING

APPLICATION OF A SINGLE-PARTICLE IMPACT*
DAMPER TO AN ANTENNA STRUCTURE

R. D. Rocke
Hughes Aircraft Company
Fullerton, California

S. F. Masri
University of Southern California

A study is made of the application of a single-particle impact damper to a high-
ly resonant radar antenna structure. A prototype damper unit was tested with a
smaller structure, which was designed to dynamically simulate the fundamental
mode of the antenna, to verify the damper design and response characteristics.
The correlation of empirical testing and theoretical analysis is emphasized. Re-
sults show that the first mode maximum amplitude of a 1200 pound cantilever type
structure can be reduced by a factor of 80 to 90 percent with the addition of 27
pound damper particle. Variations in governing parameters are shown to indicate
the range of performance characteristics obtainable. The noise level which ac-
companies an impact device of this type is also discussed.

NOMENCLATURE

A = Amplification factor of damped structure

A_s = Amplification factor of primary system in the absence of the impact damper

c = damping constant

d = clearance in which the particle is free to oscillate

e = coefficient of restitution

k = spring constant

M = mass of primary system

m = mass of particle

r = frequency ratio, Ω/ω

t = time

x = displacement of M, double amplitude

$\tilde{x}$ = base displacement, double amplitude

y = relative displacement of particle with respect to M

ζ = ratio of critical damping

μ = mass ratio, m/M

ω = natural frequency, $\sqrt{k/M}$

Ω = forcing frequency

$\dot{x}$ = velocity of M

$\dot{y}$ = relative velocity of particle

INTRODUCTION

The concept of reducing the vibration am-
plitudes of a mechanical system by attaching
to it a container in which a solid particle is
constrained to oscillate is not a new one. Anal-
ytical studies of the steady-state response of
the impact damper to sinusoidal excitations
have been made by Lieber and Jensen [1],
G-ubin [2], Arnold [3] Warburton [4], and
Masri and Caughey [5]. In addition, the feas-
ibility of using impact damping to reduce the
vibration of diverse systems as ships hulls,

*This paper not presented at Symposium.

cantilever beams, single-degree-of-freedom systems, turbine buckets, and tall flexible structures have been investigated empirically by McGoldrick [6], Lieber and Tripp[7], Sankey[8], Duckwald [9], and Reed [10], respectively.

Recently, an existing radar antenna (see Fig. 1) which had previously been qualified to

The antenna unit as shown in Fig. 1 weighs approximately 3100 pounds and the design modification was anticipated to be additional 800 pounds located on the upper part of the structure. Previous sinusoidal vibration qualification tests indicated a fundamental structural resonance at 13 Hz with the bearing (X roller type) at the array-pedestal interface being the predominant spring and the array structure itself oscillating as a rigid body. The mode shapes varied slightly according to the direction of the base input, as would be expected. In general, strong coupling existing among all three orthogonal directions for the first mode regardless of the input direction. For a base input in the X direction, the array structure responded with Point A (see Fig. 2) moving in an

FIG. 1

FIG. 2

MIL-E-16400 for shock and vibration, was changed substantially and scheduled to be retested to verify its structural capability. Because this design change incorporated a large increase in mass, but essentially no increase in strength, great concern was expressed as to the antenna's capability of sustaining a vibration endurance test at resonance. To minimize the cost and time required to perform a substantial structural redesign and refurbishment, the development of a separate single-particle impact damper package was undertaken. Previous work by the above-referenced investigators has shown the desirability of such an application. However, few actual applications are reported in the literature, i.e., other than laboratory models, and the physical size of the particle in this case was quite large. Therefore, a prototype model was constructed and tested on a resonant structure to verify the theoretical predictions and investigate design problems.

elliptical path with the larger component of response being in the X direction. With a Y direction input the major portion of the response was in the Y direction with the wings moving primarily vertically and with a 180° phase difference between them. A vertical base excitation produced a fundamental displacement mode similar to that resulting from the Y directional input.

The application of the impact damper was to reduce both the X and Y response components of the fundamental mode, regardless of the input direction, by aligning two impact damper units with the X and Y directions, respectively, at the top center portion of the structure, Point A. Maximum amplification factors (response at Point A/base input) were between

2.

16 and 20 during the structural vibration quali-
fication tests. The design goal set for the im-
pact dampers was to reduce these maximum am-
plification factors by a factor of two. Because
the antenna structure was not available for any
developmental testing, a prototype damper unit
was tested on a simulation structure to verify
the performance characteristics, see Fig. 5.

THEORETICAL CONSIDERATIONS

With the reasonable assumptions that (a)
the auxiliary mass in an impact damper moves
frictionlessly in its container and (b) the col-
lision between the particle and the primary sys-
tem is idealized to be a discontinuous process
in which the displacements of the two masses
remain stationary while their velocities change
discontinuously in accordance with the momen-
tum equation, the motion of the highly nonlinear
two-degree-of-freedom system can be treated
as a piece-wise linear process. If it is further
assumed that in steady-state motion two sym-
metric impacts occur per cycle of the sinusoi-
dal excitation at equal time increments and at
opposite sides of the container, then an exact
steady-state solution can be obtained [5]. More-
over, this type of motion has been shown [11]
to be predominant in experimental studies.

Under the stated assumptions, the motion
of the primary system (see Fig. 3) between
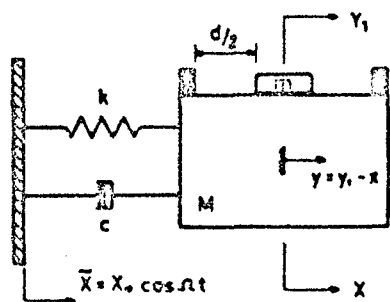
FIG. 3

impacts is given by an expression of the form
[4, 5]:

$$x = e^{-\xi \omega t} (a \sin \eta \omega t + \cos \eta \omega t) \\ + A_0 \, \tilde{x} \sin (\Omega + \tau) \quad (1)$$

where the origin of the time axis t coincides with
the occurrence of any given impact and constants
a, b, and τ are functions of the parameters of the
system and are given in Ref. [5].

The construction of a solution corresponding
to the motion of a typical system is illustrated
in Fig. 4.
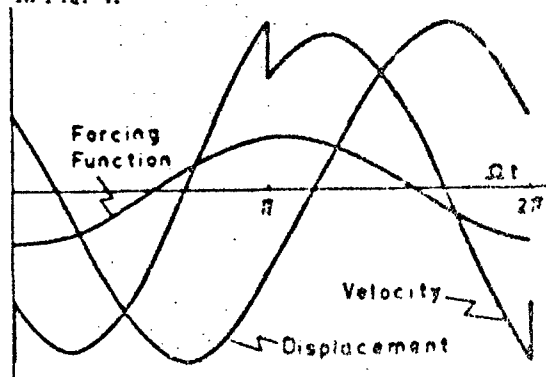
FIG 4

Whenever steady-state motion is possible, the
theory furnishes two possible solutions. To
determine which of the two possible solutions
is stable, if any, a stability analysis of the
solution must be performed. Masri and
Caughey [5] have shown that asympototic sta-
bility of the motion depends upon the modulus
of the eigenvalues of a matrix which relates to
the conditions of the system after two consecu-
tive impacts. If the modulus of each of the
eigenvalues of this conditional matrix is less
than one, the system's motion will be stable;
otherwise, steady-state motion with two sym-
metric impacts per cycle is not possible.

The theoretical solutions used in the fol-
lowing section for comparison with experimen-
tal results were obtained using the theory as
described above and identical to that found in
refs. [5, 11] with a base excitation replacing
the force excitation.

EXPERIMENTAL RESULTS

Experiments with a prototype damper model
were conducted on a resonant structure simu-
lating the antenna to gain some knowledge about
the correlation of theoretical and empirical re-
sults and the design problems to be encountered
in building and employing the actual unit during
qualification testing. Figure 5 shows the dam-
per unit mounted on the test structure. The
cantilever type test structure was designed
with a first mode natural frequency of 11.4 Hz

3

which matched that predicted for the modified antenna structure. The active weight of the structure, i.e., 33/140 of the vertical member's weight plus the weight of the top horizontal member, was 950 pounds. Provision was
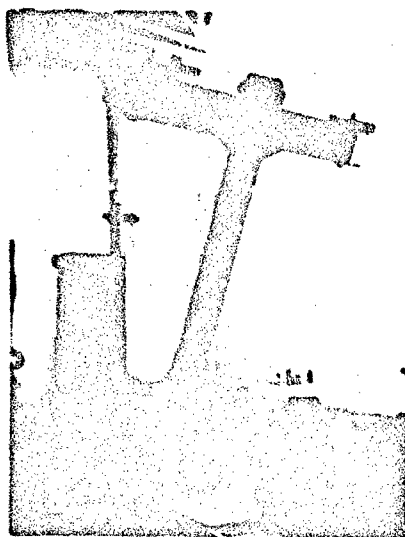
FIG. 5

made for controlling the coupling motion at the top center point of the structure by changing the balance between the weights at the ends of the top horizontal member. However, only unilateral motion in the fore and aft direction with a single damper unit was used during the study. The structural damping of the primary test structure, alone, was found to be about 0.57 percent by measuring the maximum amplification factor obtainable with small sinusoidal base input excitations.

Figure 6 shows the two damper particles used in conjunction with a steel cylindrical container. Three particle weights (56, 40, and 27 pounds) were used to obtain performance characteristics for mass ratios of 5.9, 4.2, and 2.85 percent, respectively. The majority of the work was done with the 27 pound slug, however, as it closely approximated the design goal for the antenna damper unit. To provide variation in the coefficient of restitution, the cylindrical damper particles were used with or without bonded rubber pads on the end surfaces. Shim plates (see Fig. 6) were used between the container body and the end plates to vary the clearance, d.
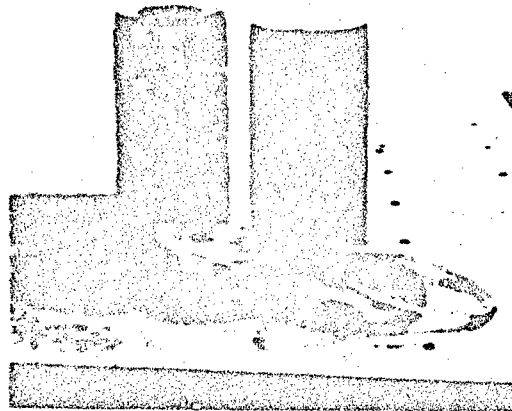
FIG. 6

The main performance characteristics sought during testing were the amplitude attenuation obtainable at the structure's resonant frequency, the region of stable two impacts/cycle motion, amplitude response as a function of frequency over a ± 10% frequency bandwidth about the structures resonance, and a quantitative measurement of the maximum noise level during operation.

The coefficient of restitution was not physically measured for a typical impact as the required [11] integrating electronics were not readily available. However, the experimental amplitude attenuation results were compared to those analytically obtained for various coefficients of restitution values. Figure 7 shows the experimental results obtained at a frequency ratio of one with and without the rubber bonded pads on the particle end surfaces as compared to the predicted values representative of e = 0.5 and e = 0.2, respectively. Of the various analytical curves used, these two for the specific coefficients given most closely matched the experimental results. Figure 8 shows how well the analytical predictions for these two coefficients are matched by the experimental results over a frequency range. Figure 7 and 8 depict the results for a mass ratio of 2.84%, i.e., the 27 pound slug. Note that the solid points in these figures represent stable two symmetric impact per cycle motion and the other points the unstable motion.

Figures 9 and 10 indicate the comparison of the frequency response characteristics for

4

Solid points indicate
stable motion

ε = 0.0057

r = 1.0

μ = 0.0284

.24
.22
.20
.18
.16
.14
.12
.10
.08

$|A|/|A_s|$

ε = 0.2

ε = 0.5

△ Steel slug

○ Rubber pads on slug

20   25   30   35   40

$d/\tilde{x}$

FIG. 7

μ = 0.0284

$d/\tilde{x}$ = 33

ε = 0.0057

△ Steel slug alone
○ Rubber pads on
    slug

Solid points indicate
stable motion

40
35
30
25
20
15
10
5
0

$|A|$

ε = 0.5

ε = 0.2

ε = 0.5

.92   .94   .96   .98   1.0   1.02   1.04   1.06

FREQUENCY RATIO — Ω/ω

FIG. 8

5

FIG. 9

FIG. 10

6
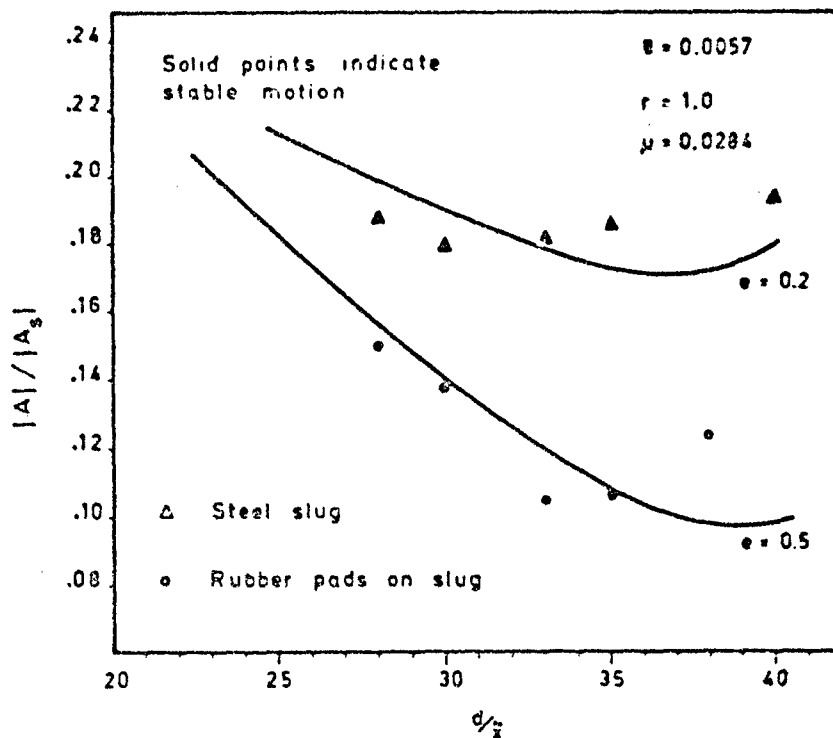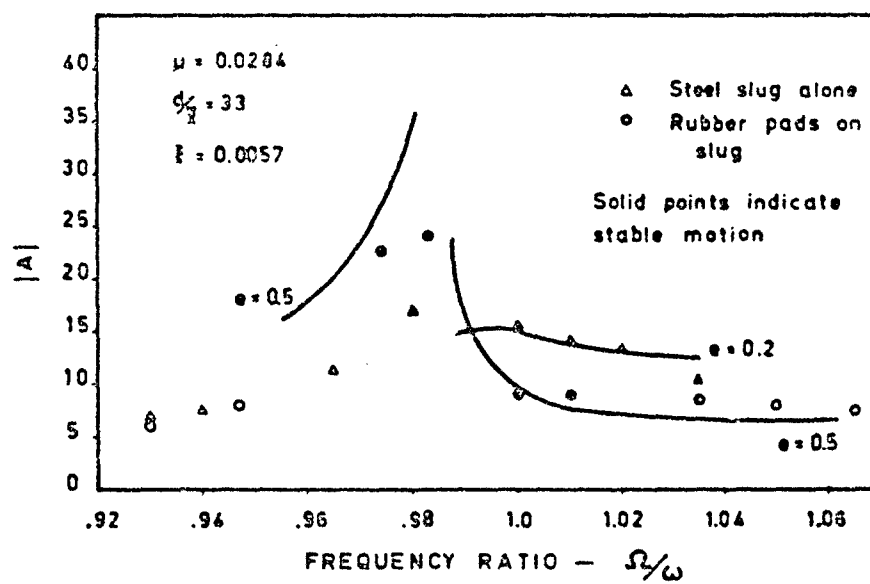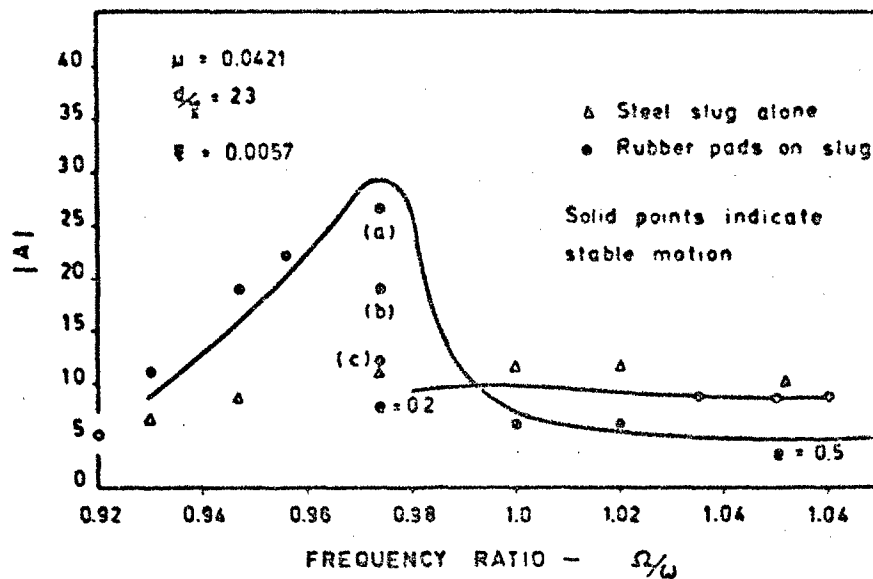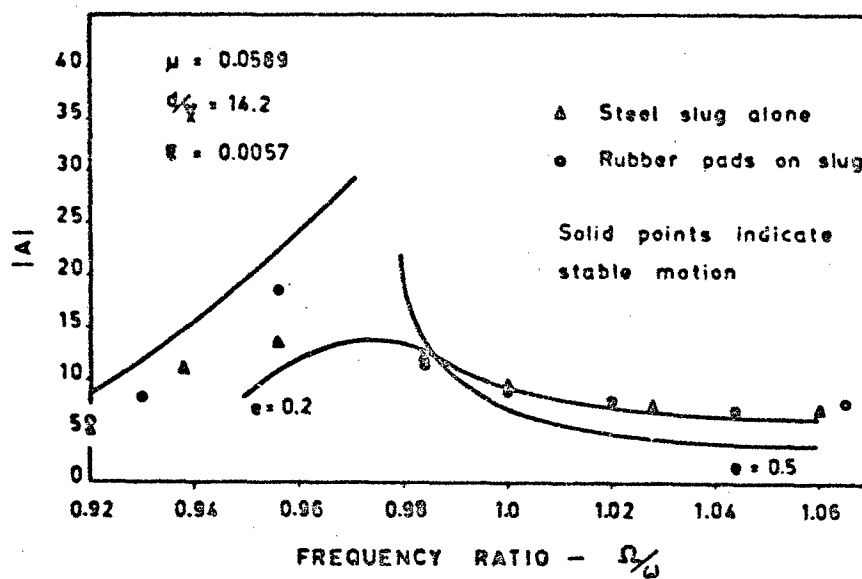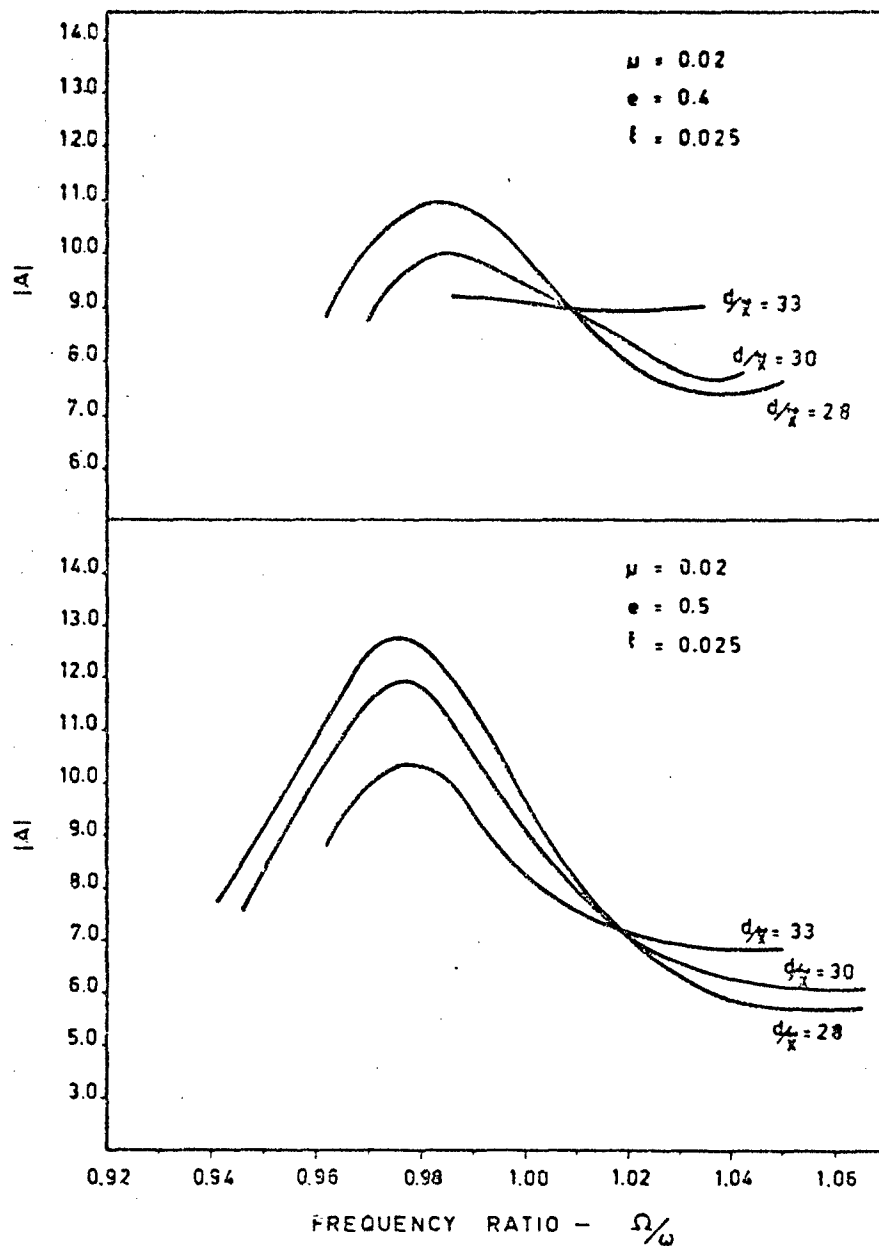
FIG. 11

the 40 and 56 pound particles. It can be seen in Fig. 10 that with the 56 pound slug the results are nearly independent of whether or not the rubber pads were used. The probable reason for this behavior is the fact that the 56 pound slug had a solid rubber pad bonded over the entire end surface, whereas the 27 and 40 pound slugs used rubber pads in the shape of annular rings, see Fig. 6. Because Possion's ratio for rubber is approximately 0.5, rubber is essentially incompressible; thus, it cannot be deflected in compression unless it is permitted to expand laterally. Therefore, with the entire end surface covered with rubber, one could expect the impact characteristics to be nearly the same as those for no rubber. Moreover, in the other two cases, the rubber annular ring allows substantial edge bulging upon compression. Because rubber is not a large energy dissipater in compression and tension, this condition provides better impact conditions and provides a higher coefficient of restitution. It is interesting to note, therefore, that the thickness and shape of the rubber pad can be utilized to obtain a variation in the coefficient of restitution.

To determine whether the performance characteristics were invariant under changes of d and $\tilde{x}$ which gave constant $d/\tilde{x}$ ratios, different clearance and excitation inputs were used. Most of the points plotted in Figs. 7 through 10 represent average responses obtained for any given $d/\tilde{x}$ ratio by using three different d and $\tilde{x}$ values which together provide the same ratio. In general, these variations resulted in slightly different response measurements with no noticeable consistent trend for specific changes. The difference in these response values in most cases was less than 15%. Figure 9 shows one particular case, however, which gave a large difference in results. For this case, a $d/\tilde{x}$ ratio of 23 was investigated using clearance values of .75, 1.0, and 1.25 inches for points (as shown) a, b, and c, respectively. Note that this occurred at a frequency ratio corresponding to the point of maximum amplification while the same three values gave equal results at a frequency ratio of one. The difference in response values was always the largest in this frequency region where the amplitude of response peaks.

The behavior of the impact damper, in general, followed that depicted in the figures. The behavior for the larger coefficients of restitution under steady-state sinusoidal excitation shows an increase in the amplification factor at a frequency ratio less than one and a decrease in level near one. To obtain more nearly optimum system response characteristics over the frequency band which includes

the primary structure's resonance, a lower coefficient of restitution is required as evidenced by the figures. This process also decreases the region, i.e., the frequency band, over which the stable two impact/cycle motion exists. In general, a broadband of stable two impact/cycle motion is not required, however, as the damper is still very effective under what is mathematically termed unstable behavior. In fact, the amplitude in the unstable region is never larger than that which would occur without the impact damper.

Based upon the general agreement of the experimental and theoretical results for the test structure and prototype damper, the basic damper parameters can be chosen for application to the antenna structure. Figure 11 shows the predicted response characteristics for the antenna based upon its inherent critical damping ratio of 2.5% and a mass ratio of 2%. These curves represent the response of stable two impact/cycle motion.

Examination of the curves in Fig. 11 indicates that the most optimum solution is that of $d/\tilde{x} = 33$ with a coefficient of restitution equal to 0.4. These parameters provide a response curve that is almost constant with frequency and equal to an amplification factor of 9 which would decrease the structure's response from that found previously by about two.

The noise level surrounding the structure during testing was measured to be about 102 dB at a ten foot radius from the unit on a General Radio broadband noise meter. The noise level was also several dB lower when using the rubber pads as compared to bare steel. Several attempts were made to lower the noise level. One approach used was to enclose the damper unit in an acoustic box which when completely sealed attenuated a 100 dB enclosed speaker source to 68 dB. This same box was modified to enclose the unit with only eight one-inch diameter studs extending through its base for mounting the damper to the beam structure. The noise level was lowered only 5 dB through this approach. Use of lead sheet and foam shrouds around the unit also provided small attenuations in noise level. From the experiments conducted it becomes obvious that the majority of the impact energy is propagated though the damper attachments to the support structure and radiated from this larger surface area. It is apparent that any application of the impact damper at low noise level must provide good attenuation in the damper attachment without deteriorating the over-all coefficient of restitution. Recent experiments with multiple particles replacing a single particle

8

have also shown significant reduction in the noise level.

CONCLUSIONS

1. In general, the experimental results obtained with the lightly damped test structure and the impact damper particles compared favorably with those response characteristics analytically defined. The analytical solution usually predicted larger amplitudes than those found empirically for frequency ratios less than one.

2. The frequency range predicted analytically for stable two impact per cycle damper motion was always larger than that determined experimentally. However, the responses termed unstable were still very effective and did not limit the parameter selection for nearly optimum damping.

3. The results indicated an 80% amplitude attenuation of the test structure by a damper whose mass ratio was 2.84%. A coefficient of restitution of 0.2 provided the best response attenuation over a frequency band of $\pm 10\%$ about the structures natural frequency. Larger attenuations can be achieved at resonance only, i.e., at frequency ratio of one, with higher coefficients of restitution.

4. Rubber pads bonded to the cylindrical damper particles end surfaces provide means of varying the coefficient of restitution of impact. Variation of this coefficient shown in the experiments was 0.2 to 0.5

5. Predictions based upon the work herein indicate that an application of a damper unit to the radar antenna structure described will fulfill the design objectives. A unit giving a mass ratio of 2% with a coefficient of restitution of 0.4 and designed for a $d/\bar{x}$ ratio of 33 is shown to limit the response amplitude for a primary system with the characteristics of the antenna structure to a value of 9.17 (see Fig. 11).

6. The broadband noise level surrounding the damper during operation was about 102 dB at a 10 foot radius with essentially no directionality indicated. Attempts to lower these acoustic levels by enclosing the unit indicate future applications of large impact dampers must provide attenuating damper attachments.

ACKNOWLEDGMENT

REFERENCES

1. Lieber, P., and Jensen, D. P., "An Acceleration Damper: Development, Design, and Some Applications," Trans. ASME, Vol. 67 (1945), pp. 523-530.

2. Grubin, C., "On the Theory of the Acceleration Damper," Journal of Applied Mechanics, Vol. 78 (1956), pp. 373-378.

3. Arnold, R.N., "Response of an Impact Vibration Absorber to Forced Vibration," Ninth International Congress of Applied Mechanics (1956).

4. Warburton, G.B., Discussion of "On the Theory of the Acceleration Damper," Journal of Applied Mechanics, Vol. 24, Trans. ASME Vol. 79 (1957), pp. 322-324.

5. Masri, S.F., and Caughey, T.K., "On the Stability of the Impact Damper," Journal of Applied Mechanics, Vol. 33, Trans. ASME, Vol. 88 (1966), pp. 586-592.

6. McGoldrick, R.T., "Experiments with an Impact Vibration Damper," David Taylor Model Basin Report No. 816.

7. Lieber, P., and Tripp, F., "Experimental Results on the Acceleration Damper," Rensselaer Polytechnic Institute Aeronautical Laboratory, Report No. TR AE 5401 (1954). See also reference list of above report.

8. Sankey, G.O., "Some Experiments on a Particle or 'Shot' Damper," Memorandum, Westinghouse Research Labs (1954).

9. Duckwald, C.S., "Impact Damping for Turbine Buckets," General Engineering Laboratory, General Electric, Report No. R55GL108 (1955).

10. Reed, Wilmer H., "Hanging-Chain Impact Dampers: A simple Method for Damping Tall Flexible Structures," presented at the International Research Seminar: Wind Effects on Buildings and Structures, Ottawa, Canada, Sept. 11-15, 1967.

11. Masri, S., "Electric-Analog Studies of Impact Dampers," Experimental Mechanics, Feb. 1967.

12. Timoshenko, S., and Young, D. H., <u>Vibration Problems in Engineering</u>, D. Van Nostrand Company, Inc., Princeton, N. J., Third Edition (1955), pp. 91.

A PROPOSED EXPERIMENTAL METHOD FOR

ACCURATE MEASUREMENTS OF THE DYNAMIC PROPERTIES

OF VISCOELASTIC MATERIALS

Kenneth G. McConnell
Associate Professor of Engineering Mechanic.
Iowa State University
Ames, Iowa
(Currently on leave at NSRDC)

The concepts behind a test method for quickly determining the properties of viscoelastic materials over a broad range of frequencies is developed. A single-degree-of-freedom model consisting of the viscoelastic test materials and a mass subjected to a sinusoidal excitation force is examined for the best physical test condition for accurately measuring the material properties. It was found that resonance was the desired condition since a ninety-degree phase shift always occurs regardless of the amount of damping present. The concept of using a combined force-acceleration feedback on the vibration shaker was added so that any desired resonant frequency could be obtained by electronically changing the mass of the original system.

The resulting test system gives the necessary flexibility to quickly test for the material properties without heat build-up while the same system can also be used to determine the change in properties due to heat build-up. Only four readily available quantities are needed for each test in order to compute the material properties.

The error analysis shows that under the most severe conditions, an error in measuring the phase angle of 0.50 degrees results in a maximum error in the material properties of less than 1.0 per cent, due to the test technique. This error drops to about 0.2 per cent when the phase angle is measured to within 0.10 degrees. The proposed test method appears to have a great degree of flexibility; the limits of which need to be determined in the laboratory.

INTRODUCTION

Several methods have been used to measure the complex stiffness of viscoelastic materials when subjected to an environment of sinusoidal oscillations. Each method appears to be limited by either the useable frequency range or the material properties. For example, the Brüel and Kjaer [1] cantilever beam technique requires relatively stiff materials to be effective while the Fitzgerald technique is limited to low frequencies.

A recent tuned damper technique [2] was used which gave results comparable with the Brüel and Kjaer method. However, the tuned damper method has certain inherent disadvantages such as requiring the acquisition of sufficient data to define a resonant peak during which the specimen properties can change due to heating as well as the inability to be used with highly damped materials where the resonant peak is not well defined due to the flatness of the response curve.

The proposed method uses the force-acceleration feedback concept to control the input forces and accelerations to the test specimen thereby simulating any desired mass to produce any desired test frequency within the capability of the equipment. A ninety-degree phase shift is used to accurately determine resonance of the test specimen.

The advantages of using this proposed technique are: (a) the test data can be obtained quickly since only four observations are needed to calculate the material properties,

11

(b) the test frequency can be easily changed by changing the input frequency, (c) the properties of highly damped materials can be measured, (d) the amplitude of motion can be easily adjusted, and finally, (e) an independent check on material properties can be obtained by recording damped oscillation data. The major disadvantage of this proposed test system is the large amount of test equipment required. This paper is devoted to developing the concepts behind the proposed test method which follows directly from a modification of the tuned damper technique [2].

ANALYSIS

The analysis is divided into two parts. First, the basic response of a single-degree-of freedom system with a viscoelastic spring material subjected to a sinusoidal force excitation will be studied. Second, the servo-shaker system will be formulated which gives many test advantages over previous methods.

RESPONSE OF BASIC TEST SYSTEM - A schematic of the proposed test method is shown in Fig. 1(a) where the material specimen is bonded to

where F_0 is the magnitude of the excitation force, $j = \sqrt{-1}$, ω is the excitation frequency, and t is time. The specimen is of length l and cross-sectional area S. An equivalent single-degree-of-freedom system is shown in Fig. 1(b).

For purposes of analysis, the stress strain relationship for the viscoelastic material is assumed to be

$$\sigma = E(1 + j\eta)\epsilon \qquad (2)$$

where σ is the normal stress, E the modulus of elasticity, η the loss factor of the viscoelastic material, and ϵ the longitudinal strain. Thus, the axial force developed in the test material is given by

$$F_a = \sigma S = \frac{ES}{l}(1 + j\eta)\,x \qquad (3)$$

where x is the displacement of the mass m. From Eq. (3), it is easily seen that the spring constant k and the damping coefficient c are given by

VISCOELASTIC TEST SPECIMEN →

IMPEDENCE HEAD →
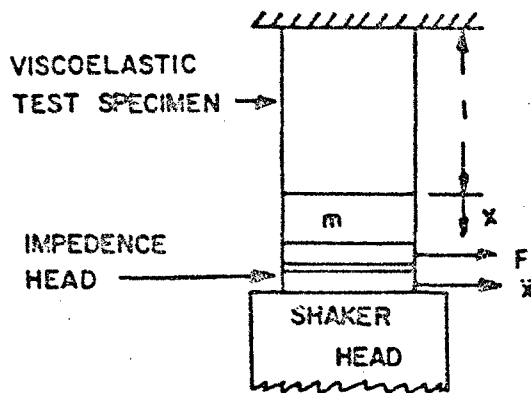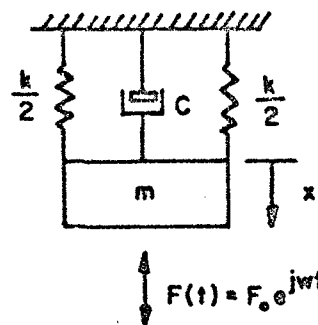
I(a)-ORIGINAL SYSTEM

I(b)-EQUIVALENT SINGLE-DEGREE-OF-FREEDOM OF ORIGINAL SYSTEM

Figure 1 - Schematic of proprosed test system

the rigid foundation A-A and is subjected to a sinusoidal force input of

$$F(t) = F_0\, e^{j\omega t} \qquad (1)$$

$$k = \frac{ES}{l} \qquad (4a)$$

$$c = \frac{k\eta}{\omega} \qquad (4b)$$

The differential equation of motion governing the system shown in Fig. 1(b) becomes

$$m\ddot{x} + \frac{ES\eta}{l\omega}\dot{x} + \frac{ES}{l}x = F_0 e^{j\omega t} \qquad (5)$$

which has the well known steady state solution of

$$x = \frac{\frac{F_0 l}{ES}}{\sqrt{(1-r^2)^2 + \eta^2}} e^{j(\omega t - \phi)} \qquad (6)$$

where

$$\tan\phi = \frac{\eta}{1-r^2} \qquad (7)$$

and

$$r^2 = \frac{ml\omega^2}{ES} \qquad (8)$$

From Eq. 7, it is seen that when r = 1.0 the phase shift between the excitation force F(t) and the responding motion x is ninety-degrees regardless of the damping present and from Eq. 6 that the amplitude of motion A becomes

$$A = \frac{F_0 l}{ES\eta} \qquad (9)$$

Equation 9 contains both material properties of E and η. A second independent equation can be obtained from Eq. 8 for r = 1.0 which gives

$$E = \frac{ml\omega^2}{S} \qquad (10)$$

from which the modulus of elasticity E is obtained directly from knowing the mass m, the the specimen length l and area S, and the resonant frequency ω (since r = 1, ω = ω_n). Substitution of Eq. 10 into Eq. 9 gives

$$\eta = \frac{F_0}{Am\omega^2} \qquad (11)$$

from which the loss factor η can be obtained by direct measurement of the quantities F_0, A, m, and ω.

The key to being able to use the simple and direct measurements of the various external quantities m, l, S, F_0, A, and ω in order to determine the material properties E and η from Eqs. 10 and 11 is the ninety-degree phase shift at the resonant condition so that r is unity. This phase-shift measurement can be done accurately by modern electronic instruments when the phase angle is in the range of ninety-degrees. Since this is the case, it would be desirable to develop means to easily change

the mass of the system. This means is available by employing some of the ideas of Otts [3] on force-controlled vibration testing.

THE SERVO-SHAKER SYSTEM – A servo controlled shaker system as shown in Fig. 2 is analyzed in this section in order to see how the mass of the system; and hence, the test frequency can be changed by employing electronic means rather than physically changing the mass m.

The basic scheme is to feedback a combination of the force transmitted (F) to the mass m by the shaker head and the responding acceleration (ẍ) of the mass. The voltage E_f represents the feedback signal and is substracted from the excitation voltage E(t) which is related to the excitation force F_0 by

$$E(t) = G_f S_f F_0 e^{j\omega t} = E_0 e^{j\omega t} \qquad (12)$$

where G_f is the gain on the force feedback signal and S_f is the sensitivity of the force transducer between the shaker head and the mass m. The resulting error signal (E_e) is the input to the power amplifier and shaker which is represented by the transfer function G(s). The force exerted by the shaker on mass m through the force transducer is given by

$$F = G(s)[E(t) - E_f] \qquad (13)$$

which is reduced by the specimen force (F_a see Eq. 3) acting on the mass m (the dashed feedback). The net force (F_n) produces an acceleration (ẍ) which generates the feedback signal

$$e_x = G_x S_x \ddot{x} \qquad (14)$$

where G_x is the acceleration feedback gain and S_x is the sensitivity of the accelerometer. Finally, the feedback signal voltage is seen to be

$$E_f = e_x + e_f = G_x S_x \ddot{x} + G_f S_f F \qquad (15)$$

The force transmitted to mass m through the force transducer can be obtained from Eq. 13 with Eqs. 12 and 15 substituted to obtain

$$F = G(s)[G_f S_f F_0 e^{j\omega t} - G_f S_f F - G_x S_x \ddot{x}] \qquad (16)$$

13

POWER AMPLIFIER AND SHAKER TRANSFER FUNCTION

EXCITATION

$$E(t) = E_0 e^{j\omega t}$$
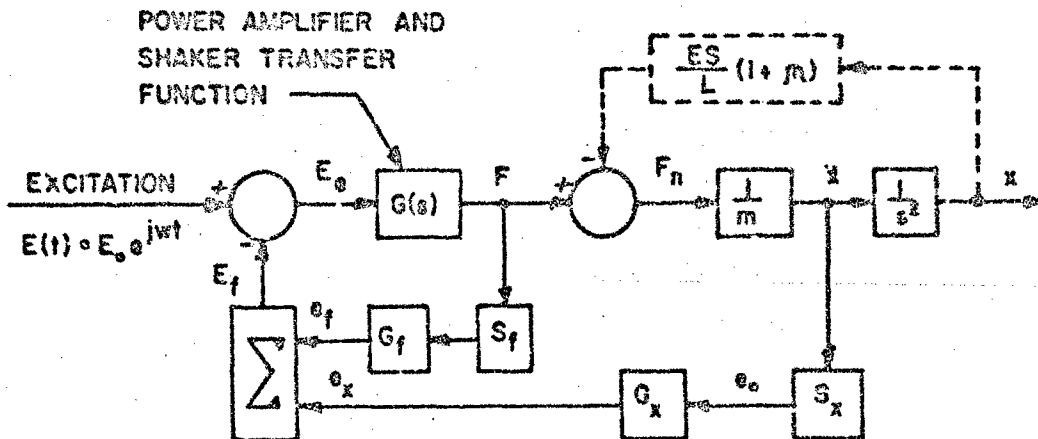
Figure 2 - Block diagram of servo controlled test system

from which

$$F = \left[\frac{G(s)\, G_f\, S_f}{1 + G(s)\, G_f\, S_f} \right] \qquad (17)$$

$$\left[F_0 e^{j\omega t} - \frac{G_x\, S_x}{G_f\, S_f} \ddot{x} \right]$$

Equation 17 reduces to

$$F = [F_c e^{j\omega t} - K G_x \ddot{x}] \qquad (18)$$

where

$$K = \frac{S_x}{G_f S_f} \qquad (19)$$

If it is assumed that the transfer function

$$\frac{G(s)\, G_f\, S_f}{1 + G(s)\, G_f\, S_f} = 1.0 + 0j \qquad (20)$$

for the frequency range of interest.

The differential equation of motion for the system composed of the test material and mass m can be obtained from a free-body-diagram of mass m to give

$$(m + K G_x)\, \ddot{x} + \frac{ESn}{l_\omega}\, \dot{x} + \frac{ES}{l}\, x = \qquad (21)$$

$$F_0 e^{j\omega t}$$

which is exactly the same as Eq. 5 except that the apparent or effective mass M becomes

$$M = m + K G_x \qquad (22)$$

Hence, the test frequency which is also the resonant frequency can be varied by changing the gain on the acceleration feedback (G_x) since this term appears as mass in the equation of motion. This gain can be either positive or negative so that the effective mass may be changed quickly by electronic means from near zero to many times m if the shaker possesses the required capability.

The previously determined expressions for the material properties; i.e. Eqs. 10 & 11, may be updated to work with the servo controlled test situation by replacing the lower case m by M as well as replacing F_0 from Eq. 12. The

14

results are simply

$$E = \frac{\omega_1^2}{S} M = \frac{\omega_1^2}{S} [m + K G_x] \qquad (23)$$

and

$$n = \frac{E_0}{G_f \, S_f \, M \, A \omega^2} = \frac{K}{[m + K G_x]} \qquad (24)$$

$$(\frac{E_0}{e_0})$$

since $A \omega^2$ is the peak acceleration and can be represented by

$$e_0 = S_x \, \ddot{x}_{max} = S_x (A \omega^2) \qquad (25)$$

It should be pointed out that E_0 and e_0 may be either peak or rms values of the excitation voltage representing the excitation force and output voltage of the accelerometer, respectively. All of the quantities in Eqs. 23 and 24 can be quite easily determined by standard measurement techniques of known accuracy.

ERROR ANALYSIS

The accuracy of Eqs. 23 and 24 is dependent on the system being in resonance at $r = 1.0$. The resonant condition is measured by the ninety-degree phase relationship between the excitation force and the resulting motion as given by Eqs. 6 and 7.

The amount of error in the frequency ratio r being other than unity can be obtained from Eq. 7. Differentiation of Eq. 7 and solving for the slope gives

$$\Delta r = \frac{n}{2} \Delta \phi \qquad (26)$$

when r is unity where Δr and $\Delta \phi$ are the variations from the assumed values. By comparing Eqs. 6, 8, 10 and 12 when $r = 1 + \Delta r$, the error can be shown to be the deviation of

$$\beta_E = \frac{4}{(2 + n\Delta\phi)^2} = \frac{E_{actual}}{E_{r=1.0}} \qquad (27)$$

and

$$\beta_n = \frac{1}{\sqrt{1+(\frac{n\Delta\phi}{2})^2(1-\frac{n\Delta\phi}{4})^2}} = \frac{n_{actual}}{n_{r=1.0}} \qquad (28)$$

from unity in Eqs. 23 and 24 where β_E and β_n are the property correction factors. The worst deviation of error due to errors in measuring ϕ occur when n is near unity. Table I shows the values of β_E and β_n for $n = 1.0$ over a range of $\Delta\phi$. It is seen that errors considerably less than one percent can be easily achieved from the test technique if the phase measurement is better than one-half degree. Modern electronic phasemeters can easily measure phase angles to this accuracy when the phase is near ninety-degrees.

POSSIBLE TEST TECHNIQUES

There are several possible test techniques that can be used with the servo-controlled test arrangement shown in Fig. 2 when the phase feedback ideas of Meso and Keller [4] are included. These feedback ideas can be used to enhance the test techniques by automating the test process and thus save time.

DISCRETE FREQUENCY - The first and most obvious test technique is to use discrete frequencies set on the excitation oscillator which generates the excitation voltage E(t) in Fig. 2. The amplitude of this voltage, E_0, will control the final amplitude of motion while the frequency of this voltage will be the resonant frequency when the acceleration gain G_x is adjusted for resonance. Once the gain G_x is set at the proper values, it is necessary to record only the frequency ω, the excitation voltage E_0, the acceleration voltage e_0, and the gain G_x in order to obtain the material properties E and n given in Eqs. 23 and 24.

The validity of these results can then be checked by recording a damped oscillation trace. This trace can be obtained by removing the excitation voltage E(t) whenever it passes through zero. The resulting test system then becomes one of a single-degree-of-freedom with initial conditions of a displacement with no velocity. The excitation voltage must be zero at removal so that the transients due to pulses from the shaker will be a minimum.

This test method can be enhanced by automating the gain G_x. The scheme is shown in Fig. 3 where the phasemeter compares the excitation signal E(t) and the accelerometer signal e_0. The resulting output voltage of the phasemeter is then used to activate a servo which adjusts G_x until resonance is achieved.

15

POWER AMPLIFIER AND
SHAKER TRANSFER
FUNCTION
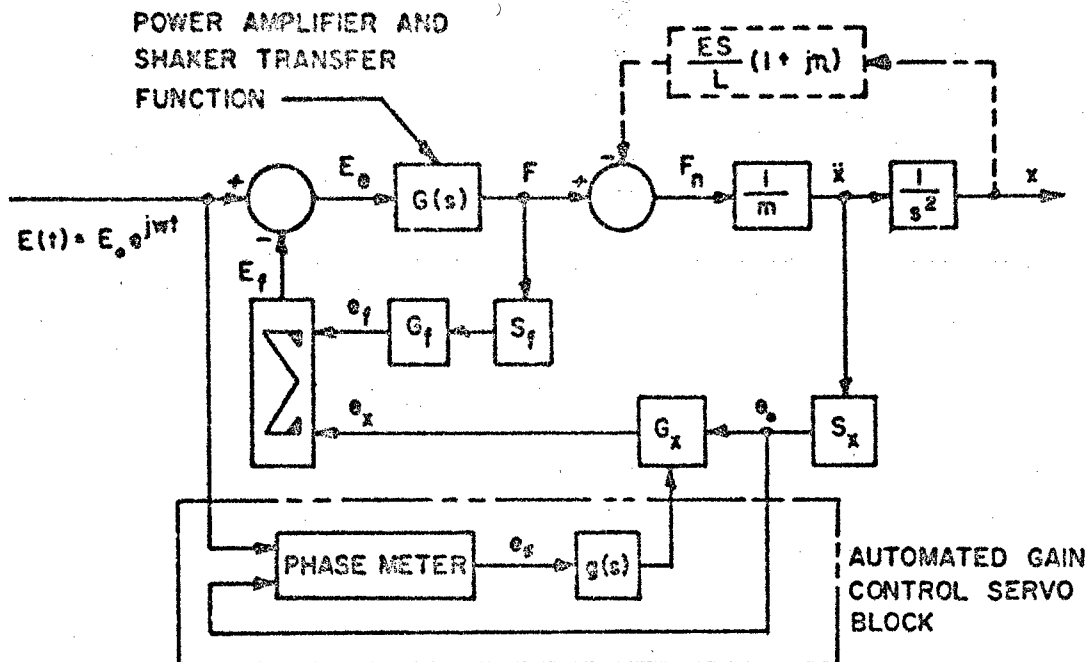
Figure 3 - Block diagram of servo controlled test system
with automated gain control

Since acceleration is being used as the signal
representing displacement, the phase angle is
plus ninety rather than minus ninety, but this
is a minor consideration since the phase
relationship is still ninety-degrees.

CONTINUOUS FREQUENCY SWEEP TESTS - This type
of test is basically one where the specimen
properties would be obtained at all frequencies
over a given range. There are basically two
methods of mechanization which can be used
here.

The first method would be to slowly change
the excitation frequency while the gain control
servo in Fig. 3 would maintain the phase at
ninety-degrees. The second method would be to
change the gain control at a slow rate while the
output of the phasemeter would be used to
control a sweep oscillator so that the ninety-
degree relationship would be maintained.

This test method is the most difficult in
that errors due to sweeping at too high a rate
will severely distort the results while
sweeping at an extremely low rate will lead to
heating of the test specimen. In addition,
there is a possibility that instability of the
two servos may result from unforeseen coupling.

PROPERTY-TEMPERATURE TESTS - A third possibility
would be to obtain property variations due to
heat build-up at a given frequency and
amplitude of motion. By using the gain control
servo in Fig. 3, it is possible to obtain a
continuous record of the material properties
at constant input frequency as the temperature
changes. The amplitude of motion could also
be controlled by an additional servo control
or the input force could remain constant.

In this section several possible test
methods were explored which indicate the
versatility of the proposed test scheme. Of
these test methods, the discrete frequency and
property-temperature tests would probably be
most useful.

SUMMARY

This paper is devoted to developing the
concepts behind a proposed test technique for
viscoelastic materials which allows for a
quick and accurate measurement of the complex
modulus of the material under a dynamic
environment without significant heating of the
test specimen. In addition, the same technique
can be used to measure the change of these
material properties as a function of temperature.

16

While the technique requires a large amount of test equipment, this equipment is readily available and is found in many vibration laboratories. The error analysis has shown the test technique should be better than one per cent when the phase angle deviates by less than one-half degree.

ACKNOWLEDGEMENTS

The author is indebted to the Department of Engineering Mechanics and the Engineering Research Institute for supporting this work.

REFERENCES

1. Nashif, A.D., "New Method for Determing Damping and Properties of Viscoelastic Materials", Shock and Vibration Bulletin 36, Part 4, pp. 4-7, January 1967.

2. Cannon, C.M. and Nashif, A.D., "Damping Measurements on Soft Viscoelastic Materials Using a Tuned Damper Technique", Paper presented to 38th Shock and Vibration Symposium, St. Louis, Missouri, May 1968.

3. Otts, J.V. "Force-Controlled Vibration Testing", Sandia Technical Memorandum SC-TM-65-31, 1965.

4. Ness, H.W. and Keller, A.C., "Resonant Dwell Test System", Test Engineering and Management, Vol. XIX, no. 6, pp. 28-33, June 1968.

TABLE I

PROPERTY CORRECTION FACTORS B_E and B_η FOR $n = 1.0$

$\Delta\phi$ Degrees	B_η	B_E
0	1.0	1.0
0.1	0.99999	0.99825
0.5	0.99996	0.99132
1.0	0.99985	0.98276
2.0	0.993828	0.96595

DISCUSSION

Mr. Ruzicka (Barry Controls): Your entire approach seems to be based upon the mass-spring—dashpot mathematical model, especially if you find a resonance by seeking out 90 degree phase. If this is a good model, which it probably is for very low damping, I think this would work. But if you have any significant degree of damping I think there is sufficient evidence that this is not a very good model for viscoelastic material.

Mr. McConnell: I realized that this question would come up when I chose the simple model. One of the limitations of the system is that the length of the specimen and the highest frequency you can use are limited when you approach the region of wave propagation. To satisfy first the simple strain model you must have a large l over d (length over diameter), for as you start to chop the length down the Poisson effects, the edge effects, certainly come into play. As the damping goes up then you get into problems if you want the Poisson effect, the radial motion. Your question is a legitimate one and that is one of the problems of proposing something. I have not done it and I know that other people who have, and will raise questions like this.

Mr. Ruzicka: I have not worried about wave effects yet. Even at a low frequency resonance if you have any significant degree of damping, say a q less than eight, I think you can readily show that the mass-spring—dashpot system will not be a very accurate model for rubber-like or viscoelastic material. One must go to many more elements in the mathematical modeling, and once you go to these additional elements the phase angle is no longer 90 degrees at resonance.

Mr. McConnell: Even at resonance?

Mr. Ruzicka: Yes sir, the phase angle goes all over the place.

Mr. McConnell: This may be a ligitimate point. For the others it may be worthwhile to investigate this as a quick method for testing it.

Mr. Henderson (AF Materials Lab): Perhaps I misunderstood part of your paper but did I understand you correctly when you said that you thought that part of the experimental portion could be conducted by cutting the force off and watching it decay? I wondered if you have considered in your model the fact that your

impedance head has a stiffness. This is not the same as having a mass suspended on a spring because your impedance head is still there, and you do not really have zero force from your impedance head, you still have the stiffness of the impedance head hooked back to ground and that might present some difficulties.

Mr. McConnell: I considered that when the force was shut off, the shaker is actually still in the picture. It has to be to make sure that the response of the system is still that of the system when it was cut off. All you are saying is that the excitation E_0 is suddenly set to zero. But you still have the feedback of the E_x, so that the shaker is still actively working within the system. The fact is that you are using both force and acceleration feedback, so that you need the impedance head. You have not really changed the system except that you now take away the excitation portion. You still have the force and the acceleration feedback.

DAMPING OF BLADE-LIKE STRUCTURES

David I. G. Jones
Air Force Materials Laboratory
Wright-Patterson AFB, Ohio 45433

and

Ahid D. Nashif
University of Dayton
Dayton, Ohio 45409

A resonant beam tuned damping device, comprising a flexible beam joined via viscoelastic links at the ends, to a vibrating structure, is described. This device has the advantage of relying on the interaction between the beam stiffness and the link stiffness for tuning, rather than on the link stiffness alone as for the conventional tuned damper, so that a weight saving possibility exists. An analysis is developed and preliminary experimental investigations are described which support the analysis and show that significant damping of a typical fan blade can be achieved by use of such dampers.

INTRODUCTION

Vibrational problems in compressor, fan and turbine blades and in helicopter rotors appear to be receiving more attention as engine performance continues to increase. The vibrational characteristics of these long, thin, blade-like structures are such that a large number of bending and torsional modes can occur at frequencies low enough for excitation to be potentially significant. These vibrations are often undesirable, as in fan blade flutter, and means are being sought to eliminate or reduce them. One of the most promising techniques for reducing these unwanted resonances is damping. However, a peculiar characteristic of these thin structures is that strains are usually small even though amplitudes of vibration may be large, so that most layered damping techniques are likely to be ineffective. In fact, one of the few well known damping techniques potentially usable is the tuned viscoelastic damper, which depends on vibration amplitude rather than strain for effective energy dissipation. Clearly, the narrow dimensions and the high centrifugal loads involved will usually preclude the use of bulky conventional tuned dampers and more useful geometrical configurations must be sought. One of these is shown in Figure 1. Shown is a resonant beam tuned damper comprising a flexible beam supported by viscoelastic links at the two ends which will be the subject of this paper.

In this paper, an analysis is developed for the energy dissipated per cycle by a resonant beam tuned damper at a point in a vibrating structure. A new parameter is defined, namely the ratio of the link stiffness to the stiffness of the resonant beam, and is shown to affect the performance of the damper, along with the better known parameters of damper mass, loss factor and resonant frequency. The effects of centrifugal forces are also considered.

In the experimental investigation, effects of centrifugal loading are measured along with the effects of the dampers on the response of a typical fan blade in the first torsional mode.

SYMBOLS

D Diameter of experimental link

D_s Energy dissipated per cycle in damper

E' Real part of Young's Modulus of link material

E'_{obs} Observed real part of Young's Modulus of link material

19

E   Young's Modulus of resonant beam material

G_o Static shear modulus of link material

h   Length of link

i $\sqrt{-1}$

I   Second moment of area of beam cross section

k   Real part of link stiffness (k/2 each end)

ℓ Length of beam

m   Isolated mass at center of beam (for tuning)

M   Net mass on conventional tuned damper

Q $1/\eta_s$ (Quality factor)

R   Radius of link

t   Time

W_D Displacement amplitude at station x of damper

W   Structure displacement amplitude at damper location

x   Distance along beam (measured from center) or distance along link in direction of shear deformation

y   Distance along link transverse to shear deformation

Γ' $k\ell^3/2$ EI - Stiffness parameter

$\Delta(\xi)$ See Equation (13)

η Loss factor of link material

η_s Composite loss factor

θ Centrifugal loading factor (g's)

λ $(\mu\omega^2/EI)^{1/4}$

μ Mass per unit length of beam

ξ $(\mu\omega^2\ell^4/EI)^{1/4}$-Frequency parameter

ξ_D $(\mu\omega_D^2\ell^4/EI)^{1/4}$-Values of ξ at damper resonance frequency

ρ Density of beam material

ρ_D Density of link material

ρ_{wD} Weight per unit volume of link material

ρ_w Weight per unit volume of beam material

σ Shear stress in link material

σ_m Maximum shear stress in link material

τ Thickness of beam

ϕ Shear strain in link material

ϕ_m Maximum shear strain

ω Frequency

ω_D Fundamental frequency of damper

ANALYSIS

Analysis of Dampers

Consider the damper shown in Figure 1.
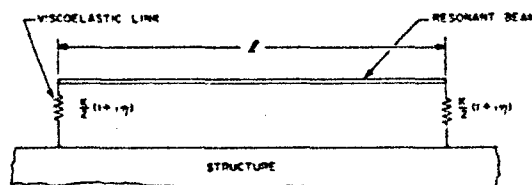
Figure 1.   Idealized Damper

Clearly, the conventional tuned damper [1-3] will be a special case in which the beam length ℓ becomes zero and the two viscoelastic links of stiffness k(1+iη)/2 combine in parallel to produce a single link k(1+iη). Let W_D be the response at a point x of the damper, measured from the center, and let W be the amplitude of vibration at the point of attachment of the damper. The Euler-Bernoulli equation

$$EI \frac{d^4W_D}{dx^4} - \mu\omega^2W = 0 \qquad (1)$$

has the general solution

$$W_D = A \, Cos(\lambda x) + B \, Ch(\lambda x) \qquad (2)$$

where $\lambda^4 = \mu\omega^2/EI$ \qquad (3)

20

where the antisymmetric terms have been rejected. The boundary condition at $x = \pm \ell/2$ are that

$$d^2 W_D/dx^2 = 0$$

$$EI(d^3 W_D/dx^3) = \frac{1}{2} k(1+in)(W_D - W) \qquad (4)$$

and the solution subject to these conditions is readily shown to be:

$$W_D(x) = \{-\Gamma'W(1+in)[Ch(\xi/2)Cos(\xi x/\ell)$$

$$+ Cos(\xi/2)Ch(\xi x/\ell)]\}$$

$$\div\{\xi^3[Sin(\xi/2)Ch(\xi/2)+Sh(\xi/2)Cos(\xi/2)]$$

$$- 2\Gamma'(1+in)Cos(\xi/2)Ch(\xi/2)\} \qquad (5)$$

where $\xi = \lambda\ell$ and $\Gamma' = k\ell^3/2EI \qquad (6)$

For values of n less than 0.2 or so, resonance occurs when:

$$\xi_D^3 [Sin(\xi_D/2)Ch(\xi_D/2)$$

$$+ Sh(\xi_D/2)Cos(\xi_D/2)]$$

$$= 2\Gamma' Cos(\xi_D/2)Ch(\xi_D/2) \qquad (7)$$

Graphs of ξ_D^2 versus $\Gamma'/4\pi^2$, representing the numerical solution of the transcendental equation (7), are shown in Figure 2.
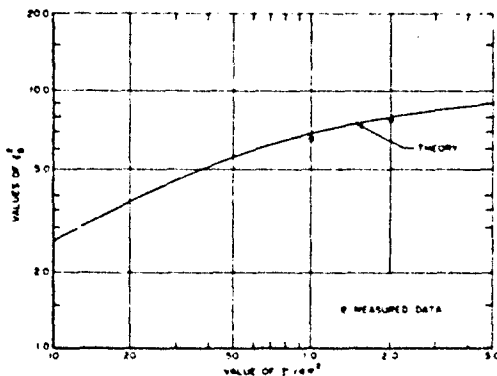
Figure 2. Graph of Experimental and Theoretical Values of ξ_D^2 Against $\Gamma'/4\pi^2$

When Γ' is very large, $Cos(\xi_D/2) = 0$ so that $\xi_D^2 \rightarrow \pi^2$ as $\Gamma' \rightarrow \infty$ and, for very small Γ':

$$\xi_D^4 = 2\Gamma' = k\ell^3/EI$$

or

$$\omega_D^2 = k/\mu\ell \qquad (8)$$

as would be expected in the limiting case of a conventional tuned damper. Other interesting results from equation (4) show that:

$$W_D(0)_{res} = \{(W/2)(1+in)/in\}$$

$$\cdot\frac{Ch(\xi_D/2) + Cos(\xi_D/2)}{Cos(\xi_D/2)Ch(\xi_D/2)} \qquad (9)$$

and

$$W_D(\ell/2)_{res} = \frac{1+in}{in} W \qquad (10)$$

and graphs of $|W_D(\ell/2)_{res}/W|$ and $|W_D(0)_{res}/W|$ against $\Gamma'/4\pi^2$, are illustrated in Figures 3 and 4 respectively.
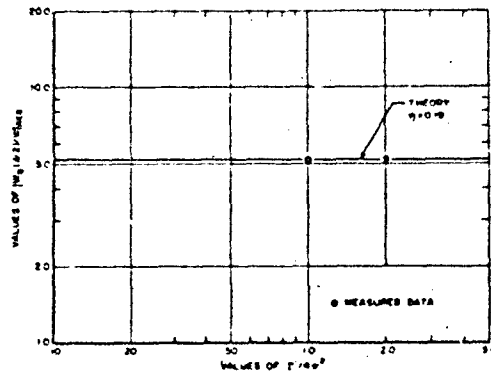
Figure 3. Graph of Experimental and Theoretical Values of $|W_D(\ell/2)_{res}/W|$ Against $\Gamma'/4\pi^2$
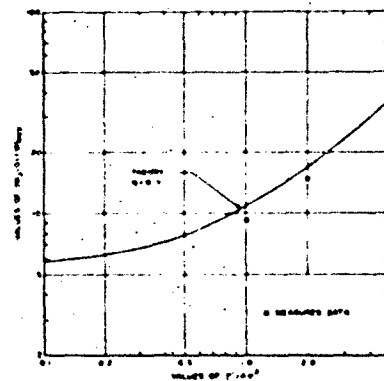
Figure 4. Graph of Experimental and Theoretical Values of $|W_D(0)_{res}/W|$ Against $\Gamma'/4\pi^2$

21

In order to determine the energy dissipated per cycle in these links, we require the values of $W_D(\ell/2)-W$

$$W_D(\ell/2)-W = \{-\xi^3 W \, [Sin(\xi/2)Ch(\xi/2)$$

$$+ Sh(\xi/2)Cos(\xi/2)]\}+\{\xi^3[Sin(\xi/2)Ch(\xi/2)$$

$$+ Sh(\xi/2)Cos(\xi/2)]$$

$$- 2\Gamma'(1+in)Cos(\xi/2)Ch(\xi/2)\} \qquad (11)$$

The energy dissipated per cycle in the two links is:

$$D_s = \pi k n \,|W_D(\ell/2)-W|^2$$

$$\therefore \ \frac{D_s}{\pi k W^2} =$$

$$\frac{n[\Delta(\xi)+2\Gamma'Cos(\xi/2)Ch(\xi/2)]}{[\Delta(\xi)]^2+[2\Gamma'nCos(\xi/2)Ch(\xi/2)]^2} \qquad (12)$$

where $\Delta(\xi) = \xi^3[Sin(\xi/2)Ch(\xi/2)$

$$+ Sh(\xi/2)Cos(\xi/2)]$$

$$- 2\Gamma'Cos(\xi/2)Ch(\xi/2) \qquad (13)$$

Graphs of $D_s/\pi k W^2$ against $(\xi/\xi_D)^2$ or (ω/ω_D) are plotted in Figure 5 for two values of $\Gamma'/4\pi^2$. If $\Gamma' = 0$, we have to take the limiting case as $\Gamma' \to 0$. It is seen that the peak D_s occurs near $\omega/\omega_D = 1$ and is the same for all Γ' but that the bandwidth over which significant amounts of energy is dissipated becomes narrower as Γ' increases. The parameter $\Gamma'/4\pi^2$ has been used instead of Γ' for convenience and for correlation with the approximate analysis of [5].

Effects of Centrifugal Loading

Consider the forces acting on an element of a viscoelastic link under a centrifugal load of θ g's as in Figure 6. The equation of equilibrium of this element is:

$$G_o \pi R^2 \Delta\phi = -\rho_{wD}\pi R^2 \Delta y\theta$$

$$\therefore \ \frac{d^2x}{dy^2} + \frac{\rho_{wD}\theta}{G_o} = 0 \qquad (14)$$

since $\phi = dx/dy$.
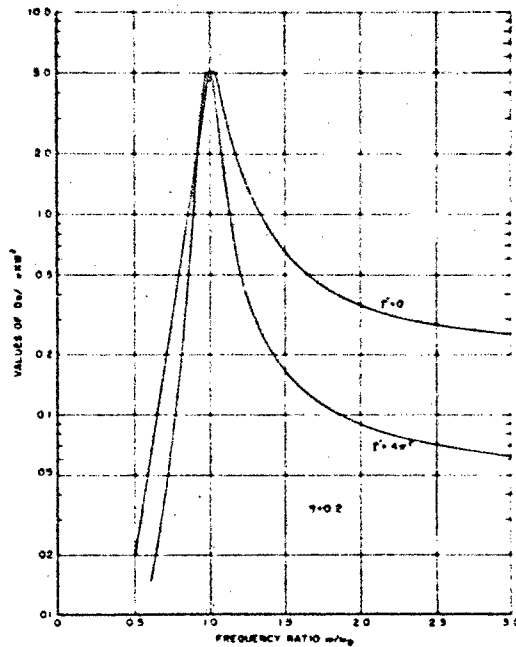
Figure 5. Graphs of Energy Dissipation Parameter Against Frequency Ratio
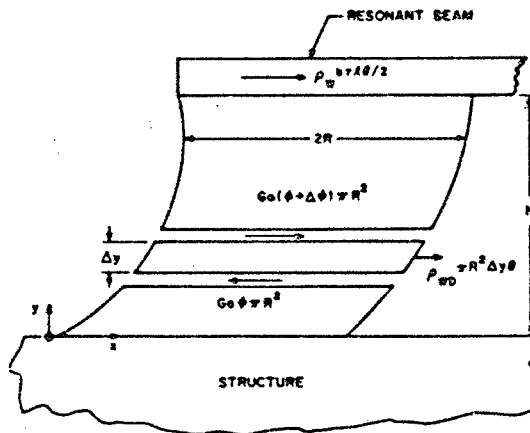
Figure 6. Sketch of Link Under Centrifugal Loading

The boundary conditions which the solution of this equation must satisfy are that $x = 0$ at $y = 0$ and the balance of forces at $y = 0$ gives:

$$\pi R^2 \, G_o(\phi)_{y=0} = \tfrac{1}{2} \rho_w b\tau\ell\theta + \rho_{wD}\pi R^2 h\theta \qquad (15)$$

22

The only solution to meet all these conditions is:

$$x = \frac{\rho_{wD}\theta}{2G_o}(2yh - y^2) + \frac{\rho_w b\tau \ell \theta}{2G_o \pi R^2} y \quad (16)$$

$$\therefore \phi = \frac{dx}{dy} = \frac{\rho_{wD}\theta}{2G_o}(2h - 2y) + \frac{\rho_w b\tau \ell \theta}{2G_o \pi R^2} \quad (17)$$

$$\phi_m = (\phi)_{y=0} = \frac{\rho_{wD}\theta h}{G_o} + \frac{\rho_w b\tau \ell \theta}{2G_o \pi R^2} \quad (18)$$

is the maximum shear strain. Also:

$$\sigma = G_o \phi = (\rho_{wD}\theta/2)(2h - 2y)$$

$$+ \rho_w b\tau \ell \theta / 2\pi R^2 \quad (19)$$

$$\sigma_m = (\sigma)_{y=0} = \rho_{wD}\theta h + \frac{\rho_w b\tau \ell \theta}{2\pi R^2} \quad (20)$$

is the maximum shear stress. The values of ϕ_m and σ_m should not exceed the limits relevant to the viscoelastic material being used. Equation (20) may be rewritten:

$$\frac{\sigma_m}{\theta \rho_w} = \frac{b\tau \ell}{2\pi R^2} + \frac{\rho_{wD}}{\rho_w} h \quad (21)$$

Design Considerations

In a specific damper design, one would wish to select the controllable parameters, namely k, ℓ and EI in such a way as to obtain the desired frequency ω_D for as low a value of Γ' as possible. Now

$$\frac{\mu \omega_D^2 \ell^4}{EI} = \xi_D^4$$

and ξ_D^4 is a function of Γ' as in Figure 2.

$$\therefore \quad \omega_D = \frac{\xi_D^2}{\sqrt{12}} \sqrt{\frac{E}{\rho}} \frac{\tau}{\ell^2} \quad (22)$$

Also:

$$\Gamma' = k\ell^3/2EI$$

$$= 6\pi \left(\frac{E'}{E}\right)\left(\frac{\ell^3 R^2}{b h \tau^3}\right)\left[1 + \frac{1R^2}{2h^2}\right] \quad (23)$$

since $k = (E' \pi R^2/h)(1 + 1R^2/2h^2)$ $\quad (24)$

where E' is the real part of the Young's Modulus of the viscoelastic material at the damper frequency ω_D and the term $1 + 1R^2/2h^2$ represents the shape effect as discussed in the experimental investigation.

Finally, the maximum stress σ_m in the viscoelastic material must not be exceeded under the imposed centrifugal field so that equation (21) must be taken into account. We now write this in the form:

$$\theta = \frac{\sigma_m / \rho_w}{b\tau \ell / 2\pi R^2 + \rho_{wD}\ell / \rho_w} \quad (25)$$

Equations (22), (23), (24) and (25) can be used to design a damper to meet a specific set of conditions. We shall not attempt to develop a specific design procedure here but will look only at the calculations for a specific geometry.

Example

Consider the damper for which

$\ell = 2.5$ ins.

$\tau = 0.04$ ins.

$h = 0.20$ ins.

$R = 0.15$ ins.

$D = 0.30$ ins.

$E' = 650$ lb/in^2

$\sigma_m = 253$ lb/in^2

$b = 2R = D = 0.30$ ins.

$\rho_w = 0.101$ lb/in^3

$E = 10^7$ lb/in^2

$\rho_{wD} = 0.0505$ lb/in^3

From equations (23) and (24):

$$\frac{\ell^3 D^2}{b h \tau^3} = \frac{15.5 \ (0.3)^2}{0.3 \times 0.2 \times (4)^3 \times 10^{-6}} = 36.2 \times 10^4$$

$$\therefore \quad \Gamma' = 266$$

From equation (22) and Figure 2

$$\omega_D = \frac{9.7}{\sqrt{12}} \sqrt{\frac{10^7 \times 386}{0.101}} \times \frac{0.040}{(2.5)^2} = 3540$$

rad/sec i.e. 562 cps.

Then, from equation (25):

$$\theta = \frac{253/0.101}{\frac{0.3 \times 0.04 \times 2.5}{2 \pi \times (0.15)^2} + \frac{0.0505 \times 0.2}{0.101}} = 8000$$

Finally, the total weight of the damper is:

$$W = \rho_w \ell_1 b + 2 \pi R^2 h \rho_{wD} = 2.03 \text{ grams}$$

and, if $G_o = 175 \text{ lb/in}^2$:

$$\phi_m = \gamma_m / G_o$$

$$= 1.45$$

This is rather high in view of the possibility of de-tuning the damper, as discussed in the experimental investigation. For this reason, θ will probably have to be restricted to 3000 g's or below, so that $\phi_m \leq 0.55$.

EXPERIMENTAL INVESTIGATION

Materials Properties Measurements for Various R/h Ratios and Static Shear Strains

In order to determine the effects of shear strain and specimen shape on the observed complex Young's Modulus, specimens were made up as shown in Figure 7 using GE-RTV-630 made in a 1:10 catalyst to material ratio at room temperature.
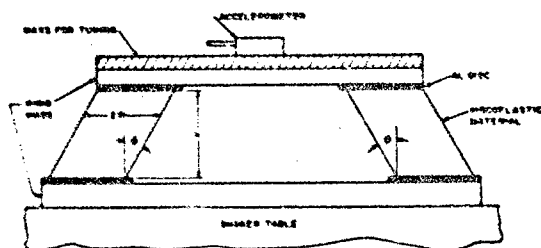
Figure 7. Experimental Links for Simulated Centrifugal Loading

Specimens were made up with h = 0.32 ins

and D = 1/4 inch, 5/16 inch, 3/8 inch and 7/16 inch and ϕ = 0, 7.5°, 18° and 32°. The specimens were then bonded to a shaker table and the resonant frequency and amplification factor at resonance measured for various input levels and tuning masses M (which must include the disc masses, the rigid upper mass, the added mass for tuning, the mass of the accelerometer and one third (1/3) the mass of the viscoelastic material in accordance with classical spring theory). Typical measurements are shown in Table 1. The results show that there is a distinct variation of E'_{obs} with the R/h ratio, but little or no variation of η or E' with ϕ. Reference [4] shows a distinct shape effect i.e. relationship between the observed E'_{obs} and the actual E' and R/h ratio. This relationship is, approximately:

$$E'_{obs} = E' \left[1 + \frac{1}{2}\left(\frac{R}{h}\right)^2\right] \qquad (26)$$

If we divide E'_{obs} by $1 + \frac{1}{2}\left(\frac{R}{h}\right)^2$ and plot E' versus ω, we should eliminate the shape effects. Figures 8 to 10 show the effects of ϕ on the values of E' and η. It is seen that the effects of ϕ are so small as to be unmeasurable and that the shape factor given in equation (26) does indeed reduce the data to a single line, within the limits of experimental scatter.
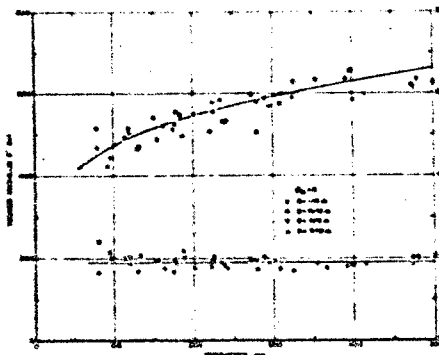
Figure 8. Graphs of E' versus ω
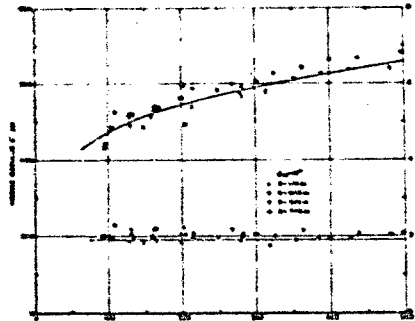
Figure 9. Graphs of E' versus ω

24

TABLE 1
Typical Measured Properties of G. E. RTV-630 at 75°F
(input = 1 g, h = 0.32 ins)

ϕ_m deg	D ins	M gm	Output g's	Freq. cps	η	E' psi
0	7/16	14.1	5.5	473	.185	652
		33.0	5.4	295	.188	598
		180.0	5.4	120	.188	530
	5/16	9.8	5.7	391	.178	652
		24.2	5.7	222	.178	519
		46.2	5.8	163	.175	535
18	7/16	17.7	5.2	427	.197	653
		72.5	5.0	198	.204	598
		104.6	5.2	163	.197	562
	5/16	9.9	5.2	387	.197	642
		33.4	5.6	199	.182	573
		72.3	5.4	129	.189	525
32	7/16	17.7	5.6	451	.181	741
		45.4	5.4	267	.190	667
		120.1	5.3	158	.192	622
	5/16	9.9	5.8	400	.176	690
		25.1	5.6	231	.182	530
		45.2	5.6	170	.182	570
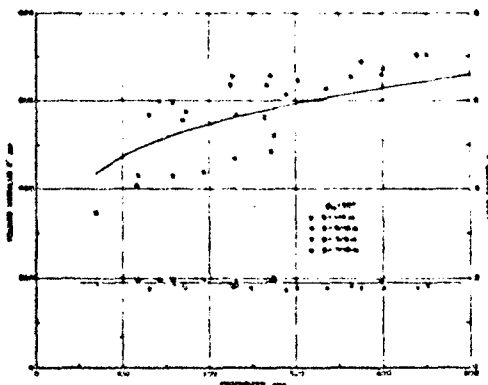
Figure 10. Graphs of E' versus ω

Figure 11. Typical Fan Blade

Measurement of Effect of Resonant Beam
Dampers on Response of Typical Fan Blade

The fan blade illustrated in Figure 11 is typical of many designs. A fixture was designed to rigidly clamp the blade at the root and this fixture was attached to a shaker table (MB-C10 shaker). Response measurements were taken at various points of the blade, for 1 g rms input level at the shaker table, using a miniature accelerometer (Endevco 2222A). Several modes were readily identified, including the first and second bending modes and the first torsional mode.

In order to make a preliminary survey of the effect of tuned dampers on the blade response, dampers of the geometries shown in Figure 12 were made, with the 0.31 in high by 1/4 in diameter links interchanged between dampers so as

25

to eliminate possible variations in viscoelastic material properties.

Each damper in turn was then placed on the fan blade and the tip resonant response measured for various tuning masses, and hence damper frequencies, and damper position. Figure 14 shows typical response spectra for the damped and undamped blade.
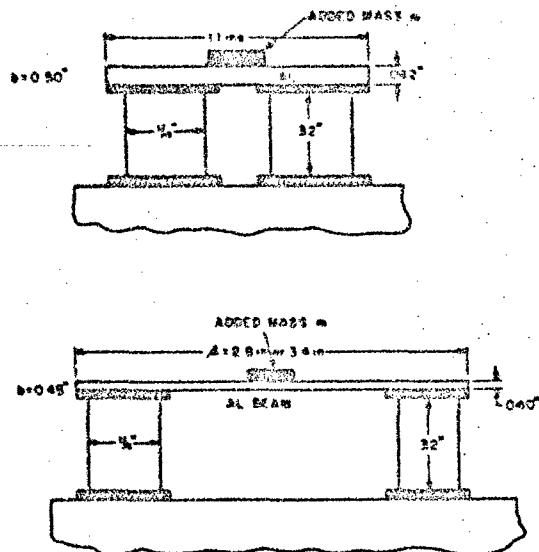
Figure 12. Experimental Tuned Dampers

The dampers were first tuned by varying the additional mass m and observing the response at the center and at the ends under shaker excitation. Typical results are shown in Table 2 and in Figure 13. It is seen that the points relating ξ_D^2 to $|W_D(\ell/2)/W|_{res}$ and $|W_D(0)/W|_{res}$ with $\Gamma'/4\pi^2$ agree well with the analysis, as shown in Figures 3 and 4 respectively.

Figure 14. Typical Response Spectra for Undamped and Damped Cases ($\Gamma'=8\pi^2$)

Figure 13. Damper Resonant Frequencies
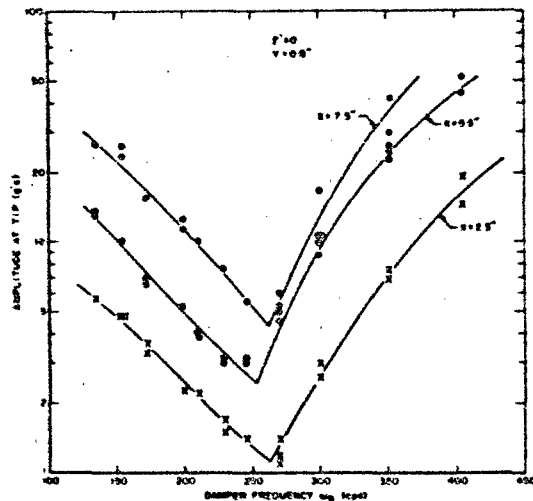
Figure 15. Graphs of Amplification Factor A, at Blade Tip, versus Damper Frequency

TABLE 2
Typical Measurements on Resonant Beam Dampers Under Shaker Excitation
(input = 1 g, h = 0.32 ins, D = 1/4 in)

ℓ ins	ℓ* = ℓ-1/2 in	m gm	Output (center) g's	Output (end) g's	Freq. cps	$\frac{\Gamma'}{4\pi^2}$	ξ^2_D
2.8	2.3	0	----	5.4	428	1.0	6.25
		0.5	8.6	5.2	380		
		1.0	9.1	5.1	344		
		2.0	9.1	4.9	287		
		4.5	9.8	4.5	214		
		8.5	9.0	3.7	168		
		12.5	9.2	4.0	137		
3.4	2.9	0	----	5.3	333	2.0	7.77
		0.5	14.0	4.1	287		
		1.0	13.2	4.1	256		
		2.0	14.5	4.2	217		
		4.5	14.7	3.9	160		
		8.5	16.5	3.9	125		
?.1	0.6	0	5.0	----	512	0	0
		6.1	5.3	----	279		
		21.5	6.1	----	174		

Figure 15 shows the variation of amplification factor A with damper frequency, ω_D, and for various damper positions for $\Gamma' = 0$ and Figure 16 shows the variation of amplification factor A with damper frequency, ω_D, and with Γ' for a fixed damper position.
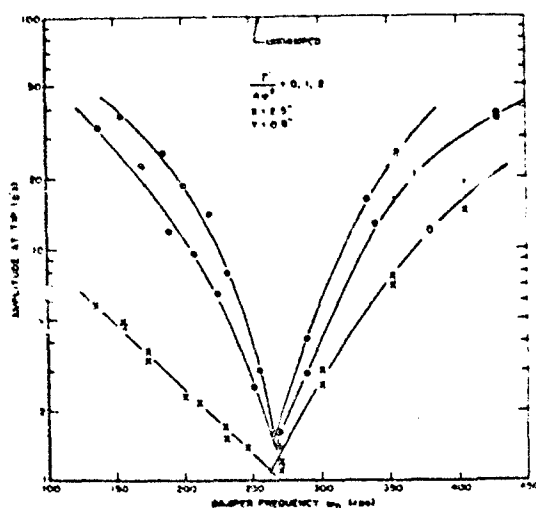
Figure 16. Typical Graphs of Amplification Factor, at Blade Tip, versus Damper Frequency for Various Values of Γ'

CONCLUDING REMARKS

An analysis has been developed, and experimentally verified in part, for the response characteristics of a resonant beam - viscoelastic link tuned damper. By proper choice of the stiffness of the two viscoelastic links and of the beam material and dimensions, this damper configuration can be tuned to any given frequency of operation for a lower weight penalty than in the case of the conventional rigid mass/viscoelastic link tuned damper. However, some sacrifice of frequency bandwidth of effective operation is involved and the beam cannot be made too light if this loss of performance is not to be too great.

The resonant beam tuned damper is a variation of the conventional tuned viscoelastic damper which appears to have considerable potential for the reduction of vibration problems in a wide variety of structures, ranging from compressor blades in jet engines to multi-span skin-stringer panels. In each specific problem area, new geometrical configurations and viscoelastic material choices will doubtless have to be made in order to take full engineering advantage of the basic concept.

For the future, work is needed to better define, measure, and make available to engineers complex modulus data, as a function of frequency and temperature, for a wide variety of viscoelastic materials possessing other useful engineering properties such as high strength.

Work is presently in hand at the AFML in this area. Further work must also be carried out to verify the effectiveness of the resonant beam damper concept under test conditions more closely approaching actual operational conditions.

REFERENCES

1. Snowdon, J. C., "Vibration of Cantilever Beams to which Dynamic Absorbers are Attached", J. Acoust. Soc. Am., Vol. 39, pp. 878-886 (1966).

2. Snowdon, J. C., "Steady State Behavior of the Dynamic Absorber", J. Acoust. Soc. Am., Vol. 31, pp. 1096-1103 (1959).

3. Jones, D. I. G., "Response and Damping of a Simple Beam with Tuned Dampers", J. Acoust. Soc. Am., Vol. 42, pp. 50-53 (1967).

4. Snowdon, J. C., Vibration and Shock in Damped Mechanical Systems. John Wiley & Sons, Inc., New York: p. 3 (1968).

5. Nashif, A. D. and Jones, D. I. G., "A Resonant Beam Tuned Damping Device", Paper No. 68-WA/GT-2, ASME Winter Annual Meeting, Gas Turbine Section, New York, Dec. 1-5, 1968.

DISCUSSION

Mr. Bouche (Endevco Corp): I have the impression that your tuned damper was tuned to the fundamental resonance of the blade. What about second mode resonance of the blade, does the damper attenuate the vibration at that resonance?

Mr. Nashif: We did limit the investigation to the first torsional mode. However this damper can be made to operate at the second bending mode and the first bending mode.

Mr. Ungar (Bolt Beranek and Newman): Did you consider damping of the beam itself? In other words using a beam made of a damping material?

Mr. Nashif: We did consider this point, however, no work has been done so far.

Mr. Ludwig (Pratt and Whitney Aircraft): Was there any consideration given to the temperature of the structure for damping? Also, I would like to know a little more about how the beam is attached to this particular blade or specimen.

Mr. Nashif: The temperature range depends on the material property itself. For a given required temperature range you have to select the proper viscoelastic material. The one we used was a good material up to about 500 degrees Fahrenheit, similar to most silicone materials. For the second question, those dampers we built in the laboratory were only an experimental kind. We have not yet started working on practical dampers, however, we shall be looking into them soon. Those dampers were put on a lathe in a slot by means of epoxy.

Mr. DiTaranto (PMC Colleges): Could you give a physical explanation of the effect of the flexibility of the beam? Why did the flexibility of the beam improve the damping over a rigid mass?

Mr. Nashif: Having the extra beam dimensions and material properties in the equation for the natural frequency of this device, all these parameters enter in and will aid us in selecting a wide range of flexibility as far as tuning goes. However, in the conventional tuned viscoelastic damper you have only the mass and the length to vary.

Mr. Jones (Air Force Materials Lab.): I just have a comment on that last question. The damping was not improved—we never claimed

this. There is a loss of frequency bandwidth of effective operation, which is the price you pay for the extra flexibility.

Mr. DiTaranto: It seems as though you are getting effective mass change with the flexibility of the beam. As you made the beam more flexible, in effect you had less energy in the beam for a given deflection, so that you should be getting a higher loss factor in that there is less energy in the beam to be dissipated.

Mr. Nashif: Actually when you make the beam very flexible or soft, all the deformation occurs in the beam and none in the viscoelastic

material. Hence little energy is dissipated that way because we are looking for maximum deformation in the high damping material, not in the beam.

Mr. Ungar: I might also mention that there is a commercial damping treatment available which uses essentially this principle but somewhat blindly, in other words undesigned. This material comes in strip form, essentially a strip of viscoelastic material which is self-adhesive. The adhering portion is about 1/2 inch wide and the paper covered portion is about 2 inches long so that there is a series of bridges formed which can resonate at an appropriate frequency.

MULTI-LAYER ALTERNATELY ANCHORED TREATMENT

FOR DAMPING OF SKIN-STRINGER STRUCTURES

Capt. D. R. Simmons
Air Force Institute of Technology
Wright-Patterson AFB, Ohio

J. P. Henderson and D. I. G. Jones
Air Force Materials Laboratory
Wright-Patterson AFB, Ohio

C. M. Cannon
University of Dayton
Dayton, Ohio

An energy analysis is developed for the prediction of the effect
of a multi-layer alternately anchored damping treatment on the
response and damping of a typical skin-stringer structural ele-
ment. Experiments are described which support the analysis and
show that it is possible to obtain significant damping in this
class of structure by proper use and optimization of the multi-
layer anchored treatment. More specifically, it is shown that
increases in the effective structure loss factor of the order of
0.04 can be achieved by use of boron-reinforced aluminum con-
straining bands for a weight penalty of only 1.5 percent of the
weight of the skin.

INTRODUCTION

The use of layered viscoelastic
damping treatments has been the subject
of a great number of reports in the last
decade, and many possible configurations
and materials have been discussed. How-
ever, most of these analyses have been
confined to relatively simple structural
systems such as beams and single bay
plates and a need has arisen for exten-
sion of analysis to the prediction of
the effect of these damping treatments
on the response and damping of more com-
plex structures such as the skin-stringer
class of structure used on aircraft and
spacecraft.

The alternately anchored version of
the constrained layer treatment proposed
by Lazan a few years ago appears to
offer the hope of considerable amounts
of damping for moderate weight additions
and, moreover, can be represented under
certain conditions in terms of an equiva-
lent free-layer treatment, thereby
greatly simplifying analysis.

In the present paper, a normal mode
analysis is used, along with strain
energy calculations, to predict the
effect of the Lazan treatment, taken as
an equivalent free layer, on the modal
damping of a typical skin-stringer
structural element. The analysis shows
how optimum configurations may be de-
signed and an experimental verification
is described.

ANALYSIS

Representation of Multi-Layer Treatment as Equivalent Free Layer

The damping treatment considered in
this paper is illustrated in Figure 1.
The detailed analysis has been carried
out by Lazan, Metherell and Sokol [1]*
and only the main results will be
utilized herein.

In cases where the surface strain
in the vibrating structure or member is
reasonably uniform over the length of
the damping configuration (vibration

*Square brackets indicate references
listed at the end of this paper.

31

wave length larger than treatment length), the behavior of the configuration may be represented with some accuracy by an equivalent layer of homogeneous damping material having (i) the same cross sectional area and length L' and (ii) attached to the structure over the distance L' as in Figure 1.

STRUCTURE

(a) UNSTRAINED CONDITION

STRUCTURE

(b) STRAINED CONDITION

STRUCTURE

(c) EQUIVALENT FREE LAYER

(note vertical scale is exaggerated for clarity)
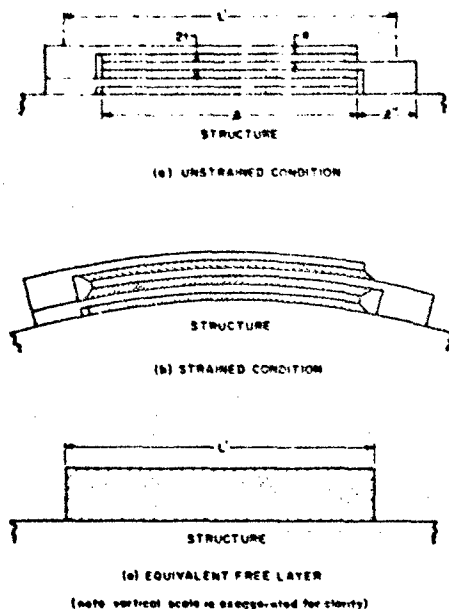
Figure 1. Multi-layer alternately anchored damping treatment

The effect of the treatment can then be considered in terms of equivalent complex Young's Modulus $E_D(1+i\eta_D)$ and the problem of predicting the effect of the damping treatment on the response is thereby greatly simplified. The expressions for E_D and η_D given in [1] are:

$$E_D = k_j' \, [L'/b(a+t)]$$

$$= [\frac{bEt}{\ell'}] \, [\frac{L'}{b(a+t)}] \, (\frac{MT + RV}{T^2 + V^2}) \quad (1)$$

$$\therefore \frac{E_D}{E} = (\frac{t}{a+t}) \, (\frac{L'}{\ell'}) \, (\frac{MT + RV}{T^2 + V^2}) \quad (2)$$

and

$$\eta_D = \frac{k_j''}{k_j'} = \frac{RT - MV}{MT + RV} \quad (3)$$

where M, R, T and V are functions of two parameters a and b alone as defined in the list of symbols. a and b in turn

are functions of the viscoelastic material loss factor η and a parameter B_0 defined by

$$B_0^2 = G(1+\eta^2)^{1/2}(\ell'^2/aEt) \quad (4)$$

being a measure of the ratio of the viscoelastic layer stiffness to the constraining band stiffness. The other symbols are defined in the nomenclature. It will be noted that in this analysis E_D and η_D do not depend on the number of layers in the treatment since they are derived from a summation of properties of typical layers. It is recognized that the first and last layers are not typical elements of the treatment and this makes equations (2) and (3) somewhat approximate for three layers or less; however the accuracy improves as the number of layers increases.

The problem has therefore been reduced to that of systematically varying the parameters ℓ', t, E, G, a, b and η. In order to make the problem more tractable the values of G and η were taken to be those appropriate to the specific viscoelastic material used in the tests, namely 3M-428* produced by Minnesota Mining and Manufacturing Company, at room temperature and over only a narrow frequency range from about 200 to 300 cps. For this case G = 52.2 psi and $\eta = 0.59$.

A major question which arises is how to determine the "effective length" L' in terms of length of viscoelastic material ℓ' and the anchor length ℓ'' as shown in Figure 1. Involved in this question is the relative stiffness of the constraining layer and structural adhesive used in the anchoring area. The assumption made in the following analysis corresponds to the case discussed by Lazan et al [1] in which the constraining layers in the anchored ends are considered to be rigid and the structural adhesive is allowed to deform in shear as the structure is strained. This assumption puts the point of effective anchoring (the plane section which remains plane after deformation) in the center of the anchored end, as shown in Figure 2. Therefore,

$$L' = \ell' + \ell''$$

---

*3M-428A, 428B, and 428C are commercially available damping tapes consisting of an aluminum foil constraining layer and a pressure sensitive adhesive damping layer, manufactured by the Industrial Tape Division, Minnesota Mining and Manufacturing Company. Some of the damping treatments used in this investigation had non-standard boron-aluminum or steel constraining layers and 3M-428 damping layer.
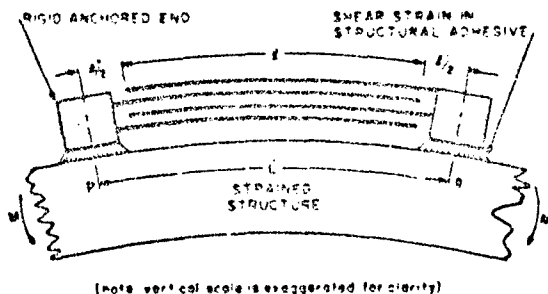
Figure 2. Shear deformation of structural adhesive with a rigid anchor

Some typical graphs of E_D and n_D for $\ell" = 1$ inch are plotted against ℓ' in Figures 3 to 5 and of $E_D n_D$, a measure of the gross damping capacity of the treatment, in Figure 6.
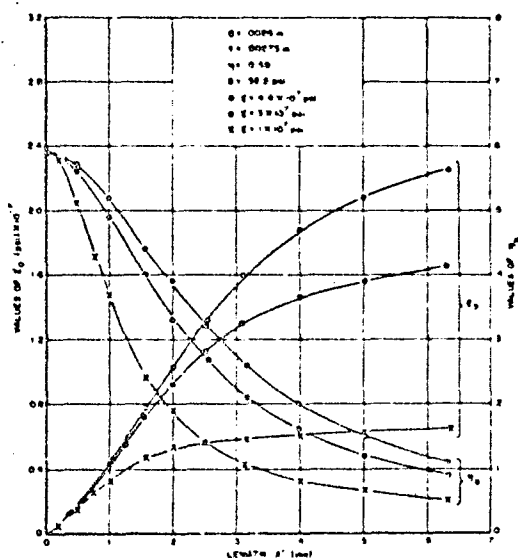
Figure 3. Equivalent free layer properties for 3M-428 with various backing materials ($76°F$)

It is seen that, for a particular selection of damping and constraining layers, an optimum length ℓ' exists for which $E_D n_D$ is a maximum. In addition, it is of interest to note that boron-reinforced aluminum[**] constraining layer gives considerable increase in damping with no increase in the weight of the

**Borsic[TM] - Aluminum Tape, Hamilton-Standard, $E = 3 \times 10^7$ psi

treatment, and that beryllium gives even higher damping.
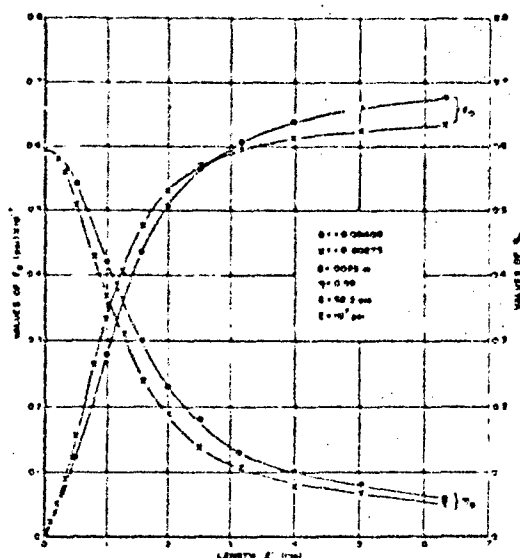
Figure 4. Equivalent free layer properties for 3M-428 with various thicknesses of aluminum backing material ($76°F$)
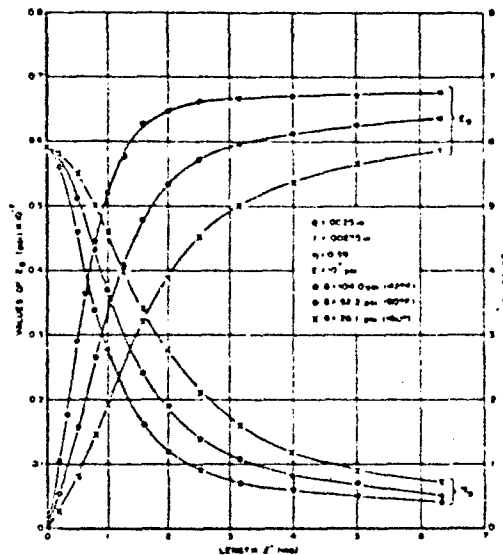
Figure 5. Equivalent free layer properties for 3M-428 at various temperatures

Modal Characteristics of Structure

This particular investigation is

concerned with the use of a multi-layer alternatily anchored damping treatment to damp resonant vibrations of a typical element of a skin-stringer structure. A wide variety of such structural configurations is utilized in the aerospace industry. The structure shown in Figures 7 and 8 is representative of the five bay test specimens used in this investigation.

Figure 6. Values of $\eta_D E_D$ for 3M-428 with various backing materials

Figure 7. Overall geometry of structural specimen

It has been shown [2, 3] that the normal modes of this type of structure fall in frequency bands, each of which is bounded on the low side by a mode in which the stringers predominantly twist, known as the stringer twisting mode, and on the high side by a mode in which the stringers mainly bend, known as the stringer bending mode.
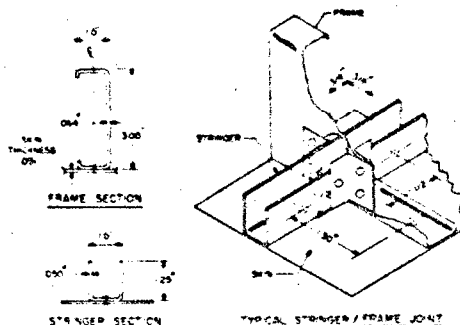
Figure 8. Detail geometry of structural specimen

When the assumption is made that the edge conditions along the frame rivet lines are simple supports, then these normal modes can be represented as:

$$W = \phi_n(x) \sin \frac{m \pi y}{\ell}$$

In the particular geometry tested, the ratio of the distance between frames to the distance between stringers was about 2.2, so that the lowest band of modes (m = 1, n = 1, 2, 3,4, 5), generally characterized by the absence of nodal lines within any of the bays of the structure, is reasonably well separated in frequency from the other bands (e.g. the m = 2, n = 1, 2, 3, 4, 5 band having one nodal line down the structure centerline parallel to the frames and the m = 1, n = 6, 7, 8, 9, 10 band having nodal lines parallel to the stringers along the center of each bay). This is not always the case, as it is possible with higher ratios of frame spacing to stringer spacing to have frequency bands, such as the m = 1, n = 1-5 band and the m = 2, n = 1-5 band, which overlap.

The subsequent analysis and experimental investigation was confined to damping of the symmetric modes in the first frequency band and no attempt was made to consider damping of the higher modal bands. It is certain, however, that these higher modal bands could also be damped by proper placing of the damping treatment.

The structure considered in the analysis was idealized as one having end conditions identical to the other stringers even though the actual structure was somewhat different. The m = 1, n = 1, 3, 5 modes and their partial derivatives, as calculated by the Transfer Matrix technique are shown in Figures 9 to 11,

34

along with the calculated resonant
frequencies [4].
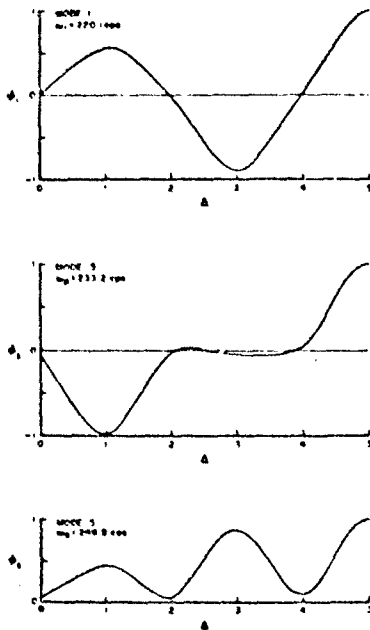
Figure 9. Theoretical mode
shapes $\phi_n(\Delta)$
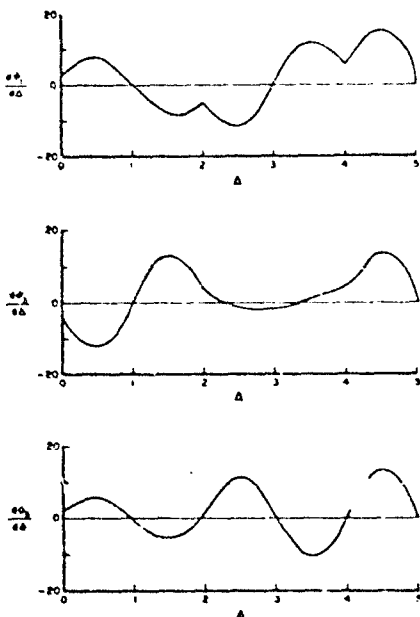
Figure 10. Theoretical values
of $\phi_n'(\Delta)$
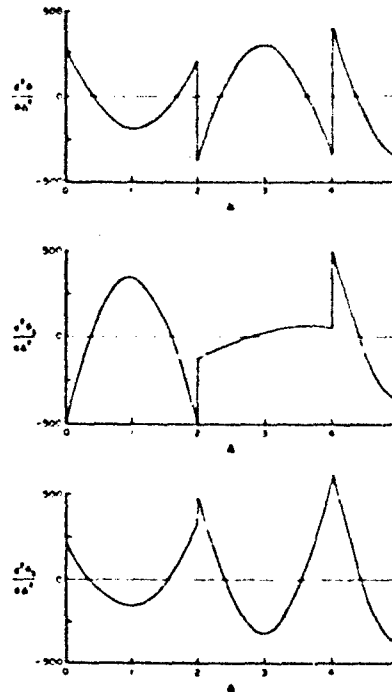
Figure 11. Theoretical values
of $\phi_n''(\Delta)$

Elastic Strain Energy in Damped Skin-Stringer Structure

Let the structure vibrate in a mode
$W = \phi_n(\Delta) \sin(\pi\delta)$ where $\Delta = x/L$ and
$\delta = y/\ell$ and the function $\sin(\pi\delta)$ repre-
sents the mode shape in the y-direction
and is assumed not to vary with mode
number n. As a concrete example, let
the structure consist of five identical
bays with six equally spaced stringers,
which are all assumed to be of identical
geometry. The frames are assumed to be
rigid and the transverse displacements
at the frames are taken to be zero.
Pinned edge conditions are assumed at
the frames, although the experimental
end conditions appear to lie somewhere
between the pinned and clamped end con-
ditions. Figures 7 and 8 show the panel
dimensions and structural details. The
total strain energy in the damped struc-
ture is:

$$U_{sn} = U_{pn} + \sum_{j=1}^{6} U_{snj} + U_{REG\ II} \qquad (5)$$

where U_{pn} is the strain energy stored in
the panel skin, U_{snj} is the strain energy
stored in the j th stringer and $U_{REG\ II}$
is the strain energy stored in the damp-
ing treatment, which occupies a part of

35

the surface of the panel. The strain energy in the frame is assumed to be zero. A viscoelastic damping treatment is added to a central area of each bay (REG II) and the remainder of the panel (REG I) is left uncovered. Equation (5) includes the elastic strain energy stored in the damping treatment. For the damping treatments considered in this paper, the area referred to as REG II will be small in comparison with the total surface area of the panel and will be located at the center of each bay. The location and size of REG II is not essential to the analysis of the strain energies, provided that it is small in relation to the total panel area so that the analysis will be applicable.

(a) Strain Energy U_{pn} in Panel Skin

An expression for the strain energy stored in a panel has been given by Timoshenko [5]:

$$U_{pn} = \frac{D}{2} \int_0^\ell \int_0^L \left\{ (W_{xx} + W_{yy})^2 \right.$$
$$\left. -2(1-\nu)[W_{xx}W_{yy}-W_{xy}^2] \right\} \, dx\,dy \qquad (6)$$

substituting $x/L = \Delta$ and $y/\ell = \delta$ and simplifying:

$$U_{pn} = \frac{D\ell L}{2} \int_0^1 \int_0^1 \left\{ \frac{1}{L^4} W_{\Delta\Delta}^2 + \frac{1}{\ell^4} W_{\delta\delta}^2 \right.$$
$$+ \frac{2\nu}{\ell^2 L^2} W_{\Delta\Delta} W_{\delta\delta}$$
$$\left. + \frac{2(1-\nu)}{\ell^2 L^2} W_{\Delta\delta}^2 \right\} \, d\Delta\,d\delta \qquad (7)$$

Since $W = \phi_n(\Delta) \sin(\pi\delta)$ for the particular panel under investigation, equation (7) yields:

$$U_{pn} = \frac{D\ell}{4L^3} \left\{ \int_0^1 \{[\phi_n''(\Delta)]^2 \right.$$
$$+ \frac{\pi^4 L^4}{\ell^4} [\phi_n(\Delta)]^2\} d\Delta$$
$$- \int_0^1 \frac{2\pi^2 L^2 \nu}{\ell^2} \phi_n(\Delta) \phi_n''(\Delta) d\Delta$$
$$\left. + \int_0^1 \frac{2\pi^2 L^2 (1-\nu)}{\ell^2}[\phi_n'(\Delta)]^2 d\Delta \right\} \qquad (8)$$

Integration of the second term in Equation (8) by parts yields:

$$U_{pn} = \frac{D\ell}{4L^3} \int_0^1 \{[\phi_n''(\Delta)]^2$$
$$+ \frac{\pi^4 L^4}{\ell^4} [\phi_n(\Delta)]^2$$
$$+ \frac{2\pi^2 L^2}{\ell^2} [\phi_n'(\Delta)]^2\} d\Delta \qquad (9)$$

Evaluating the constants in equation (9) in in-lb-sec units gives:

$$U_{pn} = .01152 \left[\int_0^1 \{[\phi_n''(\Delta)]^2 \right.$$
$$+ 3272 [\phi_n(\Delta)]^2$$
$$\left. + 112.0[\phi_n'(\Delta)]^2\} \, d\Delta \right] \qquad (10)$$

A numerical evaluation of the integrals involved in Equation (10) is given in Appendix A.

(b) Strain Energy in the Stringers

The strain energy in a stringer has been evaluated by Lin [6]:

$$U_{snj} = \frac{E}{2} \left[C_{ws} \int_0^\ell (W_{xyy})^2 dy \right.$$
$$+ I_n \int_0^\ell (W_{yy})^2 dy \left. \right]$$
$$+ \frac{GC}{2} \int_0^\ell (W_{xy})^2 dy \qquad (11)$$

where the subscript j refers to the j th stringer. Performing the indicated operations on W and simplifying yields:

$$U_{snj} = \frac{\pi^4 E C_{ws}}{2L^2\ell^3} \int_0^1 [\phi_n'(\Delta_j)]^2 \sin^2 \pi\delta \, d\delta$$
$$+ \frac{\pi^4 EI_n}{2\ell^3} \int_0^1 [\phi_n(\Delta_j)]^2 \sin^2 \pi\delta \, d\delta$$
$$+ \frac{\pi^2 GC}{2\ell L^2} \int_0^1 [\phi_n'(\Delta_j)]^2 \cos^2 \pi\delta \, d\delta$$

36

$$U_{snj} = \frac{EC_{ws}\pi^4[\phi_n'(\Delta_j)]^2}{4L^2\ell^3}$$

$$+ \frac{\pi^4 EI_n[\phi_n(\Delta_j)]^2}{4\ell^3}$$

$$+ \frac{\pi^2 GC[\phi_n'(\Delta_j)]^2}{4\ell L^2} \qquad (12)$$

For the panel used in this investigation, data was available [4] for the numerical values:

$E = 10^7$ lb/in^2

$L = 32.5$ in

$\ell = 13.5$ in

$h = .05$ in

$\nu = 1/3$

$C = 1.42 \times 10^{-4}$ in^4

$C_{ws} = 1.3825 \times 10^{-2}$ in^6

$I_n = 3.953 \times 10^{-2}$ in^4

$G = 3.76 \times 10^6$ lb/in^2

Evaluating the constants, the equation for U_{snj} becomes:

$$U_{snj} = 1.387[\phi_n'(\Delta_j)]^2$$

$$+ 3912.5[\phi_n(\Delta_j)]^2 \qquad (13)$$

in in-lb-sec units.

(c) Strain Energy $U_{REG\ II}$ in the Equivalent Free Layer

Consider a free layer damping treatment covering an area REG II of the panel. Any other type of damping treatment which can be represented in terms of an equivalent free layer treatment can be analyzed in the same manner. The actual treatment considered in this paper is the alternately anchored multiple-band treatment proposed by Lazan and discussed in the analysis. This particular analysis assumes that the surface strain in the member is reasonably uniform over the treatment area and that the treatment thickness is small compared to the panel thickness. The first assumption should be met as long as REG II is small in comparison with the panel dimensions in the direction of primary strain. The second assumption is used for the sake of simplicity so that each layer of the damping

treatment may be considered to be the same distance from the neutral axis and is therefore subjected to the same maximum total strain. There will be no appreciable change in the distance from the neutral axis for four layers or less of the 3M-428A tape used in the tests. Some effect may be noticeable for five or six layers but it should still be small. High equivalent free layer modulus values are developed only in the direction of primary strain (perpendicular to the stringers for the present investigation) and the modulus values in the other direction, parallel to the stringers, will be several orders of magnitude less. Since the flexure is also small in the transverse direction for the modes in question, there is little loss of accuracy in ignoring the energy dissipated or stored due to two-dimensional flexure in the damping treatment. Therefore:

$$U_{REG\ II} = \frac{1}{2} D_{II} \int\int_{REG\ II} (W_{xx})^2 \, dx \, dy$$

$$- \frac{1}{2} D \int\int_{REG\ II} (W_{xx})^2 \, dx \, dy \qquad (14)$$

where D_{II} is the flexural rigidity of the plate/damping layer combination allowing for the shift of the neutral axis and D is the flexural rigidity of the undamped panel about the center of the skin thickness.

(d) Total Strain Energy in the Damped Structure

If an equivalent free layer treatment is added to the structure, Equation (5) may now be written:

$$U_{sn} = \frac{D\ell H_n}{4L^3} + \sum_{j=1}^{6} U_{snj}$$

$$+ \frac{D_{II}}{2} \int\int_{REG\ II} W_{xx}^2 \, dx \, dy$$

$$- \frac{D}{2} \int\int_{REG\ II} W_{xx}^2 \, dx \, dy \qquad (15)$$

where

$$D_{II} = \frac{EI}{1-\nu^2} + \frac{E_D I_D}{1-\nu_D^2} \qquad (16)$$

and

$$H_n = \int_0^1 \left\{ [\phi_n''(\Delta)]^2 + \frac{\pi^4 L^4}{\ell^4}[\phi_n(\Delta)]^2 \right.$$

$$\left. + \frac{2\pi^2 L^2}{\ell^2}[\phi_n'(\Delta)]^2 \right\} d\Delta \qquad (17)$$

If $W = \phi_n(\Delta) \sin(\pi\delta)$ as before; the expression for U_{sn} can be rewritten as:

$$U_{sn} = \frac{D\ell H_n}{4L^3} + \sum_{j=1}^{6} U_{snj}$$

$$- \frac{D\ell}{2L^3} \int\int_{REG\ II} [\phi_n''(\Delta)]^2 \sin^2 \pi\delta\, d\Delta d\delta$$

$$+ \frac{D_{II}\ell}{2L^3} \int\int_{REG\ II} [\phi_n''(\Delta)]^2 \sin^2 \pi\delta\, d\Delta d\delta \qquad (18)$$

An expression for D_{II} which includes the effect of the shift of the neutral axis of the panel due to the damping treatment has been developed in Reference [7]:

$$D_{II} = \frac{Eh^3 A}{24(1-\nu^2)} + \frac{E_D h^3 B}{24(1-\nu_D^2)} \qquad (19)$$

where

$$e = E_D/E \qquad (20)$$

and

$$A = \frac{(1-N^2 e)^3 + [1+(2N+N^2)e]^3}{(1+N\ e)^3} \qquad (21)$$

$$B = \frac{(2N+1+N^2 e)^3 - (1-N^2 e)^3}{(1+N\ e)^3} \qquad (22)$$

where N = ratio of the equivalent damping layer thickness to panel thickness (h).

So that:

$$U_{sn} = \frac{Eh^3 \ell H_n}{48L^3(1-\nu^2)} + \sum_{j=1}^{6} U_{snj} +$$

$$+ \frac{Eh^3\ell}{48L^3(1-\nu^2)}[A-2] \int\int_{REG\ II} [\phi_n''(\Delta)]^2 \sin^2 \pi\delta d\Delta d\delta$$

$$+ \frac{BE_D h^3\ell}{48L^3(1-\nu_D^2)} \int\int_{REG\ II} [\phi_n''(\Delta)]^2 \sin^2 \pi\delta d\Delta d\delta \qquad (23)$$

Energy Dissipated in the Equivalent Free Layer Treatment

Consider a beam section of unstretched length $\lambda L/J$ (where J is the number of spans and λ is the ratio of equivalent free layer treatment length to span length in the x direction) and assume the radius of curvature in the x direction is constant over the treatment area (See Fig. 12). Consider a fiber within the viscoelastic material some distance z from the neutral axis.
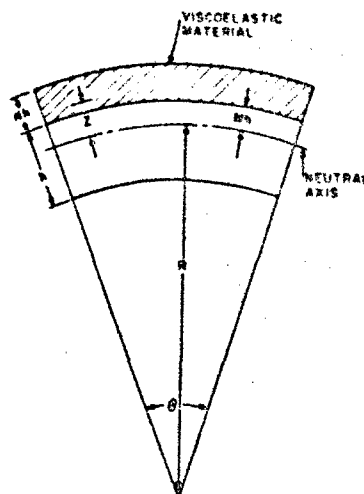
Figure 12. Deformation of element of free layer treatment

The elongation of this fiber is readily shown by elementary bending theory to be:

$$X = \frac{z\lambda L}{J} W_{xx} \qquad (24)$$

Considering the fiber as a stretched spring, the spring stiffness is given by

$$k = E_D \frac{area}{length} = \frac{E_D (\delta\ell)\delta z}{\lambda L/J} \qquad (25)$$

38

where δz is an incremental value of z and β is the ratio of the width of the treatment to the width of the span in the y direction. The extensional work done per cycle which equals the energy dissipated per cycle in a spring of stiffness k, loss factor η_D, and displacement X is [7]:

$$\delta D_{Dn} = \pi \eta_D X^2 k \qquad (26)$$

where δD_{Dn} is the portion of the energy dissipated per cycle for one fiber. Substituting Eq (24) and (25) into Eq (26) and further assuming that the curvature varies slowly the treatment length L' we have

$$\delta D_{Dn} = \pi E_D \left[\frac{\lambda \beta}{J}\right](L\ell \eta_D)(z^2 \delta z)\overline{W_{xx_i}^2} \qquad (27)$$

where

$$\overline{W_{xx_i}^2} = \frac{J}{\lambda L \delta \ell} \int\int_{\text{REG II}_i} W_{xx}^2 \, dxdy$$

is the average W_{xx}^2 in REG II_i, the portion of REG II in span i. Integrating both sides of the equation over the thickness and letting $J = 5$ results in

$$D_{Dn} = \sum_{i=1}^{5} \pi E_D \left[\frac{\lambda \beta}{J}\right] L\ell \eta_D \overline{W_{xx_i}^2} \int_{Mh}^{(M+N)h} z^2 dz \qquad (28)$$

where the symbol $\sum_{i=1}^{5}$ is used to indicate that the value of D_{Dn} must be determined for each span and added to give the total energy dissipated and Mh is the distance of the neutral axis from the common surface. Recognizing that $W = \phi_n(\Delta)\sin\pi\delta$ in the n th mode, Eq (28), in the case of panels, reduces to

$$D_{Dn} = \sum_{i=1}^{5} \frac{\pi E_D \lambda \beta L \ell \eta_D}{JL^4(1-\nu_D)^2}$$
$$\left[[\phi_n''(\Delta)]^2 \sin^2\pi\delta\right]\int_{Mh}^{(M+N)h} z^2 dz \qquad (29)$$

The integral in the above equation has been evaluated [7] so that:

$$D_{Dn} = \sum_{i=1}^{5} \frac{\pi E_D h^3 \lambda \beta \ell \eta_D B[\phi_n''(\Delta)]^2 \sin^2\pi\delta}{24L^3(1-\nu_D^2)J} \qquad (30)$$

Since the curvature in the y direction and the treatment width in the y direction are both small, the above analysis is valid for a panel, particularly in view of the low stiffness of the treatment in the y direction compared with that in the x direction.

Effective System Loss Factors

A parameter generally considered in damping analysis is the system loss factor η_{sn}, defined as:

$$\eta_{sn} = \frac{D_{sn}}{2\pi U_{sn}} \qquad (31)$$

where D_n is the total energy dissipated within the structure per cycle and U_{sn} is the total energy stored [8]. The energy dissipated within the structure can be represented as

$$D_{sn} = D_{Dn} + D_{on} \qquad (32)$$

It is frequently difficult to determine D_{on}, the energy dissipated in the nominally undamped structure, so it is convenient to define a new damping parameter η_{sn}' where

$$\eta_{sn}' = \frac{D_{Dn}}{2\pi U_{sn}} \qquad (33)$$

Rewriting Eq (31) as

$$\eta_{sn} = \frac{D_{on}}{2\pi U_{on}}\left[\frac{U_{on}}{U_{sn}}\right] + \frac{D_{Dn}}{2\pi U_{sn}} \qquad (34)$$

It is now seen that η_{sn}' is related to η_{sn} by

$$\eta_{sn} = \eta_{on}(U_{on}/U_{sn}) + \eta_{sn}' \qquad (35)$$

where η_{on} can be determined using experimental data as described later.

The theoretical value of η_{sn}' can be calculated by substituting Eq (30) and Eq (23) into (Eq (33).

$$\eta_{sn}' = \sum_{i=1}^{5} \frac{E_D h^3 \lambda \beta \ell \eta_D B[\phi_n''(\Delta)]^2 \sin^2\pi\delta}{48L^3(1-\nu_D^2)J\Psi}$$

where Ψ is defined as:

39

$$\Psi = \frac{Eh^3 \ell H_n}{48L^3(1-\nu^2)} + \frac{Eh^3 \ell (A-2)}{48L^3(1-\nu^2)} \{\zeta_n\}$$

$$+ \frac{BE_D h^3 \ell}{48L^3(1-\nu_D^2)} \{\zeta_n\} + \sum_{j=1}^{6} U_{snj} \qquad (36a)$$

where

$$\zeta_n = \int\int_{\text{REG II}} [\phi_n''(\Delta)]^2 \sin^2 \pi \delta\, d\Delta d\delta \qquad (37)$$

and H_n is given by Eq (17). Dividing numerator and denominator by $E_D h^3 \ell / 48L^3 (1-\nu_D^2)$ and simplifying,

$$\frac{n'_{sn}}{n_D} = \frac{\sum\limits_{i=1}^{5} [\phi_n''(\Delta)]^2 [\sin^2 \pi \delta](\frac{\lambda\beta}{J}) B}{\left\{ \frac{x H_n}{e} + \frac{48L^3(1-\nu_D^2)}{E_D h^3 \ell} \cdot \frac{D}{\sum\limits_{j=1}^{6} U_{snj}} \right.}$$

$$\left. + [B + \frac{X}{e}(A-2)]\{\zeta_n\} \right\} \qquad (38)$$

where $x = (1-\nu_D^2)/(1-\nu^2)$ and $e = E_D/E$. Now, recognizing that

$$\zeta_n = \frac{\lambda\beta}{J} \sum_{i=1}^{5} \overline{[\phi_n''(\Delta)]^2 \sin^2 \pi \delta} \qquad (39)$$

and dividing both numerator and denominator by the numerator, Eq (38) reduces to

$$n'_{sn} = \frac{n_D}{\frac{X}{Be}(\frac{c_n}{\lambda\beta} + A-2) + 1} \qquad (40)$$

where

$$C_n = \frac{JH_n Eh^3 \ell + 48L^3 J(1-\nu^2)\sum\limits_{j=1}^{6} U_{snj}}{Eh^3 \ell \sum\limits_{i=1}^{5} [\phi_n''(\Delta)]^2 \sin^2 \pi \delta} \qquad (41)$$

The parameter C_n has been evaluated in Appendix B. It is seen that C_n is nearly independent of the mode but does depend on the coverage as in Figure 20. n'_{sn} will therefore be approximately the same for every mode provided n_D and E_D are independent of frequency. Minor variations will occur in practice as a result of n_D and E_D changing with frequency. A computer program was written

to evaluate Eq (40) for several configurations of damping tapes. Some results are plotted in Figures 13 - 14 for $\chi=1$.
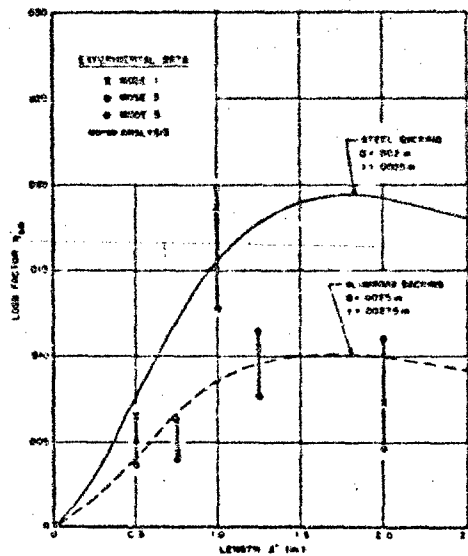
Figure 13. Theoretical and experimental variation of n'_{sn} with ℓ' for 3M-428 tape (3 layers)
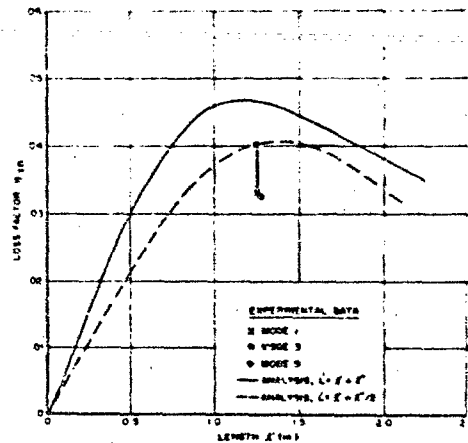
Figure 14. Theoretical and experimental variation of n'_{sn} with ℓ' for 3M-428 with Bo/Aℓ backing (6 layers)

The parameter n'_{sn} physically represents the actual damping factor only if the structure has no inherent damping. It could be used as a first order approximation to the damping factor in structures where the inherent structural

40

damping was known to be low, for example in the vacuum of outer space, or it could be used in conjunction with Eq (35) to determine the actual damping factor as defined by Lazan. The ratio of U_{on} to U_{an} has been evaluated in Appendix C and is found to be very close to unity, varying from about 0.85 to 0.99.

EXPERIMENTAL INVESTIGATION

The experimental portion of this investigation was conducted with the equipment shown in Figure 15.
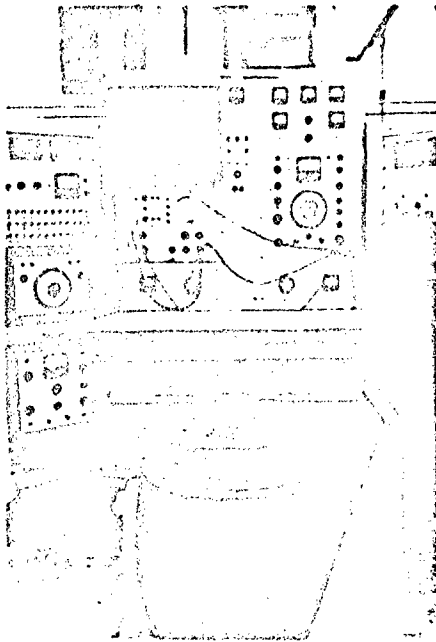
Figure 15.   Overall view of experimental apparatus

A skin-stringer-frame specimen, such as shown in Figures 7 and 8, was attached to a fixture which consisted of two aluminum I-beams connected at their flanges with 1/2 inch aluminum plates. Although the fixture was assumed to be rigid, it was carefully tested to insure that no fixture resonances existed in the frequency range of interest for the panel (200-300 cps). The specimen-fixture combination was mounted on the table of a 1200 force pound electromagnetic shaker.

Input acceleration was controlled with an accelerometer mounted on top of one of the frames. Control accelerometer location was selected to minimize variations in the input acceleration

along the frames. Panel response was measured using a 0.5 gram micro-miniature piezoelectric accelerometer placed in various positions on the vibrating panel. The 0.5 gram accelerometer was considered to be about the heaviest which could be used on this panel and still have negligible mass loading effects on the specimen mode shapes and frequencies [4]. Signal conditioning of the accelerometer output signal was accomplished by using an accelerometer amplifier with a metered output calibrated to read acceleration directly in g's. The response of the panel was measured at various positions, both undamped and with various damping configurations consisting of alternate layers of metallic backing material and viscoelastic damping material one inch wide. Configurations tested had half inch or one inch anchored ends ℓ" and 0.5, 0.75, 1.25, and 2.0 inches of viscoelastic material ℓ' and both aluminum ($E=10^7$ psi) and boron-aluminum (Bo/Aℓ) or steel ($E = 3 \times 10^7$ psi) backing. Anchoring at the ends was effected with Eastman 910 adhesive. The treatment was applied with the longer dimension perpendicular to the stringers.

Since most viscoelastic materials are temperature dependent and the damping mechanism utilized was one of energy dissipation as heat, a thermocouple was installed within the viscoelastic material and the temperature monitored in all three modes. Temperature variations with frequency were negligible with respect to the room temperature variations of 3-5°F. To all intents and purposes, temperature was constant throughout this investigation.

Initially, acceleration amplitude measurements were taken in both the transverse (y) and longitudinal (x) directions and the mode shapes so determined are shown in Figure 16 and 17.
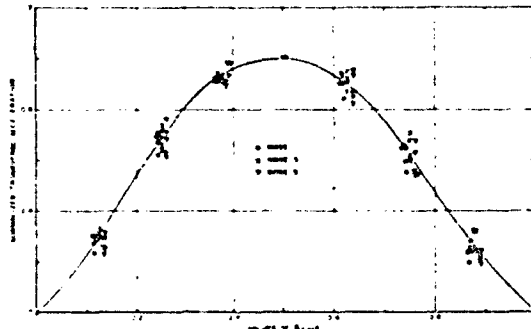
Figure 16.   Measured transverse mode shapes for undamped panel

41

It was determined that the mode shape in the transverse direction remained constant within the limits of experimental error, for all five bays, and all mode shapes, both damped and undamped. The transverse normal mode shape was approximately a half sine wave as shown in Figure 16. The transverse mode shape did tend to flatten near the frames (at $y = 0$ and $y = \ell$), but it did not depart greatly from the assumed sine form. Measured longitudinal mode shapes of the panel damped with three alternately anchored layers of 3M-428A tape are shown in Figure 18, and mode shapes for the panel damped with a similar configuration of six layers of boron reinforced aluminum constraining layers and 3M-428 adhesive are shown in Figure 19.

to predict η'_{sn} from energy calculations based on the theoretical mode shapes.
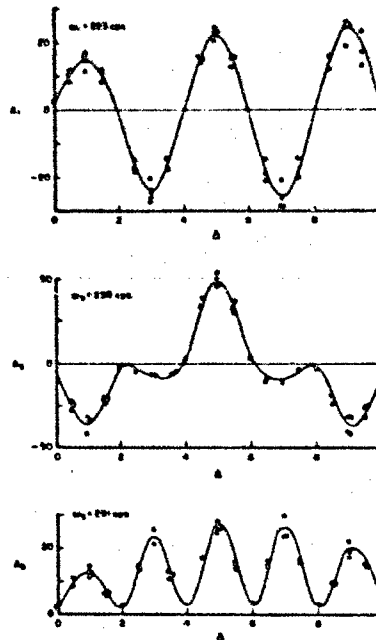
Figure 18. Typical measured mode shapes for damped panel with 3M-428A tape (3 layers), $\ell' = 0.75"$

Figure 17. Measured longitudinal mode shapes for undamped panel

There was appreciable scatter, about $\pm 10\%$, in the measurements for the undamped panel and similar scatter in the damped panel measurements. One source of the observed scatter was probably the micro-miniature accelerometer. Observed acceleration values showed a dependence on the exact position of the accelerometer on the panel and the location of the accelerometer lead.

A comparison of the theoretical mode shapes in Figure 9 with the measured mode shapes for the undamped and damped panels in Figure 17-19 gives an indication of the accuracy of the analysis used

It can be seen that the theoretical and measured undamped mode shapes agree reasonably well, the largest variation occurring in the second and fourth spans for mode 3. In addition, the measured mode shapes for the panel damped with three layers of 3M-428A tape are in reasonable agreement with the undamped measurements. However, the influence of the heavier and stiffer six layer (Bo/Aℓ) configuration on the mode shapes can be seen in Figure 19.

Typical experimentally determined values of η'_{sn} are compared with the theoretical predictions in Figure 13 and 14. These values of η'_{sn} are calculated from the relationship, derived from equations (35) and (D15),

$$\eta'_{sn} = \frac{\alpha_n \phi_n(\Delta)}{A_n(\Delta)} - \eta_{on}\left[\frac{U_{on}}{U_{sn}}\right] \qquad (42)$$

where α_n and $\phi_n(\lambda)$ are calculated from measured mode shapes of the undamped structure based on the response measurements presented in Figure 17 with the assumption that the mode shape in the

42

transverse direction is a half sine wave. $A_n(\Delta)$ is the observed amplification factor for the damped panel as plotted against Δ in Figures 18 and 19.
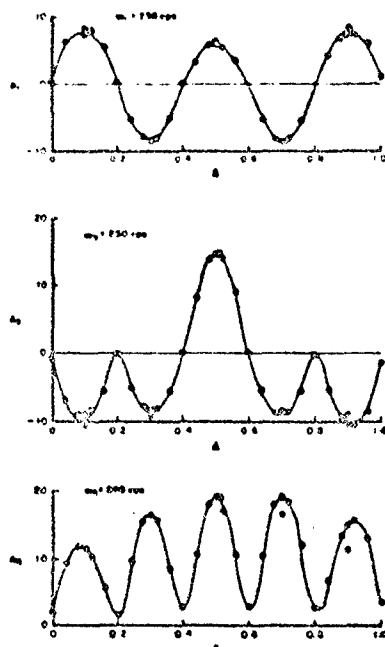
Figure 19. Measured mode shapes for damped panel with 3M-428 adhesive and Bo/Al backing (6 layers)

It should be noted that differences in the mode shapes caused by the damping treatment were neglected and $A_n(0.5)$ was used in each case. n_{on} was calculated from equation (D14) using the measured values of $A_n(0.5)$ for the undamped structure. U_{on}/U_{sn} was taken to be unity since the error introduced by this assumption (based on theoretical values of U_{on}/U_{sn} in Appendix C) is small compared to experimental scatter. Table 1 shows the values of parameters in Eq (42) used for determination of n'_{sn}.

DISCUSSION

Comparison between the theoretical predictions and the experimentally determined values of n'_{sn} shows that the theory was generally successful in predicting the amount of damping that could be expected from the application of a multi-layer alternately anchored damping treatment on this type of structure. It is noted that the theoretical analysis was more accurate for the cases in which the measured mode shapes agreed fairly

closely with the theoretical mode shapes. In mode 3, where the variation between theory and measurement was the greatest, the theory consistently predicted higher values of n'_{sn} than were observed experimentally. This seems reasonable, since if the experimental mode shape is normalized, the curvature in the first and fifth spans is lower than predicted. Thus the damping treatment experiences less strain than considered in the theory. Deviation between theory and experiment for the six layer Bo/Al configuration can be explained, in part, by the fact that the mode shapes changed due to the addition of the damping treatment.

As previously discussed, the theory in this paper is based on the assumption that $L' = \ell' + \ell''$, or that the constraining layer is rigid in the anchor area and that shear deformation occurs in the structural adhesive, as shown in Figure 2. Actually this is one of the limiting cases considered by Lazan et al [1]. The other limiting case is when the structural adhesive is considered to be rigid in shear and the constraining layers, in the anchor, strain the same as the structure. In this latter case $L' = \ell'$. Experimental measurements [1] indicate that $L' = \ell' + \ell''/2$ might be a more valid assumption (i.e. the point of effective anchoring, or undistorted normal plane, is midway between the inside edge of the anchor and the center of the anchor). The effect of making this assumption on the six layer Bo/Al data is shown by the dashed line in Figure 14, with a resulting increase of correlation between theory and experiment.

SUMMARY AND CONCLUSIONS

It has been shown that effective analysis of a multi-layer alternately anchored damping treatment applied to a skin-stringer structural element, can be accomplished using the concept of an equivalent free layer damping treatment and energy calculations based on mode shapes generated by a transfer matrix analysis. Numerical results have been presented demonstrating the effects of changes in constraining layer stiffness, adhesive thickness, temperature, and length for a damping treatment utilizing a commercially available damping adhesive. Furthermore, properly optimized and appropriately located on the structure, this type of damping treatment can give significant damping for very small addition of weight. In the case considered for the six layer boron/aluminum configuration, structural loss factors were increased by about 0.04 with 3 grams of damping treatment per span or

43

about 1.5% increase in the weight of the skin. This means that resonant amplification factors for the lightly damped modes in the untreated structure were reduced by a factor of about five.

REFERENCES

1. Lazan, B. J., Metherell, A. F. and Sokol, G., "Multiple Band Surface Treatments for High Damping", Air Force Materials Laboratory Report AFML-TR-65-269 (WPAFB, Ohio, 1965).

2. Lin, Y. K., Brown, I. D. and Deutschle, P. C., "Free Vibrations of a Finite Row of Continuous Skin-Stringer Panels", J. Sound Vib., 1, 14 (1964).

3. Mercer, C. A. and Seavey, C., "Prediction of Natural Frequencies and Normal Modes of Skin-Stringer Panel Rows", Air Force Materials Laboratory Report AFML-TR-67-234 (WPAFB, Ohio, 1967).

4. McDaniel, T. J., "Vibration of a Stringer-Panel Structure with Mass Loading, Part I. Transfer Matrix Analysis", Air Force Materials Laboratory Report AFML-TR-68-294, Part I (To Be Published).

5. Timoshenko, S. and Woinowsky - Krieger, S., Theory of Plates and Shells, McGraw-Hill Book Co., N. Y. (1959).

6. Lin, Y. K., "Free Vibration of Continuous Skin-Stringer Panels", J. Appl. Mechanics, 27, pp. 669-776 (1960).

7. Jones. D. I. G., "Some Aspects of the alysis of Damping and Vibration in Simple Structures", Air Force Materials Laboratory Report, AFML-TR-65-151 (WPAFB, Ohio, 1965).

8. Lazan, B. J., Damping of Materials and Members in Structural Mechanics, Pergamon Press, N. Y., (1968).

Appendix A

NUMERICAL RESULTS

Consider the numerical evaluation of U_{pn} and U_{snj} based on an assumed mode normalized at the center of the panel ($\Delta = .5$). Actual energy values would have to be factored by the proper number to reflect true displacements. Curves of $\phi_n(\Delta)$, $\phi'_n(\Delta)$, and $\phi''_n(\Delta)$ are plotted in Figures 9 to 11 based on calculations using a Transfer Matrix Technique [4]. The data only includes five points for each bay so that the curves are somewhat approximate. Specific integrals involved in the present analysis are given in Table 2.

It would be possible to determine numerical values for U_{pn} based on a one inch displacement at the center of the panel if desired; however, that figure is not a particularly useful parameter in this analysis, so only the ratios of energies will be considered. The same curves are used to evaluate U_{snj}, and Table 3 shows the values used in the evaluation of U_{snj}.

TABLE 1
TABLE 1
Measured Data for Undamped Structure

Mode n	1	3	5
α_n	0.228	0.599	2.08
$A_n(.5)$	37	69	30
η_{on}	0.0061	0.0087	0.0693

TABLE 2
Data for Theoretical Modes

Mode n	1	3	5
$\int_0^1 \phi_n^2(\Delta)d\Delta$	0.280	0.258	0.245
$\int_0^1 [\phi_n'(\Delta)]^2 d\Delta$	67.?	58.5	50.0
$\int_0^1 [\phi_n''(\Delta)]^2 d\Delta$	36,500	39,430	45,888
U_{on}/U_{sn} (N = .16)	.990	.990	.989
U_{on}/U_{sn} (N = .32)	.973	.973	.971
U_{on}/U_{sn} (N = .48)	.950	.950	.948
U_{on}/U_{sn} (N = .64)	.923	.924	.920
U_{on}/U_{sr} (N = .80)	.890	.893	.888
U_{on}/U_{sn} (N = .96)	.853	.855	.849

Appendix B

EVALUATION OF C_n

The equation for C_n is

$$C_n = \frac{JH_n}{\sum_{i=1}^{5} [\phi_n''(\Delta)]^2 \sin^2 \pi \delta} + \frac{48L^3 J(1-\nu^2) \sum_{j=1}^{6} U_{snj}}{Eh^3 \ell \sum_{i=1}^{5} [\phi_n''(\Delta)]^2 \sin^2 \pi \delta} \qquad (B.1)$$

where the summations shown in the denominators are over the central regions of the panel only so the $\sin^2 \pi \delta$ terms can be dropped from the analysis since they are approximately 1 at the centers of each span. Using this approximation, the expression for C_n reduces to

45

$$C_n = \frac{5H_n}{\sum\limits_{i=1}^{5} \overline{[\phi_n^{\star}(\Delta)]^2}} + \frac{48L^3J(1-\nu^2)\sum\limits_{i=1}^{6} U_{snj}}{Eh^3\ell \sum\limits_{i=1}^{5} \overline{[\phi_n^{\star}(\Delta)]^2}}$$ (B.2)

Evaluating the constants and substituting Eq (13) gives:

$$C_n = \frac{5H_r}{\sum\limits_{i=1}^{5} \overline{[\phi_n^{\star}(\Delta)]^2}}$$

$$+ \frac{434}{\sum\limits_{i=1}^{5} \overline{[\phi_n^{\star}(\Delta)]^2}} \sum\limits_{j=1}^{6} \{1.387[\phi_n'(\Delta_j)]^2 + 3912.5[\phi_n(\Delta_j)]^2\}$$ (B.3)

Recognizing that H_n is the value of the integral in Eq (10) and taking the values from Table 3, it is possible to determine the values of C_n as below for $\lambda \ll 1$, $\beta \ll 1$.

$$C_1 = \frac{5(45195)}{400950} + \frac{434}{400950}(209.8) = 0.790$$ (B.4)

$$C_3 = \frac{5(47386)}{393675} + \frac{434}{393675}(184.6) = 0.808$$ (B.5)

$$C_5 = \frac{5(52409)}{420000} + \frac{434}{420000}(140) = 0.767$$ (B.6)

For other values of λ, $\beta \sum\limits_{i=1}^{5} \overline{[\phi_n^{\star}(\Delta)]^2}$ has to be evaluated numerically. Results of these evaluations are given in Figure 20.

TABLE 3
Numerical Values for the Strain Energy in the Stringers
Based on Theoretical Modes

	Stringer Number					
	1	2	3	4	5	6
$\phi_1(\Delta)$	0	0	0	0	0	0
$\phi_1'(\Delta)$	-2.4	5.14	-6.65	-6.65	5.14	-2.4
$1.387[\phi_1'(\Delta)]^2$	7.99	35.6	61.3	61.3	35.6	7.99
$\phi_3(\Delta)$	.045	.052	.045	.045	.052	.045
$2912.5[\phi_3(\Delta)]^2$	7.93	10.58	7.93	7.93	10.58	7.93
$\phi_3'(\Delta)$	4.4	-3.42	-4.05	-4.05	-3.42	4.4
$1.387[\phi_3'(\Delta)]^2$	26.8	16.2	22.8	22.8	16.2	26.8
$\phi_5(\Delta)$	.022	.069	.10	.10	.069	.022
$3912.5[\phi_5(\Delta)]^2$	1.89	18.6	39.12	39.12	18.6	1.89
$\phi_5'(\Delta)$	-2.1	-1.65	-0.61	-0.61	-1.65	-2.1
$1.387[\phi_5'(\Delta)]^2$	6.12	3.78	0.517	0.517	3.78	6.12

46
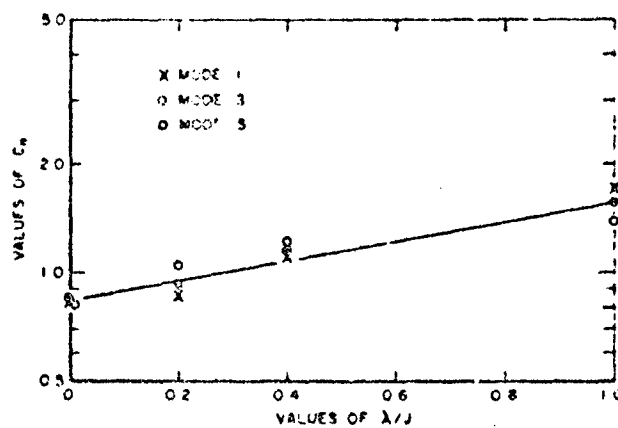
Figure 20. Variation of C_n with coverage

Appendix C

EVALUATION OF U_{on}/U_{sn}

U_{on} and U_{sn} are given by Eq (23) with and without REG II, respectively:

$$\frac{U_{on}}{U_{sn}} = \frac{\dfrac{Eh^3 \ell H_n}{48L^3(1-\nu^2)} + \sum_{j=1}^{6} U_{snj}}{\dfrac{Eh^3 \ell H_n}{48L^3(1-\nu^2)} + \sum_{j=1}^{6} U_{snj} + \dfrac{Eh^3 \ell (A-2)}{48L^3(1-\nu^2)}\{\zeta_n\} + \dfrac{BE_D h^3 \ell}{48L^3(1-\nu_D^2)}\{\zeta_n\}} \qquad (C.1)$$

where

$$\zeta_n = \int \int_{REG\ II} [\phi_n''(\Delta)]^2 \sin^2 \pi \delta\, d\Delta\, d\delta \qquad (C.2)$$

Dividing numerator and denominator by $Eh^3\ell/48L^3(1-\nu^2)$ and simplifying results in

$$\frac{U_{on}}{U_{sn}} = \frac{H_n + \dfrac{48L^3(1-\nu^2)}{Eh^3\ell}\sum_{j=1}^{6} U_{snj}}{H_n + \dfrac{48L^3(1-\nu^2)}{Eh^3\ell}\sum_{j=1}^{6} U_{snj} + (A-2+Be/\chi)\{\zeta_n\}} \qquad (C.3)$$

Now, again recognizing that

$$\zeta_n = \frac{\lambda B}{J} \sum_{i=1}^{5} \overline{[\phi_n''(\Delta)]^2 \sin^2 \pi \delta} \qquad (C.4)$$

and dividing numerator and denominator by ζ_n,

47

$$\frac{U_{on}}{U_{sn}} \approx \frac{C_n/\lambda\beta}{C_n/\lambda\beta + A-2 + \beta e/\chi} \tag{C.5}$$

Values of U_{on}/U_{sn} were calculated for several cases and are listed in Table 2.

Appendix D

RESPONSE OF THE SKIN STRINGER STRUCTURE ON THE SHAKER

Let the structure be made of a material of effective complex modulus $E(1+i\eta_o)$. Let $X_o \exp(i\omega t)$ be the input of the shaker at the frames where the frames are assumed to remain rigid and let $W(x,y) \exp(i\omega t)$ be the response of the panel relative to the frames so that a moving coordinate system is being considered. Expanding W as a series of normal modes results in

$$W(x,y) = \sum_n W_n \phi_n(x/L) \sin \pi y/\ell \tag{D.1}$$

The equation of motion becomes

$$D(1+i\eta_o)\nabla^4 W - \rho\omega^2[W + X_o] = 0 \tag{D.2}$$

or

$$D(1+i\eta_o)\nabla^4 W - \rho\omega^2 W = \rho\omega^2 X_o \tag{D.3}$$

and, for the n th normal mode,

$$D\nabla^4 \phi_n(\Delta)\sin\pi\delta = \rho\omega_n^2 \phi_n(\Delta)\sin\pi\delta \tag{D.4}$$

Substituting Eq (D.1) into Eq (D.2) results in

$$\nabla^4 \sum D(1+i\eta_{on}) W_n\phi_n(\Delta)\sin\pi\delta - \rho\omega^2 \sum W_n\phi_n(\Delta)\sin\pi\delta = \rho\omega^2 X_o \tag{D.5}$$

where η_{on} is the value of η_o appropriate to the n th mode. Expanding X_o as a series of normal modes also gives

$$X_o = \sum X_n\phi_n(x/L)\sin\pi y/\ell \tag{D.6}$$

$$\alpha_n = \frac{X_n}{X_o} = \frac{\displaystyle\int_o^1 \int_o^1 \phi_n(\Delta)\sin\pi\delta d\Delta d\delta}{\displaystyle\int_o^1 \int_o^1 [\phi_n(\Delta)]^2 \sin^2\pi\delta d\Delta d\delta} \tag{D.7}$$

Now, substituting Eq (D.6) into Eq (D.5) and using Eq (D.4),

$$\sum (1+i\eta_{on}) W_n\rho\omega_n^2\phi_n(\Delta)\sin\pi\delta - \rho\omega^2 \sum W_n\phi_n(\Delta)\sin\pi\delta =$$

$$= \rho\omega^2 \sum X_n\phi_n(\Delta)\sin\pi\delta \tag{D.8}$$

48

and performing a term by term comparison,

$$(1+i\eta_{on})\rho\omega_n^2 W_n - \rho\omega^2 W_n = \rho\omega^2 X_n \qquad (D.9)$$

therefore,

$$W_n = \frac{\alpha_n X_o (\omega/\omega_n)^2}{1+i\eta_{on} - (\omega/\omega_n)^2} \qquad (D.10)$$

and using Eq (D.1),

$$W = X_o \sum_n \frac{\alpha_n (\omega/\omega_n)^2 \phi_n(\Delta)\sin\pi\delta}{1+i\eta_{on} - (\omega/\omega_n)^2} \qquad (D.11)$$

The actual displacement at any point is $U = W + X_o$, and

$$U = X_o \left[1+\frac{W}{X_o}\right] = X_o [1+\sum_n \frac{\alpha_n (\omega/\omega_n)^2 \phi_n(\Delta)\sin\pi\delta}{1+i\eta_{on} - (\omega/\omega_n)^2}] \qquad (D.12)$$

and since both U and X_o are harmonic functions of time, and $\ddot{U}$ and $\ddot{X}_o$ are the output and input accelerations as would be measured by an accelerometer:

$$\frac{U}{X_o} = \frac{\ddot{U}}{\ddot{X}_o} = 1+\sum_n \frac{\alpha_n (\omega/\omega_n)^2 \phi_n(\Delta)\sin\pi\delta}{1+i\eta_{on} - (\omega/\omega_n)^2} \qquad (D.13)$$

If η_{on} is much less than 1, then resonance occurs at $\omega = \omega_n$, the undamped resonant frequency. The amplification factor for the undamped panel at resonance can then be expressed as

$$A_n(\Delta) = \left|\frac{\ddot{U}}{\ddot{X}_o}\right| = \left| 1 + \frac{\alpha_n\phi_n(\Delta)\sin\pi\delta}{i\eta_{on}} \right| = \frac{\alpha_n\phi_n(\Delta)\sin\pi\delta}{\eta_{on}} \qquad (D.14)$$

since $\dfrac{\alpha_n\phi_n(\Delta)\sin\pi\delta}{\eta_{on}}$ is much greater than 1. When the amplification factor at the

center of a panel is considered, the sine term in Eq (D.14) can be dropped since it will be one. If additional damping is added to the structure, Eq (D.14) becomes

$$A_n(\Delta) = \frac{\alpha_n\phi_n(\Delta)}{\eta_{sn}} \qquad (D.15)$$

SYMBOLS

A   Dimensionless parameter, see equation (21)

$A_n(\Delta)$ Resonant amplification factor, see equation (D15)

a   Thickness of damping material (in)

a $\sqrt{2}$ Bo cos $\delta/2$, where $\delta = \tan^{-1}\eta$

B   Dimensionless parameter, see equation (22)

B_o Dimensionless parameter, see equation (4)

b $\sqrt{2}$ Bo sin $\delta/2$, where $\delta = \tan^{-1}\eta$

C   Uniform torsion constant of stringer cross section (in^4)

C_n Dimensionless parameter, see equation (41)

C_{ws} Warping constant of stringer cross section with respect to axis in outer surface of skin (in^6)

49

D Bending stiffness for skin $Eh^3/12(1-\nu^2)$ (lb-in)

D_{II} Bending stiffness of panel in region II with damping treatment applied

D_{Dn} Energy dissipated per cycle in damping treatment (lb/in)

D_{sn} Total energy dissipated per cycle in the damped structure (lb/in)

D_{on} Energy dissipated in the untreated structure (lb/in)

E Young's modulus of structural material (psi)

E_D Storage modulus of the equivalent free layer damping treatment (psi)

e E_D/E

G Shear modulus of the stringer material (psi)

H_n Dimensionless parameter, see equation (16)

h Thickness of the panel skin (in)

I_D Moment of inertia of equivalent free layer damping treatment about the neutral axis of the panel (in⁴)

I_n Moment of inertia of stringer about centroidal axis (in⁴)

J Number of spans

k Stiffness or spring constant (lb/in)

k_j' Storage constant for the j th band-adhesive unit (ratio of in-phase component of force to displacement) (lb/in)

k_j'' Loss constant for the j th band-adhesive unit (ratio of out-of-phase force to displacement) (lb/in)

L Length of skin-stringer specimen (in)

L' Distance between effective fixed points on ends of multilayer damping treatment (in)

ℓ Width of skin stringer specimen (in)

ℓ' Length of viscoelastic layer

ℓ'' Length of anchored end in the damping treatment (in)

M $a \sinh a \cos b - b \cosh a \sin b$

m Mode number in the y direction

N Ratio of thickness of equivalent damping layer to thickness of panel skin

n Mode number in the x direction

R $a \cosh a \sin b + b \sinh a \cos b$

T $2 \cosh a \cos b + M + 2$

t Half the thickness of a constraining layer (in)

U Transverse displacement of panel relative to fixed area (in)

U_{sn} Total strain energy stored in damped structure (in-lb)

U_{pn} Strain energy stored in panel skin (in-lb)

U_{snj} Strain energy stored in j th stringer (in-lb)

$U_{REG\ II}$ Strain energy stored in damping treatment (in-lb)

V $2 \sinh a \sin b + R$

W Transverse displacement of the panel relative to frames (in)

$W_{xx'}$, W_{xy} etc. Partial derivatives with respect to indicated variable (i.e. $\frac{\partial^2 w}{\partial x^2}$, $\frac{\partial^2 w}{\partial x \partial y}$ etc.)

X Elongation (in), see equation (24)

X_o Amplitude of shaker input $X_o \exp(i\omega t)$

x Coordinate along frames

y Coordinate along stringers

z Coordinate normal to panel surface

α_n Dimensionless parameter, see equation (D.7)

β Ratio of width of damping treatment to width of panel

Δ x/L

δ y/ℓ

ζ_n See equation (37)

η Loss factor of damping material

η_D Loss factor of equivalent free layer damping treatment

η_{on} Loss factor, in n th mode, of untreated structure

η_{sn} System loss factor in n th mode, see equation (31)

η'_{sn} Damped system loss factor in n th mode assuming zero initial damping, see equation (33)

λ JL'/L, fractional coverage of damping treatment in x direction

ν Poisson's ratio of structural material

ν_D Poisson's ratio of equivalent free layer damping treatment

ϕ_n Normal mode shape in x direction

ϕ'_n Slope, $\dfrac{\partial \phi_n}{\partial \Delta}$

ϕ''_n Curvature, $\dfrac{\partial^2 \phi_n}{\partial \Delta^2}$

χ $(1-\nu_D^2)/(1-\nu^2)$

AN ANALYTICAL AND EXPERIMENTAL INVESTIGATION

OF A TWO-LAYER DAMPING TREATMENT

A. D. Nashif
University of Dayton
Dayton, Ohio

and

T. Nicholas
Air Force Materials Laboratory
Wright-Patterson AFB, Ohio

The temperature range of an effective layered damping treatment is extended through the use of two layers of viscoelastic materials having different glass transition temperatures with the outer layer having the higher transition temperature. In this manner, when the inner layer is within its transition region, the outer layer is still glassy and the treatment acts essentially as a constrained layer treatment. At higher temperatures the outer layer is in its transition region and the system responds as an unconstrained layer treatment. Experimental and theoretical results are presented for the vibrations of a beam with a two layered damping treatment. The treatment is then optimized with respect to thickness ratios to produce good damping over a wide temperature range.

INTRODUCTION

Many damping treatments utilizing high damping viscoelastic materials have been developed for the reduction of vibrational amplitudes in structures. In certain applications where plate or beam like structural members are subjected to a wide-band acoustical environment, the layered surface treatments are often well suited. Of these, the unconstrained layer surface treatment has been one of the most widely used because of its effectiveness and simplicity of application [1]. To introduce high damping into structures by this means, it is necessary to use a viscoelastic material that exhibits both a relatively high Young's modulus and a high loss factor. Unfortunately, most available viscoelastic materials have a high modulus only in the glassy region, where the loss factor is very small, and a high loss factor in the transition region, where the modulus falls rapidly with increasing temperature. The effectiveness of the unconstrained layer damping treatment is thus generally restricted to a narrow temperature range around the transition temperature.

A variation of this damping treatment is the constrained layer treatment where an additional layer of a stiff material, usually metal, is used to constrain the viscoelastic material thereby inducing large shear strains and hence high damping [2]. The effectiveness of this treatment depends on having a high loss factor and a relatively low stiffness for the constrained layer. As in the case of the unconstrained layer, this treatment is most effective over a limited temperature range near the transition temperature.

To overcome some of these difficulties and extend the temperature range of an effective layered damping treatment it has been proposed to apply a damping treatment composed of two layers of viscoelastic materials having different glass transition temperatures with the outermost layer having the higher transition temperature. When the inner layer is within its transition region, the outer layer is still glassy and the treatment acts essentially as a constrained layer treatment. At higher temperatures the outer layer goes into its transition region and the system responds as if an unconstrained layer treatment were applied. This technique thus admits the possibility of inducing damping in structures over a much wider temperature range than that possible with a single damping material treatment in either constrained or unconstrained

53

layer configurations.

The analysis required for this problem includes the two limiting cases of a constrained layer and an unconstrained layer treatment as specific cases. The analysis is carried out considering the shear deformation, flexural stiffness, axial stiffness, and damping of each of the two layers which are treated as linear viscoelastic materials and is an extension of the analysis of Ross, Ungar, and Kerwin [3] to include all of these effects. The analysis then allows the optimization of a treatment of any two specific materials by varying the thickness ratios of the layers to obtain the highest damping over a required temperature range and for a given frequency range.

This paper presents a detailed analysis of the vibrations of a beam with a two layered damping treatment for arbitrary material properties and geometries. The results are then applied to specific material treatments and are compared with experimental results for several geometries. The given treatment is optimized with respect to thickness ratios to produce good damping over a wide temperature range.

SYMBOLS

E   Young's modulus

G   Shear modulus

h   Thickness

I   Moment of inertia

M   Bending moment

N   Axial force

Q   Transverse shear force

t   Time

u   Axial displacement

V   Transverse shear force

w   Transverse displacement

x   Cartesian coordinate along beam axis

δ Log decrement

η Material loss factor

η_s Composite loss factor

λ Wave length

ψ Rotation of cross section

ρ Mass density

σ Normal stress

τ Shear stress

ω Frequency

Ω Reference frequency

ξ Wave number

*   Superscript denoting dimensionless quantity

ANALYSIS

The equations of motion for the three layered beam are derived by writing the separate equations for each layer and combining them while insuring continuity of displacements and tractions at the two interfaces. The base beam is denoted by subscript o, the two additional layers by subscripts 1 and 2 as shown in Figure 1.
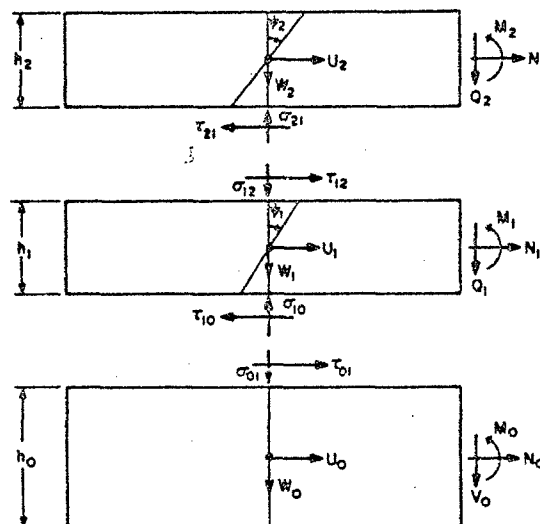
Figure 1. Notation for three-layered beam

The base beam is treated according to the elementary Bernoulli-Euler beam theory considering axial forces, the two additional layers are analyzed taking into account shear deformation as well as axial forces and flexural

54

rigidity. Only transverse inertia of each of the layers is considered. For the bottom layer or base beam, the equations of motion are:

$$\frac{\partial V_o}{\partial x} + \sigma_{oi} = \rho_o h_o \frac{\partial^2 w_o}{\partial t^2} \tag{1}$$

$$\frac{\partial N_o}{\partial x} + \tau_{oi} = 0 \tag{2}$$

$$\frac{\partial M_o}{\partial x} - V_o - \tau_{oi} \frac{h_o}{2} = 0 \tag{3}$$

where V_o, N_o, and M_o are the shear force, axial force, and bending moment respectively and σ_{oi} and τ_{oi} are the interlaminar normal and shearing stresses acting on layer 0 due to layer 1. The axial force and bending moment are related to the displacement components u_o and w_o in the axial and transverse directions respectively through

$$N_o = E_o h_o \frac{\partial u_o}{\partial x} \tag{4}$$

$$M_o = -E_o I_o \frac{\partial^2 w_o}{\partial x^2} \tag{5}$$

The equations for the middle layer are

$$\frac{\partial N_1}{\partial x} + \tau_{12} - \tau_{10} = 0 \tag{6}$$

$$\frac{\partial Q_1}{\partial x} + \sigma_{12} - \sigma_{10} = \rho_1 h_1 \frac{\partial^2 w_1}{\partial t^2} \tag{7}$$

$$\frac{\partial M_1}{\partial x} - Q_1 - (\tau_{12} - \tau_{10})\frac{h_1}{2} = 0 \tag{8}$$

where Q_1 is the transverse shearing force. Denoting the rotation of the cross section by γ_1 the force-displacement relations are

$$M_1 = -E_1 I_1 \frac{\partial \gamma_1}{\partial x} \tag{9}$$

$$N_1 = E_1 h_1 \frac{\partial u_1}{\partial x} \tag{10}$$

$$Q_1 = G_1 h_1 \left(\frac{\partial w}{\partial x} - \gamma_1\right) \tag{11}$$

In a similar manner the equations for the top layer are

$$\frac{\partial N_2}{\partial x} - \tau_{21} = 0 \tag{12}$$

$$\frac{\partial Q_2}{\partial x} - \sigma_{21} = \rho_2 h_2 \frac{\partial^2 w_2}{\partial t^2} \tag{13}$$

$$\frac{\partial M_2}{\partial x} - Q_2 - \tau_{21} \frac{h_2}{2} = 0 \tag{14}$$

$$M_2 = -E_2 I_2 \frac{\partial \gamma_2}{\partial x} \tag{15}$$

$$N_2 = E_2 h_2 \frac{\partial u_2}{\partial x} \tag{16}$$

$$Q_2 = G_2 h_2 \left(\frac{\partial w_2}{\partial x} - \gamma_2\right) \tag{17}$$

To insure continuity of displacements at the interfaces

$$U_o = U_1 - \frac{1}{2}\left(h_o \frac{\partial w_o}{\partial x} + h_1 \gamma_1\right) \tag{18}$$

$$U_2 = U_1 + \frac{1}{2}\left(h_1 \gamma_1 + h_2 \gamma_2\right) \tag{19}$$

Continuity of tractions at the interfaces is insured by

$$\begin{aligned} \tau_{12} &= \tau_{21} \\ \tau_{10} &= \tau_{01} \\ \sigma_{12} &= \sigma_{21} \\ \sigma_{10} &= \sigma_{01} \end{aligned} \tag{20}$$

Finally, thickness changes of the layers are neglected, thus

$$W_o = W_1 = W_2 = W \tag{21}$$

The system of equations (1) - (21) can be reduced by successive elimination of the variables to a set of four equations in the displacement components, w, u_1, γ_1 and γ_2,

$$-E_o I_o \frac{\partial^4 w}{\partial x^4} + E_o \frac{h_o^2}{2} \frac{\partial^3 u_1}{\partial x^3} + G_1 h_1 \left(\frac{\partial^2 w}{\partial x^2} - \frac{\partial \gamma_1}{\partial x}\right)$$

$$+ G_2 h_2 \left(\frac{\partial^2 w}{\partial x^2} - \frac{\partial \gamma_2}{\partial x}\right) = (\rho_o h_o + \rho_1 h_1 + \rho_2 h_2) \frac{\partial^2 w}{\partial t^2}$$

$$E_o h_o \frac{\partial^2 u_1}{\partial x^2} + E_1 h_1 \frac{\partial^2 u_1}{\partial x^2} + E_2 h_2 \frac{\partial^2 u_1}{\partial x^2} = 0$$

$$\tag{22}$$

$$E_1 I_1 \frac{\partial^2 \gamma_1}{\partial x^2} + G_1 h_1 \left(\frac{\partial w}{\partial x} - \gamma_1\right) + E_2 \frac{h_1 h_2}{2} \frac{\partial^2 u_2}{\partial x^2}$$

$$- E_o \frac{h_o h_1}{2} \frac{\partial^2 u_o}{\partial x^2} = 0$$

$$E_2 I_2 \frac{\partial^2 \gamma_2}{\partial x^2} + G_2 h_2 \left(\frac{\partial w}{\partial x} - \gamma_2\right) + E_2 \frac{h_2^2}{2} \frac{\partial^2 u_2}{\partial x^2} = 0$$

where the substitutions (18) and (19) are to be incorporated but have been left out for convenience in writing.

Several simple cases are derivable from the general set of equations (22). The equations for a single unconstrained layer where shear deformation is considered are given in [4] and can be obtained by setting $h_2 = 0$ in (22). The equations for a symmetrical sandwich beam [5] are obtained by setting $E_2 = E_o$ and $h_2 = h_o$. To suppress the effect of shear deformation in the top layer take $\left(\frac{\partial w}{\partial x} - \gamma_2\right) = 0$ while insuring the product $G_2 h_2 \left(\frac{\partial w}{\partial x} - \gamma_2\right)$, which represents the shear force, be non-zero by taking G_2 as infinite. The symmetrical sandwich beam equations can be further simplified by taking $E_o I_o$ and $E_2 I_2 = 0$, i.e. by neglecting the flexural rigidity of the facings and furthermore by neglecting the flexural rigidity of the core, $E_1 I_1$, which is a valid assumption for soft core materials [6].

It is to be noted at this point that the previous equations are for a three layered beam of materials which exhibit elastic behavior. Damping or viscoelasticity in the two top layers is to be incorporated later through the use of the correspondence principle once the solution for the elastic case is obtained.

Equations (22) are solved for the case of a wave travelling in the x direction with frequency ω and wave number $\mathfrak{z}$. The displacement components are taken in the form

$$w = W \exp[i(\mathfrak{z}x - \omega t)]$$
$$u_1 = U \exp[i(\mathfrak{z}x - \omega t)]$$
$$\gamma_1 = \Psi_1 \exp[i(\mathfrak{z}x - \omega t)]$$
$$\gamma_2 = \Psi_2 \exp[i(\mathfrak{z}x - \omega t)]$$

(23)

The wave number $\mathfrak{z}$ is related to the wave length of the vibration λ through

$$\mathfrak{z} = \frac{2\pi}{\lambda}$$

(24)

Substitution of the displacements (23) into the equations of motion (22) and cancelling the factor $\exp[i(\mathfrak{z}x - \omega t)]$ leads to a set of four homogeneous equations in the variables W, U, Ψ_1, and Ψ_2. For a non-zero solution, the determinant of the coefficients must be zero. Non-dimensional quantities are introduced in the form

$$E_1^* = E_1/E_o$$
$$E_2^* = E_2/E_o$$
$$x^* = h_o \mathfrak{z}$$
$$\omega^{*2} = \omega^2/\Omega^2$$
$$h_1^* = h_1/h_o$$
$$h_2^* = h_2/h_o$$

(25)

where Ω is a reference frequency taken for convenience as

$$\Omega^2 = \frac{E_o}{\rho_o h_o^2}$$

(26)

For simplicity it is assumed that the two added layers are incompressible, i.e. $E = 3G$ in all the equations. The resulting frequency equation is reduced to the form

$$\omega^{*2} = \frac{x^{*4}(c_1 + c_2 x^{*2} + c_3 x^{*4})}{(1 + h_1^* + h_2^*)(\alpha + \beta x^{*2} + \gamma x^{*4})}$$

(27)

where the following terms have been defined as

$$c_1 = \frac{E_1 E_2 h_1 h_2}{108} \Big[4E_1 h_1 (1 + h_1^2) + 4E_2 h_2 (1 + h_2^2) + 6(E_1 h_1^2 + E_2 h_2^2) + (1 + E_1^2 h_1^4 + E_2^2 h_2^4) + E_1 E_2 h_1 h_2 (4h_1^2 + 4h_2^2 + 6h_1 h_2) + 12 E_2 h_1 h_2 (1 + h_1 + h_2) \Big]$$

$$c_2 = \frac{E_1 h_1 h_2}{108} \Big[E_1 (h_1^2 + h_2^2) + 3E_1 h_1 h_2 (1 + E_1 h_1^2 + 2E_1^2 h_1^2 h_2^2) + E_1 E_2 h_1^2 (h_2 + 3h_1 h_1 - 3h_1^2 + 7h_1^2 h_2) + E_1^2 h_1 (4h_1^2 + 6h_1 h_1^2 + h_1^2 + 4h_1^2 h_1^2) + E_1 h_1^2 h_2^2 (E_2^2 h_1^2 + E_1^2 h_1^2) + 4 E_1 E_2 h_1^2 h_2 \Big]$$

$$c_3 = \frac{E_1 E_2 h_1^2 h_2^3}{108} \left(1 + E_1 h_1 + E_2 h_2\right) + \frac{E_2^2 h_1^2 h_2^4}{144}$$

(28)

$$\alpha = \frac{E_1 E_2 h_1 h_2}{9} \left(1 + E_1 h_1 + E_2 h_2\right)$$

$$\beta = \frac{E_2 h_1 h_2}{36} \Big[12 E_2 h_1 h_2 + 4E_1 (h_1^2 + h_2^2) + 4E_1 h_1 h_2 (E_1 h_2 + E_2 h_1) + E_1 (E_1 h_1^2 + E_2 h_2^2) \Big]$$

$$\gamma = \frac{E_1 h_1^2 h_2^2}{36} \Big[3E_2 h_1^2 + E_1 E_2 h_1 h_2^2 + 4E_1 h_1 h_2 + E_1 h_1^2 h_2 \Big]$$

All quantities in the above definitions (28) refer to the dimensionless parameter given by (25) with the stars omitted for simplicity.

The solution for the three layered elastic beam given by (27) can be easily extended to the case of two viscoelastic layers through the introduction of the complex moduli

$$E_1 \longrightarrow E_1(1+i\gamma_1)$$
$$E_2 \longrightarrow E_2(1+i\gamma_2) \tag{29}$$

and through the introduction of a complex frequency in the form

$$\omega \longrightarrow \bar{\omega}\left(1+i\frac{\delta}{2\pi}\right) \tag{30}$$

where δ is the logarithmic decrement and where free vibrations become free damped vibrations of the form

$$\exp(i\bar{\omega}t)\ \exp\left(-\frac{\bar{\omega}\delta}{2\pi}t\right) \tag{31}$$

Solutions to the resulting complex frequency equation are obtained by setting the real and imaginary portions equal to zero identically and solving the two resulting equations simultaneously.

The special case for zero wave number or infinite wave length is derivable from equation (27) by taking the limiting case as x^* approaches zero. Neglecting x^{*2} and x^{*4} terms compared to unity leads to the solution

$$\omega^{*2} = \frac{c_1 x^{*4}}{\alpha(1+h_1^*+h_2^*)} \tag{32}$$

which is the elementary beam solution and is derivable independently by assuming plane section remain plane and perpendicular to the deformed cross-section.

The equations were solved numerically with the aid of an IBM 7094 computer using complex Fortran IV language.

EXPERIMENTAL INVESTIGATION

In order to demonstrate the effectiveness of this two layered damping treatment, two viscoelastic materials with different transition temperatures were selected.

The first was a viscoelastic material known as LD-400, manufactured by the Lord Manufacturing Company, Erie, Pennsylvania, which has a transition temperature of approximately 80°F. The second was 3M-428 adhesive, supplied by the 3M Company, St. Paul, Minnesota, which has a transition temperature of approximately -40°F. The mechanical properties of these two materials are presented as Figures 2 and 3. These materials were applied as a two layered damping treatment by coating them on a

7.0 in long aluminum cantilever beam with the LD-400 being the outer layer and the 3M-428 being the inner layer. The thickness of the aluminum beam was .064 in.
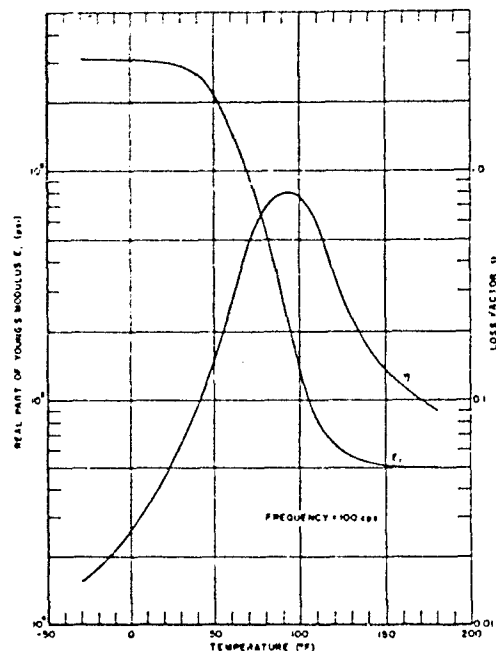
Figure 2. Mechanical properties of LD-400 [7]

For test purposes, the complex modulus apparatus and its associated electronic equipment were used as illustrated in the block diagram of Figure 4. With the specimen clamped in the mounting fixture, a harmonic force of constant amplitude was applied to the driving transducer by the oscillator. The output signal was sensed by the pickup transducer and then plotted on the recorder after being amplified. A frequency response spectrum such as that in Figure 5 was obtained in this manner at various temperatures. The frequencies at which each of the modes of vibration occurred were measured and the composite loss factor η_s in each mode was measured by the half-power bandwidth method. The composite loss factor η_s was then determined as a function of temperature for a frequency of 100 cps. Experimental results were obtained for several different thicknesses of damping treatments over a temperature range from -30°F to $+160^\circ$F.

DISCUSSION AND CONCLUSIONS

The problem of optimizing the

57

thickness ratios for best damping over a broad temperature range and over a given frequency range is not a simple one.
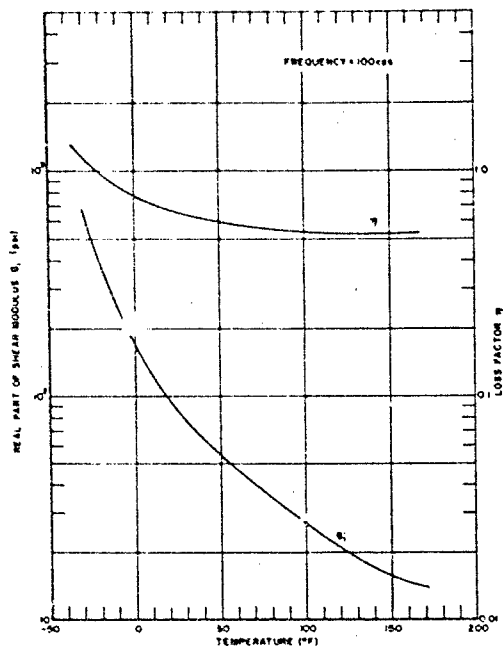
Figure 3. Mechanical properties of 3M-428 (Manufacturer's Data)
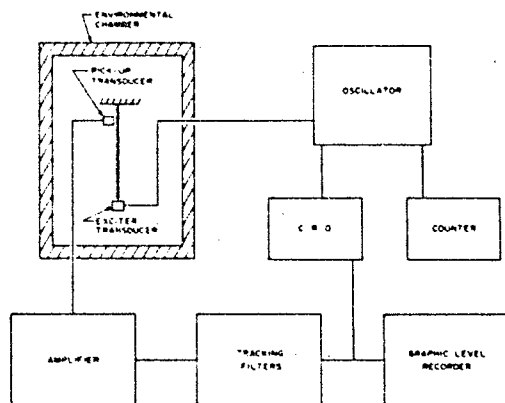
Figure 4. Block diagram of experimental setup

A large number of calculations were carried out with the aid of an IBM 7094 computer for various thickness ratios and frequencies (or wave lengths) at a number of different temperatures, i.e. for different combinations of mechanical properties. In all calculations it was assumed that the moduli and loss factor

did not vary with frequency at a given temperature and the values taken were those corresponding to 100 cps.
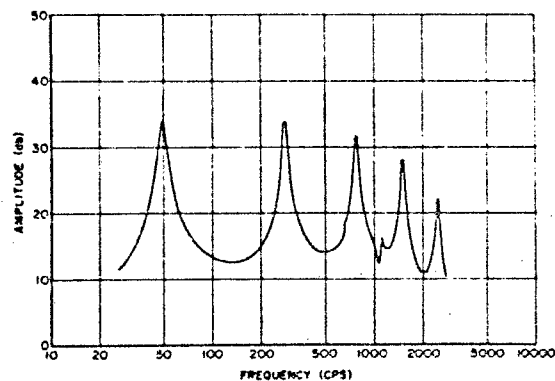
Figure 5. Typical frequency response spectrum

Figure 6 shows the sensitivity to wave length (and hence, frequency) of the log decrement or damping for two combinations of thicknesses at several different temperatures.
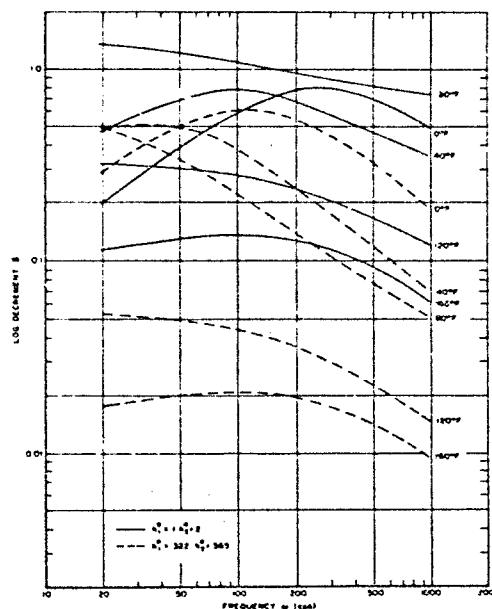
Figure 6. Frequency sensitivity of two-layered damping treatments

It can be seen from these typical results that the choice of "optimum" thickness ratios cannot be clearly defined. For simplicity, it was decided to choose thicknesses which would give

the best damping over a wide temperature range at a fixed frequency of 100 cps. Results from a large number of calculations narrowed the possible range of optimum thicknesses in which the total thickness of the damping layers also had to be considered. The damping at 100 cps is shown in Figure 7 for several thickness ratios.
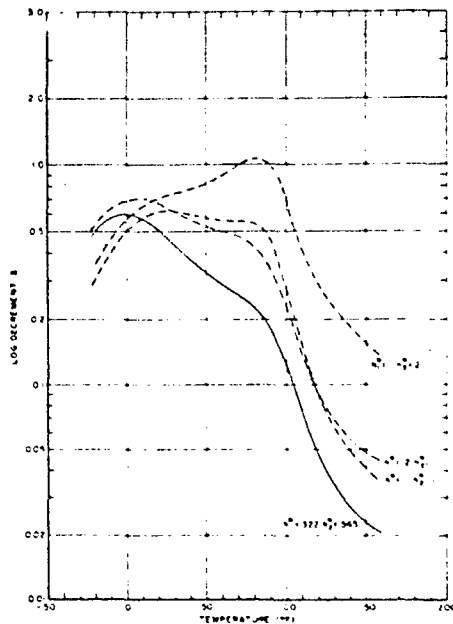
Figure 7. Effect of thickness ratios on damping

It is immediately obvious that the damping due to two layers in the initial arbitrarily chosen thicknesses as shown by the solid line can be improved by choosing other thicknesses. There is little to choose between the two curves for $h_1^* = 0.1$ and $h_1^* = 0.2$ for the same h_2^*, i.e. the results are insensitive to the thickness of the middle layer in this range. The overall damping can be increased by increasing h_1^* from 1 to 2, however, this increase of damping comes at the cost of nearly doubling the combined weight of the two damping layers. It was decided from the theoretical results shown in Figure 7 that the combinations $h_1^* = 0.1$ $h_2^* = 1.0$ and $h_1^* = 0.1$ $h_2^* = 2.0$ provided high damping over an acceptable temperature range.

Two cantilever beams were coated with the two layers of damping material described above in the thicknesses mentioned. The experimental values of the composite loss factor were obtained over a wide temperature range at 100 cps

and are presented in Figures 8 and 9 along with the theoretical predictions.
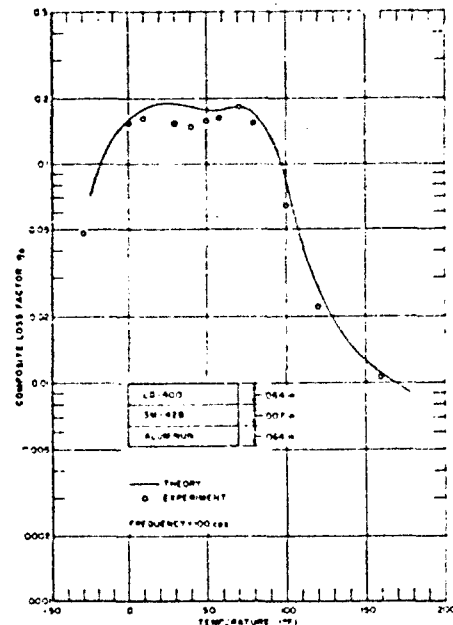
Figure 8. Experimental results for $h_1^* = 0.1$, $h_2^* = 1.0$
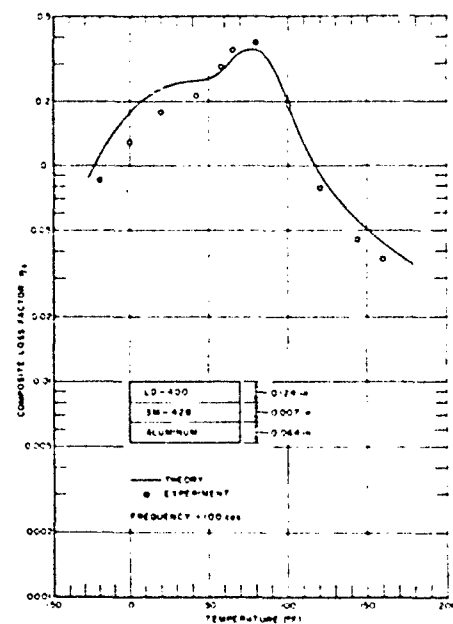
Figure 9. Experimental results for $h_1^* = 0.1$, $h_2^* = 2.0$

59

It is seen that there is excellent
agreement between experimental and theo-
retical results.

The results of this analysis and
the associated experiments indicate that
the technique of damping structural vi-
brations by applying a two-layered treat-
ment of viscoelastic materials having
different transition temperatures pro-
vides a high degree of damping over a
wide temperature range. This is illus-
trated in Figure 10 where the results
at 100 cps are presented for a single
unconstrained layer of LD-400 and for
the same layer with an additional thin
layer of 3M-428 in the middle.
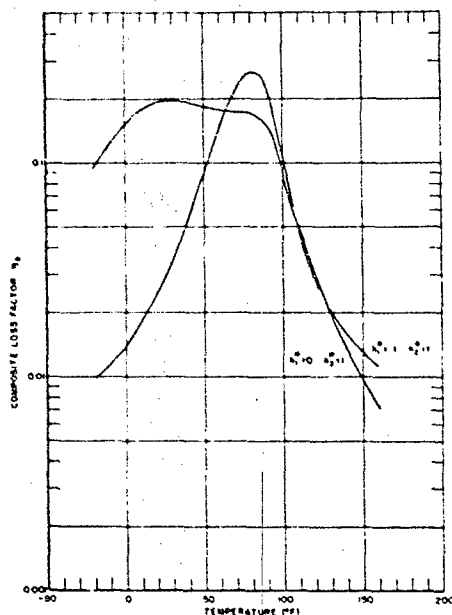
Figure 10. Comparison of uncon-
strained and two-layered damping
treatments

It is seen that good damping can be ob-
tained over a much wider temperature
range through the use of this two layer-
ed treatment with little sacrifice in
the amount of damping due to a single
unconstrained layer treatment.

The advantages of this technique
are highly dependent upon the proper
choice of thicknesses of the two layers.
In addition, the stiffnesses, damping,
and temperature dependence of the two
materials will affect the results. It
should be noted here that only limited
information is available to adequately
specify a desired range concerning the
separation of the two glass transition

temperatures. It can be stated though,
that if the difference is too great, the
damping in the intermediate range may
decrease to an undesirable level. Cal-
culations should thus be carried out to
determine the effectiveness of any spe-
cific damping treatment of the type
proposed in this paper. The analysis is
presented here to allow the calculation
of damping for any combinations of ge-
ometry and mechanical properties without
the necessity of making assumptions re-
garding relative magnitudes of damping
or stiffness and is thus broadly appli-
cable.

REFERENCES

1. Oberst, H., "Über die Dämfung der
   Biegeschwingungen dunner Bleche
   durch fest haftende Belage",
   Acustica (Acustische Beihefte)
   Heft 4, 2, 181-194 (1952).

2. Kerwin, E. M. Jr., "Damping of
   Flexural Waves by a Constrained
   Visco-Elastic Layer", Jour. Acoust.
   Soc. Am., 31, 952-962, (1959).

3. Ross, D., Ungar, E. E. and Kerwin,
   E. M. Jr, "Damping of Plate Flexural
   Vibrations by Means of Viscoelastic
   Laminae", in Structural Damping,
   ASME, 49-87 (1959).

4. Nicholas, T., "The Effects of Rota-
   tory Inertia and Shear Deformation
   on the Flexural Vibrations of a Two-
   Layered Viscoelastic-Elastic Beam",
   Shock and Vibration Bulletin (1968).

5. Plass, H. J. Jr., "Damping of Vi-
   brations in Elastic Rods and Sand-
   wich Structures by Incorporation of
   Additional Visco-Elastic Material",
   Proc. Third Midwest Conf. on Solid

Mechanics, Univ. of Michigan, 48-71 (1957).

6. Nicholas, T. and Heller, R. A., "Determination of the Complex Shear Modulus of a Filled Elastomer from a Vibrating Sandwich Beam", Experimental Mechanics, 7, 110-116 (1967).

7. Nashif, A. D., Cannon, C. M., "Wide Temperature-Range Free-Layer-Damping Treatment", Jour. Acoust. Soc. Am., 43, 1184-1185 (1968).

61

DAMPING OF PLATE VIBRATIONS BY
MEANS OF ATTACHED VISCOELASTIC MATERIAL

I. W. Jones

Applied Technology Associates, Inc.

Ramsey, New Jersey

The purpose of the investigation reported herein was to establish theory for examining the effectiveness of a viscoelastic coating for damping shock response in an elastic plate. The developed theory centers around a governing differential equation and boundary conditions for a simply-supported rectangular plate with an attached viscoelastic layer. The solution of this equation leads to response formulas for determining the amplitude of lateral motion for a general shock input and then for some specialized cases, namely; a concentrated impulsive load at the center and a concentrated step load applied at the center. The formulas are applied to an illustrative example which: (a) illustrates how they can be used on a practical problem, and (b) shows that damping of shock response by this concept is feasible in a typical case.

INTRODUCTION

The attachment of viscoelastic material to elastic beams, plates and other structural components for the sake of damping vibrations or reducing noise has become a widespread practice over the past decade. In these applications the input has been a steady-state force, pressure or edge motion. The present investigation has studied the application of this concept to problems of shock response reduction; that is, where the input is a suddenly applied force or edge motion and the response, naturally, is transient.

The mechanism of layered plate shock and vibration-damping is simple. The structural (elastic) and dissipative (viscoelastic) layers, being bonded together, are forced to undergo motion of the same amplitude in the transverse direction. Therefore the motion of the total plate is restricted by the viscoelastic layer, in which energy dissipation occurs. The viscoelastic layer is generally a rubbery or plastic material. Shear deformation in such materials is usually accompanied by a substantial amount of energy dissipation. On the other hand, these materials have little or no dissipative capacity in pure dilatational motion. Consequently, in

the design of layered plates for vibration damping one essential objective is to arrange and proportion the layers so that the deformation of the viscoelastic layer will be shearing, or distortional, rather than dilatational, to as great an extent as possible.

The foundation for the results reported herein is a governing differential equation for the flexural motion of an elastic plate with a layer of viscoelastic material attached to one face. The mathematical and physical details of the derivation of this equation are withheld from this paper since they are contained in a previous publication by the author. The equation is presented herein with only its underlying assumptions and limitations given.

The results of the solution of the equation are response formulas for calculating the transient response (specifically the deflection time-history) for a plate struck at the center by a sudden force. The transient solution to the problem was obtained by the use of Fourier series and the so-called principle of elastic-viscoelastic analogy; the latter technique involving Laplace transforms.

The equation is solved for a plate with simply supported boundaries. Response expressions for step force loading and also for impulsive loading are derived, and the effectiveness of some actual damping materials is explored in a numerical example.

LIST OF SYMBOLS

x, y, z	rectangular coordinates; x and y lie in the reference plane and z is normal to it
t	time
∇^2	$\partial^2/\partial x^2 + \partial^2/\partial y^2$
overdot, $(\dot{\ })$	derivative of ( ) with respect to time
asterisk, $(\ )^*$	coefficient of Fourier expansion of ( )
a, b	plate linear dimensions
h_i	thickness of ith layer
r	distance from reference plane to interface between layers
E_i	Young's modulus
$T, \bar{T}$	retardation time, relaxation time
ϵ_i	stiffness constant, $E/1-\nu^2$
ν_i	Poisson's ratio
μ_i	shear modulus
k_i	shear coefficient
ρ_i	density
$q(x, y, t)$	applied lateral load
$Q(x, y), q(t)$	space-dependent and time-dependent parts of applied lateral load
$w(x, y, t)$	plate transverse displacement
$w_{st}(x, y)$	transverse displacement of perfectly elastic plate under static load
$W(t)$	ratio of dynamic to static transverse displacement at center of plate

A_k	coefficient of kth component of response function
$D(m, n, t)$	magnification factor
γ	wave parameter $\left[\gamma^2 = (\frac{m\pi}{a})^2 + (\frac{n\pi}{b})^2\right]$
m, n	mode numbers
Ω	undamped natural frequency
β	damping coefficient
λ_k	root of characteristic equation
ω	damped natural frequency

PROCEDURE

The plate being considered is composed of one layer of elastic material and a second layer of viscoelastic material. The equation of motion for the plate was derived by the use of the principle of elastic-viscoelastic analogy [3]. The procedure employed for applying this principle is as follows:

i) First, derive the equation of motion and boundary conditions for a perfectly elastic two-layered plate.

ii) Next, obtain the Laplace transforms of the differential operators in the constitutive equation for the viscoelastic material.

iii) Finally, apply the Laplace transform to both sides of the equation of motion for the perfectly elastic plate, substituting the elastic constants of the layer which is to be made viscoelastic, the transformed viscoelastic operators.

The first step of this procedure, obtaining the equation of motion and boundary conditions for a two-layered perfectly elastic plate was accomplished by the author in [1] following previous work by Ren and Yu [2]. The main difference between the theory derived by the author in [1], and the earlier theory of [2] is that the author's theory was developed specifically for the solution of practical damping problems, and thus embodies several simplifying assumptions that the more classical theory of [2] does not. As a result of these assumptions the equation led to formulas that are adaptable to engineering problems.

64

EQUATION OF MOTION AND BOUNDARY CONDITIONS

The plate cross-section is shown in Fig. 1. The thickness of the upper (structural) layer is h_1. The lower (damping) layer has thickness h_2. The reference plane is arbitrarily located at a distance r above the interface between the layers. The x and y axes lie in the reference plane and the z axis is normal to it, as shown. The nomenclature used in this part of the analysis is the same as in [2]. The theory embodies the assumptions that the structural material is thin, stiff and elastic while the damping material may be relatively thick, soft and viscoelastic. The theory neglects coupling of extensional and flexural motion (an effect determined in [2] to be negligible) and shear deformation in the structural layer, which is also negligible in practical cases. Shear deformation is included in the viscoelastic layer where it is of importance. As the theory is intended for situations where flexural motion predominates over in-plane (thickness-shear, thickness-twist and extensional) motion, rotatory and in-plane inertias are also neglected. The assumptions stated above, when applied to the plate geometry, result in the following: (See Fig. 1).

i) Normals to the reference plane remain straight and unextended after deformation.

ii) Normals to the reference plane in layer 1 remain normal to the reference plane after deformation, while in layer 2 they need not.

iii) There exists a plane (the reference plane, $z=0$) which is undeformed.

Statements (i) and (ii) imply that the transverse shear strains in layer 1 and the transverse normal strains in both layers are zero. While it is known that in general a fixed neutral (undeformed) plane does not exist in a vibrating two-layered plate with layers made of different materials, it has been shown that the coupling between extension and flexure is negligible in practical cases, on the basis of this and some other assumptions an approximate neutral plane location is determined later.

The problem as outlined up to this point leads to two coupled differential equations in two variables: w, the lateral deflection and ψ_2, the rotation angle in the damping layer. A single uncoupled equation in w, the lateral deflection, was obtainable by eliminating ψ_2, but only for the case of a simply supported plate.

In deriving this equation it was assumed that the material of layer 2, the damping material, is incompressible. This is known to be a reasonable assumption for actual damping materials, and it simplifies the equation since it implies that $\epsilon_2 = 4\mu_2$ where ϵ is $E/1-\nu^2$ and μ is the shear modulus. Also, the shear coefficient in the damping layer, μ_2, is assumed to have its "engineering" value of unity. The following sixth order equation results from all of the discussed assumptions:

$$-(\frac{4h_2^3}{3}\left\{\epsilon_1\left[\frac{h_1^3}{12} + h_1(\frac{h_1}{2}-r)^2\right] + \mu_2 r^2 h_2\right\})\,\nabla^6 w$$

$$+\left\{\epsilon_1\left[\frac{h_1^3}{12} + h_1(\frac{h_1}{2}-r)^2\right] + 4\mu_2(r^2 h_2 + \frac{h_2^3}{2})\right\}\nabla^4 w$$

$$+ (1-4\frac{h_2^2}{3})\nabla^2)(\rho_1 h_1 + \rho_2 h_2)\,\ddot{w} = (1-4\frac{h_2^2}{3}\nabla^2)q \tag{1}$$

Eq. (1) reduces to the equation for a single-layered plate of thickness h_1 if we let $h_2 \rightarrow 0$. In that case, $r \rightarrow h_1/2$ see Eq. (3) and we obtain the familiar equation

$$\frac{E_1 h_1^3}{12(1-\mu_1^2)}\nabla^4 w + \rho_1 h_1\,\ddot{w} = q \tag{2}$$

The stated assumptions are satisfied if the reference plane is located according to the following equation:

$$r = \frac{h_1}{2}\frac{(1-\frac{\epsilon_2 h_2^2}{\epsilon_1 h_1^2})}{(1+\frac{\epsilon_2 h_2}{\epsilon_1 h_1})} \tag{3}$$

The boundary conditions of simple support are satisfied if:

at $x=0, a$: $\quad w = \frac{\partial^2 w}{\partial x^2} = 0$

at $y=0, b$: $\quad w = \frac{\partial^2 w}{\partial y^2} = 0$

VISCOELASTIC MATERIAL PROPERTIES

It is shown in linear viscoelasticity theory that the Laplace transform of the shear differential operator (in the case of an incompressible material) completely defines the material

65
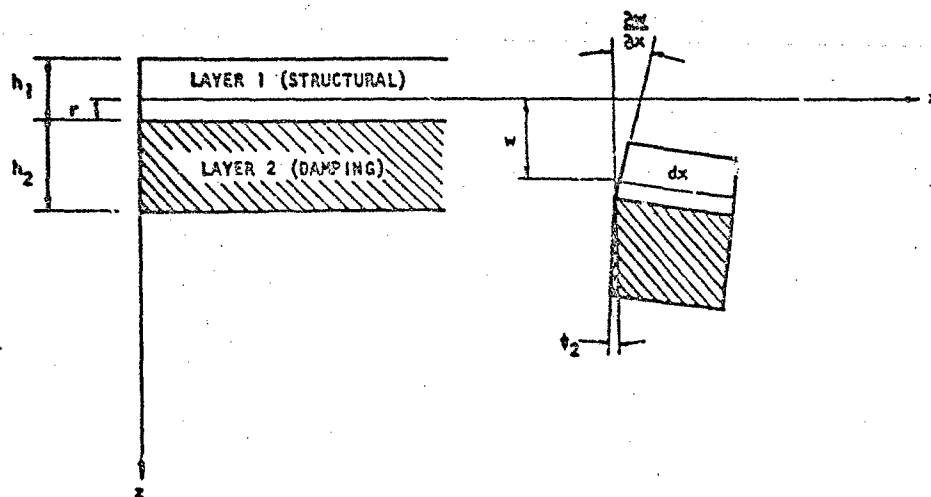
FIGURE 1 PLATE CROSS SECTION
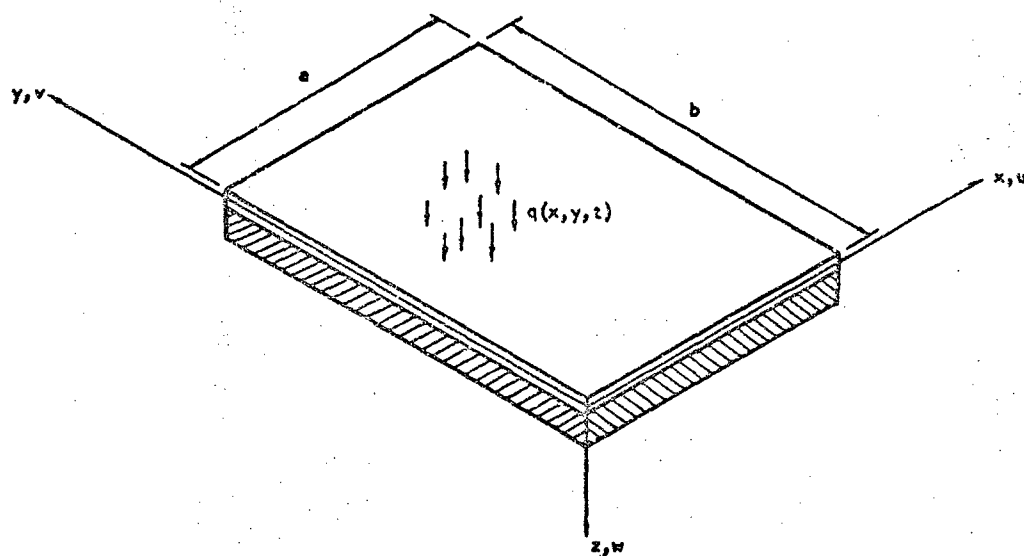
FIGURE 2 PLATE GEOMETRY

66

behavior. There are a number of tests from which this function can be determined, such as stress relaxation tests, creep tests, constant strain rate tests and sinusoidal input tests. Mathematical functions (exponentials, etc.) can be employed and their parameters adjusted so that the functions agree to some approximation with experiments. The functions chosen are often those describing the behavior of discrete element models composed of linear springs and Newtonian dashpots, which are combined into one-dimensional arrays. One of the simplest models employed is the so-called standard linear solid model, shown in Fig. (3). Its stress-deformation characteristic for shear, as given by the Laplace transform of its shear differential operator [7] is:

$$\mu(p) = \mu \ \frac{1 + \bar{T}p}{1 + Tp} \qquad (5)$$

where T is a retardation time; $\bar{T}$ is a relaxation time and the material properties μ, T and $\bar{T}$ are related to the model constants of Fig. (3) by

$$\mu = \frac{G_1 G_2}{G_1 + G_2} \qquad T = \frac{\eta}{G_2} \qquad \bar{T} = \frac{\eta}{G_1 + G_2} \qquad (6)$$

More complex models can be constructed by combining more and more springs and dashpots. The theory presented in [1], of which the present paper is a summary, implies the use of any finite number of parameters (relaxation times and retardation times, for example) to represent the viscoelastic behavior of a material. However, when a large number are attempted, even the simplest of problems can lead to mathematical and numerical difficulties. For this reason most stress and vibration analyses have been limited to two, three and four element models.

The general expression for the transformed shear operator can be written as

$$\mu(p) = \mu \ \frac{\displaystyle\sum_{k=0}^{K_2} b_k p^k}{\displaystyle\sum_{k=0}^{K_1} a_k p^k} \qquad (7)$$

It has been determined that for real materials, the orders K_1 and K_2 of the polynomials of Eq. (7) must either be the same, or K_2 must be greater by one [3]. It is also shown in [3] that the roots of the polynomials of Eq. (7) must all be real and negative.

The accuracy and validity of viscoelastic representation by discrete element models has been studied by several authors. The common approach has been to study how various models respond to stresses which vary sinusoidally with time. From a knowledge of their behavior under sinusoidal stresses, their behavior under any prescribed loading can be inferred by Fourier synthesis. The major conclusions reached in these studies, which are generally in agreement, can be summarized as follows [5,6]:

i) Most real viscoelastic solids do not behave even approximately like Voigt or Maxwell bodies. Except for certain compounds of low molecular weight, more complicated models are required.

ii) The simplest models to possess most of the general features of real viscoelastic deformation are the three-element models; however, due to the fact that there are only three material constants with which to curve-fit the response of an actual material, and there are usually not sufficient for wide time of frequency ranges, the use of these models is limited to a restricted range of time or frequency. For wide ranges of time or frequency the results are qualitative, at best. Nevertheless, the three-element models are a realistic approximation to the observed results over a frequency range of perhaps one decade.

RESPONSE OF A SIMPLY-SUPPORTED ELASTIC PLATE WITH AN ATTACHED VISCOELASTIC LAYER

For a simply-supported, perfectly elastic, two-layered plate, the response problem is completely defined by the equation of motion and the boundary conditions, Eqs. (1) and (4), respectively.

The existence of only even spacial derivatives in Eq. (1) and its boundary conditions makes it suitable for spacial solution by a Fourier sine series. Application of the standard Fourier series technique reduces Eq. (1) to an infinite number of uncoupled equations in the Fourier coefficients. Denoting the m, n^{th} coefficient by $w^*(m, n, t)$, the solution can be written as

$$w(x, y, t) = \frac{4}{ab} \sum_{m, n=1}^{\infty} w^*(m, n, t) \sin \frac{m\pi}{a} x \ \sin \frac{n\pi}{b} y \qquad (8)$$

67

To obtain a solution for $w^*(m, n, t)$ with layer 2 viscoelastic, the aforementioned principle of elastic-viscoelastic analogy is used. Replacement of the elastic constant for layer 2, μ_2, with the corresponding viscoelastic operator, $\mu_2(p)$, yields the transformed equation for the plate with a viscoelastic second layer. Then to obtain $w^*(m, n, t)$, the inverse Laplace transform of the equation is taken. For convenience the coefficient $w^*(m, n, t)$ was factored into $w_{st}^*(m, n)$, the m, n^{th} component of deflection under static load for a perfectly elastic plate, and $D(m, n, t)$, the m, n^{th} dynamic magnification factor. After application of the Laplace transform technique and much algebraic manipulation, the two factors were obtained in the following form:

$$w_{st}^*(m, n) = \left[H/\mu_2 J + \epsilon_1 K \right] q^*(m, n) \qquad (9)$$

where

$$\gamma = \left[\left(\frac{m\pi}{a}\right)^2 + \left(\frac{n\pi}{b}\right)^2 \right]^{1/2}$$

$$H = 1 + 4 \frac{h_2^2}{3} \gamma^2$$

$$J = \frac{4h_2^3}{3} r^2 \gamma^6 + 4(r^2 h_2 + \frac{h_2}{3}) \gamma^4$$

$$K = \left[\frac{h_1^3}{12} + h_1 \left(\frac{h_1}{2} - r\right)^2 \right] (4\frac{h_2^2}{3} \gamma^6 + \gamma^4)$$

and $q^*(m, n)$ is the m, n^{th} Fourier coefficient of the applied load expansion.

The formula for the m, n^{th} magnification factor, which is

$$D(m, n, t) = \sum_{k=0}^{K} A_k \frac{\Omega^2}{(\lambda_o - \lambda_k)^2 + \omega^2} \int_o^t q(\tau) \left\{ \omega e^{-\lambda_o(t-\tau)} \sin \omega(t-\tau) \right. \qquad (10)$$

$$\left. + (\lambda_o - \lambda_k) e^{-\lambda_k(t-\tau)} \left[1 - e^{-(\lambda_o - \lambda_k)(t-\tau)} \cos \omega(t-\tau) \right] \right\} d\tau$$

contains several quantities that require explanation. The coefficients A_k are given by

$$A_k = \frac{\sum\limits_{\ell=0}^{K} a_\ell (-\lambda_k)^\ell}{\prod\limits_{\substack{\ell=0 \\ \ell \neq k}}^{K} (\lambda_\ell - \lambda_k)} \qquad (11)$$

where the λ_k's are real roots of the polynomial

equation:

$$\sum_{k=0}^{K+2} \left\{ \left[a_k + \beta(b_k - a_k) \right] + a_{k-2} \right\} p^k = 0 \qquad (12)$$

The complex conjugate roots of eq. (12) are denoted $(-\lambda_o + i\omega)$. Other definitions applicable to Eq. (10) are

$$\Omega = \left[(\mu_2 J + \epsilon_1 K)/M \right]^{1/2}; M = (1 + 4 \frac{h_2^2}{3} \gamma^2)(\rho_1 h_1 + \rho_2 h_2) \qquad (13)$$

where Ω is the m, n^{th} undamped natural frequency, that is, the m, n^{th} natural frequency if the plate is perfectly elastic, and

$$\beta = \mu_2 J / (\mu_2 J + \epsilon_1 K) \qquad (14)$$

where β is a damping coefficient. Formulas for the magnification factors for some special cases have been derived as follows:

If the load $q(x, y, t)$ is applied as an instantaneous shock, or impulse, then

$$D(m, n, t) = \sum_{k=0}^{K} A_k \frac{\Omega^2}{(\lambda_o - \lambda_k)^2 + \omega^2} \left\{ \omega e^{-\lambda_o t} \sin \omega t \right. \qquad (15)$$

$$\left. + (\lambda_o - \lambda_k) e^{-\lambda_k t} (1 - e^{-(\lambda_o - \lambda_k)t} \cos \omega t) \right.$$

Finally, assume that the load is a concentrated force, P, striking the center of the plate, $(x = a/2, y = b/2)$. Then the response at the center of the plate is given by

$$w(\frac{a}{2}, \frac{b}{2}, t) = \frac{4}{ab} \sum_{m, n = 1, 3, 5 \cdots} \left[H/(\mu_2 J + \epsilon_1 K) \right]_{mn} D(m, n, t)$$

NUMERICAL EXAMPLE

A numerical example is solved to demonstrate the application of the theory, and also to

68

investigate the effectiveness of representative damping materials applied in various thicknesses to a rectangular steel plate. The plate is simply-supported and has the following geometric and material properties:

$a = 40$ in $\qquad E_1 = 30 \times 10^6$ psi

$b = 40$ in $\qquad \nu_1 = 0.3$

$h_1 = 3/8$ in $\qquad \rho_1 = 7.40 \times 10^{-4} \mathrm{lb\,sec^2/in^4}$

In the example, the viscoelastic behavior of the damping material in shear is represented by the standard linear solid model described previously. In accordance with the theory, the material is assumed to be incompressible. Thus, its viscoelastic behavior is completely defined by its transformed viscoelastic operator for shear, Eq. (5), or by the three parameters μ, the elastic shear modulus; T, a retardation time; and $\bar{T}$, a relaxation time. The elastic shear moduli of actual damping materials vary over an extremely wide range, from about 50 psi for some rubbery materials to 200,000 psi or more for stiff plastics. In the present example, representative values are taken as $\mu = 100$ psi, then 10,000 psi and finally 100,000 psi.

Pairs of numerical values of T and $\bar{T}$ are used which correspond to light damping, (T = 0.0041 sec. and $\bar{T}$ = 0.00334 sec.), and heavy damping, (T = 0.0090 sec. and $\bar{T}$ = 0.00152 sec.), in the frequency range for this problem. The density of the damping materials is assumed to be 1.4×10^{-4} lb $\mathrm{sec^2/in^4}$. The damping materials are applied in thicknesses of one, two and three times the thickness of the basic plate. The various cases described above are summarized in Table 1.

The static and dynamic characteristics of the plates, (i.e., static deflection influence coefficients, natural frequencies and decay rates) are given in Table 1 for the m=1, n=1 mode. As the response series converge fairly rapidly, the first term, the (1, 1) mode, gives a fair approximation to the total response and indicates trends which hold true when the higher mode contributions are added.

Examination of the term w_{st}^* (1, 1) reveals the reduction in static deflection due to the addition of damping material. The reduction is not significant in the case of the flexible material where $\mu = 10,000$ psi. Calculations (not shown) were also made for materials with an elastic shear modulus of 100 psi but these indicated no noticeable effect of damping material on either

static or dynamic response.

The decay rates are observed to increase with the thickness, stiffness and damping capacity of the attached materials as expected.

The applicable equation for the driving point response due to an impulsive loading is Eq. (16) with D(m, n, t) given by Eq. (15). The plate characteristics given in Table 1 were substituted into these equations and the response time-histories calculated and plotted by computer. A comparison of sample results for m, n=1 with those for m, n = 1, 3; m, n = 1, 3, 5 and m, n = 1 to 7 indicated that the series converge fairly rapidly and that the m, n=1, 3 solution gives a fairly good approximation, with the m, n=1 terms giving the dominating contribution.

The effects on response of the attached damping materials were

i) a reduction in amplitude

ii) an exponential decay of amplitude with time

iii) introduction of an out-of-phase component

iv) a change in natural frequency

The peak value of w/I for the case where a heavy damping material was applied in three times the plate thickness is 0.0098 for the plate with damping and 0.0165 for the plate without damping, indicating a reduction of 40.6% due to damping. Fig. (5) shows time-histories of the responses for this case and two other cases where the same material is applied in thicknesses of one and two times the basic plate thickness, i.e., h_2/h_1 = 1 and 2. The response of the undamped plate h_2/h_1 =0 is shown for comparison. In calculating these responses we let m and n equal 1 and 3.

This example has thus shown that a good damping material, applied in a thickness three times that of the basic plate, reduces the shock response by a very sizeable amount.

ACKNOWLEDGEMENT

thesis advisor at the Brooklyn Polytechnic
institute.

REFERENCES

1. Jones, I. W.: "Non-periodic Vibrations
   of Layered Viscoelastic Plates," Ph. D.
   Dissertation, Polytechnic Institute of
   Brooklyn, 1967.

2. Ren, Nann and Yu, Yi-Yuan: "Vibrations
   of Two-Layered Plates", AFOSR Report
   No. 65-1423, Brooklyn Polytechnic
   Institute, June 1965.

3. Nowacki, W.: Dynamics of Elastic
   Systems, John Wiley and Sons (New York)
   1963.

4. Lee, E. H.: "Stress Analysis of Viscoe-
   lastic Bodies", Quart. Appl. Math., Vol
   8, No. 2, 1955.

5. Bland, D. R.: The Theory of Linear
   Viscoelasticity, Pergamon Press, 1960.

6. Kolsky, H., and Shi, Y. Y.: " The
   Validity of Model Representation for
   Linear Viscoelastic Behavior", Brown
   University Report Nonr 562 (14)/5,
   January 1958.
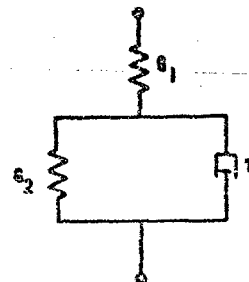
FIGURE 3 STANDARD LINEAR SOLID MODEL

TABLE 1

PLATE STATIC AND DYNAMIC CHARACTERISTICS

Case	Thickness Ratio h_2/h_1	Shear Modulus μ_2, psi	Damping	Static Defl. Coefficient $w_{st}^*(1,1)$, in.	Undamped Nat. Freq. $\Omega(1,1)$, rps	Damped Nat. Freq. $\omega(1,1)$, rps	Decay Rate $\lambda_D(1,1)$, 1/sec.
Undamped	0	--	None	0.0452	259.5	-	0
1A		10,000	Light	0.0450	259.6	259.7	0.122
2A	1	"	Heavy	0.0450	259.6	260.3	1.84
3A		100,000	Light	0.0418	269.2	270.3	1.19
4A		"	Heavy	0.0418	269.2	276.6	18.9
1B		10,000	Light	0.0434	245.5	246.0	0.598
2B	2	"	Heavy	0.0434	245.5	248.7	8.80
3B		100,000	Light	0.0311	289.7	294.8	5.16
4B		"	Heavy	0.0311	289.7	333.2	101.1
1C		10,000	Light	0.0398	240.3	241.6	1.63
2C	3	"	Heavy	0.0398	240.3	248.6	24.6
3C		100,000	Light	0.0190	348.0	361.6	11.2
4C		"	Heavy	0.0190	348.0	568.6	222.0

70
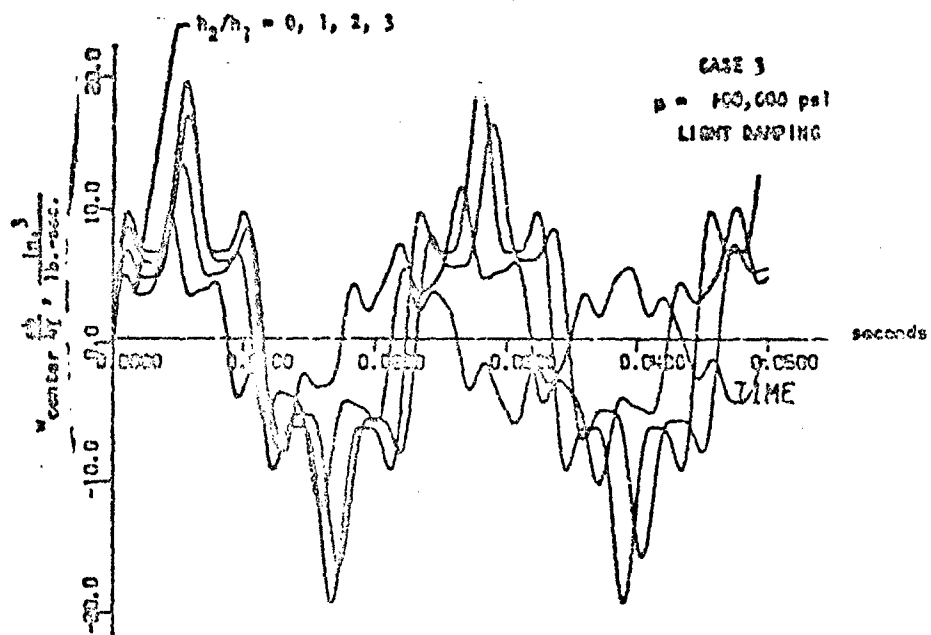
Figure 4   Response to impulsive force
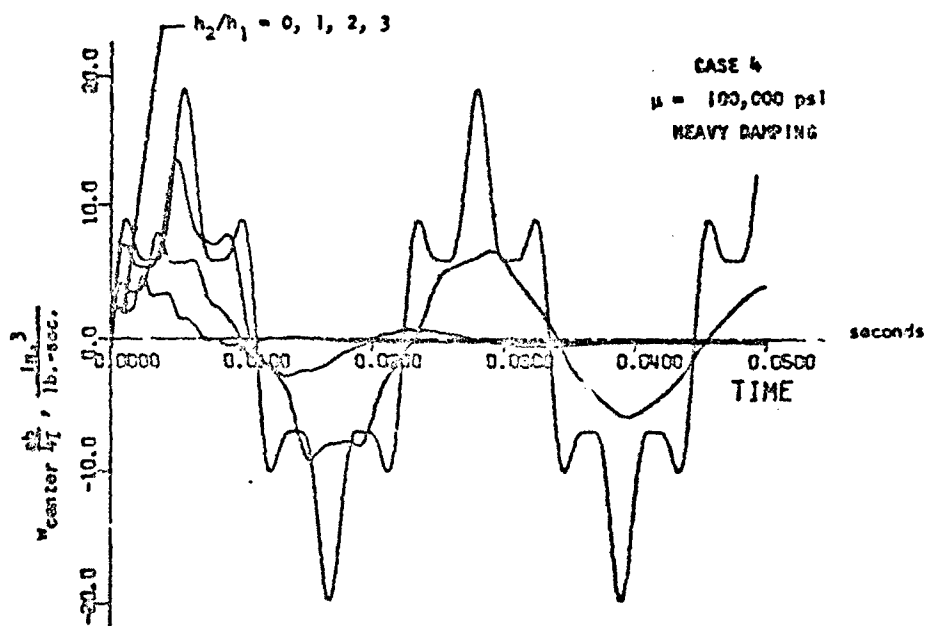
Figure 5   Response to impulsive force

DISCUSSION

Mr. Ungar (Bolt Beranek and Newman): I am struck by a problem. That is, that some of the excitation that you have used has a very broadband spectral character, whereas you said that the model that represents your material only applies to a very narrow band. How difficult would it be to generalize your analysis, say, and to use empirical data to represent material properties, say, measured data for the material since you eventually have to do numerics anyhow—use actual material data in the numerical calculations?

Mr. Jones: Well I do not know if that could be done easily with the formulation as it stands. As far as I know, numerical data are usually in the form of shear modulus or loss factor as a function of frequency. My analysis is really in the time domain, so that there would have to be some conversion. Of course, I could have done an analogous type of analysis in the frequency domain. Maybe that is what will have to be done in that case.

Mr. Arenz (Loyola University of Los Angeles): With regard to incorporating time dependent viscoelastic material properties, there are theoretical relationships to convert from a frequency dependency to a time dependency of, say, modulus of elasticity, and the loss factor is also involved. I think it could be incorporated as a time function which might be used in your equations.

Mr. Jones: Yes that is correct. If emperical data were used, I think there would still have to be some curve fitting to ascertain that the variation of properties with frequency is fairly close to that of the model used.

Mr. Foster (University of Missouri): Will your equations be in your paper when it is published?

Mr. Jones: Yes.

Mr. Foster: Is the viscoelastic material a plate that is attached through the surface tractions to the other plate, as the previous speaker did?

Mr. Jones: Yes exactly the same as the plate that has been called unconstrained layer or free layer plate.

Mr. Nicholas (Air Force Materials Lab.): Would you care to comment on the use of the standard solid model? The reason I bring up this question is that the model that you chose exhibits lower damping at the higher frequencies, and since this is a transient problem, I think you might want to put in high damping at high frequencies. You did seem to have high frequency components in the response, or is this just an arbitrary choice?

Mr. Jones: It was fairly arbitrary. It was chosen more for simplicity than for realism. The formulas that I derive in this paper permit the use of any number of spring-dashpot elements, and therefore any number of independent parameters to describe the damping behavior.

Mr. Nicholas: At the beginning I thought I understood you to say that the energy was dissipated in shear deformation of the viscoelastic layer, did you not mean extensional deformation?

Mr. Jones: Actually I think it is a combination. There is some shear deformation in this type of plate if the free layer is thick enough.

Mr. Nicholas: Usually you get the most shear deformation if you constrain it. Unless you go to a real high frequency or high thicknesses it is mostly an extensional deformation.

72

VIBRATIONS OF SANDWICH PLATES WITH ORTHOTROPIC
FACES AND CORE

Fakhruddin Abdulhadi
Reliability Engineering
IBM Systems Development Division
Rochester, Minnesota

and

Lee P Sapetta
Department of Mechanical Engineering
University of Minnesota
Minneapolis, Minnesota

The equations for stress and stress resultants (moments and forces) are derived for a rectangular sandwich plate with orthotropic core and faces through the extremization of the complementary energy integral. These and the dynamic equilibrium equations are used to obtain the equation of motion for transverse vibrations including the rotatory and shear effects. The panel consists of two membrane type orthotropic and distinct faces and one soft orthotropic core. The method of development can be used for any number of faces and cores; only the constants will change when considering additional layers. The frequency equation for the free transverse vibrations of a simply supported plate is obtained by assuming a double trigonometric series solution. The natural frequencies are tabulated for a selected example to illustrate the effect of face orthotropy.

INTRODUCTION

Vibrations of sandwich plates with isotropic faces and isotropic or orthotropic cores have been considered by many authors. Yu [1] considered the one dimensional case, including transverse shear deformation and rotatory inertia, for faces and core which are assumed to be isotropic. Cheng [2] presented the flexure theory for isotropic membrane type faces and weak orthotropic core. Liaw and Little [3] extended Cheng's theory to a plate composed of any number of isotropic faces and orthotropic cores. Falgout [4] used the method of superposing bending deflections and deflections due to transverse shear to derive the differential equation of free transverse vibrations of plates for isotropic faces and cores. Jacobson [5] used Cheng's assumptions to study the effects of orthotropic cores on the free vibrations of simply supported plates. The present investigation is also based on membrane faces and weak core construction; however, the faces and the core are considered to be orthotropic.

The sandwich plate under discussion consists of homogeneous and orthotropic membrane type faces of different thicknesses and materials. The transverse shear stress carried by the faces is negligible and the normal stress is uniformly distributed across its thickness. Thus, the flexural rigidity of an individual face is neglected. The core is considered homogeneous, orthotropic and thick relative to the faces. The entire transverse shear stress is carried by the core and is uniformly distributed across its thickness. All

other stresses in the core are considered negligible. Thus, the plate falls within the membrane face - weak core category [2, 3, 6]. The analysis is within the scope of small deflection theory.

NOMENCLATURE

A_{mn} = amplitude of free vibrations with m and n half waves

a,b = length and width of plate

c = distance between face centers (See Fig. 1)

D_x, D_y = flexural rigidities of the plate

D_{xy} = torsional rigidity of the plate

D^* = constant defined by Eq. (25)

e_{ix}, e_{iy} e_i^*, G_i = elastic constants for the ith face

f_1 = $1/(e_{1x}e_{1y} - e_1^{*2})$

f_2 = $1/(e_{2x}e_{2y} - e_2^{*2})$

G_{xz}, G_{yz} = shear moduli of the core

h = thickness of the core

H = $D^* + 2D_{xy}$

H_x = $D_x + D_{xy}$

H_y = $D_y + D_{xy}$

I = mass moment of inertia per unit area

L_1, L_2, L_3 = plate constants defined by Equations (27), (28), and (29)

m,n = number of half waves in x and y directions, respectively

M_x, M_y = bending moments per unit width

M_{xy} = twisting moment per unit width

Q_x, Q_y = shear forces per unit width

P = transverse load per unit area

R = $\rho \dfrac{\partial^2 w}{\partial t^2} - P$

S_x, S_y = core shear parameter

t = time

t_1, t_2 = thickness of upper and lower faces, respectively

V = complementary energy

x,y,z = coordinate axes (See Fig. 2)

w = transverse deflection

$\bar{w}_1, \bar{\alpha}_1, \bar{\beta}_1$ $\bar{w}_2, \bar{\alpha}_2, \bar{\beta}_2$ = generalized boundary displacements

α, β = Lagrange multipliers, rotations

$\varepsilon_{ix}, \varepsilon_{iy}$, γ_{ixy} = strains in the ith face

$\lambda_1, \ldots, \lambda_5$ = Lagrange multipliers

ρ = mass per unit area

σ_{ix}, σ_{iy}, τ_{ixy} = stresses in the ith face

Ω_{mn} = natural frequency

∇^2 = $\dfrac{\partial^2}{\partial x^2} + \dfrac{\partial^2}{\partial y^2}$

∇_0^4 = $D_x \dfrac{\partial^4}{\partial x^4} + 2H \dfrac{\partial^4}{\partial x^2 \partial y^2} + D_y \dfrac{\partial^4}{\partial y^4}$

ANALYSIS

The stress-strain relations for the ith orthotropic face are defined [7] as

$$\sigma_{ix} = e_{ix}\varepsilon_{ix} + e_i^*\varepsilon_{iy} \qquad (1)$$

74

$$\sigma_{iy} = e_{iy}\epsilon_{iy} + e_i^*\epsilon_{ix} \qquad (2)$$

$$\tau_{ixy} = G_i\gamma_{ixy} \qquad (3)$$

The stress resultants at any section may be expressed in terms of the stresses and plate dimensions, shown in Fig. 1, as

$$M_x = ct_1\sigma_{1x} \qquad (4)$$

$$M_y = ct_1\sigma_{1y} \qquad (5)$$

$$M_{xy} = ct_1\tau_{1xy} \qquad (6)$$

$$Q_x = h\tau_{xz} \qquad (7)$$

$$Q_y = h\tau_{yz} \qquad (8)$$

$$t_1\sigma_{1x} + t_2\sigma_{2x} = 0 \qquad (9)$$

$$t_1\sigma_{1y} + t_2\sigma_{2y} = 0 \qquad (10)$$

$$t_1\tau_{1xy} + t_2\tau_{2xy} = 0 \qquad (11)$$

where Eqs. (9) through (11) indicate the absence of forces in the x-y plane. The static equations of equilibrium for a differential plate element [7] are

$$\frac{\partial M_x}{\partial x} + \frac{\partial M_{xy}}{\partial y} - Q_x = 0 \qquad (12)$$

$$\frac{\partial M_y}{\partial y} + \frac{\partial M_{xy}}{\partial x} - Q_y = 0 \qquad (13)$$

$$\frac{\partial Q_x}{\partial x} + \frac{\partial Q_y}{\partial y} + P = 0 \qquad (14)$$
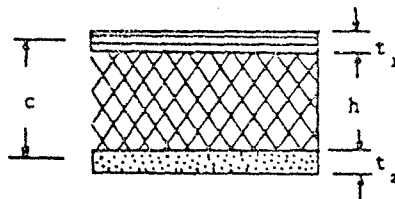
Fig. 1. Plate cross section
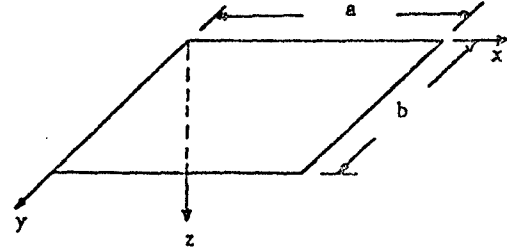
Fig. 2. Plate geometry

The strain energy of the faces and core may be written in terms of the stresses in a manner similar to that of Liaw and Little [3]. Eqs. (4) through (8) and (12) through (14) are used as the constraint conditions in conjunction with arbitrary Lagrange multipliers. Thus, the modified complementary energy can be written as

$$V = 1/2 \int_0^a \int_0^b [(t_1 f_1 e_{1y} + \frac{t_1^2}{t_2} f_2 e_{2y})\sigma_{1x}^2$$

$$+ (t_1 f_1 e_{1x} + \frac{t_1^2}{t_2} f_2 e_{2x})\sigma_{1y}^2$$

$$- 2(t_1 f_1 e_1^* + \frac{t_1^2}{t_2} f_2 e_2^*)\sigma_{1x}\sigma_{1y}$$

$$+ (\frac{t_1}{G_1} + \frac{t_1^2}{t_2 G_2}) \tau_{1xy}^2] \, dxdy$$

$$+ 1/2 \int_0^a \int_0^b h(\frac{\tau_{xz}^2}{G_{xz}} + \frac{\tau_{yz}^2}{G_{yz}}) \, dxdy$$

$$+ 1/2 \int_0^a \int_0^b [\lambda_1(M_x - ct_1\sigma_{1x})$$

$$+ \lambda_2(M_y - ct_1\sigma_{1y}) + \lambda_3(M_{xy} - ct_1\tau_{1xy})$$

$$+ \lambda_4(Q_x - h\tau_{xz}) + \lambda_5(Q_y - h\tau_{yz})$$

$$+ \alpha (\frac{\partial M_x}{\partial x} + \frac{\partial M_{xy}}{\partial y} - Q_x)$$

$$+ \beta (\frac{\partial M_y}{\partial y} + \frac{\partial M_{xy}}{\partial x} - Q_y) +$$

$$w \left(\frac{\partial Q_x}{\partial x} + \frac{\partial Q_y}{\partial y} + P \right)] \, dxdy$$

$$- \int_0^b \left| \bar{w}_1 Q_x + \bar{\beta}_1 M_{xy} + \bar{\alpha}_1 M_x \right|_{x=0}^a dy$$

$$- \int_0^a \left| \bar{w}_2 Q_y + \bar{\beta}_2 M_{xy} + \bar{\alpha}_2 M_y \right|_{y=0}^b dx \tag{15}$$

where

$$f_1 = 1/(e_{1x} e_{1y} - e_1^{*2}) \tag{16}$$

$$f_2 = 1/(e_{2x} e_{2y} - e_2^{*2}) \tag{17}$$

The first integral in Eq. (15) is the strain energy of the faces written in terms of the stresses in the upper face with the use of Eqs. (9) through (11). The second integral is the strain energy of the core. The third integral defines the constraint conditions where λ through λ, α, β, and w are arbitrary Lagrange multipliers. The line integrals represent the work done at the boundary due to the generalized displacements $\bar{w}_1$, $\bar{w}_2$, $\bar{\alpha}_1$, $\bar{\alpha}_2$, $\bar{\beta}_1$, and $\bar{\beta}_2$.

The complementary energy is minimum when the first variation of V with respect to each stress and stress resultant vanishes [8]. The minimization of Eq. (15) yields $\bar{w}_1 = \bar{w}_2 = w$, $\bar{\alpha}_1 = \bar{\alpha}_2 = \alpha$, $\bar{\beta}_1 = \bar{\beta}_2 = \beta$ and a set of equations that is reduced by the use of Eqs. (4) through (11) to the following equations:

$$M_x = D_x \frac{\partial \alpha}{\partial x} + D^* \frac{\partial \beta}{\partial y} \tag{18}$$

$$M_y = D_y \frac{\partial \beta}{\partial y} + D^* \frac{\partial \alpha}{\partial x} \tag{19}$$

$$M_{xy} = D_{xy} \left(\frac{\partial \beta}{\partial x} + \frac{\partial \alpha}{\partial y} \right) \tag{20}$$

$$\alpha = S_x Q_x - \frac{\partial w}{\partial x} \tag{21}$$

$$\beta = S_y Q_y - \frac{\partial w}{\partial y} \tag{22}$$

where

$$D_x = \frac{c^2 t_1^2 L_3}{L_1 L_3 - L_2^2} \tag{23}$$

$$D_y = \frac{c t_1^2 L_1}{L_1 L_3 - L_2^2} \tag{24}$$

$$D^* = \frac{c t_1^2 L_2}{L_1 L_3 - L_2^2} \tag{25}$$

$$D_{xy} = \frac{t_1 t_2 c^2 G_1 G_2}{t_1 G_1 + t_2 G_2} \tag{26}$$

$$L_1 = t_1 f_1 e_{1y} + \frac{t_1^2}{t_2} f_2 e_{2y} \tag{27}$$

$$L_2 = t_1 f_1 e_1^* + \frac{t_1^2}{t_2} f_2 e_2^* \tag{28}$$

$$L_3 = t_1 f_1 e_{1x} + \frac{t_1^2}{t_2} f_2 e_{2x} \tag{29}$$

$$S_x = 1/h G_{xz} \tag{30}$$

$$S_y = 1/h G_{yz} \tag{31}$$

The constants D_x and D_y are the flexural rigidities in the principal directions of orthotropy, D_{xy} is the twisting rigidity, $1/S_x$ and $1/S_y$ are the shear rigidities of the core, w is the transverse deflection (positive downward), and α and β are the rotations of a cross section about the y and x axes, respectively.

THE EQUATION OF TRANSVERSE MOTION

The dynamic equations of equilibrium of a differential plate element including the effects of transverse and rotatory inertia are

$$\frac{\partial M_x}{\partial x} + \frac{\partial M_{xy}}{\partial y} - Q_x = I \frac{\partial^2 \alpha}{\partial t^2} \tag{32}$$

$$\frac{\partial M_y}{\partial y} + \frac{\partial M_{xy}}{\partial x} - Q_y = I \frac{\partial^2 \beta}{\partial t^2} \tag{33}$$

$$\frac{\partial Q_x}{\partial x} + \frac{\partial Q_y}{\partial y} = \rho \frac{\partial^2 w}{\partial t^2} - P \tag{34}$$

76

where I is the mass moment of inertia per unit area, ρ is mass per unit area and P is the transverse forcing function per unit area.

The stress resultants M_x, M_y, M_{xy} given in Eqs. (18) through (20) are written in terms of Q_x, Q_y, w, and their derivatives by the use of Eqs. (21) and (22). The resulting equations are then used in Eqs. (32) and (33) to obtain the following:

$$I \frac{\partial^3 w}{\partial t^2 \partial x} - D_x \frac{\partial^3 w}{\partial x^3} - H \frac{\partial^3 w}{\partial y^2 \partial x}$$

$$- Q_x + D_x S_x \frac{\partial^2 Q_x}{\partial x^2} + S_x D_{xy} \frac{\partial^2 Q_x}{\partial y^2}$$

$$- I S_x \frac{\partial^2 Q_x}{\partial t^2} + S_y (H - D_{xy}) \frac{\partial^2 Q_y}{\partial x \partial y} = 0 \quad (35)$$

$$I \frac{\partial^3 w}{\partial t^2 \partial y} - D_y \frac{\partial^3 w}{\partial y^3} - H \frac{\partial^3 w}{\partial x^2 \partial y} - Q_y$$

$$+ D_y S_y \frac{\partial^2 Q_y}{\partial y^2} + S_y D_{xy} \frac{\partial^2 Q_y}{\partial x^2}$$

$$- I S_y \frac{\partial^2 Q_y}{\partial t^2} + S_x (H - D_{xy}) \frac{\partial^2 Q_x}{\partial x \partial y} = 0 \quad (36)$$

where

$$H = D^* + 2D_{xy} \quad (37)$$

Equations (34), (35), and (36) are three equations in three unknowns, namely Q_x, Q_y, and w. These equations are solved to obtain a differential equation for the transverse deflection in terms of the forcing function P. This is accomplished by considering these equations as algebraic equations with Q_x, Q_y, and w as three unknowns [9]. Solving for w by means of elimination or by determinants one obtains the following equation of transverse motion:

$$[D_{xy}(S_y \frac{\partial^2}{\partial x^2} + S_x \frac{\partial^2}{\partial y^2}) - 1] \nabla_0^4 w +$$

$$(D_x D_y - H^2) (S_x \frac{\partial^6 w}{\partial x^2 \partial y^4} + S_y \frac{\partial^6 w}{\partial x^4 \partial y^2})$$

$$+ I \frac{\partial^2 \nabla^2 w}{\partial t^2} - I (S_y H_y + S_x H_x)$$

$$\frac{\partial^6 w}{\partial t^2 \partial x^2 \partial y^2} - I S_y H_x \frac{\partial^6 w}{\partial t^2 \partial x^4}$$

$$- I S_x H_y \frac{\partial^6 w}{\partial t^2 \partial y^4} + I^2 \frac{\partial^4}{\partial t^4} [$$

$$(S_y \frac{\partial^2 w}{\partial x^2} + S_x \frac{\partial^2 w}{\partial y^2})] = [1 + S_x S_y D_{xy} \nabla_0^4$$

$$- (S_y D_y + S_x D_{xy}) \frac{\partial^2}{\partial y^2} - (D_x S_x + S_y D_{xy})$$

$$\frac{\partial^2}{\partial x^2} + S_x S_y (D_x D_y - H^2) \frac{\partial^2}{\partial x^2 \partial y^2} +$$

$$I^2 S_x S_y \frac{\partial^4}{\partial t^4} + I (S_x + S_y) \frac{\partial^2}{\partial t^2}$$

$$- I S_x S_y \frac{\partial^2}{\partial t^2} (H_x \frac{\partial^2}{\partial x^2} + H_y \frac{\partial^2}{\partial y^2})] R$$

$$(38)$$

where

$$H_x = D_x + D_{xy} \quad (39)$$

$$H_y = D_y + D_{xy} \quad (40)$$

$$R = \rho \frac{\partial^2 w}{\partial t^2} - P \quad (41)$$

$$\nabla^2 = \frac{\partial^2}{\partial x^2} + \frac{\partial^2}{\partial y^2} \quad (42)$$

$$\nabla_0^4 = D_x \frac{\partial^4}{\partial x^4} + 2H \frac{\partial^4}{\partial x^2 \partial y^2} + D_y \frac{\partial^4}{\partial y^4}$$

$$(43)$$

Equation (38) is a general equation that may be reduced for other cases of simpler sandwich construction. The effect of rotatory inertia can be removed by setting I equal to zero. If the faces are isotropic, then $D_x = D_y = H$. Further if Poisson's ratio ν is the same for both faces, then $D_{xy} = H(1-\nu)/2$. The core is

77

isotropic when $S_x = S_y$, and the effect of shear on deformation is removed when $S_x = S_y = 0$. When the faces are isotropic and rotatory inertia is neglected, Eq. (38) becomes similar to that given by Jacobson [5]. When considering the static flexure problem, all terms involving time must be removed. Equation (38) then becomes similar to that given by Cheng [2] when the faces are chosen to be isotropic and of identical materials.

A different notation for the elastic constants is used by Libov and Batdorf [9], and Plantema [10]. These constants are defined by the following:

$$\epsilon_x = \frac{1}{E_x}(\sigma_x - \nu_x \sigma_y) \qquad (44)$$

$$\epsilon_y = \frac{1}{E_y}(\sigma_y - \nu_y \sigma_x) \qquad (45)$$

$$\frac{\nu_x}{E_x} = \frac{\nu_y}{E_y} \qquad (46)$$

where E_x, E_y are elastic moduli and ν_x, ν_y are Poisson's ratios in the x, y directions, respectively. The above constants are related to those used in this investigation in the following manner:

$$e_x = \frac{E_x + \nu_x^2 E_y}{1 - \nu_x^2 \nu_y^2} \qquad (47)$$

$$e_y = \frac{e_x E_y}{E_x} \qquad (48)$$

$$e^* = \nu_y E_x = \nu_x E_y \qquad (49)$$

When the face is isotropic, these constants become

$$\nu_x = \nu_y = \nu$$

$$E_x = E_y = E$$

$$e_x = e_y = \frac{E}{1-\nu^2}$$

$$e^* = \frac{\nu E}{1-\nu^2}$$

NATURAL FREQUENCIES OF A SIMPLY SUPPORTED PLATE

When the forcing function P is equal to zero, Eq. (38) represents the equation of motion for free vibration. The following assumed solution satisfies the boundary conditions and represents the free oscillations for a simply supported plate.

$$w = \sum_{m=1}^{\infty} \sum_{n=1}^{\infty} A_{mn} \sin \frac{m\pi x}{a} \sin \frac{n\pi y}{b}$$

$$\sin \Omega_{mn} t \qquad (50)$$

The substitution of Eq. (50) in Eq. (38), and neglecting rotatory inertia, yeilds the frequency equation

$$\rho \Omega_{mn}^2 = \frac{(P1)(P2) + (P3)(P4)}{P1 + S_x S_y D_{xy}(P2) + S_x S_y (P3) + P5} \qquad (51)$$

where

$$P1 = D_{xy} S_y \left(\frac{m\pi}{a}\right)^2 + D_{xy} S_x \left(\frac{n\pi}{b}\right)^2 + 1$$

$$P2 = D_x \left(\frac{m\pi}{a}\right)^4 + 2H \left(\frac{m\pi}{a}\right)^2 \left(\frac{n\pi}{b}\right)^2 + D_y \left(\frac{n\pi}{b}\right)^4$$

$$P3 = (D_x D_y - H^2) \left(\frac{m\pi}{a}\right)^2 \left(\frac{n\pi}{b}\right)^2$$

$$P4 = S_y \left(\frac{m\pi}{a}\right)^2 + S_x \left(\frac{n\pi}{b}\right)^2$$

$$P5 = S_x D_x \left(\frac{m\pi}{a}\right)^2 + S_y D_y \left(\frac{n\pi}{b}\right)^2$$

If the rotatory inertia effect is not neglected, then the frequency equation is a lengthy cubic equation in Ω_{mn}^2.

As an example to illustrate the effect of face orthotropy on Ω_{mn}, a plate with the following dimensions and properties was selected:

$a = b = 36$ in.,

$t_1 = t_2 = 0.1$ in.,

$h = 0.4$ in.,

$G_{xz} = 18 \times 10^3$ psi,

$G_{yz} = 10 \times 10^3$ psi,

$e_{1x} = e_{2x} = 1.6 \times 10^6$ psi,

$e_{1y} = e_{2y} = 1.6 \times 10^6$ psi,

$e_1^* = e_2^* = 0.16 \times 10^6$ psi,

$G_1 = G_2 = 0.55 \times 10^6$ psi.

These chosen constants yield a degree of orthotropy $D_x/D_y = 1$. The values of e_{1x} and e_{2x} were then increased to yield $D_x/D_y = 2$, and $D_x/D_y = 3$. Resulting natural frequencies computed from Eq. (51) are given in Table 1, where

$$\sqrt{\rho} \; \Omega_{mn} = \omega_{mn} .$$

TABLE 1

Effect of Face Orthotropy on Natural Frequency

D_x/D_y	1	2	3
ω_{11}	1.98	2.28	2.53
ω_{12}	4.82	4.98	5.15
ω_{21}	4.93	6.26	7.22
ω_{22}	7.40	8.38	9.15

The values given in Table 1 indicate that as the face orthotropy increases, the deviation of the frequencies, from those obtained by assuming isotropy, increases.

CONCLUSIONS

The equation of transverse motion of a sandwich plate subject to the stated assumptions is derived. The effects of shear and rotatory inertia are included. This equation may be reduced for plates of simpler construction, i.e., for any combination of isotropic or orthotropic faces and a core. Further, the equation may be used for the study of static flexure by deleting all time dependent terms.

This analysis, by including face orthotropy, may prove useful in view of the increased use of reinforced plastics, fiberglass, etc., as facing materials.

REFERENCES

1. Y. Y. Yu, "A New Theory of Elastic Sandwich Plates - One-Dimensional Case," Journal of Applied Mechanics, ASME, Vol. 81, pp. 415-21, Sept. 1959

2. S. Cheng, "On the Theory of Bending of Sandwich Plates," Proceedings of the Fourth U.S. National Congress of Applied Mechanics, Vol. 1, pp. 511-18, 1962

3. B. D. Liaw, and R. W. Little, "Theory of Bending Multilayer Sandwich Plates," AIAA Journal, Vol. 5, pp. 301-304, 1967

4. T. E. Falgout, "A Differential Equation of Free Transverse Vibrations of Isotropic Sandwich Plates," Developments in Mechanics, Proceedings of the Seventh Midwestern Mechanics Conference, Vol. 1, pp. 223-27, 1961

5. M. J. Jacobson, "Effects of Orthotropic Cores on the Free Vibrations of Sandwich Plates," The Shock and Vibrations Bulletin No. 35, part 3, pp. 9-14, Jan. 1966

6. E. Reissner, "Small Bending and Stretching of Sandwich-Type Shells," NACA TN 1832, 1949

7. S. Timoshinko, and S. Woinowsky-Kreiger, Theory of Plates and Shells, p. 364. McGraw-Hill, New York, 1959

8. I. S. Sokolnikoff, Mathematical Theory of Elasticity, pp. 377-90. McGraw-Hill, New York, 1956

9. C. Libov and S. B. Batdorf, "A General Small-Deflection Theory of Flat Sandwich Plates," NACA TN 1526, 1948

10. F. J. Plantema, Sandwich Construction, p. 119. John Wiley, New York, 1966

THE NATURAL MODES OF VIBRATION OF BORON-EPOXY PLATES

J. E. Ashton
J. D. Anderson

General Dynamics
Fort Worth, Texas

An analytical and experimental study of the natural frequencies and mode shapes of square boron-epoxy composite plates is presented. The plates considered are laminated plies of orthotropic boron-epoxy material. Since the laminations are symmetric about the mid-plane, the plates are considered analytically as anisotropic homogeneous plates. The analysis is based on the Ritz method, using Hamilton's principle. Fully fixed boundary conditions are considered. The experimental program utilized six plates each fabricated of eight plies of boron-epoxy material. Natural frequencies and Chladni figures have been determined for each plate and compared to the analytical predictions. Excellent agreement was observed.

INTRODUCTION

The advent of the widespread use of fiber-reinforced composite materials has widened interest in the natural modes of vibration of composite plates. This paper presents an experimental and analytical study of the natural frequencies and mode shapes of square, flat boron-epoxy composite plates.

The plates considered are laminated of plies of orthotropic boron-epoxy material. However, since the principal axes of orthotropy of the plies that make up the plates are not maintained parallel to the plate edges, the plates are mathematically equivalent to generally anisotropic plates. Dynamic analyses for such generally anisotropic plates are not available in the literature, and an analytical technique has thus been developed. This analytical technique is based on the Ritz method, using Hamilton's principle. The assumed deflection series uses a 49-term expansion of characteristic functions of unit length beams. Fully fixed boundary conditions are considered. The analytical solution yields both natural frequencies and characteristic shapes.

The experimental program utilized six 13- x 13-in. plates fabricated of 8 plies of boron-epoxy composite material. The edges were fixed to prevent translation and rotation. The natural frequencies and mode shapes were determined by mechanically shaking the plate fixture at discrete frequencies with activated aluminum granules spread on the surface. Frequencies were recorded and photographs taken of the node lines at the resonant frequencies.

The natural frequencies and mode shapes were calculated for each of the plates tested, using lamina properties as determined from sandwich beam tests. The plate stiffness quantities were calculated from the lamina properties and orientations using the theory of laminated plates. Excellent agreement between the analytical and experimental results was observed. A minimum of six and a maximum of eleven of the analytically determined shapes were identified experimentally.

ANALYTICAL FORMULATION

The method of solution used herein is Hamilton's principle, with the energy solution obtained by means of the Ritz method. Young [1] has used this technique, using beam characteristic shapes to approximate the deflected shape, to obtain solutions for clamped isotropic plates. Basically, the same analysis procedure is used here, extended to include the effects of anisotropy.

The solution is obtained by equating the potential energy of the plate (shown in Fig. 1) in bending to the kinetic energy of the plate and requiring this equivalence to be stationary. That is, the solution is obtained from the requirement:

$$V - T = \text{stationary value} \qquad (1)$$

where

V = potential energy due to bending

T = kinetic energy of the plate.

81
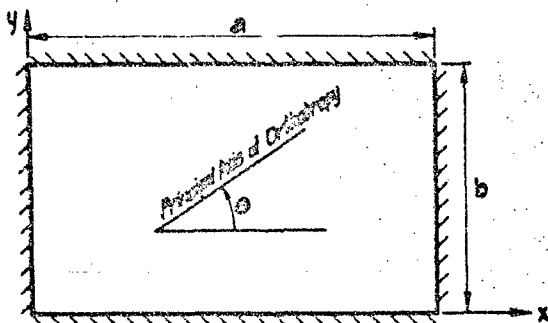
Figure 1 Plate Geometry

The potential energy due to bending, for the plate shown in Figure 1, can be written as follows:

$$V = 1/2 \int_0^a \int_0^b [M]^T [X] \; dx \; dy \qquad (2)$$

where

$$[M] = \begin{bmatrix} M_x \\ M_y \\ M_{xy} \end{bmatrix} = \text{plate moment resultants}$$

$$[X] = \begin{bmatrix} X_x \\ X_y \\ 2X_{xy} \end{bmatrix} = \text{plate curvatures} = \begin{bmatrix} W,_{xx} \\ W,_{yy} \\ W,_{xy} \end{bmatrix}.$$

W = normal deflection

and a comma denotes partial differentiation.

For anisotropic materials:

$$[M] = [D] [X] \qquad (3)$$

where $[D]$ is a fully populated symmetric matrix. If the plate in Figure 1 is fabricated of n plies of an orthotropic material, the elements of the $[D]$ matrix can be written as follows [2] :

$$D_{ij} = \frac{1}{3} \sum_{k=1}^{n} (\bar{C}_{ij})_k \; (h_k^3 - h_{k-1}^3)$$
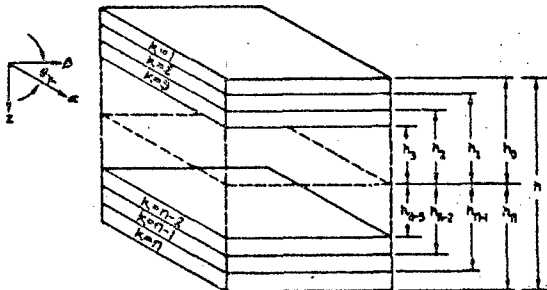
Figure 2 Layer Coordinates and Orientation for Laminates

$(\bar{C}_{ij})_k$ for each layer are given below in terms of the orthotropic elastic constants of the layer and the orientation θ_k (given with respect to axes parallel to the plate edges):

$$\bar{C}_{11_k} = C_{11_k} \cos^4\theta_k + 2(C_{12_k} + 2C_{66_k}) \cdot$$

$$\sin^2\theta_k \cos^2\theta_k + C_{22_k} \sin^4\theta_k$$

$$\bar{C}_{12_k} = (C_{11_k} + C_{22_k} - 4C_{66_k}) \cdot$$

$$\sin^2\theta_k \cos^2\theta_k + C_{12_k}(\sin^4\theta_k + \cos^4\theta_k)$$

$$\bar{C}_{22_k} = C_{11_k} \sin^4\theta_k + 2(C_{12_k} + 2C_{66_k}) \cdot$$

$$\sin^2\theta_k \cos^2\theta_k + C_{22_k} \cos^4\theta_k$$

$$\bar{C}_{16_k} = (C_{11_k} - C_{12_k} - C_{66_k}) \sin\theta_k \cos^3\theta_k$$

$$+ (C_{12_k} - C_{22_k} + 2C_{66_k}) \sin^3\theta_k \cos\theta_k$$

$$\bar{C}_{26_k} = (C_{11_k} - C_{12_k} - 2C_{66_k}) \sin^3\theta_k \cos\theta_k$$

$$+ (C_{12_k} - C_{22_k} + 2C_{66_k}) \sin\theta_k \cos^3\theta_k$$

$$\bar{C}_{66_k} = (C_{11_k} + C_{22_k} - 2C_{12_k} - 2C_{66_k}) \cdot$$

$$\sin^2\theta_k \cos^2\theta_k + C_{66_k}(\sin^4\theta_k + \cos^4\theta_k)$$

where

$$C_{11} = \frac{E_1}{1 - \nu_{12}\nu_{21}}$$

$$C_{12} = \frac{\nu_{21} E_1}{1 - \nu_{12}\nu_{21}}$$

$$C_{22} = \frac{E_2}{1 - \nu_{12}\nu_{21}}$$

$$C_{66} = G_{12}$$

where E_1, E_2, $\nu_{12} = \nu_{21} \frac{E_1}{E_2}$, G_{12} are the elastic constants of the orthotropic material.

Substituting expression (3) into expression (2), the following result is obtained:

$$V = \frac{1}{2} \int_0^a \int_0^b \left\{ D_{11} \; W^2,_{xx} + 2D_{12} \; W,_{xx} \cdot \right.$$

$$W,_{yy} + D_{22} \; W^2,_{yy}$$

$$+ 4W,_{xy} (D_{16} \; W,_{xx} + D_{26} \; W,_{yy}$$

$$\left. + D_{66} \; W,_{xy}) \right\} \; dx \; dy.$$

The kinetic energy is given by the following expression:

$$T = \frac{1}{2}\omega^2 \rho h \int_0^a \int_0^b W^2 \, dx \, dy \qquad (7)$$

where ρ = mass density

ω = angular frequency of vibration.

In order to find a solution for W that obeys condition (') (approximately), the deflection function is expanded in the following form:

$$W = \sum_{i=1}^{7} \sum_{j=1}^{7} a_{ij} Z_i(x) Z_j(y) \qquad (8)$$

where

a_{ij} = parameters to be determined

$Z_i(y)$ = characteristic shape of the ith natural frequency of a clamped-clamped beam

$= \cosh(\epsilon_i y) - \cos(\epsilon_i y)$

$- \alpha_i \left(\sinh(\epsilon_i y) + \alpha_i \sin(\epsilon_i y) \right)$

(the constants ϵ_i and α_i are tabulated in Reference 3).

The series (8) satisfies the boundary conditions of zero deflection and zero slope along the four edges.

With the assumed series (8) for the deflection, the condition (1) becomes an ordinary maximum-minimum problem in the 49 variables a_{ij}. Substituting (8) into (6) and (7) and using condition (1), the following set of linear simultaneous equations is obtained:

$$\frac{\partial V}{\partial a_{lk}} = \sum_{m=1}^{7} \sum_{n=1}^{7} d_{lkmn} a_{mn} = \frac{\partial T}{\partial a_{lk}} =$$

$$\omega^2 \rho h \; ab \qquad (9)$$

where

$$d_{lkmn} = D_{11} \Psi_{3lm} \Psi_{lkn} \frac{b}{a^3} + D_{12} \cdot$$

$$(\Psi_{5lm} \Psi_{5nk} + \Psi_{5ml} \Psi_{5kn}) \frac{1}{ab}$$

$$+ D_{22} \Psi_{1lm} \Psi_{3kn} \frac{a}{b^3} + 2D_{16} \cdot$$

$$(\Psi_{6ml} \Psi_{4kn} + \Psi_{4ml} \Psi_{4nk}) \frac{1}{a^2}$$

$$+ 2D_{26} (\Psi_{4lm} \Psi_{6nk} + \Psi_{4ml} \Psi_{6kn}) \cdot$$

$$\frac{1}{b^2} + 4D_{66} \Psi_{2lm} \Psi_{2kn} \frac{1}{ab}$$

and $\Psi_{1ij} = \int_0^1 Z_i(x) Z_j(x) \, dx = \begin{cases} 1 & i = j \\ 0 & i \neq j \end{cases}$

$$\Psi_{2ij} = \int_0^1 Z_i(x),_x Z_j(x),_x \, dx$$

$$\Psi_{3ij} = \int_0^1 Z_i(x),_{xx} Z_j(x),_{xx} \, dx$$

$$\Psi_{4ij} = \int_0^1 Z_i(x),_x Z_j(x) \, dx$$

$$\Psi_{5ij} = \int_0^1 Z_i(x),_{xx} Z_j(x) \, dx$$

$$\Psi_{6ij} = \int_0^1 Z_i(x),_{xx} Z_j(x),_x \, dx.$$

The integrals above have been given in Reference 3.

Equations (9) define a discrete special eigenvalue problem. The solution of this eigenvalue problem yields the natural frequencies and the corresponding shapes.

The above analysis has been programmed for an IBM 360-65 digital computer. This program has been used to predict natural frequencies and characteristic shapes for the plates investigated experimentally.

EXPERIMENTAL INVESTIGATION

Six panels were tested, each having a different combination of lamina orientations. The configurations are given in Table 1 in terms of the principal axis of orthotropy of the laminas. The panels were fabricated of NARMCO 5505 boron-epoxy preimpregnated tape (NARMCO Materials Division of the Whittaker Corporation).

Table 1 PANEL CONFIGURATIONS

Panel	Fiber Orientations
A	$0^\circ/90^\circ/90^\circ/0^\circ/0^\circ/90^\circ/90^\circ/0^\circ$
B	8 at 0°
C	$45^\circ/-45^\circ/45^\circ/-45^\circ/-45^\circ/45^\circ/-45^\circ/45^\circ$
D	$0^\circ/45^\circ/+45^\circ/90^\circ/90^\circ/+45^\circ/-45^\circ/0^\circ$
E	$+22.5^\circ/-22.5^\circ/+67.5^\circ/-67.5^\circ/-67.5^\circ/$ $+67.5^\circ/-22.5^\circ/+22.5^\circ$
F	8 at 45°

Each panel was in turn clamped into a relatively stiff frame constructed of 3- x 3- x 3/8-in. struc - tural steel angles welded at each corner (Fig. 3) . A 1-in. wide, 1/2-in. thick steel clamping bar fast- ened on each side of the frame with 3/8-in. bolts on 1 1/4-in. centers gripped 1/2 in. of each edge of the panels. This reduced the unsupported span of the panels to 12 x 12 in.
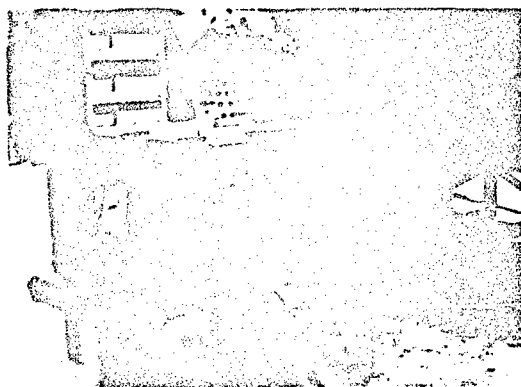
Figure 3 Mechanical Vibration Test Setup

The clamping frame was suspended above two electromechanical shakers on soft rubber cord. The shaker heads were attached to opposing sides of the frame through mechanical fuses attached to rigid angle brackets bolted to the sides of the frame. The shaker attachment brackets were located in turn on the major axes of the panel and at the panel cor- ners to prevent overlooking modes whose node lines corresponded with particular shaker attachment lo- cations.

The shakers used were two 100-pound force elec- tromechanical shakers driven by a common power supply. Synchronization of the shakers in phase or 180 degrees out of phase was accomplished by a se- lector switch. Frequency control was accomplished with a variable frequency oscillator.

When excited at a natural resonance frequency, a panel will vibrate in a characteristic mode shape. The shape is visualized by sprinkling a loose ma- terial on the surface of the panel. This material is bounced off the moving areas of the panel and accumulates on the node lines where there is rela- tively little motion. At frequencies between reso- nances, there are no stationary node lines and the loose material bounces randomly, forming no pat- tern.

Activated aluminum granules were found to have all of the properties required for the loose material. The granules used were much coarser than sand, yet were light and resilient. Their light coloring provided an excellent contrast, for photographic purposes, against the black color of the panels.

With the granules on the surface of the panel, the input frequency was slowly increased until the motion of the granules indicated a resonant condi- tion. The frequency was then tuned to produce the most clearly defined model pattern, the frequency recorded, the power cut off, and the pattern photo- graphed. The upward frequency sweep was then continued until the next resonance was encountered, tuned in, and recorded. This was continued through the frequency range of interest. The same proce- dure was repeated with the shakers oppositely phased, with the shakers attached on the other major axis of the panel and at opposite corners of the frame during in-phase and out-of-phase opera- tion. Other shaker conditions, after the initial sweep through the range, repeated most of the mo- dal patterns. However, some modes not previously excited became so because the node lines coin- cided with the shaker attachment points.

DISCUSSION AND RESULTS

A set of natural modes from the fundamental fre- quency up through approximately 1000 Hz was de- termined for each panel configuration. The modes demonstrated an interplay of two dominant charac- teristics, geometry and stiffness. Configurations A and B had the major stiffnesses coincident with the major geometric axes (specially orthotropic) and the modes were rectangular. The other config- urations involved varying amounts of anisotropy, with Panel F representing the extreme of all 45-de- gree layup. Generally, the lowest frequency modes were found to be geometrically controlled. The ef- fect of anisotropy, which causes a skewing and bending of the modal patterns, became more pro- nounced as the frequency was increased.

The six to twelve lowest natural frequencies and characteristic shapes of the panels have been cal- culated with the anisotropic plate analysis proce- dure described above. The lamina properties, based on General Dynamics sandwich beam tests [4], were taken as follows:

$$E_1 = 3.1 \times 10^7 \qquad E_2 = 2.7 \times 10^6$$
$$\nu_{12} = .28 \qquad G = .75 \times 10^6$$

The density was taken as $.192 \times 10^{-3}$ pound-sec- ond^2/inch^4.

Matched sets of experimentally photographed node lines and analytically predicted node lines for 56 natural modes are presented in Figures 4 through 9. The observed and calculated frequencies are given in the figures. The agreement between pre- dicted and observed nodal lines is excellent. The agreement between observed and predicted fre- quencies is fair.

84
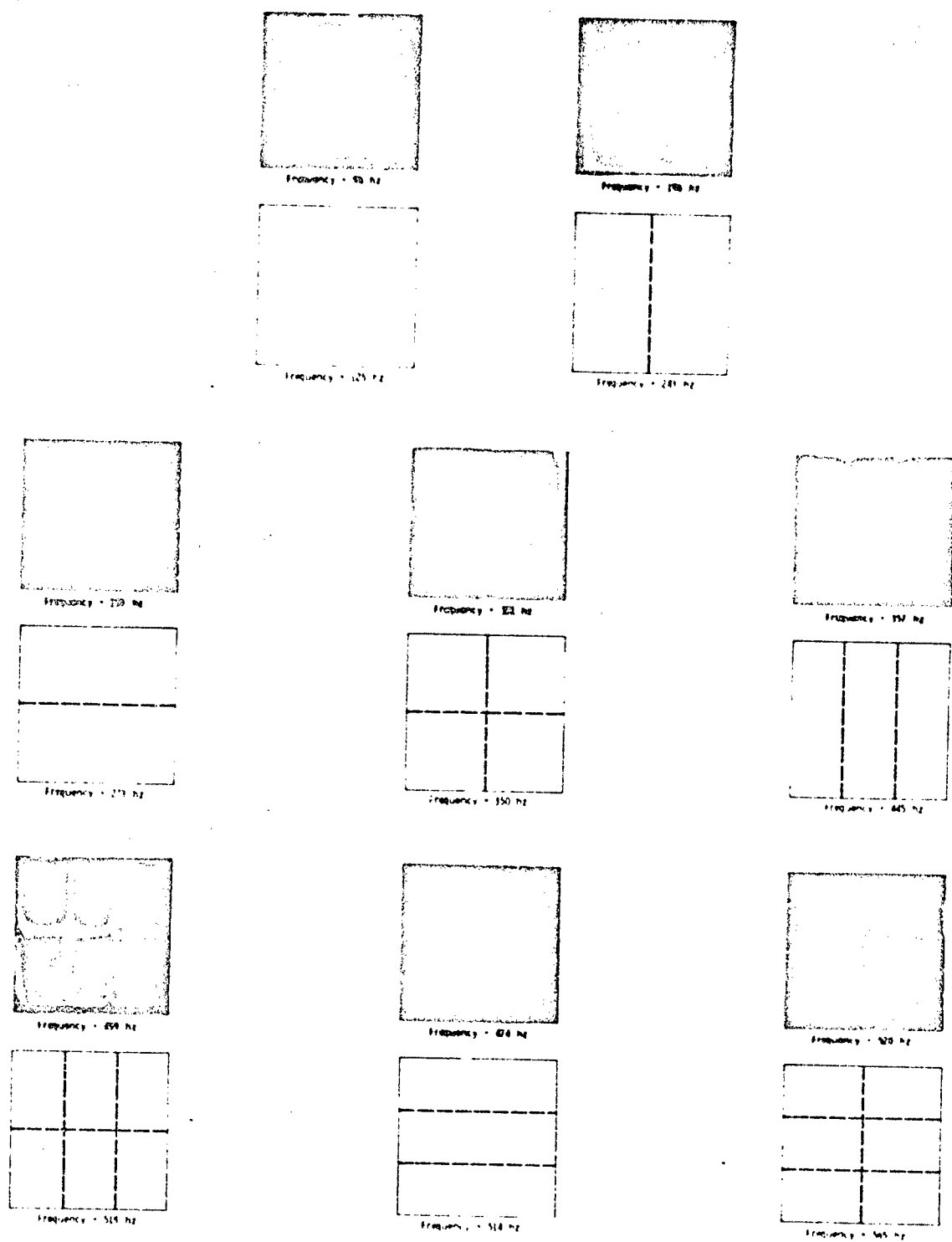
Figure 4 Frequencies and Mode Shapes,
0° - 90° Plate
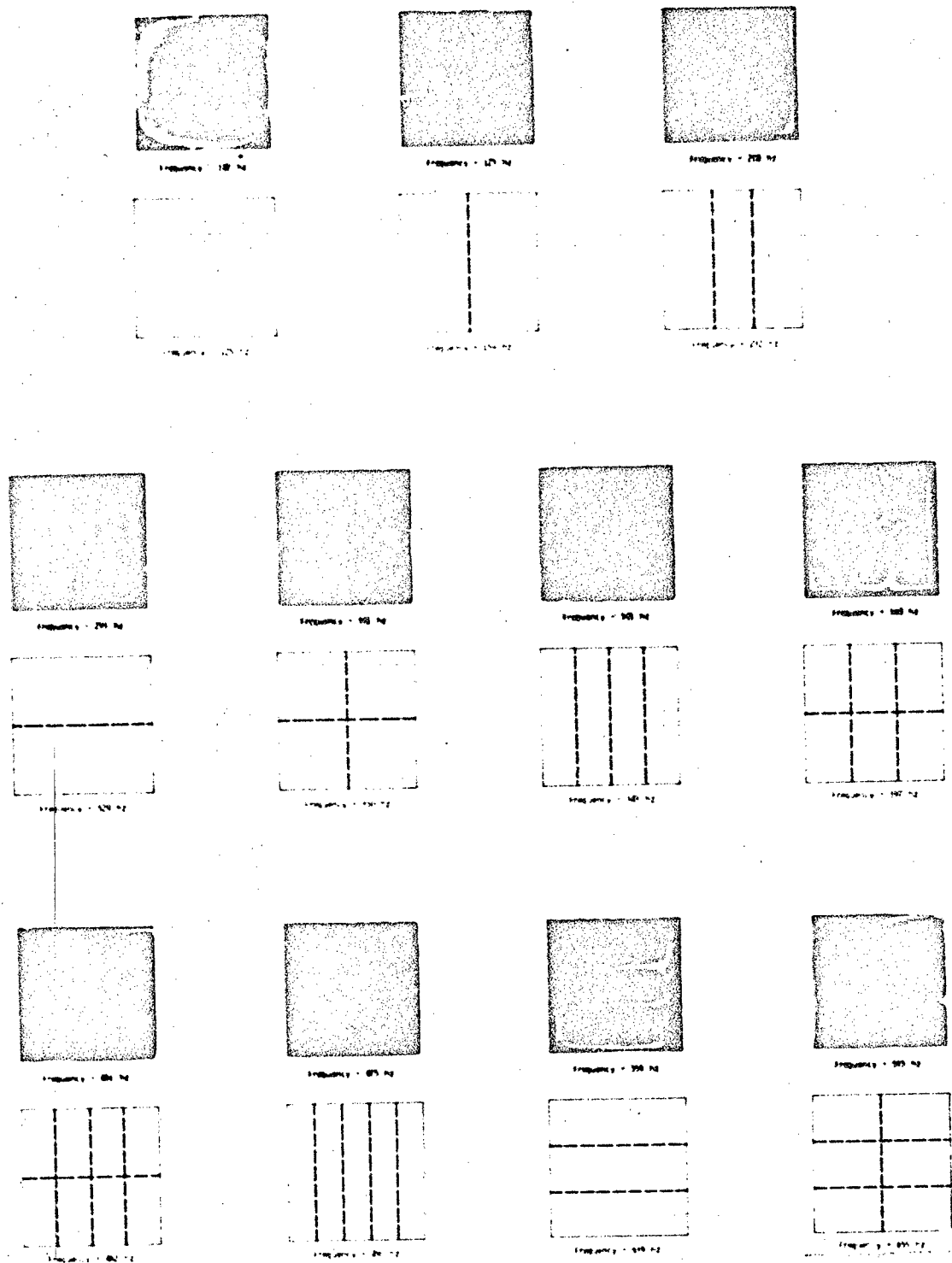
Figure 5   Frequencies and Mode Shapes,
0° Plate

86
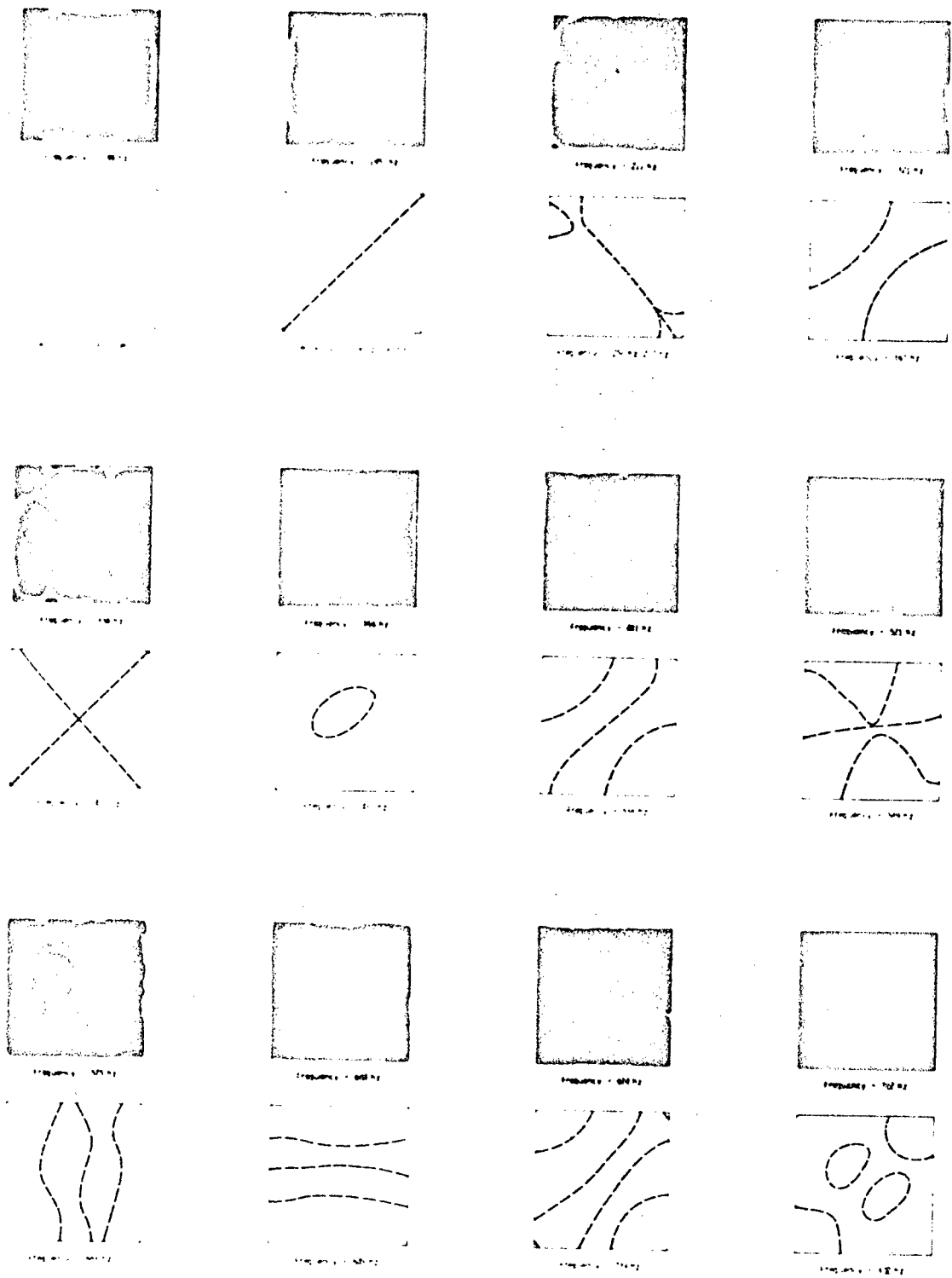
Figure 6 Frequencies and Mode Shapes,
$\pm 45^{\circ}$ Plate

87
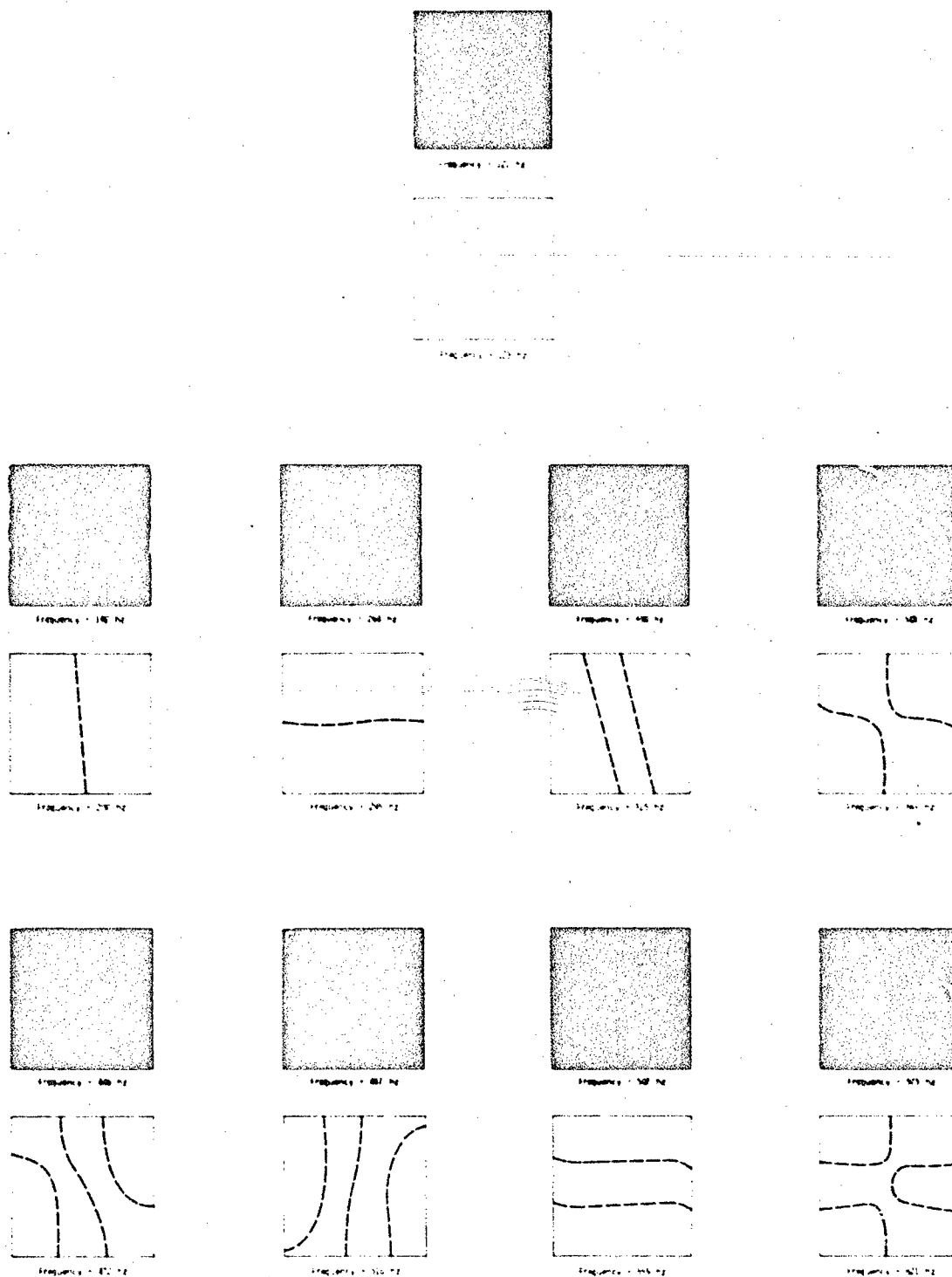
Figure 7 Frequencies and Mode Shapes,
$0^o \pm 45^o$ 90° Plate
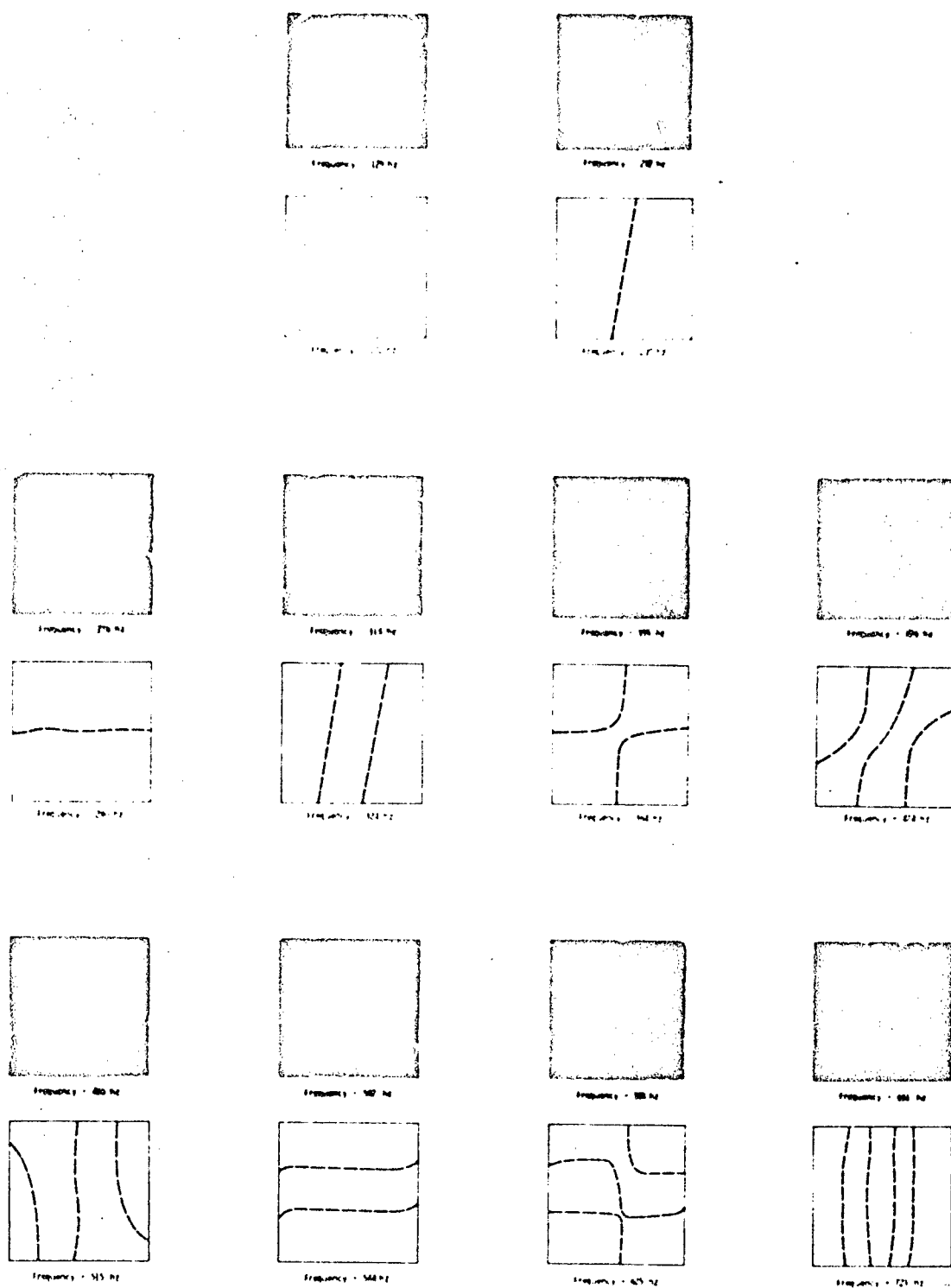
Figure 8   Frequencies and Mode Shapes,
$\pm 22.5^{\circ} \pm 67.5^{\circ}$ Plate
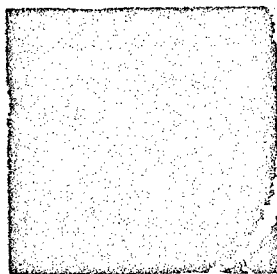
Frequency • 92 hz
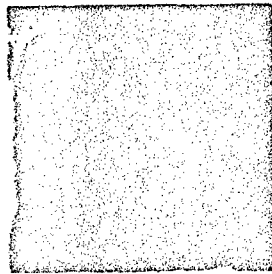
Frequency • 156 hz
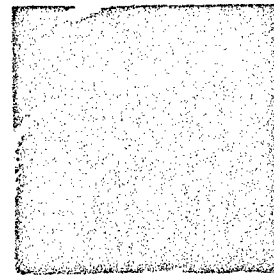
Frequency • 215 hz
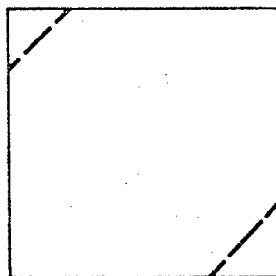
Frequency • 106 hz
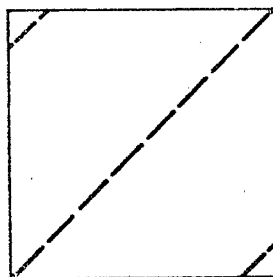
Frequency • 178 hz
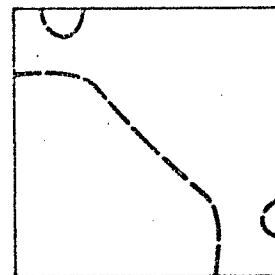
Frequency • 244 hz
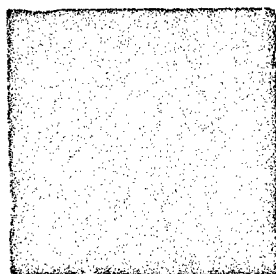
Frequency • 239 hz
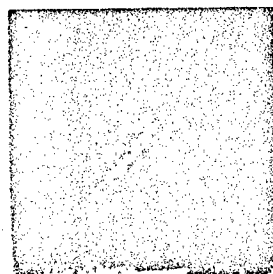
Frequency • 323 hz
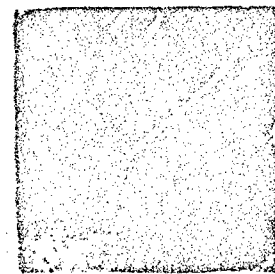
Frequency • 334 hz
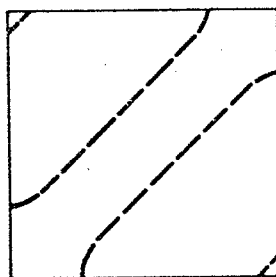
Frequency • 264 hz
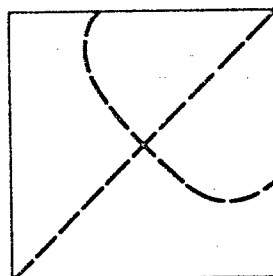
Frequency • 359 hz
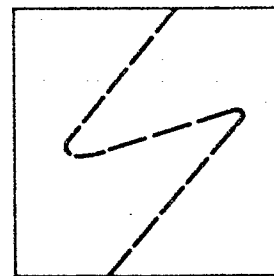
Frequency • 365 hz

Figure 9   Frequencies and Mode Shapes,
8 Plies @ 45°

90

In addition to the matched natural modes, there were several unidentifiable resonant modes within the frequency range considered with the analysis procedure. These are assumed to be modes associated with membrane or in-plane stress which undoubtedly exist in these panels. Some effects can also be expected from frame resonances which are believed to be above 500 Hz.

The experimentally determined frequencies versus the analytically predicted frequencies for the identified natural modes are shown in Figure 10. The predicted frequencies average approximately 10 percent higher than the observed frequencies. This effect is probably due to the assumption of full clamping at the boundaries for the analytical predictions, since the experimentally imposed boundary conditions provide less than rigid fixity. Unfortunately, the specific contribution of this effect would vary from panel to panel, depending on the tightening of the clamping bolts, and the panel configuration.
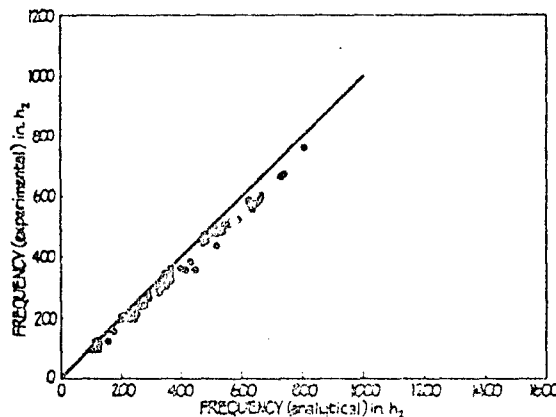
Figure 10 Experimental Vs Analytical
Frequencies

CONCLUSIONS

Experimental investigation confirms that this linear energy analysis procedure yields accurate predictions of the natural vibration mode shapes and frequencies of laminated boron-epoxy plates. It also demonstrates that the effects of anisotropy on the dynamic response are often quite pronounced.

REFERENCES

1. Young, D., "Vibration of Rectangular Plates by the Ritz Method," Journal of Applied Mechanics, December 1950.

2. Pister, K. S., et al., Analysis of Structural Laminates, ARL-76, September 1961.

3. Young, D., and Felgar, R. P., Tables of Characteristic Functions Representing the Normal Modes of a Vibrating Beam, University of Texas, Publication No. 4913, 1949.

4. Shockey, P. D., and Waddoups, M. E., "Strength and Modulus Determination of Composite Materials with Sandwich Beam Tests," presented to the American Ceramic Society Meeting, Chicago, Illinois, September, 1966.

NATURAL MODES OF FREE-FREE ANISOTROPIC PLATES *

J. E. Ashton

General Dynamics
Fort Worth, Texas

An analytical study of the natural frequencies and characteristic shapes of free-free plates is presented. The plates considered are rectangular and laminated of orthotropic plies. The principal axes of orthotropy are not maintained parallel to the plate edges. The analytical solutions are obtained with the Ritz method using beam characteristic shapes to approximate the deflected shape. Solutions are presented which illustrate the effect of varying (1) the orientation of the plies, (2) the stacking sequence, and (3) the degree of orthotropy.

INTRODUCTION

The advent of the widespread use of fiber-reinforced composite materials has renewed interest in the analysis of plates composed of laminated orthotropic materials. This paper presents an analysis of the natural frequencies and characteristic shapes of free-free rectangular plates. The plates considered are laminated of orthotropic material, but the principal axes of orthotropy of the laminas are not maintained parallel to the edges of the plate. The influence of anisotropy on the dynamic frequencies and characteristic shapes is investigated, as is the effect of varying the stacking sequence and orientations.

ANALYSIS TECHNIQUE

The method of solution used in this analysis is Hamilton's principle, with the energy solution obtained by means of the Ritz method. A 36-term series of beam characteristic shapes is used to approximate the deflected shapes.

The potential energy due to bending, for the plate shown in Figure 1, can be written as follows:

$$V = 1/2 \int_0^a \int_0^b [M]^T [X] dx\, dy \qquad (1)$$

where

$$[M] = \begin{bmatrix} M_x \\ M_y \\ M_{xy} \end{bmatrix} = \text{plate moment resultants}$$

$$[X] = \begin{bmatrix} X_x \\ X_y \\ 2X_{xy} \end{bmatrix} = \text{plate curvatures} = \begin{bmatrix} W,xx \\ W,yy \\ 2W,xy \end{bmatrix}$$
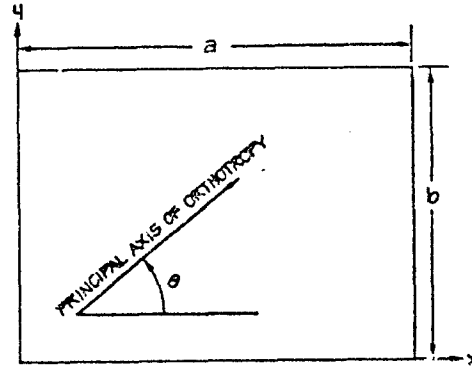
Figure 1   Plate Geometry

W = transverse deflection
and a comma denotes partial differentiation.

For anisotropic materials

$$[M] = [D] [X] \qquad (2)$$

where D is in general a fully populated matrix of stiffness coefficients which can be defined in terms of the elastic constants of orthotropic laminas and related orientations of the principal axes of orthotropy.

Substituting Equation (2) into Equation (1) and expressing the curvatures in terms of deflection, the potential energy can be expressed in terms of an integral over the area involving the stiffness terms and the deflection.

The kinetic energy is given in terms of the deflection by the following expression:

$$T = 1/2 \omega^2 \rho h \int_0^a \int_0^b W^2 dx\, dy \qquad (3)$$

*This paper not presented at Symposium.

93

where

ρ = mass density

h = plate thickness

ω = angular frequency of vibration.

An approximate solution can be obtained by equating the potential energy to the kinetic energy and requiring this energy balance to be (approximately) stationary. In the present analysis, the deflection is assumed in a series:

$$W = \sum_{i=1}^{6} \sum_{j=1}^{6} a_{ij} Z_i(x) Z_j(y) \qquad (4)$$

where

a_{ij} = parameters to be determined.

In this study, the functions $Z_i(x)$ and $Z_j(y)$ were taken as the characteristic shapes of free-free vibrating beams [1]. Although these functions only approximately satisfy the boundary conditions of zero moment and shear on the plate boundary, they allow the edge to deflect and take any slope, and thus provide a good approximation to the true free edge boundary conditions.

The condition

$$V - T = \text{stationary value} \qquad (5)$$

can be approximately satisfied by substituting the series (4) into expressions (1) and (3) and differentiating the energy balance $V = T$ with respect to a_{ij}. This results in the following systems of simultaneous equations which can be solved to give the natural frequencies and related mode shapes:

$$\frac{\partial V}{\partial a_{ik}} = \sum_{m=1}^{6} \sum_{n=1}^{6} d_{ikmn} a_{mn} = \frac{\partial T}{\partial a_{ik}} = \omega^2 \rho h \, ab \qquad (6)$$

where

$$d_{ikmn} = D_{11} \Psi_{3im} \Psi_{1kn} \frac{b}{a^3} + D_{12} \cdot$$

$$(\Psi_{5im} \Psi_{5nk} + \Psi_{5mi} \Psi_{5kn}) \frac{1}{ab}$$

$$+ D_{22} \Psi_{1im} \Psi_{3kn} \frac{a}{b^3} + 2D_{16} \cdot$$

$$(\Psi_{6mi} \Psi_{4kn} + \Psi_{6im} \Psi_{4nk}) \frac{1}{a^2}$$

$$+ 2D_{26} (\Psi_{4im} \Psi_{6nk} + \Psi_{4mi} \Psi_{6kn}) \cdot$$

$$\frac{1}{b^2} + 4D_{66} \Psi_{2im} \Psi_{2kn} \frac{1}{ab}$$

and

$$\Psi_{1ij} = \int_0^1 Z_i(x) \; Z_j(x) \; dx$$

$$\Psi_{2ij} = \int_0^1 Z_i(x)_{,x} \; Z_j(x)_{,x} \; dx$$

$$\Psi_{3ij} = \int_0^1 Z_i(x)_{,xx} \; Z_j(x)_{,xx} \; dx$$

$$\Psi_{4ij} = \int_0^1 Z_i(x)_{,x} \; Z_j(x) \; dx$$

$$\Psi_{5ij} = \int_0^1 Z_i(x)_{,xx} \; Z_j(x) \; dx$$

$$\Psi_{6ij} = \int_0^1 Z_i(x)_{,xx} \; Z_j(x) \; dx$$

The integrals are tabulated in Reference 1.

RESULTS AND DISCUSSION

A wide variety of results has been calculated to illustrate the effects of anisotropy on both the natural frequencies and mode shapes. Thirty-six terms have been used for all calculations. The comparisons presented below are restricted to square plates (a = b) so that the effects of anisotropy, and, in particular, the effects of lamination angles and sequence, can be observed with a minimum variation in geometry. The natural frequencies are presented in terms of the parameter λ defined such that

$$\omega^2 = \lambda \frac{E_2 h^2}{\rho a^4} \qquad (7)$$

where E_2 is the smaller of the two principal elastic moduli. The major Poisson's ratio term (ν_{12}) for the orthotropic laminas considered here has been taken to be .3.

Orthotropic Layers With Varying Orientations

The first four natural frequencies and mode shapes of plates composed of a single layer of orthotropic material with the principal axis of

94
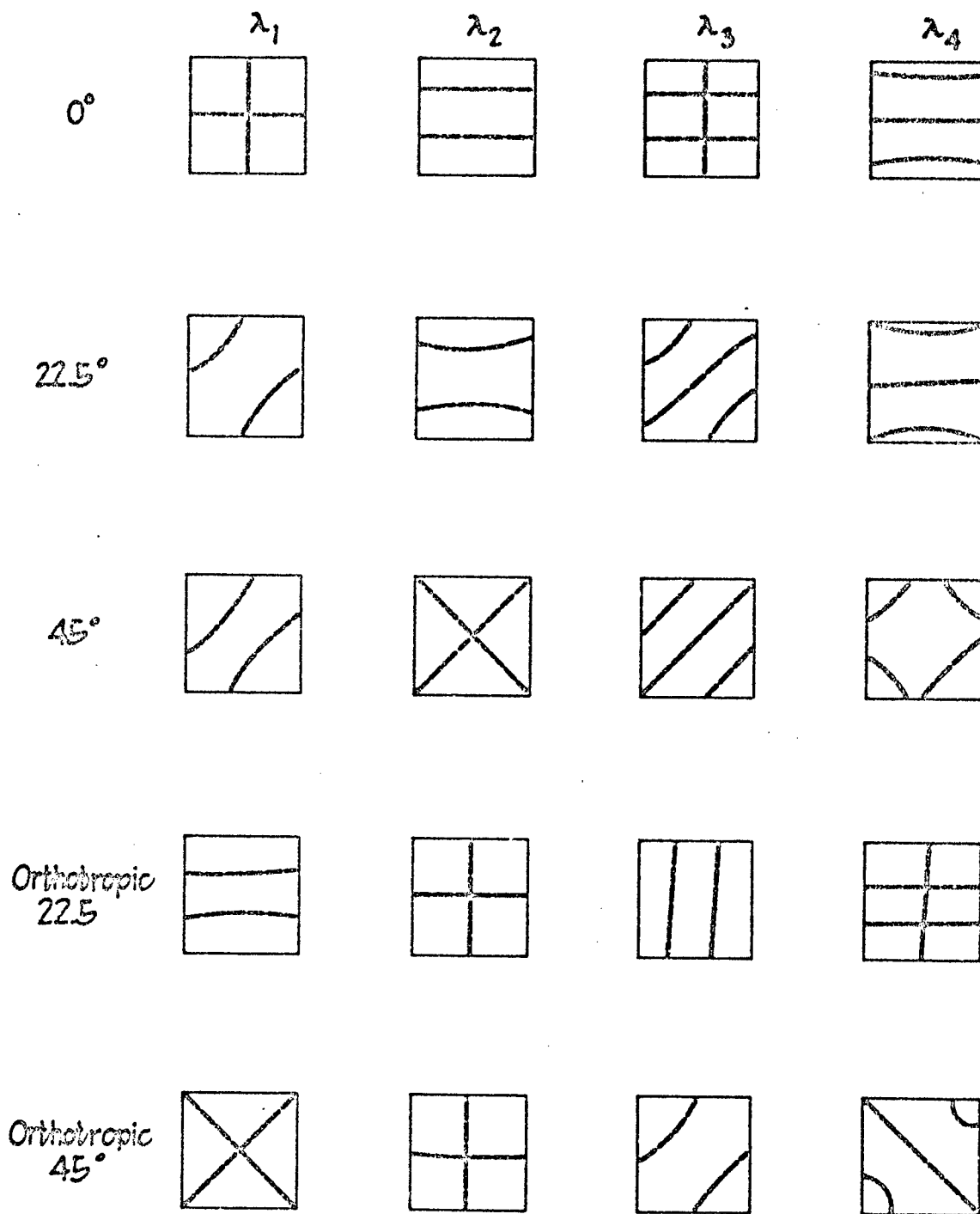
Figure 2 Characteristic Shapes for Variable
Orientation

orthotropy at angles of 0, 22.5, and 45 degrees with respect to the plate edges have been obtained for the following material property ratios:

$$\frac{E_1}{E_2} = 10 \qquad \frac{G_{12}}{E_2} = .5.$$

The $[D]$ matrix for these plates is easily computed with the following formulas [2]:

$$D_{ij} = \frac{1}{12} \bar{C}_{ij} h^3 \qquad (8)$$

where

$$\bar{C}_{11} = C_{11} \cos^4\theta + 2(C_{12} + 2C_{66}) \sin^2\theta \cdot \cos^2\theta + C_{22} \sin^4\theta$$

$$\bar{C}_{12} = (C_{11} + C_{22} - 4C_{66}) \sin^2\theta \cos^2\theta + C_{12} (\sin^4\theta + \cos^4\theta)$$

$$\bar{C}_{22} = C_{11} \sin^4\theta + 2(C_{12} + 2C_{66}) \sin^2\theta \cos^2\theta + C_{22} \cos^4\theta$$

$$\bar{C}_{16} = (C_{11} - C_{12} - 2C_{66}) \sin\theta \cos^3\theta + (C_{12} - C_{22} + 2C_{66}) \sin^3\theta \cos\theta$$

$$\bar{C}_{26} = (C_{11} - C_{12} - 2C_{66}) \sin^3\theta \cos\theta + (C_{12} - C_{22} + 2C_{66}) \sin\theta \cos^3\theta$$

$$\bar{C}_{66} = (C_{11} + C_{22} - 2C_{12} - 2C_{66}) \sin^2\theta \cdot \cos^2\theta + C_{66}(\sin^4\theta + \cos^4\theta)$$

and

$$C_{11} = \frac{E_1}{1 - \nu_{12}\nu_{21}}$$

$$C_{22} = \frac{E_2}{1 - \nu_{12}\nu_{21}}$$

$$C_{12} = \frac{\nu_{12} E_2}{1 - \nu_{12}\nu_{21}}$$

$$C_{66} = G_{12}$$

$$\nu_{12} = \nu_{21} \frac{E_1}{E_2}$$

θ = orientation of principal axis with respect to the plate edge.

The natural frequency parameter λ is presented for these orientations in Table 1. Also presented in Table 1 are the analogous results neglecting the anisotropic coupling terms D_{16}, D_{26} (orthotropic analysis) as has been frequently done in the past. Clearly, these terms are quite significant except at 0 degrees (when they are always zero). The node lines corresponding to these frequencies are presented in Figure 2. The effect of anisotropy on these shapes is also quite significant.

Table 1 EFFECT OF ORIENTATION FOR A SINGLE ORTHOTROPIC LAYER

Orientation		0°	22.5°	45°
λ_1	Anisotropic	22.1	28.9	30.4
λ_1	Orthotropic	22.1	46.0	65.1
λ_2	Anisotropic	41.8	45.5	54.9
λ_2	Orthotropic	41.8	65.6	103.8
λ_3	Anisotropic	134.7	148.3	158.5
λ_3	Orthotropic	134.7	318.6	203.4
λ_4	Anisotropic	317.0	320.4	245.7
λ_4	Orthotropic	317.0	324.2	548.4

Effect of Alternating Laminations

To illustrate the effects of laminating multiple plies at alternating $\pm \alpha$ angles (with respect to the plate edges), several $\pm 45^\circ$ laminations have been considered. The material property ratios used here are the same as used for the results discussed above. The plate stiffness matrix $[D]$ for a plate composed of n plies at $\pm \alpha$ constructed with midplane symmetry is identical to the matrix for a plate composed of a single layer at $+ \alpha$, except for the anisotropic coupling terms D_{16}, D_{26}. These terms can be computed as follows:

$$D_{16,26} = \frac{1}{3} \sum_{k=1}^{n} (C_{16,26})_k (h_k^3 - h_{k-1}^3) \qquad (10)$$

where the h_k are described in Fig. 3 and the $(\bar{C}_{ij})_k$ are given, for each lamina, in Eq. (9). For a $\pm 45^\circ$ laminate, $D_{16} = D_{26}$ and $D_{16} \longrightarrow 0$ as n becomes large. The ratio D_{16}/D_{11} is presented vs. n in Fig. 4. The first four natural frequencies have been calculated for n = 1, 4, 8, and the limiting (orthotropic) case, $n \longrightarrow \infty$. The frequencies are listed in Table 2 and the mode shapes are shown in Fig. 5. Clearly, the plate becomes effectively stiffer for alternating plies.
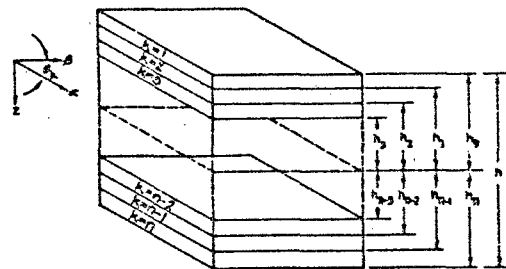
Figure 3 Layer Coordinates and Orientation for Laminates

96
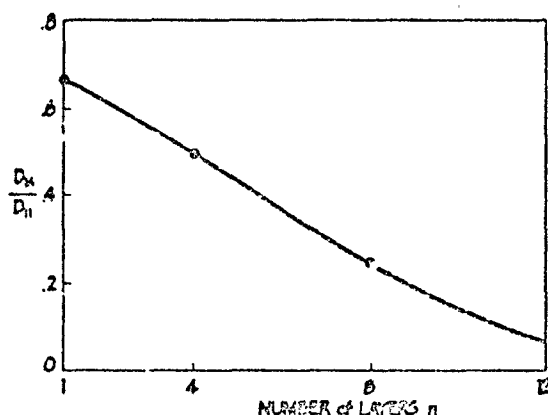
Figure 4 Variation of $\dfrac{D16}{D11}$ Vs N for $\pm 45^\circ$
Laminate

Table 2 EFFECT OF STACKING SEQUENCE
FOR A ± 45 PLATE

Laminate	λ_1	λ_2	λ_3	λ_4
1 @ +45	30.4	54.9	158.5	245.7
4 @ $\pm$45	57.9	59.8	239.6	295.4
8 @ $\pm$45	63.9	92.7	254.4	463.2
∞ @ $\pm$45 (Orthotropic)	65.1	108.8	203.4	548.4

Table 3 EFFECT OF VARIATIONS IN E_1/E_2

E_1/E_2	λ_1	λ_2	λ_3	λ_4
10.	30.4	54.9	153.5	245.7
7.5	29.3	50.6	151.2	194.6
5.0	27.7	46.0	140.6	142.4
2.5	24.4	40.7	84.4	129.0
1.0	16.7	35.9	54.7	112.4

CONCLUSIONS

The results of an analysis of the natural modes of vibration of free-free laminated plates indicate that the natural frequencies and the characteristic shapes of such plates are strongly affected (1) by the orientation of the principal axes of orthotropy of the laminas, (2) by the ratio of the principal elastic moduli, and (3) by the stacking sequence.

Variations of E_1/E_2

The results previously presented considered that the orthotropic laminas were strongly orthotropic, i.e., $E_1/E_2 = 10$. In this section, a $\pm 45^\circ$ one-ply plate is considered for decreasing values of the ratio E_1/E_2; in particular for values of $E_1/E_2 = 10, 7.5, 5, 2.5,$ and 1. In order to converge in a consistent manner to the isotropic case when $E_1/E_2 = 1$, the ratio G_{12}/E_2 has been varied linearly with E_1 from .5 when $E_1/E_2 = 10$ to .385 when $E_1/E_2 = 1$.

The first four natural frequencies are presented for these values of E_1/E_2 in Table 3. The associated mode shapes are drawn in Fig. 6. Both the frequencies and mode shapes make a continuous transition from the highly anisotropic case to the isotropic case.

97

1@+45°

4@±45°

8@±45°
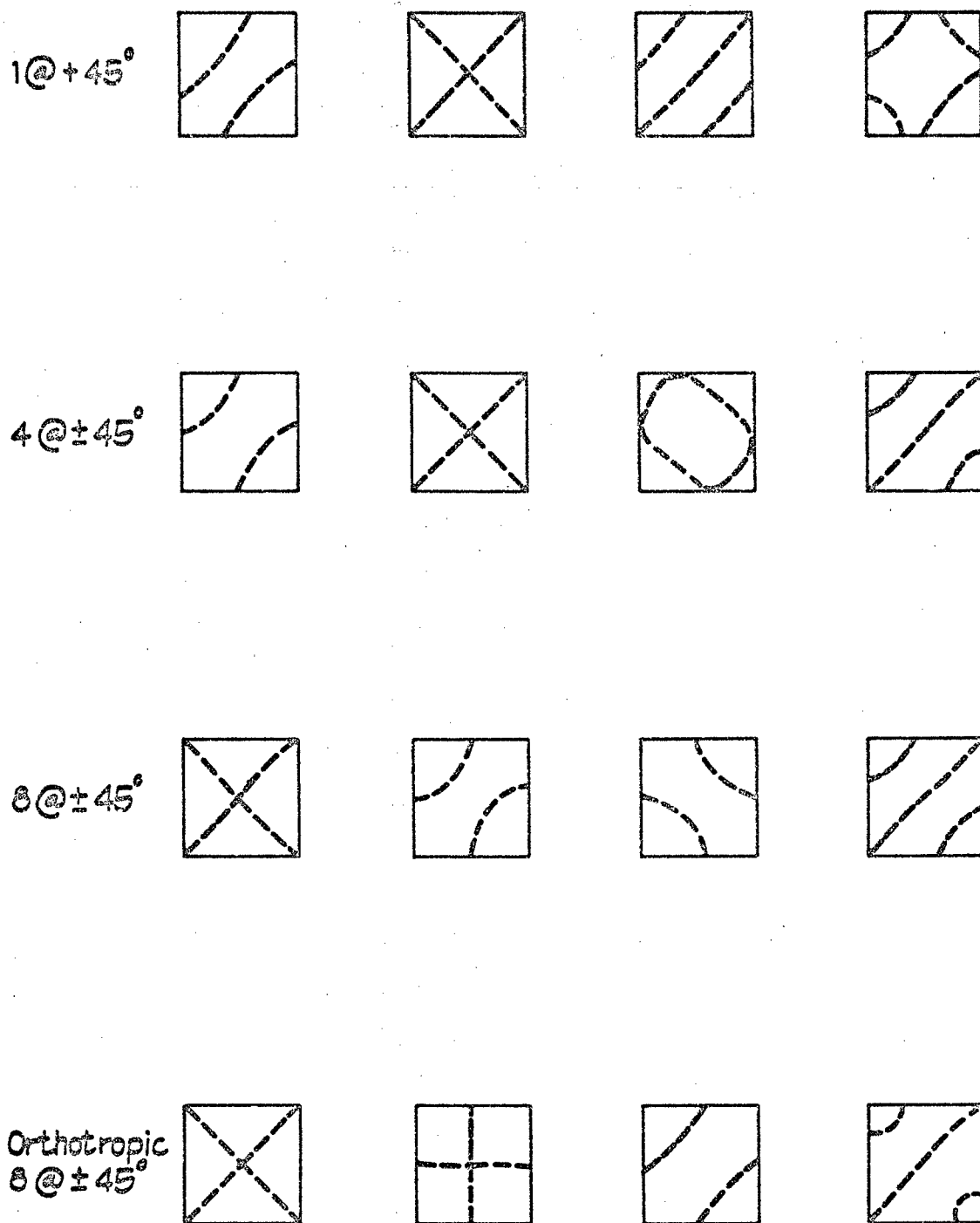
Orthotropic
8 @ ±45°

Figure 5 Characteristic Shapes for $\pm$ 45°
Laminates

$$\frac{E_1}{E_2} = 10$$

$$\frac{E_1}{E_2} = 7.5$$

$$\frac{E_1}{E_2} = 5.0$$

$$\frac{E_1}{E_2} = 2.5$$

$$\frac{E_1}{E_2} = 1$$
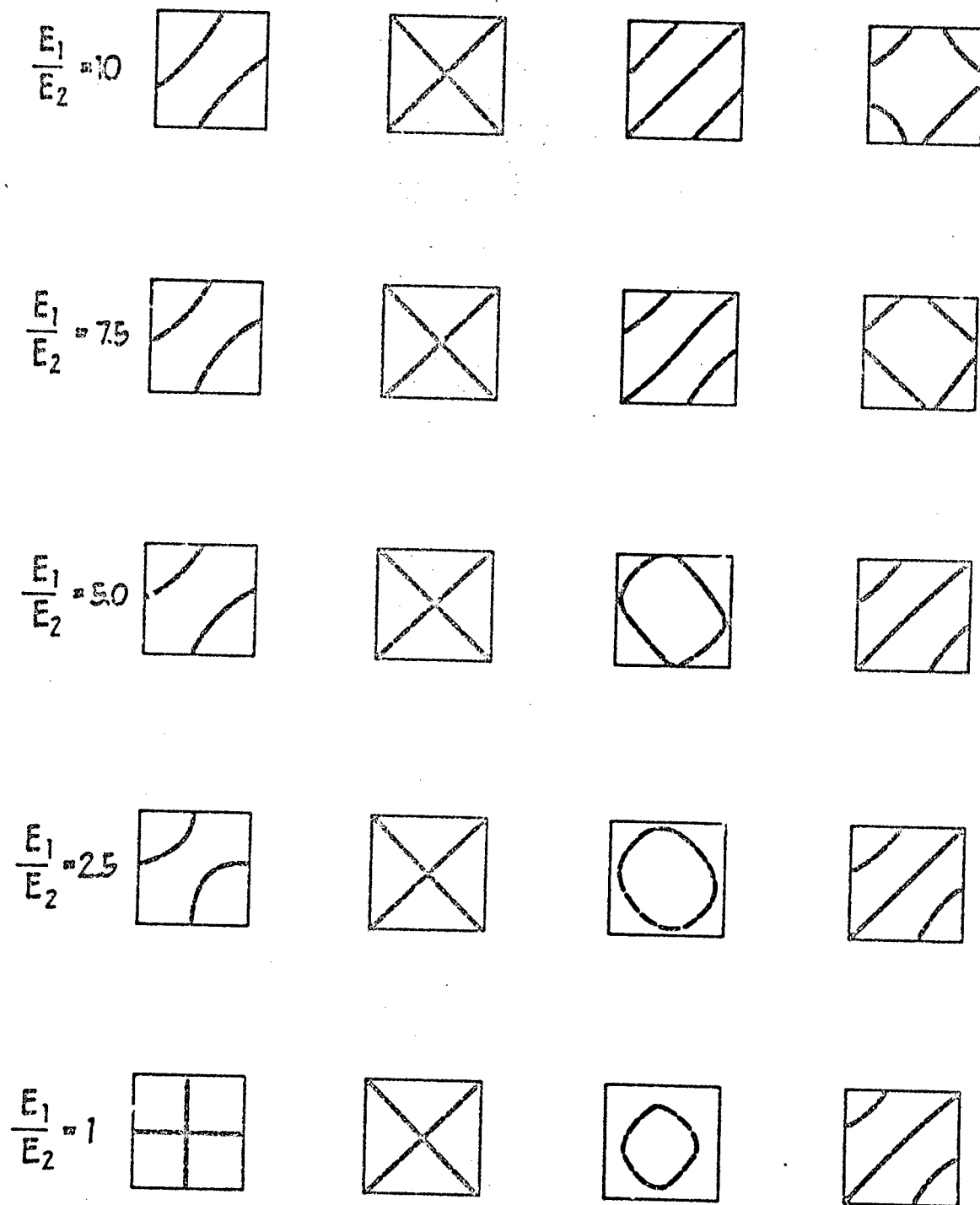
Figure 6 Characteristic Shapes for Variable
Degree of Orthotropy

ACOUSTIC TEST OF BORON FIBER REINFORCED COMPOSITE

PANELS CONDUCTED IN THE AIR FORCE FLIGHT DYNAMICS

LABORATORY'S SONIC FATIGUE TEST FACILITY

Carl L. Rupert
Air Force Flight Dynamics Laboratory
Wright-Patterson Air Force Base, Ohio

This experimental program was performed in support of research in airframe application of advanced composite material. The principal objectives were to determine the effects of fiber orientation on the response characteristics of a series of boron-epoxy panels when exposed to a high intensity sound environment, and to evaluate their sonic fatigue resistivity. The panel specimens were installed in the Air Force Flight Dynamics Laboratory's Small Scale Acoustic Test Facility and subjected to grazing incidence impingement at sound pressure levels in increments up to 160 dB (re .0002 dynes/cm^2). The pronounced nonlinear response of the panels is discussed. Representative strain levels are presented. Strain distribution patterns obtained using the brittle coating technique are shown.

INTRODUCTION

The demands of modern aerospace design stress the need for new materials with superior elastic properties, better strength-to-weight ratios, and extended high temperature applications. An example is the recent and rapid development in advanced types of fiber reinforced composite material which has generated considerable interest. Particular emphasis has been directed to boron-epoxy systems and their potential application in flight vehicle structure.

This paper presents some of the results of an experimental acoustic test program conducted in the Air Force Flight Dynamics Laboratory in support of research in airframe application of advanced composite material.

The test program objectives were (1) to determine the effects of fiber orientation on the response characteristics of a series of boron-epoxy panel specimens when exposed to a high intensity sound environment, (2) to obtain fatigue life data, and (3) to photograph strain distribution patterns from each panel configuration using the brittle coating technique.

DESCRIPTION OF TEST SPECIMENS

The specimens were 13 inch square flat panels of .040 inch nominal thickness, laminated of eight plies of boron fiber reinforced composite material. In this type of construction, each ply is essentially orthotropic as it is comprised of boron filaments aligned unidirectionally and imbedded in an epoxy matrix. The matrix material was Narmco 5505. The boron content was 50% by volume.

However, the panels were considered to be anisotropic as the angular orientation of the orthotropic axis of each ply is varied in sequence during the 8-ply lay-up. The orthotropic axes are not necessarily maintained parallel to the edges.

The six test configurations are listed in Table I. Note that the sequence of ply lay-up is symmetrical about the center line. Two configurations, the All 0° and All 45°, were included for academic reasons and not to evaluate their potential strength. All specimens were installed for test with the 0° reference axis oriented vertically.

101

SMALL SCALE TEST CHAMBER
SONIC FATIGUE FACILITY

Fig. 1 - Small scale acoustic test facility

Fig. 2 - Siren room and test set-up
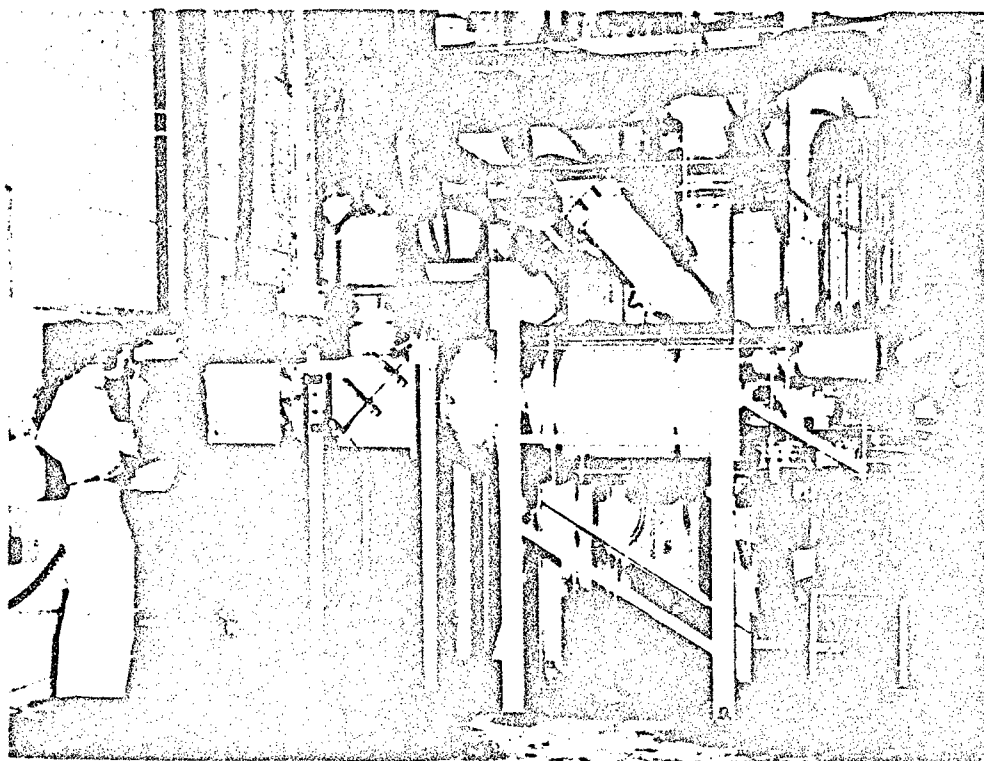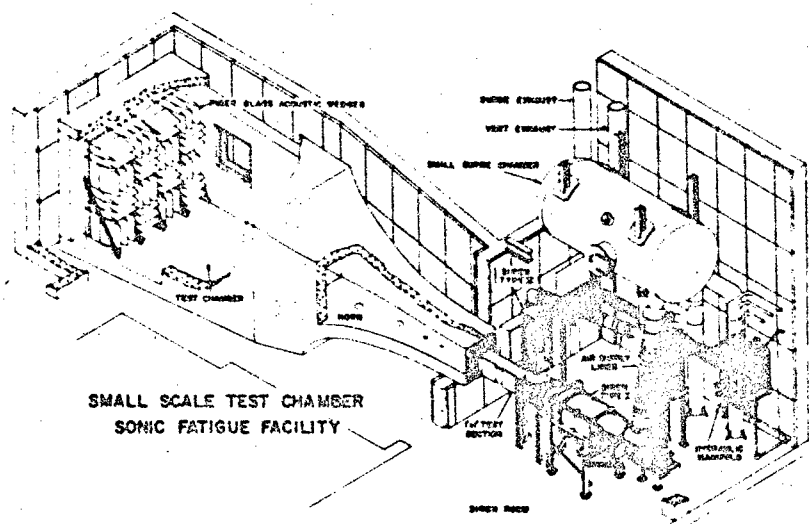
TABLE I

Fiber Orientation for 8-Ply Panel Specimens

Outer Ply	Center Line						Outer Ply
0°	90°	0°	90°	90°	0°	90°	0°
0°	0°	0°	0°	0°	0°	0°	0°
+45°	-45°	+45°	-45°	-45°	+45°	-45°	+45°
0°	+45°	-45°	90°	90°	-45°	+45°	0°
+22.5°	-22.5°	+67.5°	-67.5°	-67.5°	+67.5°	-22.5°	+22.5°
+45°	+45°	+45°	+45°	+45°	+45°	+45°	+45°

TEST INSTALLATION

The source of discrete frequency excitation required for the program was provided by the Small Acoustic Test Facility (1) shown in the cut-away of Fig. 1. It is equipped with two sirens that produce a maximum power output of 50 kw over a frequency range of 50 Hz to 10 k Hz in two overlapping increments. The sirens are coupled to an 800 cubic ft termination chamber by a 16 ft catenoidal horn. Immediately downstream of the sirens is a one-foot square test section in which sound pressure levels (SPL) up to 174 dB* can be attained and in which the panels were installed singly for exposure to grazing incidence sound energy. The test set-up (Fig. 2) shows the panel installed in a specially designed fixture which in turn is clamped to the side of the one-foot section.

Instrumentation was kept minimal. Strain gages were located perpendicularly to each panel edge on centers, plus a rosette in the geometrical center of the panel. Sound pressure levels were monitored by a microphone positioned near the test panel as shown in Fig. 3. A pulsed frequency signal was recorded from the siren to provide a frequency tracking reference for response amplitude analysis.

During preliminary check runs made on a "practice" panel it was discovered that an increase in the siren air temperature of only 10 to 15 degrees Fahrenheit could cause the panel to expand and buckle while clamped in the fixture. This tendency to "oil-can" was resolved by heating the panel while it remained loose in the fixture and then torquing it while hot. Upon removing the heat, the panel remained prestressed in the fixture so long as the siren air temperature did not exceed the pre-heat temperature.
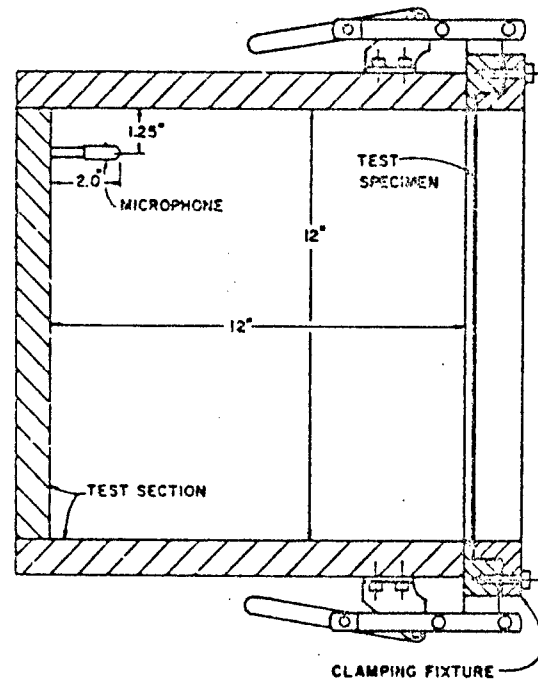
Fig. 3 - Upstream view of test section showing specimen installed for grazing incidence exposure

---

*All SPL's in this paper are referred to 0.0002 dynes/cm^2

103

LINEAR RESPONSE | SYSTEM WITH NONLINEAR RESTORING FORCES

Fig. 4 - Comparison of damped linear and damped nonlinear systems
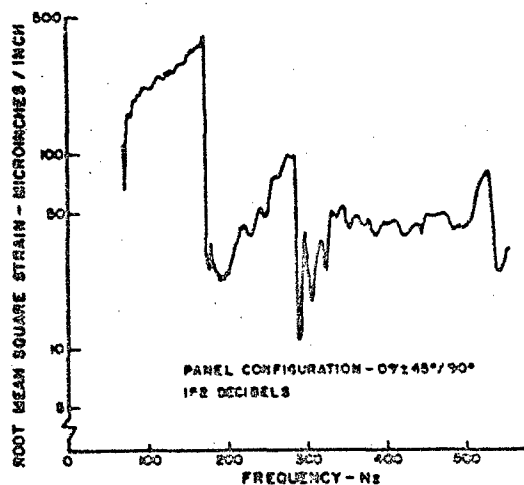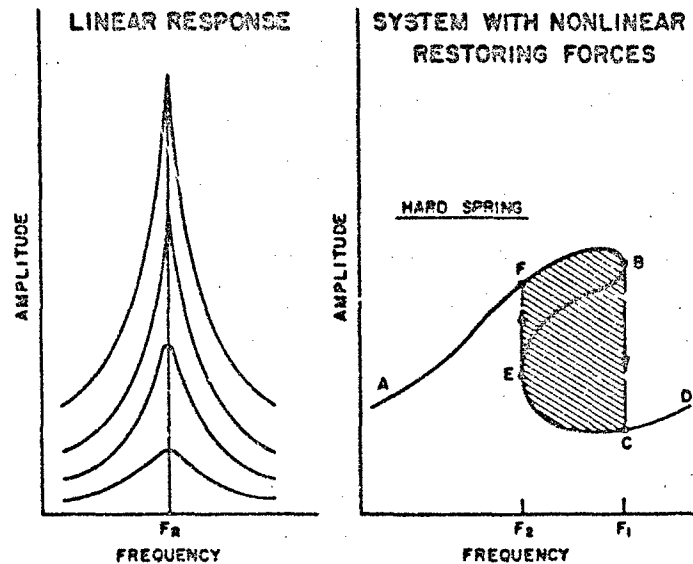
Fig. 5 - Response of 0°/+45°/-45°/90° panel during frequency sweep at constant SPL

RESPONSE TESTING

Sweep frequency data were required to determine the linearity of strain response for increases in loading, and to select the maximum responding mode of vibration for later tests-to-failure. Consequently, response runs were accomplished for each panel configuration at SPL's of 140 dB, 146 dB, 152 dB, and 158 dB,

i.e., by sweeping the siren frequency from approximately 70 Hz to 550 Hz while holding the sound pressure level constant. Each sweep run was monitored by a recording oscillograph. In addition, all gage and microphone outputs, and the tracking signal were stored on magnetic tape for later analysis.

The most significant aspect of the response data pertains to the matter of strain linearity with respect to increases in sound pressure level. To make this phase of the test more meaningful, a comparison is made between the classical damped linear and damped nonlinear response curves. These are shown in Fig. 4.

Typically, the damped linear system resonates at a natural frequency which essentially remains constant regardless of any increases in the magnitude of the exciting force.

In a damped nonlinear system, the restoring forces are not proportional to the displacement. The example shown typifies a "hard spring" system. (A "soft" system would bend the other way.) This swept-over appearance of the nonlinear response curve is explained thus: as the excitation frequency is gradually increased, the vibratory amplitude also slowly increases from A through F and continues to near B at which point a very slight increase in frequency causes the amplitude, after a transitory hesitation, to suddenly "jump-down" to C at which point stability is regained and progress toward D is resumed.

104

Fig. 6 - Family of response
curves for a damped
nonlinear system at
varying levels of
energy input

AMPLITUDE

HARD SPRING

REGION OF
INSTABILITY

EXCITATION FREQUENCY
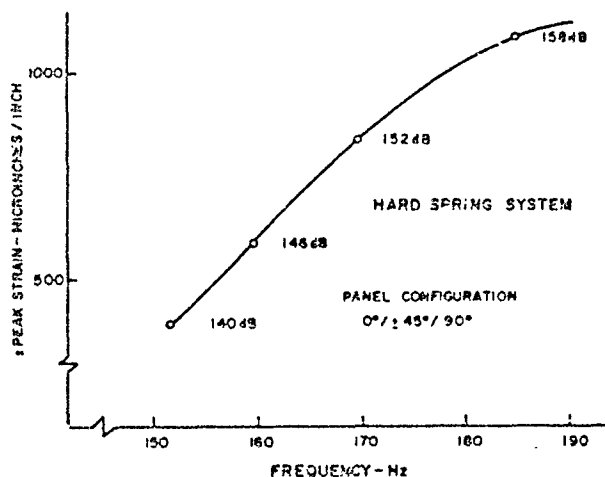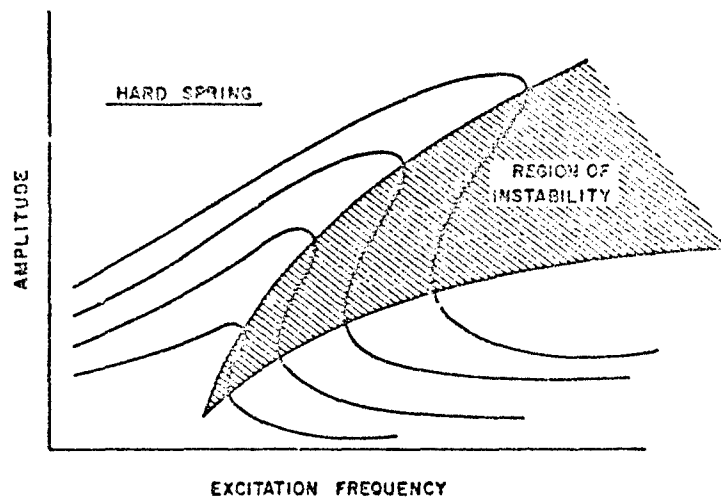
Fig. 7 - Data from the
0°/+45°/-45°/90°
panel showing
increase in natural
frequency

HARD SPRING SYSTEM

PANEL CONFIGURATION
0°/±45°/90°

Conversely, with a gradual decrease in frequency the curve, starting at D, is retraced through C to near E where the amplitude begins to hesitantly blossom and the "jump" phenomenon i· again encountered, this time from E to F where stability is achieved and the amplitude retraces the curve toward A. Thus, for any frequency falling between F_2 and F_1 there are two values of amplitude which exist while amplitudes within the shaded area are not attainable. (2, 3)

The pronounced nonlinearity of the boron-epoxy composite panels is evident in the Strain versus Frequency response charts, one of which is shown in Fig. 5. This is representative of the strain gage output from all panel configurations and demonstrates the "jump" effect that is peculiar to a hard-spring system during increasing sweep frequency.

This concept of nonlinear response can be expanded to include a family of curves, one for each level of energy input, as shown in Fig. 6. In general, the effect of increasing the exciting force is to increase the response amplitude at all frequencies while extending the resonant peak. A plot of the loci of vertical tangents to the response curves defines the region of instability. The natural frequency of the nonlinear hard-spring system follows the upper boundary of this area. This is exemplified by data recorded from the 0°/±45°/90° panel for each increment of loading, and shown in Fig. 7, demonstrating that the natural frequency shifted upward by 33 Hz over an 18 dB increase in sound pressure level. This is a typical example applying to all panel configurations.

105

PANEL B-1
ALL 0°
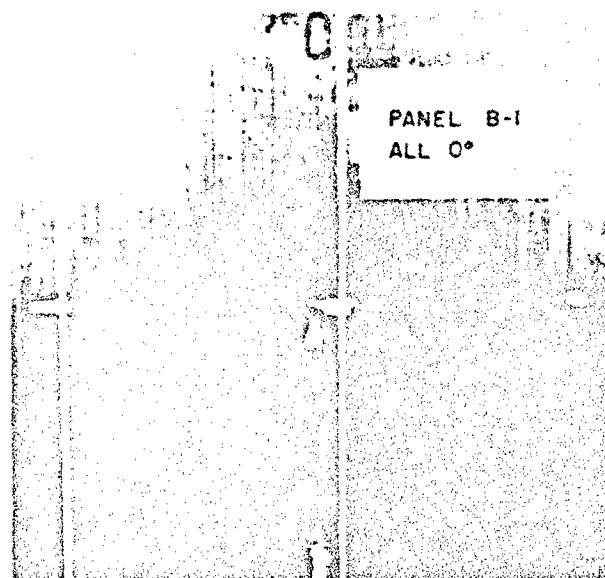
Fig. 8 - All panel failure
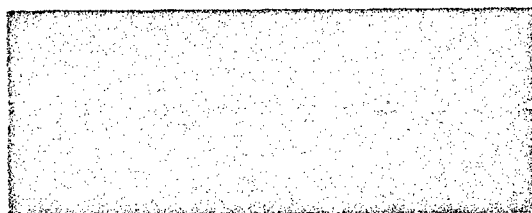
Fig. 9 - Ply separation in edge of
+45°/-45°/+45°/-45° panel

ENDURANCE TESTING

An additional objective, obtaining fatigue life data, was achieved to an extent commensurate with the limited number of specimens available, i.e., a maximum of four each of three panel configurations, and three each of the remaining configurations.

It was preferable to select a fatigue test loading that, for all panel configurations would induce failure without accumulating an excessively large number of test hours. Based on strain levels observed during response testing, it was estimated that 160 dB would be sufficient to cause failure within a reasonable period of test time.

Subsequently, all specimens were tested to failure as planned, at a sound pressure level of 160 dB. However, it is necessary to examine and account for those test variables that may have influenced the results before attempting to evaluate fatigue life.

For example, over-torquing the test fixture caused the panel specimen to distort. This, when combined with the previously described tendency to oil-can made panel installation a time consuming and sensitive procedure, and repeatable boundary conditions improbable.

It was first thought that failure could be detected visually while the panel remained installed in the test fixture. However, post-failure examination of the first several specimens revealed that damage in the outer plies was propagating undetected from the points of incipiency in the clamped area under the test fixture. Thereafter, all specimens were

106

Fig 10 - Close-up of broken
filaments in clamped
area of +22.5°/-22.5°/
+67.5°/-67.5° panel
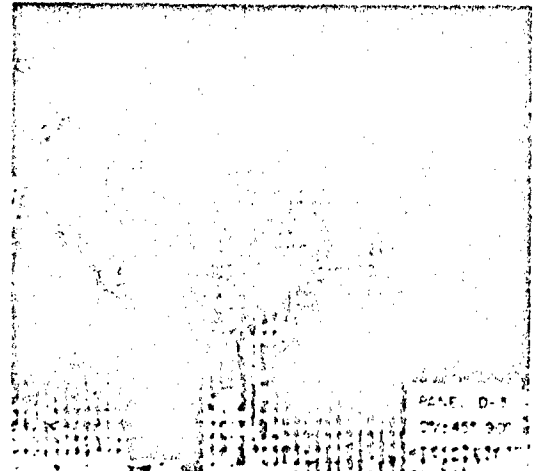
Fig. 11 - Example of extensive damage
incurred before failure was
detected

routinely removed from the fixture at regular
inspection intervals and the suspected areas
examined by microscope if failure was not
otherwise evident.

By definition, if the resonant frequency
fell-off by 10% during an endurance run, a
failure was suspected and generally found to
exist, though subsequent examination often
revealed the extent of damage to vary from
severe to nearly undetectable ply separation.
To the other extreme, detection of an incipien-
cy, sometimes only several broken filaments,
by microscope during routine inspection
intervals also was technically classified as a
failure. Consequently, "time-to-failure" by
itself is ambiguous and a function of the type
of failure and how far it had progressed before
detection. "Time-to-detection" would be more
appropriate though less meaningful.

After establishing an SPL of 160 dB at
the start of each run, it was considered good
practice to explore the region of maximum
response in order to search-out the knee of
the curve. This was done to avoid tuning-in
the specimen too fine, experience having shown
that an upward drift of several Hertz could
cause the amplitude to wander off into the
critical "jump" area.

Specimen failures were predictable only
with regard to the two panel configurations
(All 0° and All 45°) in which the orthotropic
axes of all plies were aligned in the same
direction. The failures in each occurred
parallel to filament alignment as anticipated.
As an example, Fig. 8 shows the All 0° config-
uration split cleanly in two places along the
zero (vertical) direction.

The remaining specimen failures are
grouped into either of two classifications,
ply separation as shown in Fig. 9, or failures
in or near the clamped area which usually
progressed through various stages of damage
before detection. An example of near-incipient
failure is evidenced by broken filaments in
Fig. 10 while in Fig. 11 the outer plies of the
specimen had chunked-out before failure was
detected.

Because of inconsistencies and difficulties
in detecting specimen failure, fatigue test
data are not presented. However, an estimate
of relative specimen strength can be derived
from a comparison of the response data.

Presented in Fig. 12 are load curves for
three of the configurations (+22.5°/-22.5°/
+67.5°/-67.5°, +45°/-45°/+45°/-45°, and 0°/90°/
0°/90°) which fell within a spread of 200 micro-
inches strain. This spread, also represented
by the shaded area in Fig. 13, is bracketed by
the three remaining configurations. Above the
shaded area are two "no-life" configurations
(All 0° and All 45°) with strains approaching
2000 microinches at 160 dB, while the configu-
ration that consistently exhibited the lowest
strain was the 0°/+45°/-45°/90° specimen.

Comparative data were to have been obtained
from an isotropic specimen. A single aluminum
panel of identical geometry was available at
the time of test. This panel was inadvertently
failed while recording response data at a sound
pressure level estimated at 152 dB.

107
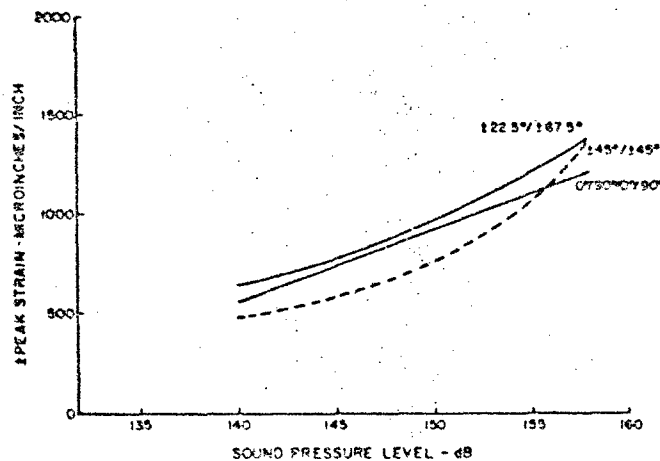
Fig. 12 - Comparison of load
curves for three
panel configurations

Fig. 13 - Comparison of load
curves for three
panel configurations.
The curves of Fig. 12
fall within the
shaded area.
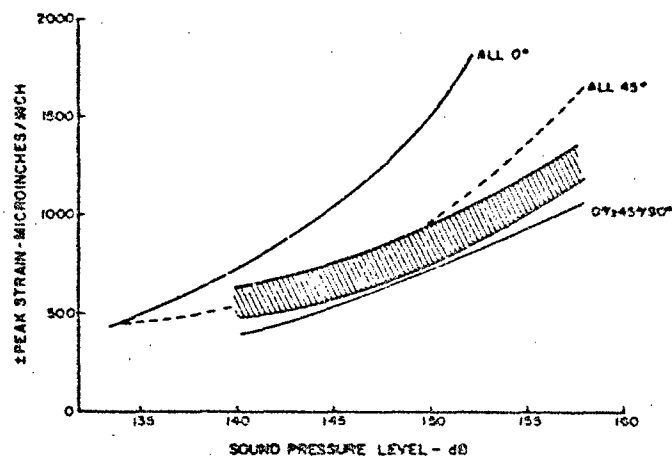
STRAIN DISTRIBUTION PATTERNS

The brittle coating method of strain analysis was successfully employed to obtain a graphic record of the distribution, direction, location, and pattern progression of tensile strains induced by successively applied loads.(4)

Briefly, the procedures and techniques of the brittle coating method are reviewed:

1. Clean the specimen surface thoroughly until completely free of all dirt and grease, using recommended solvents that do not leave deposits or other residue.

2. Spray the prepared area with a specially furnished aluminum under coating to provide a uniform background for the strain sensitive coating.

3. In accord with recommendations based on prevailing temperature and humidity conditions, select a coating that will provide the required strain threshold sensitivity.

4. Dry the coating according to specific instructions for the type of coating used. An overnight cure was typical.

5. Assuming the specimen to have been successfully loaded in the planned manner, it is necessary to "bring-out" the strain pattern in the coating by some process of crack detection. The process used in this program was the electrolyte penetrant/electrified particle method which has the advantage over dye-etchant techniques in that the process can be repeated for successive loadings without damaging the coating.

108

GRADUALLY INCREASING SOUND PRESSURE LEVEL ——→ RESONANCE | SHUT DOWN
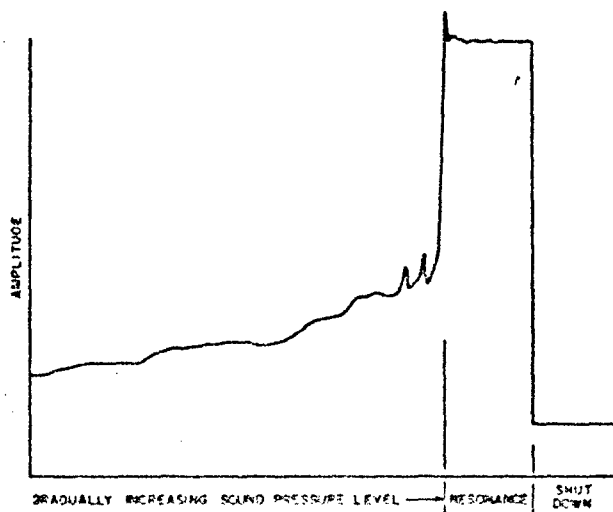
Fig. 14 – Resonating the nonlinear
system by increasing
the energy input while
holding frequency constant

6. If the resultant strain pattern
appears satisfactory, obtain photographs.
Wash-off the pattern and repeat the loading
process.

The series of brittle coatings used in
this program had a nominal strain threshold
sensitivity of 500 microinches per inch when
dried and tested at recommended temperatures,
and a craze sensitivity of 150 microinches/inch.
Since the coating sensitivity is affected by
temperature change (30 microinches/inch per
degree F), a drop of only 12°F often ruined the
coating. (5)

This tendency to craze proved critical as
the spraying/drying area was subject to drafts
and normal day-night temperature fluctuations.
Consequently, the only effective curing
procedure evolved was to coat the specimen at
the test site, provide a protective wrapping,
and isolate the area during overnight cure.

Merely loading the specimen, a process
which entailed its exposure to siren air flow
(relatively cool), often triggered the craze
tendency. This was resolved by operating the
siren air supply system for a sufficient time
to preheat the air above room ambient before
installing the specimen in the test section.
The necessity of rigid control over coating
cure temperature and test temperature cannot
be over emphasized.

A set of well defined strain patterns is
dependent on resonating the panel at the
initial load near the strain threshold sensi-
tivity of the brittle coating and choosing
succeeding load increments based on the degree
of pattern progression.

The initial approach, holding the SPL
constant while trying to search-out the
resonant frequency, proved unsatisfactory as
it was difficult to achieve a pronounced
resonance of brief duration and to predict a
load increment that would develop the strain
pattern in well-spaced stages.

A more reliable technique, shown graphical-
ly in Fig. 14, was to select a frequency for
which unstable amplitudes were known to exist,
and while holding this frequency constant,
slowly increase the SPL, driving the ampli-
tude across the lower boundary of the region
of instability at which point the panel reson-
ates quite abruptly due to the "jump" phenom-
enon. This procedure was successfully used
to produce a series of strain patterns in
progressive stages for each of the six panel
configurations. All patterns were developed
for the fundamental response.

A representative selection of strain
pattern photographs is presented for comparison
in Figs. 15 through 20 showing the general
progress of pattern development for each con-
figuration.

Obtaining quantitative strain measurements
by the brittle coating method was not a part
of the program and consequently, the procedures
involved are not treated in this paper.
However, the cracks in the coating occur
normal to the principal tensile strain, and
relative strain levels are indicated by crack
density.

109
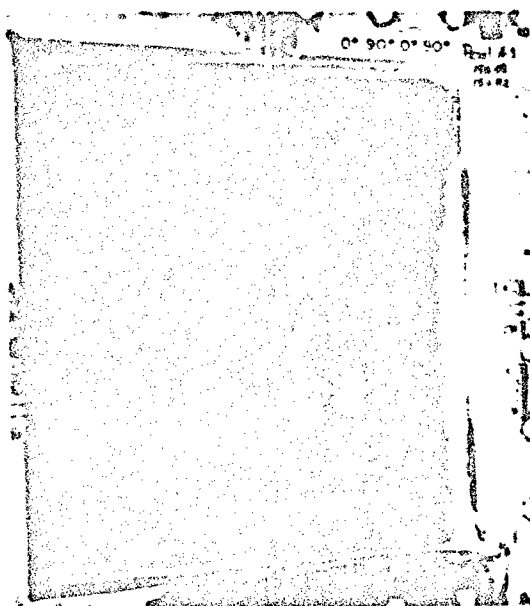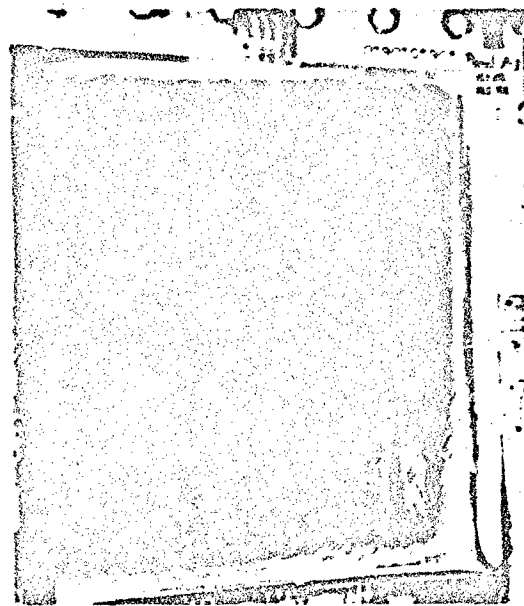
(a) - 150 dB, 150 Hz   (b) - 157 dB, 165 Hz

Fig. 15 - Strain distribution patterns for 0°/90°/0°/90° panel
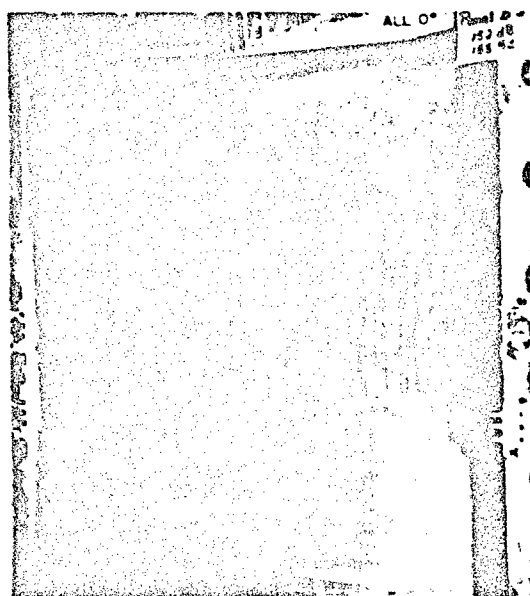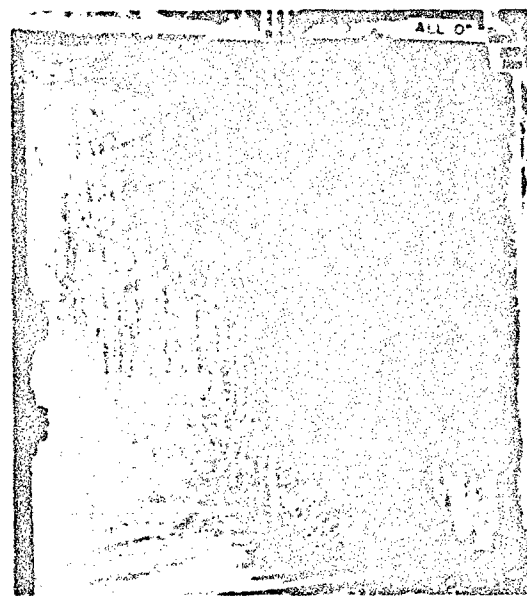
(a) - 152 dB, 155 Hz   (b) - 157 dB, 160 Hz

Fig. 16 - Strain distribution patterns for All 0° panel

110
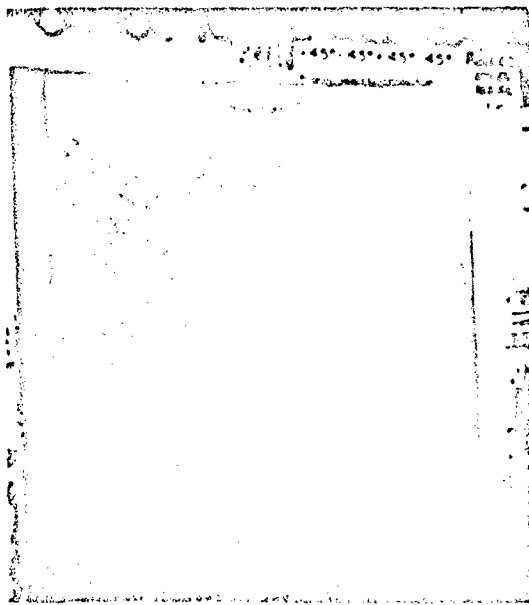
(a) - 153 dB, 165 Hz
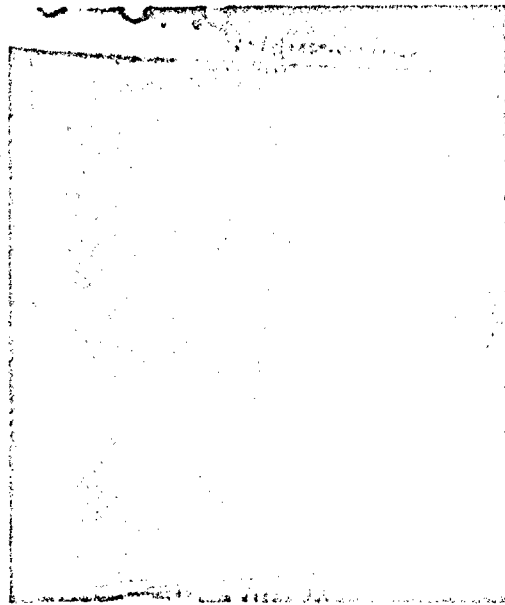
(b) - 157 dB, 175 Hz
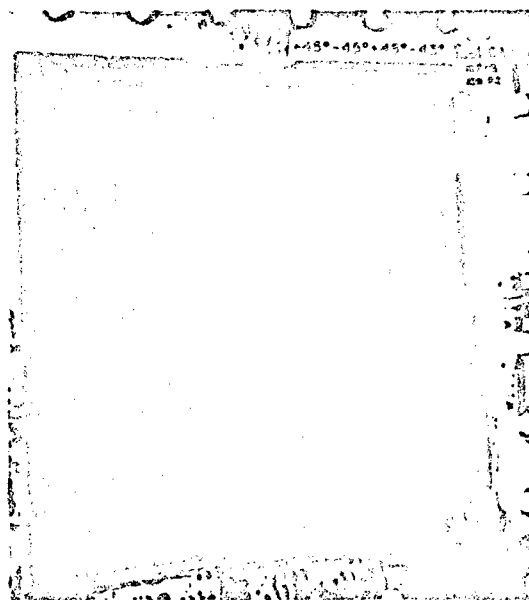
(c) - 157 dB, 180 Hz

Fig. 17 - Strain distribution
patterns for
+45°/-45°/+45°/-45°
panel
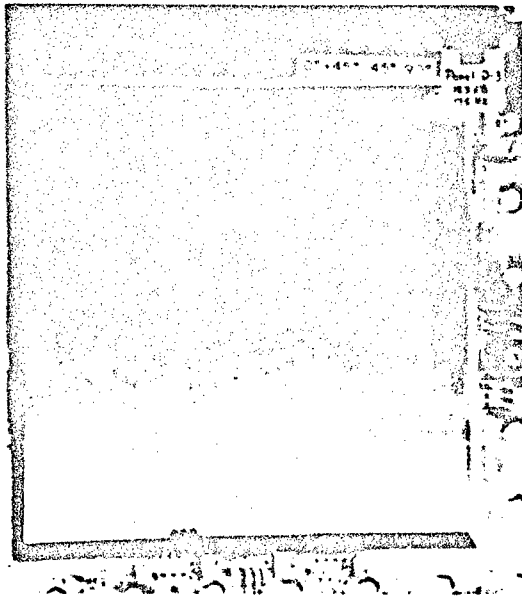
(a) - 153 dB, 175 Hz
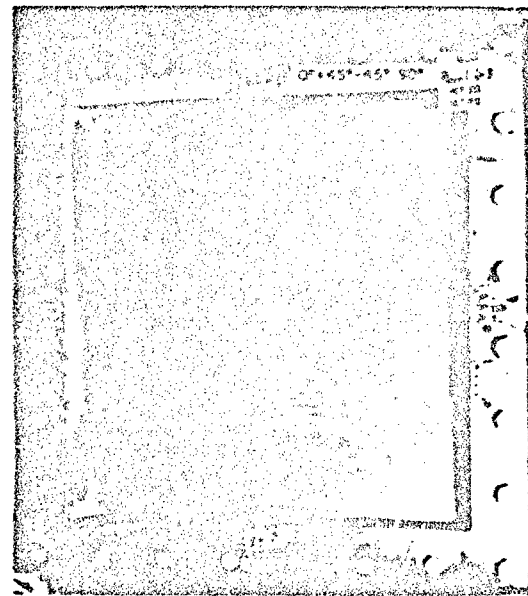
(b) - 157 dB, 187 Hz
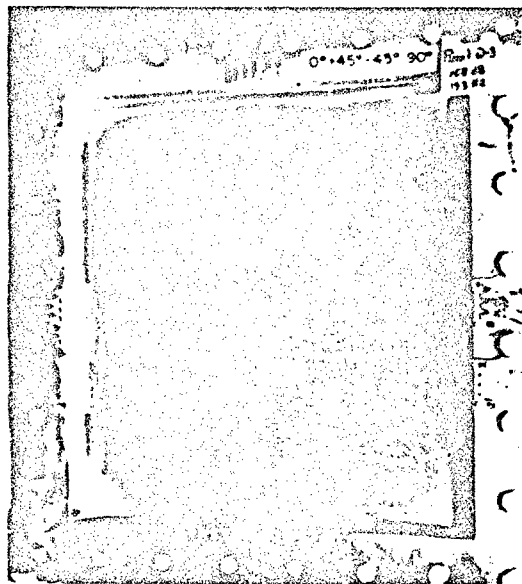
(c) - 158 dB, 193 Hz

Fig. 18 - Strain distribution
patterns for
0°/+45°/-45°/90°
panel
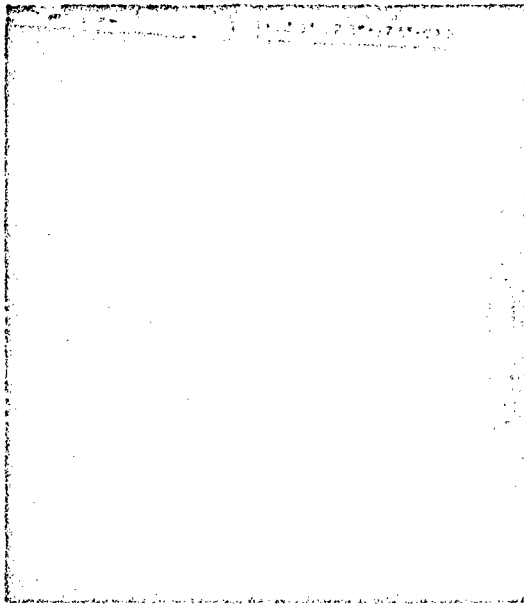
(a) - 154 dB, 180 Hz
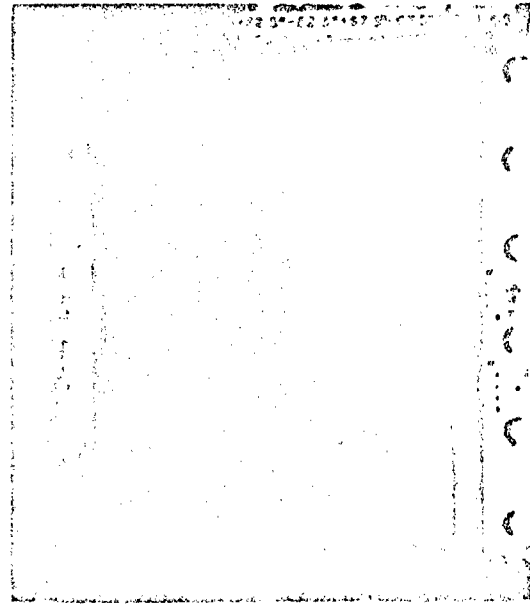
(b) - 157 dB, 185 Hz
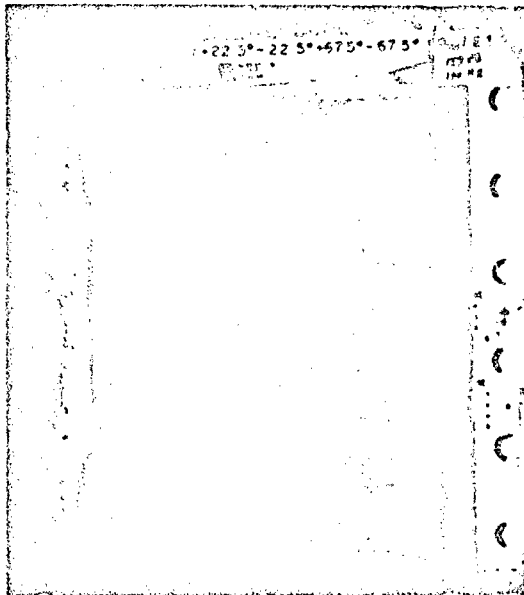
(c) - 159 dB, 190 Hz

Fig. 19 - Strain distribution patterns for +22.5°/-22.5°/+67.5°/-67.5° panel
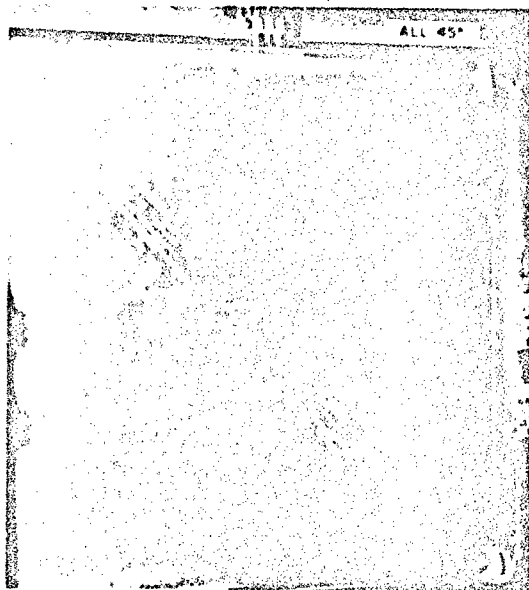
(a) – 147 dB, 145 Hz
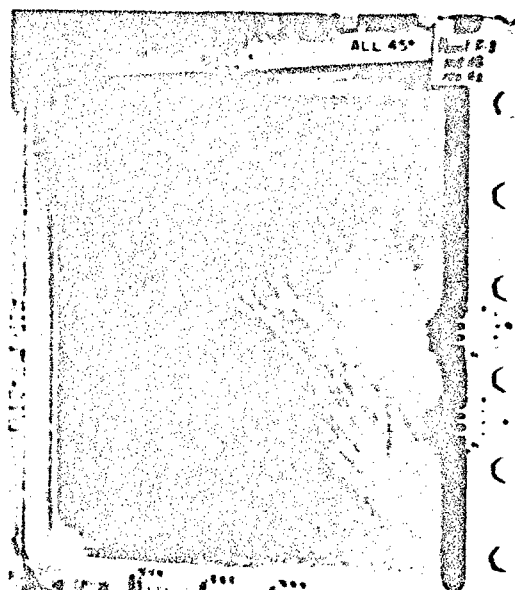
(b) – 148 dB, 150 Hz

(c) – 152 dB, 155 Hz
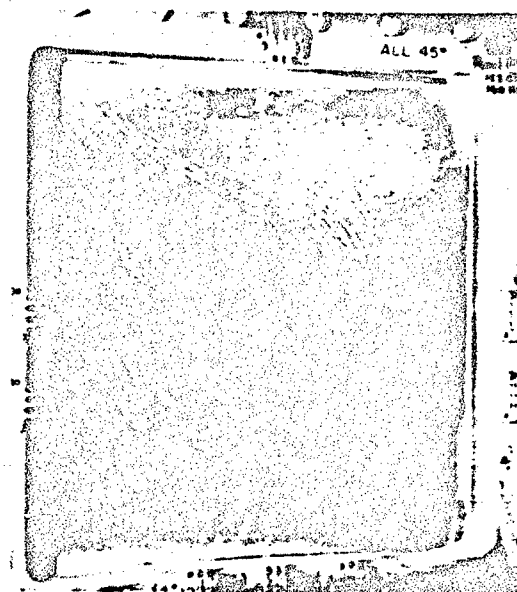
(d) – 153 dB, 160 Hz

Fig. 20 – Strain distribution patterns for All +45° panel

114
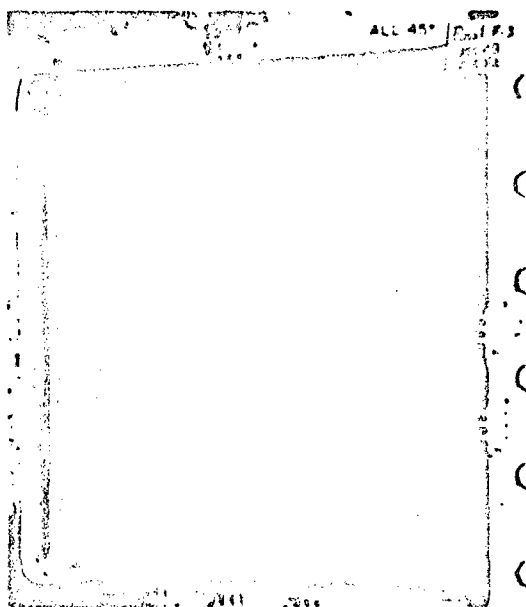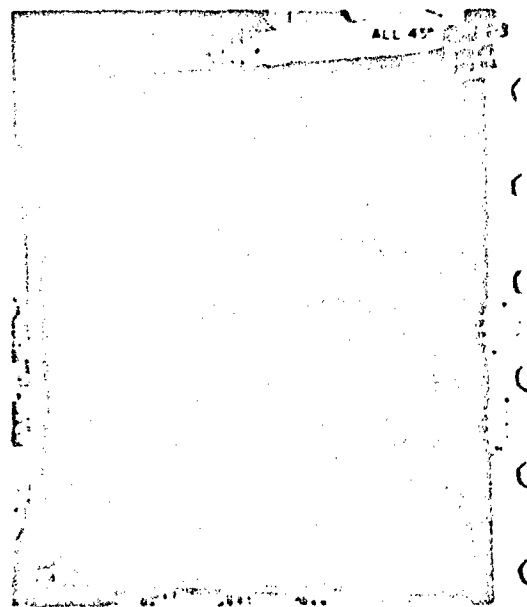
(e) - 154 dB, 165 Hz   (f) - 156 dB, 173 Hz

Fig. 20 (cont'd) - Strain distribution patterns for All +45⁻ panel

CONCLUDING REMARKS

1. It was clearly demonstrated during response tests that the boron-epoxy composite specimens respond in a manner typical of a "hard-spring" nonlinear system. This behavior was pronounced in all panel configurations and is attributed to membrane stresses resulting from large panel deflections. In addition, a comparison of strain data from the response tests provided a basis for estimating relative specimen strength.

2. Since it is not certain to what degree the endurance data were influenced by inconsistencies in detecting failure, specimen life predictions are not undertaken. A single aluminum specimen, intended to provide comparative data, failed during a response run of brief duration at an estimated 8 dB below the fatigue test level selected for the composite specimens.

3. Strain distribution patterns, from satisfactory to excellent, were photographed for all specimen configurations. The patterns were obtained from dynamic loadings using the brittle coating method. It was demonstrated that this technique can be successfully applied under adverse test conditions if appropriate precautions and procedures are devised to meet the requirements.

REFERENCES

1. A. W. Kolb and H.A. Magrath, "The RTD Sonic Fatigue Facility, Design and Performance Characteristics", Shock and Vibration Bulletin No. 37, Part 5, January 1968.

2. H. N. Abramson, "Nonlinear Vibration", Ch. 4 of Shock and Vibration Handbook, Vol. I, (C. M. Harris and C. E. Crede, Eds.) McGraw-Hill, New York, 1961.

3. S. H. Crandall, "Nonlinear Systems", Ch. 4 of Random Vibration, Vol II, (S. H. Crandall, Ed.), M.I.T. Press, Cambridge, 1963.

4. G. Ellis, F. B. Stern, and S. J. Baranowski, "Brittle Coatings", Experimental Mechanics, October 1966.

5. "Principles of Stresscoat, A Manual for Use with the Brittle Coating Stress Analysis Method", Magnaflux Corp., Chicago, 1967.

6. C. L. Rupert, "Acoustic Test of Boron-Epoxy Composite Panels to Evaluate the Effects of Varying Fiber Orientation", (AFFDL) FDD-A-7-68, in preparation.

STRENGTH CHARACTERISTICS OF
JOINTS INCORPORATING VISCOELASTIC MATERIALS

W. L. La Barge and M. D. Lamoree
Lockheed California Company
Burbank, California

This paper describes an analytical and experimental investigation of the load carrying capability of structure incorporating a constrained layer of viscoelastic material. Included in the study are the effects of the viscoelastic material on the buckling strength of panels under compression loads; on the strength of joints under static tension loads; and on the fatigue resistance of joints under axial and lateral loads. The objective of the investigation is to develop procedures for estimating the very important stress concentration factor of structures incorporating viscoelastic material as a function of the local detail design so that its influence may be properly evaluated in optimizing the structural design. The work described herein is a portion of a research and development program being conducted currently for the Air Force Materials Laboratory at Wright-Patterson Air Force Base. The purpose of the program is to develop methods of fabrication and evaluation of sonic fatigue resistant aerospace structures incorporating viscoelastic materials.

INTRODUCTION

One of the major problems confronting the designer of modern high performance jet aircraft is that of sonic fatigue. The obvious need to minimize structural weight of aircraft has resulted in highly efficient design concepts from the standpoint of strength-to-weight ratios. This type of structure is especially susceptible to fatigue failure when subjected to the high intensity acoustic fields of modern jet engines. It, therefore, becomes necessary to optimize the design of the structure from the standpoint of strength and weight when the acoustic loading is added to the other design loads.

One of the means of reducing the vibratory response level of structure due to acoustic excitation is to increase the amount of damping in the structure. The additional damping can be obtained by an "add-on" damping device; (for example, damping tape) or it may be designed into the structure. The most common way of doing the latter is to use laminated panels with a constrained core of viscoelastic material.

The reduction in vibratory response level is an indication of the potential increase in sonic fatigue life of the structure that should be attainable with viscoelastic damping. Actually, this potential is usually not realized because the addition of the viscoelastic material, in a "sandwich", for example, changes the load transfer mechanism locally (particularly in the area of rivet or other attachments) and modifies the local effective stress concentration factor. Next to the response level, the stress concentration factor is the most potent factor in determining the fatigue life of a panel or structure. The analytical determination of the stress concentration factor is very difficult except for the simplest of geometries and recourse must be had to experimental determination.

This paper describes an analytical and experimental investigation of the load carrying capability of structure incorporating a constrained layer of viscoelastic material. Included in the study are the effects of the viscoelastic material on the buckling strength of panels under compression loads; on the strength of joints under static tension loads;

and on the fatigue resistance of joints under axial and lateral loads. The objective of the investigation is to develop procedures for estimating the very important stress concentration factor of structures incorporating viscoelastic material as a function of the local detail design so that its influence may be properly evaluated in optimizing the structural design. Optimization of the structural design can proceed only when all of the design loadings are known and their effects on the structure can be estimated. Inherent in the determination of the optimum design, of course, are the manufacturing constraints necessary to permit the fabrication of flight quality hardware.

The work described herein is a portion of a program being conducted currently for the Air Force Materials Laboratory at Wright-Patterson Air Force Base. The purpose of the program is to develop methods of fabrication and evaluation of sonic fatigue resistant aerospace structures incorporating viscoelastic materials.

LIST OF SYMBOLS

D   Diameter of Fastener

E   Elastic Modulus

F   Lateral Force

G   Shear Modulus

I   Moment of Inertia

K   Stress Concentration Factor

N   Compression Load per Unit Width

P   Axial Load

R   Effectiveness Ratio

U   Strain Energy

V   Potential Energy

b   Beam Width

d   Core Thickness

l Beam Length

n   Number of Fasteners

t   Face Plate Thickness

u   Face Plate Deflection along x-Axis

v   Beam Deflection along y-Axis

α Edge Fixity Coefficient

σ Stress

Subscripts

f   Face Plate

c   Core

s   Solid Beam

v   Viscoelastic Beam

STRUCTURAL ANALYSIS

In this section analytical expressions are derived for an idealized viscoelastic beam subjected to various loading conditions. Application of appropriate limits reduces the expressions to forms applicable to solid beams. The expressions are used in conjunction with test data to assess the effective edge fixity coefficient and the effective fatigue and plastic stress concentration factors that exist at the edges of the various viscoelastic beam designs studied.

Critical Buckling Loads

The idealized model of the sandwich beam considered in this analysis consists of two face plates of equal thickness bonded to a viscoelastic core. The internal loads produced in the face plates by external forces are derived using the principle of virtual displacements whereby the variation of the total energy associated with the beam must vanish. Thus

$$\delta(U + V) = 0, \qquad (1)$$

where U is the total strain energy associated with the internal loads in the beam and V is the total potential energy associated with the applied external loads.

The strain energy terms which are included in the analysis are those associated with (1) extension and compression of the face plates, (2) bending of the face plates, (3) bending of the viscoelastic core, and (4) shear of the viscoelastic core. In general, for most viscoelastic damping materials (3) above will not contribute significantly to the total energy of the beam. It is left in the analysis, however, to facilitate checking. The total strain

energy associated with the viscoelastic beam shown in Fig. 1 can be written

$$U = 2U_1 + 2U_2 + U_3 + U_4. \qquad (2)$$
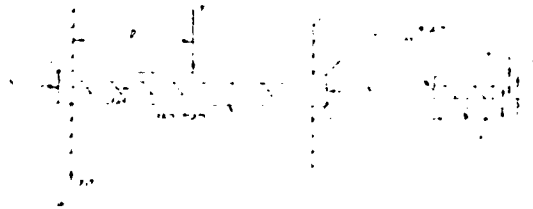
Fig. 1 - Idealized viscoelastic beam

The subscripted energy terms on the right hand side of Eq. (2) refer to the strain energies identified above. For a beam of uniform cross section it can be shown that the strain energy terms of Eq. (2) are:

$$U_1 = \frac{1}{2} E_f bt \int_0^\ell \left(\frac{du}{dx}\right)^2 dx, \qquad (3)$$

$$U_2 = \frac{1}{2} E_f I_f \int_0^\ell \left(\frac{d^2 v}{dx^2}\right)^2 dx, \qquad (4)$$

$$U_3 = \frac{1}{2} E_c I_c \int_0^\ell \left(\frac{d^2 v}{dx^2}\right)^2 dx, \qquad (5)$$

$$U_4 = \frac{1}{2} Gdb \int_0^\ell \left(\frac{d + t}{d}\right)^2 \left(\frac{2u}{d + t} - \frac{dv}{dx}\right)^2 dx. \qquad (6)$$

Implicit in the derivation of the above strain energy equations are the assumptions:

(1) loads are distributed uniformly across the width of the beam,

(2) the extension and compression of the face plates, due to bending of the beam, are small compared to the distance between the center of the core and the center of the face plates.

The potential energy associated with the axial compression loads applied at the ends of the beam is

$$V_a = -\frac{1}{2} Nb \int_0^\ell \left(\frac{dv}{dx}\right)^2 dx. \qquad (7)$$

Through the use of Eqs. (1) through (7) and the appropriate boundary conditions, it can be shown that the critical buckling load per unit width is:

$$N_{cr} = N_a \frac{N_b + Gd\left[\left(1 + \frac{t}{d}\right)^2 + \frac{N_a}{N_b}\right]}{N_a + Gd}, \qquad (8)$$

where

$$N_a = \sigma_v \frac{\pi^2}{\ell^2} \frac{E_f d^2 t}{2},$$

$$N_b = \sigma_v \frac{\pi^2}{b\ell^2} (2E_f I_f + E_c I_c).$$

The critical buckling load of a solid beam of thickness (2t) is determined from Eq. (8) by allowing the shear modulus of the core to go to infinity $(G \to \infty)$ and the core thickness to go to zero $(d \to 0)$. The buckling load equation thus reduces to the Euler equation

$$N_{cr} = \sigma_s \frac{\pi^2}{b\ell^2} 8E_f I_f. \qquad (9)$$

Comparing Eqs. (8) and (9), it is noted that the core material effects the critical buckling load in two ways. First, the core material introduces shear and adds bending rigidity to the beam and second, it alters the attachment characteristics (edge fixity coefficient, σ) of the beam. The shear modulus and

119

bending modulus of the core are properties of the material and are assumed independent of the beam design. The edge fixity coefficient, on the other hand, is assumed a function of the design configuration of the beam as well as the attachment. Values of α may vary from unity for pinned-pinned edge conditions to 4 for clamped-clamped edge conditions.

Bending Fatigue Stresses

The maximum stress developed in the face plate of a viscoelastic beam due to bending is derived using the same idealized model and analytical procedures as those used in the derivation of the critical buckling loads. Identical strain energy terms are considered. The potential energy considered is that due to the lateral force (F) applied at the center of the beam. The energy associated with this loading condition is

$$V_b = -Fv \Big|_{x=\frac{\ell}{2}}. \tag{10}$$

Using Eqs. (1) through (6) and Eq. (10) and the appropriate boundary conditions, it can be shown that the maximum stress at the outermost fiber of the face plate is

$$\sigma_v = K_v \frac{F\ell}{8} \frac{E_f}{E_f I_b + E_c I_c} \left\{ (t + \frac{d}{2}) \right.$$

$$+ \frac{t}{2} \left[\frac{E_f I_a}{2E_f I_f + E_c I_c} \right.$$

$$\left. \left. - \frac{d+t}{t} \right] \frac{\operatorname{Tanh}\left(\frac{p\ell}{4}\right)}{\left(\frac{p\ell}{4}\right)} \right\}, \tag{11}$$

where

$$I_b = 2I_f + I_a,$$

$$I_a = \frac{1}{2} bt(d + t)^2,$$

$$p = \left[\frac{2G}{E_f t d} + \frac{Gb(d + t)^2}{d(2E_f I_f + E_c I_c)} \right]^{1/2}.$$

The maximum stress in a solid beam of thickness (2t) is determined from Eq. (11) by allowing the shear modulus to go to infinity $(G \to \infty)$ and the core thickness to go to zero $(d \to 0)$. The equation thus determined is

$$\sigma_s = K_s \frac{F\ell}{64} \frac{t}{I_a}. \tag{12}$$

Comparing Eqs. (11) and (12), two effects of the core material on the maximum stresses are noted: (1) the core material introduces shear and adds bending rigidity to the beam, and (2) the stress concentration factor associated with the attachment is altered. As pointed out earlier, the shear modulus and bending modulus of the core are properties of the material and are assumed independent of the design configuration. The stress concentration factor, like the edge fixity coefficient, is assumed a function of the beam and attachment design configuration.

Tension-Compression Fatigue Stresses

In the derivation of the equation for the stress produced by an axial fatigue load, it is assumed that the axial load carrying capability of the core can be neglected and the net area of the face plate material is fully effective in transferring the load from the face plates to the fasteners. Based on these assumptions, it can be shown that the axial stress is given by

$$\sigma_v = K_v \frac{P}{(b - nD)t'}, \tag{13}$$

where t' represents the total thickness of the face plate material along the centerline of the fasteners. (See Fig. 2 for the assumed load distribution for the two basic viscoelastic beam design configurations considered in this study.)

For a solid beam, the axial stress is

$$\sigma_s = K_s \frac{P}{(b - nD)t}. \tag{14}$$

120
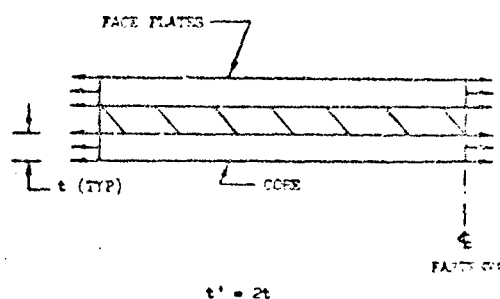
(a) Viscoelastic beam without insert
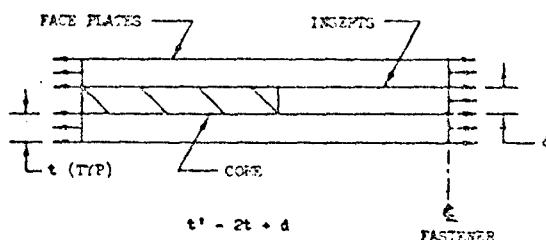
(b) Viscoelastic beam with insert

Fig. 2 - Assumed axial load distribution

Unlike previous cases discussed, the core material affects only the stress concentration factors in Eqs. (13) and (14). To simplify the notation, the same symbol (K) has been used for the stress concentration factors in Eqs. (11) through (14). They are, of course, not equal. The stress concentration factors in Eqs. (11) and (12) apply only to bending fatigue while those in Eqs. (13) and (14) are applicable to axial fatigue.

Axial Static Stresses

The analysis for the stress produced by an axial static load is identical to the analysis for the stress produced by an axial fatigue load except the stress concentration factors are plastic stress concentration factors instead of fatigue stress concentration factors. Thus, Eqs. (13) and (14) are applicable except for the interpretation of the stress concentration factors.

TEST PROGRAM

Specimen Design

The primary consideration which led to the basic specimen design configuration used in the test program was that the design should be typical of feasible aircraft type structure which could be used to carry representative aircraft loads and at the same time take maximum advantage of the damping characteristics afforded by the viscoelastic material under study. The basic configuration chosen was a sandwich configuration with a constrained viscoelastic core. The specimen face plates were fabricated from 2024-T3 clad aluminum sheet stock and the viscoelastic core from a polyurethane compound. Two types of attachments used in aircraft structure are represented. The first is where a continuous skin is attached to support structure and the second is where the edge of skin panel is attached. Specimens which represent these attachment locations are referred to as continuous beam and butt joint specimens, respectively.

The test specimens were sized such that the test loads approximated the loading of a 10 inch flat plate which might be used on an airplane as surface structure in a high noise level environment. The various test specimen designs are shown in Fig. 3. AD-5 round head rivets were used to attach all test specimens, except the static tension specimens, to the test fixtures. Steel 1/4 inch screws were used as fasteners for the static tension specimens since the shear strength of the rivets was insufficient to insure a failure of the beam specimen. All fasteners, fastener spacings, and edge distances were chosen to conform to standard design practices applicable to aircraft structure.

A total of six different joint configurations were chosen as representative designs for the test specimens. They are shown in Fig. 4.

Four of the configurations incorporated viscoelastic material in their design. They are subdivided into two groups. The first group consists of a continuous viscoelastic layer which runs the length of the beam (Configurations III and IV). In the second group (Configurations V and VI) an aluminum insert replaces the viscoelastic core along the edge of the beam which is attached to the test fixture. To simplify fabrication, the inserts were bonded to the face plates with the same

121
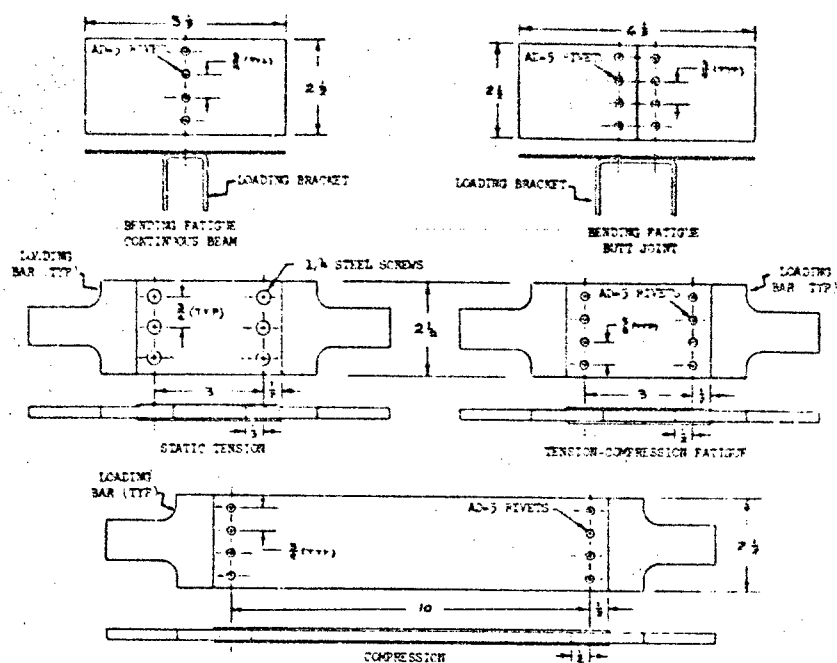
Fig. 3 - Structural element test specimens

Fig. 4 - Test specimen design configurations

TABLE 1
Test Specimen Allotment

Specimen Configuration	Core Thickness	Compression	Joint Test			
			Static Tension	Fatigue		
				Tension-Compression	Bending	
					Butt Joint	Continuous Beam
I	-	3	3	7	7	6
II	-	-	-	-	6	6
III	.02"	3	3	7	7	7
III	.05"	-	-	6	6	-
IV	.02"	-	-	6	7	-
V	.02"	-	3	7	6	-
V	.05"	-	-	-	6	-
VI	.02"	-	-	6	6	-

bonding material used to bond the core material to the plates. Two of the viscoelastic beam designs (Configurations III and V) were attached to the test fixture using only mechanical fasteners and two of the designs (Configurations IV and VI) were bonded as well as riveted to the test fixture. For most of the specimens the core thickness and face plate thickness is .02 inch. However, some of the fatigue test specimens were fabricated using .05 inch core material so that the effect of varying the core thickness could be evaluated. The remaining two design configurations were used as control specimens. They were fabricated from .05 inch aluminum sheet. The thickness of the control specimens was chosen so that the strength characteristics of the viscoelastic specimens without inserts could be compared to the strength of the control specimens on an equal weight basis. One of the configurations (Configuration I) was attached to the test fixture by means of mechanical fasteners only while the other (Configuration II) was bonded as well as riveted to the test fixture. For the sake of brevity, configurations II, IV and VI will often be referred to as bonded specimens and configurations I, III and V as unbonded specimens.

A total of 124 specimens was tested during the test program. The allotment of specimens is shown in Table 1.

Test Procedures and Results

Six test specimens were subjected to compression loads using a static test machine. The lateral deflection of the center of the specimen was measured at various load levels. The results of the tests are presented in Figs. 5 and 6 in a form suggested by R. V. Southwell. In the Southwell method, the ratio of the lateral deflection of the beam to the compression load (δ/P) is plotted against the lateral deflection (δ). The inverse of the slope of the curve is the critical buckling load of the specimen.

In the static tension test, nine specimens were tested to failure in a fifty thousand pound static test machine shown in Fig. 7. Each specimen was loaded to failure at the rate of 6000 lb/min. The failure loads determined for the specimens are listed in Table 2.

Thirty-nine specimens were subjected to tension-compression fatigue loads in the
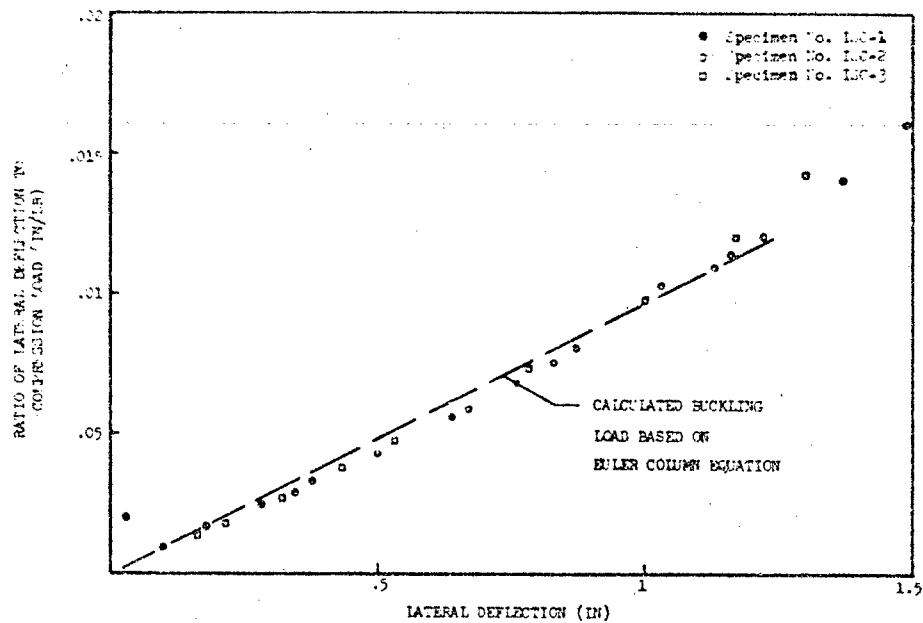
Fig. 5 – Control specimens compression
test results
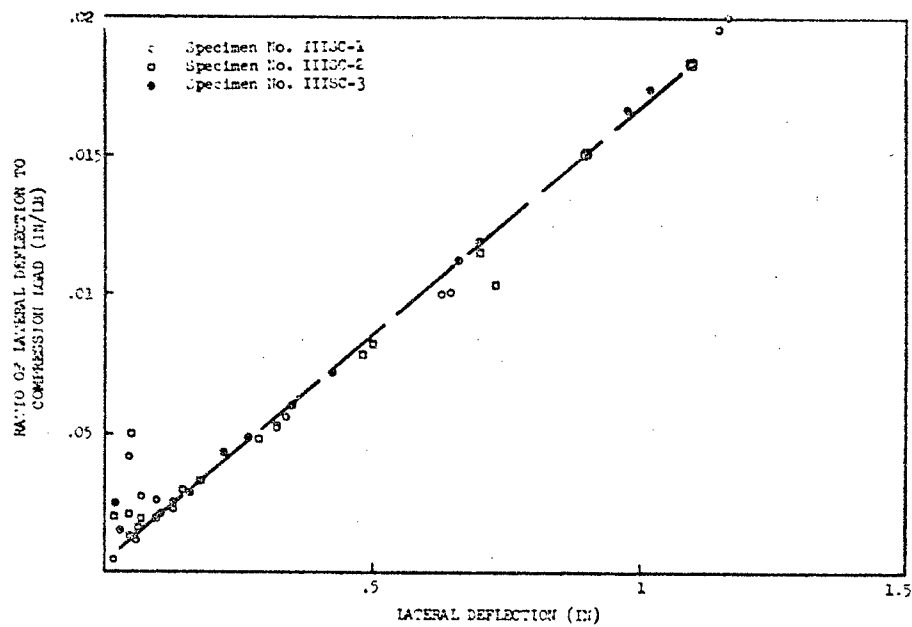
Fig. 6 – Viscoelastic specimens compression
test results
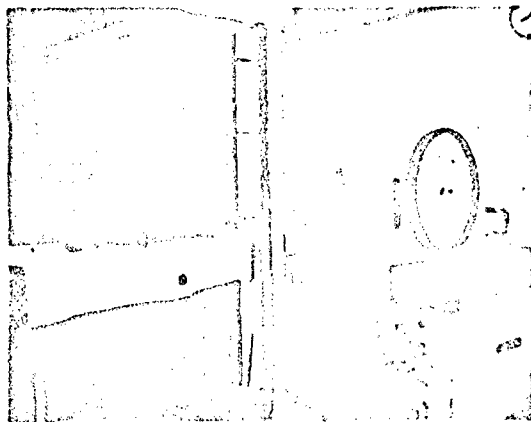
Fig. 7 - Static tension test specimen
installed in a 50K pound
static test machine

TABLE 2
Static Tension Test Data

Description of Specimen	Specimen Code	Ultimate Tension Load (lb)	Failure Mode
Control (Type I)	C3ST-1	9400	Skin
	C3ST-2	9680	Skin
	C3ST-3	9360	Skin
20 Mil V.E. without Inserts (Type III)	IIIS-1	4960	Skin
	IIIS-2	4940	Skin
	IIIS-3	4960	Skin
20 Mil V.E. with Inserts (Type V)	VS-1	8400	Skin
	VS-2	8140	Skin
	VS-3	8480	Skin

constant-amplitude, axial load fatigue test machine shown in Fig. 8. Loading was applied at the rate of approximately 30 cycles per second. The load consisted of a mean load and a cyclic load. The mean load was equivalent to a net area stress of 5,000 psi for all specimens while the cyclic load, which was held constant for any one specimen, was varied between specimens to determine stress-life
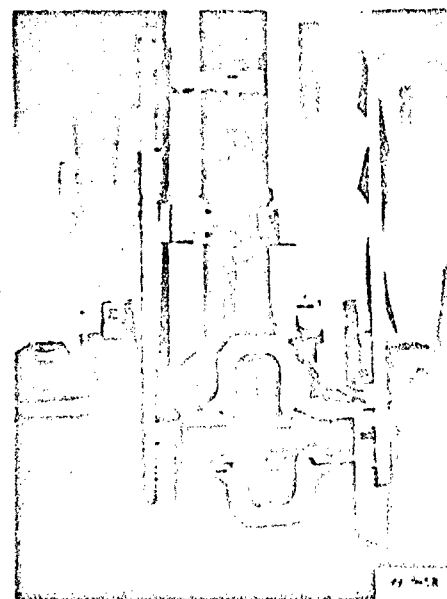
Fig. 8 - Tension-compression fatigue test specimen installed in a constant-amplitude, axial load fatigue test machine

information. Testing continued until the specimen failed or until ten million cycles were accumulated, whichever occurred first.

During testing, difficulties were encountered in the application of high compression loads which buckled some of the specimens. In order to eliminate this problem, clamps were placed at the center of the specimens as shown in Fig. 9. The clamps provided effective support to control buckling of most of the specimens but did not affect the axial fatigue load carrying capability of the specimens. The cyclic loads and cycles to failure determined for each of the specimens tested are plotted in Figs. 10 and 11.

Seventy specimens were subjected to bending fatigue loads in the servo operated test fixture shown in Fig. 12. Fatigue loads were applied at the rate of approximately 8 cps through a loading bracket attached to the specimen. The ends of the specimens were attached to the

125

test fixture by joints which were free to rotate and allowed the beam to slide freely within the joint. Fig. 13 illustrates a typical butt joint specimen installed in the test fixture. The photo is a double exposure showing the beam at two deflected positions. A constant-amplitude cyclic load was applied to each specimen. Loading continued until failure occurred or until the specimen was exposed to approximately one million cycles. Plots of cyclic load vs cycles to failure are presented in Figs. 14 through 17.

DISCUSSION OF TEST RESULTS

In this section the test results are discussed both in terms of applied loads and in terms of the resulting stresses. The first enables comparisons to be made of the load carrying capabilities of the test specimens; the second permits evaluations to be made of the effective stress concentration factors which are required for analysis. For the purpose of comparing the load carrying capabilities of the various configurations an "effectiveness ratio", R_{load}, is defined as follows

Fig. 9 - Close-up view of tension-compression fatigue test specimen showing support clamps
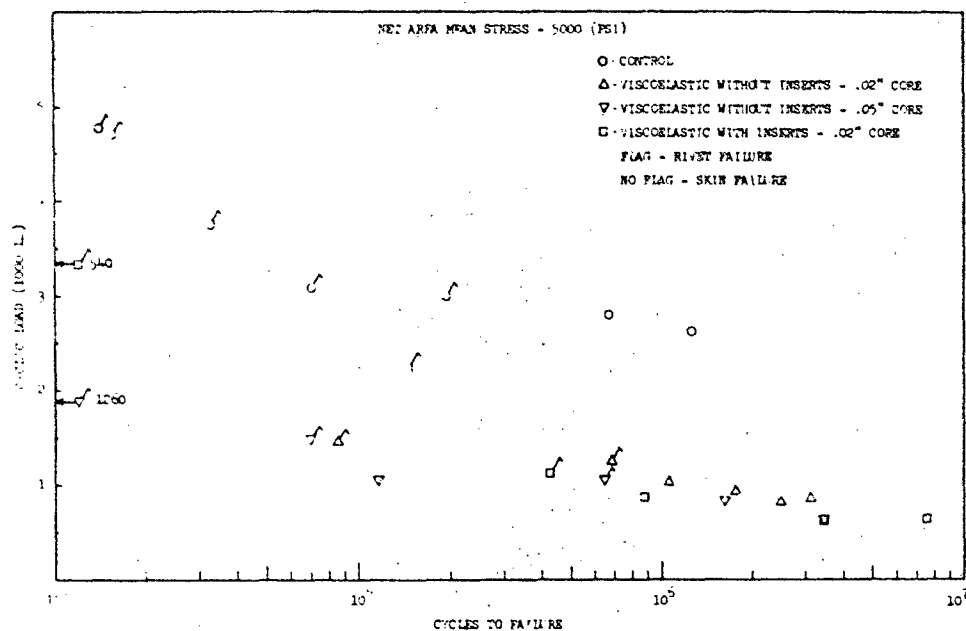
Fig. 10 - Tension-compression fatigue loads unbonded specimens
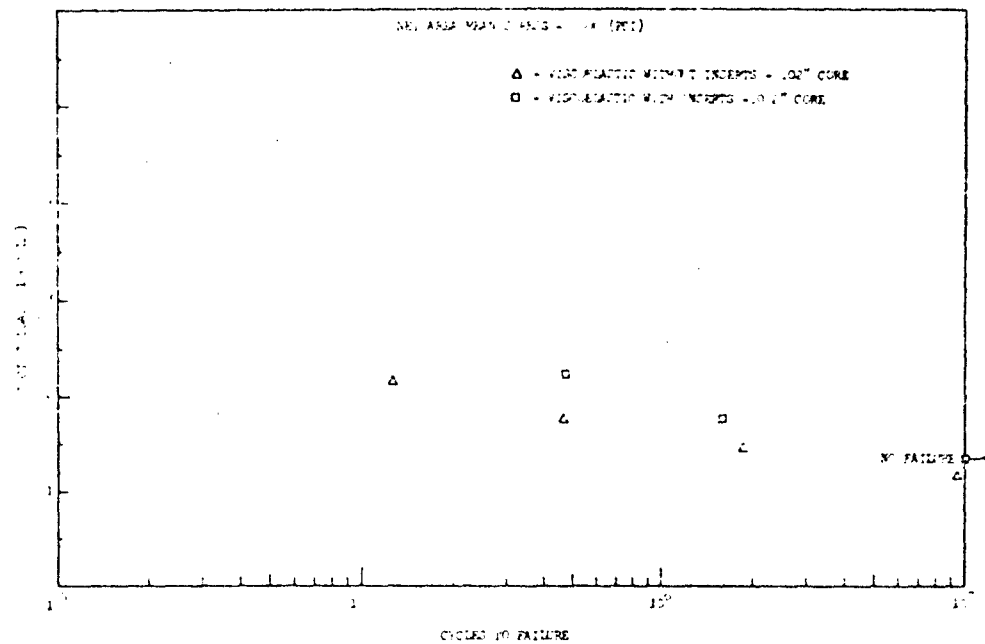
Fig. 11 - Tension-compression fatigue loads, bonded specimens
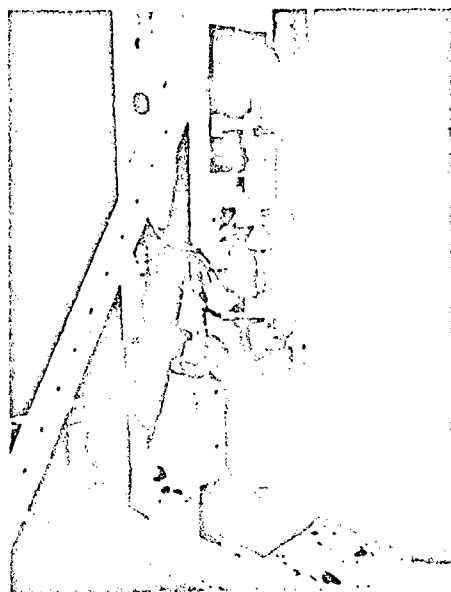
Fig. 12 - Bending fatigue specimen installed
in a servo operated bending fatigue
test fixture
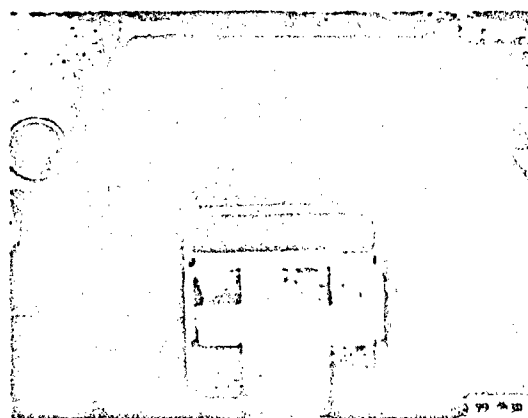
Fig. 13 - Close-up of butt joint specimen
undergoing bending fatigue test

127

Fig. 14 - Butt joint bending fatigue loads, unbonded specimens

Fig. 15 - Butt joint bending fatigue loads, bonded specimens

128
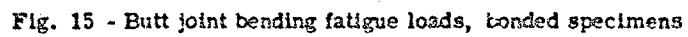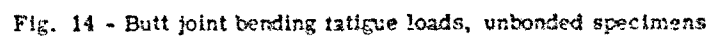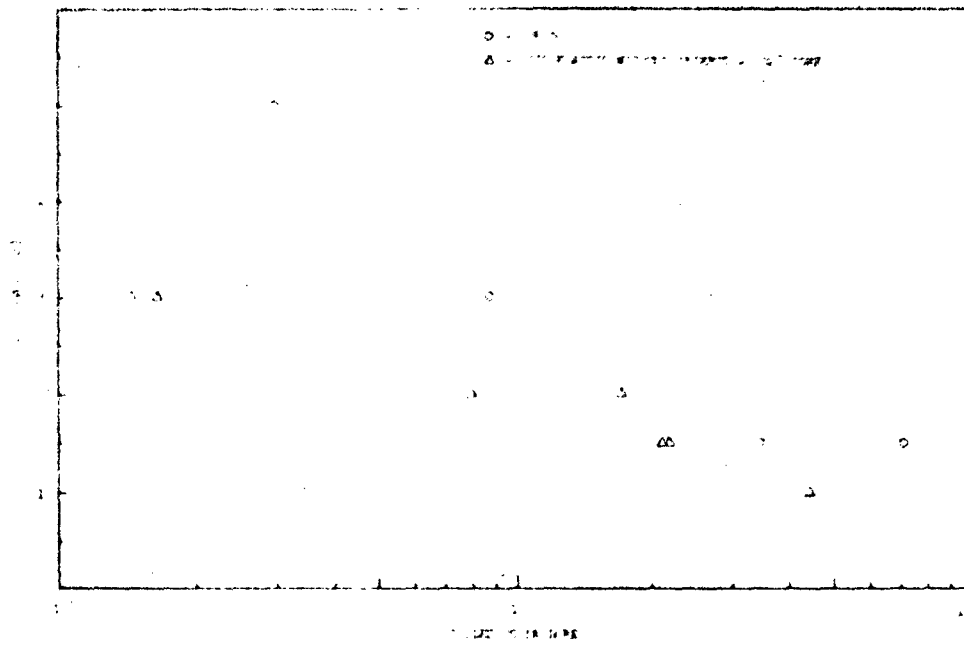
Fig. 16 - Continuous beam bending fatigue loads, unbonded specimens
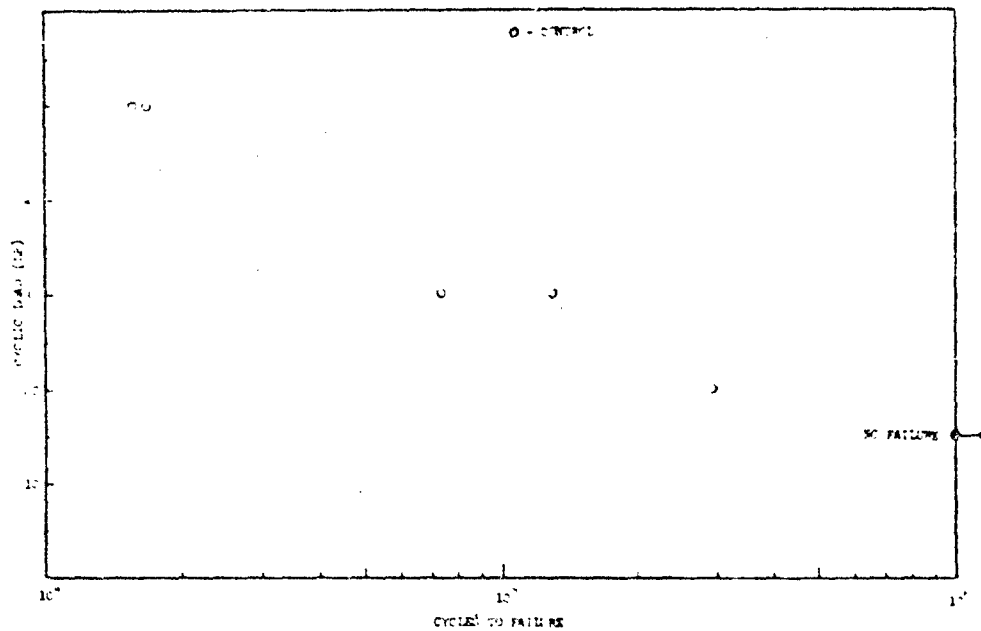
Fig. 17 - Continuous beam bending fatigue loads, bonded specimens

$$R_{load} = \frac{\text{Load carried by the visco-elastic specimen}}{\text{Load carried by the control specimen}}$$

The effectiveness ratio for each configuration will depend upon the type of loading and in the case of fatigue loading, will also depend upon the levels of the mean and varying loads.

Compression Tests

The critical buckling load of the control specimen can be calculated from Eq. (9). If the specimen is assumed to have clamped edges so that the edge fixity coefficient (o) in the equation is equal to 4, a critical buckling load of 103 lbs. is calculated. This value is compared with the test data by constructing a straight line through the test data shown in Fig. 5 with an inverse slope of 103 lbs. The calculated value is seen to be in good agreement with the test data.

The test data for the viscoelastic specimens are plotted in Fig. 6. The inverse of the slope of the line constructed through the data determines a critical buckling load of approximately 60 lbs. Thus, for critical buckling loads, the viscoelastic beam has an effectiveness ratio of approximately 60% compared to the control beam of the same weight.

The analytical expression for the critical buckling load associated with the viscoelastic beam is given by Eq. (8). The value of o is established by the edge constraints of the beam. If it is assumed that the shear modulus of the polyurethane core is 800 psi and the critical buckling load per unit width is 24 lb/in. as determined in the test, the value of o is found to be 2.25.

Two typical compression test failures are shown in Fig. 18. One of the specimens shown is a buckled control specimen and the other is a buckled viscoelastic specimen.

Static Tension Tests

Three specimens of each of the joint configurations I, III, and V were statically loaded in tension to failure. Typical failures obtained are shown in Fig. 19. Failures of the control specimens were a combination of tearing of the specimen between the fastener holes and tearing between the holes and the edges of the plate. The failures associated with the visco-
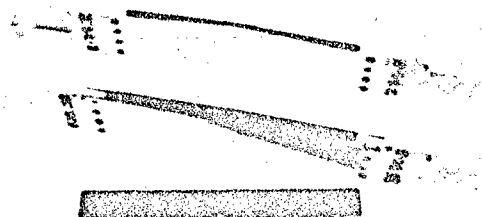
Fig. 18 - Typical compression
test failures

elastic specimens were a combination of a bearing failure of the specimen behind the fastener holes and tearing between the fastener holes. In the case of the viscoelastic specimens with inserts, the tearing extended through the face plates and inserts along the same line.

The effectiveness ratio for static tension loads are computed from test data listed in Table 2. For equal weight specimens (i.e. those without inserts), the effectiveness ratio is approximately 50%. The addition of inserts to the viscoelastic specimen increases the effectiveness ratio of the joint to approximately 85%.

Using an ultimate allowable stress of 60,000 psi for the face plate material, Eqs. (13) and (14), and the results of the static tension tests, the plastic stress concentration factors associated with each design are determined. They are 1.2 for the control specimen, 1.7 for the viscoelastic specimen without inserts, and 1.5 for the viscoelastic specimen with inserts. For equal weight specimens it is evident that the viscoelastic core increases the plastic stress concentration factor significantly. The addition of the inserts is beneficial although it does not produce a stress concentration factor equal to that of the control specimen.

130

(a) Screw head side   (b) Nut side
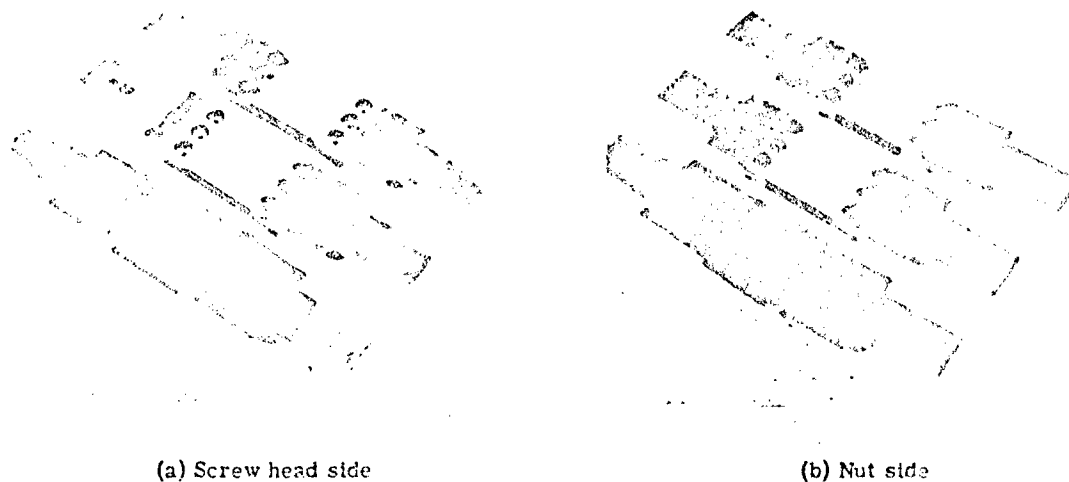
IS-1   Control
IIS-2   Viscoelastic without inserts
VS-3   Viscoelastic with inserts

Fig. 19 - Typical static tension failures

Tension-Compression Fatigue Tests

Failure modes associated with the un-
bonded specimens under tension-compression
fatigue loads were of two general types - rivet
failures and skin failures. Typical examples
of these failures are shown in Figs. 20 through
22. Examination of the rivet failures revealed
that for the control specimens the primary
mode of rivet failure was shearing of the rivet.
For the viscoelastic specimens, rivet bending
failures were the most common mode of fail-
ure for the specimens without inserts, while
rivet failures due to bending and shear were
both common modes of failure for the specimen
with inserts. All rivet failures occurred at
the interface between the loading bar and the
specimen. All skin failures consisted of tear-
ing of the face sheets between the fastener
holes. In the cases where inserts were used
in the joints, the inserts tore along the same
line as the face sheets. Referring to Fig. 10,
it is noted that at load levels for which the fa-
tigue life is less than approximately seven
hundred thousand cycles, the rivets fail. At
lower load levels all failures are skin failures.

At these lower load levels the viscoelastic
joint configuration appears to have little effect
on the cyclic load level required to produce
failure.

The effectiveness ratio of the unbonded
viscoelastic specimens for tension-
compression fatigue loads is determined by
comparing the allowable loads for the visco-
elastic specimens with those for the control
specimens. For a life corresponding to one
million cycles, the effectiveness ratio is ap-
proximately 35%.

All of the bonded specimens exhibited the
same failure mode, i.e. failure of the face
plates. Examples of this failure mode are
shown in Figs. 23 and 24. Most of the failures
occurred in the outer skin along the inside edge
of the rivet heads. One of the specimens,
failed in the face plates along the edge of the
insert.

Comparing the test results presented in
Fig. 10 with the test results presented in Fig.
11 for the bonded viscoelastic specimens, it

131

Fig. 20 - Typical tension-compression fatigue failures of unbonded control specimens
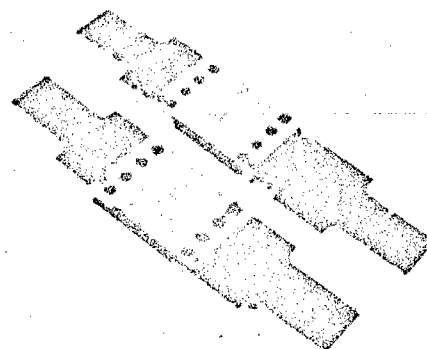
(a) .02 inch viscoelastic core

Fig. 21 - Typical tension-compression fatigue failures of unbonded viscoelastic specimens with inserts
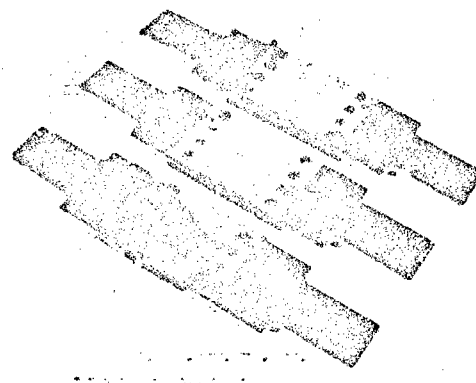
(b) .05 inch viscoelstic core

Fig. 22 - Typical tension-compression fatigue failures of unbonded viscoelastic specimens without inserts

appears that bonding the specimen to substructure

(1) makes the rivet loads less critical

(2) increases the tension-compression fatigue load resistance of the viscoelastic design configurations,

(3) improves the load carrying capability of the viscoelastic specimen with inserts more than that of the specimen without inserts.

In the analysis of the tension-compression fatigue specimens, it is assumed that existing S-N fatigue data applicable for conventional structure can be used in the design of viscoelastic specimens. The cyclic nominal fatigue stress associated with each specimen was calculated using Eqs. (13) and (14) and the cyclic load test data. The computed stresses associated with the unbonded specimens are plotted in Fig. 25. In order to assess the value of the stress concentration factor associated with specimen designs, axial S-N curves for 2024-

132
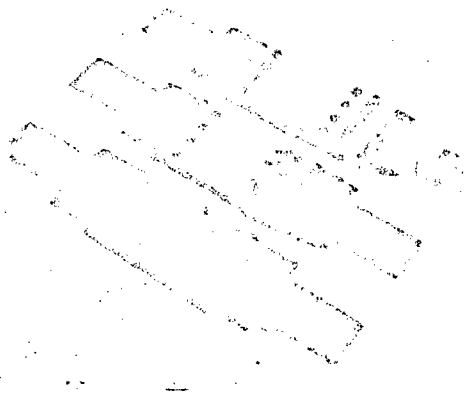
Fig. 23 - Typical tension-compression fatigue
failures of bonded viscoelastic
specimens without inserts
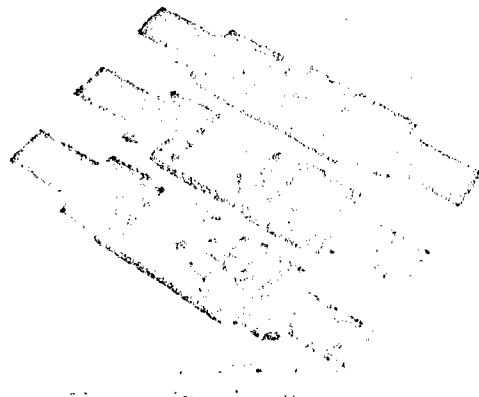
Fig. 24 - Typical tension-compression fatigue
failures of bonded viscoelastic
specimens with inserts
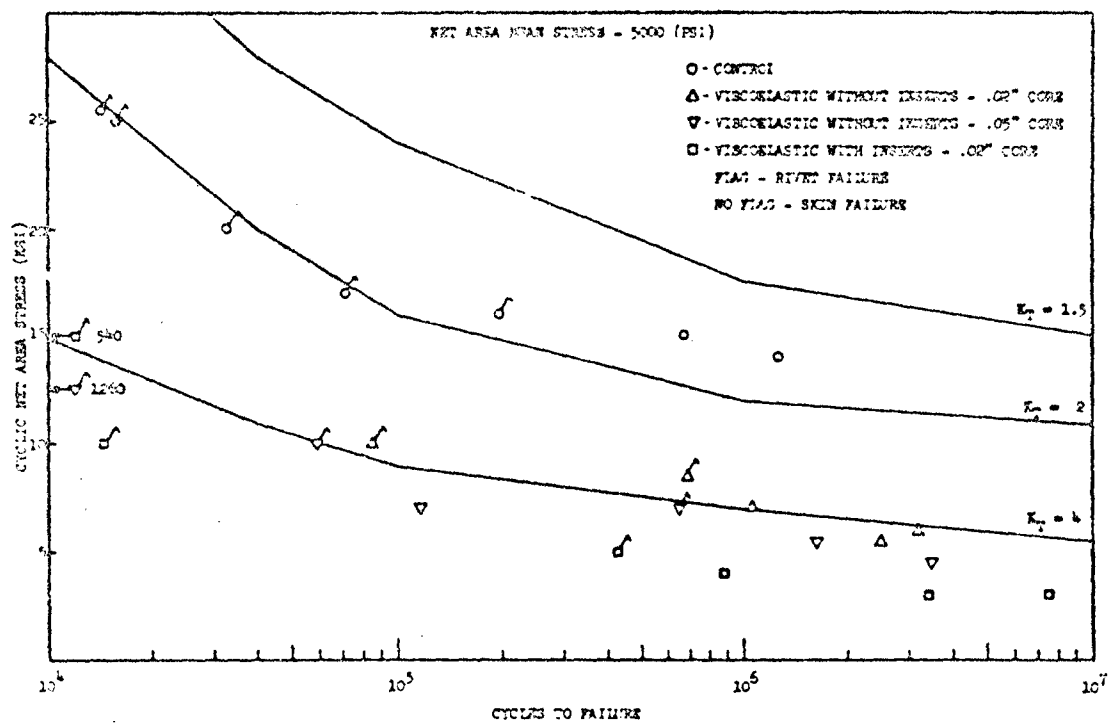
Fig. 25 - Cyclic net area axial fatigue stresses, unbonded specimens

T3 aluminum for various stress concentration factors are included in Fig. 25. The S-N curves were obtained from MIL-HDBK-5.

Based on the data for which skin failures occurred, the stress concentration factors for the viscoelastic specimens are significantly greater than for equal weight control specimens. Moreover, the effective stress concentration factors associated with the viscoelastic specimens with inserts appear to be greater than those for the specimens without inserts. This apparent anomaly is an indication that the inserts are not completely effective in transferring the axial face plate loads to the fasteners.

The calculated nominal fatigue stresses associated with the bonded test specimens are plotted in Fig. 26. Also included in the figure are S-N curves for stress concentration factors of 2 and 4. Comparing the test results presented in Figs. 25 and 26, it appears that bonding the test specimen to the support structure decreases the apparent stress concentration factors for each of the viscoelastic design configurations.

The effects of the viscoelastic layer on the load carrying capability of the rivets are demonstrated in Fig. 27. Specimen failures which occurred at load levels corresponding to a life of seven hundred thousand cycles were typically rivet failures. The sandwich construction used in the viscoelastic specimen design produces bending stresses in the rivets which, along with the shear stresses, produces a higher apparent stress concentration factor in the rivet of the viscoelastic specimens than in those of the control specimen. The data are inconclusive in determining the effects of increased core thickness and the use of inserts on the fatigue characteristics of the rivets.

Bending Fatigue Tests

In the bending fatigue tests, all specimens exhibited the same failure mode, failure of the skin across the width of the beam away from the fastener holes. Typical examples of the skin failures are shown in Figs. 28 through 31. The significant differences between the modes of failure of the specimens are the locations of the failures. The unbonded control speci-
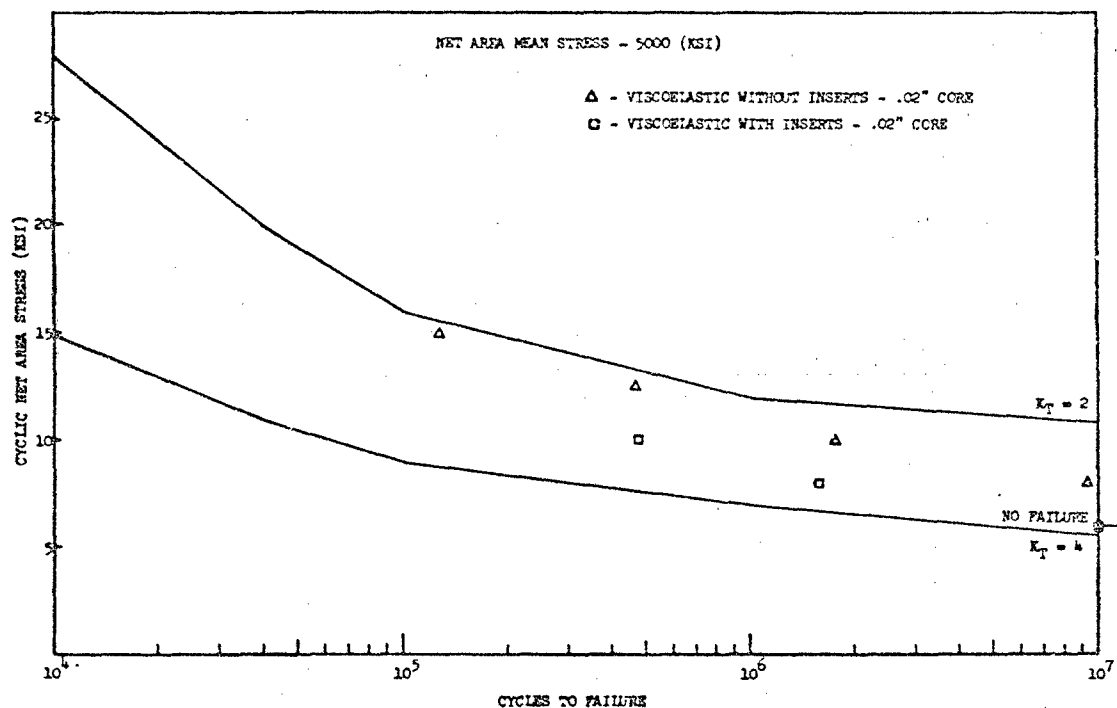
Fig. 26 - Cyclic net area axial fatigue stresses, bonded specimens

134
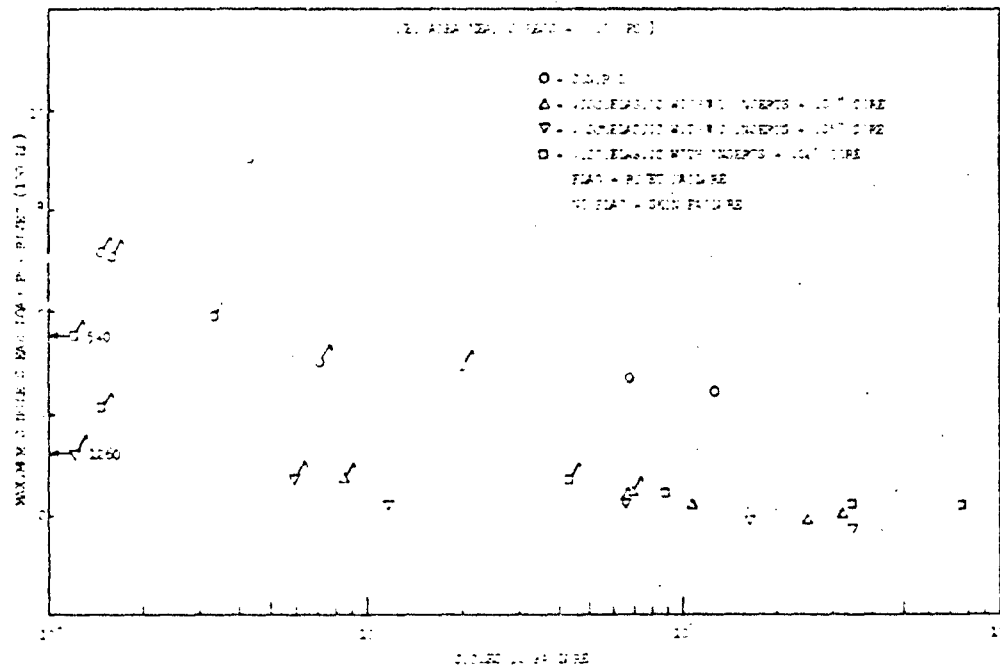
Fig. 27 – Tension-compression fatigue test, maximum rivet load, unbonded specimens
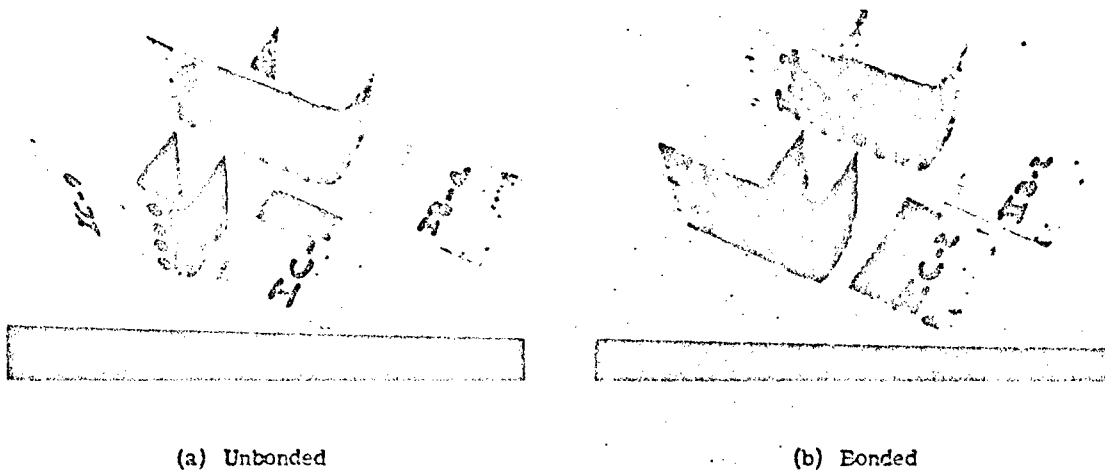
(a) Unbonded   (b) Bonded

Fig. 28 – Typical bending fatigue failures of control specimens

135

(a) Continuous beam
.02 inch viscoelastic core
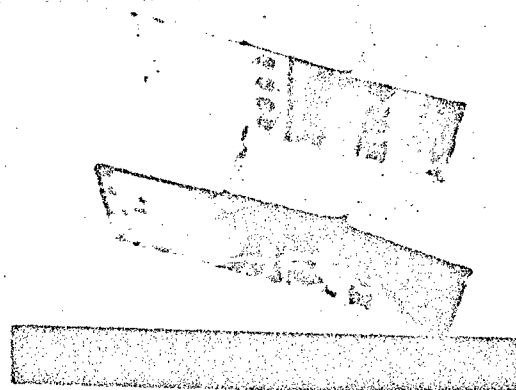
(b) Butt joint
III B2-6 .02 inch viscoelastic core
III B5-2 .05 inch viscoelastic core

Fig. 29 - Typical bending fatigue failures
of unbonded viscoelastic specimens
without inserts
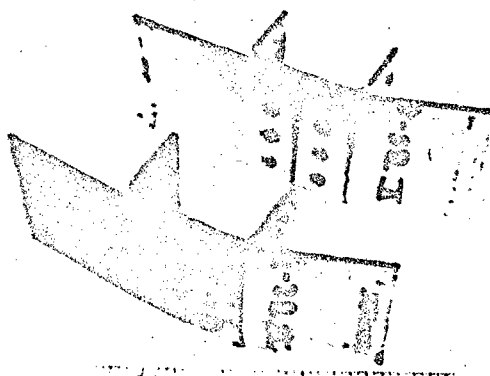
V B2-2 .02 inch viscoelastic core
V B5-4 .05 inch viscoelastic core
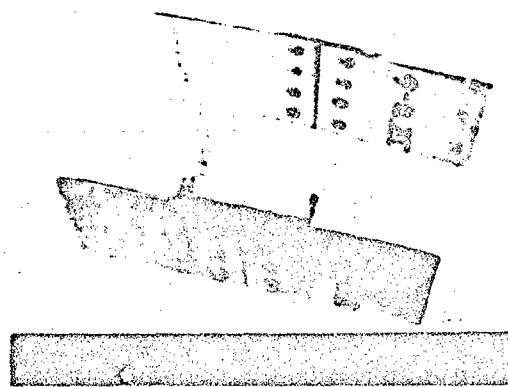
IV B-6 without inserts
VI B2-2 with inserts

Fig. 30 - Typical bending fatigue failures
of unbonded viscoelastic specimens
with inserts

Fig. 31 - Typical bending fatigue failures of
bonded viscoelastic specimens -
.02 inch core

mens and viscoelastic specimens without inserts failed along a line in front of the edge of the rivet heads. The unbonded specimens with inserts failed along the edge of the inserts. The bonded specimens all failed at the edge of the bond line.

From the standpoint of load carrying capability several trends are indicated by the test data shown in Figs. 14 through 16. First, referring to Figs. 14 and 15, it appears that the resistance to bending fatigue loads of each of the three bonded configurations is less than that of the unbonded specimens of the corresponding configuration. Referring next to Fig. 14, it appears that for the unbonded butt joint specimens, the addition of the inserts improves the bending fatigue load resistance of the viscoelastic specimens with core thicknesses of both .02 inch and .05 inch. Also for the unbonded butt joint specimens with inserts, the bending fatigue load resistance appears to be significantly greater for the specimens with .02 inch core than for the specimens with a .05 inch core. The corresponding statement for specimens without inserts appears to be true only for the higher load levels.

Nominal face plate stresses were calculated using Eqs. (11) and (12) and the bending fatigue load data discussed above. Specimen deflection measurements were made during the bending fatigue tests. The measured deflections were used to determine equivalent beam lengths, which were then used in the stress calculations. The calculated stresses for the specimens vs cycles to failure are plotted in Figs. 32 through 35. Also shown in the figure is a reverse bending S-N curve for 2024-T3 clad aluminum. The curve is for an unnotched specimen and has been extended from one hundred thousand cycles to ten thousand cycles. The trends observed in evaluating the bending fatigue load resistance of the specimens can be restated in turns of stress concentration factors by means of the data shown in Figs. 32 through 35. The stress concentration factors of the bonded butt joint design configurations shown in Fig. 35 are greater than those for the corresponding unbonded design configuration shown in Fig. 33. For the unbonded viscoelastic specimens, the inserts appear to reduce the stress concentration factors associated with the .02 inch core design and the .05 inch core design. Also, the stress concentration

factor associated with the viscoelastic specimens with inserts and .02 inch core is less than the stress concentration factor of the specimen with the .05 inch core.

Although the data indicate the above trends, it is noted that scatter does exist and tends to obscure many of the differences which may exist. It is of interest to note that data are more consistent for the continuous beam specimens than for the butt joint specimens. Also, for the butt joint specimens, there is considerably less scatter for the bonded specimens than for the unbonded specimens.

CONCLUSIONS

1. The critical buckling load of the viscoelastic beam tested is approximately 60% of that for the control beam of the same weight.

2. The use of inserts in the viscoelastic specimens increases the ultimate tensile strength of the joint from 50% to 85% of that of the control specimens.

3. The resistance of the joints containing viscoelastic material to tension-compression fatigue loads is, in general, considerably less than that of the control specimens. For the unbonded specimens, the inserts have little effect on the fatigue life of the joint at the low load levels. Bonding the specimen to the loading fixture provides a significant improvement in the tension-compression fatigue resistance of the joints containing viscoelastic material and at the same time increases the effectiveness of the insert.

4. The scatter of test data makes it difficult to evaluate the effectiveness ratios associated with the various viscoelastic design configurations for bending fatigue loads. However, in general, they are significantly higher than for tension-compression fatigue loads. Bonding the specimens to the loading fixtures changes the failure location and reduces their resistance to bending fatigue. The inserts, in general, improve the bending fatigue resistance of the joints.

137

DISCUSSION

Mr. Ungar (Bolt Beranek and Newman): You are telling us that viscoelastic inserts are not good even if you have a fatigue problem. Some of the data that you have shown, of course, showed that adding viscoelastic material reduces the fatigue resistance. What did you keep constant? I know that you had a constant load amplitude during any given test, but did you design your specimens to have a constant stress amplitude as well?

Mr. LaBarge: No we did not. I forgot to mention that we did design the specimens without inserts and the control specimens were designed such that they both had equal weight, so we held that constant. For the specimens with inserts this was just an attempt to see if we could quickly increase the fatigue resistance of the specimens without adding too much weight. When you add the inserts you have to accept this weight penalty. They did not turn out quite as well as we had anticipated, and at the present time we are looking into a chem mill process.

As a matter of fact we have already chem milled some specimens to try to increase this fatigue resistance and have had some success with it. Of course there is the problem of fabrication.

Mr. Laier (Barry Controls): Were the first specimens which you showed in the slides subjected to bending loads?

Mr. LaBarge: Yes—The first specimens were bending specimens.

Mr. Laier: And these were not set up as equals stiffness sections?

Mr. LaBarge: No, they were not equal stiffness. The control and the specimen without inserts were equal weight specimens. In the paper we present analysis to predict the stresses in the specimens and we also discuss the effects of the viscoelastic materials on the KT associated with the stress concentration factors associated with the joints.
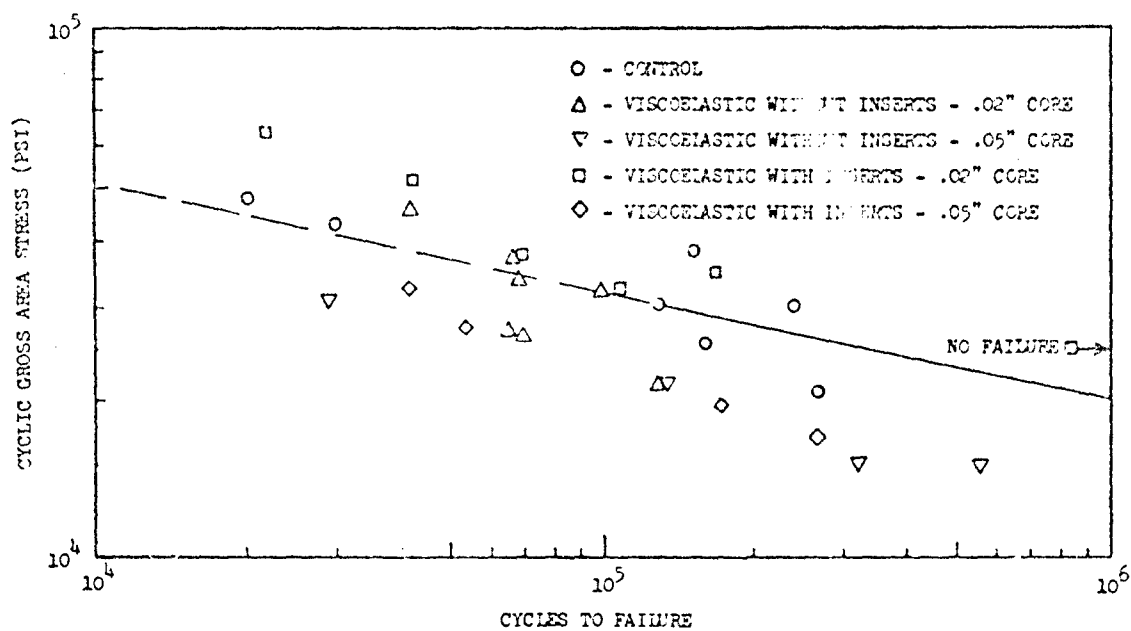
Fig. 32 - Butt joint fatigue stresses, unbonded specimens
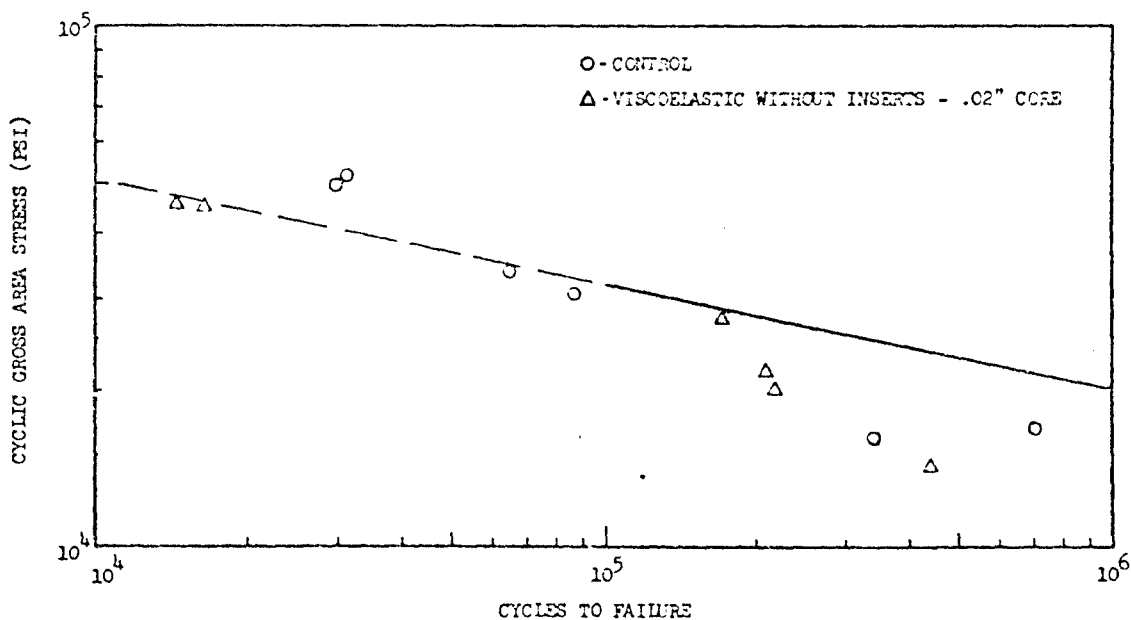
Fig. 33 - Continuous beam fatigue stresses, unbonded specimens
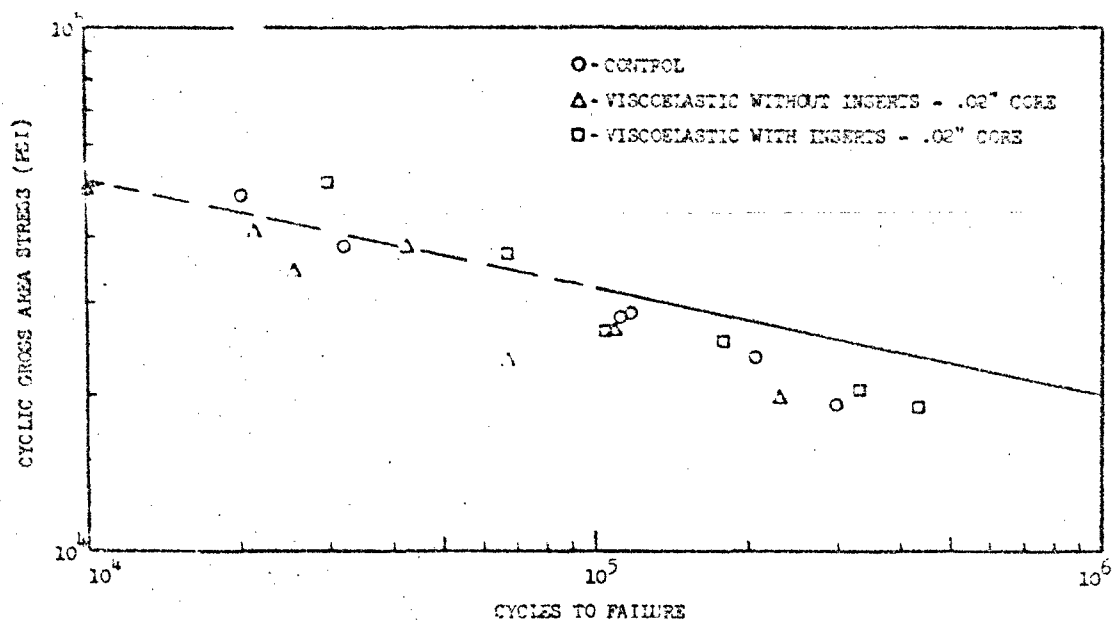
Fig. 34 - Butt joint fatigue stresses, bonded specimens
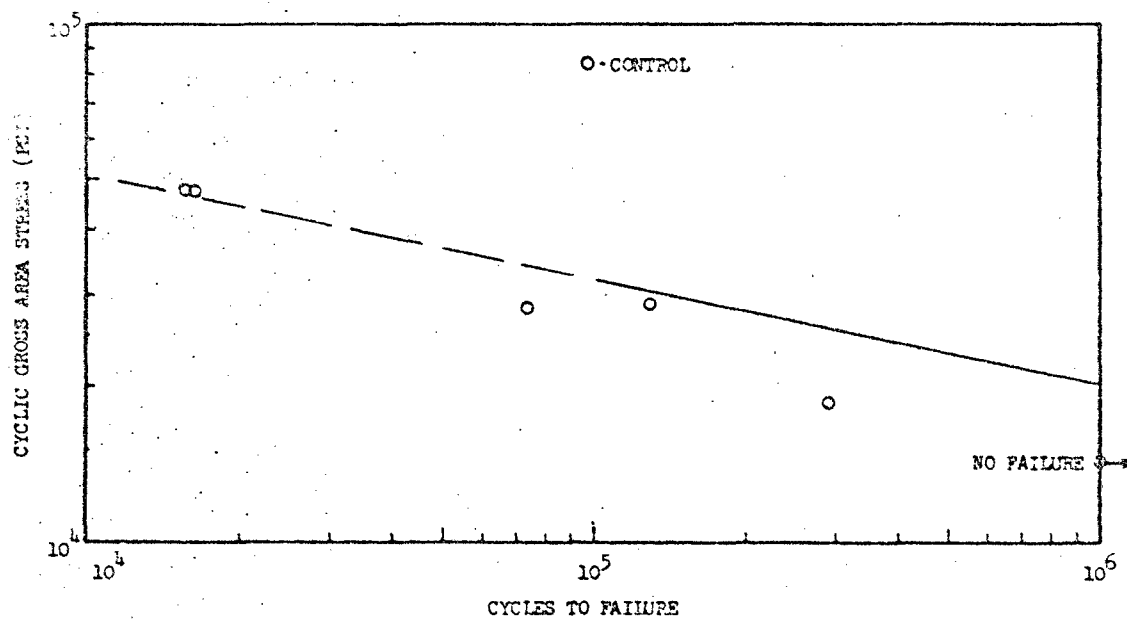
Fig. 35 - Continuous beam fatigue stresses, bonded specimens

ISOLATION

RECENT ADVANCES IN ELECTROHYDRAULIC

VIBRATION ISOLATION

Jerome E. Ruzicka and Dale W. Schubert
Barry Controls
Division of Barry Wright Corporation
Watertown, Massachusetts

This paper discusses recent advances in electrohydraulic isolation of mechanical vibration. This active isolation servomechanism, which employs electronic feedback and hydraulic actuation, has been reduced to practical operational hardware and is presently being applied in the solution of problems for which passive isolation techniques have proven inadequate. The theoretical basis for the operation of the isolation system is discussed, including consideration of system stability. Experimental data are provided for unidirectional single-mass isolation system configurations that provide limited-band isolation, broad-band isolation, single-notch isolation, combined notch and broad-band isolation, multiple notch isolation, and notch isolation with automatic frequency tracking. The results emphasize the unique performance characteristics of electrohydraulic isolation systems, including isolation of ultra low-frequency vibration, zero static and steady-state relative deflections, response substantially independent of the weight of the isolated body, and the ability to tailor the frequency response characteristics to satisfy a wide range of specific requirements.

INTRODUCTION

Vibration isolation systems may be categorized as active or passive, depending on whether or not external power is required for the isolator to perform its function. Active isolation systems are servomechanisms comprised of excitation and/or response sensors, sensor signal processors, and actuators. The sensors provide signals proportional to dynamic excitation or response quantities; the signal processors modify and combine sensor signals to create a command signal; and, the actuators apply forces or induce motions in accordance with the command signal.

Depending upon the nature of the feedback and the actuation mechanisms, active isolation systems can generally be classified as electromechanical, pure fluidic (pneumatic or hydraulic), mechanofluidic (mechanopneumatic or mechanohydraulic), electrofluidic (electropneumatic or electrohydraulic), electric-fluid (electrically conductive or magnetic fluids), and electrodynamic [1]*. Although any of these types of active isolation systems may be suitable for a specific problem, the electro-

hydraulic isolation system offers a number of advantages that make it applicable to a wide range of vibration and shock isolation problems [1-9]. The information presented in this paper represents some of the results of a continuing corporate research and development program on active isolation being conducted by Barry Controls.

Schematic diagrams of the electrohydraulic vibration isolation systems considered in this paper are illustrated in Fig. 1 for vibration excitation $a(t)$ of the foundation. The purpose of the isolator is to reduce the level of vibration response $x(t)$ of the isolated mass. The mass m for the isolation system shown in Fig. 1(a) is connected directly to the hydraulic actuator rod whereas, for the isolation system shown in Fig. 1(b), the mass m is connected indirectly to the actuator rod by a flexible mechanical coupling (passive isolator). For the purpose of this paper, it is assumed that the unidirectional single-mass isolation systems are linear and experience translational vibration only. Furthermore, both the isolated mass and the foundation are assumed rigid.

*Numbers in brackets designate References at end of paper.

141
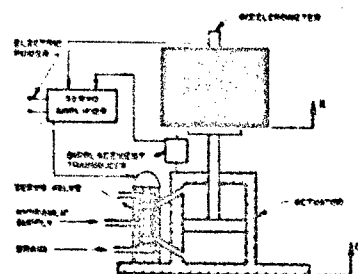
(a)
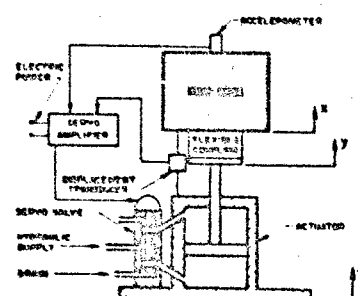
(b)

Fig. 1 – Schematic diagrams of
electrohydraulic isolation systems
(a) without and (b) with a flexible
mechanical coupling (passive isolator)

The electrohydraulic isolation systems
considered in this paper employ acceleration of
the isolated mass and relative displacement
between the mass and the foundation as the
primary feedback signals. These signals are
modified and combined in the servoamplifier to
produce a command signal that operates a
servovalve to control the flow of a relatively
incompressible fluid to and from the hydraulic
actuator (double-acting cylinder). The servo-
amplifier consists of active electronic networks
that perform amplification, attenuation, differen-
tiation, integration, addition, multiplication,
division, frequency response shaping, and
compensation functions. Consequently, the
flow through the servovalve can be made a
function of a wide variety of parameters, such
as jerk, acceleration, velocity, displacement,
time-integral of displacement, etc., where the
effect of each feedback parameter is controlled
independently by adjusting its gain.

Feedback control systems are susceptible
to instabilities that occur in various forms,
such as steady-state limit cycle oscillations
(hunting) and transient oscillations with ampli-
tudes that increase in time. Therefore, a major

consideration fundamental to the design of
electrohydraulic isolation systems is the
requirement for system stability.

NOMENCLATURE

Shown in parentheses are the units of the
parameters in terms of force (F), length (L), and
time (T). Capital letters are used to designate
the Laplace transform of time-dependent
variables denoted by low case letters; e. g.,
$P = P(s) = \mathcal{L}[p(t)]$.

PARAMETER SYMBOLS

A = average actuator area (L^2)

V = nominal actuator chamber volume (L^3)

β = bulk modulus of hydraulic fluid (F/L^2)

C_ℓ = leakage coefficient for piston $\left(\frac{L^3}{T} / \frac{F}{L^2}\right)$

ω_a = $\sqrt{\frac{2\beta A^2}{Vm}}$ = natural frequency of mass and actuator $(1/T)$

ζ_a = $\dfrac{C_\ell \omega_a m}{2A^2}$ = fraction of critical damping of mass and actuator, dimensionless

m = mass (FT^2/L)

k_c = stiffness of flexible coupling (F/L)

C_a = acceleration feedback flow gain $\left(\frac{L^3}{T} / \frac{L}{T^2}\right)$

C_v = relative velocity feedback flow gain $\left(\frac{L^3}{T} / \frac{L}{T}\right)$

C_d = relative displacement feedback flow gain $\left(\frac{L^3}{T} / L\right)$

C_i = integral-displacement feedback flow gain $\left(\frac{L^3}{T} / LT\right)$

p = pressure (F/L^2)

q = flow (L^3/T)

a = displacement of foundation (L)

y = displacement of actuator rod (L)

x = displacement of mass (L)

δ = $(x-a)$ = relative displacement of mass (L)

z = $(y-a)$ = relative displacement of actuator rod (L)

f = frequency $(1/T)$

ω = $2\pi f$ = angular frequency $(1/T)$

ω_c = $\sqrt{k_c/m}$ = natural frequency of mass and flexible coupling $(1/T)$

ω_n = N^{th} notch frequency $(1/T)$

ω_1 = lowest notch frequency $(1/T)$

ω_0 = natural frequency of second-order system $(1/T)$

ω_e = natural frequency of fixed element $(1/T)$

ζ = fraction of critical damping of second-order system, dimensionless

$G(s)$ = transfer function of electronic network, dimensionless

$H(s)$ = transfer function of fixed element, dimensionless

$T_A(s)$ = $X(s)/a(s)$ = absolute system transfer function, dimensionless

$T_R(s)$ = $\Delta(s)/a(s)$ = relative system transfer function, dimensionless

$T_o(s)$ = open-loop system transfer function, dimensionless

$E(s)$ = Laplace transform of external excitation signal $\left(\frac{L^3}{T} T\right)$

N = number of notches, dimensionless

s = Laplace operator $(1/T)$

τ = time constant (T)

t = time (T)

J_o = constant value of jerk (L/T^3)

g = acceleration of gravity (L/T^2)

j = $\sqrt{-1}$

SUBSCRIPTS

u = upper actuator chamber

L = lower actuator chamber

a = accelerometer

d = displacement transducer

sv = servovalve

c = flexible coupling

e = fixed element

GENERAL SERVOVALVE FLOW EQUATIONS

From the principle of conservation of mass, the flow into or out of the actuator is a linear combination of the flow $A\dot{z}$ resulting from the motion across the actuator, the flow $\frac{V}{\beta}\dot{p}$ resulting from storage due to compressibility, and the flow $C_L(p_L - p_u)$ resulting from leakage across the actuator piston. For an assumed positive relative velocity $\dot{z}$, the flow out of the upper chamber volume is

$$q_u = A\dot{z} - \frac{V}{\beta}\dot{p}_u - C_L(p_u - p_L) \qquad (1)$$

and the flow into the lower chamber volume is

$$q_L = A\dot{z} + \frac{V}{\beta}\dot{p}_L - C_L(p_u - p_L) \qquad (2)$$

For the purpose of a linear analysis [10], the valve flow is determined as the average of q_u and q_L, as follows:

$$q = A\dot{z} + \frac{V}{2\beta}(\dot{p}_L - \dot{p}_u) + C_L(p_L - p_u) \qquad (3)$$

For the isolation system shown in Fig. 1(a), the force generated by the actuator equals the inertia force $m\ddot{x}$, as follows

$$A(p_L - p_u) = m\ddot{x} \qquad (4)$$

Similarly, for the isolation system shown in Fig. 1(b)

$$A(p_L - p_u) = -k_c(\delta - z) = m\ddot{x} \qquad (5)$$

Substituting Eq. (4) or (5) in Eq. (3) and simplifying terms, the following relations for average valve flow for the two isolation systems shown in Figs. 1(a) and 1(b), respectively, are obtained

$$q = A\dot{\delta} + \frac{Vm}{2\beta A}\ddot{x} + \frac{C_L m}{A}\ddot{x} \qquad (6a)$$

$$q = A\dot{\delta} + \left(\frac{Am}{k_c} + \frac{Vm}{2\beta A}\right)\ddot{x} + \frac{C_L m}{A}\ddot{x} \qquad (6b)$$

These equations for average flow through the valve may be written in Laplace transform notation, as follows

143

$$Q = As\Delta + A\left(\frac{s^2}{\omega_a^2} + \frac{2\zeta_a s}{\omega_a}\right)sX \qquad (7a)$$

$$Q = As\Delta + A\left(\frac{s^2}{\omega_c^2} + \frac{s^2}{\omega_a^2} + \frac{2\zeta_a s}{\omega_a}\right)sX \qquad (7b)$$

where ω_c is the natural frequency of the rigid mass m supported by the flexible coupling stiffness k_c, and ω_a and ζ_a are the natural frequency and effective fraction of critical damping, respectively, of the rigid mass m coupled to the actuator. By expressing the valve flow Q as a function of the feedback parameters and the feedback parameter gains, Eqs. (6) or (7) provide the equation of motion for the isolation system.

SIMPLIFIED THEORETICAL ANALYSES

Simplified analyses of the electrohydraulic isolation system may be performed by assuming incompressible flow ($\beta = \infty$ and $\omega_a = \infty$), zero leakage ($C_L = 0$ and $\zeta_a = 0$), and unity transfer functions for the servovalve and feedback transducers. These assumptions are valid for vibration at frequencies considerably less than the natural frequencies associated with the actuator, servovalve and feedback transducers. As discussed later, the flexible coupling between the actuator rod and the isolated mass is employed to achieve improved high-frequency vibration isolation. Consequently, for the present low-frequency analyses, the flexible coupling stiffness k_c and, therefore, the natural frequency ω_c are assumed to be infinite. With these assumptions, the average valve flow is given simply by

$$Q = As\Delta \qquad (8)$$

In addition to establishing the fundamental roles of the feedback parameters and the feedback parameter gains, the simplified low-frequency analyses serve to demonstrate the capability of achieving extremely low isolation system natural frequencies, zero static and steady-state relative deflections, and considerable flexibility in shaping the frequency response characteristics.

BASIC SYSTEM RESPONSE

By appropriately processing the acceleration and relative displacement feedback signals in the servoamplifier, the flow through the valve can be made proportional to absolute acceleration $\ddot{x}$, relative velocity $\dot{\delta}$, and relative displacement δ, expressed as follows in Laplace transform notation

$$Q = -(C_a s^2 X + C_v s\Delta + C_d\Delta) \qquad (9)$$

where C_a, C_v and C_d represent the acceleration, relative velocity and relative displacement feedback gains, respectively. Combining Eq. (8) and (9), the following second-order equation of motion is obtained:

$$C_a s^2 X + (C_v + A)s\Delta + C_d\Delta = 0 \qquad (10)$$

Solution of this equation for the absolute transfer function $T_A(s)$ and the relative transfer function $T_R(s)$ is as follows:

$$T_A(s) = \frac{(C_v + A)s + C_d}{C_a s^2 + (C_v + A)s + C_d} \qquad (11)$$

$$T_R(s) = \frac{-C_a s^2}{C_a s^2 + (C_v + A)s + C_d} \qquad (12)$$

The form of these equations are identical to those that apply for a passive isolation system where the isolator is a parallel combination of a linear spring and a viscous damper. The feedback gains for acceleration C_a and relative displacement C_d determine the natural frequency ω_o in a manner similar to the mass and stiffness parameters in the viscous damped passive isolation system, as follows:

$$\omega_o = \sqrt{C_d/C_a} \qquad (13)$$

Furthermore, the effective fraction of critical damping ζ is given by

$$\zeta = \frac{C_v + A}{2\sqrt{C_a C_d}} \qquad (14)$$

The ability to select feedback gains C_a and C_d over a very wide range (compared to the limited ranges for the mass and stiffness counterparts of these parameters in a passive isolation system) is the basis for being able to provide extremely low natural frequencies of electrohydraulic isolation systems. Further-

144

more, since the mass m does not appear in the equations of motion, the isolation system performance characteristics are independent of the weight of the isolated body. Eq. (14) indicates that, if no velocity feedback is employed, the effective viscous damping ratio is determined solely by the actuator piston area A and the feedback gains C_a and C_d. In this case, a change in either the acceleration or displacement feedback gains will affect both the natural frequency ω_b and the fraction of critical damping ζ. The addition of relative velocity feedback, therefore, provides a means of increasing or decreasing damping without affecting the natural frequency of the isolation system.

For the special case where only acceleration feedback is employed, the absolute transfer function is a first-order lag and the relative transfer function is a first-order lead, as follows

$$T_A(s) = \frac{1}{\tau s + 1} \quad (15)$$

$$T_R(s) = \frac{\tau s}{\tau s + 1} \quad (16)$$

where the time constant $\tau = C_a/A$. The result is a resonance-free isolation system with greater degrees of high-frequency isolation provided for increasingly greater values of acceleration feedback gain C_A. In practice, it is unlikely that pure acceleration feedback can be employed because of the susceptibility of the system to voltage or current drift that may cause large undesired displacements of the isolated mass. This difficulty can be remedied by the addition of a small amount of relative displacement feedback to provide position control without materially altering the isolation characteristics.

Applying Routh's stability criteria [11] to the characteristic equation for the closed-loop responses given by Eqs. (11) and (12), the isolation system is stable for C_a, $C_d > 0$ and $C_v > -A$. Therefore, high gain acceleration feedback may be employed to achieve a natural frequency virtually as low as desired while maintaining a stable isolation system. It should be noted, however, that linear electrohydraulic isolation systems of the type described above may exhibit large dynamic deflections in response to shock excitation because of the extremely low natural frequencies that can be achieved. To avoid this situation, nonlinear electronic compensation can be introduced into the acceleration and/or relative displacement feedback loops to substantially change the loop gain for relative displacements exceeding an established linear range of operation [4]. This has the effect of

providing a hardening stiffness characteristic with greatly increased feedback control operating to limit the relative displacement severely and to rapidly reposition the isolator in its linear range of operation.

ELIMINATION OF STATIC AND STEADY-STATE RELATIVE DEFLECTIONS

In designing low-frequency isolation systems, the static and steady-state relative deflections resulting from sustained acceleration conditions are of considerable importance. For isolation systems described by a second-order equation of motion (passive or active), the static deflection $\delta_{st} = g/\omega_b^2$, where g is the acceleration of gravity and ω_b is the natural frequency. Extremely large static and steady-state relative deflections occur for low values of resonant frequency. The static and steady-state deflections can be eliminated in the electrohydraulic isolation system by introducing feedback that is a function of the time-integral of relative displacement, or by incorporating a lead network in the acceleration feedback loop.

Eq. (9) for valve flow can be modified to include integral-displacement feedback control, as follows

$$Q = -(C_a s^2 X + C_v s \Delta + C_d \Delta + C_i \Delta/s) \quad (17)$$

where the integral-displacement gain $C_i = C_d/\tau$, and τ is the time constant of an integrator in the relative displacement feedback loop. Combining Eqs. (8) and (17) results in the following third-order equation of motion:

$$C_a s^3 X + \left[(C_v + A)s^2 + C_d s + C_i \right] \Delta = 0 \quad (18)$$

Solution of this equation for the absolute and the relative transfer functions is as follows:

$$T_A(s) = \frac{(C_v + A)s^2 + C_d s + C_i}{C_a s^3 + (C_v + A)s^2 + C_d s + C_i} \quad (19)$$

$$T_R(s) = \frac{-C_a s^3}{C_a s^3 + (C_v + A)s^2 + C_d s + C_i} \quad (20)$$

Application of the final value theorem [12] to the solution for relative deflection given by Eq. (20) for the case of unit acceleration step excitation $a(s) = 1/s^3$ indicates that the static and steady-state relative deflections are zero,

as follows

$$\delta_{ss} = \overset{\text{limit}}{t \to \infty} \left[\delta(t) \right] = \overset{\text{limit}}{s \to 0} \left[s\,\Delta(s) \right] = \overset{\text{limit}}{s \to 0} \left[\frac{T_R(s)}{s^2} \right] = 0 \tag{21}$$

Applying Routh's stability criteria to the characteristic equation for the closed-loop responses given by Eqs. (19) and (20), the isolation system is stable for $C_a > 0$, $C_v > -A$, and $(C_v + A)C_d > C_aC_i$. Therefore, incorporation of time-integral of relative displacement feedback provides a means of eliminating static and steady-state relative deflections while maintaining a stable isolation system.

Eq. (9) for valve flow can be modified to include a first-order lead compensation network $\tau s/(\tau s + 1)$ in the acceleration feedback loop, as follows

$$Q = -\left[C_a\left(\frac{\tau s}{\tau s + 1}\right)s^2 X + C_v s\Delta + C_d\Delta \right] \tag{22}$$

where τ is the time constant of the lead compensation network. Combining Eqs. (8) and (22) results in the following third-order equation of motion:

$$C_a \tau s^3 X + \left[(C_v + A)\tau s^2 + (C_v + A + C_d\tau)s + C_d \right]\Delta = 0 \tag{23}$$

Solution of this equation for the absolute and the relative transfer functions is as follows:

$$T_A(s) = \frac{(C_v + A)\tau s^2 + (C_v + A + C_d\tau)s + C_d}{C_a\tau s^3 + (C_v + A)\tau s^2 + (C_v + A + C_d\tau)s + C_d} \tag{24}$$

$$T_R(s) = \frac{-C_a\tau s^3}{C_a\tau s^3 + (C_v + A)\tau s^2 + (C_v + A + C_d\tau)s + C_d} \tag{25}$$

Application of the final value theorem to the solution for relative deflection once again indicates that the static and steady-state relative deflections are zero. Routh's stability criteria applied to the characteristic equation for the closed-loop responses given by Eqs. (24) and (25) indicates that the isolation system is stable for $C_a > 0$, $C_v > -A$, and $(C_v + A)(C_v + A + C_d\tau) > C_aC_d$. Therefore, use of first-order lead compensation in the acceleration feedback loop serves to eliminate static and steady-state relative deflections while maintaining a stable isolation system.

The addition of integral-displacement feedback control or lead compensation in the acceleration loop does not materially alter the vibration isolation characteristics, since relatively low values of gain C_i or high values of the lead compensation time constant τ are generally employed. However, a radically altered transient response characteristic results for step accelerations and, to a lesser extent, for other forms of transient excitation. In addition to eliminating the static and steady-state relative deflections, the peak transient deflections of the isolation systems are reduced. It is interesting to note that, for ramp acceleration excitation $a(s) = J_0/s^2$ where J_0 is the constant value of jerk excitation, the isolation system has a constant value of steady-state relative deflection given by $-J_0\,C_a/C_i$ and $-J_0 C_a\tau/C_d$ for integral-displacement feedback and acceleration lead compensation, respectively.

NOTCH ISOLATION CHARACTERISTICS

There are instances where it is desired to obtain both resonant vibration control and a degree of vibration isolation greater than that provided by the basic electrohydraulic isolation system, as expressed by Eqs. (11), (19) and (24). For example, a high degree of isolation at a particular frequency may be preferred over broad-band isolation characteristics. Networks for shaping the frequency response characteristics of the electrohydraulic isolation system may be incorporated in the acceleration loop, as the following discussion demonstrates relative to achieving single-notch and multiple-notch isolation characteristics. This type of electrohydraulic isolation system is particularly

146

well suited to adaptive control since a feedback control signal proportional to frequency can be employed to have the notch-frequency automatically track the frequency of excitation.

Single-Notch Isolation

A very high degree of vibration isolation may be obtained at a discrete frequency by incorporating a frequency response shaping network having an undamped resonance characteristic in the acceleration loop. One such network is represented by the transfer function $\omega_n^2/(s^2 + \omega_n^2)$, which applies for a simple undamped second-order oscillator. This network provides an infinite gain in the acceleration feedback loop at the frequency $\omega = \omega_n$, thereby resulting in zero transmission of vibration as demonstrated below.

Modifying Eq. (9) to include the second-order oscillator network in the acceleration loop gives

$$Q = -\left[C_a\left(\frac{\omega_n^2}{s^2 + \omega_n^2}\right) s^2 X + C_v s\Delta + C_d \Delta\right] \tag{26}$$

Combining Eqs. (8) and (26) results in the following third-order equation of motion:

$$C_a \omega_n^2 s^2 X + \left[(C_v + A) s^3 + C_d s^2 + (C_v + A) \omega_n^2 s + C_d \omega_n^2\right] \Delta = 0 \tag{27}$$

Solution of this equation for the absolute and relative transfer functions is as follows:

$$T_A(s) = \frac{\left[(C_v + A)s + C_d\right](s^2 + \omega_n^2)}{(C_v + A)s^3 + (C_a \omega_n^2 + C_d)s^2 + (C_v + A)\omega_n^2 s + C_d \omega_n^2} \tag{28}$$

$$T_R(s) = \frac{-C_a \omega_n^2 s^2}{(C_v + A)s^3 + (C_a \omega_n^2 + C_d)s^2 + (C_v + A)\omega_n^2 s + C_d \omega_n^2} \tag{29}$$

Upon substituting $s = j\omega$, these equations indicate that the absolute transmissibility is zero and the relative transmissibility is unity for $\omega = \omega_n$. Consequently, this form of the electrohydraulic isolation system is ideal for the isolation of vibration excitation having a single discrete frequency. An additional advantage is the relatively small relative deflections that occur in response to shock excitation. Routh's stability criteria applied to the characteristic equation of the closed-loop responses given by Eqs. (28) and (29) indicates that the isolation system is stable for C_a, $C_d > 0$ and $C_v > -A$.

Multiple-Notch Isolation

Notch isolation characteristics may be obtained at more than one frequency by using several second-order oscillator networks arranged in parallel in the acceleration loop. The frequency response shaping network is represented by the transfer function $\sum_{n=1}^{N} (\omega_1/\omega_n)\left[\omega_n^2/(s^2 + \omega_n^2)\right]$, which represents the summation of N single-notch networks having arbitrarily spaced natural frequencies, and a gain relationship of ω_1/ω_n to provide equal percentage bandwidths of each notch. This network provides infinite gain in the acceleration feedback loop at each notch natural frequency $\omega = \omega_n$, thereby resulting in zero transmission of vibration as demonstrated below.

Modifying Eq. (9) to include N parallel second-order oscillator networks in the acceleration loop gives

$$Q = -\left[C_a \sum_{n=1}^{N} \left(\frac{\omega_1 \omega_n}{s^2 + \omega_n^2}\right) s^2 X + C_v s\Delta + C_d \Delta\right] \tag{30}$$

147

Combining Eqs. (9) and (30) results in the following $(2N + 1)^{th}$-order equation of motion

$$C_a \sum_{n=1}^{N} \left(\frac{\omega_1\, \omega_n}{s^2 + \omega_n^2} \right) s^2 X + (C_v + A) s \Delta + C_d \Delta = 0 \tag{31}$$

Solution of this equation for the absolute and relative transfer function is as follows:

$$T_A(s) = \frac{\left[(C_v + A)s + C_d \right] \prod_{n=1}^{N} (s^2 + \omega_n^2)}{C_a \left[\sum_{n=1}^{N} \left(\frac{\omega_1\, \omega_n}{s^2 + \omega_n^2} \right) \prod_{n=1}^{N} (s^2 + \omega_n^2) \right] s^2 + \left[(C_v + A)s + C_d \right] \prod_{n=1}^{N} (s^2 + \omega_n^2)} \tag{32}$$

$$T_R(s) = \frac{-C_a \left[\sum_{n=1}^{N} \left(\frac{\omega_1\, \omega_n}{s^2 + \omega_n^2} \right) \prod_{n=1}^{N} (s^2 + \omega_n^2) \right] s^2}{C_a \left[\sum_{n=1}^{N} \left(\frac{\omega_1\, \omega_n}{s^2 + \omega_n^2} \right) \prod_{n=1}^{N} (s^2 + \omega_n^2) \right] s^2 + \left[(C_v + A)s + C_d \right] \prod_{n=1}^{N} (s^2 + \omega_n^2)} \tag{33}$$

Upon substituting $s = j\omega$, these equations indicate that the absolute transmissibility is zero and the relative transmissibility is unity for each notch frequency $\omega = \omega_n$. Consequently, this form of the electrohydraulic isolation system is ideal for the isolation of periodic vibration excitation comprised of any number of discrete frequency components [7]. Routh's stability criteria applied to the characteristic equation of the closed-loop responses given by Eqs. (32) and (33) indicates that the isolation system is stable for C_a, $C_d > 0$ and $C_v > - A$.

EFFECT OF FIXED ELEMENT DYNAMICS

The isolation system transfer function and stability conditions examined thus far have been for ideal system elements (actuator, servovalve, accelerometer, flexible coupling, and displacement transducer) having unity transfer functions. This simplification was introduced to demonstrate clearly the basic low-frequency response characteristics of the electrohydraulic isolation system. As a practical matter, however, the effect of fixed element dynamics on the isolation system performance must be considered, as well as the use of compensation techniques to ensure stability. Block diagrams are shown in Fig. 2 and 3 for the electrohydraulic isolation systems illustrated in Fig. 1(a) and 1(b), respectively, where H represents the transfer function for isolation system fixed elements and G
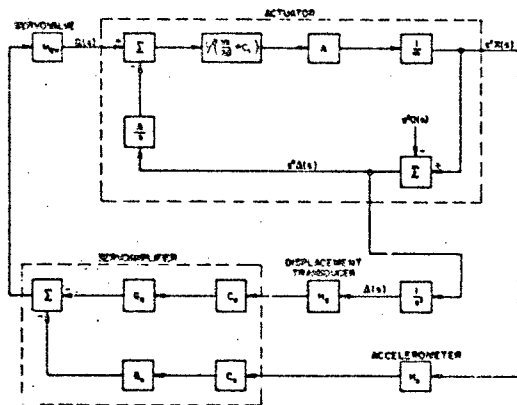
Fig. 2 - Block diagram of electrohydraulic isolation system without a flexible coupling (passive isolator)
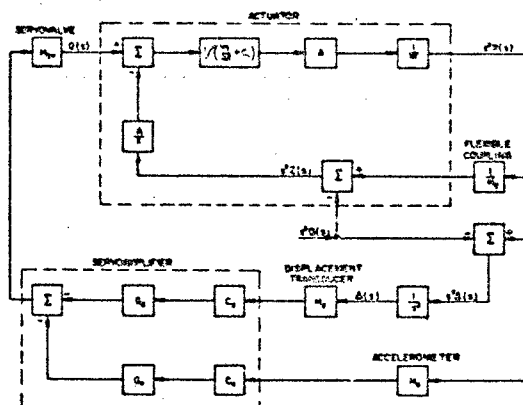
Fig. 3 - Block diagram of the electro-hydraulic isolation system with a flexible coupling (passive isolator)

148

represents the transfer function for compensation or frequency response shaping networks.

The open-loop transfer function $T_o(s)$ for the isolation system block diagram shown in Fig. 3 is obtained by substituting an external sinusoidal signal E for the acceleration feedback signal $C_a G_a H_a s^2 X$ and solving for the open-loop transfer function, defined as follows:

$$T_e(s) = \frac{C_a G_a H_a s^2 X}{-E} \qquad (34)$$

The flow from the servovalve for the open-loop condition is

$$Q = -H_{sv}(E + C_d G_d H_d X) \qquad (35)$$

where $X = \Delta$ since $a(s)$ is assumed zero. Combining Eqs. (35) and (7b), solving for X in terms of E, and placing this result in Eq. (34) gives the following general expression for the open-loop transfer function:

$$T_o(s) = \frac{C_a G_a H_a s^2 H_{sv}}{As\left[1 + \frac{2\zeta_a s}{\omega_a} + \frac{s^2}{\omega_a^2} + \frac{s^2}{\omega_c^2} + \frac{C_d}{As} G_d H_d H_{sv}\right]} \qquad (36)$$

The open-loop transfer function for the isolation system block diagram shown in Fig. 2, which does not include the flexible coupling, is obtained by setting $\omega_c = \infty$.

Relative velocity feedback is not shown in Figs. 2 or 3 or in Eq. (36) since it is generally obtained by differentiation of the relative displacement signal by use of a network having the transfer function

$$G_d = 1 + \frac{C_v s}{C_d}\left(\frac{1}{1 + \tau s}\right) \qquad (37)$$

where τ is the time constant of a lag compensation network employed to wash out the velocity feedback signal for frequencies greater than $\omega = 1/\tau$.

The dynamics of the accelerometer, displacement transducer, and servovalve can be represented as a damped second-order transfer function, as follows

$$H_e = \frac{\omega_e^2}{s^2 + \zeta_e \omega_e s + \omega_e^2} \qquad (38)$$

where ω_e is the natural frequency and ζ_e is the fraction of critical damping for the element in question (generally specified by the manufacturer). The dynamics of the servovalve and actuator greatly influence the stability state of the isolation system because the natural frequencies of these elements are relatively low. The natural frequency of the servovalve is generally between 50 and 200 Hz, and the effective natural frequency of the mass supported by the actuator without a flexible coupling is also generally between 50 and 200 Hz. The fraction of critical damping for the mass and actuator system generally ranges between 0.1 and 0.3, depending upon whether the damping is provided by the actuator seals alone or whether significant damping due to leakage exists. Accelerometers and displacement transducers can generally be selected that have relatively high natural frequencies (e.g., above 1000 Hz) and, therefore, represent minor influences on stability.

Referring to Eq. (36) with $s = j\omega$, the open-loop phase angle for the uncompensated system ($G_a = G_d = 1$) at frequencies approaching zero is $+180°$. At intermediate frequencies ($\omega < \omega_a, \omega_{sv}$) where the value of the displacement feedback term becomes small compared to the other terms, the open-loop phase angle approaches $+90°$. For higher frequencies, the phase angle is lagged strongly by the dynamics of the servovalve and actuator ($-180°$ phase lag for each element), thereby resulting in a phase angle less than $-180°$ and a total gain far in excess of unity, which indicates that the system is grossly unstable. The system can be stabilized by using low-frequency lag, lag-lead, quadratic or a combination of these compensation networks, as represented by G_a in the acceleration loop, to lower the acceleration gain below unity at the frequency where the open-loop phase angle is $-180°$. These compensation networks can provide adequate stability for the system, but at the sacrifice of vibration isolation at high frequencies (see Experimental Results, Fig. 5 for example). Lead-lag and pole-cancellation compensation networks cannot be used since they require excessive gain and the natural frequencies of the system fixed elements vary with excitation amplitude and actuator position because of nonlinearities.

A form of mechanical compensation may be obtained by connecting the mass to the actuator rod through a flexible coupling, as shown by the schematic diagram in Fig. 1(b) and the block diagram in Fig. 3. Since the stiffness of the flexible coupling is in series with the actuator stiffness, the effective natural frequency of the actuator and mass is lowered to less than ω_c. Therefore, a low-stiffness flexible coupling can be employed to attenuate the acceleration loop gain and at the same time offer passive vibration isolation at higher frequencies (see Experimental Results, Figs. 5 and 7, for example). However,

electronic compensation networks generally are still required to achieve satisfactory margins of stability.

EXPERIMENTAL RESULTS

A photograph of a single-mass laboratory experimental model of the electrohydraulic vibration isolation system attached to a vibration shaker is shown in Fig. 4. The hydraulic actuator, servoaccelerometer, direct current differential transformer displacement transducer (DCDT), servovalve and flexible coupling are standard commercially available components, whereas the servoamplifier (not shown) is a custom assembly employing operational amplifiers and various types of frequency response shaping networks and compensation networks.
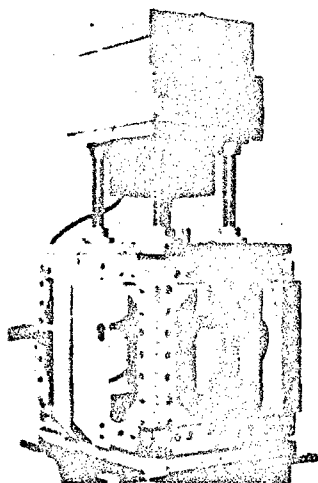
Fig. 4 – Photograph of the laboratory experimental model of the electro-hydraulic vibration isolation system

The hydraulic actuator (5-inch stroke, 2-1/2 inch bore) is supported within a rigid structural frame that houses four linear bearing and shaft assemblies for constraining the motion of the rigid payload in vertical translation. The isolated weight was 150 or 250 lbs., depending on the isolation system configuration. The overall height of the isolator (18 inches) was selected for convenience in conducting experimental research.

The servoaccelerometer (force-balance type) attached to the payload mass provides the acceleration feedback signal and the DCDT connected between the mass and the structural frame (representing a rigid foundation) provides the relative displacement feedback signal. The servoamplifier processing these feedback signals provides a flow command signal to drive the servovalve torque motor. The servovalve connected to the actuator by a manifold regulates the flow of hydraulic fluid from a hydraulic power supply (not shown) that has a 3. gpm flow capacity at 1500 psi pressure.

The performance of the vibration isolation system was measured in terms of the absolute transmissibility, which is defined as the ratio of the harmonic vibration response amplitude of the isolated mass to the amplitude of harmonic vibration excitation imposed on the foundation. Vibration excitation was imposed on the isolation system foundation (the structural frame) by use of a specially modified mechanical shaker over the frequency range of 0.02 to 10 Hz, and a standard electrodynamic shaker over the frequency range of 5 to 500 Hz. The vibration response of the isolated rigid mass was measured by an external DCDT at low frequencies and a piezoelectric accelerometer at high frequencies.

Open-loop transfer functions were measured by disconnecting the acceleration feedback signal and, in its place, substituting an external excitation signal from an oscillator. The magnitude of the open-loop transfer function represents the ratio of the amplitude of the disconnected acceleration feedback signal to the amplitude of the external signal substituted in its place. The phase angle of the open-loop transfer function represents the phase difference between the disconnected acceleration signal and the externally applied signal. The displacement loop remained closed, thereby maintaining the actuator in its null position which was required for testing purposes.

Experimental transmissibility curves are presented in Figs. 5 to 15 with system parameters selected to provide limited-band isolation, broad-band isolation, single-notch isolation, combined notch and broad-band isolation, multiple-notch isolation, and notch isolation with automatic frequency tracking. For each system tested, open-loop transfer functions (magnitude and phase) were measured to determine the margin of stability in terms of gain and phase margins [13]. The gain margin is defined as the additional gain that just makes the system unstable; that is, the magnitude (db) of the open-loop transfer function when the phase angle is -180°. The phase margin is defined as the additional decrease in phase angle that just makes the system unstable for a unity gain (0 db magnitude) of the open-loop transfer function; that is, the phase margin equals 180° plus the negative phase angle corresponding to a magnitude of 0 db.

LIMITED-BAND ISOLATION

Transmissibility curves for limited-band isolation are shown in Fig. 5 for the electro-hydraulic isolation system with no flexible
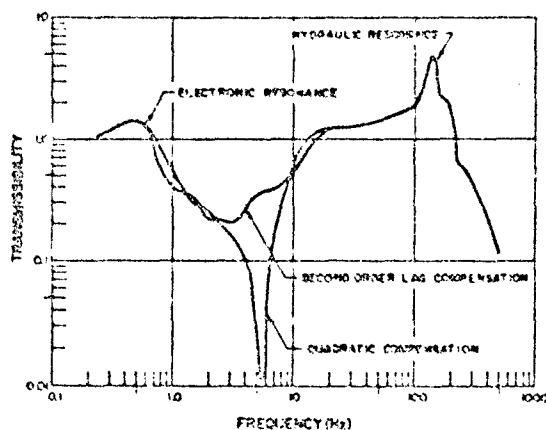
Fig. 5 - Experimental transmissibility curves for limited-band isolation systems employing second-order lag and quadratic compensation

Fig. 6 - Experimental Bode diagrams of open-loop transfer function for limited-band isolation system with quadratic compensation

Fig. 7 - Experimental transmissibility curves for broad-band isolation systems with elastomeric (f_c = 10 H$_z$) and helical spring (f_c = 3 hz) flexible couplings.

coupling. The isolated weight was 150 lbs., and an electronic resonance was created at 0.5 Hz with a resonant transmissibility of 1.4. Second-order lag and quadratic compensation were employed in the acceleration loop to stabilize the isolation system. The transmissibility curve demonstrates the limited bandwidth of isolation that is provided by the electrohydraulic isolation system with no flexible coupling. A transmissibility less than 0.5 was provided over the frequency range of approximately 1 to 10 Hz, and the system with quadratic compensation generally provided better isolation than the system with second-order lag compensation. The hydraulic resonance in the region of 150 Hz is primarily due to the hydraulic fluid compressibility effects. The degree of amplification at the hydraulic resonance is a function primarily of the actuator damping characteristics, and passive isolation is provided for frequencies greater than 200 Hz in accordance with the passive isolation characteristics of the hydraulic actuator.

The open-loop transfer function for the isolation system with quadratic compensation is shown in Fig. 6 in the form of Bode diagrams (magnitude and phase angle versus frequency). Determination of the gain and phase margins from the Bode diagrams is as indicated in Fig. 6; the gain margin is 8 db and the phase margin is 45°.

BROAD-BAND ISOLATION

Transmissibility curves for broad-band isolation are shown in Fig. 7 for the electrohydraulic isolation system with flexible couplings (passive isolators) employed to

provide high-frequency vibration isolation. The isolated weight was 250 lbs., and an electronic resonance was created at 0.5 Hz with a resonant transmissibility of 1.5. An elastomeric isolator was employed to achieve f_c = 10 Hz while a helical spring was used to achieve f_c = 3 Hz. The transmissibility curves demonstrate that lowering the stiffness of the flexible

151

coupling improves high-frequency vibration isolation. In this case, isolation of vibration occurs for frequencies greater than 0.8 Hz, with greater than 75 percent isolation provided for frequencies greater than 2 Hz, and greater than 90 percent isolation provided for frequencies greater than 10 Hz. The high-frequency attenuation rate is approximately 6 db/octave. For the system in which f_c = 12 Hz, the gain margin was 5 db and the phase margin was 50° whereas, for the system in which f_c = 3 Hz, the gain margin was 9 db and the phase margin was 90°. The isolation system having the lower value of flexible coupling stiffness, therefore, exhibited better isolation characteristics and higher margins of stability.

Transmissibility curves for broad-band isolation are shown in Fig. 8 for the electro-hydraulic isolation system with a flexible coupling (f_c = 3 Hz), an isolated weight of 250 lbs., and various resonant frequencies created electronically. Changing the acceleration feedback gain provided resonant frequencies of 0.05, 0.1 and 0.5 Hz, respectively,
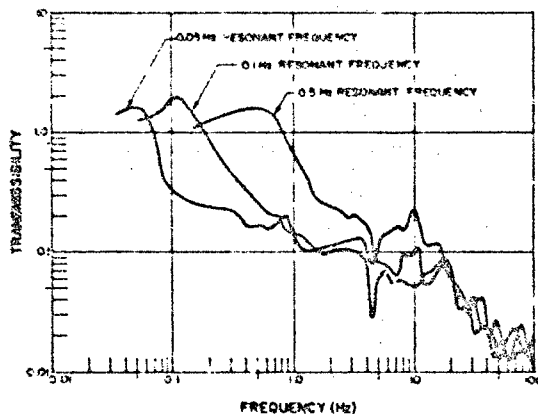
Fig. 8 - Experimental transmissibility curves for broad-band isolation systems with flexible coupling (f_c = 3 Hz) and resonant frequencies of 0.05, 0.1 and 0.5 Hz

with resonant transmissibilities ranging between 1.5 and 2.0. For frequencies greater than 15 Hz, the transmissibility is essentially the same for all three systems. It is interesting to note that passive isolation systems with 0.05, 0.1 and 0.5 Hz resonant frequencies would exhibit static deflections of approximately 320 feet, 82 feet, and 3 feet, respectively, whereas the electrohydraulic isolation system has a zero static deflection. The gain margins for the 0.05, 0.1 and 0.5 Hz resonant frequency systems were 10 db, 9 db and 8 db, respectively, and the phase margins were 38°, 30°, and 90°, respectively.

SINGLE-NOTCH ISOLATION

A transmissibility curve for single-notch isolation is shown in Fig. 9 for the electro-hydraulic isolation system with no flexible coupling. The isolated weight was 150 lbs. and a single notch (antiresonance) was created
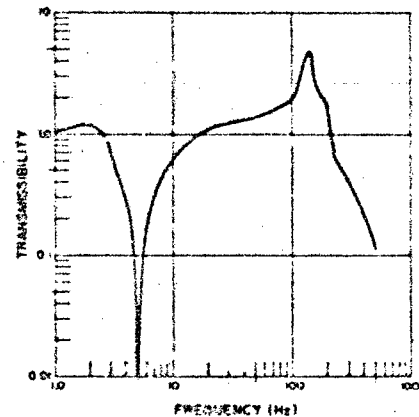
Fig. 9 - Experimental transmissibility curve for a single-notch isolation system with the notch antiresonance at 5 Hz

at 5 Hz. Approximately 99 percent isolation was provided at the notch frequency and the nominal bandwidth of the notch (measured at a transmissibility of 0.5) was 100 percent. A resonance condition existed at approximately 2 Hz, with a resonant transmissibility of 1.2. The gain margin of the single-notch isolation system was 10 db and the phase margin was 94°.

Transmissibility curves for single-notch isolation systems with various notch bandwidths are shown in Fig. 10 for a notch frequency of 5 Hz, at which greater than 99 percent isolation was provided. The low, medium and high gains in the acceleration loop result in bandwidths (measured at a transmissibility of 0.5) of nominally 10, 50 and 100 percent, respectively. The higher the acceleration loop gain, the greater the bandwidth and the higher the res-onant transmissibility, which had values of 1.05, 1.15 and 1.2, respectively, for the three increasingly greater values of gain. Furthur-more, for a given notch frequency, an increase in acceleration loop gain decreases the reso-nant frequency of the isolation system, which had values of 3.5, 2.0 and 1.75, respectively, for the three increasingly greater values of gain. The margins of stability for the three single-notch isolation systems were as follows: low gain, 28 db gain margin and 109° phase margin; medium gain, 14 db gain margin and 109° phase margin; and high gain, 10 db gain margin and 94° phase margin.

152
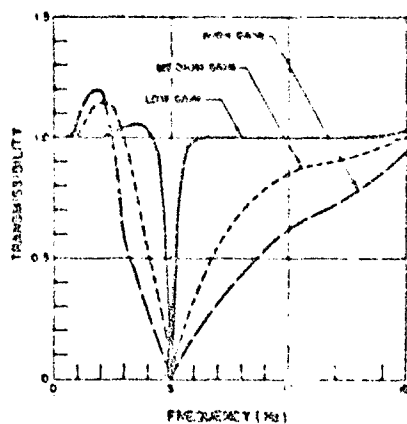
Fig. 10 - Experimental transmissibility
curves for single-notch isolation systems
with various degrees of acceleration
feedback gain and the notch antiresonance
at 5 Hz

Fig. 11 - Experimental transmissibility
curves for broad-band and combined
notch and broad-band isolation systems
with flexible coupling ($f_c = 10$ Hz) and
the notch antiresonance at 5 Hz

An increase in the acceleration gain for a
single-notch isolation system increases the
bandwidth of the notch, decreases the resonant
frequency, increases the resonant transmissibil-
ity, and decreases the margin of stability. For
frequencies substantially greater than the notch
frequency, the transmissibility is independent
of the notch characteristics, with a hydraulic
resonance occurring in the region of 150 Hz.

COMBINED NOTCH AND BROAD-BAND ISOLATION

Transmissibility curves for broad-band
isolation, with and without a single notch at
5 Hz, are shown in Fig. 11 for the electro-
hydraulic isolation system with elastomeric
flexible coupling ($f_c = 10$ Hz). The isolated
weight was 250 lbs., and an electronic reso-
nance was created at 0.5 Hz with a resonant
transmissibility of 1.5. The transmissibility
characteristics of the broad-band isolation
system were previously discussed with
reference to Fig. 7. The transmissibility
curve providing combined notch and broad-
band isolation characteristics is essentially
the same as without the notch, except in the
region of the notch frequency, at which
greater than 99 percent isolation is provided.
For the broad-band isolation system without
the notch, the gain margin was 5 db and the
phase margin was 50° whereas, for the
isolation system providing combined notch and
broad-band isolation, the gain margin was 5 db
and the phase margin was 35°. Consequently,
a slight decrease in the margin of stability is
associated with the addition of the single-notch
isolation characteristic.

MULTIPLE-NOTCH ISOLATION

A transmissibility curve for multiple-notch
isolation is shown in Figure 12 for the electro-
hydraulic isolation system with no flexible
coupling. The isolated weight was 150 lbs.,
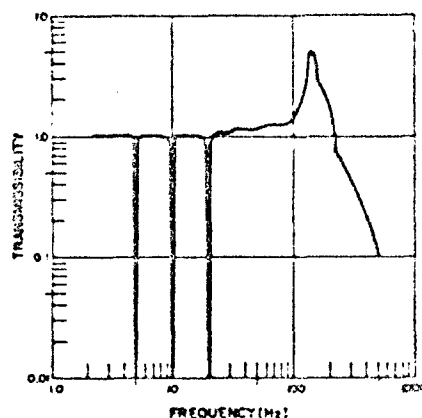
Fig. 12 - Experimental transmissibility
curve for a multiple-notch isolation system
with the notch antiresonances at 5, 10
and 20 Hz

and the frequencies associated with the three
notches are related harmonically. At 5, 10 and
20 Hz, greater than 99 percent isolation is
provided and the nominal bandwidths of the

153

notches (measured at a transmissibility of 0.5) was 8 percent. No apparent resonance condition existed and the transmissibility was equal to or less than unity between the notch frequencies. However, for frequencies greater than the highest notch frequency, the transmissibility exceeded unity with a hydraulic resonance occurring in the region of 150 Hz. The gain margin of the three-notch isolation system was 9 db and the phase margin was 65°.

The transmissibility curve shown in Fig. 13 is for a three-notch isolation system,
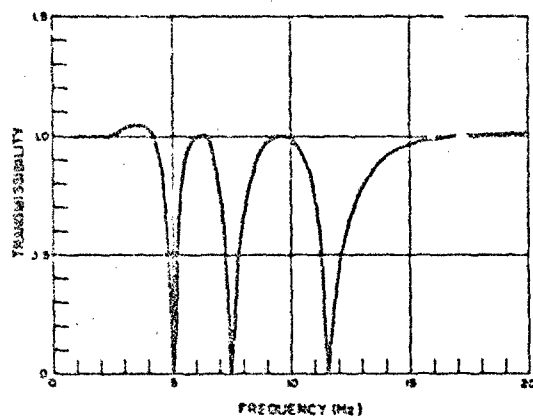
Fig. 13 - Experimental transmissibility curve for a multiple-notch isolation system with the notch antiresonances at 5, 7.5 and 11.5 Hz

where the notch frequencies are not related harmonically and the notch bandwidths (measured at a transmissibility of 0.5) are 8 percent. At the notch frequencies of 5, 7.5 and 11.5 Hz, greater than 99 percent isolation is provided. A resonance condition existed for this isolation system, where the resonant frequency was 3.5 Hz and the resonant transmissibility was 1.05. For frequencies greater than approximately 20 Hz, the transmissibility curve is essentially that shown in Fig. 12. The gain margin of the three-notch isolation system was 8 db and the phase margin was 74°.

NOTCH ISOLATION WITH AUTOMATIC
FREQUENCY TRACKING

Transmissibility curves are shown in Figs. 14 and 15 for single-notch electrohydraulic isolation systems with automatic notch-frequency tracking capability. The automatic frequency tracking is achieved by employing a feedback signal proportional to the frequency of vibration excitation to drive an adaptive single-notch electronic shaping network to continuously change the notch frequency so

that it corresponds to the frequency of vibration excitation. The isolated weight was 150 lbs., and the bandwidth of the notch (measured at a transmissibility of 0.5) was 8 percent.
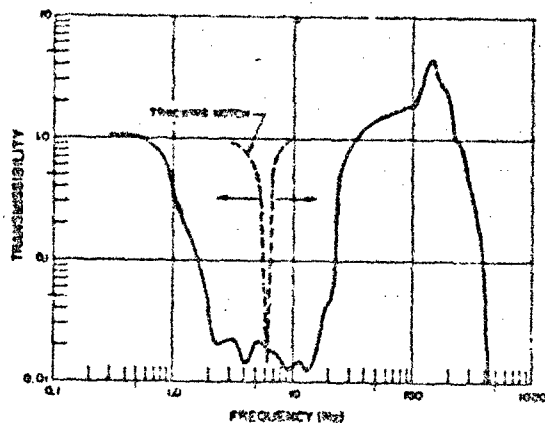
Fig. 14 - Experimental transmissibility curve for a notch isolation system with automatic frequency tracking using a frequency-detection network in the acceleration feedback loop
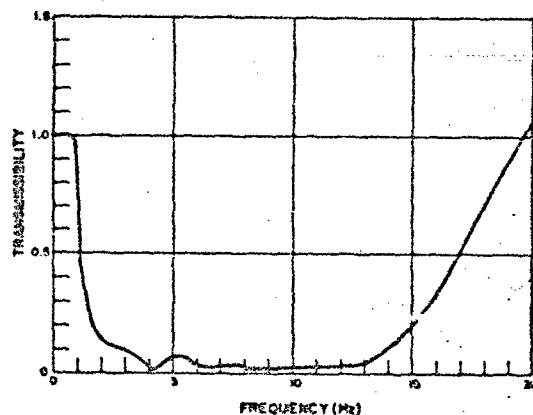
Fig. 15 - Experimental transmissibility curve for a notch isolation system with automatic frequency tracking using tachometer feedback

The transmissibility curve shown in Fig. 14 was obtained by processing the acceleration feedback signal through a frequency-detection network to obtain the control signal required to adapt the notch frequency of the frequency response shaping network to the frequency of vibration excitation. The notch automatically tracked the excitation frequency over the frequency range of approximately 1.0 to 25 Hz, with greater than 90 percent isolation

154

provided between 1.5 and 23 Hz, and greater than 98 percent isolation provided between 2.5 and 17 Hz. The transmissibility exceeds unity when the bandwidth of automatic frequency tracking is exceeded, and a hydraulic resonance occurs in the region of 150 Hz. The margin of stability is essentially that of a single-notch isolation system where the notch frequency is at the highest frequency in the automatic frequency tracking band. In this case, the gain margin was 5 db and the phase margin was 59°.

The transmissibility curve shown in Fig. 15 was obtained by using a tachometer feedback signal to adapt the notch frequency to the frequency of vibration excitation. The notch automatically tracked the excitation frequency over the frequency range of approximately 1.0 to 17 Hz, with greater than 90 percent isolation provided between 3 and 14 Hz, and greater than 95 percent isolation provided between approximately 4 and 13 Hz. In the high-frequency region (frequencies greater than the highest frequency in the automatic frequency tracking band), the transmissibility is essentially the same as that shown in Fig. 14. The gain margin for this isolation system was 5 db, and the phase margin was 69°.

CONCLUDING REMARKS

This paper has reported on the results of a theoretical and experimental investigation of electrohydraulic vibration isolation systems. Only single-mass isolation system configurations were considered and, while the theory assumed a rigid isolated body and foundation, consideration of flexibility of the isolated body and foundation were inherent in the experimental studies. In practice, the isolated body and foundation structural resonances must be considered because of their effect on stability.

With acceleration of the isolated mass and relative displacement between the mass and the foundation as the primary feedback signals, it has been demonstrated that isolation of ultra low-frequency vibration is feasible. Resonant frequencies substantially less than 0.1 Hz can be achieved while providing a zero static deflection. Purely active systems can provide limited-band isolation, single-notch isolation, multiple-notch isolation and notch-isolation with automatic frequency tracking. Broad-band isolation and combined broad-band and notch isolation can be provided by inserting a mechanical flexible coupling (passive isolator) between the isolated mass and the actuator rod. The flexible coupling provides mechanical compensation that attenuates the acceleration loop gain and offers passive vibration isolation at high frequencies. For this active-passive isolation system, isolation of vibration is provided by active means in the low-frequency region where the flexible coupling essentially has a unity transfer function, while the flexible coupling provides isolation in the high-frequency region, where the excitation frequency is beyond the frequency band over which the active system is operative.

Because of the acceleration feedback, the electrohydraulic isolator stiffness is unilateral; that is, a very low stiffness is presented to the vibration environment existing at the foundation, but a high stiffness is presented to forces acting on the isolated mass. If force feedback is employed in lieu of acceleration feedback (obtained by use of a load cell in series with the actuator, for example), the isolator stiffness is bilateral; that is, the isolator presents a very low stiffness to both the vibration environment and to forces acting on the isolated mass. Identical vibration isolation characteristics can be achieved with either acceleration or force feedback; however, the system with acceleration feedback will be relatively insensitive to dynamics of the isolated body compared to the system employing force feedback.

Electrohydraulic isolation systems are capable of providing performance characteristics that far surpass those demonstrated for passive or other active isolation systems investigated to date. It is anticipated that this active isolation concept will provide unique solutions to a wide range of vibration isolation problems.

REFERENCES

1. J. E. Ruzicka, "Active Vibration and Shock Isolation." SAE Paper No. 680747, Oct. 1968.

2. H. S. Ripley, "Investigation of a Crew Seating System For Advanced Aerospace Vehicles." Air Force Report AFFDL-TR-66-214 (DDC Report AD 817028), Nov. 1966.

3. P. C. Calcaterra, "Performance Characteristics of Active Systems for Low Frequency Vibration Isolation." SM Thesis, MIT, June 1967.

4. P. C. Calcaterra and D. W. Schubert, "Research on Active Vibration Isolation Techniques for Aircraft Pilot Protection." Air Force Report AMRL-TR-67-138 (DDC Report AD 664090), Oct. 1967.

5. J. S. Pepi, "Vibration Isolation of Optical Reconnaissance Sensors." Air Force Report AFAL-TR-67-277 (DDC Report AD 822872), Oct. 1967.

6. J. A. Joseph, "Active Isolation of Vehicle Equipment From Shock and Vibration." Air Force Report AFFDL-TR-67-168 (DDC Report AD 828043), Dec. 1967.

7. P. C. Calcaterra and D. W. Schubert, "Isolation of Helicopter Rotor-Induced Vibrations Using Active Elements." Shock and Vibration Bulletin 37, Part 6, Jan. 1968, pp. 29-37.

8. J. S. Pepi, "Active Vibration Isolation of Aerial Cameras." IES Proceedings, April 1968, pp. 389-399.

9. J. D. Leatherwood and G. V. Dixon, "Active Vibration Isolation for Flexible Payloads." IES Proceedings, April 1968, pp. 407-413.

10. J. J. D'Azzo and C. H. Houpis, Feedback

Control System Analysis and Synthesis. (Second Edition), McGraw-Hill Book Co., New York, 1966, p. 39.

11. Ref. 10, p. 121.

12. Ref. 10, p. 91.

13. Ref. 10, p. 344.

DISCUSSION

Mr. Mustain (McDonnell-Douglas): We are looking into isolating a rather large vehicle for modal surveys and we are being forced down to the 1/2 cycle or better isolation system. We are looking) air springs which your people have been working on. How well advanced are you on this system to try to isolate such a big structure?

Mr. Ruzicka: At the present time most of our work has been with a single mass unidirectional system. The logical steps would be as follows:- systems requiring three degrees of freedom which would be basically pitch, roll and yaw; then the six degree of freedom problem, on which we are working theoretically. We have got a computer program set up to analyse, for example, cross coupling effects in six degrees of active control.

The second paper this morning will show you a typical application which is a single direction application - the isolation of a pilot seat. To date these have been primarily unidirectional applications.

(The following statement was made by Mr. Ruzicka later in the program to amplify his response to the question. Ed.)

The question had to do with what sort of stiffness characteristics do you get out of electro-hydraulic isolation system. It is interesting that you can have either bi-lateral or unilateral stiffness characteristics. All passive devices are unilateral, that is, you get the same characteristic whether you push them in the plus or in the minus direction. For example if you load a spring in the plus direction and run a load-deflection test, turn the spring over and run that test again you get the same identical characteristics. With acceleration feedback one obtains what we are calling unilateral characteristics.

That is, it has different stiffness characteristics in the plus and minus directions. This is apparent when you think of it because if you put a force on top of this system with acceleration feedback, the force begins to create an acceleration of the mass, the acceleration is sensed and fed back; and in this sense the acceleration feedback acts as a mass multiplier. Therefore the mass will respond very little to forces applied to it. Now an alternative to acceleration feedback would be force feedback, i.e., put a load cell in series with the isolator and feedback force. When you do this you get a bilateral stiffness characteristics; that is, the characteristic is the same whether it is in the plus or the minus direction. There are some cases in which you would like softness in two directions, and in other cases you would like softness in one direction and stiffness in the other. I intended to make this point in the second paper because this is an example of the case in which you would like a unilateral characteristic. In the pilot seat you would like a very soft stiffness pointing at the environment; that is, one wants to isolate the pilot from the vibration coming from the fuselage. But it must not be soft for the pilot looking down. If it were, you could very easily drive the system. If you push a half-cycle on 1/10th cycle system it is going to want to move. This was a half-cycle system. For the pilot pushing pedals and applying control forces - these could very well drive the system which would be undesirable. For this application with the acceleration feedback, the system appeared very stiff to the pilot. To put numbers on this, the stiffness needed to get a half cycle system for a 250 lb payload is about six lbs per inch, and that is the stiffness that this isolator presented to the aircraft. The stiffness presented to the pilot was 50,000 lbs per inch. We are approaching if you like, a mechanical diode that is, it exhibits zero impedance in one direction and infinite impedance in the other direction.

156

ACTIVE ISOLATION OF HUMAN SUBJECTS

FROM SEVERE AIRCRAFT DYNAMIC ENVIRONMENTS *

Peter C. Calcaterra and Dale W. Schubert
Barry Controls
Division of Barry Wright Corporation
Watertown, Massachusetts

An investigation was conducted to evaluate the feasibility of protecting pilots
from the vertical dynamic excitations experienced during low-altitude, high-
speed (LAHS) flight by means of active isolation techniques. Performance
specifications for candidate isolation systems were evolved based on defini-
tion of the expected dynamic environment, human tolerance levels, and cockpit
clearance. Required vibration isolation and maximum relative displacement
values were postulated. Analyses of existing isolation techniques indicated
that, for the selected dynamic environment typically experienced during LAHS
flights in the vertical direction (i.e., combined vibration and sustained accel-
eration excitations), passive systems cannot provide the required degree of
vibration isolation while simultaneously limiting the maximum relative
displacement to the desired values. Various active isolation techniques were
evaluated. An active hydraulic system was selected, employing acceleration
and displacement feedback mechanisms. Analyses were conducted to define
the type of compensation and loop gains required to provide the desired isola-
tion, limit the dynamic deflection, and maintain system stability. A laboratory
model for experimental research was designed and tested. Test results show
that the developed active hydraulic isolation technique provides the vertical
isolation and displacement control postulated to be required for pilot protection
during LAHS flight. In addition, the system exhibits zero static deflection, and
is essentially insensitive to forces applied at the isolated payload, and to
human-body resonance coupling effects. Recommendations are made regarding
human subject performance evaluation tests, consideration of multiaxial
dynamic excitations, and further research efforts required prior to the appli-
cation of similar active isolation techniques in operational systems for a given
aircraft.

INTRODUCTION

Advances in military aircraft performance
have given rise to dynamic environments which
can cause decrements in human sensorimotor
and cognitive functions. Occurrence of pain,
discomfort, fatigue and other subjective
responses to the environment together with the
task difficulty have a bearing on human perform-
ance. The tactical necessity for low-altitude
high-speed (LAHS) flight requires that pilots
perform precise terrain-following, navigation,
target identification and aircraft control tasks
during exposure to levels of dynamic excitation
considered to be in excess of tolerable limits.
Successful generation of design criteria to
provide the necessary protection must then be
based on the results of research in three major

areas: (1) development of techniques for
protecting the pilot against the complex accel-
erations encountered during LAHS flight; (2)
evaluation of the ability of the pilot so protected
to perform the various tasks required by the
mission; and (3) consideration of operational
requirements, such as weight, applicable mili-
tary aircraft standards and compatibility with
cockpit space, and pilot-control interface. The
investigation reported herein deals with the
first area of research.

A laboratory research model utilizing an
active hydraulic isolation system was developed,
built and tested. System selection and design
were based on: (a) dynamic environment

157

characteristics typical of those encountered during LAHS flight; (b) analysis and evaluation of various shock and vibration isolation techniques; (c) limits of tolerable acceleration levels for seated human subjects; and (d) maximum allowable dynamic deflections of the isolated mass. The feasibility of utilizing active hydraulic isolation techniques is demonstrated on the basis of the response of a rigid-mass payload, so isolated, to combined sinusoidal vibration and ramp-sustained acceleration excitations in the vertical direction.

Further uses of the model in the laboratory will allow evaluation of the pilot's ability to perform the tasks required by the LAHS flight mission while being afforded the degree of vertical acceleration protection dictated by human tolerance limits. Evaluation can also be made of the effect of additional protective devices such as seat cushions and body and head restraints. Results of such human subject evaluation tests and consideration of specific environmental and operational requirements will determine the direction to be followed in adapting the active hydraulic isolation system approach to a particular aircraft.

DYNAMIC EXCITATION AND DESIGN CRITERIA

The dynamic environment associated with low-altitude high-speed flight is a complex one [1-13]**. It can be characterized in terms of periodic and random vibrations and transient and sustained accelerations occurring separately or simultaneously in the vertical, horizontal and angular directions. Although newer aircraft have wing loadings such that the flight is smoothed out during gust encounters, accelerations perpendicular to the flight path of the aircraft excite the normal bending modes of the structure. Low frequency harmonic vibrations are generated due to flexibility of the structure and distribution of aerodynamic pressures over large portions of the aircraft. Random vibration excitations are experienced due to atmospheric turbulence and buffeting. Terrain following maneuvers result in relatively fast rates of change of acceleration, followed by sustained accelerations during climb (or descent) occurring over a period of several seconds. In order to evaluate the feasibility of applying active isolation techniques for protecting pilots during LAHS flights, the dynamic environment was defined by the Vibrations and Impact Branch, Biodynamics Division of the Aerospace Medical Research Laboratories, WPAFB, in terms of vertical sinusoidal vibration and ramp-sustained acceleration, occurring both separately and simultaneously. Application of the techniques in the more realistic complex environment would follow the successful solution to the simplified problem.

Fig. 1 shows the levels of vertical sinusoidal vibration selected for the feasibility

study. In the region from 3.5 to 33 Hz, two levels were chosen. The lower level (0.3 g vector) is indicative of the acceleration experienced at the cockpit of existing aircraft. It is anticipated that future generation aircraft will exhibit the high levels of excitation (2 g vector). Fig. 2 shows the character and level of the ramp-sustained accelerations selected for the investigation. These accelerations were chosen based on typical aircraft loadings experienced during terrain following maneuvers [1, 5, 11].
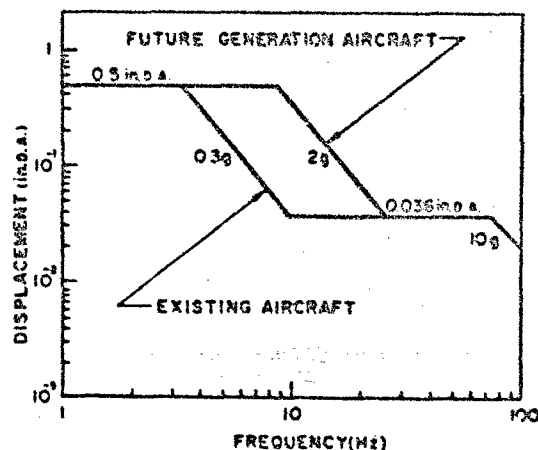
Fig. 1. Vertical sinusoidal vibration excitation levels selected for low-altitude high-speed flight
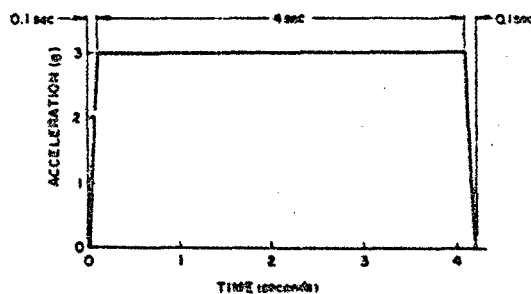
Fig. 2. Level of ramp-sustained acceleration excitation selected for low-altitude high-speed flight

** Numbers in brackets designate references at end of paper.

158

The ability of man to tolerate a given environment must be based not only on physical injury criteria, but also on pain, discomfort, and performance requirements associated with specific tasks which he is to carry out while being subjected to that environment. For the case of LAHS flight, limited subjective and performance data is available for actual [4-7], and simulated [8-12] flights. More extensive data is available on the levels of acceleration which can be tolerated by human subjects in the laboratory under sinusoidal vibration [13-21], sustained accelerations [13, 22-25], shock and impact [26-28], and combined rectilinear and oscillatory accelerations [29]. The tolerance level data, as reported by various experimenters, show considerable variability. The type and duration of excitation, frequency at which excitation occurs, restraint conditions, physical condition of the individual, antici-pation of the excitation, and the relative degree of control of the test environment by the subject, influence the individual's ability to sustain a given level of excitation without pain or discomfort and/or be able to perform given tasks. The data show, however, that the response of the human body to unidirectional sinusoidal vibration can be defined in terms of the frequency of the excitation.

Mechanical representation of the human body by means of lumped parameter systems composed of mass, spring and damping elements helps in understanding and describing the response of the human body to dynamic exci-tations [30-36]. Below approximately 2 Hz, the body acts as a rigid mass. In the regions from 4 to 15 Hz, resonances occur. During human subject testing, pain and discomfort in the back, abdomen and chest occur in the frequency range from 4 to 10 Hz; and degra-dation of visual acuity and tracking capabilities occur in the frequency range from 6 to 15 Hz due to head motions. Taking into consideration (a) the frequency ranges where body resonances occur, (b) the subjective response tolerance levels; (c) levels above which performance deteriorates; and (d) existing specifications (WADD "Vibration Tolerance Curve for Military Aircraft, ")[13], the maximum acceleration levels shown in Figure 3 were selected for the investigation to correspond to approximately one hour tolerance for a seated subject in the vertical direction (z-axis).

The maximum allowable relative deflection between the isolated mass and the source of the excitation was selected to be ± 2.5 inches under either vibratory, transient or combined dynamic excitation conditions, based on evaluation of expected clearances between a seated pilot and cockpit envelope.

Fig. 4   shows the allowable isolation system transmissibility based on the selected sinusoidal vibration excitations and human tolerance limits. In the region from 3.5 to 33 Hz, two levels of allowable transmissibility
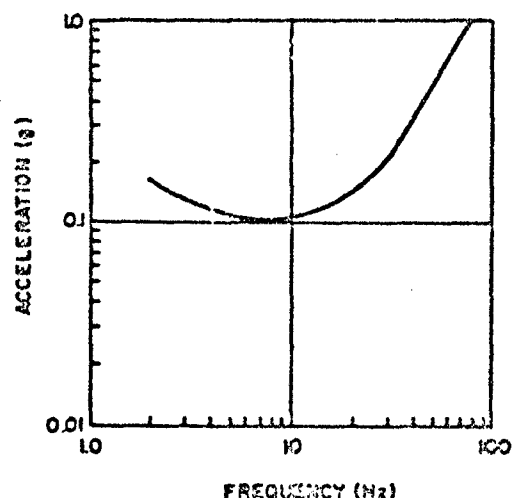
Fig. 3. Selected values of tolerable accel-eration for seated human subject under vertical sinusoidal vibration
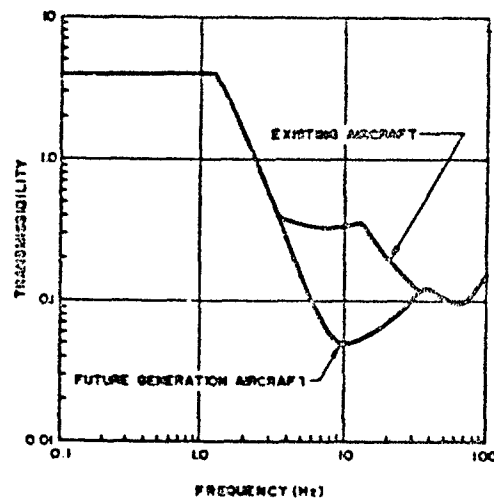
Fig. 4. Required values of transmissibility based on selected vertical sinusoidal vibra-tion excitation and human subject tolerance levels

are shown, for existing and future aircraft, respectively, which correspond to the two levels of excitation selected for the investi-gation. For frequencies below 1 Hz, a maxi-mum transmissibility of 4 was selected based on the maximum input level 0.25 inches single amplitude, and the portion of allowable deflection over which the system is linear; namely; 1 inch either side of the null position.

159

Critical dynamic environment during LAHS flight occurs for conditions of combined vibration and sustained accelerations. The values of transmissibility shown in Fig. 4 and the maximum relative deflection of ± 2.5 inches serve to define the required isolation system characteristics under separate sinusoidal vibrations and ramp-sustained accelerations, respectively. However, the essential requirement of the approach to be selected is the ability to provide vibration isolation while simultaneously limiting the relative deflection under the combined excitation conditions.

Feasibility evaluation of the approach was based on analysis and performance of the system with a rigid mass payload. A range from 210 to 270 lb was chosen to be representative of the total expected pilot, personal equipment, seat structure, and restraint mechanism weights. A nominal rigid load of 245 lbs was selected for the active system design and test. Selection of system design, though based on a rigid mass payload, included consideration and evaluation of the effect of human body mechanical characteristics on the system performance.

SYSTEM ANALYSIS AND DEVELOPMENT

A variety of isolation system techniques were evaluated during the investigation in light of the postulated design and performance requirements. Linear and nonlinear standard passive elements [37-39], and a variety of active isolation mechanisms (i.e., electrically activated fluids, pneumatic and hydraulic) [40-47] were considered.

Passive systems both linear and nonlinear, employing either conventional or relaxation damping mechanisms, cannot be designed to satisfy the requirements of ± 2.5 inches maximum deflection under the combined levels of sinusoidal vibration and sustained acceleration, while simultaneously providing, on the average, 80 percent isolation from 5 to 20 Hz for the duration of the combined excitation conditions. The degree of vibration isolation shown in Fig. 4 can be attained by a passive system having a resonant frequency of 1 Hz. The static deflection of such a system is approximately 10 inches. Even if the static deflection were eliminated by use of an auxiliary spring, a linear passive 1 Hz resonant frequency system will deflect 30 inches when subjected to a 3 g sustained acceleration. Nonlinearities in the spring element can be introduced to limit the deflections under sustained accelerations, and the dynamic deflections would thus be limited to the desired values. However, the vibration isolation requirements would not be met, since during conditions of sustained acceleration, the system would exhibit the isolation characteristic associated with a resonant frequency much greater than 1 Hz.

Active elements can be introduced to generate a force proportional to the integral of the relative displacement, such that the static deflection is eliminated and the mass is returned to its neutral position during sustained acceleration excitations. Therefore, the vibration isolation characteristics of the system will be those of a 1 Hz resonant frequency system during the greater portion of the duration of sustained accelerations. However, the performance of such a system with integral displacement feedback is affected by changes in supported weight. In addition, for a non-rigid payload such as a human subject, coupling effects between the human body and the seat will affect the performance of the system.

The required protection and motion limitation can be attained independent of the dynamics of the isolated mass by means of an active system which generates forces to control the motions of an actuator as a function of both the relative displacement between the mass and the source of excitation and the acceleration of the mass. Of the active isolation mechanisms considered, only those employing hydraulic elements exhibit capabilities for fast speed of response, are linear and relatively incompressible, and can be designed to respond over the frequency range of interest. Although hydraulic components are commonly used in control systems, such systems provide primarily accurate position and force-displacement control [44-47]. What is required is position control and simultaneous isolation of vibration excitations. An active hydraulic system, incorporating acceleration and relative displacement feedback, was selected to provide the specified vibration isolation and displacement control under the combined excitation conditions.

Analyses were performed, using analog and digital computers, to define the required type of feedback and compensation mechanisms, and the associated gains to achieve the desired performance while maintaining system stability. Development of the system block diagram and associated open and closed loop system transfer functions is discussed in Appendix I. Transfer functions were defined for the accelerometer, servovalve, actuator, and flexible coupling, based on the expected and/or known characteristics of each component. The predicted vibration transmissibility was calculated from the absolute value of the system closed loop transfer function $|x(j\omega)/a(j\omega)|$. The predicted system stability was defined in terms of the open loop transfer function $B(j\omega)/E(j\omega)$.

A series of development tests were conducted to define actual system stability margins, develop feedback mechanisms, and evaluate the final system design. These tests included low and high frequency sinusoidal vibration using mechanical and electrodynamic shakers, and

160

ramp-sustained acceleration testing by means
of a synthesized excitation technique developed
to measure the response of the system to tran-
sient excitations.

Final system testing was conducted with
a 245-lb rigid mass payload shown in Fig. 5.
The performance of the system with the rigid
mass served to verify the feasibility of employ-
ing active isolation techniques to provide the
postulated degree of protection during LAHS
flight. Test results were obtained for various
levels of vibratic input, variation in payload
weight, and for conditions of combined vibra-
tory and sustained accelerations.
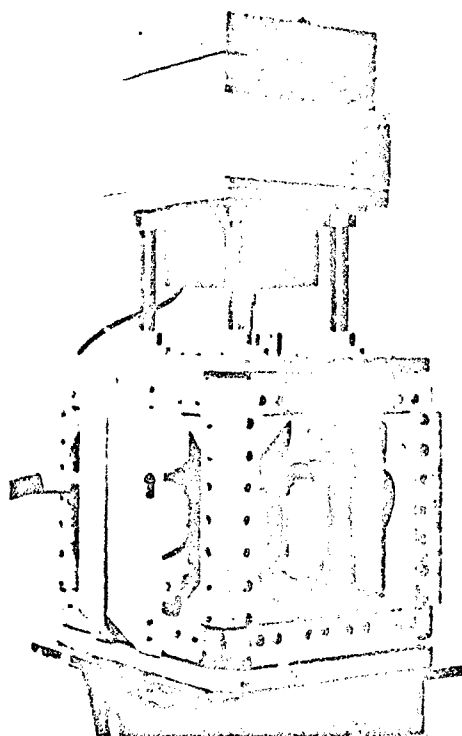
Fig. 5. Active hydraulic isolation
system with rigid payload

In order to arrive at successful genera-
tion of protective design criteria for LAHS flight
missions, the ability of the pilot to perform the
required tasks while being afforded the degree
of isolation provided by the active hydraulic
isolation system must be evaluated. To allow
use of the active isolation system approach
with a human subject, a laboratory test model
was developed by replacing the rigid mass with
a seat structure. The model, shown in Fig. 6,
consisted of a 33.5-lb metal seat plus a 145-lb
rigid weight. Modifications were made on the
rigid mass system gains and feedback compen-
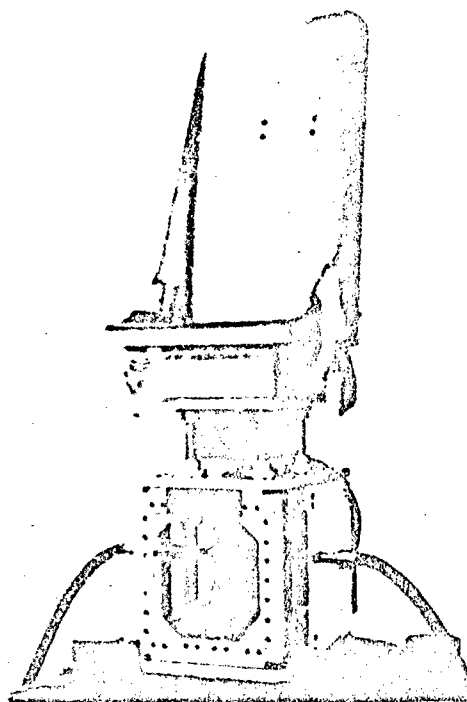
Fig. 6. Laboratory test model; active
hydraulic isolation system with metal seat

sations to provide dynamic performance and
stability margins for the laboratory model equiv-
alent to those attained with the rigid mass. It
is anticipated that the laboratory test model
with the seat structure will be used by the
Aerospace Medical Research Laboratory to con-
duct studies on human subject response and
performance, and evaluate seat and body
restraint systems.

SYSTEM DESCRIPTION AND OPERATION

The active hydraulic isolation system is
a multiple loop feedback control system designed
to act as a very low frequency vibration isolator
and position controller. Figs. 7, 8, and 9 show
the system with rigid payload in pictorial,
schematic, signal flow and block diagram form,
respectively. It consists of feeback trans-
ducers, a servoamplifier, a servovalve, and a
hydraulic actuator with flexible coupling.
Signals from the transducers proportional to the
acceleration of the mass and the relative
displacement between the mass and the exci-
tation are modified, summed, and compensated
in the servoamplifier to deliver a signal to the
servovalve. Flow from a hydraulic power source
is supplied to the hydraulic actuator as a
function of the signal delivered to the servovalve.
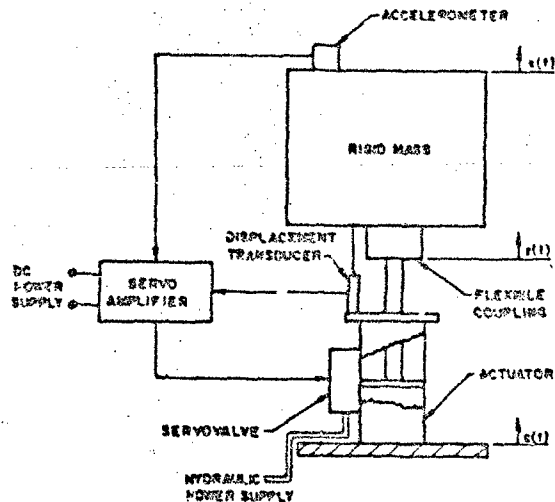
Fig. 7. Schematic representation of the active
hydraulic isolation system with rigid payload

Actuator forces are thus generated to:
(a) limit the acceleration experienced by the
mass; (b) limit the relative displacement
between the mass and the excitation source;
and (c) return the mass to its neutral
position after the onset of a sustained
acceleration.

Two feedback transducers are used. A
servoaccelerometer capable of responding from
DC to frequencies above those of interest,
generates the acceleration feedback signal. The
transfer function of the accelerometer is repre-
sented by $\Box_a$. A differential transformer gene-
rates the relative displacement signal. Over
the frequency range of interest, the transfer
function of the displacement transducer is unity.

The acceleration and displacement
signals are fed into a servoamplifier wherein
they are transformed and summed to generate
the flow command signal supplied to the servo-
valve. The servoamplifier consists of five
sections. The first section consists of two
solid state operational amplifiers and circuitry
to convert the current signal from the
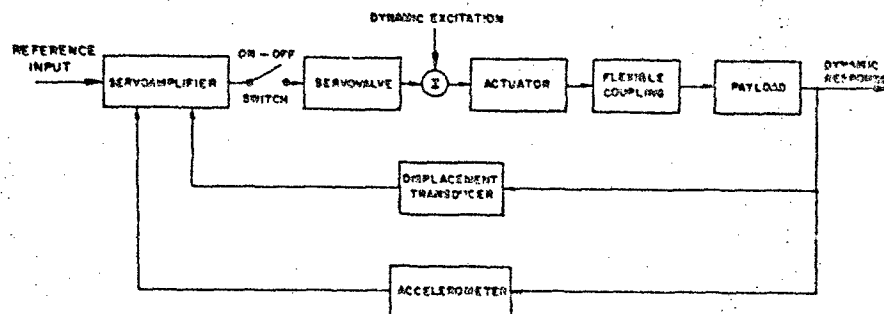
Fig. 8. Signal flow diagram of the active hydraulic isolation system
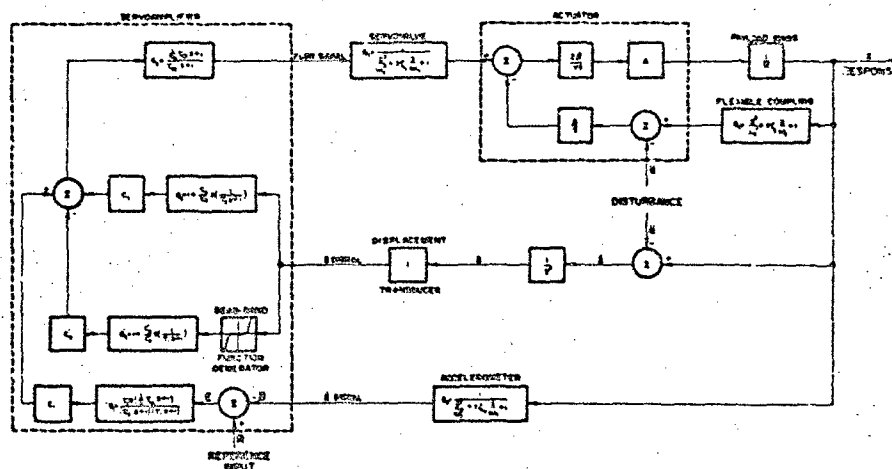
Fig. 9. Block diagram of the active hydraulic isolation system

162

accelerometer to a voltage signal of the proper scale factor. A compensator of transfer function G_1 was designed to operate on the acceleration signal to insure the required displacement control at low frequencies. The second section consists of one solid state operational amplifier and circuitry designed to attenuate the relative displacement signal at high frequencies. A compensator of transfer function G_2 was designed to operate on the relative displacement signal and provide the proportional and differential displacement control required to return the payload to its neutral position during conditions of sustained acceleration. The third section consists of three operational amplifiers and circuitry designed to form a deadband function generator to change the gain in the displacement loop as a function of displacement. A compensator of transfer function G_3' was designed to operate on the relative displacement signal and provide proportional and differential displacement control for relative displacements in excess of ± 1 inch. The fourth section consists of one operational amplifier and circuitry designed to sum the compensated acceleration and relative displacement signals. A compensator of transfer function G_7 was designed to operate on the summation to attenuate the combined signal at high frequencies. The fifth and final section is a constant current differential amplifier used to drive the servovalve. This amplifier provides a current signal proportional to the voltage output of the fourth section described above. The amplifier acts as a current source and thus compensates for the inductance of the torque motor in the servovalve.

The servovalve is a two-stage flow control valve which can deliver a maximum flow of 30 in.^{3}/sec at a valve pressure drop of 1,000 psid. The transfer function of the servovalve is represented by G_v. The actuator is a 3,000 psi working pressure, 2.5 in. bore, 5 in. stroke, double acting, single rod hydraulic cylinder with adjustable needle valve cushions. The actuator uses special seals and packings for minimum friction under working pressure. The flexible coupling is an elastomeric element of dynamic stiffness selected to yield a resonant frequency of 16 Hz for a system payload of 245 lb. The dynamic characteristics for the actuator and coupling are shown in Appendix I.

The system hydraulic and electrical power requirements are: (a) 30 in.^{3}/sec at 3,000 psi maximum; and (b) 115 volts AC, 250 ma, 50-400 Hz.

TEST PROCEDURES

During the investigation, individual component and system development tests served to define the required loop gains and compensator characteristics. Final system performance and stability characteristics for a rigid payload were determined in terms of measured open loop transfer function, transmissibility values for sinusoidal vibration, variation of system

resonant frequency with load, and system response to sustained acceleration and combined excitations. The performance of the laboratory test model with a metal seat was defined in terms of measured open loop transfer function and transmissibility values for sinusoidal vibrations.

System Open Loop Transfer Function

An approximation of the expected margin of stability for the active isolation system was determined by measuring the magnitude and phase of the open loop transfer function $B(j\omega)/E(j\omega)$. This measurement was performed by disconnecting the accelerometer from the servoamplifier (see Fig. 3), injecting a command signal equivalent to E from an oscillator, and observing the phase and magnitude relationships between the returned acceleration signal B, and the command signal E. The magnitude of the signal levels used for the command signal was maintained as near as possible to the voltage levels observed during normal closed loop operation to ensure that any system nonlinearity with actuating signal level would be properly incorporated in the measured open loop transfer function. Polar plots were made from the measured values of the system open loop transfer functions.

Vibration

Two vibration testing machines were used during development testing of the isolation system. A low frequency mechanical testing machine capable of generating a maximum double amplitude excitation level of 0.125 in. was used over the frequency range of from 0.1 to 15 Hz. An electrodynamic vibration machine, capable of generating the input levels shown in Fig. 1 for frequencies above 10 Hz, and limited to a maximum double amplitude displacement level of 0.4 in. from 5 to 10 Hz, was used for high frequency development testing. Final system testing was performed on an electrohydraulic vibration machine, capable of generating the vibration levels of Fig. 1 over the entire frequency range (0.1 to 100 Hz).

The excitation and system response vibration levels at low frequencies (below 5 Hz) were measured by utilizing a rectilinear potentiometer which yielded an output voltage proportional to the relative displacement between its attachment points. Piezoelectric accelerometers were used for the measurement of the input and response vibration levels at frequencies above 5 Hz. Vibration signals obtained from the piezoelectric accelerometers were passed through a sharp cutoff low-pass filter set to a cutoff frequency four times the vibratory excitation frequency. Transmissibility values were calculated as the ratio of response to input vibration level at each frequency.

Sustained Acceleration

To generate the ramp-sustained accelerations shown in Figure 2 would require use of a centrifuge. Since no such test facilities were

available at Barry Controls, an excitation
synthesis approach was developed to define the
response of the system to the required transient
excitations. The method, described in
Appendix II, is based on introducing an elec-
trical acceleration command signal into the
servoamplifier proportional to the magnitude of
the specified acceleration level. If the frequency
of the command signal and/or system response
is lower than approximately 5 Hz, the response
acceleration $\ddot{X}(t)$ is equivalent to the error
signal $E(t)$. The synthesized excitation tech-
nique was used to record the input acceleration
$\ddot{a}(t)$, the equivalent acceleration response
function $\ddot{X}(t)$, and the system relative deflection
$\delta(t)$, on an X-Y plotter as a function of time.

Combined Vibration and Sustained Acceleration

        The method described for sythesizing the
ramp-sustained acceleration excitation was used
in conjunction with the mechanical vibration
machine to determine the equivalent system
response to combined excitations.

DISCUSSION

        It is shown that, on the basis of the
simplified, unidirectional definition of the
dynamic environment, the performance require-
ments associated with the protection of pilots
from the accelerations experienced during LAHS
flight conditions cannot be met with a passive
isolator. Having established the need for
active isolation techniques, the procedure used
to develop a feasible approach followed the
various typical steps required to design active
control systems to a set of specifications.

        Analysis were initially performed using
a simplified representation of an active system.
In order to achieve the degree of required iso-
lation at low frequencies and not exceed the
maximum allowable dynamic deflections under
sustained acceleration, both acceleration and
relative displacement feedback were required.
The characteristics of basic components such
as accelerometer, displacement transducer,
hydraulic actuator, flexible coupling, and servo-
valve were selected. Selection was based on
one or more of several criteria, among them
linearity over the frequency and dynamic exci-
tation ranges under consideration, speed of
response, friction, and reliability. The charac-
teristics of the various basic elements were
expressed in terms of transfer functions which
did not consider any of the nonlinearities
exhibited by real components. Analyses were
then performed based on the selected transfer
functions to determine the type of compensation
and gains required in the servoamplifier, which
would result in a stable system and meet the
specified performance requirements. Having
analytically defined the required compensation
networks, the basic components were designed
and constructed, and the overall system tested.
Final adjustments in the compensation networks
and gains were based on actual test results.
Adjustment from the calculated values were

necessary due to the differences between the
analytical component transfer functions used in
the calculations, and the transfer functions of
actual hardware.

Fig. 10. Polar plot of predicted system open
loop transfer function $B(j\omega)/E(j\omega)$ with rigid
payload
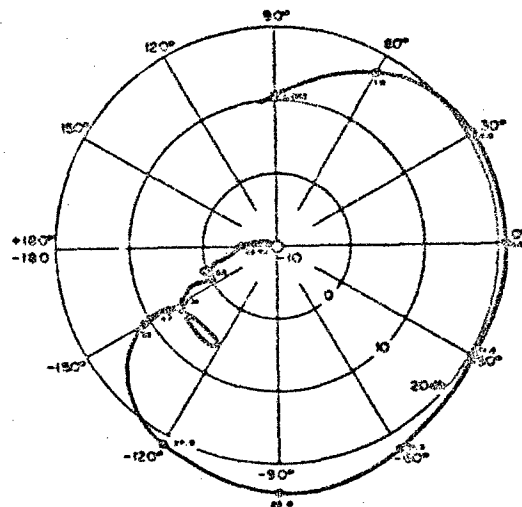
Fig. 11. Polar plot of measured system open
loop transfer function $B(j\omega)/E(j\omega)$ with rigid
payload

164

System Stability

For the case of the rigid payload, the calculated open-loop transfer function shown in Fig. 10 indicates a phase margin of approximately 25° and a gain margin in excess of 11 db. The measured open-loop transfer function shown in Fig. 11, indicates a slightly lower value of phase margin and a gain margin of about 9 db. Differences between the calculated and measured open-loop transfer functions were also found for the system with a metal seat as indicated by Figs. 18 and 19. The differences are more pronounced at higher frequencies. These differences are due either to (a) nonlinearities in the system components and/or (b) error in the measurement of system open-loop response.

At higher frequencies the performance of the system is dominated by the dynamics of the servovalve and the flexible coupling. Both elements are nonlinear. The resonant frequency of the servovalve varies inversely with the flow output of the valve. The value of the valve resonant frequency used in the calculation of the open-loop response was that recommended by the manufacturer at a flow output of 25 percent capacity. However, in the frequency region of expected valve resonance, the servovalve operates at approximately 0.1 percent capacity. At this lower flow the servovalve resonant frequency is higher than the value used in the analysis. Moreover, since the excitation and isolation requirements are a function of frequency, the flow requirements, and, therefore, the servovalve response, would vary both with excitation vibration level and frequency. The resonant frequency of the flexible coupling is a function of the amplitude of the dynamic excitations imposed on it. The values used in the

analysis apply for low amplitude excitations. However, as the excitation amplitude increases, the resonant frequency of the flexible coupling decreases, which tends to improve the margin of stability of the system as a whole. In addition, errors can be introduced in the measurement of the open loop transfer function particularly at higher frequencies, where low values of and distortion in the signals make the measurement difficult.

It must be recognized that for systems employing other than unity feedback (such as the active hydraulic isolation system), the technique of evaluating the system margin of stability on the basis of open loop response gives only an indication of the expected gain and phase margins. To verify the margins of system stability, the closed loop response of the system was checked with dynamic inputs and payloads which exceeded the design values. Also, the closed loop system response with gains higher than those required to obtain the desired performance was checked with both the rigid payload and the metal seat. Results of these tests indicate that the system margins of stability are at least those shown by the measured and calculated open loop responses.

Fig. 12. Predicted system transmissibility
$|\ddot{X}(j\omega)/\ddot{a}(j\omega)|$ with rigid payload
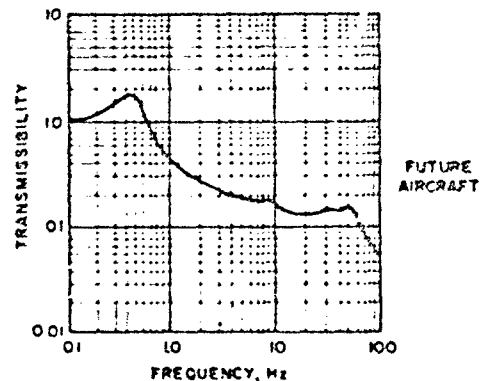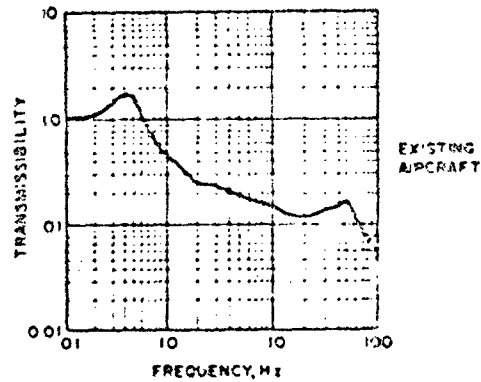
Fig. 13. Measured system transmissibility
$|\ddot{X}(j\omega)/\ddot{a}(j\omega)|$ with rigid payload

165

System Dynamic Response

Values of the analytically predicted transmissibility for the system with the rigid payload shown in Fig. 12 differ from the values based on results of vibration tests, shown in Figs. 13 and 14. In the region from 2 to 10 Hz the measured transmissibility is higher than the predicted one, whereas from 10 to 100 Hz the opposite is true. Differences can be attributed to previously discussed nonlinearities in the various components, primarily those exhibited by the servovalve. The predicted values are based on approximate linear representation of the dynamic characteristics of the various components. The dynamic response of the servovalve varies in proportion to the valve flow. In the region from 5 to 10 Hz the flow requirements are a maximum and the predicted system performance in this region is better than the measured performance. In the region above 20 Hz the flow requirements are minimized and the servovalve performance is better than predicted. Other component nonlinearities not accounted for by the transfer functions used in the analysis, such as those exhibited by the flexible coupling and actuator, also contribute to the differences between predicted and measured values of transmissibility.

Results of vibration excitation tests with a rigid payload indicate that the vibration isolation characteristics of the system are independent of the level of vibration excitation. System performance with different vibration levels is demonstrated by the transmissibility curves shown in Figs. 13 (a) and (b). Fig. 14 shows the average transmissibility based on the values shown in Figs. 13 (a) and (b). Evaluating the system vibration performance in terms of this averaged transmissibility is justifiable since the minor differences which exist between the curves shown in Fig. 13 can be accounted for, almost on the basis of experimental error alone.

The system average transmissibility shown in Fig. 14 is well within the required values for existing aircraft vibration excitation levels, in the region below 30 Hz. For vibration inputs corresponding to future generation aircraft, the required transmissibility in the region from 5 to 50 Hz is lower than the attained transmissibility. Compensation networks in the servoamplifier can be designed to result in values which meet the levels required based on the excitation corresponding to future generation aircraft. However, the needed loop gains would result in an unstable system at frequencies higher than 20 Hz. The final selection of system parameters was based on attaining the required performance for existing aircraft vibration inputs. At the same time, the system was designed to provide the best possible isolation for the higher inputs. The feasibility of the approach suggests that with further research and development efforts, the transmissibility requirements for future generation aircraft can be attained, while maintaining safe margins of stability.

The system linearity was demonstrated in terms of a payload variation. Fig. 15 shows values of transmissibility for frequencies in the region of system resonance, measured with rigid payloads ranging in weight from 145 to 350 lb. Results indicate that the system resonant frequency and maximum transmissibility at resonance are independent of payload weight, for the range of payloads considered.
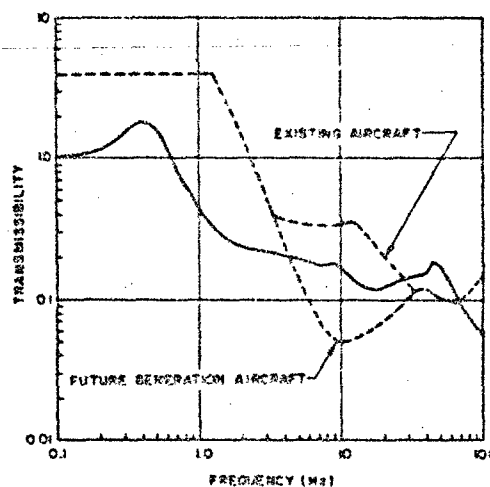
Fig. 14. Comparison of required transmissibility for LAHS flight to measured transmissibility with rigid payload
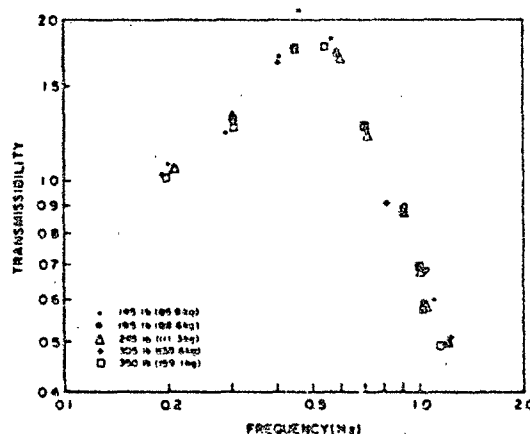
Fig. 15. Effect of rigid payload weight transmissibility in the neighborhood of system resonance
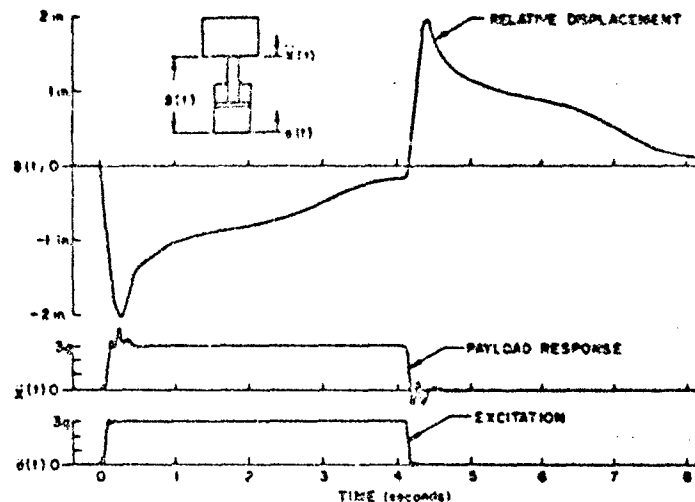
Fig. 16. Experimental response of system with rigid payload to ramp-sustained acceleration excitation
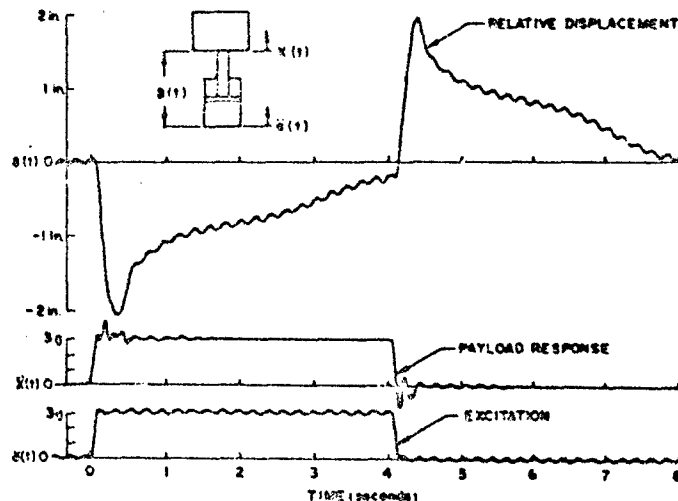
Fig. 17. Experimental response of system with rigid payload to combined sinusoidal vibration and ramp-sustained acceleration excitation

The response of the active hydraulic isolation system with a 245-lb rigid payload to ramp-sustained acceleration and combined excitations is shown in Figs. 16 and 17, respectively. The top trace in each figure shows the relative displacement between the payload and the system attachment point. The middle and lower traces show the payload acceleration response and the acceleration excitation, respectively. Fig. 16 indicates that the maximum deflection under a 3g peak, 4-second duration sustained acceleration excitation with a rise time of 0.1 seconds does not exceed the maximum required value of 2.5 inches. In addition, the payload is automatically returned towards the neutral position after onset of the sustained acceleration excitation.

Under combined excitation conditions, the maximum relative deflection is less than the required 2.5 inches. The ability of the active isolation system to provide vibration isolation during conditions of combined excitation is clearly shown in Fig. 17. The combined acceleration excitation shown in the bottom trace of Fig. 17 consists of the 3g, 4-second duration ramp-sustained acceleration generated by the synthesis technique, and a 0.125-inch double amplitude vibration at 5 Hz, generated by a mechanical vibration machine. The maximum deflection is ± 2.1 inches and the maximum payload response acceleration is approximately 5g. However, as the 3g level of acceleration is maintained for 4 seconds, the active isolation system returns the payload to the null

167

position and provides isolation from the simultaneously experienced vibration. The servo-amplifier circuitry was designed so that when the payload, after the onset of sustained acceleration, is returned to within ± 1 inch of the null position, vibration isolation is provided to the payload equal to that shown in Figs. 13 and 14. As indicated in the top trace of Fig. 17, within approximately one second after onset of the ramp-sustained acceleration excitation, the relative deflection δ, is within ± 1 inch of null. From this time on , and for the duration of the combined excitation condition, the payload is isolated from the vibration excitation. The degree of isolation is indicated in the middle trace of Fig. 17.

To allow evaluation of the active isolation techniques developed for a rigid mass with a human subject, a laboratory test model as constructed as shown in Fig. 6, by replacing the rigid payload with a metal seat structure. Several changes were introduced in the design of the system to insure that the same approximate degree of isolation would be provided as for the system with rigid payloads, while maintaining equivalent stability margins. The seat exhibits structural resonances not present in the rigid mass for which the system was developed. To avoid instabilities lower values of loop gain had to be used to compensate for the seat resonances at high frequencies. A rigid weight of 145 lb was added and changes were made in the servoamplifier circuitry, to achieve equivalent stability margins. The calculated and measured open loop transfer functions for the metal seat plus rigid weight, shown in Figs. 18 and 19, respectively, indicate the approximate phase and gain margins of

stability. Fig. 20 shows a comparison between the measured transmissibility for the system with a rigid payload and with the seat. At frequencies lower than 10 Hz, the degree of isolation attained with either system is approximately the same. The higher values of transmissibility measured with the seat for frequencies above 10 Hz are due to the lower values of loop gain which had to be used in order to insure the same stability margins.
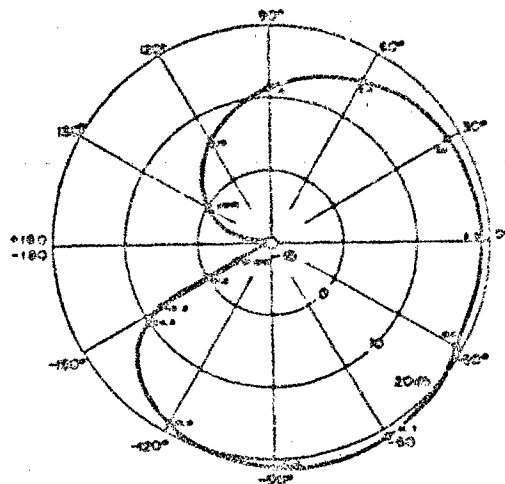

Fig. 19. Polar plot of measured system open loop transfer function $B(j\omega)/E(j\omega)$ with metal seat
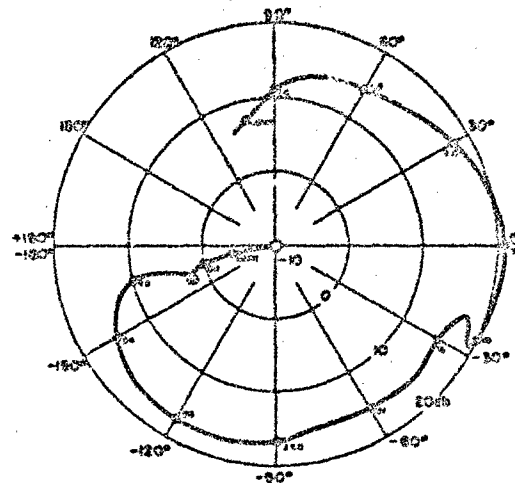
Fig. 18. Polar plot of predicted system loop transfer function $B(j\omega)/E(j\omega)$ with metal seat
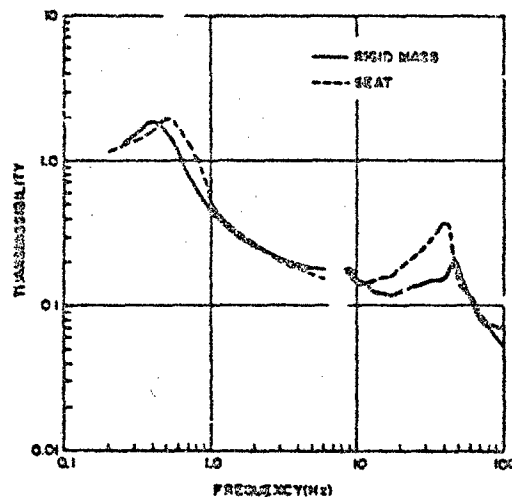
Fig. 20. Comparison of measured transmissibility with rigid payload to measured transmissibility with metal seat

168
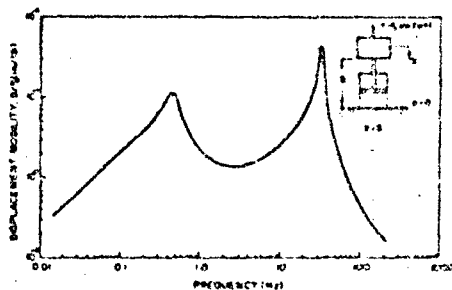
Fig. 21. Values of point displacement mobility for forces applied at the payload

Finally, the most significant characteristic of the active hydraulic isolation system developed during the investigation can be described in terms of the displacement mobility, δ/F_0, versus frequency curve shown in Fig. 21 for the system with the rigid payload. The ratio δ/F_0, calculated as shown in Appendix III, defines the point displacement mobility at the payload, where F_0 is the amplitude of a sinusoidal force $F = F_0 \sin 2\pi f t$, applied at the rigid payload, and δ is the relative displacement between the payload and the isolation system attachment point due to application of the force F.

For the pilot seat application the results shown in Fig. 21 imply that the system performance is unaffected by slowly applied reaction forces resulting from application of foot pressure on pedals or other control members. For forces which are applied to the payload at frequencies other than approximately zero, the effect on the system performance is negligible. Consider, for example, the human-body coupling effects. The dynamics of the human body can be represented by a model having a 5 Hz resonant frequency. Let the magnitude of force acting on the system at the payload attachment point due to human-body coupling effects F_0, be 100 lb. The deflection of the system δ, due to such a force applied at a frequency of 5 Hz would be less than 0.002 inches. Therefore, it can be stated that the dynamic performance of the active hydraulic isolation system is essentially unaffected by human-body resonance coupling effects and/or external forces applied to the isolated mass.

CONCLUSIONS

Based on the analyses and results of the investigation, the following conclusions are made:

1. The active hydraulic isolation system represents a feasible approach to provide the acceleration reduction and displacement control required to protect pilots from the vertical dynamic environment encountered during low-altitude high-speed flight.

2. Tests on a laboratory model developed for experimental research, show that the active hydraulic isolation technique can be used to provide at least 80 percent vertical vibration isolation to a 245-lb rigid mass at frequencies above 5 Hz under combined vibratory and sustained (3 g) accelerations and for the duration of the sustained acceleration (4 sec), while limiting the maximum dynamic deflections to ± 2.1 inches and automatically initiating return of the mass to its neutral position after onset of sustained acceleration. The model resonant frequency is 0.5 Hz, with maximum transmissibility at resonance less than 2.

3. Static deflection of the model is zero.

4. Dynamic performance of the model is essentially independent of load, for the range of rigid payloads associated with human subject weights.

5. Dynamic performance of the model is essentially unaffected by human body resonance coupling effects, and/or external forces applied to the isolated mass.

6. Dynamic performance of the model is independent of vibratory excitation level, for the range of vertical vibration levels expected during low-altitude high-speed flights.

7. Research efforts should be directed to several areas of investigation prior to final definition of design criteria for pilot protective systems employing active isolation techniques. These include: (a) human subject performance evaluation tests with the laboratory model; (b) evaluation of system response to multiaxial and random excitations; (c) effect of additional protective devices such as seat cushions and body and head restraints; (d) effects of load and input impedance on the dynamic performance of the system; (e) techniques for varying system performance by means of different feedback and compensation mechanisms; (f) cockpit structural interface considerations; and (g) weight, space and other operational system requirements for given aircrafts.

NOMENCLATURE

a   displacement excitation, in.

A   average actuator cross sectional area, $in.^2$

B   feedback signal from accelerometer, $\dfrac{volts}{in./sec^2}$

C_1 acceleration loop gain, $\dfrac{in.^3/sec}{in./sec^2}$

C_s relative displacement loop gain, $\dfrac{in.^3/sec}{in.}$

C_s relative displacement loop gain for $|\delta| > 1$ in., $\dfrac{in.^3/sec}{in.}$

C_3 relative velocity loop gain, $\frac{\text{in.}^3/\text{sec}}{\text{in.}/\text{sec}}$

C_3' relative velocity loop gain for $|\delta| > 1$ in., $\frac{\text{in.}^3/\text{sec}}{\text{in.}/\text{sec}}$

E actuating error signal, $\frac{\text{volts}}{\text{in.}/\text{sec}^2}$

f frequency, Hz

F force excitation, lb

G_1 compensator transfer function, dimensionless

G_2 compensator transfer function, dimensionless

G_3 compensator transfer function, dimensionless

G_3' compensator transfer function, dimensionless

G_a accelerometer transfer function, dimensionless

G_c flexible coupling transfer function, dimensionless

G_v servovalve transfer function, dimensionless

j represents $\sqrt{-1}$

M supported mass, lb sec^2/in.

Q_v flow from servovalve, $\frac{\text{in.}^3/\text{sec}}{\text{ma}}$

R reference input, $\frac{\text{volts}}{\text{in.}/\text{sec}^2}$

s Laplace operator, sec^{-1}

t time, sec

V actuator chamber volume, in.^{2}

x displacement of supported mass, in.

z displacement of actuator rod, in.

a_1 constant, dimensionless

a_2 constant, dimensionless

β bulk modulus of hydraulic fluid, lb./in.^{2}

δ relative displacement between supported mass and actuator, in.

ΔP differential pressure across actuator, lb./in.^{2}

ζ_a damping ratio for accelerometer, dimensionless

ζ_c damping ratio for flexible coupling, dimensionless

ζ_v damping ratio for servovalve, dimensionless

τ_1 time constant, sec

τ_2 time constant, sec

τ_3' time constant, sec

τ_{c_1} time constant, sec

τ_{c_2} time constant, sec

ω frequency, radians/sec

ω_a undamped natural frequency of accelerometer, radians/sec

ω_c undamped natural frequency of coupling and supported mass radians/sec

ω_v undamped natural frequency of servovalve, radians/sec

Appendix I

ACTIVE SYSTEM OPEN AND CLOSED LOOP TRANSFER FUNCTIONS

This appendix deals with generation of the system block diagram and the associated transfer functions. Figs. 8 and 9 show a schematic representation of the active hydraulic system and the relationship between the various elements in the system, respectively. The servoamplifier modifies and adds signals from the displacement transducer and the accelerometer, and delivers a flow command signal to the servovalve. The actuator, through the flexible coupling, generates forces as a function of the flow delivered by the servovalve. These forces act on the isolated mass to attenuate the effects of distrubing excitations.

The flow from the servovalve Q_v can be expressed in terms of the relative actuator piston displacement and the compressibility of the hydraulic fluid in the actuator [45, p. 37].

$$Q_v = A(\dot{z} - \dot{\delta}) + \frac{V}{2\beta}\, \dot{\Delta P} \tag{1}$$

170

The symbols used throughout the appendices are defined in the nomenclature.

Based on performance data for the type of flexible coupling used in the system, the dynamics of the coupling can be represented by

$$\ddot{x} + 2\zeta_c\omega_c\dot{x} + \omega_c^2(x - z) = 0 \tag{2}$$

The acceleration of the isolated mass is described in terms of the actuator force output by

$$M\ddot{x} = \Delta P A \tag{3}$$

Substituting Eqs. (2) and (3) in Eq. (1), and rearranging terms,

$$\frac{Q_v}{A} = \left[\frac{1}{\omega_c^2} + \frac{V}{2\mu}\frac{M}{A^2}\right]\ddot{x} + \frac{2\zeta_c}{\omega_c} + \dot{x} - \dot{a} \tag{4}$$

Using the Laplace operator notation, the acceleration of the isolated mass is given by

$$s^2x(s) = \frac{Q_v(s)\frac{s}{A} + s^2 a(s)}{\left[\frac{1}{\omega_c^2} + \frac{VM}{2\beta A^2}\right]s^2 + 2\zeta_c\frac{s}{\omega_c} + 1} \tag{5}$$

The flow command signal to the servovalve Q_v is the sum of the compensated acceleration and displacement signals. The flow from the servovalve in terms of the accelerometer transfer function $G_a(s)$, the servovalve transfer function $G_v(s)$, the loop gains C_1 and C_2, and the compensator transfer functions $G_1(s)$, $G_2(s)$ and $G_3(s)$, is given by Eq. (6), (minus sign implies negative feedback)

$$Q_V(s) = -[C_1 G_1(s)G_a(s)\ddot{x}(s) + C_2 G_2(s)\delta(s)]G_3(s)G_V(s) \tag{6}$$

where.

$$\delta = x - a$$

$$G_1(s) = \frac{\pi s(\frac{1}{\alpha_1}\tau_{c_1}s + 1)}{(\tau_1 s + 1)(\tau_{c_1}s + 1)}$$

$$G_2(s) = \frac{\frac{1}{\alpha_2}\tau_{c_2}s + 1}{\tau_{c_2}s + 1}$$

$$G_3(s) = 1 + \frac{C_3}{C_2}s\left[\frac{1}{\tau_3 s + 1}\right]$$

$$G_a(s) = \frac{1}{\frac{s^2}{\omega_a^2} + \zeta_a\frac{s}{\omega_a} + 1}$$

$$G_v(s) = \frac{1}{\frac{s^2}{\omega_v^2} + 2\zeta_v\frac{s}{\omega_v} + 1}$$

Fig. 9 shows the block diagram of the system based on Eqs. (5) and (6). For the system under consideration $\frac{1}{\omega_c^2} >> \frac{VM}{2\beta A^2}$ ($10^{-4} >> 10^{-6}$). Therefore, from Fig. 9, the open loop transfer function, $\frac{B(s)}{E(s)}$, is given by

$$\frac{B(s)}{E(s)} = \frac{\frac{C_1}{A}G_1(s)G_2(s)G_a(s)G_v(s)s^2}{G_c(s)s + \frac{C_2}{A}G_2(s)G_3(s)G_v(s)} \tag{7}$$

171

where, from Eq. (2)

$$G_c(s) = \frac{s^2}{\omega_c^2} + \frac{2\zeta_c}{\omega_c} s + 1$$

The system closed loop transfer function relating the system acceleration respons $\ddot{x}$, to the disturbance acceleration $\ddot{a}$, can be obtained from Eqs. (5) and (6) and is given by

$$\frac{\ddot{x}(s)}{\ddot{a}(s)} = \frac{s + \frac{C_2}{A} G_2(s)G_3(s)G_V(s)}{\frac{C_1}{A} G_1(s)G_2(s)G_3(s)G_V(s)s^2 + G_c(s)s + \frac{C_2}{A} G_2(s)G_3(s)G_V(s)} \tag{8}$$

Eqs. (7) and (8) were solved on a digital computer for the system with a 245-lb. rigid payload, using the following values of system constants:

$$\frac{C_1}{A} = 1.58 \text{ sec}$$

$$\frac{C_2}{A} = 4.5 \text{ sec}^{-1}$$

$$\frac{C_3}{C_2} = 0.51 \text{ sec}$$

$$\tau_1 = 0.315 \text{ sec}$$

$$\tau_2 = 0.0263 \text{ sec}$$

$$\omega_V = 1100 \text{ sec}^{-1}$$

Results are presented in Figs. 10 and 11 which show polar plots of the amplitude and phase angle of the system open loop transfer function $\frac{B(j\omega)}{E(j\omega)}$, and Fig. 12, which shows a plot of the magnitude of the closed loop transfer function $\frac{\ddot{x}(j\omega)}{\ddot{a}(j\omega)}$ as a function of frequency, respectively.

Fig. 18 shows a polar plot of the amplitude and phase angle of the system open loop transfer function $\frac{B(j\omega)}{E(j\omega)}$ obtained from Eq. (7) for a 33.5-lb metal seat plus a 145-lb rigid weight. The same constants as shown above apply for this case except for the following:

$$\frac{C_1}{A} = 0.84 \text{ sec}$$

$$\frac{C_2}{C_2} = 0.30 \text{ sec}$$

$$\tau_{C_2} = 0.05 \text{ sec}$$

$$\omega_c = 113 \text{ sec}^{-1}$$

Appendix II

SYSTEM ERROR TRANSFER FUNCTION

In this appendix, it is shown how the reference input signal $R(t)$ may be used to represent an acceleration disturbance into the active hydraulic isolation system. The system error transfer function $\frac{E(s)}{R(s)}$, can be derived using the block diagram shown in Fig. 9 and Eq. (7) in Appendix I, and is given by:

172

$$\frac{E(s)}{R(s)} = \frac{1}{1 + \frac{R(s)}{E(s)}}$$

$$\frac{E(s)}{R(s)} = \frac{G_c(s)s + \frac{C_2}{A} G_a(s)G_3(s)G_v(s)}{\frac{C_1}{A} G_1(s)G_2(s)G_3(s)G_v(s)s^2 + G_c(s)s + \frac{C_2}{A} G_a(s)G_3(s)G_v(s)} \tag{9}$$

The system closed loop transfer function $\frac{\ddot{X}(s)}{\ddot{\sigma}(s)}$, is given by Eq. (8). From Eqs. (8) and (9) the ratio $\frac{E(s)}{X(s)}$ is given by

$$\frac{E(s)}{X(s)} = \frac{G_c(s)s + \frac{C_2}{A} G_a(s)G_3(s)G_v(s)}{s + \frac{C_2}{A} G_a(s)G_3(s)G_v(s)} \tag{10}$$

If a command signal $R(t)$ equivalent to the disturbance $\ddot{\sigma}(t)$ is introduced into the system shown in Fig. 9, the measured error signal $E(t)$ will be equivalent to the system acceleration response $\ddot{X}(t)$ as long as the ratio $\frac{E(s)}{X(s)}$ given by Eq. (10) is near unity. Values of the amplitude and phase angle of $\frac{E(j\omega)}{X(j\omega)}$ were calculated on a digital computer as a function of frequency and are tabulated below.

AMPLITUDE AND PHASE ANGLE OF $\frac{E(j\omega)}{X(j\omega)}$

FREQUENCY		AMPLITUDE		PHASE
Rad/sec	Hz	Ratio	db	degrees
0.063	0.01	0.10000E+01	-0.00	0.0
0.100	0.02	0.99999E+00	-0.00	0.0
0.158	0.03	0.99999E+00	-0.00	0.0
0.251	0.04	0.99996E+00	-0.00	0.0
0.398	0.06	0.99990E+00	-0.00	0.0
0.631	0.10	0.99985E+00	-0.00	0.0
1.000	0.16	0.99953E+00	-0.00	0.0
1.585	0.25	0.99913E+00	-0.01	0.0
2.512	0.40	0.99852E+00	-0.01	0.1
3.981	0.63	0.99738E+00	-0.02	0.2
6.310	1.00	0.99476E+00	-0.05	0.3
10.000	1.59	0.98811E+00	-0.10	0.4
15.849	2.52	0.97033E+00	-0.26	0.6
25.119	4.00	0.92179E+00	-0.71	1.0
39.811	6.34	0.80306E+00	-1.91	2.9
63.096	10.04	0.55093E+00	-5.18	10.6
100.000	15.92	0.20591E+00	-13.73	109.7

It can be seen that the system acceleration response $\ddot{X}(j\omega)$ is within 10 percent of the value of the error signal $E(j\omega)$, for values of frequency lower than approximately 5 Hz. Therefore, if a reference input signal $R(j\omega)$, equivalent to a disturbance $\ddot{\sigma}(j\omega)$, is electronically introduced into the system at the appropriate location (see Fig. 9), values of the measured error signal $E(j\omega)$ will be equivalent to the acceleration response $\ddot{X}(j\omega)$, as long as the frequency of the disturbance and of the response is below 5 Hz. Such a synthesized excitation technique was used for evaluating the system response to the ramp-sustained acceleration excitation, where neither the frequency of the disturbance nor the frequency of the system was greater than 5 Hz.

173

Appendix III

DISPLACEMENT MOBILITY

Referring to Fig. 7, the equations of motion governing the actuator and the flexible coupling for a force disturbance $F(t)$ applied at the isolated mass (i.e., $\ddot{a}(t) = 0$) are given by

$$Q_v = A(\dot{z}) + \frac{V}{2\beta}\,\dot{\overline{\Delta P}}$$ (11)

and

$$\frac{F}{M} = \ddot{x} + 2\zeta_c\,\omega_c\,\dot{x} + \omega_c^2\,(x-z)$$ (12)

The acceleration of the isolated mass is described in terms of the actuator force output and the applied force by

$$M\ddot{x} = \Delta PA + F$$ (13)

Combining Eqs. (11), (12), and (13), and solving for x using the Laplace operator notation

$$x(s) = \frac{\dfrac{Q_v(s)}{As} + \dfrac{F(s)}{\omega_c^2 M} + \dfrac{F(s)}{2\beta A^2/V}}{\dfrac{1}{\omega_c^2} + \dfrac{M}{2\beta A^2/V}\,s^2 + 2\zeta_c\,\dfrac{s}{\omega_c} + 1}$$ (14)

As indicated in Appendix I, for the system under consideration $\dfrac{1}{\omega_c^2} >> \dfrac{M}{2\beta A^2/V}$. The expression then becomes

$$x(s) = \frac{\dfrac{Q_v(s)}{As} + \dfrac{F(s)}{\omega_c^2 M}}{\dfrac{s^2}{\omega_c^2} + 2\zeta_c\,\dfrac{s}{\omega_c} + 1}$$ (15)

Substituting the expression for valve flow Q_v represented by Eq. (6) of Appendix I, solving for $\frac{x}{F}$, and recognizing that since $\delta = x - a$, $x = \delta$ for $a = 0$, the point displacement mobility $\frac{\delta}{F}$, is given by Eq. (16)

$$\frac{\delta(s)}{F(s)} = \frac{\dfrac{s}{\omega_c^2 M}}{\dfrac{C_1}{A}G_1(s)G_2(s)G_a(s)G_v(s)s^2 + G_c(s)s + \dfrac{C_2}{A}G_2(s)G_3(s)G_v(s)}$$ (16)

The magnitude of the $\frac{\delta}{F}$ ratio was calculated as a function of frequency with the values of constants shown in Appendix I for a 245-lb rigid payload. These results are shown in Fig. 21.

174

REFERENCES

1. H. A. Magrath, O. R. Rogers, C. K. Grimes, Shock and Vibration in Aircraft and Missiles, Shock and Vibration Handbook (edited by C. M. Harris and C. E. Crede), Vol. 3, Chap. 47, McGraw-Hill Book Co., New York, 1961

2. C. B. Notess, "A Triangle-Flexible Airplanes, Gusts, Crew", FDM No. 343, AD469378, Cornell Aeronautical Laboratory, Inc., Buffalo, N. Y., May 1963

3. J. W. Miller, "Visual, Display, and Control Problems Related to Flight at Low Altitude", ONR Symposium Report ACR-95, AD602823, March 1964

4. T. H. Kerr, J. E. Nethaway, and H. W. Chinn, "Aircraft Tests in High Speed Low-Level Flight, Including Impressions of a Spring-Mounted Seat", Report 442, AD431313, Advisory Group for Aeronautical Research and Development, Paper Presented at the 22nd Meeting of the Flight Mechanics Panel, Torino, Italy, April 16-19, 1963

5. G. C. Dyer, "Effect of Aircraft Speed on Low-Altitude Acquisition of Ground Targets (Phase III)", APGC-TR-65-73, AD481113, Deputy for Effectiveness Test, Air Proving Ground Center, Elgin AFB, Florida, November 1965

6. J. J. McGrath, W. E. Osterhoff, and G. J. Borden, Geographic Orientation in Aircraft Pilots: Chart Scale and Pilot Performance", Technical Report 751-4, AD619780, Human Factors Research, Inc., Los Angeles, California, July 1965

7. J. W. Miller, "A Critical Review of the Human Aspects of Low-Level, High-Speed Flight", AD460383. Paper Presented at 21st Aerospace Medical Panel Meeting, Advisory Group for Aeronautical Research and Development, NATO, Lisbon, Portugal, September 17-22, 1964

8. G. J. Hurt, "Rough-Air Effect on Crew Performance During a Simulated Low-Altitude High-Speed Surveillance Mission", NASA Technical Note D-1924, August 1963

9. M. Sadoff and E. Wempe, "Pilot Vehicle System Simulation for Low-Altitude, High-Speed Flight", NASA Technical Note D-2793, June 1965

10. H. E. Rawson, et al., "Flight Simulator Study of Human Performance During Low-Altitude, High Speed Flight", TRECOM TR 63-52, AD431739, North American Aviation, Inc., Columbus, Ohio, November 1963

11. S. M. Soliday and B. Schohan, "A Simulator Investigation of Pilot Performance During Extended Periods of Low-Altitude, High-Speed Flight", NASA CR-63, June 1964

12. S. M. Soliday, "Effects of Task Loading on Pilot Performance During Simulated Low-Altitude High-Speed Flight", USATRECOM Technical Report 64-69, North American Aviation, Inc., Columbus, Ohio, February 1965

13. D. E. Goldman, and H. E. von Gierke, Effects of Shock and Vibration on Man, Shock and Vibration Handbook (edited by C. M. Harris and C. E. Crede), Vol. 44, McGraw-Hill Book Co., New York, 1961

14. C. S. Harris, and R. W. Shoenberger, "Human Performance During Vibration", AMRL-TR-65-204, AD624196, Aerospace Medical Research Laboratories, Wright-Patterson AFB, Ohio, November 1965

15. C. S. Harris, W. D. Chiles, and R. M. Touchstone, "Human Performance as a Function of Intensity of Vibration at 5 CPS", AMRL-TR-64-83, AD607760, Behavioral Sciences Laboratory, Wright-Patterson AFB, Ohio, September 1964

16. R. E. Chaney, "Subjective Reaction to Whole-Body Vibration", Report No. DC-6474, AD607462, Boeing Aircraft Co., Wichita, Kansas, September 1964

17. G. H. Ziegenruecker and E. B. Magid, "Short Time Human Tolerance to Sinusoidal Vibrations", WADC TR 59-391, D227341, Wright Air Development Center, Wright-Patterson AFB, Ohio, July 1959

18. N. F. Clarke, G. C. Mohr, J. W. Brinkley, J. H. Henzel, and H. E. von Gierke, "Evaluation of Peak vs. RMS Acceleration in Periodic Low Frequency Vibration Exposures", AMRL-TR-65-67, AD630785, Aerospace Medical Research Laboratories, Wright-Patterson AFB, Ohio, November 1965

19. E. B. Magid, R. R. Coermann, and G. H. Ziegenrueckler, "Human Tolerance to Whole Body Sinusoidal Vibration", Aerospace Medicine, November 1960, pp. 915-924

20. G. C. Mohr, J. N. Cole, E. Guild and H. E. von Gierke, "Effects of Low Frequency and Infrasonic Noise on Man", AMRL-TR-65-69, Aerospace Medical Research Laboratories, Wright-Patterson AFB, Ohio, September 1965 (AD 627420)

21. H. E. von Gierke, "On Noise and Vibration Exposure Criteria", Archives of Environmental Health, September 1965, Vol. 11, pp. 327-339

22. N. P. Clarke, H. Taub, H. F. Scherer, W. F. Temple, H. E. Vykukal, and M. Matter, "Preliminary Study of Dial Reading Performance During Sustained Acceleration and Vibration", AMRL-TR-65-110, AD622298, Aerospace Medical Research Laboratories, Wright-Patterson AFB, Ohio August 1965

23. R. Margaria, and T. Gualtierotti, "Body Susceptibility to High Accelerations and to Zero Gravity Condition", Paper reprinted from Advances in Aeronautical Sciences, Vols. 3-4, Pergamon Press Ltd., AD 631880, 1961

24. T. M. Fraser, "Human Response to Sustained Acceleration", NASA SP-103, 1966

25. A. S. Hyde, and h. Raab, "A Summary of Human Tolerance to Prolonged Acceleration", AMRL-TR-65-36, AD615570, Biophysic Laboratory, Wright-Patterson AFB, Ohio, February 1965

26. D. H. Weir, and A. V. Phatak, "Model of Human Operator Response to Step Transitions in Controlled Element Dynamics", NASA CR-671, January 1967

27. P. Foster, "An Investigation of the Relationship Between Experience Parameters and Subject Acceleration Response in Experimental Impact", ARL-TR-66-8. 6571st Aeromedical Research Laboratory, Holloman AFB, New Mexico, March 1966

28. A. E. Hirsch, "Man's Response to Shock Motions", Structural Mechanics Laboratory, Research and Development Report 1797, Department of the Navy, David Taylor Model Basin, Washington, D. C., January 1964

29. C. B. Dolkas, and J. D. Stewart, "Effect of Combined Linear and Oscillatory Acceleration on Pilot Attitude-Control Capabilities", NASA TN D-2710, March 1965

30. H. E. von Gierke, "Biodynamic Response of the Human Body", Applied Mechanics Reviews, Vol. 17, No. 12, December 1964

31. S. Barret and P. R. Payne, "Responses of a Linear Damped Dynamic System to Selected Acceleration Inputs", Aerospace Medical Research Laboratories, Wright-Patterson AFB, Ohio, 1965, (AMRL-TR-65-40) (AD 616643)

32. Anon., "A Study of the Dynamic Model Technique in the Analysis of Human Tolerance to Acceleration", NASA TN D-2645, March 1965

33. E. P. Hanavan, Jr., "A Mathematical Model of the Human Body", AMRL-TR-64-102, AD 608463, Behavioral Sciences Laboratory, Wright-Patterson AFB, Ohio, October 1964

34. D. McRuer, D. Graham, E. Krendel and W. Reisener, Jr., "Human Pilot Dynamics in Compensatory Systems", AFFDL-TR-65-15, AD 470337, Air Force Flight Dynamics Laboratory, Wright-Patterson AFB, Ohio July 1965

35. R. G. Edwards, and K. O. Lange, "A Mechanical Impedance Investigation of Human Response to Vibration", AMRL-TR-65-91, AD 609006, Biophysics Laboratory, Wright-Patterson AFB, Ohio October 1964

36. R. R. Coermann, "The Mechanical Impedance of the Human Body in Sitting and Standing Position at Low Frequencies", ASD TR 61-492, Wright-Patterson Air Development Center, Ohio, September 1961

37. C. E. Crede, and J. E. Ruzicka, "Theory of Vibration Isolation, Shock and Vibration Handbook (edited by C. M. Harris and C. E. Crede), Vol. 2, Chap. 30, McGraw-Hill Book Co., New York, 1961

38. J. E. Ruzicka, "Vibration Control", Electro-Technology, Vol. 72, No. 2, p. 63, August 1963

39. J. E. Ruzicka, and R. D. Cavanaugh, "New Method for Vibration Control", Machine Design, p. 114, October 16, 1958

40. S. K. Oleson, and J. J. Eige, "Development of Automatically Hardening Shock Mounts", AD 438143, Southwest Research Institute, San Antonio, Texas, September 1963

41. R. D. Cavanaugh, "Air Suspension and Servo-Controlled Isolation Systems," Shock and Vibration Handbook (edited by C. M. Harris and C. E. Crede, Vol. 2, Chap. 33, McGraw-Hill Book Co., New York, 1961

42. C. E. Crede, and R. D. Cavanaugh, "Feasibility Study of an Active Vibration Isolator for a Helicopter Rotor", WADC 58-183, Wright Air Development Center, Wright-Patterson AFB, Ohio, 1958

176

43. L. E. Snelien, P. Marshall, and
    R. Gates, "A Servo Controlled Rotor
    Vibration Isolation System for the Reduc-
    tion of Helicopter Vibrations", IAS Paper
    No. 62-34, Institute of Aerospace
    Sciences, January 1962

44. J. F. Blackburn, G. Reethof, and J. L.
    Shearer, Fluid Power Control, The MIT
    Press, Cambridge, Mass., 1960

45. J. J. D'Azzo, and C. H. Houlis, Feed-
    back Control System Analysis and
    Synthesis, McGraw-Hill Book Co.,
    New York, 1960

46. F. H. Raven, Automatic Control
    Engineering, McGraw-Hill Book Co.,
    New York, 1960

47. A. W. Langill, Jr., Automatic Control
    Systems Engineering, Vol. 1, Prentice-
    Hall, Inc., Englewood Cliffs, N. J.,
    1965

ELASTIC SKIDMOUNTS FOR MOBILE EQUIPMENT SHELTERS

R. W. Doll, R. L. Laier
Barry Controls
Division Barry Wright Corporation
Burbank, California

A study of the dynamic environment associated with the transportation and operation of relatively fragile mobile systems pointed out the need for designing a shock attenuation system which would protect delicate equipment and structure from shock damage due to dropping, towing and transportation environments, as required by such specifications as MIL-STD-810, MIL-E-4970 and MIL-S-52059.

A skidmount isolation system was developed which exhibits a decreasing stiffness spring rate effect. This characteristic substantially increases energy absorbing capability for a given force-deflection point, resulting in a lower height skidmount than could be obtained if a linear spring rate characteristic was used.

The configuration is shown and the shock response characteristics of a typical skidmount are described and compared to predicted values for rotational drops.

INTRODUCTION

With the advent of sophisticated weapons systems for field use, the concept of light-weight mobile shelters, housing complex and delicate electronic systems, has been introduced. When these shelters and their equipment are subjected to the dynamic environments associated with the transportation and operation of field equipment, the integrity, service life and reliability of both shelter and electronic equipment may be degraded, unless shock and vibration protection is provided. With this in mind, a shock mount design that would also serve as a skid for towing purposes was initiated.

The following primary criteria were initially set up as requirements for an acceptable skidmount design:

1. Adequate shock protection under flat and rotational drops.

2. Long term service life.

3. Capability of being towed.

4. Usable for many drops.

5. Economically producible.

6. Adaptable to a wide variety of supported weights in a given length.

Other desirable characteristics of the design were:

1. Capability of provision for lifting by a forklift.

2. Capability of not needing rigid blocking out other than simple tie down ropes during a wide range transportation environments.

3. Light weight.

The following types materials were considered for the working element of the skid:

1. Rubber Foam

2. Elastomer

3. Steel Springs

Since one requirement for an acceptable skid design was reusability, crushable honeycomb, buckling metal and frangible rings were not considered. Foam and springs were discarded in favor of elastomers because of greater energy storage capability per volume or pound, as well as packaging, strength and cost considerations. The isolator configuration, called a skidmount and as shown in Figure 1, was ultimately developed.

179

DESIGN CONSIDERATIONS

As Figure 1 shows, the skidmount section
consists of two elastomer elements inclined at
an angle such that at a predetermined dynamic
load, the elastomer will continue to deflect
without an appreciable increase in load. This
results in a greater amount of energy storage
capability for a given overall height than could
be obtained if a linear load-deflection char-
acteristic was used.
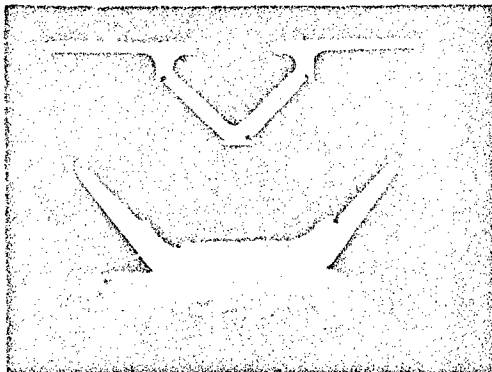
Figure 1
Skidmount Cross Section

Other reasons for the particular configur-
ation shown was efficient usage of support
structural and horizontal stability under side
loads. Also, since the skidmounts must be cap-
able of being towed over various terrain, the
angled sides provide ramps that would allow the
skid to slide over the dirt, rather than dig
into it as would be the case with vertical
sides.

To show that the skidmount is a more efficient
shock attenuation system than a linear system,
a comparison of the deflection required for both
systems is made in Table I. This example shows
that for a drop height of approximately 10
inches, the linear spring would require approxi-
mately 30% more deflection than the skidmount
configuration. As Table I points out, the skid-
mount was optimized for a 10 inch drop height
but the same configuration can be optimized for
other drop heights.

In order to facilitate prediction of re-
sponse characteristics for various package
weights and inertias, the dynamic translational
load-deflection data were obtained from a test
specimen and these data were used to develop
the spring rate equation for the rotational
edge drop analysis. The data were compared to
actual rotational drop test values in order to
verify the accuracy for use in design evalu-
ations.

TABLE I
Comparison of Skidmount and
Linear Spring Performance

DROP HEIGHT (in)	ACCELERATION (g)	DEFLECTION (in)	
		SKIDMOUNT	LINEAR
7.5	11.4	1.23	1.60
.9	12.5	1.55	1.90
.8	.40	1.90	2.00
.5	1.55	1.56	2.07

TEST PROCEDURES

The static load-deflection properties were
first determined by slowly loading a section in
a Tinius Olsen Test Machine. This data was used
to verify the non-linear characteristics of the
design and determine the static load carrying
limits of the mount.

The dynamic load-deflection characterist-
ics were determined by dropping a mass with a
skidmount section attached, onto a rigid base
and measuring the deceleration of the mass and
the deflection of the skidmount.

A crystal accelerometer, charge amplifier
and oscilloscope were used to monitor deceler-
ation, while a sliding friction device was used
to measure deflection. Figure 2 shows the test
setup.
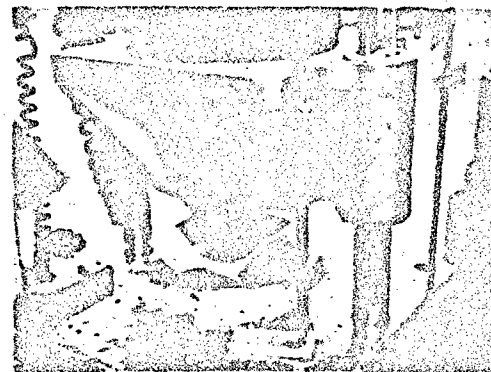
Figure 2

Test Setup For Determining Dynamic
Load-Deflection Data

The resulting static and dynamic load-deflection curves are compared in Figure 3. As is normal, the dynamic stiffnesses are slightly higher than the static stiffnesses.

The acceleration versus drop height data are plotted on Figure 4. Similar results would be expected from a full size rigid package mounted on skidmounts, which had the same relative load per unit length of elastomer.
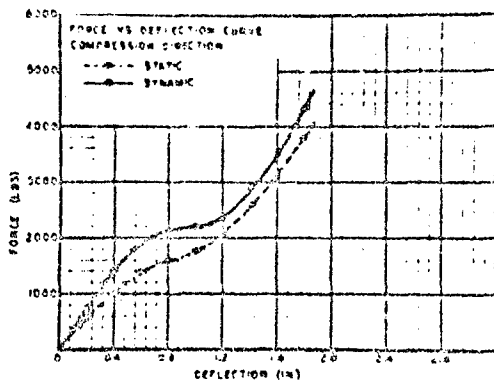
Figure 3

A 2518 pound mockup was used as a simulated shelter with dimensions of 7 feet long by 4 feet wide by 3.5 feet high. The moment of inertia was calculated as 4500 inch-lb-sec^2 with the center of gravity 26 inches up. Figure 5 shows the configuration.
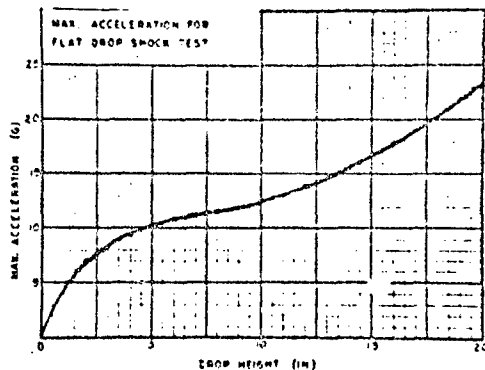
Figure 4

Two skidmounts were bolted to the mockup. One end was raised and dropped from various heights. Accelerations were measured at the corner farthest from the pivot point and at the center of gravity.
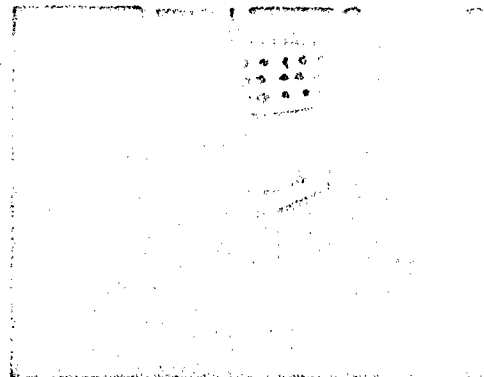
Figure 5

Test Setup For Rotational Drop Data

ANALYSIS OF EDGE ROTATIONAL DROP ABOUT THE LATERAL AXIS

Nomenclature

b = Horizontal distance from c.g. to elastic center of elastomer

c = Vertical distance from c.g. to elastic center of elastomer

F(z) = Spring Force

h = Drop Height

I_o = Moment of Inertia about point of rotation "0"

I_{xx} = Moment of Inertia about c.g.

L = Overall length of test package

R = Radius from point of rotation to c.g.

V = Potential energy

v_o = Velocity at impact

T = Kinetic energy

W = Weight of test package

θ = Angle between bottom of skid and R

φ = Angle between horizontal and R

η_o = Rotational Velocity at impact

181
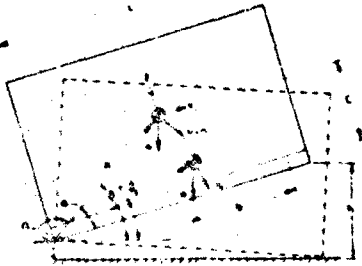
Figure 6

Mathematical Model for Rotational Drop

Using the translational dynamic load-deflection data, a mathematical model for the vertical spring rate was derived. The predicted response for the rotational drop was calculated. The assumptions are as follows:

1. The mass pivots about the Point "0" without linear translation.

2. The mass is rigid and inert compared to the skidmounts.

3. The deflection of the skidmount is small compared to the drop height.

The initial rotational impact velocity is first computed using potential and kinetic energy relationships:

$$dT = - dV \tag{1}$$

$$T_2 - T_1 = V_1 - V_2 \tag{2}$$

where,

$$T_1 = 0 \quad \text{and} \quad T_2 = \frac{I_0 \Omega_0^2}{2} \tag{3}$$

$$V_1 - V_2 = \int_{\phi_1}^{\phi_2} (W \cos\phi) \; r d\phi \tag{4}$$

Therefore,

$$\frac{I_0 \Omega_0^2}{2} = - Wr(\sin\phi_2 - \sin\phi_1) \tag{5}$$

Or,

$$\Omega_0 = \sqrt{\frac{2Wr}{I_0} (\sin\phi_1 - \sin\phi_2)} \tag{6}$$

From the geometric relations between the angle ϕ, the drop height (h) and package dimensions R, L and C are related as follows:

$$\sin\phi = \left(\frac{2C}{L} + \frac{(h-4)(L^2 - 4C^2)}{2 rL^2} \right) \tag{7}$$

Substituting this Equation into Equation (6) and noting that $h_1 = h$, $h_2 = 0$, the angular velocity reduces to,

$$\Omega_0 = \sqrt{\frac{Wh}{I_0} \left(1 - \frac{4C^2}{L^2} \right)} \tag{8}$$

Then the magnitude of the velocity at c.g. is,

$$v_0 = R\Omega_0 \tag{9}$$

With a direction perpendicular to the Radius R.

Then the velocity directed along the principle axes of the shelter is as follows:

$$v_z = v_0 \cos\theta = \Omega_0 R \cos\theta \tag{10}$$

$$v_y = v_0 \sin\theta = \Omega_0 R \sin\theta \tag{11}$$

Substituting Equation (8) into the above equations, yields

$$v_z = \frac{L}{2} \sqrt{\frac{Wh}{I_0} \left(1 - \frac{4C^2}{L^2} \right)} \tag{12}$$

$$v_y = C \sqrt{\frac{Wh}{I} \left(1 - \frac{4C^2}{L} \right)} \tag{13}$$

Now that the initial velocities (Ω_0, v_z, v_y) have been defined, the Equations of Motion are written for the Edge Rotational Drop. Due to the symmetry of the elastomer elements, the Y and α modes will be the only coupled modes, therefore, these Equations of Motion describing the response to the Edge Rotational Drop are as follows:

$$m\ddot{z} = -4F(z) \tag{14}$$

$$m\ddot{z} + 4 \; [1843.59z^4 -1434.75z^3$$
$$-6954.48z^2 + 13749.57z -227.67] \tag{15}$$

Where F(z) was written in the form of a polynominal in z as derived from the dynamic load-deflection data by a least square approximation of test data. The resulting relationship is as follows:

182

$$F(z) = 1843.59z^4 - 1434.75z^3 - 6954.48z^2 \quad (16)$$
$$+ 13749.57z - 227.67$$

$$m\ddot{z} + 4\,[1843.59z^4 - 1434.75z^3 - 6954.48z^2 \quad (17)$$
$$+ 13749.57z - 227.67]$$

$$m\ddot{y} = + 4F_y \, C_1 - 4K_y Y \quad (18)$$

$$m\ddot{y} + 4K_y Y - 4K_y \, C_1 = 0 \quad (19)$$

$$I_{xx}\ddot{a} = 4\,K_y\,C_y - 4K_y C^2{}_1 + 4F(\,b)b \quad (20)$$

$$I_{xx}\ddot{a} + 4K_y C^2{}_1 - 4b[1843.59b^4 a^4 \quad (21)$$
$$-1434.75b^3 a^3 - 6954.48b^2 a^2$$
$$+13749.58 a - 227.67] - 4K_y C_y = 0$$

The above Equations of Motion were solved numerically using the Runge-Kutta Method for simultaneous second order differential equations. The results of this analysis are shown graphically for the response accelerations at c.g. and at the corner Figures 7 and 8.

The actual test results show values which are approximately 10% to 20% less than the theoretical results. This is good agreement when instrumentation, assumptions and variances are taken into account.
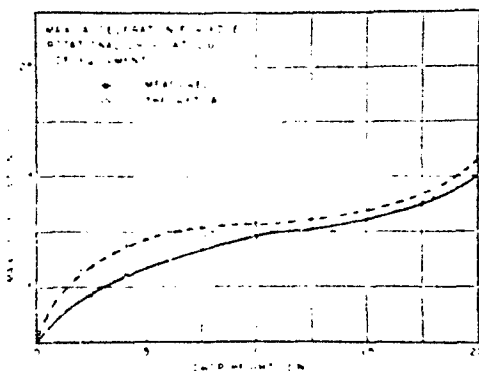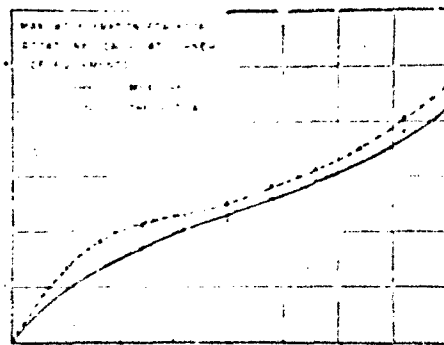
Figure 8

CONCLUSIONS

The design approach described herein will provide low shock response levels combined with a very efficient use of available mount space. Shock response values can be calculated with a high degree of accuracy for both straight and rotational drops, thus providing a means of optimizing each application.

BIBLIOGRAPHY

1) Cyril M. Harris and Charles E. Crede, "Shock and Vibration Handbook", Vol. 2, Pg. 31-1 to 31-33, McGraw-Hill, New York, 1961.

2) James B. Scarborough, "Numerical Mathematical Analysis", pp 355-361. Johns Hopkins Press, Baltimore, 1961

3) R. D. Mindlin, "Dynamics of Package Cushioning", Bell System Technical Journal B-1369, Oct. 1945.

Figure 7

183

DISCUSSION

Mr. Denner (Hughes Aircraft Co.): Do you have any typical weights for these skid systems for common sizes of shelters?

Mr. Doll: The skid averages out to about 7 lbs per foot, including the tow weights on the end which are a little bit larger than the extrusions. For a typical 12 foot shelter, it would weigh less than 90 lbs.

Mr. Gertel (Kinetic Systems): I was curious about the statement you made on the non-linear and linear equivalents. I believe you said the non-linear mount gave a lower deflection than the equivalent linear mount?

Mr. Doll: Yes. If you draw a straight line from the origin thru a point on the load-deflection curve before it stiffins up, both systems would have the same force level, but the skid mount would be more efficient. It would have more energy underneath the curve at that particular point.

Mr. Gertel: I made a fairly short standard package cushioning deflection calculation which would indicate that, the optimum linear mount would have considerably lower deflection than the equivalent situation which you described.

Mr. Doll: Once you got past the flat portion of the curve there is a cross over point where the deflection of a linear spring would equal that of the skid mount.

Mr. Gertel: The linear mount probably would have a higher stiffness. Based on the simple package cushioning equations, the deflection equals twice the drop height divided by the acceleration. Looking at your table, in almost every case the optimum linear mount would have roughly the same deflection as your own non-linear mount.

COMPUTER-AIDED DESIGN OF OPTIMUM SHOCK-ISOLATION SYSTEMS

E. Sevin, W. D. Pilkey, A. J. Kalinowski
IIT Research Institute
Chicago, Illinois

A computer-aided optimization method, termed indirect synthesis, for the design of a class of multidegree-of-freedom, multi-isolator shock-isolation systems is described. Such systems are characterized by (1) linear structural elements interconnected by nonlinear isolator elements and (2) constraints and a performance index that can be expressed as linear functions of the system state variables. Any number of degrees of freedom can be considered and no restrictions are imposed on the nonlinearity of the isolator elements. The indirect synthesis method also can be used to determine tradeoff relationships between performance index and response constraints, thereby providing a quantitative measure of the effectiveness of any proposed isolator concept and the theoretical performance improvement margin.

INTRODUCTION

The design of an optimum shock-isolation system requires synthesizing portions of an otherwise-specified assemblage of structural elements so that an index of over-all system performance is optimized (i.e., minimized or maximized) and specified constraints on the system response are satisfied under the action of an external shock excitation. This is essentially a variational-type problem for which most success, to date, has resulted from mathematical programming formulations. Even so, because of computational difficulties, these have been limited to relatively small and simple systems. The reasons for this state of affairs can be understood by considering the following characteristics of what might be termed the "conventional direct-synthesis approach" to design optimization:

● The entire system dynamics must be solved for each trial set of design parameters considered.

● If more than one isolator is present in the system, all parameters contained in all isolators must be sought simultaneously.

● Nonlinear programming search codes are required to execute the performance minimization. The unknown parameters invariably appear implicitly

and nonlinearly in the mathematical representations for both the performance index and response constraints. The nonlinearity aspect rules out the use of efficient linear programming techniques: The implicit appearance of the parameters rules out the use of high-speed "gradient-type" nonlinear programming codes. The only alternative is that less efficient, slower-converging mathematical programming codes, such as the "pattern-search" type, be employed.

In this paper we will consider a new computer-oriented approach, called indirect synthesis. It treats the same general class of problems, yet holds promise of avoiding many of the disadvantages of the direct approach. The method is intended for many-degree-of-freedom systems whose structural elements are linearly elastic. The isolator elements may be highly nonlinear, thus the over-all system dynamics are nonlinear. Further, both the performance index and constraints must be linear functions of the state variables (e.g., displacements, velocities, forces).

The method of indirect synthesis comprises two distinct phases, (1) Time-Optimal Synthesis, and (2) System Identification. The first phase involves the determination of the force-time variation in each of the isolator elements for which the performance index is optimized and the constraints satisfied. For the

class of systems described, finding the
optimum isolator for consists of solv-
ing a linear programming problem whose
dimension depends on the number of iso-
lators and constraints rather than on
the degrees of freedom of the over-all
system. The linear programming formula-
tion is possible since the isolator ele-
ments, despite the possibility of their
being nonlinear in their respective state
variables, enter the equations of motion
as unknown functions of time. While it
is possible to handle nonlinear struc-
tural systems by other means (e.g., dy-
namic programming), the practical appli-
cation of the method for truly large
systems and present generation computers
depends on the linear programming ap-
proach.

Repetitive solution of the time-
optimal synthesis phase for different
constraint levels results in a perform-
ance index/constraints relationship that
represents the best performance possible
for the totality of admissible isolator
elements (for the prescribed loading)
When the optimization proceeds by con-
ventional direct-search techniques this
information is generally unavailable
since specific isolation-element config-
urations must be specified in advance.

The system identification phase con-
sists of determining the open parameters
of some prescribed isolator element. This
is done by causing the response of iso-
lator elements to approximate the ideal
synthesized response, thereby avoiding
the necessity of solving a constrained
minimization problem. In a multi-iso-
lator problem, this can be accomplished
one isolator at a time. Knowledge of
the tradeoff relationship between opti-
mum performance and constraint serves to
terminate the identification process.

TIME-OPTIMAL SYNTHESIS

The practicality of the indirect
synthesis method stems from the fact that
the time-optimal synthesis phase is eas-
ily accomplished for an important class
of large isolation systems. This is a
consequence of the linear form of the
defining equations, even though the iso-
lator elements under consideration may
be nonlinear when expressed in terms of
the system state variables. The general
dynamic system under consideration will
consist of an arbitrary arrangement of
linearly elastic structural elements
interconnected by isolation elements.
The structural elements are assumed to
be the known (and fixed) portions of the
system, and the isolator elements the
unknown portions. The most general ar-
rangement is shown in Fig. 1:
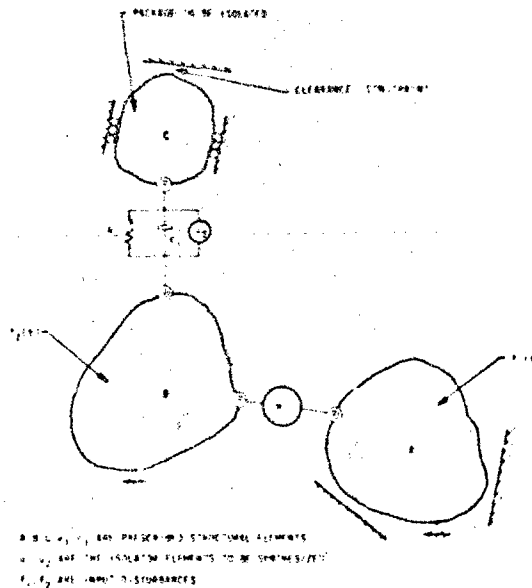
Fig. 1 - Multi-isolator, multidegree-
of-freedom system

Less general configurations, which are
considered later, are shown in Fig. 2.

To establish a mathematical state-
ment of this general shock isolation
problem we introduce the following nomen-
clature:

u_j; $j=1,\ldots,J$ = forces in the J
(unknown) isolator elements.

$C_k(t,u_j)$; $k=1,\ldots,K$ = response func-
tions (relative motions or func-
tions of relative motions) at
positions in either a structural
or an isolator element, or a
combination of these, where time
is denoted by t. (According to
the design requirements, the C_k
must lie within some prescribed
(time-dependent or invariant)
bounding values, say, between
C_k^L and C_k^U. The C_k are referred
to as the "constraint functions"
and there may be K such inequal-
ities specified.)

$h(t,u_j)$ = response function whose
maximum or integrated value over
time represents the index of
performance to be optimized
(minimized or maximized). De-
note this functional of h by Q,
the performance index. If the
maximum absolute value in time
of h is of prime concern, then
$Q=\max_t h(t,u_j)$ for all $0 \leq t < t_f$;

if an integral of the response

186

is the performance index, then

$$Q = \int_0^{t_f} h(t, u_j) dt.$$

t_f = final value of the time interval of interest.

$f_j(t)$; $j=1,2,\dots L$ = external shock excitations.

The optimum design problem for the general shock isolation system considered thus amounts to determining the J isolator elements (i.e., the u_j) such that the K constraints

$$C_k^L \leq C_k(t, u_j) \leq C_k^U; \quad k=1,\dots,K \quad (1)$$

are satisfied and the performance index, Q, takes on a minimum (or maximum) value.

The choice of performance index is of utmost importance since it establishes the sense in which the isolation system design is optimized. The choice of constraints, on the other hand, restricts the range of candidate designs relative to which the optimum is selected.

In general, both the performance index and constraints can consist of any linear combination of response quantities. Since we are limiting consideration to structural elements that respond linearly to either the external shock excitation or to prescribed forces at the attachment points of the isolator elements, the method of superposition applies. Thus, any of the state variables, or a linear combination of the state variables, can be written in the form of a convolution integral involving the response of the (known) structural elements to unit forces and the (unknown) isolator element forces. The response function, therefore, can be written as

$$h(t, u_j) = h_o(t) + \sum_1^J \int_0^t R_j(t-\tau) u_j(\tau) d\tau, \quad (2)$$

where the $R_j(t)$ are the values of h due to a unit impulse applied at the attachment point of the jth isolator element, and $h_o(t)$ is an analogous response due to the applied disturbances $f_j(t)$. Similarly, linear constraint functions can be written as

$$C_k(t, u_j) = C_{ok}(t) + \sum_{j=1}^J \int_0^t R_{kj}(t-\tau) u_j(\tau) d\tau. \quad (3)$$

Expressions (2) and (3) assume zero initial conditions as is usually the case

for shock problems. However, the appropriate solution to the homogeneous equations of motion can be added to both equations to include situations where nonzero initial conditions prevail.

For computational purposes, it may be more convenient to obtain solutions to the original system for unit step-functions $\tilde{R}_j(t)$, rather than for unit impulses. As the response of a system to a unit impulse is the derivative of the response to a unit step-function, so $R_j(t)$ can be computed from $d\tilde{R}_j(t)/dt$.

In particular circumstances, the performance index and constraint functions may be reduced to special cases of these general forms. For example, the response function h could be a linear combination of J of the isolator forces

$$h(t, u_j) = \sum_1^J A_j u_j(t), \quad (4)$$

where A_j are prescribed constants. Similarly, a constraint might be reduced to a linear combination of the form

$$C_k(t, u_j) = C_{ok}(t) + \sum_{j=1}^J A_{jk} u_j(t) \quad (5)$$

where A_{jk} are known constants. Still another possible constraint form would involve the terminal value of a response, i.e., its value at time t_f

$$C_k(t_f, u_j) = \sum_{j=1}^J \int_0^{t_f} {}_j(t_f - \tau) u_j(\tau) d\tau. \quad (6)$$

The time-optimal synthesis for systems with these types of performance index and constraints becomes a problem of linear programming where, in discrete form, we seek to establish the i-components (i=1,\dots,I) characterizing each of the J isolator forces u_{ji}, such that Q is minimized subject to the linear constraints

$$C_{ki}^L \leq C_k(t_i, \quad \dots, K). \quad (7)$$

As state ther the form

$$Q = \max_{t_i} h(\quad \leq t_i \leq t_f \quad (8)$$

or

$$Q = \int_0^{t_f} h(\quad (t_i, u_{ji}) t_i. \quad (9)$$

187

Also, it is possible to have the integral of the absolute value of h as the performance index and still retain the linearity in u_{ji} required to formulate the problem as one of linear programming.

The functions h and C_k are arbitrary in that either can represent stresses, displacement, forces, or practically any other physical quantity of interest to the system.

Details of the linear programming formulation and a code to implement it are given in Ref. [1]. Of importance here is the observation that the size of the linear programming problem does not depend on the number of degrees of freedom characterizing the dynamic system. Rather, the size of the program, from a computational point of view, is proportional to the quantity IJK, where I is the number of discrete time steps used to characterize the isolator forces, K is the number of response constraints and J is the number of isolator elements. Moreover, the dynamic analysis is conducted only once to determine the influence-type functions which appear as the coefficients of the u_j in Eqs. (2), (3), and (6).

Time-optimal synthesis results in isolator functions u_j for the optimal isolators and the minimum value of Q. If the synthesis is executed for a range of values of the constraints, a hypersurface showing the optimal performance possible for various combinations of constraints can be constructed. The isolation system designer can use such information to learn if proposed designs can ever meet the required performance. Also, a measure of his success at various stages of his design efforts is now available, since the performance of his candidate system can be compared to that of the best possible.

The time-optimal synthesis process can be conveniently considered in terms of three computational steps.

Step 1 - System Dynamics. Structural-dynamic codes are used to obtain the required response history of the individual structural elements resulting from both the external loading and the unit impulses at the isolator element attachment points, i.e., determine $h_o(t)$ and $C_{ok}(t)$ appearing in Eqs. (2), (3) and (5) and R_j and R_{kj} appearing in Eqs. (2), (3), and (6).

Step 2 - Linear Program Preprocessor (LLP). The response information of Step 1, the form of the performance index, and the nature of the constraints to be met must be converted to standard linear

programming form. The mechanics of accomplishing this for a single-degree-of-freedom system are given in Ref. [2]. For the general problem, this task can be automated by a linear programming preprocessor (LPP). The standard linear programming problem may be stated as: Find the vector $\bar{Z}$ that minimizes $\varsigma = \bar{C}\,\bar{Z}$ subject to the linear constraints $\bar{A}\,\bar{Z}=\bar{B}$, where the components of $\bar{Z}$ must be positive. In essence, the LPP code sets up the $\bar{A}$, $\bar{B}$, $\bar{C}$ matrices using the response output and other essential information. Such an LPP code that accepts quite general forms of constraints and performance indices is available. The formulation and implementation, including the FORTRAN IV listing and users manual, are provided in Ref. [1].

Step 3 - Linear Program Solver. This step employs existing large-scale[†] linear programming codes that accept the output of Step 2 (i.e., the coded $\bar{A}$, $\bar{B}$, $\bar{C}$ matrices) and compute the minimum ς (say ς^*) and corresponding minimizing vector $\bar{Z}^*$. The optimum isolator functions u_j^*, any desired response functions, and also the optimum performance Q^* for the specified constraints can be subsequently determined from ς^* and $\bar{Z}^*$.

SYSTEM IDENTIFICATION

The second phase in the indirect synthesis process is termed system identification. This phase results in the selection of design parameters associated with the candidate isolator element configuration that satisfy the originally stated optimization problem. This is accomplished by curve-matching techniques that mold the candidate isolator force-time characteristics to the ideal response as determined from the time-optimal synthesis phase.

The design parameters are determined for each isolator separately, rather than simultaneously as required by the direct-synthesis method. The optimum isolator forces $u_j^*(t)$, used as the reference for curve-matching, need be computed only once. This is equivalent to performing the system dynamics but once.

Assume that the force in the jth isolator element (u_j) can be expressed as an arbitrary algebraic or transcendental function of the relative displacement (x_j) and relative velocity ($\dot{x}_j$)

[†]Available linear programming codes include CDC Allegro, IBM MPS 360, IBM LP 90, and UNIVAC FMPS.

between the isolator terminals[‡] [e.g., Fig. 2(a)] and the M_j unknown design parameters $\bar{\alpha}_j = \alpha_{j1}, \alpha_{j2}, \ldots, \alpha_{jM_j}$. That is,

$$u_j = u_j^c(x_j, \dot{x}_j, \bar{\alpha}_j). \qquad (10)$$

the optimal history of $u_j, u_j^*(t)$, for the J values of j. The same dynamic system equations employed to compute $u_j^*(t)$ are used to obtain the corresponding relative motion trajectories $x_j^*(t)$ and $\dot{x}_j^*(t)$. Knowledge of $(u_j^*, x_j^*, \dot{x}_j^*)$ permits us to compare the force in the jth candidate
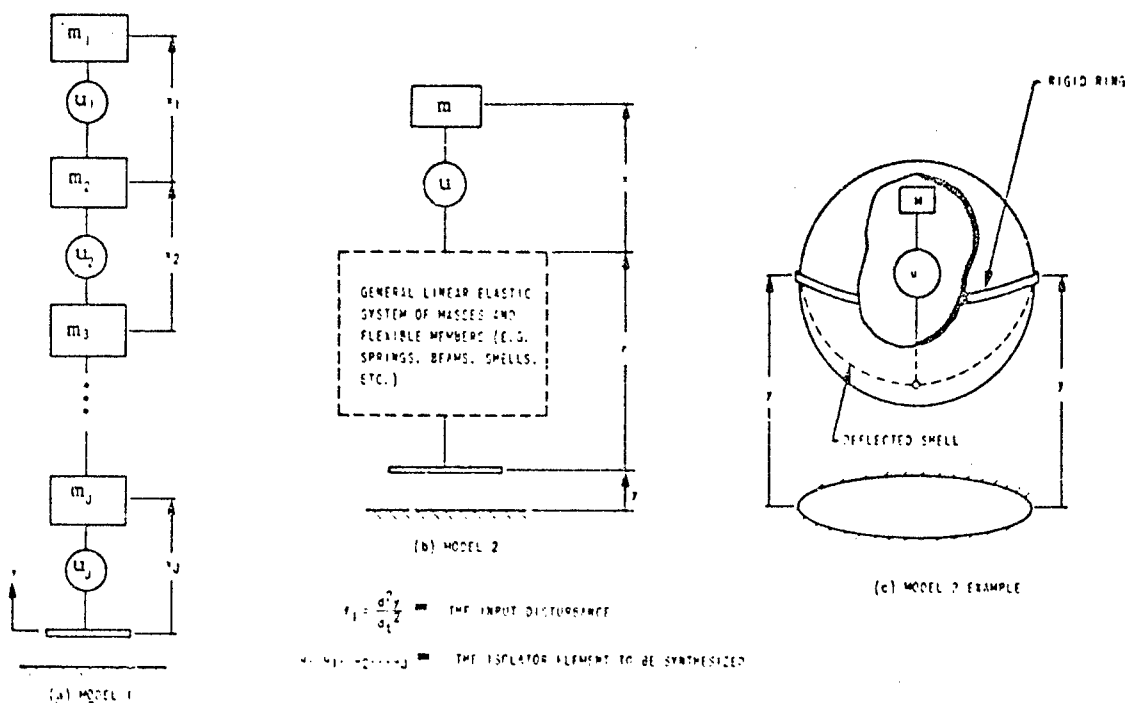
Fig. 2 - Example shock isolation systems

One such form is

$$u_j^c = \sum_{n=1}^{N_j} \gamma_{nj} x_j^n + \sum_{n=1}^{N_j'} \beta_{nj} \dot{x}_j^n , \qquad (10a)$$

where the $(N_j + N_j')$ values γ_{nj}, and β_{nj} refer to the M_j values of $\bar{\alpha}_j$.

The optimum synthesis problem is to select numerical values for the M_j design parameters $\bar{\alpha}_j$ for each of the J isolators such that Q is minimized (or maximized) and the constraints on C_k are satisfied. Recall that we have already determined

isolator (under the assumption that it can respond optimally) with u_j^* and to select the design parameters to minimize the difference between the two. That is, from the difference function,

$$\Delta_j(t) = u_j^*(t) - u_j^c(x_j^*, \dot{x}_j^*, \bar{\alpha}_j), \qquad (11)$$

we can select the $\bar{\alpha}_j$ such that

$$H(\bar{\alpha}_j) = \int_0^{t_f} \left[\Delta_j(\tau)\right]^2 d\tau \qquad (12)$$

is minimized.

The relation (12) can be approximated with a finite sum so that the design parameters are determined by solving

---

[‡]Additional considerations that arise when derivatives of u_j appear in the expression relating force and relative motion (e.g., for a spring and dashpot in series) are discussed in Ref.[1]. This is a situation not fundamentally different from that considered here.

the least-square optimization problem[**]

$$H(\overline{\tau}_j^*) =$$

$$\min_{\overline{a}_j}\left[\sum_{i=1}^{I}\left[u_j(t_i)-u_j^c(x_j^*(t_i),\dot{x}_j^*(t_i),\overline{a}_j)\right]^2 \Delta t_i\right]$$

(13)

where $\overline{\tau}_j^*$ refer to the minimizing parameters and Δt_i is the integration time interval. If the parameters $\overline{a}_j$ appear linearly in Eq. (10) [.g., Eq. (10a)], (13) becomes a problem of ordinary least-square curve-fitting: If they appear nonlinearly, the parameters must be determined with a nonlinear search code [5].

The determination of $\overline{a}_j^*$ is the step previously referred to as molding the jth candidate isolator's force-time characteristics to those of the time-optimal response. The suboptimization problem (13) involves each M_j set of parameters independent of those appearing elsewhere in the system, i.e., system identification is performed an isolator element at a time.

If perfect curve-matching, $\Delta_j(t) = 0$ for all $0 \le t \le t_f$ and for all J-isolators, is realized, then a solution to the system equations containing the candidate isolators with $\overline{a}_j = \overline{a}_j^*$ (i.e., $u_j(x_j,\dot{x}_j,\overline{a}_j^*)$ in place of $u_j^*(t))$ will be $x_j(t) = x_j^*(t)$. The corresponding Q and $C_k(t)$ will be the same as those obtained from time-optimal synthesis since both are expressible as functions of x_j [1].

If the curve-matching is performed imperfectly, some degree of error will be introduced into the candidate isolator trajectories, and the extent to which the resulting performance and constraints are satisfied will be affected. Some indication of how the accumulation of the individual curve-fitting errors will affect the final response of the dynamic system designed by the indirect synthesis method is given in subsequent examples.

A flow chart illustrating the overall indirect-synthesis computational process is shown in Fig. 3. The first three steps constitute the time-optimal synthesis phase and provide the optimal

---

[**]The minimax (or Chebychev) definition of curve fitting, which minimizes the maximum deviation being matched, may also be used in place of the least square measure of curve-fitting error [Eq. (12)].

TIME-OPTIMAL SYNTHESIS (Steps 1,2,3)

STEP 1 (SYSTEM DYNAMICS)

Determine system response functions for unit impulse loadings

STEP 2 (LINEAR PROGRAM PREPROCESSOR)

Use the response functions and the specification of the constraint functions and performance indices to construct the $\overline{A},\overline{B},\overline{C}$ matrices that define the standard linear programming problem: Find the vector $\overline{Z}$ that minimizes $\tau = \overline{C}\overline{Z}$ subject to $\overline{A}\overline{X} = \overline{B}$

STEP 3 (LINEAR PROGRAM SOLVER)

Use a linear programming code to solve for the minimum $\tau = \tau^*$ and corresponding $\overline{Z}^*$. Next, determine the time-optimal performance Q* and optimum trajectories $u^*(t)_j$ of the jth isolator $j=1,2,....J$ from $\tau^*,\overline{Z}^*$

SYSTEM IDENTIFICATION

$j=j+1$

Select the configuration (i.e., $u_j^c(x_j,\dot{x}_j,\overline{a}_j)$) of the jth isolator

Assume an initial set of parameters for the jth isolator $(\overline{a}_j)_n$ where $n=1$ corresponds to the initial estimate

$n=n+1$

Compute the measure of curve-matching $H(\overline{a}_j)_n$

Logic of the curve-fitting routine or the mathematical programming code establishes a new set of parameters $(\overline{a}_j)_{n+1}$ that tend toward the minimization of $H(\overline{a}_j)$

Is $H(\overline{a}_j)$ minimized? — No

Yes

Are all J candidate isolators synthesized? — No

Yes

Substitute the optimized parameters, i.e., $(\overline{a}_j^*)$ $j=1,....J$, into the candidate system equations and compute
• Candidate system performance
• Response constraints

Are both the level of performance and degree of satisfaction of the response constraints acceptable?

No — Select other candidate isolators

Yes — STOP: Satisfactory system is achieved

Fig. 3 - Indirect synthesis flow chart

190

performance Q^*, the optimum forces u_j^*, and trajectories $x_j^*, \dot{x}_j^*$ necessary for the system-identification phase. The n-loop refers to the iteration, for a fixed j, on the $\bar{\tau}_j$ values in the process of minimizing $H(\bar{\tau}_j)$ and the j-loop refers to the determination of the parameters in each of the J candidate isolators. The outermost loop refers to the process of redesign. If a set of parameters $\bar{\alpha}_j$ that results in a satisfactory curve match for the postulated isolator configuration does not exist, then other candidate isolator elements can be used. This involves repeating part of the system identification loop, but does not require a fresh time-optimization solution.

To illustrate the important features of the indirect synthesis method, two representative shock isolation configurations will be considered. The first of these is the rectilinear multi-degree-of-freedom, multi-isolator system shown in Fig. 2(a), referred to as Model 1. The second type of system [Fig. 2(b)] consists of a single isolator interposed between a rigid (isolated) mass and an arbitrary linearly elastic base structure which may be some combination of continuous or lumped mass members such as springs, beams, and shells. This is referred to as Model 2. A specific example of this latter system is shown in Fig. 2(c), where the base structure is represented by a shell-type housing. Although more complicated systems consisting of combinations of the types shown in Fig. 2(a) and 2(b) can be conceived (e.g., the general problem shown in Fig. 1), the essential features of multi-isolator, multidegree-of-freedom isolation system design can be sufficiently explored with the two problem types selected.

Model 1

The problem is to synthesize the J shock isolators appearing in the system shown in Fig. 2(a), such that the absolute value of the peak acceleration of mass m_1 is minimized, subject to prescribed constraints on the relative displacement between each neighboring mass. In the time-optimal synthesis phase, the J candidate isolator forces are expressed as explicit functions of time; consequently, the equations of motion for the system represented in Fig. 2(a) can be written as the following system of first-order differential equations:

$$\dot{X} = \begin{bmatrix} \dot{X}_j \\ ---- \\ \dot{X}_{j+J} \end{bmatrix} =$$

$$\begin{bmatrix} X_{j+J} \\ ---------------------- \\ \frac{1}{m_{j+1}}u_{j+1}(t) - (\frac{1}{m_{j+1}} + \frac{1}{m_j})u_j(t) + \frac{1}{m_j}u_{j-1}(t) \end{bmatrix}_{j=1,2,\ldots J}$$

subject to initial conditions

$$\begin{bmatrix} X_j(0) \\ ------- \\ X_{j+J}(0) \end{bmatrix} = \begin{bmatrix} \bar{d}_0 \\ --- \\ \bar{v}_0 \end{bmatrix}_{j=1,2,\ldots J} \qquad (14)$$

where the notation

$X_j = x_j =$ Relative displacement across the terminals of the jth isolator

$X_{j+J} = \dot{x}_j =$ Relative velocity across the terminals of the jth isolator; u_0, u_J/m_{J+1} are both defined as zero, and u_{J+1}/m_{J+1} is defined as $-d^2y/dt^2$ (the rigid base input acceleration which corresponds to f_1 in terms of the general notation given earlier)

is introduced.

The time-optimal synthesis response characteristics are obtained by performing the three steps outlined. Let the performance index be the maximum absolute acceleration of the mass m_1, i.e., $h = u_1/m_1$ [see Eq. (4)] where

$$Q = \max_t \left[\left| \frac{u_1(t)}{m_1} \right| \right] \qquad 0 \le t \le t_f .$$

We seek to determine the u_j such that Q is minimized, i.e.,

$$Q^* = \min_{u_j} \left[Q \right] \qquad j=1,2,\ldots J ,$$

and relative displacement constraints for each isolator of the form

$$|X_j(t)| \le \tilde{X}_j \text{ for all } 0 \le t \le t_f, \ j=1,2,\ldots J$$

[see Eq. (7)] are satisfied for prescribed values of $\tilde{X}_j$.

191

To illustrate the general notation of Eq. (3), consider the special case $J=1$. The response quantity to be constrained is the relative displacement $X_1(t) = C_1(t)$. The net contribution to Eq. (3), for $k=1$ is made up of three parts:

(1) The solution to Eq. (14) due to only $u_1(t)$ [i.e., with $\ddot{y}(t)=0$] subject to homogeneous initial conditions $X_1(0) = X_2(0) = 0$;

$$\frac{1}{m_1} \int_0^t R(t-\tau) u_1(\tau) d\tau$$

where $R(t-\tau) = -(t-\tau)$.

(2) The solution to Eq. (14) due to only $\ddot{y}(t)$ [i.e., $u_1(t)=0$] subject to homogeneous initial conditions $X_1(0) = X_2(0) = 0$;

$$\int_0^t R(t-\tau)\, \ddot{y}(\tau)\, d\tau$$

(3) The homogeneous solution to Eq. (14) [i.e., both $y(t)$, $u_1(t)$ taken as zero] subject to the nonhomogeneous initial conditions;

$$(v_o)_1 t + (d_o)_1$$

The net response $C_1(t)$ is the sum of these three terms:

$$C_1(t) = -y(t)+y(0)+(d_o)_1+[(v_o)_1 + \dot{y}(0)]t$$

$$+ \frac{1}{m_1} \int_0^t (t-\tau) u_1(\tau) d\tau$$

To obtain an explicit expression for the constraint relation (7) in terms of the variable u_{11}, a discretization scheme must be selected. For example, a piecewise constant representation of u_1 is:

$$u_1(t) = \sum_{r=1}^{I} [u_{1r}-u_{1(r-1)}] H(t-t_r),$$

where H is the unit step-function. With this expression the constraint Eq. (7) now appears as

$$-\widetilde{X}_1 \le -y(t_i)+y(0)+(d_o)_1+[(v_o)_1+\dot{y}(0)]t_1$$

$$+\frac{1}{m_1}\sum_{r=1}^{I}[u_{1r}-u_{1(r-1)}]\int_0^{t_i} H(\tau-t_r)[\tau-t_i]\,d\tau \le \widetilde{X}_1$$

$$\text{for } i=1,2,\ldots I$$

where, since the bounds on the constrained quantity are the same for all t, $C_{11}^U = \widetilde{X}_1$ and $C_{11}^L = -\widetilde{X}_1$. The linear form in which the discretized components of $u_1(t)$ appear in both the expression for the performance and constraints, provides the basis for formulating the problem of minimizing Q as one of linear programming [2].

The solution to the time-optimal synthesis problem provides both the optimum performance index Q^* and the corresponding optimum force, displacement and velocity trajectories ($u_j^*(t), x_j^*(t), \dot{x}_j^*(t)$). This information constitutes the results of the time-optimal synthesis phase, and is used as input for the system identification phase. The values for the system parameters are obtained by evaluating relation (13) for each isolator in the system.

Next we consider the consequence of imperfect curve-matching. An indication of how the accumulation of the J individual curve-fitting errors will affect the final response of the system [i.e., $u_j^c(x_j,\dot{x}_j,\bar{\alpha}_j^*)$ in place of u_j in Eqs. (14)] designed by the indirect synthesis method can be obtained from analysis of a specially defined system composed of a collection of isolators that satisfy the linear property

$$u_j^c(x_j+v,\dot{x}_j+w,\bar{\alpha}_j)=u_j^c(x_j,\dot{x}_j,\bar{\alpha}_j)+u_j^c(v,w,\bar{\alpha}_j).$$

$$(15)$$

For example, a linear spring and dashpot is parallel (Eq. (10a) with $N_j = N_j' = 1$ satisfies this criterion.

The relation

$$\bar{\delta}(t) = \bar{X}(t) - \bar{X}^*(t) \qquad (16)$$

defines $\bar{\delta}$ as the difference between the trajectory determined from the time-optimal synthesis problem and the trajectory obtained by integrating the equations of motion of the candidate system, (i.e., Eq. (14) with $u_j^c(x_j,\dot{x}_j,\bar{\alpha}_j^*)$ in place of $u_j(t)$). The parameters $\bar{\alpha}_j^*$ appearing in $u_j^c(x_j,\dot{x}_j,\bar{\alpha}_j^*)$ are the results obtained from the sequence of curve-fitting problems defined by Eq. (13).

A relationship between the J curve-fitting errors $\Delta_j(t)$ and the trajectory error $\bar{\delta}(t)$ can be obtained by first substituting $\bar{X} = \bar{X}^* + \bar{\delta}$ into the candidate system equations; then substituting $\bar{X}=\bar{X}^*$ and $u_j = u_j^*(t)$ into the time-optimal system equations [i.e., into Eqs. (14) with $u_j = u_j^*(t)$] and subtracting these two differential equations and initial conditions; and using (15) to cancel out like terms. Thus, the error differential equation

192

$$\dot{\overline{z}} = \begin{bmatrix} \dot{\delta}_j \\ ----- \\ \dot{\delta}_{j+J} \end{bmatrix} =$$

$$\begin{bmatrix} \delta_{j+J} \\ ------------------------------ \\ \frac{1}{m_{j+1}} u^c_{j+1}(\delta_{j+1}, \dot{\delta}_{j+1}, \overline{\alpha}^*_{j+1}) - \left[\frac{1}{m_{j+1}} + \frac{1}{m_j}\right] \cdot \\ ------------------------------ \\ \cdot u^c_j(\delta_j, \dot{\delta}_j, \overline{\alpha}^*_j) + \frac{1}{m_j} u^c_{j-1}(\delta_{j-1}, \dot{\delta}_{j-1}, \overline{\alpha}^*_{j-1}) \end{bmatrix}$$

$$- \begin{bmatrix} \overline{0} \\ ------------------------------ \\ \frac{1}{m_{j+1}} \Delta_{j+1}(t) - \left[\frac{1}{m_{j+1}} + \frac{1}{m_j}\right]\Delta_j(t) + \frac{1}{m_j} \Delta_{j-1}(t) \end{bmatrix}$$

$$j = 1, 2, \ldots J \quad (17)$$

is obtained subject to initial conditions

$$\begin{bmatrix} \delta_j(0) \\ ------- \\ \delta_{j+J}(0) \end{bmatrix} = \begin{bmatrix} \overline{0} \\ ----- \\ \overline{0} \end{bmatrix}_{j=1,2,\ldots J} \quad (17a)$$

where

$$u^c_o = 0; \quad \Delta_o = 0; \quad \frac{u^c_{J+1}}{m_{J+1}} = 0; \quad \frac{\Delta_{J+1}}{m_{J+1}} = 0;$$

$$\frac{u^c_J}{m_{J+1}} = 0; \quad \text{and} \quad \frac{\Delta_J}{m_{J+1}} = 0.$$

Let the variable $\delta^o_{jn}(t)$ denote the solution to Eqs. (17) subject to a unit impulse applied in the nth row of the nonhomogeneous portion of Eq. (17), i.e., the second column vector. (All other terms in the nonhomogeneous vector taken as zero.) Then the trajectory error across the jth isolator that is due to the expression

$$\frac{1}{m_{n+1}} \Delta_{n+1}(t) - \left[\frac{1}{m_{n+1}} + \frac{1}{m_n}\right] \Delta_n(t)$$

$$+ \frac{1}{m_n} \Delta_{n-1}(t)$$

appearing in only the nth row of the nonhomogeneous portion of Eq. (17) is given by

$$\delta_{jn}(t) = \int_0^t -\delta^o_{jn}(t-\tau)\left[\frac{1}{m_{n+1}} \Delta_{n+1}(\tau)\right.$$

$$\left. -\left[\frac{1}{m_{n+1}} + \frac{1}{m_n}\right] \Delta_n(\tau) + \frac{1}{m_n} \Delta_{n-1}(\tau)\right] d\tau. \quad (18)$$

The total error across the nth isolator is the contribution from all the $n=1,2, \ldots J$ rows of the lower partition of the nonhomogeneous term in Eq. (17)

$$\delta_j(t) = \sum_{n=1}^J \delta_{jn}(t) \quad j=1,2,\ldots 2J. \quad (18a)$$

The expressions (18) illustrate the manner in which the trajectory error $\delta_j(t)$ for the jth isolator depends upon the accumulated curve-fitting errors experienced at each isolator in the system. The form of the error solution given by Eqs. (18) does not depend on the particular performance or constraint definition (i.e., peak acceleration of mass m_1 and constraints across each isolator) selected for illustration, but holds for the general criteria definitions given earlier.

In Eqs. (18), note that, as the peak value of each $\Delta_n(\tau)$ curve tends toward zero ($0 \leq \tau \leq t_f$), the peak value of the $\delta_j(t)$ quantity tends toward zero, thus indicating that the indirect synthesis trajectory is approaching the time-optimal synthesis trajectory. Consequently, any constraints imposed on the state variables in the originally defined optimization problem tend toward being satisfied exactly as the curve fitting errors get smaller.

Since the system performance depends upon the $\overline{X}(t)$ trajectories, it too will be affected by the accumulated curve-fitting error. The performance obtained by indirect synthesis will tend toward the time-optimal synthesis performance Q^* as curve-fitting errors tend toward zero.

If any of the $\Delta_n(t)$ functions are substantially large, the $\delta_j(t)$ quantity may lead to candidate system trajectories $x_j(t) = x^*_j(t) + \delta_j(t)$ that exceed the originally imposed constraints. Such a situation may be rectified by selecting other candidate isolator configurations containing more open parameters that consequently may result in closer curve fitting, hence smaller trajectory errors.

Model 2

The system of Fig. 2(b) has been selected to illustrate some system identification techniques for situations in which a single isolator is interposed between a mass and a general linear elastic structure (e.g., a configuration of interconnected beams, shells, springs). Two different approaches to the system identification problem are discussed. The first is essentially the same as that of Model 1, wherein the determination of the optimum system parameters $\overline{a}^*$ are found through curve-matching on the isolator force. The second approach differs in that the curve-matching is performed on the response trajectories rather than on force. In addition to providing an alternate method for performing the parameter identification, this second approach holds the promise of more closely satisfying the response constraints by emphasizing curve-matching to the response trajectories instead of to the isolator forces. Expressions relating the curve-matching error to the trajectory error is made for both approaches.

During the time-optimal phase the isolator forces are expressed as explicit functions of time. This leads to system equations for Model 2 in the form

$$m[\ddot{y} + \ddot{r} + \ddot{x}] + u(t) = 0$$

$$r = g(\ddot{y},t) + \int_o^t R(t-\tau)u(\tau)d\tau \qquad (19)$$

subject to

$$x(0) = d_o, \quad \dot{x}(0) = v_o \qquad (19a)$$

Since there is only one isolator in this problem, the nonessential subscript one on $m, x, R,$ and u have been omitted.

The term $R(t-\tau)$ is the elastic structure relative displacement response [i.e., the distance between the rigid base and the isolator attachment point in Fig. 2(b)] due to a unit impulse applied at the isolator attachment point. The term $g(\ddot{y},t)$ contains both the response contribution of the base input acceleration alone and the homogeneous solution (i.e., the response with $\ddot{y}$ and $u(t)$ both zero, subject to any nonhomogeneous initial conditions or r and $\dot{r}$).

There is nothing fundamentally new in the determination of the time-optimal synthesis characteristics for this model. The only computational difference between Models 1 and 2 is that, in the latter, the calculations involving the unit impulse responses are more involved.

We start the system identification phase by assuming the time-optimal synthesis phase is completed, i.e., the optimum force u^* and trajectories $x^*, \dot{x}^*, r^*$ are known such that the performance is optimum and the constraints are satisfied.

First Approach. The candidate system equations are defined by replacing $u(t)$ in Eq. (19) with $u^c(x, \dot{x}, \overline{a})$. The determination of the optimum parameters $\overline{a}^*$ is essentially the same as the general case, where j assumes the value 1 in relations (10), (11), and (13). The effect of imperfect curve-matching for the class of isolators defined by Eq. (15) can be ascertained for Model 2 in the same fashion as for Model 1. The error differential equation relating the curve fitting error $\Delta(t)$ and the trajectory error $\delta(t)$ (where $x(t) = x^* + \delta$) is given by

$$m\left[\ddot{\delta}(t) + \frac{d^2}{dt^2}\int_o^t u^c(\delta(\tau), \dot{\delta}(\tau), \overline{a}^*)R(t-\tau)d\tau\right]$$

$$+ u^c(\delta(t), \dot{\delta}(t), \overline{a}^*) \qquad (20)$$

$$= \Delta(t) + m\frac{d^2}{dt^2}\int_o^t \Delta(\tau)R(t-\tau)d\tau$$

subject to

$$\delta(0) = \dot{\delta}(0) = 0 \qquad (20a)$$

This form is valid for time-varying $\overline{a}$ coefficients, since Eq. (15) is the only assumption made regarding the functional form of u^c. In the special, but important, case where the coefficients $\overline{a}$ are constant, a solution to Eqs. (20) can be expressed as

$$\delta(t) = \int_o^t \Delta(\tau)W_1(t-\tau)d\tau, \qquad (21)$$

where

$$W_1(t) = \mathcal{L}^{-1}\left[\frac{1+s^2mR(s)}{ms^2+[1+s^2mR(s)]\,u^c(1,s,\overline{a}^*)}\right] \qquad (22)$$

The operator $\mathcal{L}^{-1}$ represents the inverse Laplace transform, $R(s)$ is the Laplace transform of $R(t)$, and s is the transform variable on time.

194

Equation (21) leads to the relation

$$\delta(t) \; \leq \; \max_{\tau} |\Delta(\tau)| \int_0^t |W_1(t-\tau)| d\tau \qquad (23)$$
$$0 \leq \tau \leq t,$$

which illustrates that the upper bound on $\delta(t)$ is reduced, according to the peak magnitude of the curve-fitting error, and in the limit as the peak $\Delta(\tau)$ approaches zero. It follows that the time-optimal and candidate system trajectories approach each other.

Second Approach. In this approach, curve-matching is performed by fitting the time-optimal synthesis trajectory $x^*(t)$ to a specially constructed version of the candidate system equations obtained by replacing $x,\dot{x}$ with $x^*,\dot{x}^*$ in only the expression for r

$$m[\ddot{y}(t)+\ddot{r}'(t)+\ddot{x}'(t)]+u^c(x'(t),\dot{x}'(t),\overline{a})=0$$

$$r'(t)=g(\ddot{y}(t),t) \qquad (24)$$

$$+\int_0^t u^c(x^*(t),\dot{x}^*(t),\overline{a})R(t-\tau)d\tau$$

subject to

$$x'(0) = d_o, \quad \dot{x}'(0) = v_o \qquad (24a)$$

The notation x' and r' rather than x, r is used to emphasize that the dependent variables of this set differ from those of the actual candidate equations. The essential difference is that a solution of Eqs. (24) requires solving a simple second-order (generally nonlinear) differential equation. This is a consequence of r' being a known function of time (depending only upon $\overline{a}$). In contrast, the solution to the actual candidate system equations requires analysis of the entire system including the structural elements, because the unknowns, $x,\dot{x}$ appear in the integral expressions for r.

For a candidate isolator configuration, the design parameters $\overline{a}^*$ are determined such that

$$H'(\overline{a}) = \int_0^{t_f} [\Delta'(\tau)]^2 d\tau \qquad (25)$$

is minimized, where

$$\Delta'(t) = x^*(t) - x'(t,\overline{a}), \qquad (26)$$

x^* is the time optimal trajectory, and $x'(t,\overline{a})$ is a solution to the Eqs. (24). Analogous to Eq. (12), Eq. (25) can be approximated with a finite sum, and the optimum design parameters are determined as the solution to

$$H'(\overline{a}^*) = \min_{\overline{a}} \left[\sum_{i=1}^I [\Delta'(t_i)]^2 \Delta t_i \right] (27)$$

Because the determination of $x'(t_i,\overline{a})$ can be rapidly computed from Eqs. (24) for an assumed set of trial parameters $\overline{a}_i$, Eq. (27) can be minimized with a mathematical search code without much difficulty. This approach has an advantage in that the curve matching is performed on the relatively smooth $x^*(t)$ curve rather than on the less smooth $u^*(t)$ curve required with the first approach.

A relation between the curve fitting-error $\Delta'(t)$ (for an isolator that satisfies Eq. (15) with constant $\overline{a}$) and the trajectory error $(\delta(t) = x(t)-x^*(t))$ can be obtained in a similar manner, and is given by the expression

$$\delta(t) = \int_0^t \Delta'(\tau)W_2(t-\tau)d\tau \qquad (28)$$

where

$$W_2(t) = \mathcal{L}^{-1}\left[\frac{u^c(1,s,\overline{a}^*)}{ms^2+[ms^2R(s)+1]\,u^c(1,s,\overline{a}^*)} \right] (29)$$

Consider another method for performing the curve-matching on $x^*(t)$. This approach eliminates the repetitive integration of Eqs. (24) previously required to attain the minimum value of $H'(a)$. The first step is to construct an integral equation of the form

$$x'(t) = x^p(t) + \int_0^{t_f} K(t,\tau)F(\tau)d\tau \quad (30)$$

from the equation $\ddot{x}'(t) = F(t)$,

where

$$F(t) = -\ddot{y}(t)-\frac{u^c}{m}(x'(t),\dot{x}'(t),\overline{a})-g(\ddot{y}(t),t)$$

$$-\frac{d^2}{dt^2}\int_0^t u^c(x^*(\tau),\dot{x}^*(\tau),\overline{a})R(t-\tau)d\tau$$

$$\qquad (31)$$

$$= \tilde{F}(t,x',\dot{x}',\overline{a}).$$

195

The kernal $K(t,\tau)$ is constructed so as to satisfy one of four possible types of homogeneous conditions,

(1) $x'(0)=0$, $x'(t_f)=0$ and
x^P meets $x^P(0)=x^*(0)$, $x^P(t_f)=x^*(t_f)$

(2) $x'(0)=0$, $\dot{x}'(t_f)=0$ and
x^P meets $x^P(0)=x^*(0)$, $\dot{x}^P(t_f)=\dot{x}^*(t_f)$

(3) $\dot{x}'(0)=0$, $x'(t_f)=0$ and
x^P meets $\dot{x}^P(0)=\dot{x}^*(0)$, $x^P(t_f)=x^*(t_f)$

(4) $x'(0)=0$, $\dot{x}'(0)=0$ and
x^P meets $x^P(0)=x^*(0)$, $\dot{x}^P(0)=\dot{x}^*(0)$,

and x^P is constructed to satisfy the actual corresponding nonhomogeneous boundary condition, with $F(t)=0$.

For example, the $K(t,\tau)$ function and corresponding $x^P(t)$ term for the first type are given by

$$K(t,\tau) = \begin{cases} \tau(\frac{t}{t_f}-1) & 0 \le \tau \le t \\ t(\frac{\tau}{t_f}-1) & t \le \tau \le t_f \end{cases}$$

and $x_p = t[x^*(t_f)-x^*(0)]/t_f + x^*(0)$. Other kernals are tabulated in Ref. [1] Note that $K(t,\tau)$ does not depend on the functional form of the candidate isolator hence does not have to be reconstructed for other candidate isolator configurations. For this method, the curve-fitting deviation is obtained by first substituting $x'=x^*(t)$ and $\dot{x}'=\dot{x}^*(t)$ into Eq. (31), then Eq. (31) into Eq.(30) and finally that result into Eq. (26) to give

$$\Delta'(t) = x^*(t)$$

$$-\left[x^P(t)+\int_o^{t_f} K(t,\tau)\widetilde{F}(\tau,x^*(\tau),\dot{x}^*(\tau),\bar{a})d\tau\right]. \quad (32)$$

Consider the particular case wherein u^c can be written so that its unknown design parameters, or functions G_n of the unknown parameters, factor so that

$$u^c(x,\dot{x},\bar{a}) = \sum_n G_n(\bar{a})U_n(x,\dot{x}) \quad (33)$$

For example, the isolator Eq. (10a) is one of this type. When Eq. (33) is substituted into (32), $\Delta'(t)$ becomes

$$\Delta'(t) = x^*(t)-T(t)-\sum_n G_n(\bar{a})S_n(t) \quad (34)$$

where

$$T(t)=x^P(t)-\int_o^{t_f} [\ddot{y}(\lambda)+\ddot{g}(y(\lambda),\lambda)]K(t,\lambda)d\lambda$$

and $\quad (35)$

$$S_n(t)=\int_o^{t_f}\left[U_n(x^*(\lambda),\dot{x}^*(\lambda))\right.$$

$$\left.+\frac{d^2}{d\lambda^2}\int_o^\lambda U_n(x^*(\tau),\dot{x}^*(\tau))R(\lambda-\tau)d\tau\right]d\lambda.$$

The quantities $T(t)$, $S_n(t)$ are functions of time that do not have to be re-evaluated for different values of $\bar{a}$: Consequently, when Eq. (34) is substituted into Eq. (27), the computations for $h'(\bar{a})$ can be made without repetitive integration of Eqs. (24) as previously required. Equation (27) is then minimized to obtain the optimum design parameters. If assumption (33) does not apply, the more general expression (32) can be used directly in Eq. (27). The minimization computing time of $H'(\bar{a})$ will be increased since re-evaluation of the integral appearing in Eq. (32) will be required for each trial $\bar{a}$.

The relation between the curve-fitting error $\Delta'(t)$ (for an isolator satisfying Eq. (15) with constant $\bar{a}$) and the trajectory error $\delta(t)=x(t)-x^*(t)$ is given by

$$\delta(t)=\int_o^t \Delta'(\lambda)W_3(t-\lambda)d\lambda+\Delta'(0)\int_o^t W_3(\lambda)d\lambda$$

$$+\dot{\Delta}'(0)\int_o^t\int_o^\lambda W_3(\tau)d\tau d\lambda \quad (36)$$

where

$$W_3(t)= \pounds^{-1}\left[\frac{-ms^2}{ms^2+[ms^2R(s)+1]u^c(1,s,\bar{a}^*)}\right]$$

Note that, $\Delta'(0) = 0$ if type 1 or type 2 boundary conditions are used; $\Delta'(0) = 0$ if type 3 is used; and both $\Delta'(0) = 0$ and $\dot{\Delta}'(0) = 0$ if type 4 is used.

The $\delta(t)$ error differs, depending on which of the four types is selected. Once a computational scheme has been set up to implement the formulation, it is a simple matter to experiment with any or

196

all of these four kernals. Our current experience with the method, based on several example problems, indicates that the second and third types result in a smaller trajectory error than the first or fourth.

Other System Identification Techniques

The literature contains a variety of system identification techniques other than those treated here. Most of these methods are concerned with the problem of matching a variable that occurs as a dependent variable in a differential equation. Some of the earlier methods for parameter identification are the so-called equation-of-motion methods (e.g., the Laplace transform method, the Fourier transform method and the derivative method) which are discussed in Ref. [4]. These methods are limited in that linearity in the variable to be fitted is required. A generalization of these methods, Shinbrot's method function, Ref. [5] overcomes this restriction and has been successfully applied to an isolation design (Ref. [1]) by the indirect-synthesis method. A more recent technique, termed quasilinearization, [6], [7], [8], is also a general identification method which accepts nonlinearities in the variable to be fitted.

CONCLUDING REMARKS

The complete success of the indirect synthesis method depends largely upon the magnitudes of the curve-matching deviations ($\Delta(t)$ or $\Delta'(t)$) experienced during the system identification phase. If a candidate isolator has a great degree of flexibility, in that its response characteristics can be made to closely conform to those of the time-optimal synthesis characteristics, the method should work quite effectively. Results with single isolators [1] have been encouraging. The application of the method to multi-isolator problems has yet to be demonstrated, although it appears promising. Its success depends on the accumulation of curve-fitting errors [e.g., as demonstrated with Model 1, Eqs. (18)].

If a candidate configuration is not capable of responding in a near optimum fashion regardless of the design parameters selected, the trial configuration can be rejected and replaced with one possessing a greater potential for conforming to the time-optimal response (e.g., a configuration with more open parameters). To a degree, this redesign step is one of trial and error; however, because the indirect synthesis method allows evaluation of each of

these candidates without reanalysis of the entire system dynamics, a series of candidate configurations can be rapidly analyzed.

If excessive curve-fitting errors result in a set of design parameters that leads to an unacceptable candidate system response (i.e., the constraints imposed by the originally stated optimization problem are violated), then in such situations it may be desirable to employ direct synthesis. The indirectly synthesized parameters may already be in the same neighborhood of an optimum solution and can be used as intelligent starting values for the initiation of a direct search.

REFERENCES

1. W. D. Pilkey, et al., "Shock Isolation Synthesis Study," SAMSO Report on Contract F04694-67-C-0136, to be published

2. T. Liber and E. Sevin, "Optimal Shock Isolation Synthesis," Shock & Vibrations Bull. No. 35, Part 5, pp. 203-215, Feb. 1966

3. D. W. Marquardt, "Least Square Estimation of Nonlinear Parameters," Share Program Library SDA 3094-01

4. H. Greenberg, "A Survey of Methods for Determining Stability Parameters of an Airplane from Dynamic Flight Measurements," NACA TN-2340, 1951

5. M. Shinbrot, "On the Analysis of Linear and Nonlinear Dynamical Systems from Transient Response Data," NACA TN-3288, 1954

6. R. Bellman and R. Kalaba, Quasi-Linearization and Nonlinear Boundary Value Problems, pp. 132-139, American Publishing Inc., New York, 1965

7. R. Bellman, H. Kagiwada, and R. R. Kalaba, "Quasi-Linearization, Systems Identification and Prediction," Rand RM-3812-PR, Aug. 1963

8. R. Bellman, "On the Construction of a Mathematical Theory of the Identification of Systems," Rand RM-4769-PR, Nov. 1966.

DISCUSSION

Mr. Howard (Aerospace Corp.): Have you gotten any results from more than a one degree freedom system?

Mr. Pilkey: Yes, we have results at the moment from only a single isolator, but we do have results from multi-degree of freedom systems. Also the paper deals with error analyses for multi-degree-of-freedom multi-isolator systems.

Mr. Howard: Do you feel you have the computational facilities to handle multi-degree of freedom multi-isolator problems?

Mr. Pilkey: Yes, the paper refers to a computer code developed for the linear programming problem which will accept any structural analysis as input as long as it is linear, and it may have an arbitrary number of isolators. The code is developed, running and debugged.

ANALYTIC INVESTIGATION OF BELOWGROUND SHOCK-ISOLATING

SYSTEMS SUBJECTED TO DYNAMIC DISTURBANCES

J. Neils Thompson, Ervin S. Perry, Suresh C. Arya
The University of Texas at Austin
Austin, Texas

This paper presents an analytical method used to determine a closed-form solution of the response characteristics of belowground circular concrete liner packing systems when subjected to dynamic disturbances. A mathematical model consisting of a two-degree-of-freedom system with lumped masses and springs having distributed weight was used to represent the system. Piecewise continuous linear equations of motion were developed for the trilinear phases of crushing of the backpacking material and solved by use of principal coordinates on a digital computer.

This study showed that low crushing strength and large thicknesses of backpacking are desirable characteristics of backpacking materials. So long as crushing takes place in the backpacking layer, liner accelerations due to a dynamic input disturbance will stay below the maximum input accelerations. An increase in the mass of the backpacking results in increases to both the deformation of the backpacking layer and the acceleration of the liner, but it acts also as a damping agent in decaying vibrations in the liner.

INTRODUCTION

Shock-isolating systems for belowground-protective-structures have been given more attention during the past few years due to the need for developing structures that are capable of withstanding explosion-generated ground motions and accelerations. The motion generated may be due to close-in nuclear bursts or detonations of other high-powered explosions.

The types of belowground structures most commonly built have been in the form of circular rings of reinforced concrete. They are mainly used as galleries and passages to serve as chambers to house equipment and personnel. Recently protective structures normally consisted of reinforced concrete placed in direct contact with the surrounding rock or soil medium. The design criteria generally used for such systems were that the primary structure must be adequate to resist the external forces. Various shock-isolating devices have been used to protect sensitive equipment.

The anticipated serious damage due to extremely high energy explosions requires that the strength of the primary structure be extremely high unless the structure is buried very deep in rock and has complex shock-isolating devices to protect the equipment. To avoid such expensive and complex solutions, more attention is being given to isolating the entire structure from the surrounding medium.

The purpose of shock-isolating systems is to reduce the shockwave that reaches the structure by providing a medium of crushable, energy-absorbing material outside the structure. The important features of such a system are that:

1. With every shockwave, the energy and acceleration should be damped through the permanent deformation of the backpacking layer.

2. The permanent deformation of the back-packing layer should not exceed its bottoming strain from either a single shockwave or from a specified number of smaller successive shockwaves.

3. The acceleration of the liner structure should not exceed certain specified limits or

the input acceleration.

4. For certain systems, required to withstand multiple shots, the backpacking layer should retain as much as possible its original shape.

The broad objectives of the research study being reported here were to determine analytically the response characteristics and structural behavior of the reinforced concrete cylindrical liner, as well as the energy-absorbing, backpacking layer. The designer of protective structural systems can use these results to formulate approximations for developing a design and to aid in determining the effects of various parameters on the system.

Previous research on such systems consisted of experimental work on laboratory models and the testing of actual systems in the field. (Refs. 1, 2 and 5.) A few analytical investigations have also been conducted on shock-isolating, energy-absorbing materials and reported in Refs. 3 and 4, and have provided guidance for the conduction of this research.

Structural System Investigated

The structural system investigated consisted of a reinforced concrete liner of cylindrical shape encompassed by a low-strength, lightweight concrete backpacking layer. The parameters of the system were as follows: (1) A structural concrete liner with radii varying from 3.5' to 8.0' and with a minimum percentage of reinforcement (total 1%) with ratio of thickness to mean liner radius = 0.2, as shown in Fig. 1, and (2) a backpacking layer with thickness varying from 4.0' to 8.0' made of low-strength concrete with density varying from 30 to 50 lbs/cft and compression yield strength varying from 15 to 200 psi.

A disturbance function of ground displacement with amplitudes varying from one to four feet and a residual permanent displacement of 50% was used. The period of disturbance function was 400 msec. Corresponding velocity and acceleration curves were obtained from the first and second derivations of the displacement curve, respectively.

To investigate this structural system analytically, it was necessary to establish an equivalent mathematical model, which would provide a similar response and state of stress. In the field of structural dynamics, a spring-mass system has been found to be a convenient

representation of an actual structure. To achieve that objective, dynamic equivalent parameters were used in this sytem. The important parameters involved were the masses and stiffness of the liner and of the backpacking and the forcing functions. The equivalent system is shown in Fig. 2.
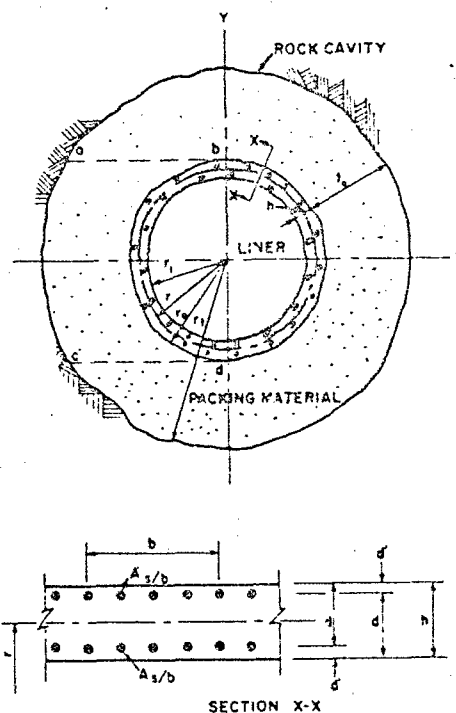
Fig. 1 - Liner backpacking system
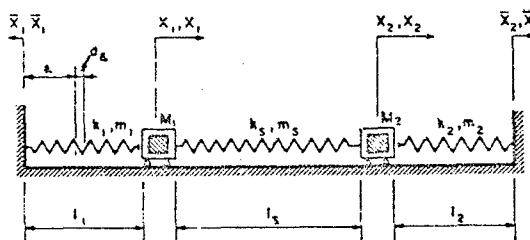
Fig. 2 - Spring mass system in equilibrium position

200

The stiffness of the liner was established such that the deflection of the lumped masses under concentrated loads was the same as that for the corresponding point on the liner under circular segmental distributed pressure (i.e., at points of maximum deflection). The approximate value obtained is given by Eq. 1.

$$k_s = \frac{11.5E_cI}{r^3} \qquad (1)$$

This liner spring stiffness (k_s) was assumed to behave elastically and the same in both tension and compression.

The equivalent spring stiffness for the backpacking layer was obtained by giving a horizontal displacement A_1 to the liner (this caused deformation in the backpacking layer of the same magnitude A_1), which varied cosisoidal towards the vertical diameter. After ignoring the second order strain terms and making the assumption that either the backpacking layer was fully in the elastic phase or fully in the plastic phase, the variable strains were integrated and from that expression the total force acting on the liner was obtained as given by Eq. 2.

$$P_e = \frac{-A_1E_er}{2t_p} \qquad (2)$$

The unit elastic spring stiffness was obtained by dividing Eq. 2 by the ground displacement amplitude A_1 and as given by Eq. 3.

$$k_e = \frac{-E_e\,r_o}{2t_p} \qquad (3)$$

For the range of plastic phase, the unit plastic spring stiffness was obtained by using the modulus of backpacking E_p instead of E_e in Eq. 4.

$$k_p = \frac{-E_p\,r_o}{2t_p} \qquad (4)$$

The structural behavior of the backpacking spring for unloading and reloading was assumed to have the same modulus as the initial elastic stiffness. The paths of loading and unloading are shown in Fig. 3.
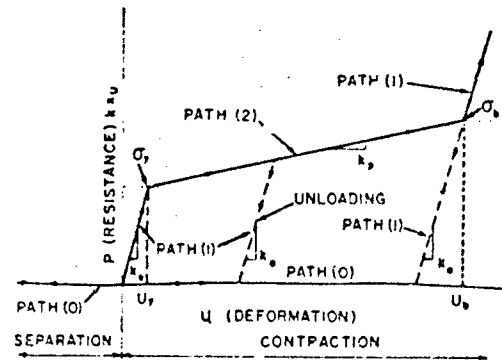
Fig. 3 – Assumed structural behavior of backpacking

The mass elements for the liner were obtained by distributing the actual mass of the liner, lumped 10% at each end of the spring k_s and the rest of the 20% uniformly distributed in the spring k_s. The dynamic equivalence in harmonic motion was 50% of the static mass but the actual mass of the liner was used with the understanding that in most cases the tunnel liner would be used for housing equipment and instruments. The additional mass for these fixtures, when moving in phase with the liner, will add their masses to the liner mass.

The backpacking material used could be cellular or vermiculite concrete. Their strengths and properties are given in Table I. A typical stress-strain curve is shown in Fig. 4.

The mass of the backpacking layer was included in this analysis and was assumed to be distributed in the springs k_1 and k_2. Only that volume of the backpacking layer was included in the mass which lies in the region a,b,c,d, drawn on the exterior dimension of the liner as shown in Fig. 1.

The forcing function employed was in the form of a ground displacement disturbance caused by the nuclear blast. This function was approximate and was based on a mixture of theoretical studies made for ideal conditions

TABLE I

PROPERTIES OF BACKPACKING CONCRETES

Type of Concrete	Density (w) Lb/Ft^3	Yield Stress (σ_y) PSI	Bottoming Stress (σ_b) PSI	Yield Strain (ε_y) %	Bottoming Strain (ε_b) %	Modulus of Elasticity (E_e) PSI	Tangent Modulus (E_p) PSI	Elastic Spring Stiffness (k_e)k/ft*	Plastic Spring Stiffness (k_p)k/ft*
** Cellular	20	20	40	2	40 to 60	1000	34	$226\frac{r_o}{t_p}$	$7.7\frac{r_o}{t_p}$
** Vermiculite	50	200	330	2	40	10000	342	$2260\frac{r_o}{t_p}$	$77.3\frac{r_o}{t_p}$

* Per ft. of width of backpacking layer, See Eqs. 3 and 4 respectively.
** Ref. (4)
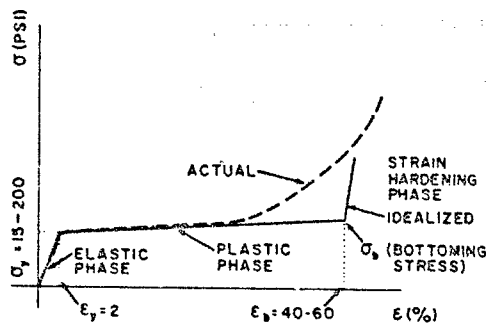
Fig. 4 – Stress–strain curve for low–strength concretes

and actual field conditions. The displacement curve is shown in Fig. 5. To use this displacement curve in this analytical solution, a tenth order polynomial function was derived by the method of least-square-fit and is given by Eq. 5(a).

$$x_1 = \sum_{i=1}^{10} a_i (t)^i \quad (a)$$

$$t_d = (t - t_r) \quad (5)$$

$$x_2 = \sum_{i=1}^{10} a_i (t_d)^i \quad (b)$$

The effect of a time lag in the ground motion experienced by the windward and leeward sides was found to be negligible and hence was ignored in the actual results but was included in the mathematical formulation. The displacement on the leeward side is given by Eq. (5b) which includes the effect of time lag. Instead of deriving separate polynomials for the velocity and accelerations of the ground, these were respectively obtained by single and double differentiations of Eq. 4.

Development of Solution

The lumped mass system shown in Fig. 2 was assumed to represent the actual liner-backpacking structure as shown in Fig. 1. Due consideration was given to the use of the two-degree-of-freedom system instead of the multi-degree-of-freedom system. The investigations reported in Refs. 3 and 4 showed that the rigid body response of the multi-degree system differs to the extent of about 5% from the rigid body response of the single-degree-of-freedom system. Except for very low amplitudes in the two-degree-of-freedom system, rigid body response was always greater than the body deformation of the liner; therefore, the error involved in the general solution would not be significant.

The equations of motion for the spring-lumped-mass system for Fig. 2 are developed in the Appendix. The effect of damping was ignored due to the unknown nature of the damping coefficient. The mass of stiffness springs

202
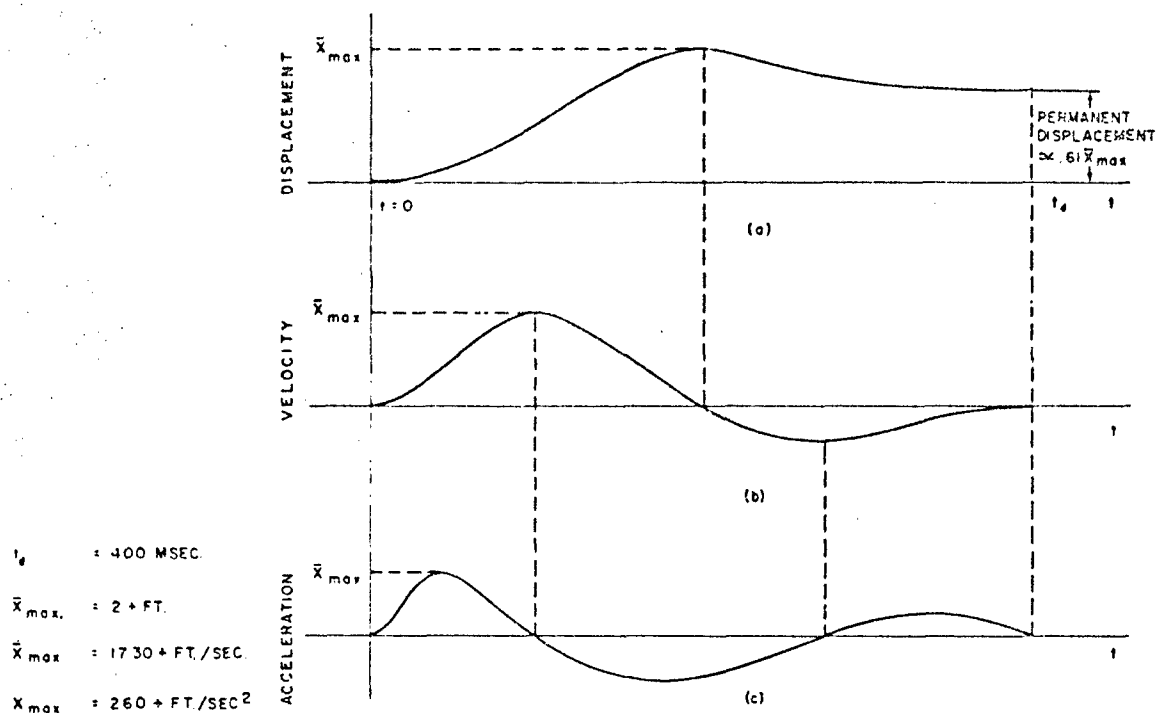
Fig. 5 - Idealized wave form for direct-
transmitted ground shock

t_d : 400 MSEC.

$\bar{x}_{max.}$: 2 + FT.

$\dot{\bar{x}}_{max}$: 17 30 + FT./SEC.

$\ddot{x}_{max}$: 260 + FT./SEC^2

of the backpacking layers and tunnel liner were taken into consideration. The general solution was obtained by the use of principal coordinates and is given by Eq. 11, in the Appendix. The solution in x-coordinates can be obtained by using the transformation relationship as given by Eq. 6, in the Appendix.

In the solution of Eq. 11, the parameters k_1, k_2, m_1 and m_2 change in value depending upon the elasto-plastic conditions of springs k_1 and k_2 and the contact of the liner with the backpacking layer. The elasto-plastic conditions and the resulting natural frequencies of the system during those phases are shown in Fig. 6. Upon combining the change of spring stiffnesses k_1 and k_2 of the windward and leeward sides respectively, it resulted in nine sets of piecewise continuous equations of motions to provide a complete response.

The solution of these nine piecewise continuous equations of motion was made

continuous in x-coordinates by the use of the following boundary conditions:

Initial Conditions (at t = 0):

$$x(0) = 0+ \qquad (a)$$

$$\dot{x}(0) = 0+ \qquad (b)$$

$$\ddot{x}(0) = 0+ \qquad (c)$$

Boundary Conditions (at $t = t'$):

$$x_\ell(t') = x_n(t') \qquad (d)$$

$$x_\ell(t') = \dot{x}_n(t') \qquad (e) \qquad\qquad (6)$$

The subscripts ℓ and n refer to equation of motions, which provide for continuity between two phases of deformation of the backpacking material.

203
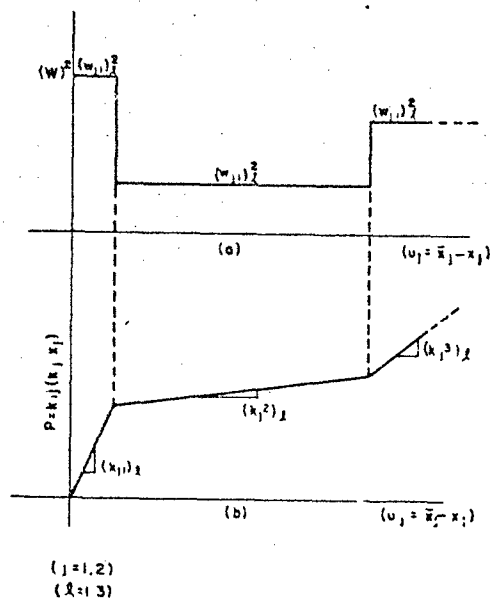
Fig. 6 - Natural frequency and backpacking stiffness relationship

Whenever the liner was not in contact with either side of the backpacking layer, it was assumed that the backpacking layer stayed in contact with the rock cavity rather than with the liner. The equation of motion (Eq. 9 in Appendix) was modified for the rigid body as given by Eq. 7 below:

$$\ddot{r}_1 = 0 \qquad \text{(a)}$$
$$\ddot{r}_2 + \omega_{22}^2 \, r_2 = 0 \qquad \text{(b)} \tag{7}$$

The solution of these equations was simple and the constant of integration was evaluated by the initial and boundary conditions.

The solutions for the responses of displacement, velocity, acceleration of liner masses and the liner deformation were computed at successive intervals of time using a Control Data CDC 6600 digital computer.

Discussion of Results

The significant results obtained from analytical work, as previously described, are presented in this section. The main study was directed towards showing the response characteristics of the backpacking layer as a shock-isolating agent. Parameters associated with

the system that were varied included backpacking thickness (t_p), radius of liner (r_i), amplitude of the input displacement pulse (A_1), mass of the tunnel liner (M) and the mass of the backpacking layer (m). In this paper only the most important parameters connected with the design criteria, such as backpacking layer thickness (t_p), inside radii of the tunnel liner (r_i) and the amplitude of the displacement pulse (A_1) are discussed. The other parameters, such as yield strength (σ_y), density of backpacking material, and liner stiffness $(k_s) = 5{,}000$ kips per ft per ft width were kept as common variables.

Case I. Variation of backpacking layer thickness (t_p).

$$t_p = 1.0', 2.0', 4.0' \text{ and } 8.0'$$

$$A_1 = 2.0'$$

$$r_i = 3.5'$$

Case II. Variation of inside radius of liner (r_i).

$$t_p = 4.0'$$

$$A_1 = 2.0'$$

$$r_i = 3.5', 5.0', 6.0', 7.0' \text{ and } 8.0'$$

Case III. Variation of amplitude of input displacement pulse (A_1).

$$t_p = 4.0'$$

$$A_1 = 1.0', 2.0' \text{ and } 4.0'$$

$$r_i = 3.5'$$

In order to facilitate the explanation, the side of the system which first encounters the shockwave is called the "windward" side or the loaded side, and the other side is referred to as the "leeward" side or the unloaded side.

For all the cases studied, the results with respect to time are shown for the maximum responses of acceleration $(\ddot{x}_1)$, of the liner mass (M_1), and backpacking layer deformation (u_1) of windward side of the backpacking layer for different values of yield strength of the material (σ_y). The reason that only the response of the windward side of the system is presented is that the leeward side of the system was not directly put into motion by the input pulse of the shockwave but by the momentum of the system generated by its inertial

forces. The influence of inertial forces was assumed to encounter appreciable damping, and consequently the system would slow down or would stop with time. The internal damping of the system would also be appreciable after the shockwave had passed; therefore the system was studied only for the duration of the shockwave.

Case I. In Fig. 7 are shown the structural systems investigated. Their results are presented in Fig. 8, which show the crushing of the windward side of the backpacking layer and the acceleration response ($\ddot{x}_1$) for the windward mass (M_1) for different yield strengths (σ_y) of the material. It will be noticed that the
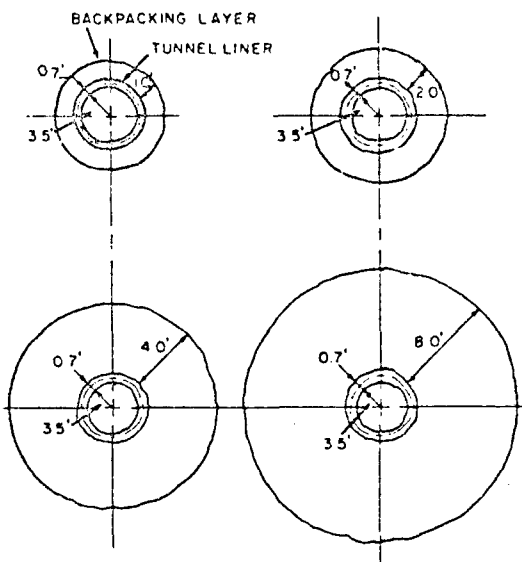
Fig. 7 - Case I - Structural systems with variation in backpacking thickness (t_p)

backpacking layer undergoes three stages of deformation as the shockwave passes through the system. The first stage of the deformation was up to the elastic limit, which was recoverable with the passing of the shockwave. On studying the acceleration of the mass M_1, in this stage, it will be noted that its value exceeded the input acceleration ($\ddot{x}_1$), or in other words, the resulting liner acceleration was greater than the input acceleration. With the increase of the yield strength of the material and/or of the backpacking layer thickness, the range of deformation in the elastic stage increased, but this did not cause the reduction

in the acceleration of the liner. Another function of the backpacking layer is to curb the transmission of external forces to the liner. This action does not take place in the elastic phase because the backpacking does not crush and thus does not reduce the forces transmitted. Also, this results in the liner moving essentially with the ground displacement. For the elastic phase it can be concluded that the backpacking layer serves a very limited purpose.

During the second stage of the deformation, which lies between the elastic and bottoming limit of the backpacking material and which is larger than the elastic stage, significant reduction occurred in the acceleration of the liner. As the yield strength of the material was decreased, the resulting acceleration of the liner also decreased. Therefore, the use of a low yield strength material for the backpacking layer is an effective means of reducing acceleration of the liner.

The contribution of the backpacking layer thickness in the second stage was found to be twofold. First, the use of a larger thickness reduced the liner acceleration. The second effect was found to be that the larger thickness permits a larger range of material yield strength compared to the smaller thickness. Therefore, for materials that change strength with time, the greater thickness provides a longer period of usable life.

The third stage which the backpacking layer might undergo lies beyond the bottoming limit. During this stage it was noted that the acceleration of the liner stayed below the input acceleration but the external forces were transmitted to the liner which negated the further usefulness of the backpacking.

Summarizing these stages of behavior of the backpacking layers, we find that in the elastic stage only the net force on the liner was reduced; in the plastic stage both acceleration and net force on the liner were reduced. In the bottoming stage, only the acceleration of the liner was reduced.

Case II. It was noted in this case that the systems with the larger radii had the same effect on all three of the main characteristics, namely, acceleration of the liner, deformation of the backpacking layer and available range of yield strength of material were similar in nature as discussed in Case I.

MAXIMUM INPUT
ACCELERATION

$t_p = 8'0"$
$t_p = 4'0"$
$t_p = 2'0"$
$t_p = 1'0"$

$\bar{X}_1$ (MAX. ACCELERATION OF LINER) FT./SEC^2

400   360 200   200   100

ELASTIC LIMIT

$t_p = 8'0"$
$t_p = 4'0"$
$t_p = 2'0"$
$t_p = 1'0"$

BOTTOMING LIMIT

$u_1 = \bar{X}_1 - X_1$ $u_2 = X_2 - \bar{X}_2$

σ_y (YIELD STRENGTH OF MATERIAL) PSI

150

100

50

0   2   .4   .6   .8   1.0   1.2   1.4   1.6   1.8

U_1 (MAX. CRUSHING DEFORMATION OF BACKPACKING) FT.

PARAMETERS
ε_y	YIELD STRAIN	2%
ε_b	BOTTOMING STRAIN	40%
σ_b	BOTTOMING STRESS	1.67 σ_y
r_i	INSIDE RAD. OF LINER	3.5'
h	THICKNESS OF LINER	0.2r
A_1	INPUT DISP PULSE AMP	2! +
t_d	INPUT DISP PULSE PER.	400 m sec

Fig. 8 - Acceleration and deformation responses for
variation of backpacking thickness (t_p)

Case III. One purpose of this case was to
determine the relationship of results when
different magnitudes of input displacement pul-
ses were applied to a single structural system.
Associated with these input pulses are veloc-
ities and accelerations. The magnitudes of
these quantities are shown in Fig. 9.

In Fig. 10 are presented the results for
these forcing quantities.

The effect of variation of the input pulse
on the acceleration of the liner was quali-
tatively different but was quantitatively in pro-
portion to their variation in certain ranges of
yield strength of material. This proportionality
also existed in the peak crushing of the back-
packing layer. The other effect of this case
was that as long as the peak amplitude of the
pulse was less than the bottoming limit, the
backpacking layer never crossed into the
bottoming phase. The resulting effect on avail-
able range of yield strength was similar as in
Cases I and II. The higher magnitude pulses
caused larger ranges of yield strength to be

effective. The magnitude of range of yield
strength was the same for all values of pulses,
thus indicating that the responses on the sys-
tem were linearly proportional to the magnitude
of the shockwave applied.

Conclusions

1. Low crushing strengths and large thick-
nesses are desirable characteristics of back-
packing materials for use in shock-isolating
systems.

2. For the imposed damaging accelerations,
it is necessary to design the backpacking layer
such that permanent crushing will occur if the
external forces that are transmitted to the liner
are to be reduced.

3. Crushing in the backpacking layer will
not exceed the bottoming limit as long as the
magnitude of the input displacement pulse is
less than the product of the bottoming strain
and the thickness of the backpacking layer.

206

BACKPACKING LAYER
TUNNEL LINER

$r_i = 35'$
a

$r_i = 50'$
b

$r_i = 60'$
c

$r_i = 70'$
d

$r_i = 80'$
e
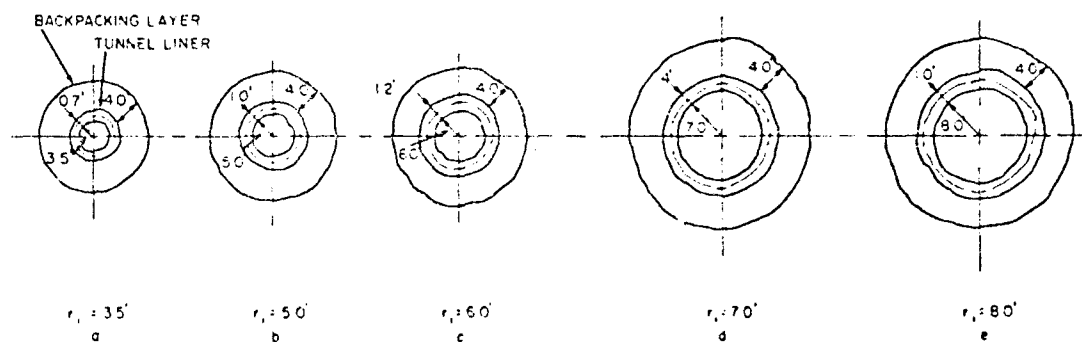
Fig. 9 - Case II - Structural systems with variation in inside radius of liner (r_i)

MAXIMUM INPUT ACCELERATION

$\dot{X}_1$ (MAX ACCELERATION OF LINER) FT./SEC.^{2}

σ_y (YEILD STRENGTH OF MATERIAL)PSI

ELASTIC LIMIT

BOTTOMING LIMIT

u_1 (MAX CRUSHING DEFORMATION OF BACKPACKING)FT.

PARAMETERS

ξ_y	YIELD STRAIN	2%
ξ_b	BOTTOMING STRAIN	40%
σ_b	BOTTOMING STRESS	$1.67\sigma_y$
h	THICKNESS OF LINER	$0.2r$
t_p	THICKNESS OF BACKPACKING	$4.0'$
t_d	INPUT DISP PULSE PER.	400 m sec
A_1	INPUT DISP PULSE AMP	2.' +

Fig. 10 - Acceleration and deformation responses for variation of inner radius of liner (r_i)

207

4. Liner acceleration from a dynamic input disturbance will stay below the maximum input acceleration as long as crushing in the backpacking exceeds the elastic phase. It is possible for the liner acceleration to exceed slightly the input acceleration for short periods of time if the backpacking remains in the elastic phase.

5. The maximum crushing deformation in the backpacking layer varies inversely linearly with the yield stress of the backpacking material for the same output.

6. The deformation of the liner is reasonably small during the crushing phase of the windward side of the backpacking. However, if the bottoming phase is reached in the subsequent phases, the deformation would be sufficient to result in failure of the liner provided damping resistance is negligible in the system.

7. With an increase in the thickness of the backpacking only, the results indicate:

    a. A decrease in the acceleration of the liner.

    b. An increase in the range of useful yield strength of the backpacking material.

    c. An increase in the deformation of the backpacking.

8. With an increase in the inner radius of the liner only, the results indicate:

    a. A decrease in the acceleration of the liner.

    b. An increase in the range of useful yield strength of the backpacking material.

    c. An increase in the deformation of the backpacking.

9. With an increase in the amplitude of the input displacement pulse only, the results indicate:

    a. An increase in the range of useful yield strength of the backpacking material.

    b. An increase in the acceleration of the liner.

    c. An increase in the rattling of the liner.

    d. An increase in the deformation of the backpacking.

Acknowledgments

APPENDIX

The symbols adopted for use in the following formulation are given at the end of the Appendix. The equations of motion for the system as shown in Fig. 2, as well as their solutions, are also presented in this section.
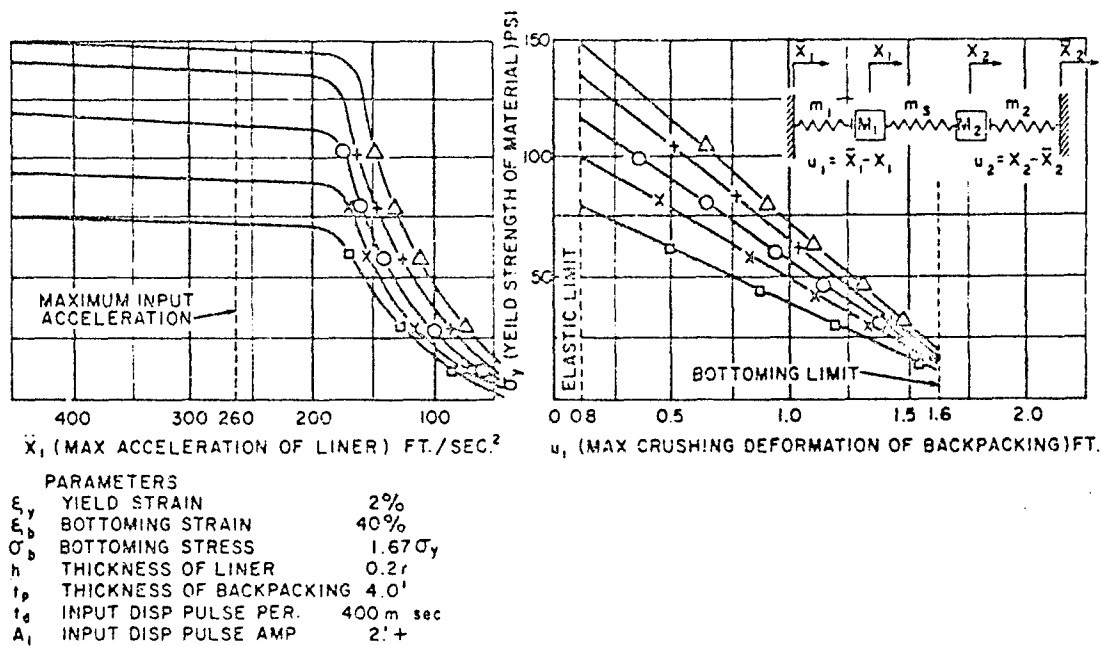
The kinetic and the potential energies of the system measured at the equilibrium position are given by Eq. 1, assuming that the velocity varies linearly along the length of springs.

$$
\begin{aligned}
K.E. &= 1/2 M_1\, \dot{x}_1^2 = 1/2 M_2\, \dot{x}_2^2 + 1/2\, \frac{m_1}{\ell_1} \\
&\quad \int_0^{\ell_1} \left[\dot{\bar{x}}_1 + (\dot{x}_1 - \dot{\bar{x}}_1)\, \varepsilon/\ell_1 \right]^2 d\varepsilon \\
&\quad + 1/2\, \frac{m_s}{\ell_s} \int_0^{\ell_s} \left[\dot{x}_1 = (\dot{x}_2 - \dot{x}_1)\, \varepsilon/\ell_s \right]^2 d\varepsilon \\
&\quad + 1/2\, \frac{m_2}{\ell_2} \int_0^{\ell_2} \left[x_2 + (\dot{\bar{x}}_2 - \dot{x}_2)\, \varepsilon/\ell_2 \right]^2 d\varepsilon
\end{aligned}
$$

$$
\begin{aligned}
P.E. &= 1/2\, k_1\, (x_1 - \bar{x}_1)^2 + 1/2\, k_s\, (x_2 - x_1)^2 \\
&\quad + 1/2\, k_2\, (\bar{x}_2 - x_2)^2
\end{aligned} \tag{1}
$$

Equation 1 when employed in Lagrange's equation, assuming a conservative force field, resulted in a pair of equations of motion. The effect of damping in Eq. 1 was ignored because of the unknown nature of the magnitude.

Equation 2 is a set of linear differential equations of second order and it is evident that coupling between them is due to k_s and m_s.

208

$$\left(M_1 + \frac{m_1 + m_s}{3}\right) \ddot{x}_1 + \frac{m_s}{6}\ddot{x}_2 + (k_1 + k_s)x_1 -$$

$$(k_s)x_2 = k_1 \dot{x}_1 - m_1 \ddot{x}_1$$

$$\left(\frac{m_s}{6}\right)\ddot{x}_1 + \left(M_2 + \frac{m_2 + m_s}{3}\right)\ddot{x}_2 - (k_s)x_1 +$$

$$(k_2 + k_s)x_2 = k_2 \dot{x}_2 - m_2 \ddot{x}_2 \qquad (2)$$

These equations can be solved by the use of principal coordinates (normal coordinates) such that the equations of motion will appear in a diagonalized form and can be uncoupled. The equations are arranged first in the matrix symbolic form as shown by Eq. 3.

$$M\{\ddot{x}\} + K\{x\} = \{C\} \qquad (3)$$

Equation 3 can be written as given by Eq. 4 by multiplying by M^{-1} and defining a dynamic matrix by $H = M^{-1}k$:

$$\{\ddot{x}\} + H\{x\} = M^{-1}\{C\} \qquad (4)$$

Introducing principal coordinates, Eq. 4 appears as given by Eq. 5.

$$\{\ddot{r}\} + \Lambda\{r\} = \{Q\} \qquad (5)$$

where Λ is a diagonal matrix with λ_{jj} as its diagonal elements.

Since $\{x\}$ and $\{r\}$ describe the same physical system, these coordinates can be transformed into each other. Assuming a linear relationship, this transformation is represented by Eq. 6.

$$\{x\} = [\mu]\{r\} \qquad (a)$$

$$\{\dot{x}\} = [\mu]\{\dot{r}\} \qquad (b)$$

$$\{\ddot{x}\} = [\mu]\{\ddot{r}\} \qquad (c) \qquad (6)$$

Substituting Eq. 6 into Eq. 4 and premultiplying it by $[\mu]^{-1}$, Eq. 7 is obtained.

$$\{\ddot{r}\} + [\mu]^{-1}H[\mu]\{r\} = [\mu]^{-1}M^{-1}\{C\} \qquad (7)$$

Comparing Equations 5 and 7, then $[\mu]^{-1}H[\mu] = \Lambda$ and $[\mu]$ is a modal matrix.

In order to obtain the modal matrix $[\mu]$, and the natural frequencies of the system, the determinate of the homogeneous part of Eq. 5 must be zero. Therefore, the characteristic function of the matrix H is given by Eq. 8.

$$\Delta(\lambda) = \lambda I - H = 0 \qquad (8)$$

From eigenvalues λ_{jj}, eigenvectors can be obtained which will form transformation matrix $[\mu]$. The matrix $[\mu]$ when employed in Eq. 7 will diagonalize the matrix H. Now Eq. 5 is rewritten in expanded forms with the definition $\lambda_{jj} = \omega_{jj}^2$.

$$\ddot{r}_j + \omega_{jj}^2 r_j = \bar{c}_{1j}\bar{x}_1 + \bar{c}_{2j}\ddot{\bar{x}}_1 + \bar{c}_{3j}\bar{x}_2 +$$

$$c_{4j}\ddot{\bar{x}}_2 \quad (j = 1,2) \qquad (9)$$

Wherein $\bar{c}_{ij}$ are known constants made up of the mass matrix.

The general solution of Eq. 9 consists of homogeneous and particular parts. The homogeneous solution is simple and is given by Eq. 10.

$$r_j = A_j \sin \omega_{jj} t + B_j \cos \omega_{jj} t$$

$$x_i = \sum_{j=1}^{2} \mu_{ij} r_j \quad (i = 1,2)\,(j = 1,2) \quad (10)$$

The particular solution of Eq. 8 can be found by the use of Laplace transforms. The resulting solution is as follows:

$$r_j(t) = A_j \sin \omega_{jj} t + B_j \cos \omega_{jj} t$$

$$+ \bar{c}_{1j} \left[\sum_{i=1}^{10} a_i \prod_{p=1}^{i+1} (i - p + 1)! \right.$$

$$\left. \frac{\cos(p-1)\pi}{2(\omega_{jj})^{p+1}} t^{(i-p-1)} \right]$$

$$+ \bar{c}_{2j} \left[\sum_{i=2}^{10} (i)(i-1)a_i \prod_{p=1}^{i-1} (i-p-1)! \right.$$

$$\frac{\cos(p-1)^-}{2(\imath_{jj})^{p+1}} \quad {}^{(i-p-1)}]$$

$$+ \bar{c}_{3j} [\sum_{i=1}^{10} a_i \, {}^{(i-1+1)} \, {}^{i+1}_{p=1} !$$

$$\frac{\cos(p-1)^-}{2(\imath_{jj})^{p+1}} \, t_d \, {}^{(i-p+1)}]$$

$$+ \bar{c}_{4j} [\sum_{l=2}^{10} a_i \, (i)(i-1) \, {}^{i-1}_{p=1} \, {}^{(i-p-1)} !$$

$$\frac{\cos(p-1)^-}{2(\imath_{jj})^{p+1}} \, t_d \, {}^{(i-p-1)}]$$

$$i-p-1 \geq 0 \quad (j = 1, 2) \qquad (11)$$

The first and second derivatives of Eq. 11 will give velocities and accelerations in r-coordinates. The general response can be obtained in x-coordinates by the use of Eq. 6 (a, b, and c).

Symbols and Notations

A	=	area of cross section.
A_1	=	maximum amplitude of input displacement pulse.
A_j	=	constant of integration of "jth" equation.
A_s, A'_s	=	area of tensile and compressive steel reinforcement.
b	=	unit length of cylindrical tunnel liner.
c	=	seismic velocity of rock media surrounding the cavity.
$\bar{c}_{ij}$	=	coefficients of particular solution obtained from "ith" and "jth" equations.
d	=	effective depth to steel reinforcement.
d'	=	concrete cover.
E_c	=	modulus of elasticity of structural concrete.
E_e	=	modulus of elasticity of backpacking material in compression.
E_p	=	modulus of backpacking material in compression in plastic phase.
E_s	=	modulus of elasticity of reinforcing steel.
f_y	=	yield strength of reinforcing steel in the liner.
f_c	=	compressive strength of the structural concrete in the liner.
h	=	thickness of cylindrical tunnel liner.
h_m	=	ordinate of mass of liner on horizontal diameter.
I	=	moment of inertia of liner thickness for unit length.
k	=	general spring stiffness of backpacking layer.
k_e, k_p	=	spring stiffness of backpacking layer in compression in elastic and plastic phases respectively.
k_s	=	liner elastic stiffness.
k_1, k_2	=	spring stiffness of windward and leeward sides of backpacking layer.
ℓ_s	=	length of equivalent spring of liner.
ℓ_1, ℓ_2	=	spring lengths of windward and leeward sides of backpacking layer.
M	=	mass of liner.
M_1, M_2	=	lumped masses of liner.
m	=	mass of backpacking layer.
m_s	=	total distributed mass of liner spring k_s.
m_1, m_2	=	total distributed masses of backpacking layer springs k_1 and k_2.
P_e	=	total horizontal pressure of backpacking layer on liner per unit length.
p	=	radial pressure of backpacking layer on liner per unit length.
r_j	=	"jth" coordinate in principal axes.
r, r_i, r_o	=	mean, inside and outside radii respectively of liner.
r_t	=	inside radius of rock cavity.
t_d	=	time period of input displacement pulse.
t_p, t_θ	=	thickness of backpacking without deformation and with deformation at central angle θ respectively.
t_r	=	transit time of shockwave traversing rock cavity diameter.
u	=	deformation of backpacking layer.
u_1, u_2	=	elastic deformations of crushing deformations on windward and leeward sides of backpacking layer.
x_1, x_2	=	displacements of lumped masses M_1 and M_2 respectively.
$\bar{x}_1, \bar{x}_2$	=	input displacements on windward and leeward faces of rock cavity due to shockwave.
$\ddot{x}$	=	maximum input acceleration.
γ	=	specific weight of structural concrete.
δ_d	=	horizontal deformation of liner.

$\varepsilon_e, \varepsilon_b$	=	strains of backpacking material at elastic and bottoming points respectively.
θ	=	central angle (polar coordinates).
λ_{ij}	=	eigenvalue of i, j modal columns.
σ_y, σ_b	=	compression stresses of backpacking material at yield and bottoming points respectively.
$\sigma_r(\theta)$	=	radial stress in backpacking at angle.
ω	=	natural circular frequency of dynamic system, radians per second.
ω_{ij}	=	natural frequency of "ith", "jth" mode of system.

Superscripts

$\cdot$	=	$\dfrac{d}{dt}$
$\cdot\cdot$	=	$\dfrac{d^2}{dt^2}$
$+$	=	slightly greater

References (Reports)

1. C. J. Costantio and R. L. Marino, Jr., "Response of Cylindrical Shells Encompassed With Isolation Material to a Plane Pressure Pulse," I. I. T. Research Institute, Chicago, Ill. Research Report AFWLTR-76-122, February, 1966.

2. W. R. Cox, "Interaction of Cylindrical Lining and Packing System with Rock Deformation," PhD Thesis, University of Illinois, Urbana, 1964.

3. W. P. Dawkins, "Dynamic Response of a Tunnel Liner-Packing System," PhD Thesis, University of Illinois, Urbana, Ill., 1966.

4. M. Salah Nossier, Ervin S. Perry and J. Neils Thompson, "A Study of the Response of Backpacking Material Encasing a Tunnel Liner Subjected to a Dynamic Disturbance," Structural Mechanics Research Laboratory, The University of Texas, Austin, Texas, December, 1966.

5. R. H. Sievers, Jr., and A. R. Stacy, "Structural Response and Permanent Displacement Measurement," U. S. Army Engineer Research and Development Laboratories, Fort Belvoir, Va., Operation Hardtack, June, 1960.

211

GAS DYNAMICS OF ANNULAR CONFIGURED SHOCK MOUNTS

W.F. Andersen
Westinghouse Electric Corp.
Sunnyvale, California

A rigorous analytical solution of the gas dynamics phenomena of annular configured shock mounts has been achieved. The results of this study are of particular interest in shock isolation applications where the rattle space thickness-to-diameter ratio is small, on the order of 1:50. The specific case for which the solution was developed and applied was in the lateral shock support portion of the Poseidon Fleet Ballistics Missile System. The solutions for several shock inputs have been obtained, and experimental verification of the analytical results has been produced. It was found that loads on the missile from the air effects were of the same magnitude of those from the lateral support material. Other important findings included pressure distributions affecting missile buckling strength and high frequency oscillations affecting missile components. In addition, a simplified mathematical model is presented, consisting of linear spring, mass, and damper elements, which adequately duplicates the forcing function response of the gas dynamic effects of the special case considered.

INTRODUCTION

Recent trends in the shock hardening of large missiles have been toward the use of a shock mitigating material such as flexible foam or elastomer structure in the annulus between the missile and its container. The space efficiency obtained with this kind of lateral shock isolator makes it an attractive choice for retrofitting larger diameter missiles into existing launch tubes or silos, and for cases where costs are sensitive to container diameters. There are two primary design considerations relating to the shock mitigation properties of such a system. The first is the stiffness of the foam or elastomer structure. This may be controlled by changes in polymer formulation and/or structural properties. The other consideration is that of air compression and gas dynamics. Gas dynamics effects are an important feature of any shock isolator employed in an annular space envelope where the thickness-to-diameter ratio is small.

In order to demonstrate the acceptable performance of a complex spring-mass system, it is often necessary to model the system mathematically and show through analytical means that the system will function adequately. To accomplish this, the system components must first be modeled and tested separately, then combined and tested with the design input.

This paper deals with the modeling of the gas dynamics effects inherent in an annular configured shock mount. The specific case analyzed is the lateral support portion of the Poseidon Missile System. The Poseidon (C-3) lateral support system as shown in Figure 1, consists of a series of elastomer pads placed around the missile in several annular rings. The basic internal structure is that of a pre-buckled column as shown in Figure 2. The pad is normally free breathing, except during shock when the inertial effects of air have to be considered.

During relative motion between the missile and launch tube, the air trapped in the annulus will be compressed on one side and will be expanded on the other side. (Hereafter, the locations around the missile will be referred to as indicated on Figure 3.) To relieve this pressure
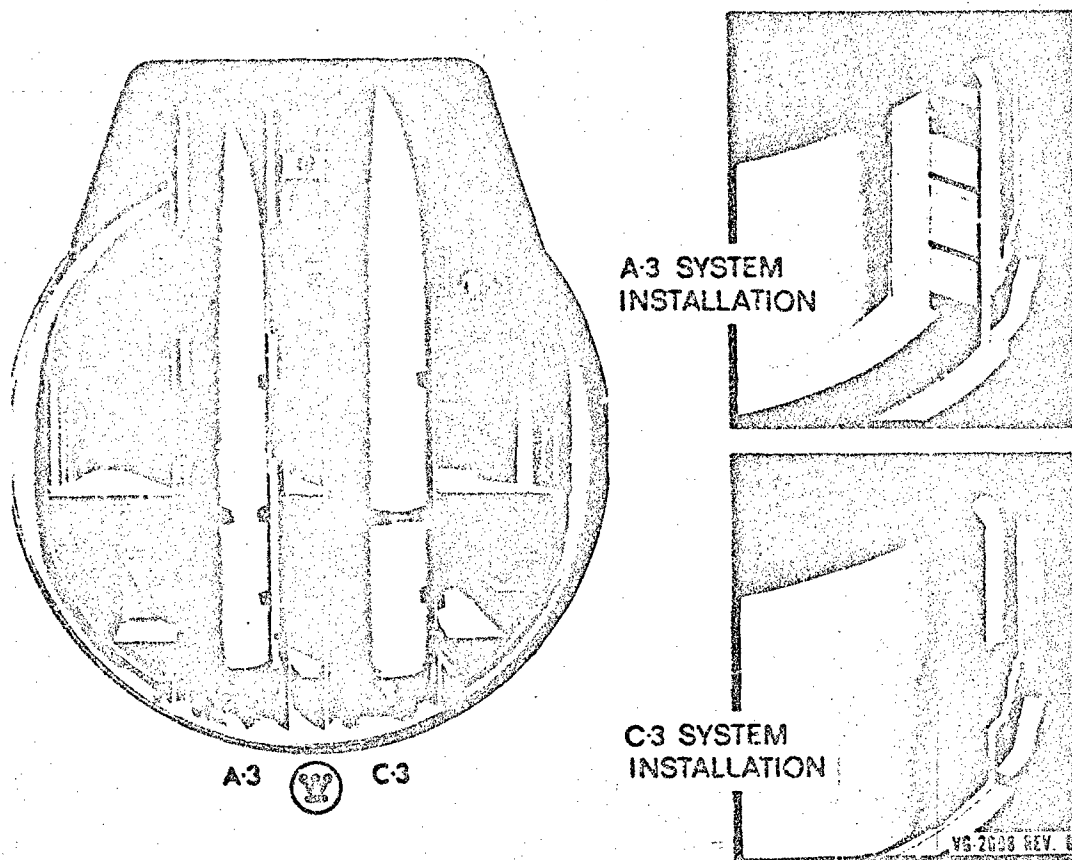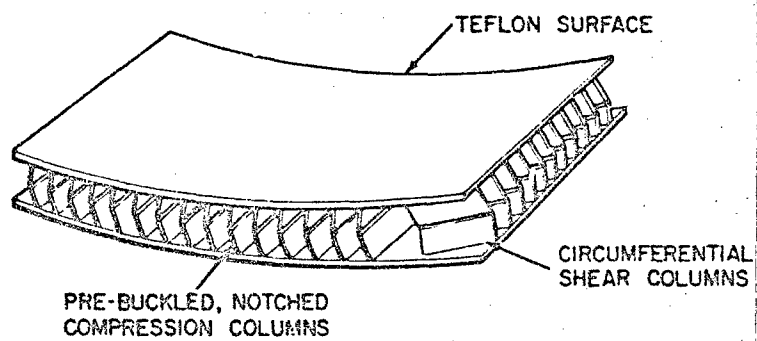
Figure 1. Poseidon (C-3) Lateral Support System

A·3 SYSTEM INSTALLATION

C·3 SYSTEM INSTALLATION

A·3   C·3

TEFLON SURFACE

CIRCUMFERENTIAL SHEAR COLUMNS

PRE-BUCKLED, NOTCHED COMPRESSION COLUMNS

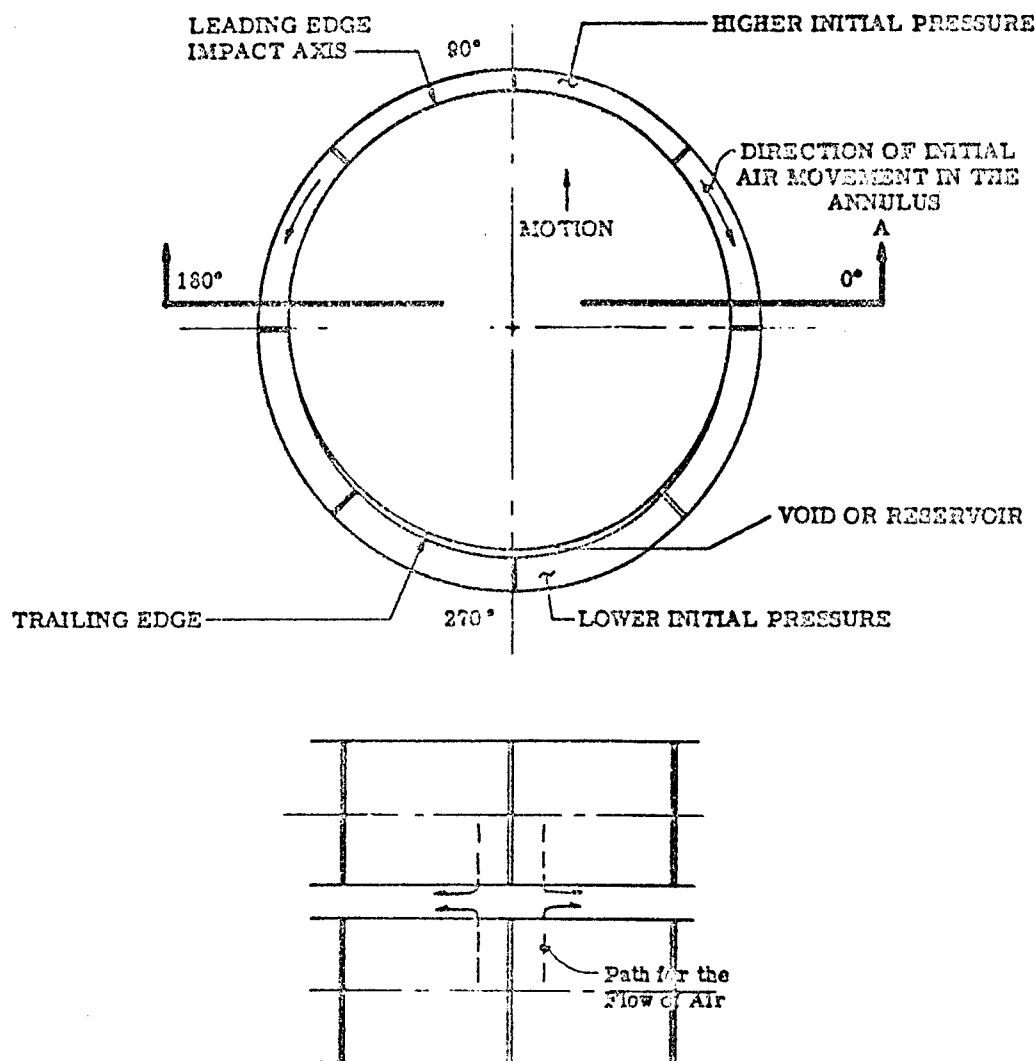Figure 2. Pad Construction Details

214

SECTION A-A

Figure 3. Location Terminology and Configuration Effects

differential, air will flow from the pressurized region to the region of lower pressure. An oscillation will be created due to wave reflection, and thus an oscillatory forcing function will be applied to the missile. As a result of the configuration of the shock mitigation pads, the process for equilibrium of air pressure is quite complex.

Due to the construction of the missile, two limitations are present during shock. The first is the acceleration of the missile, and the second is the maximum skin pressure to which the missile can be subjected. The dynamic effects of air have a large effect on both of these lateral shock constraints; therefore, time and effort was devoted to understanding and predicting the effects of air under shock loading. Gas dynamics theory in conjunction with configuration parameters was incorporated into an Airflow Analysis which was used to predict pressure profiles and forces. To check the validity of the Airflow Analysis, tests were run at the Partial Full-Scale Test

215

Machine (PFSTM) facility at Hunter's Point, San Francisco, and then the Airflow Analysis and the PFSTM tests were modified until satisfactory agreement was obtained. The next step was to use the Airflow Analysis to predict the response to the design shock input. The analysis is complex and time consuming even though it is carried out on a high speed digital computer. For this reason, a simplified mechanical model was developed which accurately duplicated the force-time history from the analytical gas dynamics solution. This simplified mechanical model was then used for the total shock model and allowed many different cases to be run economically.

AIRFLOW ANALYSIS

Gas dynamics theory and the configuration parameters (diameter of missile, thickness of annulus, elastomeric pad design and spacing, etc.) were incorporated into an Airflow Analysis. Of the features included in the analysis, the mass injection characteristics (see Figure 3), where air from the pad is forced into the horizontal stream of flow, have the greatest effect on the final results, as they directly control the amount of mass transfer, the speed of wave propagation, and the magnitude of pressure build up. The effects of mass injection can be increased and decreased however, by proper vertical spacing of the elastomeric pad segments. This is the primary design parameter used to vary the total force-time history of the dynamic air effects.

Because the pads have a free height which is less than the sum of the initial clearance and the maximum missile excursion, a reservoir or void is created on the trailing edge as illustrated by Figure 3. This effect is achieved mathematically by allowing the horizontal annulus to expand when missile excursions create a void.

A number of simplifying assumptions were made to allow the airflow analysis to become manageable. These were:

1. The shear columns have no effect on the vertical flow in the pads.

2. The control volume has a constant height.

3. The flow is frictionless.

4. The effect of bending the flow into a circular path is neglected.

5. Axial symmetry is assumed about the 90° - 270° axis.

The constraints and assumptions mentioned previously were incorporated into a computer program "AIRFLOW" to predict pressure distributions and forces as a function of time. Figures 4 and 5 show an element of the annulus and the vectorial equations used to derive the final differential equations on Figure 6. The equations are a modification of those proposed by Shapiro in The Dynamics and Theromodynamics of Compressible Fluid Flow for one-dimensional flow with area change and mass injection.

To obtain the solution, the pad and the space where considered as separate control volumes and the equations of continuity, momentum, and energy in conservation form for each were written. An isothermal state equation was assumed for the pad-space combination, and an empirical mass injection momentum loss equation was used for the pad.

Integration of the differential equations on Figure 6 was accomplished through the use of a Runge-Kutta numerical integration technique. The spatial derivatives were calculated by the approximation

$$\frac{\partial f}{\partial x} = \frac{f_{i+1} - f_{i+1}}{2x}$$

To assure numerical stability, the time steps used for the Runge-Kutta routine always satisfied the Courant stability criterion,

$$(|u| + c)\frac{\Delta t}{\Delta x} \leq 1.0 ,$$

for one-dimensional flow. However, a rigorous stability analysis involving the mass injection and area change terms would probably show a more stringent stability criterion, but by stepping time in smaller increments, this difficulty was overcome. The Airflow Analysis was then ready to be checked with experimental data.

PARTIAL FULL-SCALE TEST MACHINE-PFSTM

The experimental tool used to verify the Airflow Analysis was a shock test apparatus called the Partial Full-Scale Test Machine (PFSTM). It is a drop test machine sealed to represent a 60" vertical section of the missile, elastomeric liner, and launch tube (Figure 7). To conduct a shock test, the missile-launch tube assembly, supported by parallelogram linkages, is raised to various heights and then released to impact against a concrete and steel buttress. At impact, an approximate step velocity is imparted across the annulus, and the frame or launch tube is latched into place. The missile segment is then free to respond to the force from the elastomer segments and the airflow effects. During the tests, data is collected by displacement, acceleration, and pressure measuring transducers and recorded on a high speed oscillograph.
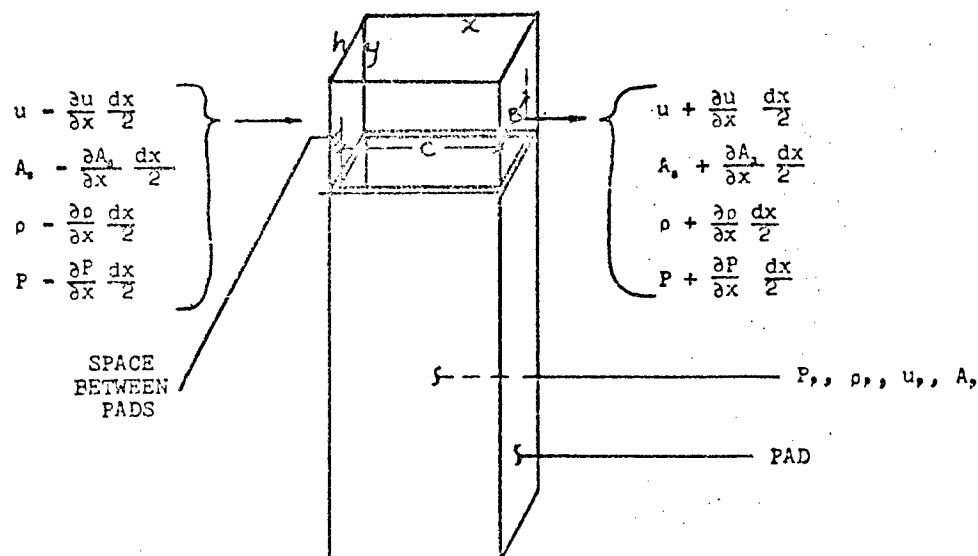
THE VECTOR EQUATIONS FOR THE ELEMENT ABOVE CAN BE WRITTEN
IN CONSERVATION FORM AS:

$$\frac{\partial}{\partial t}\begin{bmatrix} \rho_{,} \\ \rho \\ \rho u \\ \rho e \end{bmatrix} + \frac{\partial}{\partial x}\begin{bmatrix} 0 \\ \rho u \\ (\rho u^2 + P) \\ \rho(e+\frac{P}{\rho})u \end{bmatrix} + \begin{bmatrix} \frac{A_1}{A_,}\frac{X}{C}\dot{m}^1 \\ -\dot{m}^1 \\ 0 \\ -\dot{m}^1 h_{,} \end{bmatrix} = \begin{bmatrix} \rho_{,}\dot{V}_{,}^{\ 1} \\ -\rho A_{,} \\ -\rho u A_{3} \\ -(\rho e+P)A_{3} \end{bmatrix}$$

<u>FLUID EQUATIONS</u>   <u>MASS INJECTION TERMS</u>   <u>PAD & SLOT COMPRESSION</u>

OR, MORE CONVENTIONALLY

$$\frac{\partial \vec{U}}{\partial t} + \frac{\partial \vec{F}}{\partial x} + \vec{H} = \vec{I}$$

WHERE $\vec{U}$, $\vec{F}$, $\vec{H}$ & $\vec{I}$ ARE THE FOUR DIMENSIONAL
VECTORS DESCRIBED ABOVE

Figure 4. Control Volume Element and
Vectorial Equations

RESULTS

The relative displacement-time results from a PFSTM test were used as input to the Airflow Analysis in order to test the validity of the configuration phenomena and gas dynamics theory. The pressures at various azimuths generated by the Airflow Analysis are plotted with respect to time and are compared with those obtained at PFSTM. A typical cross section of the test configuration is shown on Figure 8.

Figure 9 shows the pressure-time history of various locations around the missile for a PFSTM test. Also plotted on Figure 9 are the curves generated by the airflow analysis. Figure 10 shows the displacement time history. Note particularly that the pressures are not in phase with the displacement, consequently, an integrated force-deflection curve of the airflow characteristics is very unusual as illustrated by Figure 11. The hysteresis loop is very

$$T_{p} = T \longrightarrow \frac{P_{p}}{\rho_{p}} = \frac{P}{\rho} \longrightarrow P_{p} = P\left(\frac{P_{p}}{\rho}\right)$$

(ISOTHERMAL)

$$h_{p} = \left(\frac{k}{k-1}\right)\frac{P}{\rho}$$

$$e = \left(\frac{1}{k-1}\right)\frac{P}{\rho} + \frac{u^{2}}{2}$$

$$\dot{A}_{s} = \frac{1}{A_{s}}\left(\frac{\partial A_{s}}{\partial t} + u\frac{\partial A_{s}}{\partial x}\right)$$

$$\dot{V}_{p}{}^{1} = \frac{1}{A_{p}C}\frac{\partial}{\partial t}(A_{p}C)$$

$$\dot{m}^{1} = \frac{\dot{m}}{A_{s}X}$$

$$\dot{m} = \text{MASS PER UNIT TIME} \atop \text{LEAVING THE PAD}$$

WHERE $\dot{m} = f\left(\dfrac{P_{p}-P}{\rho\,\frac{u^{2}}{2}}\right)$

THE EQUATIONS IN FIGURE 4 ARE SUITABLE FOR SOME TYPES OF INTEGRATION ROUTINES, HOWEVER FOR THE INTEGRATION ROUTINE USED IN THIS STUDY, THE EQUATIONS HAD TO BE REARRANGED AS IN FIGURE 6.

Figure 5. Definition of Terms

large, thus a large amount of energy is dissipated by the effects of the air flow.

The predicted pressures on the trailing edge azimuths do not agree with those recorded during PFSTM testing. The reason for the apparent anomaly is that during testing the seals on the trailing edge azimuths did not function properly, and vented air to the atmosphere. The correlation for the other azimuths however is good, thus leading to the conclusion that the Airflow Analysis is able to reproduce test data, and should therefore be able to be used for predictions with other shock inputs.

When the design input was used, similar results were obtained (Figure 12). Once again the peculiar phasing effects are prominent. Figure 13 shows a particularly significant pressure profile which occurred at 16 milliseconds after impact. This pressure profile has an effect on the missile analogous to stepping on a tin can. The effect only lasts a few milliseconds, but could aggravate the buckling strength capabilities of the missile. The integrated pressures gave a force-time plot which had very nearly a full cycle of force-time history (Figure 14) for only a half cycle of displacement time history.

MATHEMATICAL MODEL

As mentioned previously, the gas dynamics approach to modeling the air pressure force response, although accurate, would be cumbersome and time consuming in the total shock model. To overcome this problem, a simplified math model producing the force developed by the air pressure was desired.

THE REARRANGED SIMULTANEOUS PARTIAL DIFFERENTIAL EQUATIONS TO BE SOLVED ARE:

1) $\dfrac{\partial \rho_{p}}{\partial t} = \dfrac{\left(-\dot{m} + LX\rho_{p}\frac{\partial h_{p}}{\partial t}\right)}{A_{p}C}$

2) $\dfrac{\partial \rho}{\partial t} = -\rho\dfrac{\partial u}{\partial x} - u\dfrac{\partial \rho}{\partial x} + \dfrac{\dot{m}}{A_{s}X} - \dfrac{\rho}{A_{s}}\dfrac{\partial A_{s}}{\partial t} - \dfrac{\rho u}{A_{s}}\dfrac{\partial A_{s}}{\partial x}$

3) $\dfrac{\partial u}{\partial t} = -u\dfrac{\partial u}{\partial x} - \dfrac{1}{\rho}\dfrac{\partial P}{\partial x} - \dfrac{u\dot{m}}{\rho A_{s}X}$

4) $\dfrac{\partial \rho}{\partial t} = c^{2}\left(\dfrac{\partial \rho}{\partial t} + u\dfrac{\partial \rho}{\partial x}\right) - u\dfrac{\partial P}{\partial x} + \dfrac{(k-1)}{A_{s}X}\dfrac{\dot{m}u^{2}}{2}$

WHERE $\dot{m} = f\left(\dfrac{P_{p}-P}{\rho\frac{u^{2}}{2}}\right)$

$A_{s} = hy + (h-h_{0})L_{s}$ for $h > h_{0}$

$A_{s} = hy$ for $h < h_{0}$

$h_{0} = $ free height of the pad

$L_{s} = \dfrac{h-h_{0}}{\alpha h}$ WHERE $\alpha \cong 0.04$

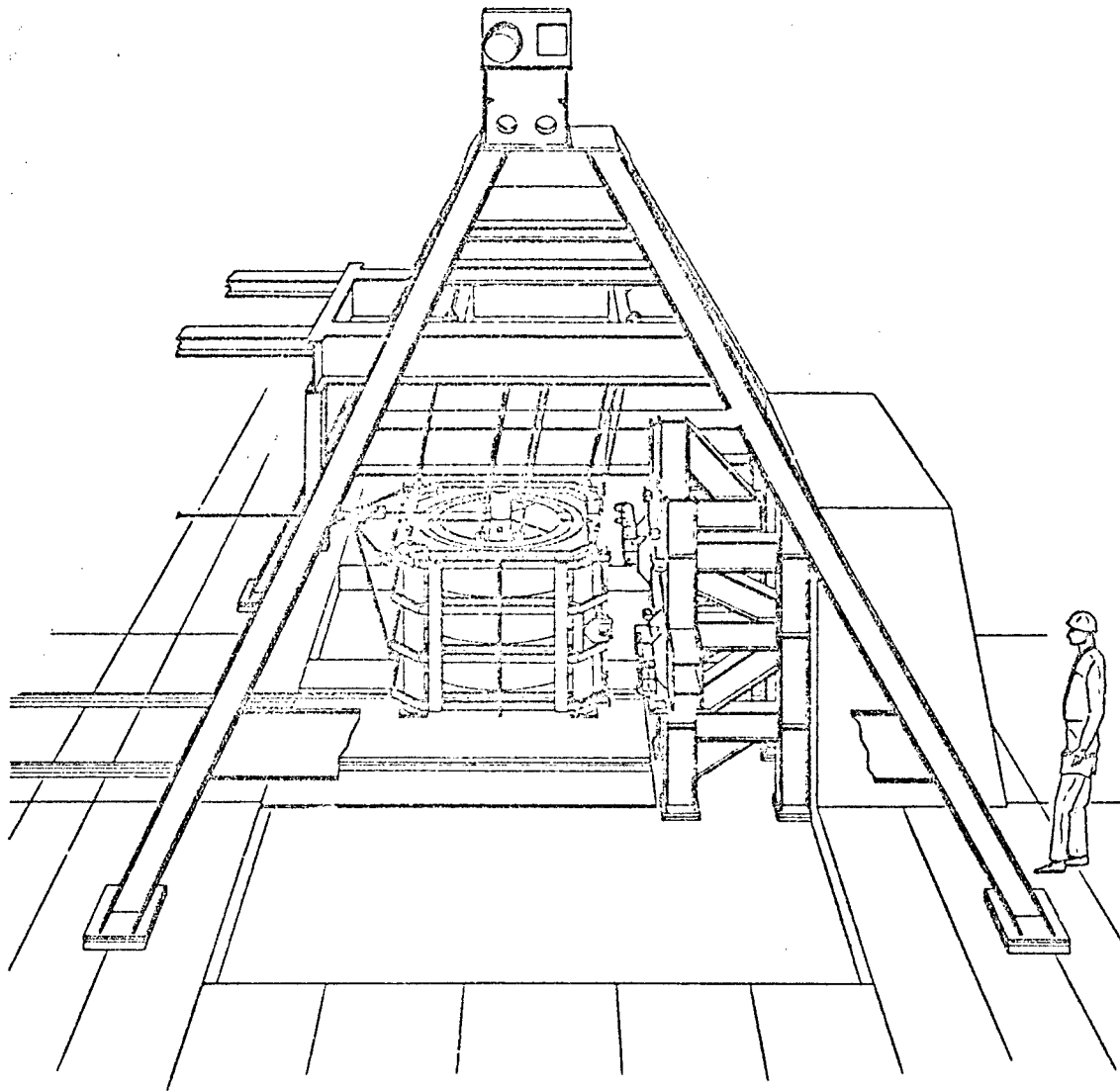Figure 6. Final Differential Equations

Figure 7. Partial Full-Scale Test Machine (PFSTM)

Figure 14 shows the integrated force from the air pressure as obtained from the "AIR-FLOW" program. It is interesting to note that from a very non-linear process, a continuous curve, approaching a sine wave for the first cycle, is generated. The smooth shape of the curve is probably due to the integration of the pressures around the missile. as integration usually provides a smoothing effect. The shape of the curve obtained strongly suggests a simple spring-mass-damper system to produce forces similar to the one shown. Classical vibration theory provides direction by suggesting the hy-

draulic system shown on Figure 15 as an effective analogy to the system in consideration. The launch tube-missile configuration is a complex pneumatic system where the compressibility of air has distinct effects, but since the force-time curve is very near a sine wave for the first cycle, the hydraulic analog is relatively good.

The forces developed by the dynamic effects of air only occur as a function of relative displacement. To include this constraint in the math model, a linkage (Figure 16) was used to insure

AIR ENTRAPMENT SEALS
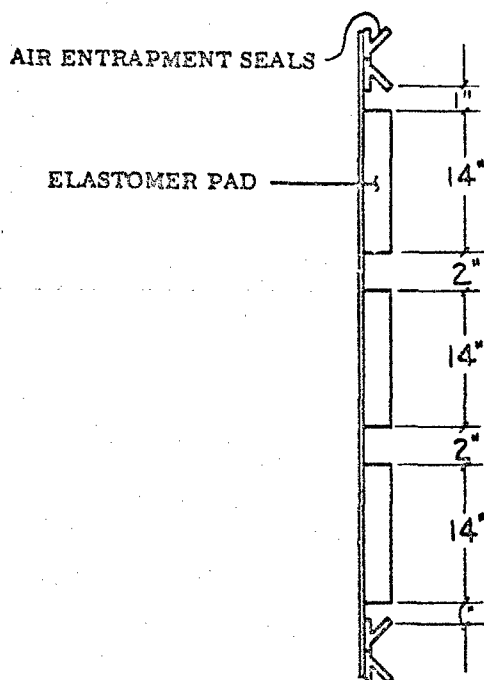
ELASTOMER PAD

1"

14"

2"

14"

2"

14"

Figure 8. Typical PFSTM
Test Assembly

that forces could only be developed during relative motion. Assuming an infinitesimal displacement, the point connecting the spring to the linkage has the same velocity as the relative velocity between the missile and the launch tube. Once the model was developed, the next task was to specify the constants to be used for the three elements of the model. This was accomplished through the use of a parametric study with the same time-displacement input used in "AIRFLOW" to produce the theoretical curve to be matched. The correlation between the force-time outputs from "AIRFLOW" and the mechanical model is very good as evidenced by Figure 17.

Note specifically the ability of the mechanical model to reproduce the characteristic full cycle of force-time history for the half cycle time-displacement history. Due to the good agreement obtained, it is felt that the mechanical model is adequate for use in the complete shock model.

CONCLUSIONS

The results of the Airflow Analysis developed in this study show an important aspect of the lateral shock capabilities of any shock mitigation system where the thickness-to-diameter ratio is small. The Airflow Analysis provides valuable information as to the pressure distributions applied to the missile and the forcing function response of the airflow characteristics. The simplified mathematical model adequately represents the dynamic effects of air and reproduces all of the important basic phenomena. It is useful for the specific case involved, however when different shock profiles are used, when different pad configurations are considered, or when the basic dimensions of the system change, the constants of the mathematical model will no doubt have to be changed.

REFERENCES

1. Ascher H. Shapiro, The Dynamics and Thermo Dynamics of Compressible Fluid Flow, Vol. 1 and 2. Ronald Press, New York, 1953.

2. R.D. Richtmyer and K.W. Morton, Difference Methods for Initial Value Problems, Second Edition. Interscience Publishers, New York, 1967.
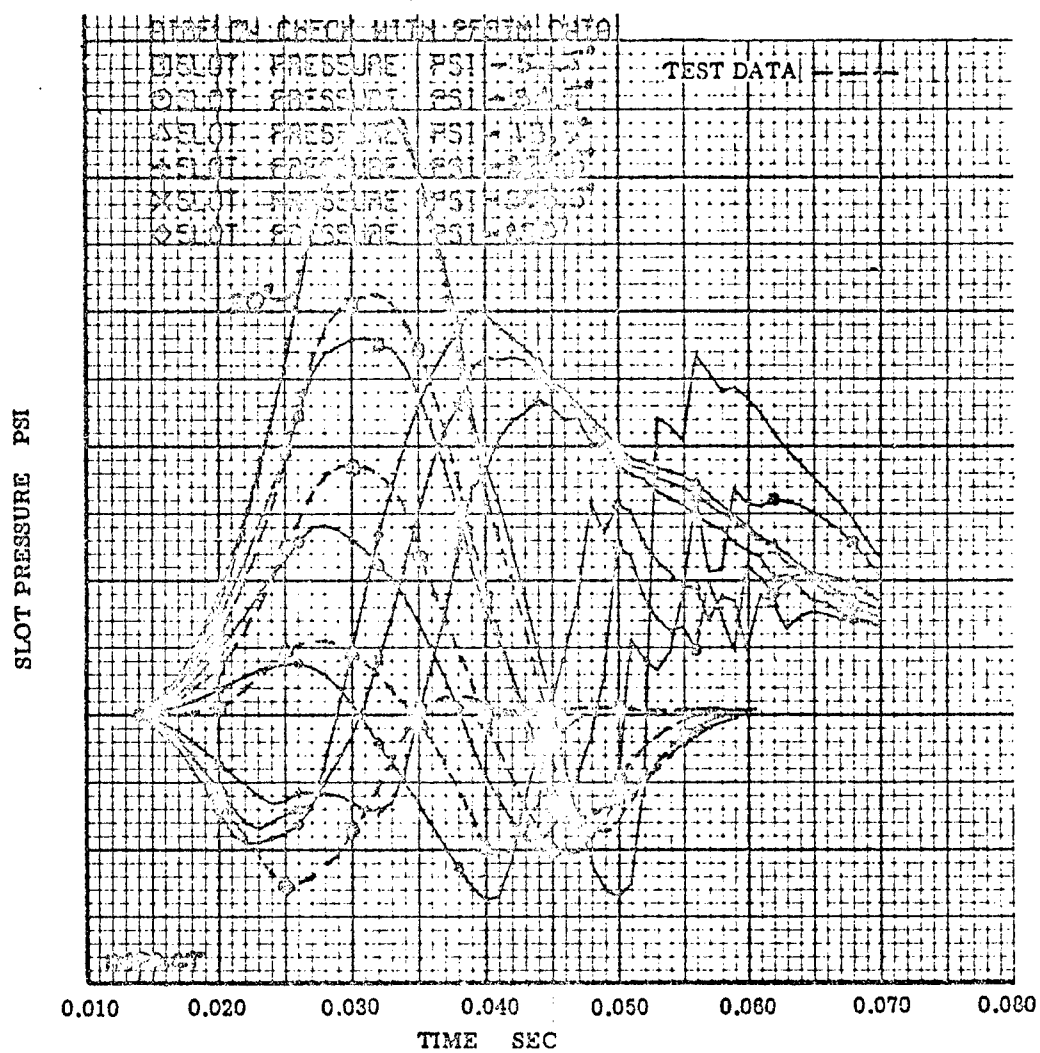
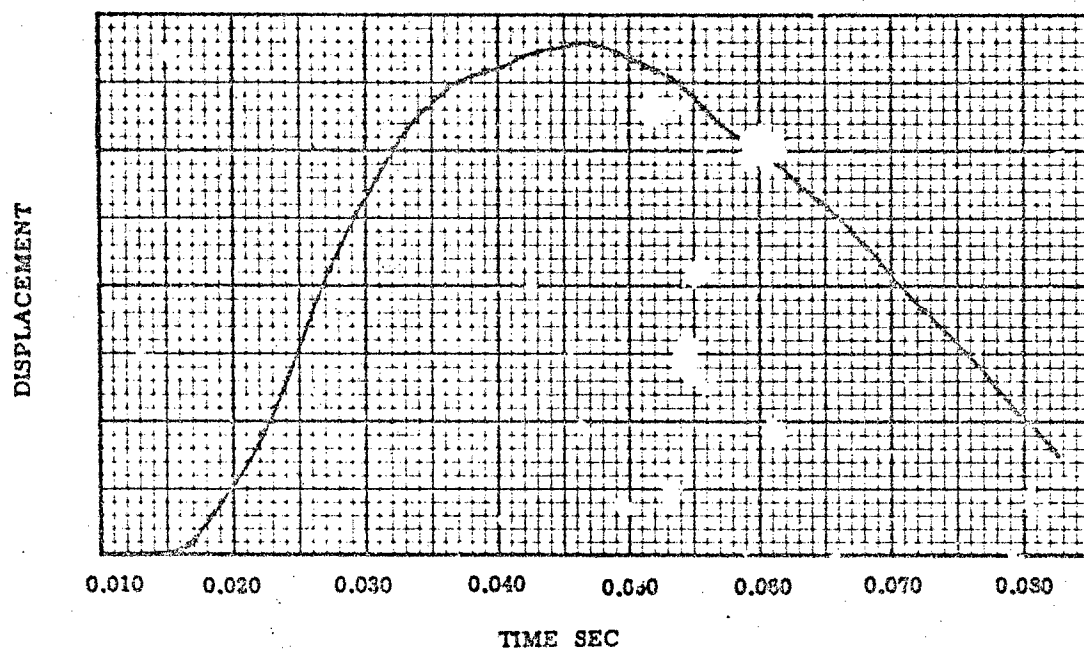Figure 9. Pressure-Time History With PFSTM Input

221

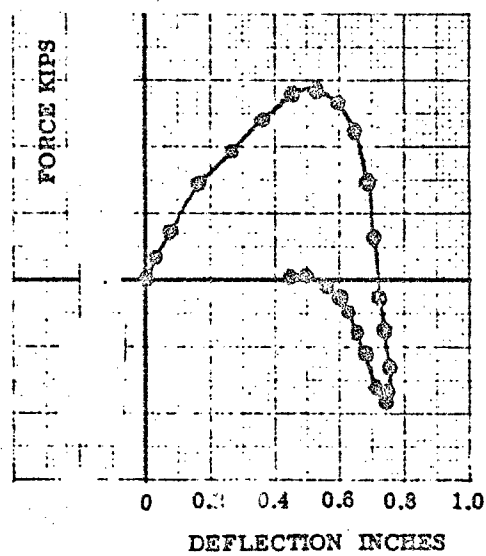Figure 10. Displacement-Time History of PFSTM

Figure 11. Force-Deflection Curve Due to Calculated Airflow Effects

222

Figure 12. Pressure-Time History with Design Input
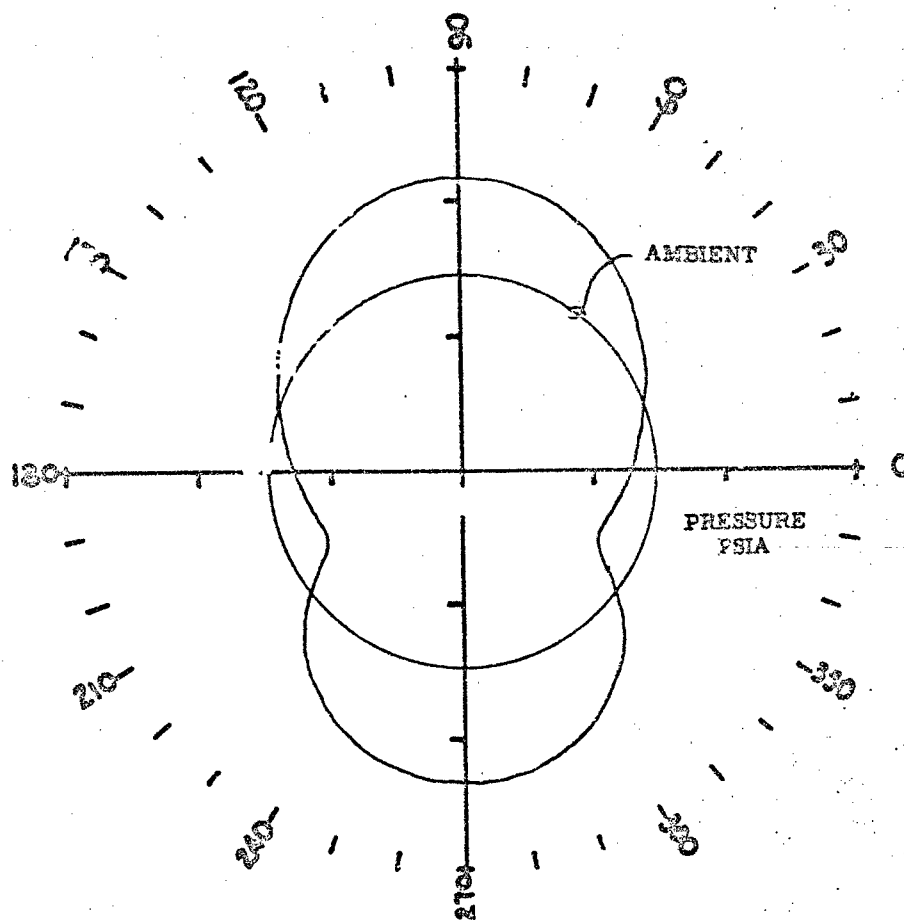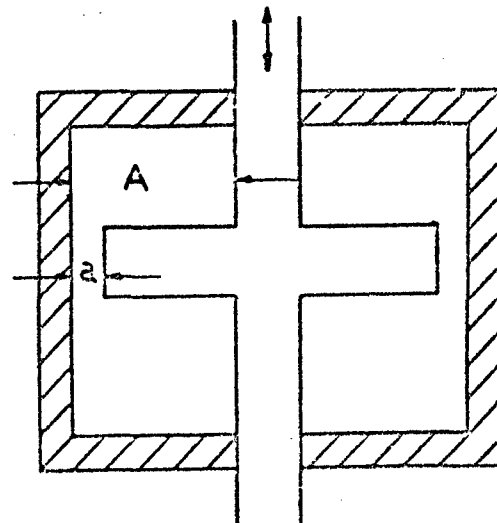
Figure 13. Pressure Profile at 16 milliseconds after Impact for Design Input

A = FLUID AREA

a = CLEARANCE AREA

DURING MOTION OF THE PISTON, FORCES
ARE DEVELOPED BY THE MOVING FLUID.
THIS IS SIMILAR TO THE MISSILE-LAUNCH
TUBE CONFIGURATION
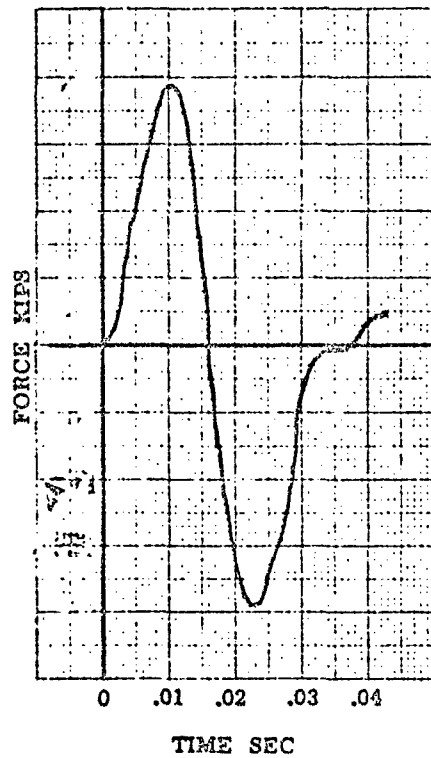
Figure 14. Total Integrated
Force Due to Airflow Effects
with the Design Input
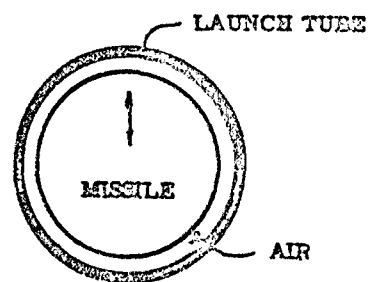
Figure 15. Hydraulic Analogy

225
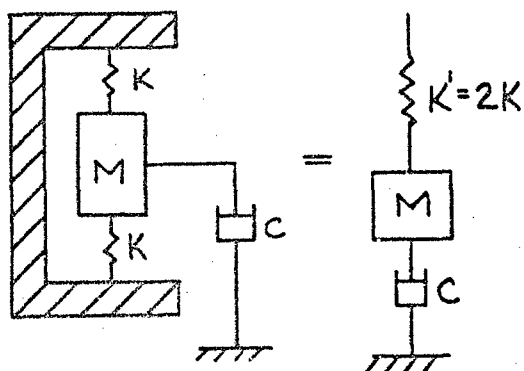
WHERE $M \propto m' \left(\frac{A}{a}\right)^2$
and m' = MASS OF AIR IN
CLEARANCE AREA

REF: W.T. THOMSON, VIBRATION THEORY
AND APPLICATIONS, pg 34, #42,
PRENTICE HALL, 1965.

TO OBTAIN FORCE ONLY AS A FUNCTION
OF RELATIVE DISPLACEMENT, THE FOL-
LOWING LINKAGE WAS USED.
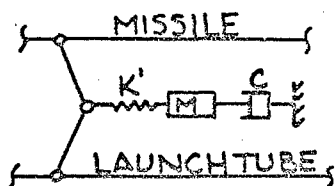
Figure 16. Mechanical Equivalent of the
Hydraulic Analogy
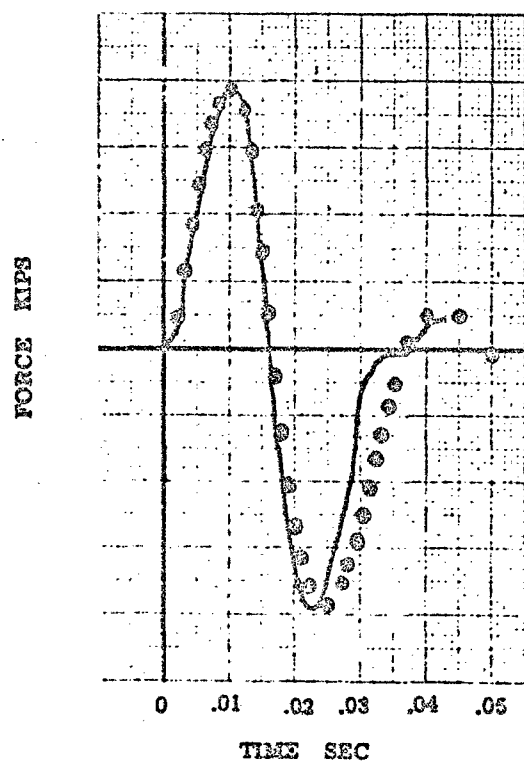
GAS DYNAMICS AIRFLOW ————

MATHEMATICAL MODEL ⊕⊕⊕⊕⊕

Figure 17. Comparison of Force-Time
Histories from "AIRFLOW" and the
Mathematical Model

A SCALE MODEL STUDY OF CRASH ENERGY

DISSIPATING VEHICLE STRUCTURES

D.J. Bozich and G.C. Kao
Research Staff, Wyle Laboratories
Huntsville, Alabama 35806

The objectives of this paper are to show that the energy
dissipation mechanisms of motor vehicle structures can be
simulated by scale model experiments and that the experi-
mental results can be of significant value toward the for-
mulation of an analytical model. The crash models were
designed to represent a one-tenth scale passenger car using
gravitational scaling laws. The scale weight of the model
can be varied to represent actual vehicle weight from about
2,500 to about 5,000 pounds. A scaled mannequin and seat-re-
straint system, and restrained cargo were added as options
for a few of the experiments to study the effect of the range
of energy dissipators on their responses. Accelerometers were
attached to the model structure, the mannequin and the cargo.

Tests were conducted on a ballistic pendulum at several
different drop heights to simulate impact speeds up to about
40 miles per hour. Three types of barriers, namely, a small
area barrier (SAB), a medium area barrier (MAB), and a
wedge barrier (WB) were used during the tests. Five basic
scaled energy dissipating materials were used to construct
several different types of energy absorbers to simulate
multiple structural zones of a vehicle.

This paper offers an approach to study the energy absorbing
characteristics of motor vehicles as well as to set prelimi-
nary criteria for the design of more efficient structural
systems for absorbing collision forces.

INTRODUCTION

The crashworthiness of a vehicle
structure is closely related to, among
other things, the amount of impact energy
which can be dissipated through struc-
tural deformation. In order to achieve
this objective, vehicle structures should
be designed to deform effectively during
impact collisions so as to reduce g-loads
on occupants. Analytical models for ve-
hicles, as well as component structures
are needed to predict responses and to
provide design information for vehicle
systems and testing.

A recent study on structural re-
sponses of vehicle structures [1] has
revealed that the peaks and valleys of
deceleration response curves actually
represent the successive collapse (or
failure) of structural components which
react to impact collisions. This find-
ing leads to a hypothesis that the re-
acting structural components act as
energy dissipating mechanisms (or energy
dissipators). The problem is reduced to
finding suitable analytical models to

represent multiple energy dissipators rather than to deal with the more complicated motor vehicles.

The objectives of this paper are to show that the energy dissipating mechanisms of motor vehicles can be simulated by scale model experiments and that the experimental results can be of significant value toward the formulation of analytical models. Since scale model experiments can be conducted with a high degree of accuracy and repeatability; this advantage would greatly enhance the reliability of analytical models. On the other hand, scale model experiments cannot be used to simulate all the structural characteristics and crash environments of impact collisions. Therefore, cautions must be exercised in choosing the desired crash parameters used in crash testing.

In this investigation, scale models were designed and fabricated to represent one-tenth scale medium range passenger cars using gravitational scaling laws.

Two types of model vehicles were used in the experimental tests. The first model was designed to simulate deceleration response only, and had a scale weight of 40 pounds. The second model comprised a scaled vehicle, mannequin and cargo; and had a scale weight of 43.6 pounds. Both mannequin and cargo were equipped with restraining wires to represent respective restraint systems. The objective here was to study the relative effect of the range of energy dissipators on the mannequin and cargo responses. Accelerometers were used to measure and acquire the impact response signals.

Tests were conducted on a ballistic pendulum at several different drop heights to simulate full-scale impact speeds up to 40 miles per hour. Three types of barriers were used during the tests; namely, a small area barrier (SAB), a medium area barrier (MAB), and a wedge barrier (WB). Five basic scaled energy dissipating materials were used to construct thirteen different types of energy dissipators to simulate multiple structural zones of a vehicle. Over one hundred and eighty tests were performed.

An analytical model was developed in an attempt to predict model vehicle re-

sponses. The analytical model uses the elasto-plastic deformation characteristics of energy dissipating materials to obtain responses of medium area barrier impact tests. Satisfactory comparisons between analytical and experimental results were obtained.

This paper presents the feasibility of using scale model experiments in formulating analytical models, and in simulating effects of barrier size, shape, and impact velocity to the responses of scaled elements (i.e., vehicle, mannequin and cargo, etc.); it also illustrates the effectiveness of "programmed" structural deformation techniques in reducing deceleration response.

DYNAMIC MODELING AND SCALING LAWS

The state-of-the-art in dynamic modeling has been well treated in many text books and the literature. Ref. [2] is particularly good and one of the better sources for a complete treatment on this particular subject. The theory of dynamic modeling is, therefore, not presented here, but rather moderately reviewed.

The use of scale models for simulation of complex or expensive engineering problems has been found to be particularly valuable in several respects:

(i)   to obtain experimental data for quantitative evaluation of a particular theoretical analysis,

(ii)   to explore the fundamental behavior involved in the occurrence of little-understood and particular types of phenomena,

(iii)   to obtain quantitative data for use in prototype design problems, particularly when mathematical theory is overly complex, or non-existent,

(iv)   to obtain qualitative and quantitative data with minimum expense and effort.

Two general types of dynamic modeling techniques are recognized. Geometrically similar modeling is widely used and its technique is well developed due to less complexity in relating the

228

model and the full-scale prototype.
Wind-tunnel tests of aircraft and aerospace vehicles are well-known applications of this technique. A skew model is a distorted model of the prototype that gives a possible amplified response of a portion of a structure, which is of interest to the investigator. Skew modeling is generally less popular in model testing because of inherent complexities in the basic model-to-prototype relationship, such as less accuracy in predicting the prototype's dynamic behavior from the model's. A geometrically similar model was used for this experimental study.

Geometrically similar modeling branches in several directions; each of which has scaling laws which depend on the items or quantities that are or interest to the investigator. The quantities, to name a few, may be stress, strain, frequency, force, acceleration, etc. It has been found generally, however, that complete geometrical similarity between the model and the prototype is unattainable and dissimilarity between some less important quantities must be accepted. The vehicle model for studying crashworthiness must satisfy laws of similitude dealing with acceleration - and consequently, the human deceleration tolerance and structural behavior as well as geometric similarity. Gravity scaling laws (also known as Froude's law) therefore were applied throughout this experimental study. These scaling laws were used because the model vehicle and a full-scale automobile will both experience the same deceleration levels in g units (1g = 32.2 ft/sec^2), upon impact. Let the geometrical (length) scale factor be λ, then Table I summarizes the essential ratio between model and full-scale prototype parameters. It can be shown that some less important parameters, such as Young's Modulus, stress, and others, are not scaled. However, they were of no significant importance to the experimental crashworthiness model program.

DESCRIPTION OF TEST MODEL ELEMENTS

An automobile model was fabricated for the experimental crashworthiness study. A geometrical scale factor λ of 1/10 was selected. It was shown in the previous section that the gravity scaling laws require the length and width of the model to be 1/10th those of the full size automobile. However, if the vehicle model's weight is 1/100th that of a full-scale automobile, then the material density of the model should be ten times greater.

TABLE I

Table of Gravity Scaling Laws

Quantity	Ratio of Model to Prototype (λ)	Numerical Ratio for a 1/10 Scale Model
Acceleration	1	1
Area	λ^2	0.01
Deflection	λ	0.10
Density	$1/\lambda$	10.0
Energy	λ^2	0.01
Frequency	$1/\sqrt{\lambda}$	3.16
Length	λ	0.1
Mass	λ^2	0.01
Modulus of Elasticity	1	1*
Strain	1	1*
Stress	1	1*
Time	$\sqrt{\lambda}$	0.316
Velocity	$\sqrt{\lambda}$	0.316
Volume	λ^3	0.001

* Unity only when density ratio is made to equal $1/\lambda$. In many practical cases, density ratio can not be controlled.

The average American automobile weighs approximately 4000 pounds, and occupies a volume of approximately 500 to 700 cubic feet. The material density (made of steel and void) is approximately 5 lb/cu ft. The vehicle model, weighing 37.7 pounds, is made of steel which has a known density of 490 lb/cu ft. The "density" of the model vehicle volume is about 49 lb/cu ft, or about ten times that of an average full-scale automobile, thus satisfying the gravity scaling laws.

Two types of crash simulation models were used in the experiments. The type I model, as shown in Figure 1, was used to simulate vehicle response only. The type II model, as shown in Figure 2, was used to simulate, respectively, the motions of the vehicle, the mannequin and the cargo block. Statistics of these two models are listed in Table II.
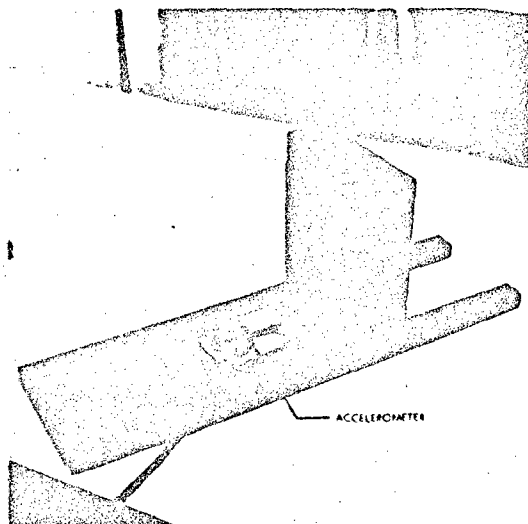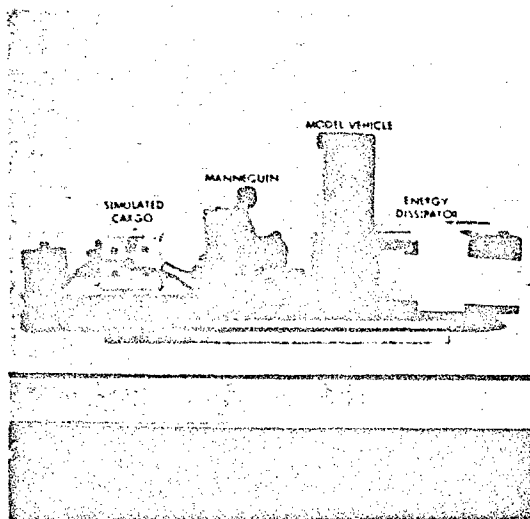

Figure 1. Type I Model

Figure 2. Type II Model

TABLE II

Statistics of Crash Simulation Models

Item	Type I	Type II
Width	5.9 in.	5.9 in.
Overall Length	20.25 in.	18.8 in.
Thickness	9.75 in.$^+$	1.3 in.*
Vehicle Weight	40.0 lbs	37.70 lbs
Mannequin	-	1.35 lbs
Cargo	-	4.51 lbs
Total Weight	40.0 lbs	43.56 lbs

+ Bottom to top of channel

* Base plate only

The same gravity scaling law applies to the mannequin. The material density of the mannequin should be ten times that of a human being. A human being comprised of solid, liquid, air, and visco-elastic components has a specific gravity of approximately 1.0. A commercial material, having a specific gravity of 10.0 could not be found, therefore, a compromise was made and the mannequin was made of brass which had a specific gravity of 8.6. The material was also chosen because it was easily machinable.

The design profile of the mannequin and the construction of the joints (specially designed for seated position) were guided by the research report of Ref. [3]. The width of the body, the extremities, head, and neck are so proportioned that the mannequin has the same weight distribution as that of an actual human being. The mannequin weighs 1.35 pounds, which is 1/100th of an average adult's weight (male and female). The legs and hands of the mannequin are free to move within the same effective limitations that a human may experience in a forward seating position. Figure 3 is a photograph of the final mannequin assembly.

The material elasticity is not proportionally scaled in this mechanical mannequin to that of a living body. The entire body is known to be elastic in nature. The internal organs, suspended

and inter-related within a body framework can be considered as a multiple-degree-of-freedom system in dynamic behavior. The natural vibration frequencies, the material elasticities, and the material damping play important roles in the study of human deceleration tolerance during an abrupt change of velocity. Obviously the mechanical mannequin does not attempt to simulate the biochemical nature of the human body under dynamic loads; rather, it is primarily intended to study only the flexing of the extremities, and the "jacknifing" of the upper torso of a human body under abrupt deceleration.
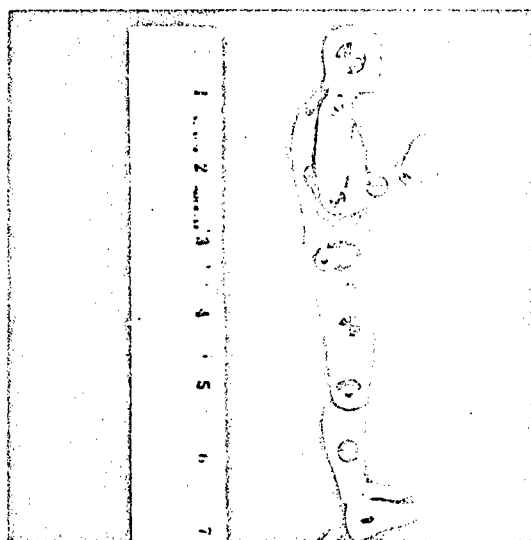

Figure 3. Actual Size of the 1/10 Scale Mannequin

A 2.5 inch cube, made of Brass, weighing 4.51 pounds was fabricated to simulate a cargo load of 450 pounds, carried inside an automobile or in the bed of a pickup truck, etc. This load, when used, was restrained only in a forward direction by a piano wire, which breaks at a predetermined force of 320 pounds.

Most head-on collisions display deceleration time curves which are characterized by the following:

(i)   Several deceleration peaks occur in the early half of the time-history during collisions.

(ii)   Time duration lasts from 0.1 to 0.25 seconds.

(iii) 60 to 90 percent of the area under the curve is contained in the early half of the time duration.

(iv) Peak deceleration ranging from 20 g to 150 g are commonly found depending on the vehicle's initial impact velocity, type of vehicle, and the struck object.

Therefore, it is important to be able to simulate experimentally the deceleration-time curve, peak deceleration, and energy distribution during an impact collision of the vehicle mode; and later, perhaps, to control and to improve the deceleration-time history and the energy absorption characteristics of an automobile design through the evaluation of the model test data.

In order to achieve similarity of the deceleration-time curves of the vehicle model and of the full-scale prototype, several energy absorbing materials and their combinations were used to absorb crash energy of the vehicle model upon collision with various types of barriers. Five types of materials were selected. They are as follows:

Materials	Symbol
Fiber Glass	F
Styrofoam	S
Acoustic Tile	T
Paper Honeycomb, load parallel to cell	P
Aluminum Honeycomb, 350 psi strength, load parallel to cell	A_{3P}
Aluminum Honeycomb, 350 psi strength, load vertical to cell	A_{3V}
Aluminum Honeycomb, 150 psi strength, load parallel to cell	A_{1P}

The elements were cut to give a nominal size of 3" x 6" x 2". Three different elements were put together in series to form an energy-dissipating block, of size 3" x 6" x 6". The elements were separated from each other by a 3" x 6" x 1/32" aluminum plate, to ensure that

each element would not interfere with the others when the entire block was being deformed. An extra aluminum plate was also located in the front of the energy absorbing block. The arrangements of the elements in a block were varied. Thirteen arrangements of the energy absorbing blocks were formed and tested. Their arrangement, signations, and average weights are listed in Table III. Figure 4 shows one of these energy dissipators.

TABLE III

Description of Energy Dissipators

Material Combiniations (Front to Bock)	Test Series Designation	Average Weight (lb)
P - S - T	100	0.66
P - S - F	200	0.40
P - F - T	300	0.86
S - P - A	400	0.39
S - F - T	500	0.70
P - F - A	600	0.45
P - T - A	700	0.75
S - F - A	800	0.42
S - T - A	900	0.70
F - T - A	1,000	0.80
P - T - A_{1P}	700 A	0.70
S - A_{3V} - A_{1P}	800 A	0.37
S - T - A_{3P}	900 A	0.73

The deceleration response of an automobile in an accident varies significantly upon impact with various struck objects. Three barrier designs were employed in the experimental study. They consist of:

    A Pole Barrier - Small Area Barrier
       (SAB)
    A Wedge Barrier (90° Angle) - (WB)
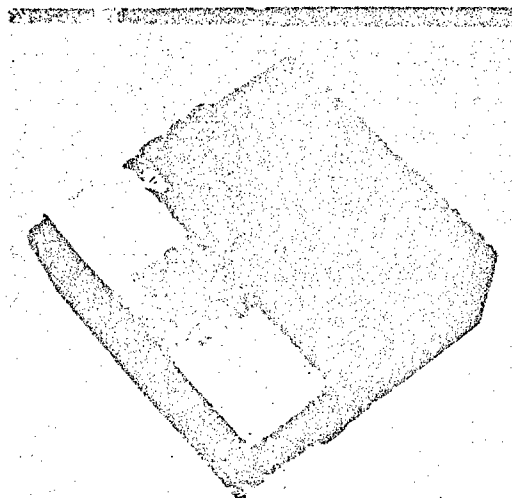   A Flat Barrier - Medium Area Barrier
       (MAB)

Figure 4. Typical Material Arrangement of an Energy Dissipator

These barriers simulate the collision of a vehicle with a rigid utility pole, a rigid corner of a heavy object such as a bridge abutment or a 45 degree head-on collision with another vehicle, and a rigid flat barrier. Figures 5, 6, and 7 show photographs of the three barrier designs used in this study.
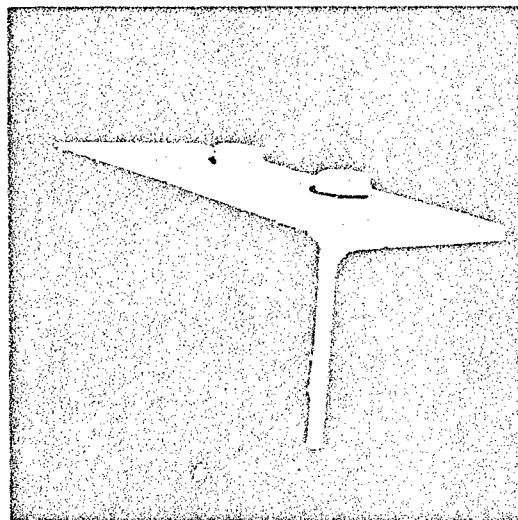
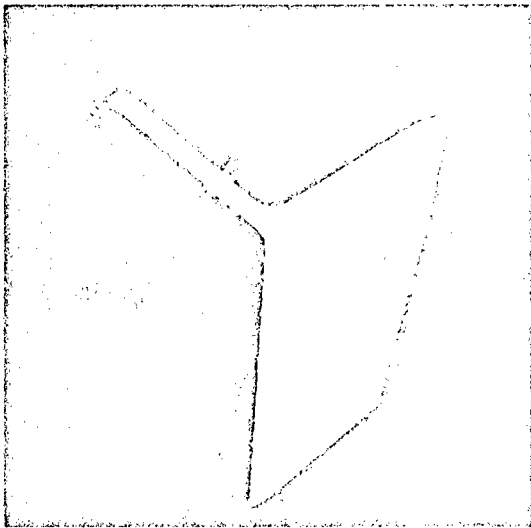

Figure 5. Medium Area Barrier (MAB)
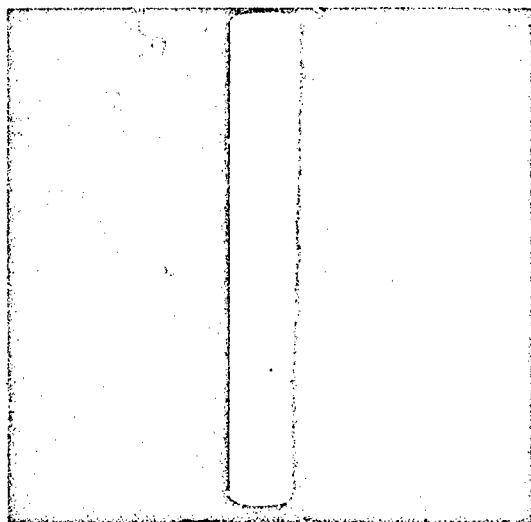
Figure 6. Wedge Barrier (WB)

Figure 7. Small Area Barrier (SAB)

DESCRIPTION OF EXPERIMENTS

A U-shape wooden framework is secured on the top surface of the pendulum platform. A 2' x 6' teflon sheet (1/16 inch thick) forms the bottom floor inside this wooden framework. The test vehicle model is placed on the teflon sheet a few inches from the leading edge of the open end of the wooden framework, and secured slightly by paper tape to the teflon floor and to the sides of the wooden framework to prevent any premature movement of the vehicle. Upon impact the vehicle model is free to slide backward on the "frictionless" teflon floor. The platform and the initial location of the vehicle model with respect to the platform are so designed that the vehicle model hits the designed barrier at the platform's lowest position, after its release from a predetermined initial raised position. After a time delay sufficient to acquire the model impact response data, the platform impacts the large reaction mass which is made of reinforced concrete with a steel covering and frame. The scaled barrier is welded to the reaction mass. Figure 8 is a photograph of the experimental facility.
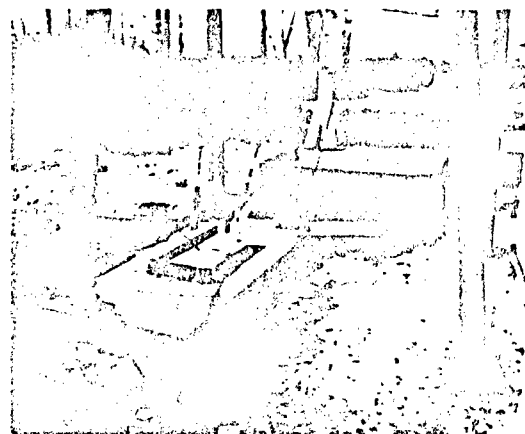

Figure 8. General View of Shock Test Facility

The actual impact velocity of the model vehicle at the moment of impact can be calculated from the conversion of potential energy into kinetic energy, namely:

$$V = \sqrt{2\,gh}$$

where V = actual impact velocity, ft/sec

g = 32.2 ft/sec^2

h = platform drop height, ft.

233

The simulated impact velocity of the model vehicle is related to the actual velocity by the scaling laws, discussed previously. It can be shown that

$$V_{simulated} = \frac{1}{\sqrt{\lambda}} \, V \text{ actual}$$

The geometrical scale factor is 1/10 in this experiment. Figure 9 gives a design chart of platform drop height vs. simulated automobile impact velocity. Three drop height values, 2.0 ft., 3.5 ft., and 5.0 ft., were used in the experiments to simulate a prototype vehicle traveling at 24.4, 32, and 39 mph, respectively.
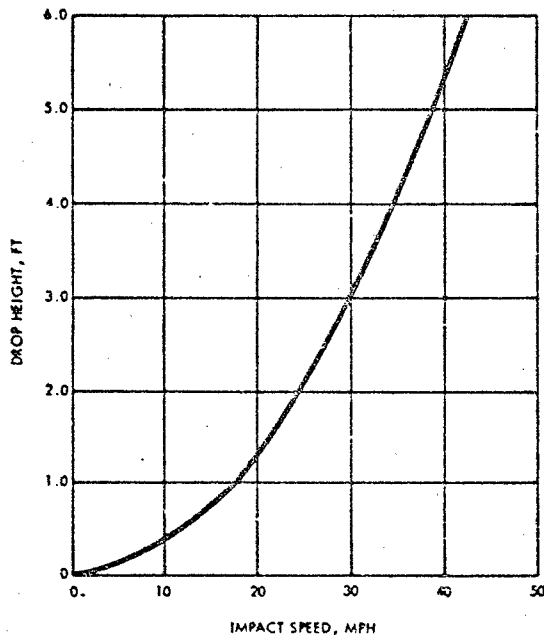
Figure 9. Drop Height vs. Simulated Impact Speed

Two laboratory test series were conducted in this program. The first laboratory test series was designed to give more insight and knowledge about the energy absorption problem, and to simu-late the deceleration-time history of an actual automobile crash. Type I model was used in the tests. Ten arrangements of energy dissipating blocks, series 100 through 1000, the three drop heights, and the three barriers formed a 10 x 3 x 3 lattice of experiments (that is, a total of 90 tests). Forward deceleration of the vehicle model and the platform were recorded by a two-channel visi-corder. The deceleration of the plat-form was needed just to ensure that there was enough time delay between the vehicle model impacting the barrier, and the platform impacting the large barrier. The mechanical mannequin and the simulated cargo load were not in-stalled in the vehicle model in this first test series.

After a careful study of the test data compiled from the first test series, a second laboratory test series was con-ducted a few days later on the 200, 700A, 800A, and 900A series of energy dissi-pating blocks. The type II model was used in the tests. Two drop heights (2.0 ft. and 3.5 ft.) and the three barriers were used to give a total of 24 tests. A scaled seat mannequin, re-strained by a simulated seat belt only, and the simulated cargo load, restrained in a forward direction by a piano wire restraint, were added to the vehicle model in this second test series. The breaking forces of the simulated seat belt wires and the cargo restraint piano wire were tested and found to be 55 and 315 pounds, respectively. Selection of these two load values was based on simu-lating the dynamic failure of actual full-scale seat belts and restraint belts for heavy loads. The estimated failure loads of the simulated seat belt and the piano wire were 70 g and 100 g loads, respectively.

The forward deceleration responses were recorded by a four-channel direct writing oscillograph (visicorder) for positions on the platform, the vehicle model, head of the mannequin, and the load. High speed movies were also used in this second series of tests. A
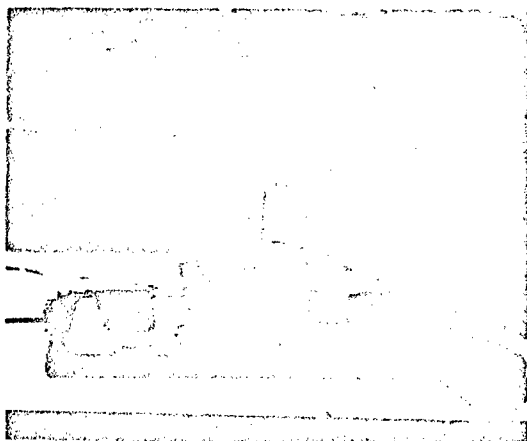
234

Figure 10. A Typical Model Vehicle
Impact Scene

typical model vehicle impact scene is
presented in Figure 10. The stress dis-
placement curves of the energy dissipa-
ting blocks, series 200, 700A, and 900A
were similarly tested against three de-
signed barriers, namely, a pole barrier,
a wedge barrier, and a flat barrier. The
force displacement curves are shown in
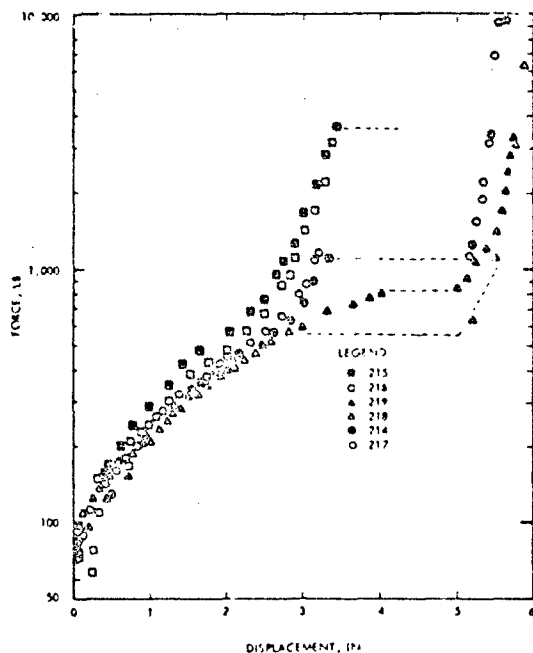Figures 11 through 13.

Figure 12. Force Displacement Curves of
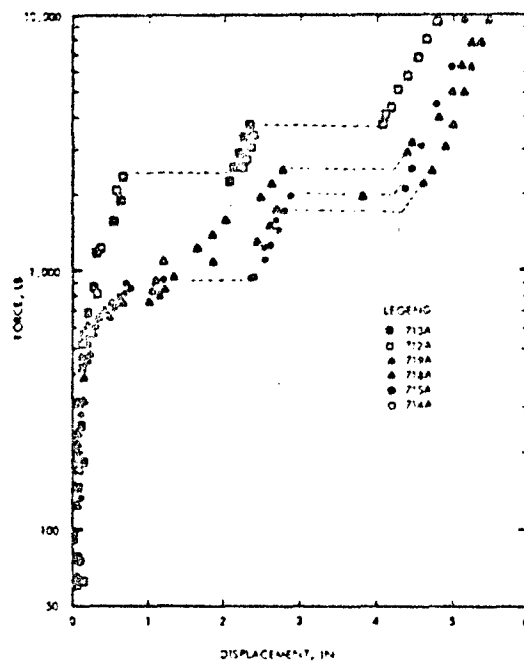Series 700A Energy Dissipators

Figure 11. Force-Displacement Curves of
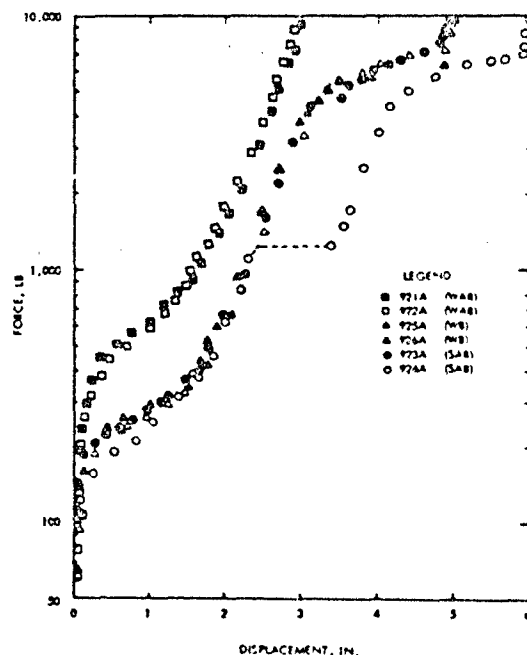Series 200 Energy Dissipators

Figure 13. Force-Displacement Curves of
Series 900A Energy Dissipators

235

Test results for the pendulum drop tests of the model vehicles and static compression tests of the energy dissipations have been reduced to graphical form. They are presented as follows:

a. Figures 14 through 23 represent the Peak-g responses of Type I model.

b. Figures 24 through 26 represent deceleration responses of Type II model, mannequin, and cargo subject to a 32 mph impact velocity with the three barriers.

Figure 16. Peak g Response - Series 300 Energy Dissipator Subject to Three Impact Velocities

Figure 14. Peak g Response - Series 100 Energy Dissipator Subject to Three Impact Velocities
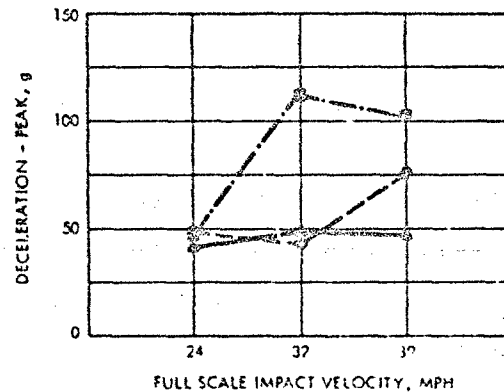
Figure 17. Peak g Response - Series 400 Energy Dissipator Subject to Three Impact Velocities

Figure 15. Peak g Response - Series 200 Energy Dissipator Subject to Three Impact Velocities
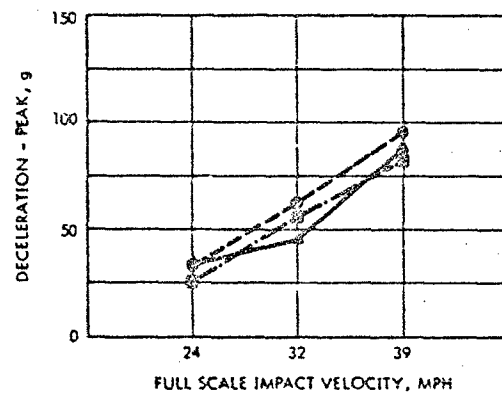
Figure 18. Peak g Response - Series 500 Energy Dissipator Subject to Three Impact Velocities
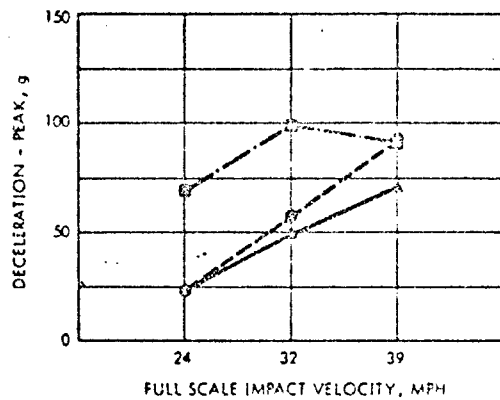
Figure 19. Peak g Response - Series 600
Energy Dissipator Subject to
Three Impact Velocities
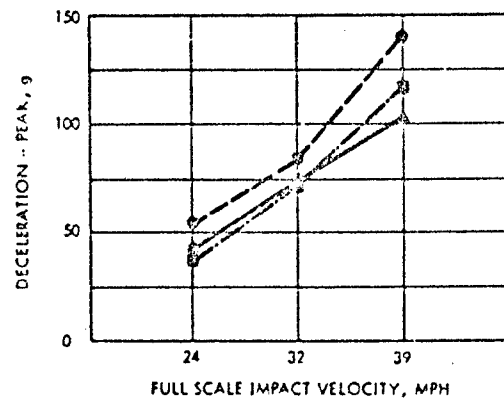
Figure 22. Peak g Response - Series 900
Energy Dissipator Subject to
Three Impact Velocities
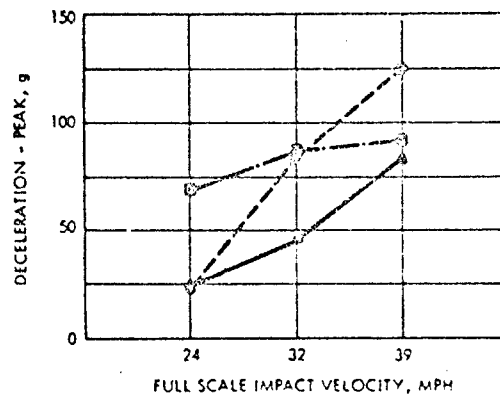
Figure 20. Peak g Response - Series 700
Energy Dissipator Subject to
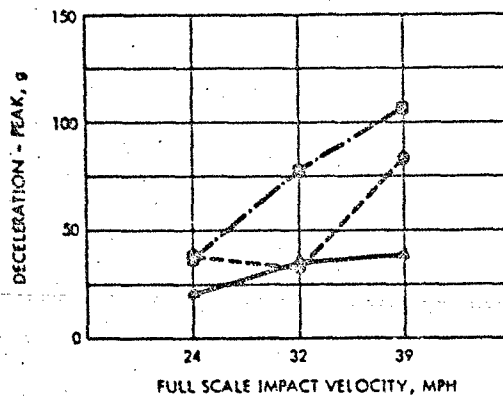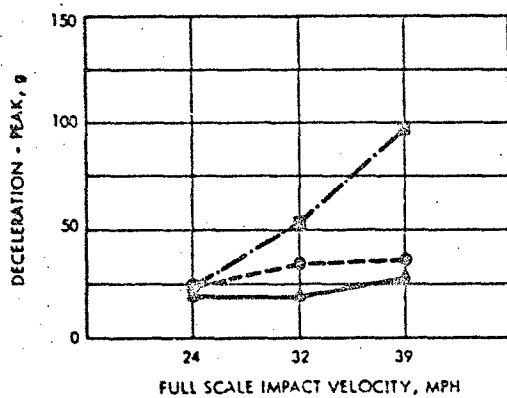Three Impact Velocities
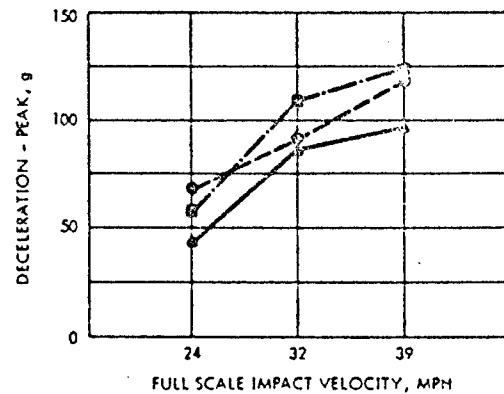
Figure 23. Peak g Response - Series 1000
Energy Dissipator Subject to
Three Impact Velocities
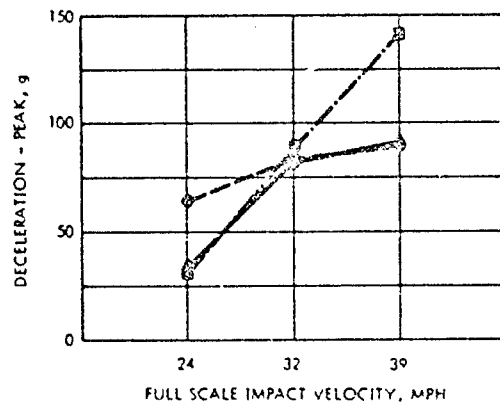
Figure 21. Peak g Response - Series 800
Energy Dissipator Subject to
Three Impact Velocities

The conclusions on the test results
can be summarized as follows:

a. Energy dissipation is, in general,
dependent on impact velocity. This
phenomenon is demonstrated by the
peak g vs. impact velocity curves,
as shown in Figures 14 through 23.

b. Energy dissipation is dependent
upon barrier shape. The wedge
barrier would render lower peak
g responses than that of the me-
dium and small area barriers.

237
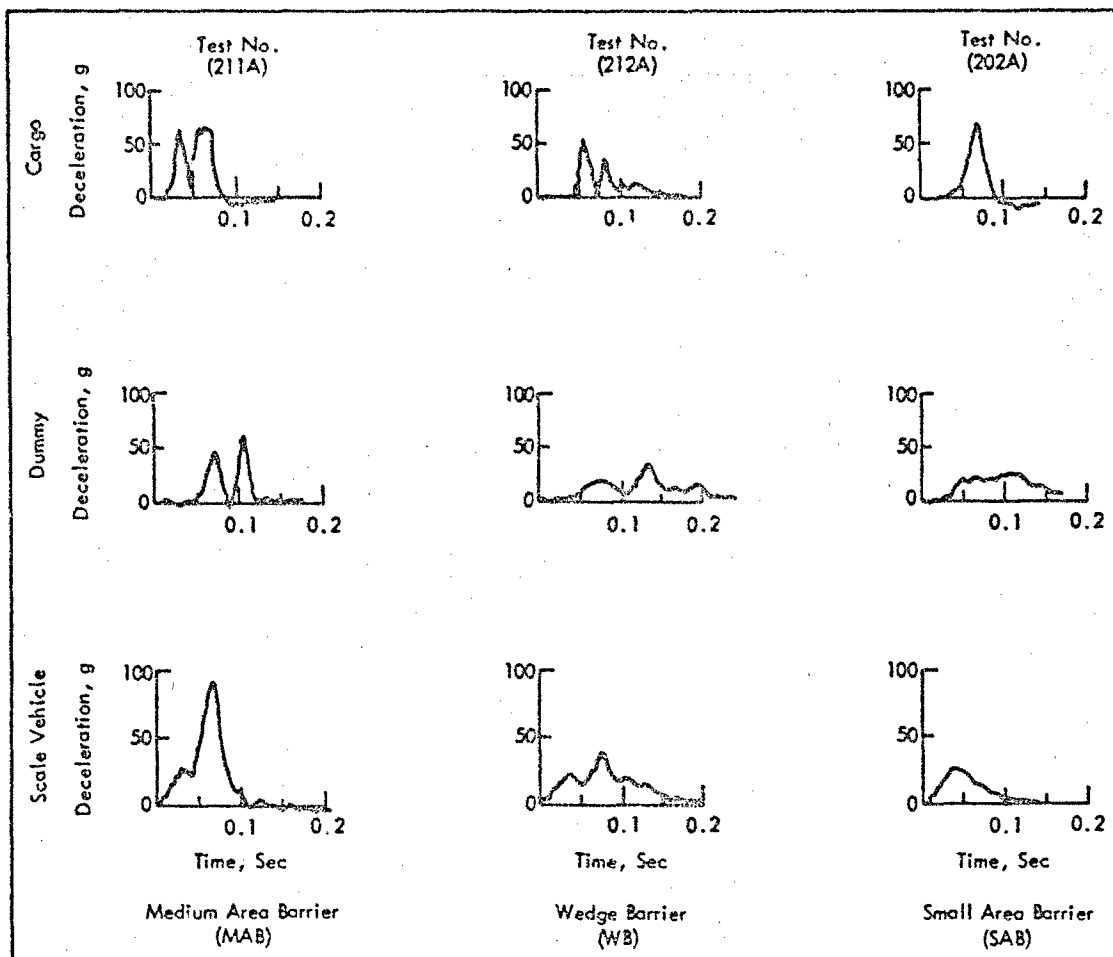
Figure 24. Responses of Cargo, Dummy and Scale Vehicles with Series 200
Energy Dissipator Subject to 32 Miles Per Hour Impact

238
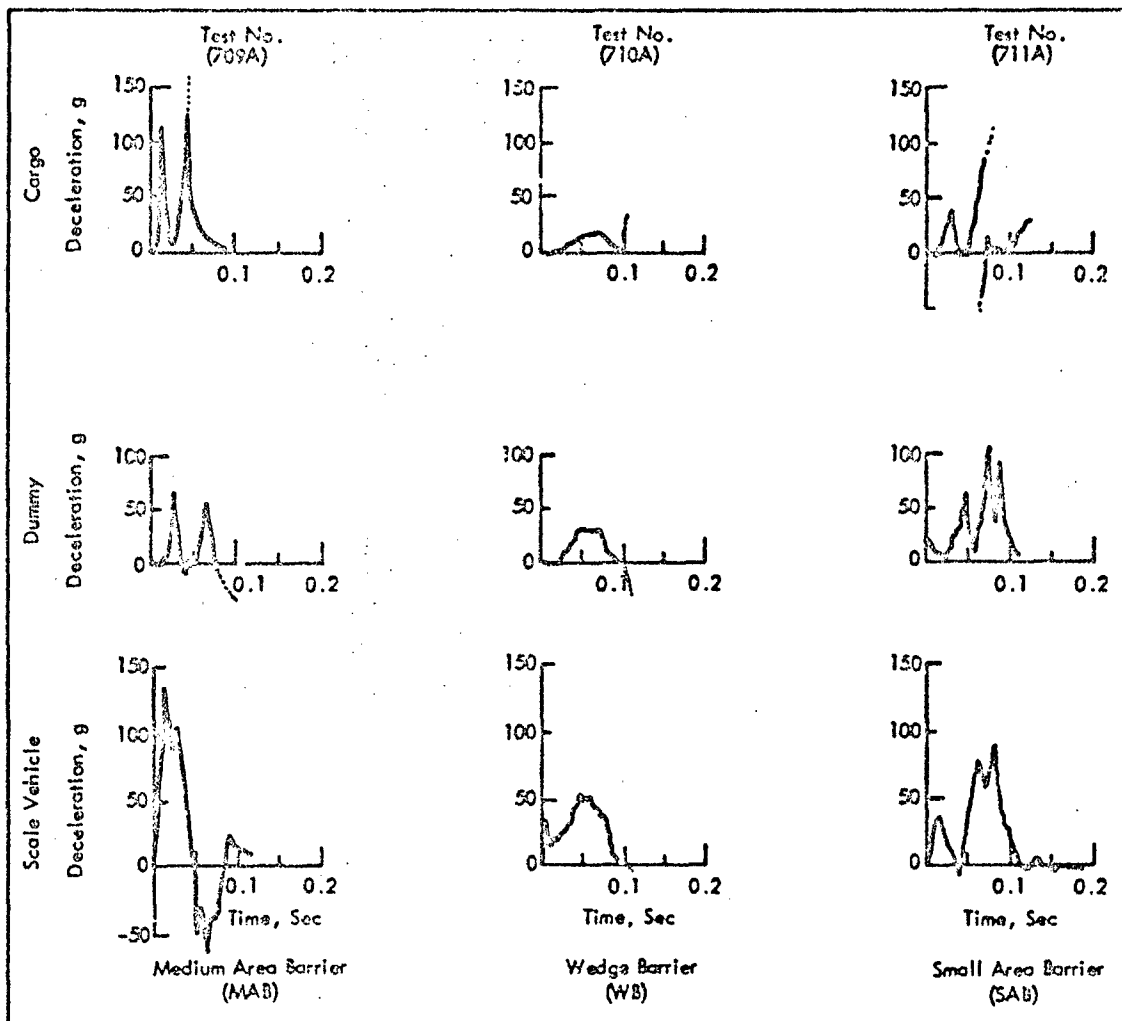
Figure 25. Responses of Cargo, Dummy and Scale Vehicles with Series 700A
Energy Dissipator Subject to 32 Miles Per Hour Impact
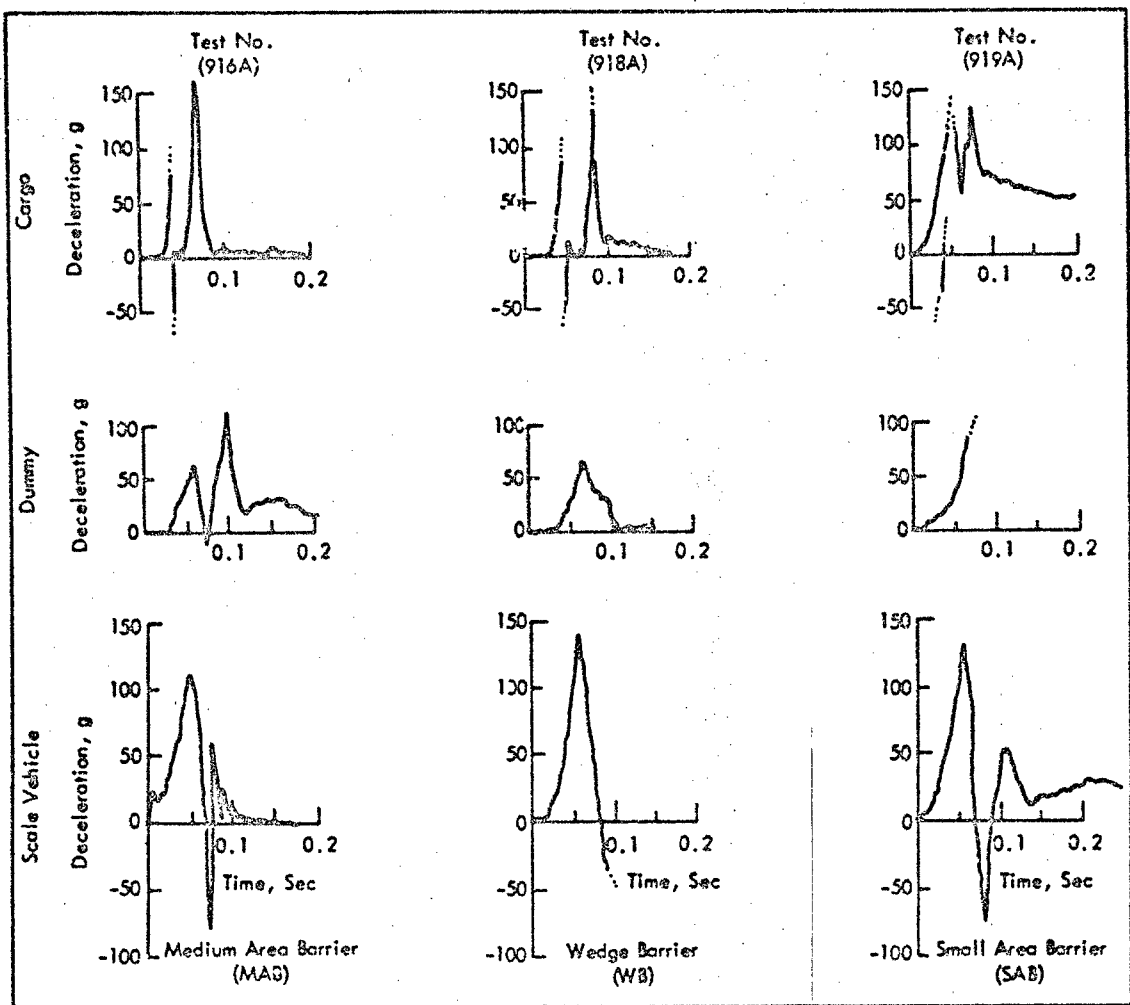
Figure 26. Responses of Cargo, Dummy and Scale Vehicles with Series 900A
Energy Dissipator Subject to 32 Miles Per Hour Impact

240

c. Certain energy dissipators, such
as Series 100, 200 and 400,
when interacting with the wedge
and pole barriers tend to main-
tain relatively low and yet con-
stant peak responses of the model
vehicle, as shown in Figures 14,
15, and 17, respectively. Fur-
thermore, the responses of the
mannequin and the simulated car-
go to wedge barrier impact tests,
as shown in Figures 24 through
26, are comparatively lower than
that of other barrier impacts;
and the responses of the dummy,
in particular, are considered
as tolerable for humans to sur-
vive. This phenomenon may sug-
gest that the principal energy
dissipating mechanisms gener-
ated between these dissipators
and the barriers could be uti-
lized to design structural sys-
tems of prototype vehicle
which would respond in the same
manner as that of the experimen-
tal model.

d. The one-tenth scale mode   d
in the tests have shown
factory results in
energy dissipating   in
of barrier collisions. F.
example, Figure 27 represe..cs a
comparison between the barrier
collision responses of a 1937
Plymouth [4] and the type I
model with a series 200 energy
dissipator. Figure 28 repre-
sents a comparison between the
responses of a 1949 Chevrolet
[5] and the type I model with
a Series 700 energy dissipator.
The similarity of the curves in
these examples are remarkable.
The discrepancy in the early
peaking of the model vehicle
can be eliminated by modifying
the material properties of the
energy dissipator.
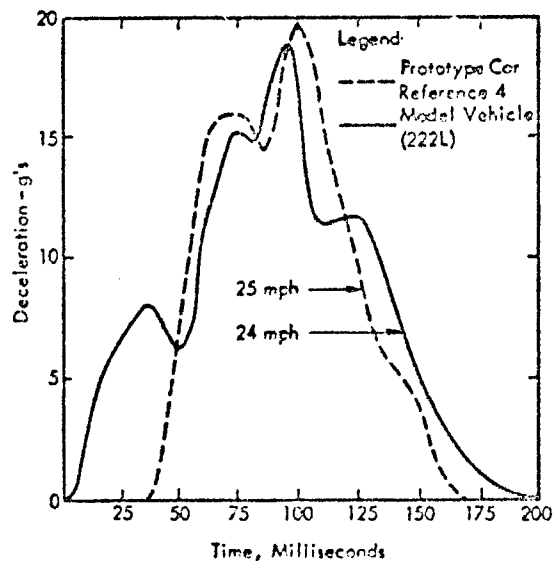
Figure 27. Comparison of Deceleration
Responses of a Prototype Car
and Type I Model Vehicle
with a 200 Energy Dissipator
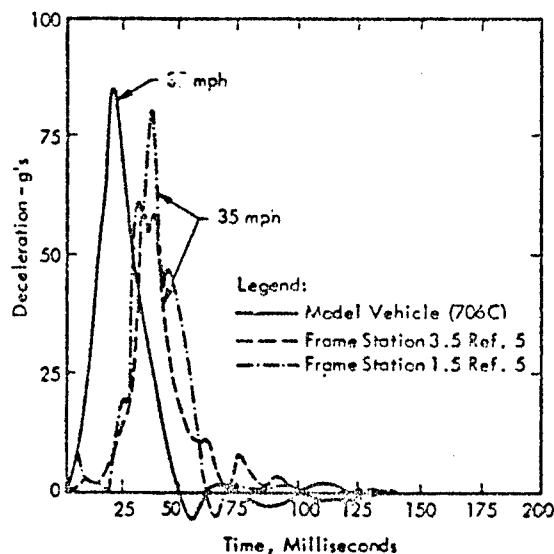
Figure 28. Comparison of Deceleration
Responses of a Prototype Car
and Type II Model Vehicle
with a 700 Energy Dissipator

241

PREDICTION OF SCALE MODEL VEHICLE RE-
SPONSES TO MEDIUM-AREA-BARRIER IMPACT

The mathematical model used in this
analysis, as shown in Figure 29, con-
sists of a vehicle V of mass m_v travel-
ing at an initial velocity v_o striking an
infinitely rigid barrier. The front of
the vehicle is protected by a series of
three crushable energy dissipators of
thicknesses L_1, L_2, L_3. The cross-
sectional area A is common to the front
of the vehicle, the three dissipators
and the barrier.
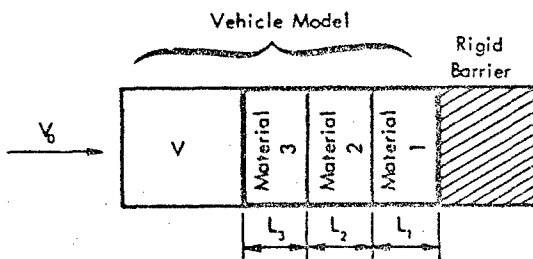
Figure 29. Analytical Model of the
Scale Vehicle

The stress-strain characteristics of
the three dissipating materials are
known; their idealized characteristics
are shown in Figure 30. For the pur-
pose of the present analysis, it is
assumed that dissipator 1 reaches its
yield point $(\sigma_{c_1} \epsilon_{c_1})$, collapses to its
plastic state $(\sigma_{p_1} \epsilon_{p_1})$, and then reaches
the end of its plastic state $(\sigma_{p_1} \epsilon_{c_1})$,
after which it is crushed to its mini-
mum thickness and then becomes inert.
The stress begins to rise again, until
dissipator 2 reaches its yield point,
and so on. We assume that there is no
"stress overlap", i.e., that

$$\sigma_{c_3} > \sigma_{p_3} > \sigma_{c_2} > \sigma_{p_2} > \sigma_{c_1} > \sigma_{p_1}$$

We also assume that $\epsilon_p > \epsilon_c$, and that the
gradient of the characteristic becomes
infinite at $\epsilon = \epsilon_{L_1}$.

Strain, ϵ (In./In.)
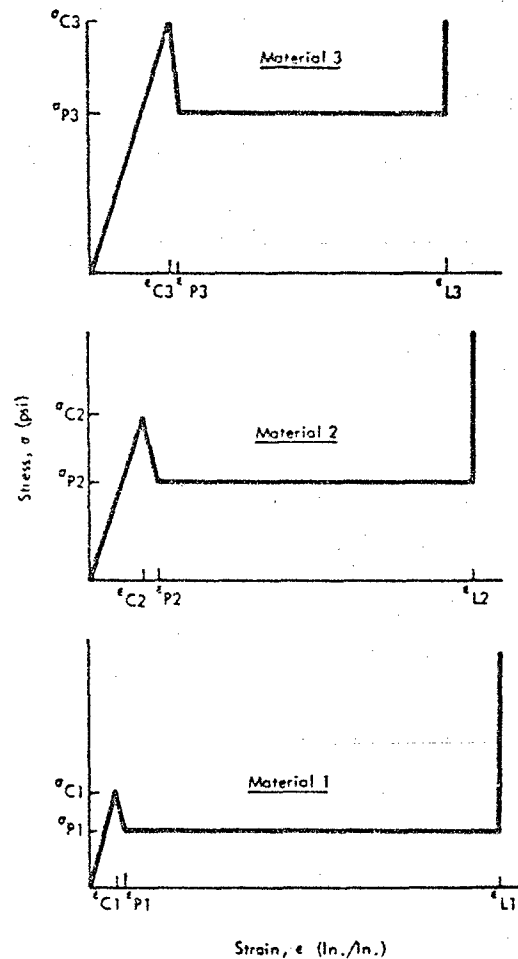
Figure 30. Idealized Stress-Strain
Characteristics of Energy
Dissipators

Having estimated the stress-strain
characteristics for the three materials
comprising the energy dissipator under
consideration, the analysis divides the
post-impact behavior into nine phases.
For the purposes of the analysis, it has
to be assumed that one material reaches
its yield point, passes through its
plastic mode and becomes compressed to
its maximum limit, (after which it is
energetically inert), before the stress
has reached the yield point of the next
material. The first material to yield
is denoted dissipator 1, the second as
2, and the third as 3. For a non-
collapsible material, it is assumed that

the plastic mode is very limited, i.e., that the maximum crushing limiting strain is only very slightly greater than the hypothetical "yield strain."

The analysis of the vehicle model, is divided into nine phases, each phase being evaluated numerically in small increments of either σ or ϵ. The principal assumption is that the stress is constant throughout the system at any given instant in time; that is, that the same stress is applied to each dissipator in each increment. The nine phases of the analysis outlined in Table III are:

Phase 1

The stress excursion during Phase 1 is divided into a number (say 25) of increments $\Delta\sigma$, where

$$\Delta\sigma = \sigma_{c_1}/25 \qquad (1)$$

The final stress at the end of the n-th increment is $n\Delta\sigma$. If we denote the gradient of the elastic portion of the stress-strain curves at m_i, then the compression at the end of the n-th increment for dissipator i is given by

$$\Delta s_i' = n\Delta\sigma \cdot \frac{L_i}{m_i} \qquad (2)$$

where L_i is the initial length of the dissipator. If we denote by $\Sigma\Delta s_i$ the compression at the beginning of the increment, the compression which took place during the increment is given by

$$\Delta s_i = n\Delta\sigma \frac{L_i}{m_i} - \Sigma\Delta s_i \qquad (3)$$

Now, strain energy absorbed is given by the general expression

$$\Delta E = \sigma A \Delta s \qquad (4)$$

TABLE IV

Nine Phases of the Analysis

	Stress		#1 Strain		#2 Strain		#3 Strain		Mechanical Condition of Dissipation			Energy Transfer of Dissipation		
	Initial	Final	Initial	Final	Initial	Final	Initial	Final	#1	#2	#3	#1	#2	#3
1	0	σ_{c_1}	0	ϵ_{c_1}	0	*	0	*	Elastic	Elastic	Elastic	Absorb	Absorb	Absorb
2	σ_{c_1}	σ_{p_1}	ϵ_{c_1}	ϵ_{p_1}	*	*	*	*	Failing	Elastic	Elastic	Absorb	Emit	Emit
3	σ_{p_1}	σ_{p_1}	ϵ_{p_1}	ϵ_{L_1}	-	-	-	-	Plastic	Stationary	Stationary	Absorb	Inert	Inert
4	σ_{p_1}	σ_{c_2}	Inert	Inert	*	ϵ_{c_2}	*	*	Inert	Elastic	Elastic	Inert	Absorb	Absorb
5	σ_{c_2}	σ_{p_2}			ϵ_{c_2}	ϵ_{p_2}	*	*		Failing	Elastic		Absorb	Emit
6					ϵ_{p_2}	ϵ_{L_2}	-	-		Plastic	Stationary		Absorb	Inert
7	σ_{p_2}	σ_{c_3}			Inert	Inert	*	ϵ_{c_3}		Inert	Elastic		Inert	Absorb
8	σ_{c_3}	σ_{p_3}					ϵ_{c_3}	ϵ_{p_3}			Failing			Absorb
9	σ_{p_3}	σ_{p_3}					ϵ_{p_3}	ϵ_{L_3}			Plastic			Absorb

* Intermediate Strain to be Computed

243

where $\bar{\sigma}$ = mean stress acting,

A = cross-sectional area, and

Δs = stroke during the increment. Now we have, for the n-th increment,

$$\bar{\sigma} = \left(n - \frac{1}{2}\right)\Delta\sigma \qquad (5)$$

and hence

$$\Delta E_i = \left(n - \frac{1}{2}\right)\Delta\sigma A \Delta s_i \qquad (6)$$

where Δs_i is given by Equation (3).

The total energy absorbed during the increment is given by

$$\Delta E_t = \sum_1^3 \Delta E_i \qquad (7)$$

and this quantity is known. Now if the initial velocity at the beginning of the increment is v_o', and the final velocity $(v_o' - \Delta v)$, we may calculate Δv from the equation of conservation of energy in the form

$$\Delta E_t = \frac{1}{2}\frac{m_v}{g}\left[v_o'^2 - (v_o' - \Delta v)^2\right] \quad (8)$$

Now the total distance traveled during the increment by the vehicle is given by

$$\Delta s_t = \sum_1^3 \Delta s_i \qquad (9)$$

and the mean speed of the vehicle during the increment is

$$\bar{v} = \frac{1}{2}\left[v_o' + (v_o' - \Delta v)\right] \qquad (10)$$

Thus we may calculate the time occupied by the increment as

$$\Delta t = \frac{\bar{v}}{\Delta s_t} \qquad (11)$$

the mean deceleration during the increment as

$$g = \frac{\Delta v}{\Delta t} \qquad (12)$$

and the rate of change of deceleration as

$$\dot{g} = \frac{g}{\Delta t} \qquad (13)$$

Phase 2

Dissipator 1 has passed its yield point and is collapsing towards the plastic state. As the stress falls, dissipators 2 and 3 elastically expand and give up energy to the system. Analogous to Equation (1) we have

$$\Delta\sigma = \frac{1}{25}\left(\sigma_{c_1} - \sigma_{P_1}\right) \qquad (14)$$

If we denote the gradient of the failing portion of the stress-strain characteristics as m_{c_1}, then, using the same arguments as previously we have for the n-th increment

$$\Delta s_i = \left(\epsilon_{c_1} + \frac{n\Delta\sigma}{m_{c_1}}\right)L_1 - \Sigma\Delta s_1 \quad (15)$$

where we have assigned a negative sign to m_{c_1}. Thus the energy absorbed by 1 is given by

$$\Delta E_1 = \left[\sigma_{c_1} - \left(n - \frac{1}{2}\right)\Delta\sigma\right]A\Delta s_1 \quad (16)$$

Dissipators 2 and 3 have expanded again, their strokes being given by

$$\Delta s_i = \Sigma\Delta s_i - L_i\left(\hat{\epsilon}_i - \frac{n\Delta\sigma}{m_i}\right) \quad (17)$$

where $\hat{\epsilon}_i$ = the strain of that dissipator at the beginning of the phase. The energy given up by 2 and 3 is

$$\Delta E_i = \left[\sigma_{c_1} - \left(n - \frac{1}{2}\right)\Delta\sigma\right]A\Delta s_i \quad (18)$$

Thus, noting that

$$\Delta s_t = \Delta s_1 - \Delta s_2 - \Delta s_3$$

$$\Delta E_t = \Delta E_1 - \Delta E_2 - \Delta E_3 \tag{19}$$

we may compute Δv, Δt_1, g, and $\dot{g}$ as before

Phase 3

Dissipator 1 is absorbing energy in its plastic mode at constant stress σ_{p_1}. Dissipators 2 and 3 are inert and stationary. We now consider the strain excursion ϵ_{p_1} to ϵ_{L_1} as being divided into increments $\Delta\epsilon$ given by

$$\Delta\epsilon = -\frac{1}{25}\left(\epsilon_{p_1} - \epsilon_{L_1}\right) \tag{20}$$

For the n-th increment the compression of 1 is given by

$$\Delta s_1 = \left(\epsilon_{p_1} + n\Delta\epsilon\right) L_1 - \Sigma\Delta s_1 \tag{21}$$

and the energy absorbed is given by

$$\Delta E_1 = \sigma_{p_1} A \Delta s_1 \tag{22}$$

Noting that $\Delta E_t = \Delta E_1$ and $\Delta s_t = \Delta s_1$, we may compute Δv, Δt, g, and $\dot{g}$ as before.

Phase 4

Dissipator 1 is totally collapsed and henceforth is inert. Dissipators 2 and 3 are absorbing energy in their elastic modes, and the calculations are similar to those presented for Phase 1.

Phase 5

Dissipator 2 reaches its yield stress and collapses towards its plastic state, absorbing energy. Dissipator 3 expands elastically as the stress falls, giving

up energy. The calculations are similar to those for Phase 2.

Phase 6

Dissipator 2 is collapsing in its plastic state, absorbing energy at constant stress. Dissipator 3 is temporarily stationary and inert. Calculations as Phase 3.

Phase 7

Dissipator 2 is totally collapsed and henceforth inert. Dissipator 3 is absorbing energy in its elastic mode again. Calculations as Phase 1.

Phase 8

Dissipator 3 reaches its yield point and collapses towards its plastic state, absorbing energy. Calculations as Phase 2, except of course, no energy is given up by other dissipators.

Phase 9

Dissipator 3 absorbing energy in its plastic mode at constant stress.

The analysis permits the calculation of the complete displacement, velocity, deceleration, and rate-of-change of deceleration histories, from the moment of impact, through as many of the phases as are utilized, until either all the incident kinetic energy has been absorbed, or until the dissipators are all totally expended. Vehicle rebound is ignored and only the case of impact against a flat barrier of area equal to the cross-sectional area of the dissipators is considered.

In order to predict analytical responses, numerical computations have been performed to evaluate medium area impact responses with Series 200, 700, and 900 energy dissipators. The idealized stress-strain curves of the energy dissipating materials are presented in Figures 31 through 33. The analytical results are compared with the following test cases:
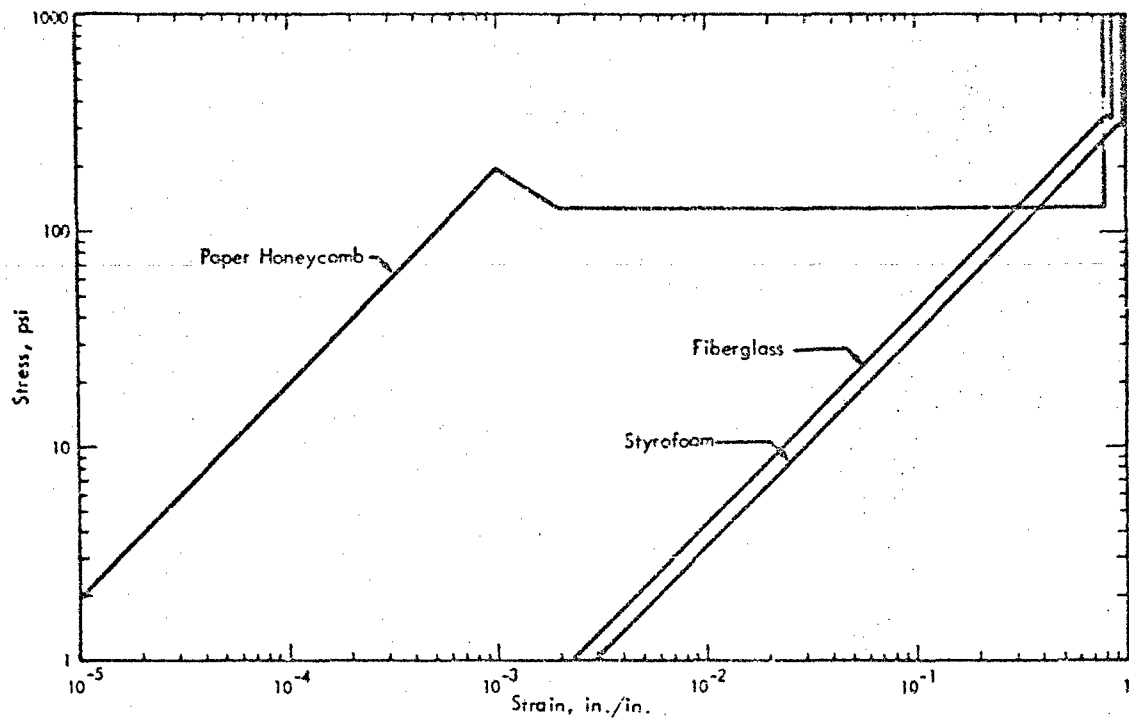
Figure 31. Component Stress-Strain Curves of Series 200 Energy Dissipator
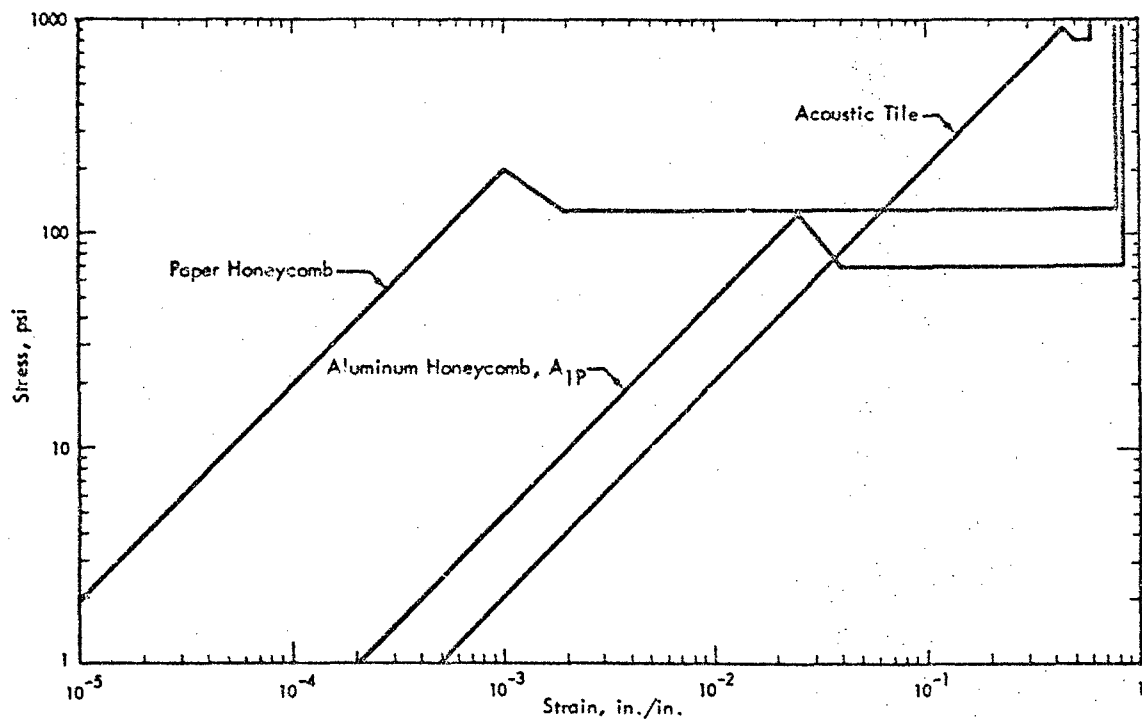
Figure 32. Component Stress-Strain Curves of Series 700 Energy Dissipator
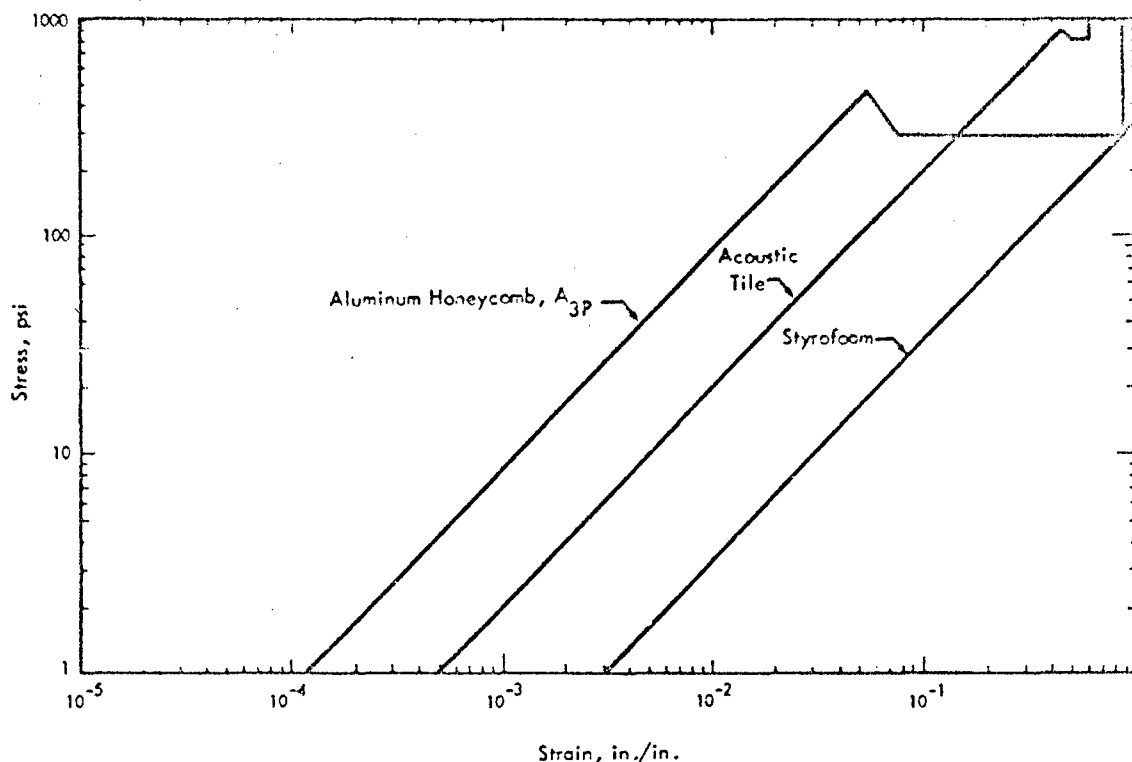
Figure 33. Component Stress-Strain Curves of Series 900 Energy Dissipator

Case I: Series 200 dissipator (paper
          honeycomb, fiberglass and styro-
          foam) at impact velocity of 32
          mph. Comparison between analy-
          tical and experimental results
          for Test No. 206C is presented
          in Figure 34.

Case II: Series 700 dissipator (paper
          honeycomb, aluminum honeycomb
          and acoustic tile) at impact
          velocity of 24 mph. Comparison
          between analytical and experi-
          mental results for Test Nos.
          701B and 703G is presented in
          Figure 35.

Case III: Series 900 dissipator (alumi-
          num honeycomb, acoustic tile
          and styrofoam) at impact velo-
          city of 39 mph. Comparison be-
          tween analytical and experi-
          mental results for Test No.
          905F is presented in Figure 36.
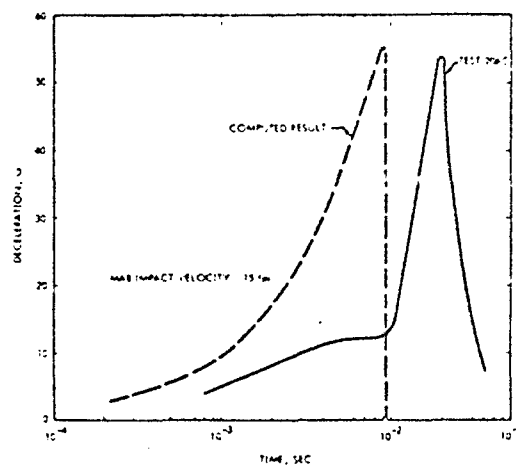
Figure 34. Comparison of Analytical
           and Experimental Vehicle
           Responses with Series 200
           Energy Dissipator

247
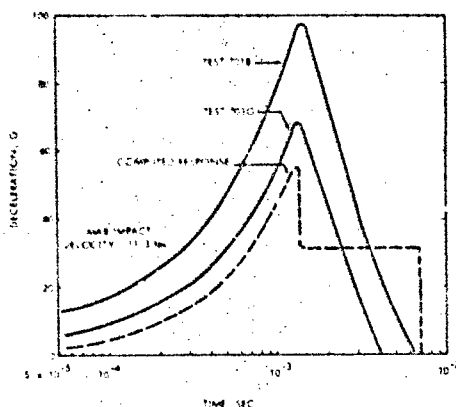
Figure 35. Comparison of Analytical
and Experimental Vehicle
Responses with Series 700
Energy Dissipator
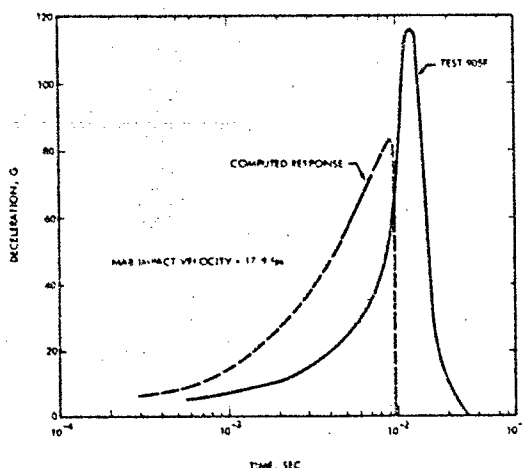
Figure 36. Comparison of Analytical
and Experimental Vehicle
Responses with Series 900
Energy Dissipator

The comparison between experimental
and analytical response curves is quite
encouraging. Although there exists
certain disagreements in response ampli-
tudes, the general shapes of analytical
curves are quite satisfactory. It is
believed that accuracy in analytical
prediction could be achieved with im-
proved stress-strain curves.

SUMMARY AND CONCLUSIONS

The test data obtained through simu-
lated crash experiments have revealed
several interesting results, namely:

● Peak-g levels of Wedge Barrier
Impacts are usually lower than
those of Medium Area Barrier and
Small Area Barrier, and for some
cases, responses are not sensitive
to impact speeds;

● The models respond severely to
Medium Area and Small Area Bar-
riers at high impact speeds. The
cargo restraining system broke
loose on series 700A, 800A and
900A dissipators at 32 mph impact
speeds. Series 200 dissipators
with softer composite material
properties performed well to pro-
tect both the occupant and the
cargo;

● Series 100, 200 and 400 dissipa-
tors are relatively insensitive
to Wedge Barrier impacts, and
peak-g levels are substantially
lower than those of the other
groups.

The objectives of this study were to
show that the energy dissipation mecha-
nisms of motor vehicle structures can be
simulated by scale model experiments,
and that the experimental results can be
of significant value toward the formu-
lation of an analytical model.

The results of the scale-model exper-
imental study have provided a significant
understanding of structural impact mech-
anisms; and have shown the effectiveness
of experimental models for simulating
vital crash parameters which may be en-
countered during full-scale tests.   In
particular, the following concluding re-
marks can be made:

● The crash model performed remark-
ably well in simulating collision
responses.

● The response prediction model de-
veloped in this report provides
satisfactory agreement in predic-
ting decelerating responses to
medium area barrier impacts.

248

- Energy dissipation of the crash models is dependent upon impact velocity, barrier shape and cross-sectional area. Test results also indicate that the model impacts with the wedge-type barrier demonstrated energy dissipation characteristics which provided smoother and substantially lower deceleration loads to the occupant and cargo than did the other barriers.

- It is possible to design optimum energy dissipators which are independent of impact velocities for each type of barrier.

ACKNOWLEDGEMENTS

REFERENCES

1. Kao, G., Conticelli, V., "Responses and Classifications of Vehicle Structures," Wyle Laboratories Research Report WR-68-3, Volume IV of V (March 1968).

2. Baker, W.E., Editor, "Use of Models and Scaling Laws in Shock and Vibration," The American Society of Mechanical Engineers Publication (November 1963.

3. Dempster, W.T., "Space Requirements of the Seated Operator," WADC TR 55-159 (July 1955).

4. Severy, D.M., and Mathewson, J.H., "Automobile-Barrier Impacts – Series II," Clinical Orthopaedics Vol. 9, 1955.

5. Severy, D.M., Mathewson, J.H., and Siegel, A.W., "Barrier Collisions, IV. An Evaluation of Motorist Force and Injury Control Systems," Highway Research Board Proceedings, Vol. 40, 1961.

DISCUSSION

Mr. Hanks (NASA, Langley): What is the purpose for this study, do you plan to use this to study the human effects in a crash?

Mr. Kao: The purpose of this study is two-fold. First we try to develop a technique to use the scale model vehicle to simulate the true or equivalent collision environment. The scale model testing program is relatively inexpensive and you can try it out on a very small size and can test out all the pertinent test parameters that you would like to test later on for the prototype vehicle. We ran about 120 scale model tests in a 10 day period, and collected much good data. Then we can decide what would be the most important parameter to look for in the prototype testing. Secondly, we try to establish

---

an analytical model to predict the response of the vehicle structure.

Mr. Hanks: I was more intrigued by the small human model.

Mr. Kao: We did not intend to predict analytically the response of the human model.

Mr. Verga (Hazeltine Corp.): I am curious as to who is budgeting this program? Is it an in-house Wyle project or are there auto industries looking into this and should we look forward to seeing a crash proof compartment in addition to the fire wall in passenger cars in the near future?

Mr. Kao: This program was sponsored by the Department of Transportation. Currently we are looking into the possibility of conducting secondary collision type of testing.

Mr. Renius: I would like to add that to my knowledge all the automotive manufacturers are

looking into the same sort of materials application for future automobiles.

Mr. Kapur (Aerospace Corp.): What kind of material properties did you use - dynamic material properties or static ones?

Mr. Kao: These are the static material properties. That may be the reason that our analytical results do not quite agree w.th experiment.

Mr. Kapur: I think you will get much better correlation if you use dynamic material properties.

Mr. Kao: In the future I think we will do that.

Mr. Westine (Southwest Research Institute): I have some comments. I have a friend who defines modeling as the art of skilial approximation. Among the things that you approximate is the strength of the mannekin. How does one decide what is the strength in the muscles in the man's arm, particularly when you know a real individual tenses up. What are the load-deflection characteristics of a mannekin when he is getting smashed. This means of course that you have made approximations. The other thing I would note is that the form of modeling which you chose used a true time scale and the model which you used simulated lumped inertial effects, gravitational effects and constitutive effects, or stress-strain effects of material, you did this by distorting what I would call distributed inertial effects. You approximated them with lump inertial effects. Why did you pick this form of a model over what I would call a Cauchy model? Some people might call it a mock one, others a replica model. That form of model simulates distributed inertial effects, lumped inertial effects, load de-

flection or constitutive effects and distorts gravitational effects. It is a question of what one approximates. Why, for example, did you think that gravitational effects mattered and had to be simulated in making the model?

Mr. Kao: To answer your first question about the use of human volunteers. I think you can get human volunteers. In fact we did contact an association in Los Angeles and learned that you can get 3 men for two weeks for $5,000. To answer your second question - the true parameter that we tried to simulate was the deceleration versus time. That is why we chose the gravitation scaling law which gives 1 to 1 ratio without any modification. If we do this we have to sacrifice other parameters. Because this is such simple model we did not try to complicate the other scaling parameters.

Mr. Westine: The replica model to which I referred which simulates distributed inertia, lumped inertia and constitutive effects would use scale time as the length ratio and forces as the square of the length ratio which you did. It would just be a question of how you interpret time. For example, I noted that your peak forces and accelerations seem to match pretty well but you seem to have a little trouble with your time scales. You simulated gravitational effects and I do not think they matter.

Mr. Kao: I agree with you. The reason we have to take the time into consideration is because the human impact tolerance limit is inversely proportional to the time duration. The human can take a high g input for a very short period of time. However, he cannot sustain a low g input for a sustained period of time and that is why we look into the time factor as well. Your comment is very worthwhile.

DESIGN OF RECOIL ADAPTERS

FOR ARMAMENT SYSTEMS

A. S. Whitehill, T. L. Quinn
Lord Manufacturing Company
Erie, Pennsylvania

Placement of guns in aircraft has always presented interesting
engineering problems. At one time, it was necessary to syn-
chronize the firing rate with the rotation of the propeller to
prevent the pilot from shooting himself down. Today's rapid
firing weapons producing high recoil forces demand adequate
protection for the aircraft structure.

The gun on its supports must be considered a six degree of free-
dom system. Proper evaluation of the problem of placing guns in
aircraft must consider the dynamics of the entire system includ-
ing the stiffnesses of the support points and the motion of the
gun in response to the forces and torques resulting from recoil.
It is possible to make several valid assumptions, however, which
will simplify the analysis without sacrificing understanding of
the problem. The new approach in designing recoil adapters
views the gunfire as a forced vibration rather than a series of
shock pulses. The concepts presented reveal new avenues leading
to a significant reduction in recoil dither forces.

INTRODUCTION

Since the advent of supersonic tac-
tical fighters, there has been a con-
tinuing emphasis on the development of
a more versatile firing platform. The
Vietnam conflict has clearly demon-
strated the need for both missiles and
guns on fighter aircraft to eliminate
any performance gaps which one or the
other may possess.

Today, fighter aircraft carry both
missiles and guns. At a range of 1.5
to 5 miles, missiles using radar to
lock onto the target are available to
the pilot. However, he is often re-
luctant to use this weapon due to the
identification problem at this dis-
tance. Vietnam is one warfare arena
where the chances that a blip on the
radar screen may be a commercial air-
liner are as great as being a MiG.

At distances less than 1.5 miles or
8,000 feet, the pilot will generally use
visual identification to determine
friend or foe. In this case, the infra-
red homing missile can be used against
the MiG. Due to acceleration restric-
tions (the effectiveness of the missile
decreases with increasing lateral accel-
eration) the pilot must stay on the
MiG's tail to achieve any degree of suc-
cess. In addition, in the event of pilot
error, a heat-seeking missile is capable
of homing in on closer, friendly aircraft
rather than the more distant enemy.

Since the heat-seeking missile is in-
capable of tight, fast maneuvers, the
gun is still the most effective weapon
in close-in dogfighting. The chart on
the next page depicts the effective
range of the various weapons in the fir-
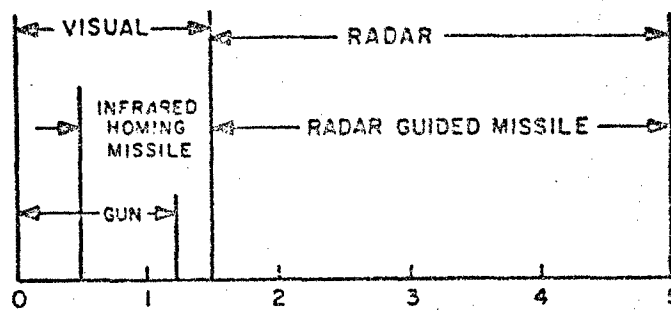ing platform of the modern fighter.

Fig. 1 - Distance From Launch (Mi.)

While the gun has clearly demonstrated its value, externally mounted gun pods on aircraft have the disadvantages of detracting from the aircraft's ability to maneuver and of costing some aircraft speed. While this may be unimportant during missions involving support fire of ground troops, it could prove deadly in dogfights with highly maneuverable MiGs. The resolution of this problem involves placement of the gun within the aircraft structure, usually in the nose of the plane.

Recoil adapters are of prime importance in a project of this type. If a 20mm gun were hard mounted, the peak recoil force per round would be approximately 32,000 pounds occurring each time the gun fires. Lord Manufacturing Company became involved in one project through efforts in developing an improved recoil adapter to reduce this recoil force.

DISCUSSION

In the past, the philosophy surrounding the design of recoil adapters has been to treat each firing pulse as an individual shock problem. The approach used was to design sufficient damping into the adapter to dissipate the energy of the recoiling gun and return the weapon to its original position before the next round was fired.

This method remains legitimate for low rate weapons, such as grenade launchers. The recoil adapters are designed with the same principles involved in the designing of shock mounts. The energy to be stored and dissipated is calculated from

$$E = \frac{1}{2} \frac{I^2}{m}$$

where   I = the impulse from the round
        m = the mass of the gun

Generally, a principal system constraint is the allowable recoil deflection. If the energy is to be stored in a spring, the linear spring rate can be calculated from

$$K = \frac{2E}{d^2}$$

where   K = spring rate of the adapter
        d = allowable recoil deflection

The corresponding peak recoil force is then calculated from

$$F_{PK} = Kd = \frac{2E}{d} = \frac{I^2}{md}$$

A linear spring is considered a 50% efficient energy storage device; that is, the energy stored is equal to one-half its peak force times the maximum deflection, or

$$E = \frac{1}{2} F_{PK} d$$

The corresponding load-deflection curve is shown in Fig. 2. The energy storage capability is proportional to the area under the curve.
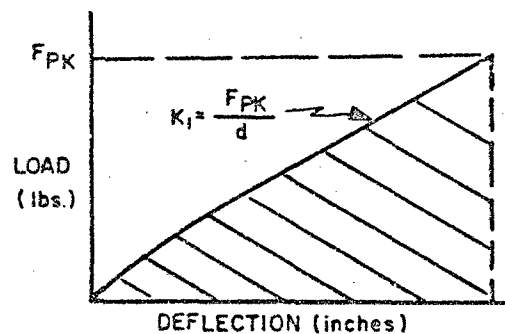

Fig. 2 - Load-Deflection Curve For A Linear Energy Storage Device

252

By using a softer, preloaded spring, the efficiency of the device can be greatly increased as shown in Fig. 3.

LOAD
(lbs)

$(1-n)F_{PK}$

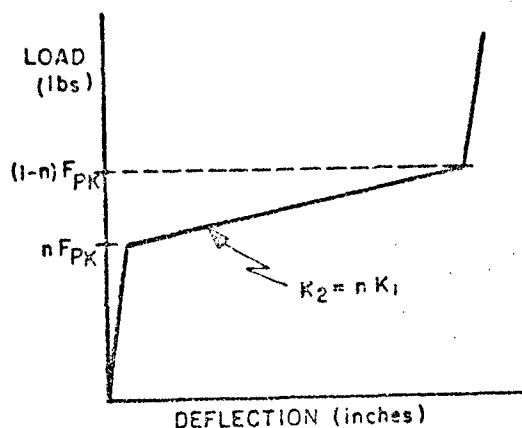nF_{PK}

$K_2 = nK_1$

DEFLECTION (inches)

Fig. 3 - Load-Deflection Curve
For A Preloaded Or Bi-Linear
Energy Storage Device

Thus, a bi-linear recoil adapter is capable of storing the same amount of energy as a linear adapter with equal deflection but with a much smaller recoil force. For example, if the preload of the bi-linear system is 1/3 F_{PK}, then the maximum recoil force from the bi-linear adapter will be only 2/3 the peak force from the linear system assuming the spring in the bi-linear device has 1/3 the stiffness as that in the linear adapter.

To dissipate the stored energy before the next round is fired, damping is required. The amount of damping needed is dependent upon the firing rate of the weapon. If the firing rate is low, the natural frequency of the adapters could be set sufficiently high such that the system may oscillate through several cycles between rounds. In this case, the amount of damping required is usually not too high.

As the firing rate is increased, however, the time available for dissipating the energy of the gun becomes shorter. In this situation, the amount of damping required increases which results in a higher peak recoil force.

Modern weapon technology has increased the firing rates of guns to the point that some fire at rates of up to

6,000 rounds per minute or 100 rounds per second. It was this development which led to the treatment of each burst of gunfire as a high-frequency, forced vibration rather than an individual shock.

MULTI-DEGREE OF FREEDOM SYSTEM

A gun on its supports should be considered as a six degree of freedom system capable of translating along and rotating about the three principal axes. However, because the recoil force is always in one direction, the gun will tend to translate in that direction and rotate about the pitch and yaw axes which are perpendicular to the recoil axis. The rotation is a result of the torques caused by the center of gravity of the gun and the center of elasticity of its supports not lying in the line of action of the recoil forcing pulse—that is, the firing barrel.

This rotation is considered highly undesirable because it could cause wide dispersion of the shells. To resolve this problem, guns have been placed in very stiff structures to permit translational recoil motion only. However, if the eccentricities are significant, the resulting torques must be reacted by equal and opposite torques somewhere in the system. To prevent the structure from responding to the firing pulse from each round, the pulse period must be more than six times the natural period of the structure. The period of a gunfire pulse is usually low (on the order of .002 seconds). Since the natural period of a simple spring-mass system is

$$T = 2\pi\sqrt{\frac{M}{K}}$$

and if T is one-sixth the gunfire pulse period:

$$T = \frac{.002}{6} = 3.3 \times 10^{-4} \text{ seconds}$$

Then, the needed spring rate of the structure can be calculated from

$$K = \frac{4\pi^2 M}{T^2} = \frac{4\pi^2 w}{T^2 g}$$

For a gun weighing 386 pounds, the structural stiffness needed to prevent response to the gunfire pulse is 3.6 X 10^8 lbs/in, a fantastic stiffness to expect from practical structures.

TWO DEGREE OF FREEDOM ANALYSIS

A diagram of the system to be analyzed is shown in Fig. 4.

253
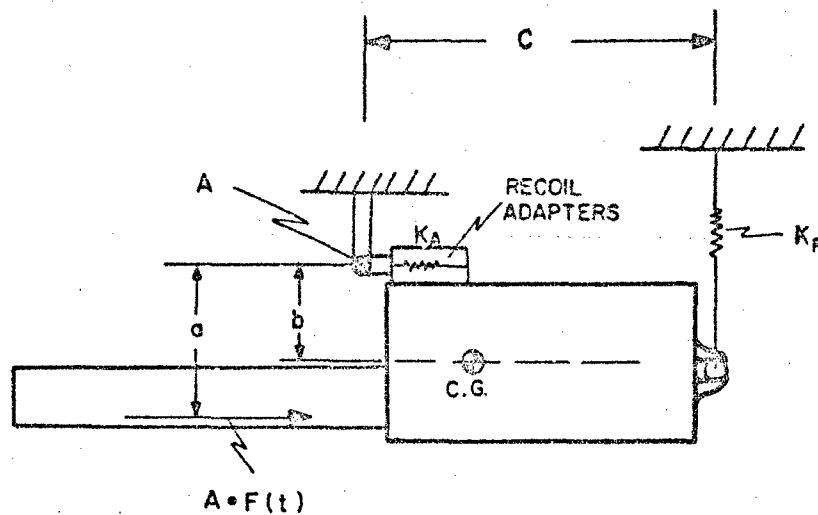
Fig. 4 - Typical Gun System

NOTATIONS

A = Pivot point

a = Distance between "A" and the center of gravity

b = Distance between "A" and the firing barrel

c = Distance between "A" and the rear support

AF(t) = Recoil forcing pulse as a function of time

K_A = Axial spring rate of the recoil adapters

K_R = Radial spring rate of the rear support

M = Mass of the gun

X = Linear motion along the recoil axis as measured at the recoil adapter

$\ddot{X}$ = Acceleration along recoil axis

θ = Angular motion about "A"

$\ddot{\theta}$ = Angular acceleration about "A"

I_A = Moment of inertia about "A"

r = Radius of gyration about "A"

f = Firing frequency in cps

f_n = Axial natural frequency

w = 2-f = circular firing frequency

w_n = $\sqrt{K/M}$ = 2-f = circular natural frequency

X_{AVE} = Set back in the recoil direction

X_{DIT} = Dither motion about X_{AVE}

θ_{AVE} = Angular windup about "A"

θ_{DIT} = Angular dither motion about θ_{AVE}

t = Time (seconds)

F_{AVE} = Time averaged recoil force

T_{AVE} = Time averaged windup torque about "A"

KE = Free recoil kinetic energy

V = Free recoil velocity

I = Recoil impulse

E_T = Energy stored in translation

E_R = Energy stored in rotation

254

The assumptions involved in the analysis are as follows:

1. The firing barrel, the center of gravity of the gun, the elastic center of the recoil adapters, and the rear ball support lie in the same plane.

2. The system has two degrees of freedom and is capable of translation along the recoil axis and rotation about the attaching pin through the recoil adapter inner member.

3. The recoil adapters are linear springs with little or no damping.

4. The rear support has some spring rate in the radial direction, regardless how high.

The differential equations of motion involving two dependant variables X and θ and one independent variable are written:

$$\Sigma P = 0 = M(\ddot{X} + a\ddot{\theta}) + K_A X - AF(t) \quad (1)$$

$$\Sigma M_A = 0 = aM(\ddot{X} + a\ddot{\theta}) - bAF(t) + I_A \ddot{\theta} + c^2 K_R \theta \quad (2)$$

These two equations can be combined, eliminating the recoil forcing pulse

AF(t) and resulting in a linear second order differential equation with two unknowns.

$$\left[aM(a-b) + I_A \right] \ddot{\theta} + c^2 K_R \theta = -M(a-b)\ddot{X} + b K_A X \quad (3)$$

Solutions were assumed of the form

$$X = X_{AVE} + X_{DIT} \sin \omega t \quad (4)$$

$$\theta = \theta_{AVE} + \theta_{DIT} \sin_n t \quad (5)$$

In these equations, X_{AVE} is an average recoil deflection and θ_{AVE} is an average angular windup about "A". X_{DIT} and θ_{DIT} are the vibratory or dither motion superimposed on the average recoil deflection and the dither oscillation about the average windup respectively. This form generally agrees with the appearance of the oscillograph traces of gun motion.

The second derivatives are taken with respect to time to obtain the linear and angular acceleration of the system.

$$\ddot{X} = -X_{DIT} \omega^2 \sin \omega t \quad (6)$$

and

$$\ddot{\theta} = -\theta_{DIT} \omega^2 \sin \omega t \quad (7)$$

Substitution into (3) yields:

$$\theta_{DIT} \sin \omega t \left\{ c^2 K_R - \omega^2 \left[aM(a-b) + I_A \right] \right\} + c^2 K_R \theta_{AVE} = \quad (8)$$

$$X_{DIT} \sin \omega t \left\{ b K_A + \omega^2 M(a-b) \right\} + b K_A X_{AVE}$$

Since,

$$X_{AVE} = \frac{F_{AVE}}{K_A} \quad (9)$$

$$\theta_{AVE} = \frac{T_{AVE}}{c^2 K_R} = \frac{b F_{AVE}}{c^2 K_R} \quad (10)$$

then,

$$\theta_{DIT} = \frac{b + \left(\frac{\omega}{\omega_n}\right)^2 (a-b)}{c^2 K_R/K_A - \left(\frac{\omega}{\omega_n}\right)^2 \left[a(a-b) + r \right]} X_{DIT} \quad (11)$$

A second equation containing the same unknowns of X_{DIT} and θ_{DIT} can be derived on the basis of the conservation of energy in the system. The total free recoil energy is equal to the energy stored in translation plus the energy stored in rotation.

$$KE = E_T + E_R \quad (12)$$

$$E_T = \frac{1}{2} MV^2 = 2 X_{DIT} F_{AVE} \quad (13)$$

therefore,

$$V = \sqrt{\frac{4 X_{DIT} F_{AVE}}{M}} \quad (14)$$

$$E_R = \frac{1}{2} I_A \dot{\theta}^2 = 2 \theta_{DIT} b F_{AVE} \quad (15)$$

255

therefore,

$$\Delta = \sqrt{\frac{4\,\Theta_{DIT}\,b\,F_{AVE}}{I_A}} \qquad (16)$$

Another equation involving the conservation of momentum can also be written:

$$I = M\,(\Delta V) + \frac{I_A\,(\Delta\dot\theta)}{b} \qquad (17)$$

or,

$$I = 2\,(MV + \frac{I_A\dot\theta}{b}) \qquad (18)$$

Substitution of equations (14) and (16) into (18) eventually yields:

$$X_{DIT} = \left[\frac{1}{4}\sqrt{\frac{I}{M\,f}} - r\sqrt{\frac{\Theta_{DIT}}{b}}\right]^2 \qquad (19)$$

Equations (11) and (19) can be solved in the conventional manner and solutions for X_{DIT} and Θ_{DIT} can be obtained in terms of system geometry, gun mass and radius of gyration, recoil adapter natural frequency, firing frequency, and the ratio of the rear support spring rate to the recoil adapter spring rate.

$$X_{DIT} = \frac{I}{16\,Mf}\; \frac{\left\{c^2\left(K_R/K_A\right) - \left(\frac{f}{f_n}\right)^2\left[a(a-b)+r^2\right]\right\}}{\left\{c^2\left(K_R/K_A\right) - \frac{f}{f_n}\left[a(a-b)+r^2\right] + \frac{c}{\sqrt{b}}\sqrt{b+\left(\frac{f}{f_n}\right)^2\,(a-b)}\right\}^2} \qquad (20)$$

$$\Theta_{DIT} = \frac{I}{16\,Mf}\; \frac{\left[b + \left(\frac{f}{f_n}\right)^2\,(a-b)\right]}{\left\{c^2\left(K_R/K_A\right) - \left(\frac{f}{f_n}\right)^2\left[a(a-b)+r^2\right] + \frac{c}{\sqrt{b}}\sqrt{b+\left(\frac{f}{f_n}\right)^2\,(a-b)}\right\}^2} \qquad (21)$$

SAMPLE PROBLEM

A typical gun system might have the following parameters:

$a = 4$ inches $M = .90\ \frac{\#\cdot sec^2}{in.}$

$b = 8$ inches $r = 20$ inches

$c = 20$ inches $f_n = 13$ cps

$K_A = 6250\ \#/in.$ $I = 31.6\ \frac{\#\cdot sec}{round}$

A computer program was utilized to calculate values of X_{DIT} and Θ_{DIT} versus the firing rate for several values of the K_R/K_A ratio. The resulting plots of the data are shown in Fig. 5 and Fig. 6. Note that the curves are for $2X_{DIT}$ and $2\Theta_{DIT}$ which corresponds with the peak-to-peak values of the translational and rotational dither motions.

Several conclusions may be drawn from these curves. First, the motions are more or less independent of spring rate except in a small frequency band near the resonant frequencies. This indicates that most of the recoil force is reacted by the mass-acceleration force rather than the spring deflection force. Therefore, the dither forces transmitted to the supporting structure at both the recoil adapters and the third point of support are proportional to the various spring rates except at frequencies near a resonance.

Second, the natural frequencies must be located as far as possible from the firing frequency in all cases. When this is accomplished, the dither motions are then only frequency dependent. It is also obvious, then, that the softer the springs in all directions at all locations, the lower the vibratory forces will be whether they are caused by translation or rotation.

Third, the angle through which the gun rotates is quite small; and for steady state conditions, the angular position in space should be the same for each projectile leaving the weapon. Thus, for the high firing rate guns, dispersion on the target becomes more or less independent of the support rigidity. Therefore, when the firing rates are high, the support spring should be made as soft as possible in all directions to reduce the vibratory forces transmitted to the structure while having little effect on target dispersion. On the other hand, for low firing rates, the angular motions become large; hence, there is a practical limitation for each system which must be evaluated on an individual basis.

SINGLE DEGREE OF FREEDOM ANALYSIS

Although the angular dither motions of the weapon are quite small, this rotation can be eliminated if there are no eccentricities or offsets about the
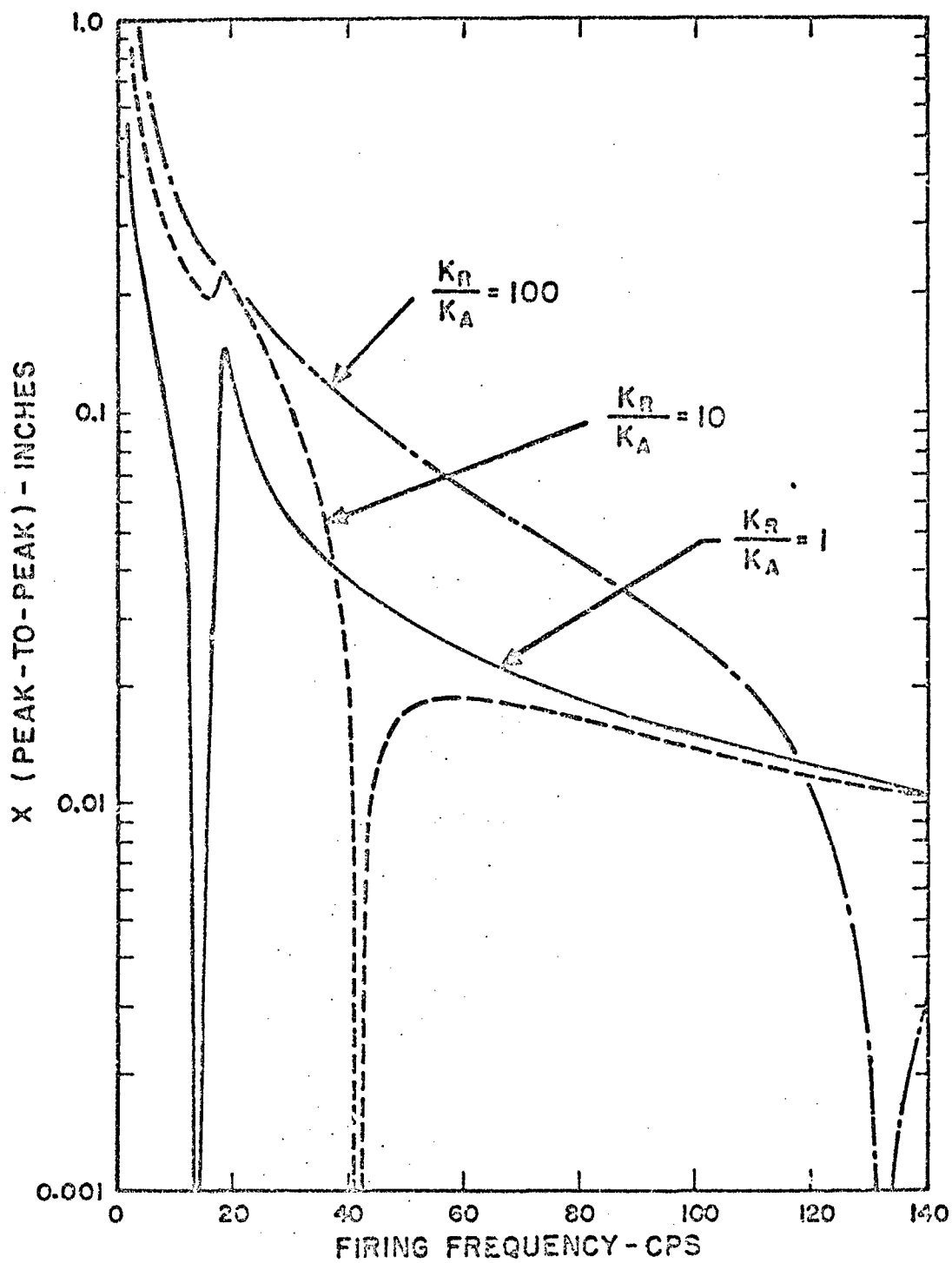
Fig. 5 — Peak-To-Peak Dither Motion Versus
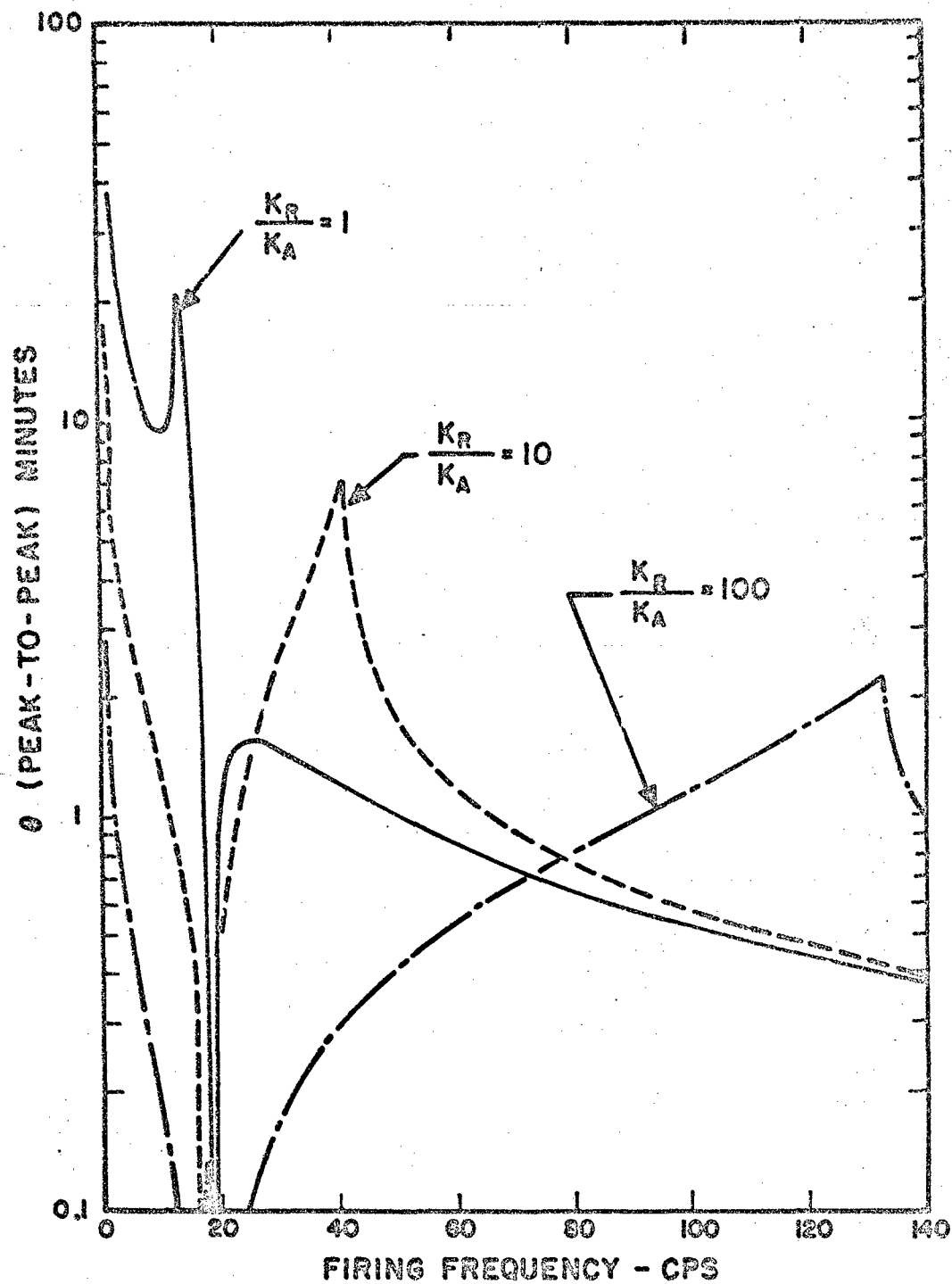Firing Frequency For Various Ratios of K_R/K_A

257

Fig. 6 – Peak-To-Peak Angular Dither Motion Versus
Firing Frequency For Various Ratios or K_R/K_A

pitch and yaw axes between the center of elasticity of the recoil adapters, the center of gravity of the gun, and the firing barrel. This is determined from equation (21); to make $\theta_{DIT} = 0$, it is necessary that $a = b = 0$. When this is accomplished, then equation (2) can be reduced to

$$X_{DIT} = \frac{I}{16 \, Mf}$$

This equation, when considered in conjunction with typical load-deflection curves of recoil adapters, provides an indication of the improvement in performance which can be achieved by considering the adapter for a high rate gun a vibration isolator. Fig. 7 depicts the load-deflection curve for a typical recoil adapter system designed to be an energy-dissipative device.
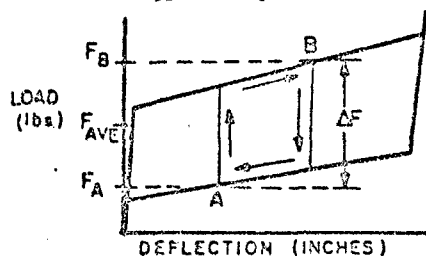

Fig. 7 – Load-Deflection Curve
Of Low Rate Adapter

If these adapters are used in a high firing rate application, when steady state firing is reached, the adapters must react a force (F_{AVE}) equal to the impulse times the firing rate.

$$F_{AVE} = I \left(\frac{lbs. \cdot sec}{round}\right) \times f \left(\frac{rds}{sec}\right)$$

The gun will oscillate about F_{AVE} through a deflection $X = 2 \, X_{DIT}$. The total recoil dither force transmitted into the structure is given by $F = F_B - F_A$.

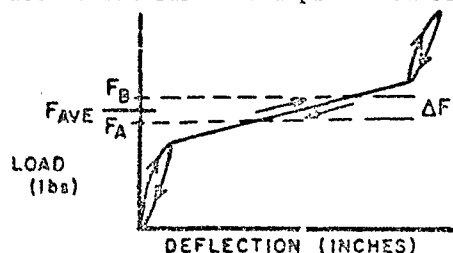An adapter designed specifically for high firing rate would have a load-deflection curve as depicted in Fig. 8.

Fig. 8 – Load-Deflection Curve
of High Rate Adapter

Again, the average force will be as calculated above. The dither motion will also be the same as given above. The gun will recoil until it reaches point B. It will then move forward in counter recoil until it reaches point A, at which time the next round is fired, causing the gun to return to B. However, as the curves indicate, the absence of high damping in the high rate adapter results in a much lower recoil dither force being transmitted into the structure as compared with that from the adapters which were designed for lower firing rates.

SUMMARY AND CONCLUSIONS

The design of suspension systems for rapid-fire weapons must consider the gun and its supports as a multi-degree of freedom system. Spring rates in all directions must be assigned to each point of support, and it must be recognized that the gun will translate and rotate in response to the forces and torques resulting from recoil.

It has been demonstrated that the stiffness of the supporting structure must be so great as to be impractical in order to prevent gun rotation arising from offsets between the elastic center, the center of gravity, and the firing barrel. If the eccentricities cannot be eliminated, the analysis has shown that provided the natural frequency of the supports is not in the region of the firing frequency, the dither angle is of the same order of magnitude whether the supports be "soft" or "stiff." Thus, the designer may as well use "soft" supports to reduce the vibratory forces transmitted into the structure.

Finally, the engineer must decide whether the system loading may be treated as a series of independent shocks or a high frequency vibration. This decision is based on such factors as firing rate, the available weapon travel, and the maximum acceptable force transmitted. If the gunfire can be treated as a vibratory input, then it is possible to design a system including recoil adapters which will result in low vibratory forces being transmitted to the support structure and will utilize parts having greater reliability and durability by eliminating friction dampers which may tend to exhibit change in performance characteristics over time and have a shorter service life.

259

A DYNAMIC VIBRATION ABSORBER FOR TRANSIENTS*

Dirse W. Sallet
University of Maryland
College Park, Maryland
and
U. S. Naval Ordnance Laboratory
White Oak, Silver Spring, Maryland

The principle of the dynamic vibration absorber was applied to reduce in a defined manner transient vibrations of a one degree of freedom system. Ten rules were developed which relate the position of the roots of the characteristic equation to the physical parameters; three of these rules, based upon an approximation which is often justified in engineering practice, can be used directly to determine the spring and damping coefficients of the absorber to approximate the defined ideal response. The concept of the "relative" and the "absolute influence position" is introduced; these new definitions refer to a particular position of the roots of the characteristic equation when only the spring constant, or, respectively, the spring constant and the damping coefficient between the masses are variable.

INTRODUCTION AND PROBLEM FORMULATION

The idea of eliminating detrimental vibrations of a machine, a structural part of a machine or any mass, or to reduce the amplitude of vibrations with a tuned dynamical vibration absorber has been known since 1905 and is extensively discussed in the literature. However, dynamic vibration absorbers generally are only applied when the force causing the vibrations is sinusoidal and when only the steady state is of interest.

The following question is now posed: Is the principle of dynamic vibration absorption, namely, the transmitting of the energy from the vibrating main mass to a secondary mass on which the vibrations can be tolerated, applicable to transients? As is customary in automatic control theory, a step input to the system for the investigation of transients is prescribed.

A practical example, for which the transient vibrations are of interest, is the motion of a model in a shock tunnel. Typical for a shock tunnel is, first, the relatively short running time and therefore short measuring time, and, second, the step function force input acting on the model. Because of the first point the transient vibrations are of specific interest, and because of the second point those transients which are due to a step input are of interest. The obvious solution, eliminating the transients or greatly reducing their amplitude by installing a suitable damper between the vibrating mass and the inertial reference system, is, in this case, not satisfactory. Such a damper, between the model and the tunnel wall, would influence the flow around the model. In other practical applications in which the amplitude of the transient vibrations is to be reduced, the installation of a damper between the vibrating mass and the reference system may not be possible for design reasons. The possiblity that some damping of the main mass may already exist shall not be excluded; in this case, however, the damping coefficient is considered to be constant.

A pure damper converts the vibration energy into heat, while an undamped dynamical vibration absorber assumes the energy from the main mass but does not reduce the total energy

---

*This paper not presented at Symposium.

of the system. Therefore, when the vibration energy is large, the dynamical vibration absorber will influence the vibration of the main mass sooner than a damper. This advantage, offered by a dynamic vibration absorber, is important when the early transients are to be reduced in magnitude.

The tuning of the vibration absorber is to be carried out in view of the following requirements:

1. The main mass is to assume that position which it would assume at the time $t = \infty$ if there were damping in the system, and if the forcing function were a true step input.

2. At this position the velocity of the main mass is to be zero.

3. The requirements 1 and 2 are to be approached simultaneously during the time $t^*-\Delta t < t < t^*+\Delta t$ where t^*-t_o is to be as small as possible.

4. The time duration $2\Delta t$ is to be a maximum.

Meaningful measurements can be obtained at the vibrating aerodynamic model if these requirements are at least approximately satisfied. It then may be of no importance if, and to whatever degree, the vibration damper feeds the energy back to the mainspring mass system.

BASIC EQUATIONS AND THEIR SOLUTIONS

The differential equations for the idealized system (see Fig. 1) are:

$$m_1 X_1'' + b_1 X_1' + k_1 X_1 - b_2 (X_2' - X_1') - k_2 (X_2 - X_1) = F(t) \quad (1)$$

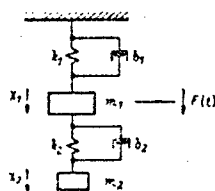$$m_2 X_2'' + b_2 (X_2' - X_1') + k_2 (X_2 - X_1) = 0. \quad (2)$$

Fig. 1 - Idealized mechanical system

where X_1 and X_2 are the deflections from the position of equilibrium of the main and absorber mass, respectively, X'' and X' are the second and first differentiation of X with respect to time t, and $F(t)$ is a step forcing function having the magnitude F_0 and acting on m_1 at $t \geq 0$. The damping constants are designated by b and the spring constants are designated by k.

The initial conditions are:

$$X_1 = X_2 = 0 \quad , \quad X_1' = X_2' = 0 \quad for \quad t = 0. \quad (3)$$

By introducing new variables the Eq. (1) to (3) are made dimensionless as follows:

$$X_1 = X_{1 max} \cdot x_1, \quad X_2 = X_{2 max} \cdot x_2 \quad , \quad \tau = \lambda t.$$

where x is a function of τ and λ is an arbitrary constant having the dimension (time)$^{-1}$. Let

$$\lambda = \sqrt{\frac{k_1}{m_1}} .$$

Equations (1) and (2) now become:

$$\ddot{x}_1 + a_1 \dot{x}_1 + c_1 x_1 - d_1 \dot{x}_2 - e_1 x_2 = g , \quad (4)$$

$$\ddot{x}_2 + a_2 \dot{x}_2 + c_2 x_2 - d_2 \dot{x}_1 - e_2 x_1 = 0 . \quad (5)$$

The initial conditions are:

$$\left. \begin{array}{l} x_1 = x_2 = 0 \\ \dot{x}_1 = \dot{x}_2 = 0 \end{array} \right\} \quad for \quad \tau = 0, \quad (6)$$

where $\ddot{x}$ and $\dot{x}$ are the second and first derivatives of x with respect to τ, and a, c, d, e and g follow from the transformation.

The Eq. (4) and (5) with the initial conditions (6) yield the solution in the form

$$\bar{x}_1(s) = G_1(s) f(s), \quad (7)$$

where

$$G_1(s) = \frac{s^2 + \frac{1}{\lambda}\frac{b_2}{m_2}s + \frac{1}{\lambda^2}\frac{k_2}{m_2}}{\Delta(s)} = \frac{(s - z_1)(s - z_2)}{(s - p_1)(s - p_2)(s - p_3)(s - p_4)}$$

$$(8)$$

262

and $f(s)$ is the Laplace transformation of $g(\tau)$, the input function. The characteristic equation, which is obtained by setting the denominator of the transfer function equal to zero, is:

$$s^4 + s^3 \frac{1}{2}\left[\frac{b_1}{m_1} + \frac{b_2(m_1 + m_2)}{m_1 m_2}\right] + s^2 \frac{1}{2}\left[\frac{k_1}{m_1} + \frac{k_2(m_1 + m_2) + b_1 b_2}{m_1 m_2}\right] + s \frac{1}{2^3} \cdot \frac{b_1 k_2 + k_1 b_2}{m_1 m_2} + \frac{1}{2^4} \frac{k_1 k_2}{m_1 m_2} = 0. \qquad (9)$$

For the case for which four different poles exist and none of those poles coincides with the zeros of the transfer function, Eq. (7) is rewritten as follows, [2].

$$x_1(t) = K_0 + K_1 e^{p_1 t} + K_2 e^{p_2 t} + K_3 e^{p_3 t} + K_4 e^{p_4 t}. \qquad (10)$$

where

$$K_0 = \lim_{s \to 0} [s \, x(s)]$$

and

$$K_i = \lim_{s \to p_i} [(s - p_i) x(s)], \qquad (i = 1, 2, 3, 4)$$

If a double pole is present which does not coincide with the zeros, Eq. (7) becomes:

$$x_1(t) = K_0 + K_{11} t e^{p_1 t} + K_{22} e^{p_2 t} + K_{33} t e^{p_3 t} + K_{44} e^{p_4 t}. \qquad (11)$$

where

$$K_j = \lim_{s \to p_m} [(s - p_m)^2 x(s)], \qquad (j = 11, 33; \ m = 1, 2)$$

and

$$K_k = \lim_{s \to p_n} \left[\frac{d}{ds}\{(s - p_n)^2 x(s)\}\right]. \qquad (k = 22, 44; \ n = 1, 2)$$

If a pair of poles coincides with the pair of zeros, (7) becomes an equation similar to (10), however, without the last two expressions. This case may be regarded to be of no further interest since two sinusoidal expressions are necessary for beats, and since the coefficients which belong to the same pair of poles are complex conjugates of each other. Also, the case for which a double pole exists is at this time of no further interest because of the factor t with K_{11} and K_{33} in Eq. (11).

Equation (10), with the given coefficients and for the case $b_2 \leq b_2(crit)$, may now be written in the following convenient form:

$$x_1(t) = \frac{K \, r_I r_{II}}{r_1 r_2} + \frac{K}{r_3 r_4}\left[\frac{r_{I1} r_{II1}}{m_1 r_2} e^{-\sigma_1 t} \cos(\omega_1 \lambda t + \xi_1) + \frac{r_{I3} r_{II3}}{m_3 r_4} e^{-\sigma_3 t} \cos(\omega_3 \lambda t + \xi_3)\right] \qquad (12)$$

$$\dot{x}_1(t) = \frac{K}{r_3 r_4}\left[\frac{r_{I1} r_{II1}}{m_1} e^{-\sigma_1 t} \cos(\omega_1 \lambda t + \xi_{11}) + \frac{r_{I3} r_{II3}}{m_3} e^{-\sigma_3 t} \cos(\omega_3 \lambda t + \xi_{31})\right]. \qquad (13)$$

In the above two equations the Roman numerals indicate zeros and the Arabic numerals indicate poles of the transfer function; e.g., r_{II3} signifies the distance from the zero II to the pole 3 (see Fig. 2). The angles are also
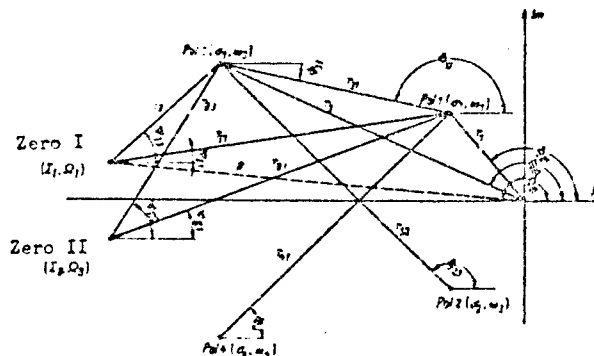
Fig. 2 – Nomenclature for the zeros and poles of the transfer function

dependent upon the position of the poles and zeros; e.g., ξ_1 is the sum of all angles formed by the segments connecting the pole 1 with all zeros and the positive x-axis minus the sum of all angles formed by the segments connecting the pole 1 with all poles and the positive x-axis. It is interesting to note that the expression $r_{31} \, r_{32}$, which is the product of the segments pole 3-pole 1 and pole 3-pole 2, can be factored in both equations. The particular significance of this product, which becomes apparent at this point, will be discussed at length later.

263

MATHEMATICAL FORMULATION OF THE TUNING CRITERIA

The time-dependent part of the Eq. (12),

$$y = A e^{-n_1 \lambda t} \cos(\omega_1 \lambda t + \xi_1) + B e^{-n_2 \lambda t} \cos(\omega_2 \lambda t + \xi_2). \quad (14)$$

with

$$A = \frac{r_{11} r_{111}}{r_{21} r_{31} \omega_1 r_1} \quad (15)$$

and

$$B = \frac{r_{13} r_{113}}{r_{21} r_{31} \omega_3 r_3} \quad (16)$$

is now rewritten, [3]

$$y = C \cos\left(\frac{(\omega_1 + \omega_2)\lambda t + \xi_1 + \xi_3}{2} + \varphi^*\right), \quad (17)$$

where

$$C = \left[A^2 e^{-2 n_1 \lambda t} + B^2 e^{-2 n_2 \lambda t} + \ldots \right.$$

$$\left. \ldots + 2 A B e^{-(n_1 + n_2)\lambda t} \cos[(\omega_1 - \omega_2)\lambda t + \xi_1 - \xi_2] \right] \quad (18)$$

and

$$\varphi^* = \arctan\left[\frac{A e^{-n_1 \lambda t} - B e^{-n_2 \lambda t}}{A e^{-n_1 \lambda t} + B e^{-n_2 \lambda t}} \tan \frac{(\omega_1 - \omega_2)\lambda t + \xi_1 - \xi_2}{2}\right] \quad (19)$$

Then:

$$|A e^{-n_1 \lambda t} - B e^{-n_2 \lambda t}| \leq C \leq |A e^{-n_1 \lambda t} + B e^{-n_2 \lambda t}|. \quad (20)$$

The period of the envelope C follows from (19):

$$T_C = \frac{2\pi}{(\omega_1 - \omega_2)\lambda}. \quad (21)$$

The minima of this envelope occur when

$$t = t^* = \frac{n\pi - (\xi_1 - \xi_2)}{(\omega_1 - \omega_2)\lambda}, \quad (n = 1, 3, 5 \ldots) \quad (22)$$

The same development for Eq. (13) yields:

$$y' = A' e^{-n_1 \lambda t} \cos(\omega_1 \lambda t + \xi_{11}) + B' e^{-n_2 \lambda t} \cos(\omega_2 \lambda t + \xi_{22}). \quad (23)$$

$$A' = \frac{r_{11} r_{111}}{r_{21} r_{31} \omega_1} \quad (24)$$

$$B' = \frac{r_{13} r_{113}}{r_{21} r_{31} \omega_3} \quad (25)$$

$$y' = C' \cos\left(\frac{(\omega_1 + \omega_2)\lambda t + \xi_{11} + \xi_{22}}{2} + \varphi^{**}\right). \quad (26)$$

$$C' = \left[A'^2 e^{-2 n_1 \lambda t} + B'^2 e^{-2 n_2 \lambda t} + \ldots \right.$$

$$\left. \ldots + 2 A' B' e^{-(n_1 + n_2)\lambda t} \cos[(\omega_1 - \omega_2)\lambda t + \xi_{11} - \xi_{22}] \right]. \quad (27)$$

$$\varphi^{**} = \arctan\left[\frac{A' e^{-n_1 \lambda t} - B' e^{-n_2 \lambda t}}{A' e^{-n_1 \lambda t} + B' e^{-n_2 \lambda t}} \tan \frac{(\omega_1 - \omega_2)\lambda t + \xi_{11} - \xi_{22}}{2}\right]. \quad (28)$$

with

$$|A' e^{-n_1 \lambda t} - B' e^{-n_2 \lambda t}| \leq C' \leq |A' e^{-n_1 \lambda t} + B' e^{-n_2 \lambda t}|. \quad (29)$$

Both envelopes have the same period; the minima of the envelope C' (see Eq. (27)) occur when

$$t = t^{**} = \frac{n\pi - (\xi_{11} - \xi_{22})}{(\omega_1 - \omega_2)\lambda}, \quad (n = 1, 3, 5 \ldots). \quad (30)$$

The ideal requirements for the motion of the main mass posed in the first paragraph may now be expressed as conditions to be satisfied by the geometry of the poles and zeros of the transfer function. The requirement 1 becomes:

$$A e^{-n_1 \lambda t} - B e^{-n_2 \lambda t} = 0. \quad (31)$$

with

$$t^* - \Delta t \leq t \leq t^* + \Delta t.$$

The requirement 2 becomes:

$$A' e^{-n_1 \lambda t} - B' e^{-n_2 \lambda t} = 0, \quad (32)$$

with

$$t^{**} - \Delta t \leq t \leq t^{**} + \Delta t.$$

The requirement 3 becomes:

$$t^* \to t^{**}. \quad (33a)$$

$$t^* = 0 \qquad \sigma_3 \tau = n \cdot 1. \qquad (33b)$$

The requirement Δ becomes:

$$\frac{2\gamma}{(m_1 - m_2)\lambda} \qquad (34)$$

is to be a maximum since this expression is proportional to Δt.

The numerical values of the expressions (31) and (32) may directly be used as a criterion of the motion of the main mass for the type of application considered. The particular application of the dynamic vibration absorber will determine the choice of n for the determination of t* and t**. The period of the envelope, expression (34), is a measure of the duration $2\Delta t$, but not the duration itself. For any specific application, a compromise must be found between the conditions (33b) and (34) which cannot be satisfied simultaneously. In the following derivation of the equations for the direct determination of the tuning parameters (k_2 and b_2) at first only conditions (31) and (32) are taken into account. It is shown that in this way the tuning parameters are determined and that within the given approximation, condition (34) is adequately approached. Consideration of condition (33b) will lead to a less satisfactory approach to the other conditions.

DERIVATION OF THE TUNING RULES AND
  EQUATIONS

A comparison of the coefficients of the Eq. (8) yields the following expressions for the real, imaginary and absolute values of the zeros (Σ, Ω and R) and for the real, imaginary and absolute values of the poles (σ, ω and r):

$$\Sigma = \frac{1}{\lambda} \frac{b_2}{2 m_2}. \qquad (35)$$

$$\Omega = \frac{1}{\lambda} \sqrt{\frac{k_2}{m_2} - \left(\frac{b_2}{2 m_2}\right)^2}. \qquad (36)$$

$$R = \frac{1}{\lambda} \sqrt{\frac{k_2}{m_2}}. \qquad (37)$$

For two complex conjugate roots of Eq. (9) one obtains:

$$2(\sigma_1 + \sigma_3) = \frac{1}{\lambda}\left[\frac{b_1}{m_1} + \frac{b_2(m_1 + m_2)}{m_1 m_2}\right]. \qquad (38a)$$

$$r_1^2 + r_3^2 + 4\sigma_1\sigma_3 = \frac{1}{\lambda^2}\left[\frac{k_1}{m_1} + \frac{k_2(m_1 + m_2) + b_1 b_2}{m_1 m_2}\right]. \qquad (39a)$$

$$2(\sigma_3 r_1^2 + \sigma_1 r_3^2) = \frac{1}{\lambda^2} \cdot \frac{b_1 k_2 + k_1 b_2}{m_1 m_2}. \qquad (40a)$$

$$r_1^2 r_3^2 = \frac{1}{\lambda^4} \cdot \frac{k_1 k_2}{m_1 m_2}. \qquad (41a)$$

$$\sigma_{1,3}^2 + \omega_{1,3}^2 = r_{1,3}^2 \qquad (42)$$

If two roots (σ_3 and σ_4) become real, then Eq. (38) to (41) become:

$$2\sigma_1 + \sigma_3 + \sigma_4 = \frac{1}{\lambda}\left[\frac{b_1}{m_1} + \frac{b_2(m_1 + m_2)}{m_1 m_2}\right]. \qquad (38b)$$

$$r_1^2 + \sigma_3\sigma_4 + 2\sigma_1(\sigma_3 + \sigma_4) = \frac{1}{\lambda^2}\left[\frac{k_1}{m_1} + \frac{k_2(m_1 + m_2)}{m_1 m_2} + \frac{b_1 b_2}{m_1 m_2}\right]. \qquad (39b)$$

$$r_1^2(\sigma_3 + \sigma_4) + 2\sigma_1\sigma_3\sigma_4 = \frac{1}{\lambda^2} \cdot \frac{b_1 k_2 + k_1 b_2}{m_1 m_2}. \qquad (40b)$$

$$r_1^2\sigma_3\sigma_4 = \frac{1}{\lambda^4} \cdot \frac{k_1 k_2}{m_1 m_2}. \qquad (41b)$$

If all roots become real, then Eq. (38) to (41) become:

$$\sigma_1 + \sigma_2 + \sigma_3 + \sigma_4 = \frac{1}{\lambda}\left[\frac{b_1}{m_1} + \frac{b_2(m_1 + m_2)}{m_1 m_2}\right]. \qquad (38c)$$

$$(\sigma_1 + \sigma_2)(\sigma_3 + \sigma_4) + \sigma_1\sigma_2 + \sigma_3\sigma_4 = \frac{1}{\lambda^2}\left[\frac{k_1}{m_1} + \frac{k_2(m_1 + m_2)}{m_1 m_2} + \frac{b_1 b_2}{m_1 m_2}\right]. \qquad (39c)$$

$$\sigma_1\sigma_2(\sigma_3 + \sigma_4) + \sigma_3\sigma_4(\sigma_1 + \sigma_2) = \frac{1}{\lambda^2} \cdot \frac{b_1 k_2 + k_1 b_2}{m_1 m_2}. \qquad (40c)$$

265

$$\sigma_1 \sigma_2 \sigma_3 \sigma_4 = \frac{1}{\lambda^4} \frac{k_1 k_2}{m_1 m_2}. \qquad (41c)$$

Rule 1. Complex conjugate zeros of the transfer function may only exist if the relative damping constant b_2 of the dynamic vibration absorber (considered as a system by itself) is smaller than its critical value. If the relative damping constant has a value equal to the critical value, then the transfer function has a double zero. The position of the zeros is independent of the absolute damping constant b_1.

From Eq. (38a), (38b) and (39c) follows:

Rule 2. The sum of the real parts of all poles is independent of the relative spring constant k_2.

From Eq. (41a), (41b) and (41c) follows:

Rule 3. The product of the absolute values of all poles is independent of the damping constants of the system.

With the conditions (31) to (34) given in the section, Mathematical Formulation of the Tuning Criteria, and with the above rules, the vibration absorber could be tuned in a more direct fashion than by trial and error. Since, in general, none of the systems of Eq. (38) to (41) can be explicitly solved, formulae for the physical constants of the dynamic vibration absorber resulting in the tuned motion of m_1 according to conditions (31) to (34) cannot be derived.

The process of approaching the stated requirements by tuning the two degree of freedom system so that beats occur will mainly be of interest when the absolute damping constant b_1 is small. Also, the mass of the absorber m_2 will be smaller for most technical applications than the main mass m_1, and since beats are to occur, b_2 will be smaller than $b_{2\ crit}$. In this case, as shown below, the product of the real parts of the complex poles is negligible when compared with the sum of the squared magnitudes of these poles; consequently, Eq. (38a) to (41a) may explicitly be solved. One obtains:

$$\sigma_{1,4} = \frac{1}{\lambda W}\left[-F + \frac{D}{2}(E + W)\right], \qquad (43)$$

$$\sigma_{3,4} = \frac{1}{\lambda W}\left[F - \frac{D}{2}(E - W)\right]. \qquad (44)$$

$$r_{1,4} = \frac{1}{2\lambda^2}[E + W], \qquad (45)$$

$$r_{3,4} = \frac{1}{2\lambda^2}[E - W], \qquad (46)$$

and with (42)

$$\omega_{1,4} = \frac{1}{\lambda}\sqrt{\frac{1}{2}(E + W) - \frac{1}{W}\left[-F + \frac{D}{2}(E + W)\right]^2}; \qquad (47)$$

$$\omega_{3,4} = \frac{1}{\lambda}\sqrt{\frac{1}{2}(E - W) - \frac{1}{W}\left[F - \frac{D}{2}(E - W)\right]^2}, \qquad (48)$$

where the symbols are defined as follows:

$$W = \sqrt{E^2 - 4C}. \qquad (49)$$

$$D = \frac{1}{2}\left[\frac{b_1}{m_1} + \frac{b_2(m_1 + m_2)}{m_1 m_2}\right]. \qquad (50)$$

$$E = \frac{k_1}{m_1} + \frac{k_2(m_1 + m_2) + b_1 b_2}{m_1 m_2}, \qquad (51)$$

$$F = \frac{b_1 k_2 + b_2 k_1}{2 m_1 m_2}. \qquad (52)$$

$$C = \frac{k_1 k_2}{m_1 m_2}. \qquad (53)$$

With the above expressions the motion of the main mass may now be expressed explicitly as a function of time and the parameters of the physical system using Eq. (12) and (13). For the general case, this leads to a long and complex expression.

For a given problem, it is important to estimate the error ϵ, which is introduced in Eq. (39a) by neglecting $4\sigma_1\sigma_3$.

Let

$$\epsilon = \frac{4\sigma_1\sigma_3}{r_1^2 + r_3^2 + 4\sigma_1\sigma_3},$$

then from Eq. (38a) and (39a)

$$\epsilon \leq \frac{\left(\frac{b_1}{m_1} + \frac{b_2(m_1 + m_2)}{m_1 m_2}\right)^2}{4\left(\frac{k_1}{m_1} + \frac{k_2(m_1 + m_2)}{m_1 m_2} + b_1 b_2\right)} \cdot \tag{54}$$

The largest possible error ϵ may already be computed from the second and third coefficient of the characteristic Eq. (9).

To express the maximum error ϵ in a more convenient manner the following nomenclature is introduced:

$$n_1 = \frac{b_1}{b_{1\,krit.}}, \qquad n_2 = \frac{b_2}{b_{2\,krit.}}, \qquad n = \frac{m_2}{m_1},$$

$$\lambda = \sqrt{\frac{k_1}{m_1}}, \qquad \lambda_2 = \sqrt{\frac{k_2}{m_2}}.$$

Equation (54) may now be rewritten:

$$\epsilon \leq \frac{[n_1 \lambda + n_2 \lambda_2 (1 + n)]^2}{\lambda^2 + \lambda_2^2 (1 + n) + 4 n_1 n_2 \lambda_2}. \tag{55}$$

If the above-described approximations are obtained by $\sigma_1^2 \ll \omega_1^2$ and $\sigma_3^2 \ll \omega_3^2$ and if $r_{31} r_{32} \neq 0$, then the conditions (31) and (32) may be expanded as follows:

$$\frac{r_{11} r_{111}}{m_1 r_1} e^{-\sigma_1 t} - \frac{r_{13} r_{113}}{m_3 r_3} e^{-\sigma_3 t}$$

$$= \lambda t (\sigma_3 - \sigma_1) - \frac{t^2 \lambda t}{r_1^2 r_3^2}(r_1^2 \sigma_3 - r_3^2 \sigma_1) + \frac{t^3}{r_1^2 r_3^2}(r_1^2 - r_3^2). \tag{56}$$

$$\frac{r_{11} r_{111}}{m_1} e^{-\sigma_1 t} - \frac{r_{13} r_{113}}{m_3} e^{-\sigma_3 t}$$

$$= \lambda t (\sigma_3 - \sigma_1) - \frac{t^2 \lambda t}{r_1 r_3}(r_1 \sigma_3 - r_3 \sigma_1) + \frac{t^3}{r_1 r_3}(r_1 - r_3). \tag{57}$$

It is now seen that conditions (31) and (32) are satisfied within the given approximation if

$$\left.\begin{aligned}\sigma_3 &= \sigma_1 \\ \Omega &= 0\end{aligned}\right\} \tag{58}$$

or if

$$r_1 = r_3 = \Omega \tag{5}$$

or if

$$\left.\begin{aligned}r_1 &= r_3 \\ \sigma_3 &= \sigma_1\end{aligned}\right\} \tag{60}$$

From these three possible solutions one may conclude as follows:

In general, condition (58) can physically not be realized as the following reasoning will demonstrate. The compatibility condition of Eq. (38a) to (41a) for σ_1 equal to σ_3 yields:

Rule 4. If all the poles of the transfer function have equal real parts, then

$$[b_1 n + b_2 (1 + n)]^2 - 4 n [b_1 n$$

$$+ b_2 (1 + n)] [m_2 k_1 n - k_2 (1 + n) - b_1 b_2]$$

$$+ 8 n^2 m_1 [b_1 k_2 + k_1 b_2] = 0 \tag{61}$$

must hold true, where n is the ratio of the mass of the damper to the main mass.

Setting the absolute damping constant in Eq. (61) equal to zero, one obtains the simple expression

$$k_2 = \frac{8 n^2 k_1 m_1 (1 - n) + b_2^2 (1 + n)^3}{4 n m_1 (1 + n)^2}. \tag{62}$$

Letting

$$b_2^2 = 4 k_2 n m_1.$$

in other words, Ω is equal to zero (see (36)), then from Eq. (62)

$$\frac{k_2}{k_1} = \frac{1 - n}{(1 + n)^2}.$$

Rule 5. A system having only relative damping and having an absorber mass to main mass ratio of equal to or less than one, can only have complex poles with equal real parts if the zeros of the transfer function are complex roots.

Condition (59) also cannot be physically realized, because, as in condition (58), this would require negative parameters. From the compatibility condition of Eq. (38a) to (41a) for r_1 equal to r_3 one obtains:

Rule 6. If all poles of the transfer function lie on a circle around the origin of the complex plane, then

$$k_1^2 k_2^2 + k_2 \left[2 k_1 b_1 k_1 \ldots \right] + k_1 b_2^2 = 0 \tag{63}$$

Again setting the absolute damping constant b_1 equal to zero, Eq. (63) becomes:

$$k_2 = (1 + m)^2 k_1 \tag{64}$$

Suppose r_1 is equal to r_2, then it follows with the condition $\Omega = r$:

$$\left(\frac{k_2}{k_m}\right)^2 = \frac{k_2}{m_1}$$

Rule 7. For a system with only relative damping, poles and zeros of the transfer function cannot lie on the same circle around the origin of the complex plane; their relationship is

$$r^2 = N^2 + \frac{k_2}{k_1}$$

The condition (60) is only to be approached as indicated by the arrows, as otherwise a double pole would occur, and, in this case, the solutions (12) and (13) and their subsequent development would not be valid. The question now posed is, in which way is condition (60) to be approached. The actual task is to eliminate the vibrations of the main mass. To accomplish this by means of beats of a two-mass system, it becomes important that the vibrations are damped as much as possible in order for the minima of the envelope to approach the eventual final position of the main mass as soon as possible. In order to extract a maximum amount of energy from the system with variable b_2 or k_2 during the time $t_2 - t_1$,

$$M = \int_{t_1}^{t_2} [b_1 x_1^2 + b_2 (x_1 - x_2)^2] \, dt \tag{65}$$

must be a maximum with respect to b_2 or k_2. The integrand of Eq. (65) is

where

$$\xi_{III} = 2\Phi_{II} - \Phi_{II} - \Phi_{2I} - \frac{\pi}{2}$$

$$\xi_{IIII} = 2\Phi_{0I} - \Phi_{II} - \Phi_{2II} - \frac{\pi}{2}$$

A consideration of the root locus plot of the characteristic equation shows that for small values of b_1 a change of b_2 or k_2 influences the product $r_{31} r_{32}$ much more than the value J_2, where

$$J_1 = \frac{k^2}{(r_n r_2)^2} J_2.$$

If M has a maximum with respect to k_2 or b_2, then $r_{31} r_{32}$ must have a minimum in respect to k_2 or b_2. The fact that M does possess a maximum for a system which is only relatively damped follows from physical considerations; namely, if b_2 equals zero, then M equals zero. If b_2 approaches infinity, $x_1 - x_2$ becomes zero, and M again equals zero. Now, considering k_2 as a variable, if k_2 approaches infinity, $x_1 - x_2$ and therefore M equals zero. If k_2 approaches zero, then the beat phenomenon due to the motions of the two masses is lost, i.e., the energy is no longer continuously transferred from one mass to the other, and the decrease in energy due to the coupling b_2 becomes smaller.

From the second part of the condition (60) follows, within the approximation stated in this section, that

$$r_{31} r_{32} = r_1^2 + r_2^2 \tag{66}$$

Employing Eq. (45) and (46) to set

$$\frac{\partial r_{31} r_{32}}{\partial k_2} = 0.$$

(the exceptional case for $r_1 = r_2$ is excluded since it was already covered in Rule 6) one obtains:

268

$$\lambda_3 \quad \frac{n(1-m)k_1}{(1-m)^2} \quad \frac{b_1 b_2}{m_1(1-m)} \qquad (67)$$

The product $r_{31} r_{32}$ is a minimum, if Eq. (67) holds true. The importance of the product $r_{31} r_{32}$ was already recognized in Eqs. (12) and (13): the smaller $r_{31} r_{32}$ becomes, the larger the non-steady part of the motion of the main mass. The Eq. (65) shows the influence of $r_{31} r_{32}$ upon the energy which is led away from the system.

To simplify the further description of the system, the position of the roots of the characteristic equation at which the product $r_{31} r_{32}$ becomes a minimum by varying only the relative spring constant, k_2, will be called the relative influence position. If the relative damping constant is variable also, then the position of the roots at which $r_{31} r_{32}$ is a minimum is called the absolute influence position.

From Eq. (67) follows:

Rule 8. If the product of the real parts of the roots of the characteristic equation is negligible when compared to the sum of the squared magnitudes of these roots, then the relative influence position will be approached if

$$\lambda_3 \quad \frac{n(1-m)k_1}{(1-m)^2} \quad \frac{b_1 b_2}{m_1(1-m)}$$

A comparison of Eq. (67) with (62) and noting Rule 1 yields:

Rule 9. If the product of the real parts of roots of the characteristic equation is negligible when compared to the sum of the squared magnitudes of these roots, then the relative influence position will be approached for a system which has only relative damping if the roots have equal real parts.

For the case for which the relative damping constant (the damping constant between mass 1 and mass 2) b_2 is adjustable also, the damping and spring constant values resulting in the influence position (in this case, the absolute influence position) may be obtained by applying Rules 4 and 6. The results are given in Rule 10.

Rule 10. If the product of the real parts of the roots of the characteristic equation is negligible when compared to the sum of the squared magnitudes of these roots, and if the real parts are of the same order of

magnitude, or if $b_1 \ll b_1$ crit, then the absolute influence position is approached if

$$\lambda_3 \quad \frac{\lambda_1}{2\lambda_1}\left[n(b_1 + b_2)^2 + b\left(\frac{1}{n} + 2\right) \right.$$
$$\left. - \left[\left[n(b_1 + b_2)^2 + b\left(\frac{1}{n} + 2\right) \right]^2 + 4 b_2^2 b_1^2 \right] \right]. \qquad (68)$$

where

$$\cdot \ b_2 \quad \left| \left(b_1 \frac{\cdot}{\cdot m} \right)^2 b_1^2 \dots \right| \qquad (69)$$

For a system only relatively damped, an accurate tuning for the absolute influence position (in this case, a double pole is possible by setting

$k_2 = \dfrac{n}{(1+n)^2} k_1$ and letting b_2 equal the

value given in Eq. (69).

APPLICATION

For the investigated example the values are: $m_1 = 0.01441 \dfrac{kp\ s^2}{cm}$,

$m_2 = 0.00131 \dfrac{kp\ s^2}{cm}$, $k_1 = 355.604 \dfrac{kp}{cm}$

and $b_1 = 0.12466 \dfrac{kp\ s}{cm}$. The values of

b_2 are 0.00169; 0.00423; 0.01693; 0.04233 (arbitrarily chosen) and

$0.10810 \dfrac{kp\ s}{cm}$ (calculated with Eq. (67)).

Figures 3 to 6 show the displacement and velocity (dotted line) of mass m_1. For parts (a) of these pictures k_2 was tuned according to Rule 8 and Rule 10 (Fig. 6a), while for parts (b) k_2 was tuned to give exactly the influence position. For part (c) of the figures, k_2 was obtained with Rule 4. In this case, the roots of the characteristic equation have equal real parts. (The figures were obtained by simulating the systems on a PACE analog computer.)

Table 1 gives the numerical values for the product $r_{31} r_{32}$ and for the four stated requirements (the first minimum for the conditions 2 and 3) of Fig. 3 through 6; Table 2 shows a comparison between the true values of the characteristic equation (accurate to five decimal places) and the values obtained by means of Eq. (43), (44), (47) and (48).
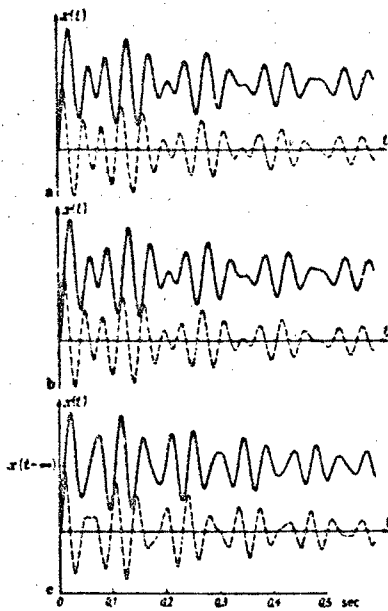
Fig. 3 - b_2 = 0.00169 kp s/cm
       (a) k_2 = 24.67878 kp/cm
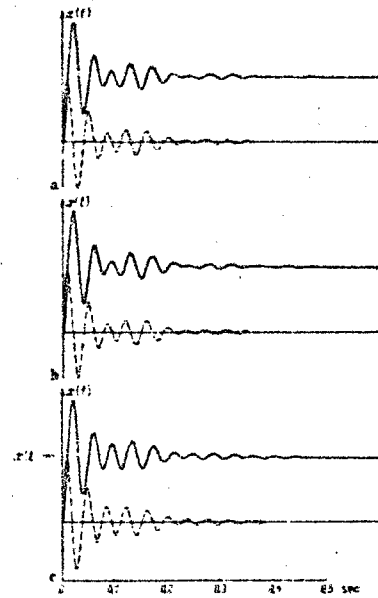   (b) k_2 = 24.8000 kp/cm
       (c) k_2 = 38.16737 kp/cm

Fig. 5 - b_2 = 0.04233 kp s/cm
       (a) k_2 = 24.35552 kp/cm
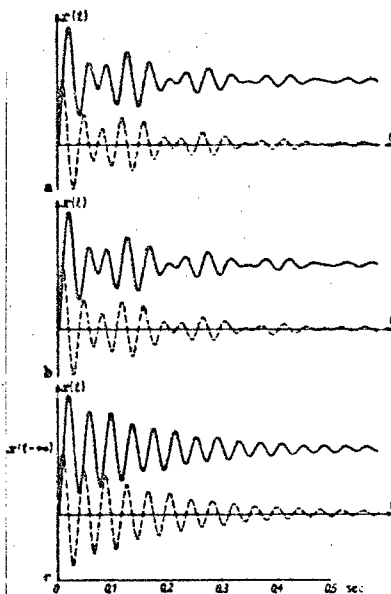   (b) k_2 = 24.80000 kp/cm
       (c) k_2 = 22.28056 kp/cm

Fig. 4 - b_2 = 0.01693 kp s/cm
       (a) k_2 = 24.55793 kp/cm
       (b) k_2 = 24.60000 kp/cm
       (c) k_2 = 13.40205 kp/cm
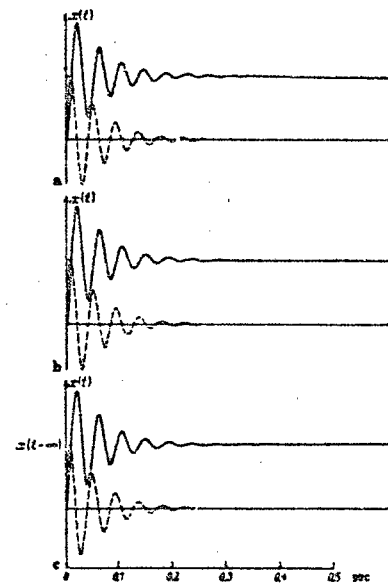
Fig. 6 - b_2 = 0.10890 kp s/cm
       (a) k_2 = 23.82872 kp/cm
       (b) k_2 = 26.50000 kp/cm
       (c) k_2 = 26.25163 kp/cm

270

TABLE 1. Numerical Values of the Product $r_{31}\, r_{32}$ and of the Requirements 1 to 4 for the Vibrations Shown in Fig. 3 to 6

vibration	$r_{31}\, r_{32}$	Requirement 1 Eq (31) n = 1	Requirement 2 Eq (32) n = 1	Requirement 3 t* n = 1	Requirement 3 t** n = 1	Requirement 4 Exp (34)
3a	0,55190	0,19185	0,30313	0,06587	0,06562	0,13731
3b	0,55183	0,18605	0,29777	0,06593	0,06563	0,13747
3c	0,71395	0,35033	0,22283	0,05635	0,05644	0,11832
4a	0,55080	0,14865	0,23541	0,07239	0,07230	0,13733
4b	0,55080	0,14669	0,23357	0,07242	0,07232	0,13739
4c	0,66981	0,60409	0,68847	0,05331	0,05367	0,09874
5a	0,52451	0,09488	0,14417	0,08722	0,08744	0,14343
5b	0,52429	0,07603	0,12637	0,08753	0,08758	0,14413
5c	0,53242	0,18404	0,22342	0,08458	0,08512	0,13821
6a	0,32537	0,02044	0,01202	0,21522	0,21948	0,24709
6b	0,21276	0,00018	0,00010	0,31205	0,31294	0,35500
6c	0,21476	0,00017	0,00023	0,30789	0,30900	0,34930

TABLE 2. Roots of the Characteristic Equation for the Vibrations Shown in Fig. 3 to 6

Vibration	σ_1 exact	σ_{1A} Eq (43)	υ_3 exact	σ_{3A} Eq (44)	$*_1$ exact	$*_{1A}$ Eq (47)	ω_3 exact	ω_{3A} Eq (48)
3a	0,02363	0,02362	0,00839	0,00840	1,09157	1,09235	0,80025	0,79768
3b	0,02357	0,02355	0,00846	0,00847	1,09251	1,09330	0,80153	0,80095
3c	0,01601	0,01603	0,01601	0,01599	1,22495	1,22563	0,85688	0,68024
4a	0,04372	0,04392	0,02870	0,02860	1,08087	1,09478	0,73261	0,73503
4b	0,04375	0,04385	0,02857	0,02857	1,09020	1,09510	0,79905	0,73543
4c	0,03621	0,03649	0,03621	0,03593	1,02927	1,03327	0,62417	0,62176
5a	0,07584	0,07750	0,06391	0,06225	1,07392	1,09733	0,80003	0,79628
5b	0,07713	0,07863	0,06263	0,06112	1,08229	1,10120	0,80435	0,79106
5c	0,06988	0,07218	0,06988	0,06758	1,06452	1,08308	0,77510	0,76187
6a	0,12141	0,16579	0,19478	0,15040	0,93554	1,10012	0,83366	0,75695
6b	0,16335	0,18419	0,15284	0,13209	0,99635	1,11396	0,83368	0,79746
6c	0,15810	0,18251	0,15810	0,13368	0,99497	1,11711	0,88045	0,73487

271

A comparison of the given vibration plots shows:

1. A difference between the vibrations (a) and (b) is not noticeable as long as b_2 is small. Only from the respective numerical values given in the tables does a difference in the motions become apparent.

2. It is the relative influence position (see (a) and (b) on figures) and not the pole position $\sigma_1 = \sigma_3$ which results in distinct beats, as long as b_2 is smaller than the b_2 required to give the absolute influence position.

3. The absolute influence position is the best position of the roots if rapid permanent damping of the vibration of the main mass is desired. This fact is supported by Fig. 7: the relative damping constant b_2 for this system is larger than the damping constant necessary to obtain the absolute influence position.

4. The influence of the spring constant k_2 upon the motion of m_1 is insignificant if the relative damping constant b_2 is equal to or larger than the constant b_2 necessary to obtain the absolute influence position (compare Fig. 6 with Fig 7).

The values given in Tables 1 and 2 check the statement 1, 2 and 4. Interesting and of practical importance is the close agreement of the values for the roots of the characteristic equation obtained with the Eq. (42), (44), (47) and (48) which are based on the stated approximation and the exact values for these roots (see Table 2). As shown in Eq. (54), the approximations will increasingly deviate from the true value with increasing b_2.

The application of the damper to reduce transient vibrations of a model in a shock tunnel, mentioned in section 1, was experimentally tested [4]. Figure 8 shows the model and the lever mechanism to simulate the lift. When the hooks (shown below the model) are disengaged, the weight is suddenly released and the model swings around its new position of equilibrium. The motions are recorded with an oscillograph from strain gages fixed to the sting. The vibration absorber, which fits in the detachable front of the model, consists of an elliptic lead cylinder fixed by two leaf springs to an oil-tight housing (see Fig. 9). The spring constant may be varied by changing the length of the leaves, while the relative damping constant depends upon the viscosity of the oil,
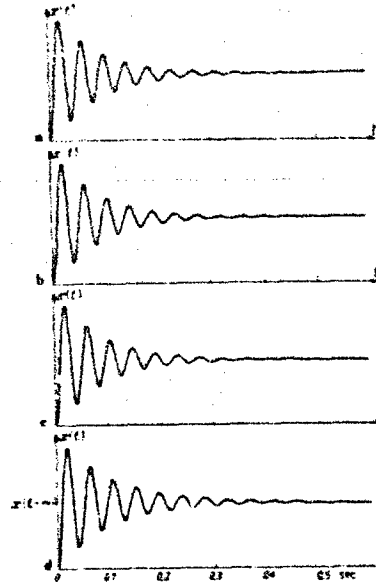

Fig. 7 — $b_2 = 0.16934$ kp s/cm
(Only the displacement of m_1 is shown)

(a) $k_2 = 20.68350$ kp/cm

(b) $k_2 = 27.35440$ kp/cm

(c) $k_2 = 29.78750$ kp/cm

(d) $k_2 = 37.69380$ kp/cm

Fig. 8 — Lever mechanism and model

272

Fig. 9 - Vibration absorber

in which the leaden cylinder swings.
Figure 10 shows the vibrations of the
model without, and with, the presence
of the described damper. The tuning
was carried out with the parameters
given in Fig. 5; the spring constant

of the damper was $k_2 = 25.2 \frac{kp}{cm}$. The

value is close to that given in Fig. 5b.
The distortion of the first three
maxima of the vibration shown in
Fig. 10a, and of the first maximum in
Fig. 10b, is due to exceeding the
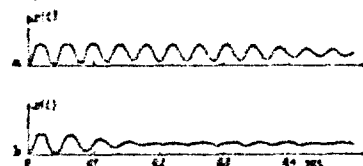limitation of the recording device.

Fig. 10 - Model vibrations without (a),
and with, (b), absorber

REFERENCES

1. D. W. Sallet, "Ein Schwingungstilger
    zur Abstimmung von Einschwing-
    vorgangen," Dissertation,
    T. H. Stuttgart, 1966

2. P. A. Crafton, Shock and Vibration
    in Linear Systems,
    New York, 1951

3. K. Magnus, Schwingungen, Stuttgart,
    1961

4. A. Weise, Jahresbericht 1964 and
    die Deutsche Forschungsgemein-
    schaft zum Forschungsvorhaben,
    "Untersuchungen mit instationaren
    Verdichtungsstossen," Institut fur
    Aerodynamik und Gasdynamik,
    T. H. Stuttgart, Az.: We 11/24